The Modeling of Hydrological Cycle and its Interaction with Vegetation in the Framework of Climate Change

Dissertation

submitted to and approved by the

Department of Architecture, Civil Engineering and Environmental Sciences
University of Braunschweig – Institute of Technology

and the

Faculty of Engineering
University of Florence

in candidacy for the degree of a
Doktor-Ingenieur (Dr.-Ing.) /
Dottore di Ricerca in "Riduzione del Rischio da Catastrofi Naturali su Strutture ed Infrastrutture" *)

by
Simone Fatichi
Born 26-04-1982
from Arezzo, Italy

Submitted on	18 March 2010
Oral examination on	07 May 2010
Professorial advisors	Prof. E. Caporali Prof. M. Schöniger Prof. V.Y. Ivanov

2010

*) Either the German or the Italian form of the title may be used.

Abstract

There is a growing interest to extend climate change predictions to smaller, catchment-size scales and identify their implications on hydrological and ecological processes. Small scale processes are expected to respond to climate change in a non-linear fashion, producing local effects and feedbacks. This thesis presents a blueprint methodology for studying climate change impacts on eco-hydrological dynamics at the plot and catchment scales. Downscaling climate change scenarios to the fine temporal and spatial scales offers the opportunity of making inferences about changes in flood or drought risks and in complex interactions, such as the coupled dynamics of hydrological cycle and vegetation. A weather generator, *AWE-GEN*, is developed to produce input meteorological variables to hydrological and eco-hydrological models. The generator is capable of reproducing numerous climate statistics over a range of temporal scales, from extremes, to low-frequency inter-annual variability. The weather generator is also used for the simulation of future climate scenarios, as inferred from climate models. Using a Bayesian technique, a stochastic downscaling procedure derives the distributions of factors of change for several climate statistics from a multi-model ensemble of outputs of General Circulation Models. The factors of change are subsequently applied to the statistics derived from observations to re-evaluate the parameters of the weather generator. The time series of meteorological variables are generated for the two scenarios corresponding to the current and expected future climates. A probability distribution of climate statistics is used for the latter. The time series serve as input to a newly developed eco-hydrological model *Tethys-Chloris*. The hydrological model reproduces essential components of the land-surface hydrological cycle, solving the mass and energy budget equations. The vegetation model parsimoniously parameterizes essential plant life-cycle processes, including photosynthesis, phenology, carbon allocation, and tissue turnover. The methodology is applied to simulate the present (1961-2000) and future (2081-2100) hydrological regimes for the area of Tucson (Arizona, U.S.A.). A general reduction of precipitation and a significant increase of air temperature are inferred with the downscaling procedure. The eco-hydrological model is successively used to detect changes in the surface water partition and vegetation dynamics for a desert shrub ecosystem, typical of the semi-arid climate of southern Arizona. The ensemble simulation results for the future climate account for uncertainties in the downscaling and are produced in term of probability density functions. A comparison of control and future scenarios is discussed in terms of changes in the hydrological balance components, energy fluxes, and indices of vegetation productivity. An appreciable effect of climate change can be observed in metrics of vegetation performance. The negative impact on vegetation due to amplification of water stress in a warmer and dryer climate is partially offset by the effect of the augment of carbon dioxide concentration. This implies a positive shift in plant water use efficiency. Additionally, an increase of runoff and a depletion of soil moisture with consequence in deep recharge are detected. Such an outcome affects water availability and risk management in semi-arid systems and might expose plants to more severe and frequent droughts.

Sommario

Estendere previsioni di cambiamento climatico alle piccole scale tipiche dei bacini idrografici e l'identificazione delle possibili conseguenze nei processi idrologici ed ecologici è un problema di notevole e crescente interesse. Le dinamiche alle piccole scale potrebbero, infatti, rispondere al cambiamento climatico in maniera non-lineare con retroazioni ed effetti locali. Questa tesi traccia una strada per lo studio degli impatti del cambiamento climatico sulla dinamica eco-idrologica alla scala di cella e di piccolo bacino idrografico. Il downscaling di scenari di cambiamento climatico ad alta risoluzione spaziale e temporale fornisce l'opportunità di effettuare analisi relative a rischi come quello idraulico o di siccità e permette di capire meglio l'evoluzione di interazioni complesse quali la dinamica congiunta di ciclo vegetativo ed idrologico. In questo contesto, un weather generator, *AWE-GEN*, è stato sviluppato al fine di generare variabili meteorologiche in ingresso a modelli idrologici ed eco-idrologici. Il generatore è capace di riprodurre numerose statistiche climatiche in un ampio intervallo di scale temporali, dai processi estremi ai quelli con basse frequenze come la variabilità inter-annuale. Il weather generator è anche utilizzato per simulazioni di scenari climatici futuri che vengono inferiti dai risultati dei modelli climatici. Distribuzioni di fattori di cambiamento delle statistiche climatiche sono derivate da un insieme di uscite di modelli di circolazione globale utilizzando una procedura di downscaling stocastico che usa a sua volta una tecnica Bayesiana. I fattori di cambiamento sono in seguito applicati alle statistiche derivate dalle osservazioni per rivalutare i parametri del weather generator. Serie temporali di variabili meteorologiche sono così generate corrispondenti a scenari di clima presente e di clima atteso nel futuro. Nel caso di clima futuro si può generare un'intera distribuzione di probabilità delle statistiche climatiche. Le serie temporali così ottenute servono come ingressi ad un modello eco-idrologico, *Tethys-Chloris*, sviluppato nella tesi. La componente idrologica modella il ciclo superficiale dell'acqua, risolvendo le equazioni di bilancio di massa ed energia. La componente di dinamica della vegetazione parametrizza in maniera essenziale i processi del ciclo di vita della pianta, quali la fotosintesi, il ciclo fenologico, l'allocazione del carbonio, e il ricambio dei tessuti vegetali. La metodologia proposta è applicata nell'area di Tucson (Arizona, U.S.A.), con lo scopo di simulare il regime idrologico presente (1961-2000) e futuro (2081-2100). La procedura di downscaling permette di prevedere una generale riduzione delle precipitazioni e un significativo incremento della temperatura. Il modello eco-idrologico è successivamente utilizzato per valutare possibili cambiamenti nelle varie componenti del ciclo idrologico e nella dinamica della vegetazione di un ecosistema composto di arbusti tipici del clima semi-arido dell'Arizona meridionale. I risultati delle simulazioni per il clima futuro tengono conto dell'incertezza derivata dalla procedura di downscaling e sono mostrati attraverso funzioni di densità di probabilità. Gli scenari presenti e futuri sono confrontati in termini di cambiamenti nelle componenti del bilancio idrologico, nei flussi energetici e negli indici di produttività della vegetazione. Il cambiamento climatico sembra produrre un effetto molto significativo nel comportamento della vegetazione. L'impatto negativo di un clima più caldo e secco e con un maggiore stress idrico è in parte attenuato dall'effetto positivo dell'aumento della concentrazione di anidride carbonica. Questo risultato ha ripercussioni positive incrementando l'efficienza delle piante nell'usare l'acqua. Una diminuzione della ricarica agli acquiferi profondi è inoltre evidenziata come conseguenza di un maggiore deflusso superficiale e di una minore umidità media del suolo. Questi risultati potrebbero avere implicazioni importanti nella disponibilità di risorsa idrica e nella gestione del rischio in ambienti semi-aridi e possono esporre le piante a periodi di siccità più severi e frequenti.

Zusammenfassung

Es besteht derzeit ein wachsendes wissenschaftliches Interesse daran, Vorhersagen zum Klimawandel auch auf eine kleinere Skala zu übertragen und deren Einfluss auf hydrologische und ökologische Prozesse zu beschreiben. Auf Ebene eines Einzugsgebiets sind diese Prozesse dem Klimawandel in der Regel auf nicht-lineare Weise unterworfen und führen zu lokalen Effekten und Rückkopplungen. Diese Arbeit präsentiert eine Vorgehensweise um Einflüsse des Klimawandels auf ökologisch-hydrologische Dynamiken auf der Einzugsgebietskala nachzuvollziehen. Auf dieser Ebene können aus den Klimawandelszenarien Rückschlüsse auf Flut- bzw. Dürrerisiken sowie weitere komplexe Wechselwirkungen wie gekoppelte Dynamiken des hydrologischen Wandels und der Vegetation gezogen werden. Dazu wurde ein Wettergenerator, *AWE-GEN*, entwickelt, der meteorologische Variablen für hydrologische und ökologische Modelle ausgibt. Der Generator ermöglicht das Nachvollziehen zahlreicher Klimastatistiken über eine Bandbreite von Zeitskalen, von extremen bis hin zu seltenen zwischenjährlichen Variabilitäten. Der Wettergenerator wird darüber hinaus für die Simulation zukünftiger Klimaszenarien genutzt, die aus den Klimamodellen hervorgehen. Mittels einer Bayes-Technik werden stochastische Downscaling-Prozeduren zur Verteilung der Wechselfaktoren für verschiedene Klimastatistiken aus einem Multimodell-Ensemble ermittelt, die auf Daten des Globalen Klimamodells beruhen. Die Wechselfaktoren werden danach auf die aus Beobachtungen erhaltenen Statistiken angewendet, um die Parameter des Wettergenerators zu überprüfen. Zeitreihen von meteorologischen Variablen wurden für zwei Szenarien generiert, die der heutigen sowie zukünftigen Klimadaten entsprechen. Eine Wahrscheinlichkeitsverteilung von Klimastatistiken wird auf letztere angewendet. Die Zeitreihen dienen als Ausgangsdaten für das neu entwickelte öko-hydrologische Modell *Tethys-Chloris*. Das hydrologische Modell bildet essentielle Komponenten des hydrologischen Oberflächen-Kreislaufs nach und löst die Massen- und Energiebilanz-Gleichungen. Das Vegetationsmodell parametrisiert die notwendigen Lebenszyklen der Pflanzen inklusive Photosynthese, Phänologie, Kohlenstofffixierung und Gewebedurchsatz. Dieser Methode wird angewendet, um die momentanen (1961-2000) sowie zukünftigen (2081-2100) hydrologischen Regime im Gebiet von Tucson (Arizona, U.S.A.) zu simulieren. Dabei lie sich eine generelle Reduzierung des Niederschlags und eine Zunahme der Lufttemperatur beim Downscaling-Prozess ableiten. Das öko-hydrologische Modell wurde im Anschluss genutzt, um änderungen in der Verteilung der Oberflächengewässer und der Vegetationsdynamik für ein Wüsten-Buschland ökosystems nachzuweisen, wie es für das semi-aride Klima von Südarizona typisch ist. Die Ergebnisse der Gesamtsimulationen für das zukünftige Klima tragen den Unsicherheiten des Downscaling-Prozesses Rechnung und sind als Wahrscheinlichkeitsdichte-Funktionen dargestellt. Ein Vergleich der zukünftigen Szenarien mit den Kontrolldaten wird in Hinsicht auf Änderungen der hydrologischen Balancekomponenten, Energieflüsse und Indizes der Vegetationsproduktivität diskutiert. Ein nennenswerter Effekt des Klimawandels kann in den Metriks der Vegetationsleistung beobachtet werden. Der negative Einfluss auf die Vegetation aufgrund von Wassermangel in einem wärmeren und trockeneren Klima wird teilweise ausgeglichen durch den Effekt einer verbesserten Kohlendioxidversorgung. Darin eingeschlossen ist eine positive Veränderung bei der Effizienz der Wassernutzung. Zusätzlich wird eine Erhöhung des (Oberflächen-)Abflusses und eine Verringerung der Bodenfeuchtigkeit und als Konsequenz der Grundwasserneubildung beobachtet. Diese Ergebnisse beeinflussen die Wasserverfügbarkeit und das Risikomanagement in semi-ariden System und Pflanzen schwereren und häufigeren Dürren aussetzen.

Contents

Abstract II
Sommario III
Zusammenfassung IV
List of Figures XXIX
List of Tables XXXII
List of Main Symbols LX
List of Acronyms LXI

1 INTRODUCTION **1**
1.1 Scope of research 1
1.2 Implications of the research in risk assessment and mitigation 4

2 "AWE-GEN" AN HOURLY WEATHER GENERATOR **7**
2.1 Introduction 7
2.2 Data and model validation 10
2.3 Precipitation 10
2.3.1 Neyman-Scott Rectangular Pulse model 13
2.3.2 Parameter fitting procedure 14
2.3.3 Low-frequency properties of the rainfall process 16
2.3.4 Results and validation 19
2.4 Cloud cover 24
2.4.1 Model 24
2.4.2 Results and validation 26
2.5 Air temperature 29
2.5.1 Model 29
2.5.2 Results and validation 31
2.6 Shortwave incoming radiation 36
2.6.1 Direct and diffuse radiation for clear sky conditions 37
2.6.2 Direct and diffuse radiation for overcast conditions 39
2.6.3 Results and validation 42
2.7 Vapor pressure 45
2.7.1 Model 45
2.7.2 Results and validation 46
2.8 Wind speed 50
2.8.1 Model 50

2.8.2 Results and validation 51
2.9 Atmospheric pressure 53
2.10 Covariance between variables 54
2.11 Application of AWE-GEN in climate change studies 57

3 DOWNSCALING AND MULTI-MODEL ENSEMBLE 59
3.1 Introduction 59
3.2 Stochastic downscaling 60
3.2.1 Methodology 63
3.2.2 Factors of change 64
3.2.3 Multi-model ensemble approach to predict future conditions 66
3.2.4 Application of the multi-model ensemble approach 71
3.2.5 Extension of precipitation statistics to finer time scales 80
3.3 General Circulation Models (GCMs) and scenarios 81

4 "TETHYS" A HYDROLOGICAL MODEL 87
4.1 Introduction 87
4.1.1 Model overview 89
4.1.2 Basic computational element 91
Topographic representation 91
Land cover composition 96
Vegetation composition and attributes 97
4.2 Radiative fluxes 99
4.2.1 Shortwave fluxes 100
Vegetated surface 100
Non-vegetated surface 104
4.2.2 Surface albedos 104
Canopy radiative transfer scheme 105
Ground albedo 108
Snow albedo 109
Water albedo 110
4.2.3 Long-wave fluxes 110
Vegetated surface 111
Non-vegetated surface 113
4.2.4 Net radiation 113
4.2.5 Single-temperature simplification 114
4.3 Soil-vegetation-atmosphere mass and heat transfer scheme 115
4.3.1 Sensible heat 116
Vegetated surface 117
Non-vegetated surface 118
4.3.2 Latent heat, evaporation and transpiration 118
Vegetated surface 119
Non-vegetated surface 120
4.3.3 Ground heat 120

4.3.4 Incoming heat with precipitation . . . 123
4.3.5 Numerical solution for surface temperature . . . 124
4.4 Energy and mass transfer resistances . . . 124
4.4.1 Aerodynamic resistance . . . 125
4.4.2 Undercanopy resistance . . . 132
4.4.3 Leaf boundary resistance . . . 134
4.4.4 Soil resistance . . . 137
4.4.5 Stomatal resistance and photosynthesis . . . 143
Canopy partition . . . 143
Scaling of nitrogen . . . 145
Biochemical model of photosynthesis and stomatal aperture . 145
4.5 Snow hydrology . . . 159
4.5.1 Precipitation partition . . . 159
4.5.2 Snowpack energy and mass balance . . . 160
4.5.3 Snow interception . . . 162
4.5.4 Snowpack water content . . . 165
4.5.5 Snow depth and density . . . 166
4.6 Canopy interception and erosion . . . 168
4.6.1 Throughfall . . . 168
4.6.2 Canopy storage capacity . . . 170
4.6.3 Model of interception . . . 170
4.6.4 Rainfall erosion . . . 171
4.7 Subsurface water dynamics . . . 173
4.7.1 Infiltration and infiltration excess runoff . . . 173
4.7.2 Soil sealing and crust . . . 176
4.7.3 Governing equation . . . 179
4.7.4 Soil properties and pedotransfer functions . . . 185
4.7.5 Saturation excess runoff . . . 189
4.7.6 Subsurface flow . . . 189
4.8 Surface water dynamics . . . 191

5 "CHLORIS" A DYNAMIC VEGETATION MODEL 193
5.1 Introduction . . . 193
5.1.1 Model overview . . . 195
5.1.2 Vegetation structure . . . 195
5.2 Carbon pool dynamics . . . 199
5.2.1 Net Primary Production and plant respiration . . . 199
5.2.2 Carbon allocation and translocation . . . 202
5.2.3 Tissue turnover and leaf environmental stresses . . . 208
5.2.4 Carbon balance . . . 211
5.3 Vegetation phenology . . . 213
5.3.1 Dormant state to maximum growth . . . 214
5.3.2 Maximum growth to normal growth . . . 216

5.3.3 Normal growth to senescence state 216
5.3.4 Senescence to dormant state 216
5.3.5 Leaf age 217

6 "TETHYS" AND "CHLORIS" (T&C) TESTING 219
6.1 Introduction 219
6.2 Lucky Hills, Arizona, USA 220
6.3 San Rossore, Italy 227
6.4 Reynolds Creek, Mountain East, Idaho, USA 231
6.5 Bayreuth-Waldstein, Germany 234
6.6 Walker Branch, Tennessee, USA 238
6.7 Sensitivity to land cover composition 241

7 USING CLIMATE CHANGE PREDICTIONS IN ECOHYDROLOGY, A CASE STUDY 247
7.1 Introduction 247
7.2 Case study characterization 248
7.3 Ecohydrological modeling validation 251
7.4 Generation of present and future climate with AWE-GEN 255
7.5 Point scale results 265
7.6 Distributed results 278

8 CONCLUSIONS AND OUTLOOKS 289

A APPENDIX CHAPTER TWO 297
A.1 Rainfall disaggregation 297
A.1.1 Random cascade dissagregation model 298
A.1.2 Microcanonical model 300
A.1.3 Results 302
A.2 Statistical properties of the *NSRP* model 305
A.3 Cloud cover parameter estimation 306
A.4 Definition of sun variables 310
A.5 Solution of the ODE for deterministic air temperature 311
A.6 Air temperature parameter estimation 312
A.7 Clear sky radiation parameterizations 314
A.7.1 Direct beam irradiance 314
A.7.2 Diffuse irradiance 317
A.8 Overcast sky radiation parameterizations 318
A.8.1 Direct beam irradiance 319
A.8.2 Diffuse irradiance 320
A.9 Terrain effects 321

B APPENDIX CHAPTER THREE 327
B.1 Posterior PDF calculation using MCMC simulations 327

C APPENDIX CHAPTER FOUR **329**
C.1 Parameters of canopy radiative transfer model 329
C.2 Aerodynamic resistance to momentum 330
C.3 Model parameters 331

D APPENDIX CHAPTER FIVE **333**
D.1 Vegetation structural properties 333
D.2 Model parameters 334

List of Figures

1.1 Stages of operational risk management, adapted from *Plate* (2002). Hazard determination in a changing climate is the aspect investigated in this research (red square). 4

2.1 Schematic representation of Neyman-Scott and Bartlett-Lewis models with rectangular pulses. 12

2.2 The annual precipitation simulated with the *NSRP* model (red line) after the external selection based on the AR(1) precipitation series (magenta dots) has been carried out. The vertical bars denote the $\check{p} = 2.5\%$ of the long-term average annual precipitation. 18

2.3 A comparison between observed (red) and simulated (green) monthly statistics of precipitation (mean, variance, lag-1 autocorrelation, skewness, frequency of non-precipitation, transition probability wet-wet), for the aggregation period of 1 hour. 19

2.4 A comparison between observed (red) and simulated (green) monthly statistics of precipitation (mean, variance, lag-1 autocorrelation, skewness, frequency of non-precipitation, transition probability wet-wet), for the aggregation period of 24 hours. 20

2.5 A comparison between observed (red) and simulated (green) monthly statistics of precipitation (mean, variance, lag-1 autocorrelation, skewness, frequency of non-precipitation, transition probability wet-wet), for the aggregation period of 48 hours. 20

2.6 A comparison between observed (red) and simulated (green) monthly precipitation. The vertical bars denote the standard deviations of the monthly values. 21

2.7 A comparison between the observed (red crosses) and simulated values of extreme precipitation (green crosses) at (a) 1-hour and (b) 24-hour aggregation periods; (c) extremes of dry and (d) wet spell durations. Dry/wet spell duration is the number of consecutive days with precipitation depth lower/larger than 1 $[mm]$. 23

2.8 A comparison between observed (red) and simulated (green) fractions of time with precipitation larger than a given threshold [1−10−20mm] at different aggregation periods (a). The same comparison for dry spell length distribution (b), i.e. consecutive days with precipitation depth lower than 1 [mm] and for wet spell length distribution (c), i.e. consecutive days with precipitation depth larger than 1 [mm]. E_{obs} and σ_{obs} are the observed mean and standard deviation and E_{sim} and σ_{sim} are the simulated ones. 23

2.9 A comparison between the observed (cyan) and simulated (magenta) fair weather cloud cover distribution for every month. E_{obs} and σ_{obs} are the observed mean and standard deviation and E_{sim} and σ_{sim} are the simulated ones. 27

2.10 A comparison between the observed (cyan) and simulated (magenta) total cloud cover distribution, for every month. E_{obs} and σ_{obs} are the observed mean and standard deviation and E_{sim} and σ_{sim} are the simulated ones. 28

2.11 A comparison between the observed (red) and simulated (green) average air temperature for every month, aggregation periods of 1 [h] (a) and 24 [h] (b). The vertical bars denote the standard deviations. 31

2.12 A comparison between the observed (red) and simulated (green) daily maximum (a) and minimum (b) air temperature for every month. The vertical bars denote the standard deviations. 32

2.13 A comparison between the observed (red) and simulated (green) air temperature distribution (a) and average daily cycle (b). The triangles are the standard deviations for every day hour, E_{obs} and σ_{obs} are the observed mean and standard deviation and E_{sim} and σ_{sim} are the simulated ones. 32

2.14 A comparison between the observed (red) and simulated (green) extremes of air temperature. a) Maxima of hourly temperature. b) Minima of hourly temperature. c) Maxima of daily temperature. d) Minima of daily temperature. 34

2.15 A comparison between the observed (red) and simulated (green) occurrence of heat (a) and cold (b) waves, i.e. consecutive days with temperature higher than the 90 percentile or lower than 10 percentile. 34

2.16 A comparison between the observed (red) and simulated (blue) daily cycle of global (a), direct (b) and diffuse (c) shortwave radiation for clear sky condition. 39

2.17 A comparison between the observed (red) and simulated (green) mean monthly shortwave radiation. a) Global radiation. b) Direct beam radiation. c) Diffuse radiation. The vertical bars denote the standard deviations of the monthly values. 43

2.18 A comparison between the observed (red) and simulated (blue) daily cycle of global (a), direct (b) and diffuse (c) shortwave radiation for all sky conditions. 44
2.19 A comparison between the observed (red) and simulated (green) annual cycle of global shortwave radiation for different local time hours. The global shortwave fluxes are expressed in $[W\ m^{-2}]$. 44
2.20 A comparison between the observed (red) and simulated (green) mean monthly vapor pressure for 1 $[h]$ (a) and 24 $[h]$ (b) aggregation time periods. The vertical bars denote the standard deviations of the monthly values. 47
2.21 A comparison between the observed (red) and simulated (green) relative humidity daily cycle (a) and vapor pressure probability density function (b). The triangles in (a) represent the daily cycle of relative humidity standard deviation. E_{obs} and σ_{obs} are the observed mean and standard deviation and E_{sim} and σ_{sim} are the simulated ones. . 48
2.22 A comparison between the observed (red) and simulated (green) dew point temperature (a) and relative humidity (b) probability density functions. E_{obs} and σ_{obs} are the observed mean and standard deviation and E_{sim} and σ_{sim} are the simulated ones. 48
2.23 A comparison between the observed (red) and simulated (green) mean monthly relative humidity for aggregation periods of 1 hour (a) and 24 hours (b). The vertical bars denote the standard deviations of the monthly value. 49
2.24 A comparison between the observed (red) and simulated (green) monthly dew point temperature for aggregation periods of 24 hours. a) Mean dew point temperature. b) Maximum dew point temperature. c) Minimum dew point temperature. The vertical bars denote the standard deviations of the monthly value. 49
2.25 A comparison between the observed (red) and simulated (green) wind speed probability density function (a) and daily cycle of wind speed (b). E_{obs} and σ_{obs} are the observed mean and standard deviation and E_{sim} and σ_{sim} are the simulated ones. 52
2.26 A comparison between the observed (red) and simulated (green) extremes of wind speed at aggregation periods of 1 hour (a) and 24 hours (b). 52
2.27 A comparison between the observed (red) and simulated (green) atmospheric pressure probability density function. E_{obs} and σ_{obs} are the observed mean and standard deviation and E_{sim} and σ_{sim} are the simulated ones. 53
2.28 Simulated hourly values of hydro-meteorological variables with AWE-GEN: a.) precipitation; b.) cloud cover, c.) air temperature, d.) global shortwave radiation, e.) relative humidity, f.) vapor pressure, g.) wind speed, and h.) atmospheric pressure. 54

2.29 A comparison between the observed (cyan) and simulated (black) monthly number of wet days (a) and cloud cover (b). 55

2.30 A comparison between the observed (red) and simulated (green) cross-correlation between: daily temperature amplitude and cloudiness (a), global solar radiation and cloudiness (b), global solar radiation and wind speed (c), and global solar radiation and relative humidity (d). 56

3.1 Representation of the partition between land cover (100%) and sea cover (0%) in CCSM-3.0, for the Italian region. 61

3.2 The subplots illustrate sensitivities of the computed probability density functions of the factors of change with respect to the metrics of natural variability (the parameter λ_0 in text). These are expressed using either the standard deviation of monthly temperatures (subplot (a)) or the coefficient of variation for precipitation statistics (subplots (b) and (c)). The presented analysis is for the location of Tucson, the month of April a.) Sensitivity of the factor of change for mean monthly temperature; the circles denote the mean of the posterior PDFs and the vertical bars give the 10-90 percentile intervals of the PDF. b.) The factor of change for mean precipitation at the aggregation period of 24 hours; the circles denote the mean of the PDFs and the vertical bars give the 10-90 percentile intervals of the PDF. c.) The factor of change for precipitation variance at the aggregation period of 24 hours; the circles denote the mean of the PDFs, and the vertical bars give the 10-90 percentile intervals of the PDF. 73

3.3 Same as Figure 3.2 for the month of July. 74

3.4 The posterior probability density functions (PDF) obtained from the multi-model ensemble for the location of Tucson airport, the month of September. a.) The PDF of mean September temperature for the CTS (yellow bars) and the FUT (red bars) scenarios. Also shown are the observation (OBS) and results from the individual models for the CTS (green dots) and FUT (magenta dots). b.) The PDF of the additive factor of change for air temperature, $\Delta T = \nu - \mu$, (blue bars) and predictions by the individual models (black dots). c.) The PDF of mean September precipitation for the CTS (yellow bars) and the FUT (red bars) scenarios. Also shown are the observation (OBS) and results from the individual models for the CTS (magenta dots) and FUT (green dots). d.) The PDF of the product factor of change for precipitation, $FC = \nu/\mu$, (blue bars) and predictions by the individual models (black dots). 75

3.5 Same as Figure 3.4 for the month of February. 76

3.6 The factors of change estimated for different precipitation statistics at the aggregation interval of 24 hours. The mean (black circles) and the 10-90 percentile intervals (red lines) are computed from the posterior PDFs of these statistics. a.) Mean precipitation. b.) Variance of precipitation. c.) Skewness of precipitation. d.) Logit transformed frequency of no-precipitation. 77

3.7 Same as Figure 3.6 for aggregation periods of 96 hours. 77

3.8 The effect of the factors of change on the annual cycles of monthly temperature and precipitation for the location of Tucson airport. a.) The observed mean monthly temperature for the period 1961-2000 (black line); the predicted mean monthly air temperature (green dashed line) and the 10-90 percentile intervals (vertical bars, cannot be seen for all months because of the small magnitude) computed from the posterior distributions of the factors of change applied to the observed cycle. b.) The mean monthly temperature change (black dots) and the 10-90 percentile bounds (blue vertical bars). c.) The observed mean monthly precipitation for the period 1961-2000 (black line); the predicted mean monthly precipitation (green dashed line) and the 10-90 percentile intervals (vertical bars) computed from the posterior distributions of the factor of changes applied to the observed cycle. 79

3.9 The time series of mean monthly temperature calculated from eight GCMs: CCSM3, CGCM3.1(T63), CSIRO-Mk3.5, ECHAM5-MPI-OM, GFDL-CM2.1, INGV-SXG, IPSL-CM4, and MIROC3.2(medres) for the location of Tucson airport, including observations (OBS). a) Control scenario (CTS) 1961-2000. b) Future scenario (FUT), 2081-2100. c) Additive factors of change for mean monthly temperature. . 85

3.10 The time series of total monthly precipitation calculated from eight GCMs: CCSM3, CGCM3.1(T63), CSIRO-Mk3.5, ECHAM5-MPI-OM, GFDL-CM2.1, INGV-SXG, IPSL-CM4, and MIROC3.2(medres) for the location of Tucson airport, including observations (OBS). a) Control scenario (CTS) 1961-2000. b) Future scenario (FUT), 2081-2100. c) Multiplicative factors of change for monthly precipitation. . 86

4.1 Components of "Tethys" showing the coupling between hydrological, energy, and biochemical processes. The model is forced with atmospheric inputs and it returns to the atmosphere energy and mass fluxes. All the components and symbols are detailed in the text. . . 90

4.2 A visual scheme of the components included in the hydrological and energy balance schemes. 90

4.3 Representation of topographic attributes using a regular square grid. a.) Digital Elevation Model. b.) Slope fraction [−] calculated with the maximum steepness method. c.) Aspect in angular degree [°] from North. All the attributes refer to the Cerfone creek watershed in Tuscany (Italy). 93

4.4 Representation of topographic and hydrological features for a small zero-order catchment, i.e., Digital Elevation Model (left panel) and arrows outlining the flow directions (right panel). The domain is the one of the Biosphere 2 Hillslope Experiment (*Hopp et al.*, 2009). . . 93

4.5 Maps of flow accumulation, i.e. upslope area according to the calculated flow directions. a.) D-infinity *Tarboton* (1997) method. b.) Single flow method of *Orlandini et al.* (2003) using lateral transversal deviation with $\lambda = 0$. The domain is the Cerfone creek watershed in Tuscany (Italy). 95

4.6 An illustration of the land cover composition of a general *basic computational element*. (a) The area is subdivided into vegetated, bare soil, water, urban, and rock covered, surfaces. (b) The presence of snow $C_{sno} = 1$ alters the composition. 96

4.7 An illustration of vegetation representation at the element scale. The area is subdivided into patches of bare soil, and patches of vegetation (*Crown Areas*) that may included up two *PFTs*, one denoting the upper canopy (High-vegetation H_v) and one the lower canopy (Low-vegetation L_v). Note that species competition is not enabled in this version of the model. 98

4.8 An illustration of the vertical composition of vegetation at the element scale. 98

4.9 A schematic diagram of the beam and diffuse solar radiation absorbed, transmitted, and reflected by a general layer of vegetation with and underneath surface s. The scheme is valid for both the wavebands $\Lambda 1$ and $\Lambda 2$. 101

4.10 A schematic diagram of the beam and diffuse solar radiation absorbed, transmitted, and reflected by high-vegetation, low-vegetation, and under-canopy ground. In this case the underneath surface is bare ground $s = g$, with albedos $\alpha^{\mu}_{soil,\Lambda}$-$\alpha_{soil,\Lambda}$. The scheme is valid for both the wavebands $\Lambda 1$ and $\Lambda 2$. 102

4.11 Interaction between snow depth and vegetation height used to determine the values of the albedos. The fourth scheme, with *high vegetation* completely covered by snow is not taken into account into "Tethys". The schemes are valid for both the wavebands $\Lambda 1$ and $\Lambda 2$ and for direct beam (μ) and diffuse radiation. 103

4.12 A schematic cartoon of long-wave radiation fluxes absorbed, transmitted, reflected, and emitted by vegetation and under-canopy surface. In the illustrated scheme the surface underneath the vegetation is bare ground ($s = g$). L_{atm} is the downward atmospheric longwave radiation flux, $L_v \downarrow_{(H_v)-(L_v)}$ are the downward longwave radiation fluxes from the vegetation canopies, $L \uparrow_g$ is the upward longwave radiation flux from the ground, and $L_v \uparrow_{(H_v)-(L_v)}$ are the upward longwave radiation fluxes from the canopies. L_{abs,H_v}, L_{abs,L_v}, $L_{abs,g}$ are the absorbed longwave radiation fluxes for high and low vegetation layers, and understory ground respectively. 112

4.13 A conceptual diagram of sensible heat flux including resistances for a vegetated patch (*Crown Area*) without snow cover, for the definition of symbols refer to the text. 116

4.14 A conceptual diagram of sensible heat including resistances for a vegetated patch (*Crown Area*) in the presence of snow, for the definition of symbols refer to the text. 117

4.15 A conceptual diagram for latent heat including resistances in a vegetated patch (*Crown Area*) without snow cover, for the definition of symbols refer to the text. 118

4.16 Illustration of the assumption made for the wind vertical profile between the land surface and the atmospheric surface layer, where $u(z)$ is the wind velocity, z_{atm} is the reference height, d is zero-plane the displacement, z_{om} is the roughness for momentum, and H_c is the canopy height. 125

4.17 Signs of some quantity in case of stable or unstable conditions of the atmospheric surface layer. The potential temperatures, θ, are replaced with conventional temperatures T. This is possible since the reference height, z_{atm}, is relative close to the surface and changes in atmospheric pressure are negligible. 130

4.18 Aerodynamic resistance, r_{ah} [$s\ m^{-1}$], sensitivity to wind speed at the reference height, u_a [$m\ s^{-1}$], and instability of the atmosphere, $T_s - T_a$ [$^{\circ}C$], calculated with the complete solution of the Monin-Obukhov similarity theory (c) and (d), and with the approximation proposed by *Mascart et al.* (1995); *Noilhan and Mafhouf* (1996) (a) and (b), for a vegetated area with $H_c = 12$ [m] (a) and (c), and for a bare soil area (b) and (d). A fixed $T_a = 15$ [$^{\circ}C$] is used. 132

4.19 Undercanopy resistance, $r_a{}'$, function of the LAI in the parametrization proposed by *Zeng et al.* (2005) (red-line) and by *Choudhury and Monteith* (1988) with different values of the attenuation coefficient, α, (dashed black-lines). The $r_a{}'$ are calculated with a fixed $H_c = 12$ [m] and $u_a = 5$ [$m\ s^{-1}$]. 133

4.20 Illustration of leaf boundary layer concept. A leaf boundary layer with thickness, δ, surrounds the leaf creating a resistance, r_b, in the mass-energy transfer from the leaf surface-subsurface to the atmosphere. A diffusive sub-layer between the proper leaf boundary layer and the leaf surface seems plausible (*Vesala*, 1998), although it is not considered in "Tethys". 135
4.21 Illustration of the implications of equation (4.119) in the determination of α' [−]. a.) Logarithmic and exponential profile of wind speed forced to produce the same value of wind speed u at the canopy height H_c. b.) Values assumed by α' for different canopy heights. 137
4.22 Sensitivity analysis of leaf boundary resistance, r_b [$s\ m^{-1}$], to wind speed at the reference height, u_a [$m\ s^{-1}$], and leaf dimension, d_{leaf} [cm]. The vegetation height is fixed to $H_c = 12$ [m] and $LAI = 1$. . . 138
4.23 Illustration of the scheme assumed to describe soil resistance to evaporation. Both α and β methods are outlined in the figure. The scheme is drawn from *Mahfouf and Noilhan* (1991). 139
4.24 Values assumed by soil resistance r_{soil} and β parameter as a function of soil moisture, θ, for a sand loam soil. The graphs are obtained from equations 4.124 and 4.125. 142
4.25 Values of relative maximum Rubisco capacity, V_m/V_{max}, function of leaf temperature, T_v [$°C$], for different values of activation energy, H_a [$kJ\ mol^{-1}$] with $\Delta S = 0.649$ (a), and entropy factor ΔS [$kJ\ mol^{-1}\ K^{-1}$] with $H_a = 72$ (b). 150
4.26 Diagram of the resistance scheme for CO_2 transfer from the leaf interior to the atmospheric surface layer for high and low vegetation layers. The variables c_a, c_{ac}, c_s, and c_i are the atmospheric, canopy space, leaf surface, and leaf interior CO_2 concentrations, respectively. The other variables are defined in the text. 153
4.27 Values of maximum photosynthetic capacity, A_{max}, and minimum stomatal resistance, $r_{s,min}$, function of V_{max}. A sensitivity analysis to atmospheric CO_2 concentration, c_a [ppm], and to the empirical coefficient, a [−], is shown. The graphics are calculated with $LAI = 1$ [−], $\epsilon = 0.081$ [$\mu molCO_2\ \mu mol^{-1}\, photons$], $H_a = 72$ [$kJ\ mol^{-1}$], $\Delta S = 0.649$ [$kJ\ mol^{-1}\ K^{-1}$] for a C3 plant; $a = 9$ [−] in the subplots (a) and (b); $c_a = 380$ [ppm] in the subplots (c) and (d). 155
4.28 Sensitivity analysis of net assimilation rate, A_{nC}, stomatal resistance, r_s, and leaf interior CO_2 concentration, c_i, to atmospheric CO_2 concentration, c_a [ppm]. The relationships are calculated for a C3 plant in well watered conditions with $LAI = 1$ [−], $T_v = 25$ [$°C$], $\Delta e = 0$ [Pa], $\epsilon = 0.081$ [$\mu molCO_2\ \mu mol^{-1}\, photons$], $H_a = 72$ [$kJ\ mol^{-1}$], $\Delta S = 0.649$ [$kJ\ mol^{-1}\ K^{-1}$], $PAR_{abs} = 300$, $a = 9$ [−], $g_0 = 0.02$ [$mol\, CO_2\ m^{-2}\, s^{-1}$], $\Delta_0 = 1500$ [Pa], $V_{max} = 60$ [$\mu mol\ CO_2\ m^{-2}\ s^{-1}$], $r_a = 75$ [$s\ m^{-1}$], and $r_b = 50$ [$s\ m^{-1}$]. 156

4.29 Sensitivity analysis of net assimilation rate, A_{nC}, stomatal resistance, r_s, internal leaf CO_2 concentration, c_i, and dark respiration, R_{dC}, to environmental factors such as Δe $[Pa]$ and T_v $[^\circ C]$. The relationships are calculated for a C3 plant in well watered condition with $LAI = 1$ $[-]$, $\epsilon = 0.081$ $[\mu molCO_2\ \mu mol^{-1}\, photons]$, $H_a = 72$ $[kJ\ mol^{-1}]$, $\Delta S = 0.649$ $[kJ\ mol^{-1}\ K^{-1}]$, $c_a = 380$ $[ppm]$, $a = 9$ $[-]$, $g_0 = 0.02$ $[mol\, CO_2\ m^{-2}\, s^{-1}]$, $\Delta_0 = 1500$ $[Pa]$, $V_{max} = 60$ $[\mu mol\ \mathrm{CO_2}\ m^{-2}\ s^{-1}]$, $PAR_{abs} = 300$ $[W\ m^{-2}]$, $r_a = 75$ $[s\ m^{-1}]$ and $r_b = 50$ $[s\ m^{-1}]$. 157

4.30 Sensitivity analysis of net assimilation rate, A_{nC}, and stomatal resistance, r_s, to environmental dependence such as PAR_{abs} $[W\ m^{-2}]$ and θ_R $[-]$. The relationship are calculated for a C3 plant with with $LAI = 1$ $[-]$, $T_v = 25$ $[^\circ C]$, $\Delta e = 0$ $[Pa]$, $\epsilon = 0.081$ $[\mu molCO_2\ \mu mol^{-1}\, photons]$, $H_a = 72$ $[kJ\ mol^{-1}]$, $\Delta S = 0.649$ $[kJ\ mol^{-1}\ K^{-1}]$, $c_a = 380$ $[ppm]$, $a = 9$ $[-]$, $g_0 = 0.02$ $[mol\, CO_2\ m^{-2}\, s^{-1}]$, $\Delta_0 = 1500$ $[Pa]$, $V_{max} = 60$ $[\mu mol\ \mathrm{CO_2}\ m^{-2}\ s^{-1}]$, $r_a = 75$ $[s\ m^{-1}]$, $r_b = 50$ $[s\ m^{-1}]$, $\Psi_{ss} = 400$ $[kPa]$, and $\Psi_{wp} = 4000$ $[kPa]$ in a generic sand loam soil. 158

4.31 An example of snow intercepted by vegetation. Picture taken in February in a mixed deciduous-evergreen wood in Tuscany. 163

4.32 Temporal evolution of intercepted snow $In_{S_{WE}}$ after a snowfall of 10 $[mm]$ in a evergreen forest with $LAI = 4.0$ and $T_a = -5^\circ C$. 165

4.33 Scheme of the interception process in absence of snow where two vegetation layers, *high* and *low-vegetation* are considered. The variable P_{r,H_v} and P_{r,L_v} represent the precipitation reaching the high and low layers of vegetation. The other terms are defined in the text. 169

4.34 Infiltration capacity, I_f^C, varying with soil water content of the shallower part of soil, θ_F, values refer to a generic sand loam soil. The dashed line represent the vertical saturated hydraulic conductivity $K_{s\,v}$.175

4.35 Values of saturated hydraulic conductivity, $K_{s\,v,cr}$ $[mm\ h^{-1}]$, of a sealed soil for a sandy-loam subject to a 30 $[mm\ h^{-1}]$ rainfall lasting one hour. The effects of cumulative rainfall at different depths are shown. 178

4.36 A graphical scheme illustrating the discrete soil column and the principal variables used in the computation of subsurface water dynamics. The subscript i identify the soil layer. The term $\Psi_{e,i}$ $[mm]$ is the water potential at the bubbling pressure at the center of the layer, $K_{s,i}$ $[mm\ h^{-1}]$ is the saturated conductivity at the center of layer (Section 4.7.4), L_{kb} $[mm\ h^{-1}]$ is the bottom leakage subsurface flow (Section 4.7.6). The soil water content is θ_i $[-]$, q_i $[mm\ h^{-1}]$ is the vertical outflow from layer i, $Z_{s,i}$ $[mm]$ is the depth from the surface to the layer upper boundary, $d_{z,i}$ $[mm]$ is the layer thickness, and $D_{z,i}$ $[mm]$ is a positive distance between the layer center and the precedent layer center. Note the first value of Z_s is always zero, corresponding to the surface. Rather than define the mesh resolution a priori, in each simulation the soil column can be properly subdivided. Typically between 8 and 20 layers are used with a coarser mesh resolution at greater depths for computational efficiency. 182

4.37 Soil water retention and unsaturated conductivity curves, i.e., unsaturated hydraulic conductivity K_v $[mm\ h^{-1}]$ (a) and soil water potential $-\Psi$ $[kPa]$ (b) function of soil water content, θ. The curves are calculated for a generic sand loam soil. 186

4.38 Illustration of the saturated hydraulic conductivity, $K_{s\,v}$, decay with soil depth, z_d, in a generic sand loam soil, values obtained with the parameter $m_f = 320$ $[mm]$. 188

5.1 Components of "Chloris" showing the different biochemical and physiological processes. The model is forced with atmospheric and soil environmental conditions calculated in "Tethys". It returns the Leaf Area Index and vegetation properties. All the components and symbols are detailed in the text. 196

5.2 Conceptual diagram of carbon fluxes simulated by the model and of the involved processes. The four carbon pools are leaves, fine roots, living sapwood, and carbohydrate reserve. Boxes outlined with dashed lines illustrate processes that affect the carbon balance. The red arrows indicates the general patterns of productivity. The blue solid-line arrows show allocation fluxes, while the magenta ones show translocation. The black dashed-line arrows indicates turnover from carbon pools. The yellow arrows indicate allometric constraints and controls. 196

5.3 Behavior of relative senescence induced turnover, $d_{leaf,a} \cdot A_{cr}$ $[-]$, function of the relative age, Ag_L/A_{cr} $[-]$, for evergreen ($\Xi = 0$), deciduous ($\Xi = 1$), and grass species ($\Xi = 2$). 210

5.4 A conceptual scheme of phenology phases. The plant passes from the dormant state ($\Phi = 1$) to maximum growth ($\Phi = 2$) at the begin of the favorable season (t_{MG}). For deciduous species and grasses ($\Xi = 1,\ 2$) it corresponds to leaf onset. After a prescribed period d_{MG} $[day]$ the plant passes in a normal growth state ($\Phi = 3$), until the arrival of the unfavorable season, where a senescence state begins ($\Phi = 4$). In the senescence state (t_{SE}) leaf shed becomes dominant and carbon is allocated exclusively to carbohydrate reserves for $\Xi = 1,\ 2$. When all the leaves are shed (t_{DO}) the plants return into a dormant state ($\Phi = 1$) until the arrival of a new favorable season. In evergreen species ($\Xi = 0$) the senescence and dormant states are considered as a single state similar to normal growth in which carbon is still allocated to all the compartments but $f_f = 0$. In crops ($\Xi = 3$), the green biomass is lost after a prescribed harvesting date, thus senescence and dormant states do not exist. 215

5.5 An example of leaves with different ages, picture taken in late October in a chestnut (Castanea sativa) deciduous wood in Tuscany. 218

6.1 Shrub plant community at the Lucky hills flux tower. Source: *www.tucson.ars.ag.govunitgiswg.html*. 221

6.2 A comparison between observed and simulated average daily cycle of energy fluxes, where R_n is the net radiation, H the sensible heat, λE the latent heat, and G the ground heat. 222

6.3 A comparison between observed and simulated monthly average daily cycle of net radiation, R_n. 223

6.4 A comparison between observed and simulated monthly average daily cycle of latent heat, λE. 223

6.5 A comparison between observed and simulated monthly average daily cycle of sensible heat, H. 224

6.6 A comparison between observed and simulated soil water contents at different depths: 5 $[cm]$, top panel, 15 $[cm]$ central panel, 30 $[cm]$, bottom panel. 224

6.7 Monthly partition of the principal hydrological budget components expressed in $[mm\ yr^{-1}]$ averaged over the simulation period. 225

6.8 A comparison between simulated and remote sensing observations of GPP and NPP. MOD-SPT is the MODIS estimation of the vegetation productivity in the pixel containing the flux tower, MOD-AVE is the average in a surrounding area of 7x7 $[km^2]$. 226

6.9 A comparison between simulated and remote sensing observation of Leaf Area Index. MOD-SPT is the MODIS estimation of LAI in the pixel containing the flux tower, MOD-AVE is the average in a surrounding area of 7x7 $[km^2]$. 226

6.10 Aerial view of the San Rossore flux tower, source: Google® maps (left); and illustrative details of maritime pine (Pinus pinaster) (right). 227
6.11 A comparison between observed and simulated average daily cycle of energy fluxes, where R_n is the net radiation, and λE the latent heat. 228
6.12 A comparison between observed and simulated monthly average daily cycle of latent heat, λE. 228
6.13 Monthly partition of the principal hydrological budget components expressed in $[mm\ yr^{-1}]$ averaged over the simulation period. 229
6.14 A comparison between simulated and remote sensing observations of Leaf Area Index (top panel), GPP and NPP (bottom panel) and the time evolution of simulated, β_R, moisture stress factor (central panel). 230
6.15 Climate, snow, and precipitation measurement site near fir forest in the southern, higher-elevation region of the Reynolds Creek Experimental Watershed, from *Slaughter et al.* (2001). 232
6.16 A comparison between simulated and observed snow water equivalent at the Reynolds Creek Mountain East snow pillow location. 232
6.17 A comparison between simulated and observed snow depth at the Reynolds Creek Mountain East snow pillow location. 233
6.18 A comparison between simulated and observed soil moisture at the Reynolds Creek, Mountain East neutron probe location. a) Soil moisture at 15 $[cm]$. b) Soil moisture at 30 $[cm]$. c) Soil moisture at 60 $[cm]$. 233
6.19 Images of the forest stand and flux tower at the Bayreuth-Waldstein FLUXNET site. Source: *www.fluxnet.ornl.gov fluxnet Cd-1 web _start_here.html.* 234
6.20 A comparison between observed and simulated monthly average daily cycle of net radiation, R_n. 235
6.21 A comparison between observed and simulated monthly average daily cycle of latent heat, λE. 236
6.22 Monthly partition of the principal hydrological budget components expressed in $[mm\ yr^{-1}]$ averaged over the simulation period. 236
6.23 Simulated Leaf Area Index (top panel) and a comparison between observed and simulated snow depth below the canopy (bottom panel). 237
6.24 Images of the Walker Branch deciduous forest during wintertime (left) and late summer (right). 238
6.25 A comparison between observed and simulated monthly average daily cycle of latent heat, λE. 239
6.26 A comparison between observed and simulated Leaf Area Index. . . 240
6.27 Simulated Leaf Area Index for the different vegetation types. a.) Temperate deciduous forest. b.) Temperate evergreen forest. c.) Grassland. d.) Crops. e.) Grass below deciduous trees. f.) Deciduous and evergreen mixed forest. 246

7.1 Deserts in the USA Southwest and Mexico Northwest. The circle indicates the area interested by the presented analysis, the cross indicates the location where the eco-hydrological model is validated. Source: *http://www. desertmuseum.org/desert/sonora.php*. 249

7.2 Plant of Whitethorn Acacia (Acacia Constricta). Source: *http:// ag.arizona.edu/pima/gardening/ aridplants/Acacia_constricta.html*. . 250

7.3 Plant of Creosote bush (Larrea Tridentata). Source: *http://www. mojavenp.org/larrea_tridentata_ mojave_national_preserve.htm*. . . . 250

7.4 Representation of topographic attributes of the Lucky Hills experimental watershed. a.) Digital Elevation Model. b.) Slope fraction [−] calculated with the maximum steepness method. 251

7.5 The results of spatially-distributed ecohydrological simulations averaged over the simulation period: a.) Incoming shortwave radiation. b.) Bare soil evaporation flux. c.) Transpiration flux. 252

7.6 The results of spatially-distributed ecohydrological simulations averaged over the simulation period: a.) Lateral subsurface flow. b.) Infiltration flux. c.) Soil moisture content. 253

7.7 The results of spatially-distributed ecohydrological simulations averaged over the simulation period: a.) Leaf Area Index. b.) Above Ground Net Primary Productivity. c.) Surface radiative temperature. 254

7.8 A comparison between the observed (solid line) and simulated (dashed line) cumulative runoff. 254

7.9 A comparison between the means of the observed (yellow dot) and simulated climatic variables for the control scenario (black dot) and the multiple future scenarios expressed as a PDF (blue (a) and red bars (b)). a.) Mean annual precipitation. b.) Mean air temperature. 259

7.10 A comparison between the means of the observed (yellow dot) and simulated climatic variables for the control scenario (black dot) and the multiple future scenarios expressed as a PDF (green (a) and magenta (b)). a.) Mean vapor pressure. b.) Mean shortwave radiation. 260

7.11 A comparison between the observed (black dots, subplots (a), (b), and (f), and cyan bars, subplots (c), (d), and (e)) and simulated meteorological variables for the CTS (red) and FUT (blue) scenarios. a.) The mean monthly precipitation, the vertical bars denote the standard deviations of monthly values. b.) The fraction of time with precipitation larger than a given threshold $[1-10mm]$ for different aggregation periods. c.) The frequency distribution of dry spell length. Dry spell duration is a number of consecutive days with precipitation depth lower than 1 $[mm]$. d.) The frequency distribution of cloud cover. e.) The frequency distribution of air temperature. f.) The mean daily cycle of air temperature. The triangle symbols denote the standard deviations of hourly values. E_{obs} is the observed mean, E_{cts} and E_{fut} are the simulated means for the control and future climate scenarios. 262

7.12 A comparison between the observed (dashed line with black diamonds) and simulated values of extreme precipitation for CTS (red crosses) and FUT (blue crosses) scenarios at (a) 1-hour and (b) 24-hour aggregation periods; (c) extremes of dry and (d) wet spell durations. Dry/Wet spell duration is the number of consecutive days with precipitation depth lower/larger than 1 $[mm]$. 263

7.13 A comparison between the observed (black dots, subplots (a), (b), (c), (d), (e), and (h), and cyan bars, subplots (f), (g), and (i)) and simulated meteorological variables for CTS (red) and FUT (blue) scenarios. a.) The mean daily cycle of global radiation. b.) The mean daily cycle of direct beam radiation. c.) The daily cycle of diffuse radiation. d.) The mean monthly global shortwave radiation. The vertical bars denote the standard deviations of monthly values. e.) The daily cycle of relative humidity. The triangle symbols denote the standard deviations of hourly values. f.) The frequency distribution of vapor pressure. g.) The frequency distribution of wind speed. h.) The mean daily cycle of wind speed. The triangle symbols denote the standard deviations of hourly values. i.) The frequency distribution of atmospheric pressure. E_{obs} is the observed mean, E_{cts} and E_{fut} are the simulated means for the control and future climate scenarios. 264

7.14 Monthly partition of the principal hydrological budget components averaged over the simulation period in $[mm\ yr^{-1}]$ (left panel) and in fractions (right panel). Results for the present climate. 267

7.15 Time series of simulated Leaf Area Index. Results for the present climate. The vertical yellow dashed lines are one year equally spaced. 268

7.16 Monthly partition of the principal hydrological budget components averaged over the simulation period in $[mm\ yr^{-1}]$ (left panel), and in fractions (right panel). Results for the *mean* future climate. 269

7.17 Time series of simulated Leaf Area Index. Results for the *mean* future climate. The vertical yellow dashed lines are one year equally spaced. 269
7.18 Vegetation productivity indexes for the control scenario (black dots) and an ensemble of future scenarios expressed as Probability Density Functions. a.) Gross Primary Production. b.) Net Primary Production c.) Aboveground Net Primary Production. d.) Leaf Area Index. 271
7.19 Drought stress and leaf onset dates for the control scenario (black dots) and an ensemble of future scenarios expressed as Probability Density Functions. a.) Leaf onset date for deciduous shrubs. b.) Bud burst date for evergreen shrubs. c.) Drought stress coefficient, β_R. 272
7.20 Evaporation and transpiration fluxes for the control scenario (black dots) and an ensemble of future scenarios expressed as Probability Density Functions. a.) Total evapotranspiration. b.) Transpiration from plants. c.) Bare soil evaporation. 272
7.21 Energy fluxes for the control scenario (black dots) and an ensemble of future scenarios expressed as Probability Density Functions. a.) Latent heat flux. b.) Net radiation flux. c.) Sensible heat flux. . . . 273
7.22 Soil water content at different depths of the soil column for the control scenario (black dots) and an ensemble of future scenarios expressed as Probability Density Functions. 274
7.23 Fraction of precipitation re-evaporated to the atmosphere and infiltration excess runoff (Horton Runoff) for the control scenario (black dots (a,c); black diamonds (b,d)) and an ensemble of future scenarios (PDFs (a,c); crosses (b,d)). 275
7.24 Vegetation productivity indexes vs precipitation and water and rain use efficiencies for the control scenario (black diamonds) and an ensemble of future scenarios (crosses). a.) Gross Primary Production vs precipitation. b.) Net Primary Production vs precipitation c.) Aboveground Net Primary Production vs precipitation. d.) Water Use Efficiency. e.) Rain Use Efficiency. 276
7.25 Time series of simulated Leaf Area Index. Results for the present climate. Point scale results (red line) and spatially averaged results over the distributed domain (blue dashed line). 281
7.26 Time series of simulated Leaf Area Index. Results for the *mean* future climate. Point scale results (red line) and spatially averaged results over the distributed domain (blue dashed line). 281
7.27 Spatial distribution of soil moisture, time averaged quantities for each basic computational element. A comparison between the control, CTS, (a) and future, FUT, scenarios (b). 282
7.28 A comparison between the cumulative discharge simulated at the Lucky Hills outlet in the control (green line) and future (blue line) scenarios. 282

7.29 Spatial distribution of infiltration rates, time averaged quantities for each basic computational element. A comparison between the control, CTS, (a) and future, FUT, scenarios (b). 283

7.30 Spatial distribution of deep recharge fluxes, time averaged quantities for each basic computational element. A comparison between the control, CTS, (a) and future, FUT, scenarios (b). 284

7.31 Spatial distribution of Leaf Area Index, time averaged quantities for each basic computational element. A comparison between the control, CTS, (a) and future, FUT, scenarios (b). 285

7.32 Spatial distribution of transpiration rates, time averaged quantities for each basic computational element. A comparison between the control, CTS, (a) and future, FUT, scenarios (b). 286

7.33 Spatial distribution of ANPP, time averaged quantities for each basic computational element. A comparison between the control, CTS, (a) and future, FUT, scenarios (b). 286

7.34 Spatial distribution of GPP, time averaged quantities for each basic computational element. A comparison between the control, CTS, (a) and future, FUT, scenarios (b). 286

A.1 Graphical representation of a two branches multiplicative random cascade process. 298

A.2 Moment scaling relationships (a), and the $\tau(q)$ function compared with simple scaling and Mandelbrot-Kahane-Peyriere (MKP) function (b). Results are obtained with observed rainfall at Lucky Hills (AZ) for a ten years (1999-2009) period and aggregation time 1 minute. . 299

A.3 Parameters of the microcanonical model. a.) Probability that the cascade weight, W, is 0 or 1, P_{01}, against the time scale, T. The solid circles indicate the time scales over which the model disaggregates rainfall, and the dashed line is a fitted logarithmic function. b.) Beta distribution parameter, a, for the weights, W_x, against the time scale, T. The open circles indicate the time scales over which the model disaggregates rainfall, and the dashed line is a fitted power law. The time scale, T, refer to the scale, n, in the breakdown $n-1 \rightarrow n$. Results are obtained with observed rainfall at Lucky Hills (AZ) for a ten years (1999-2009) period and aggregation time 1 minute. 301

A.4 A comparison between observed (blue) and simulated (red) cumulative distribution function of 5-min rainfall amounts from observations and a simulation with the microcanonical model (a). Fractions of time with precipitation larger than a given threshold 1, 10 $[mm]$ at different aggregation periods. Results obtained with observed rainfall at Lucky Hills (AZ) for a ten years (1999-2009) period and aggregation time 1 minute. 303

A.5 A comparison between the observed (red crosses) and simulated values of extreme precipitation (blue crosses) at (a) 5 minutes, (b) 15 minutes, and (c) 1 hour aggregation periods. Note that for 1 hour the simulated and observed values are the same. Results obtained with observed rainfall at Lucky Hills (AZ) for a ten years (1999-2009) period and aggregation time 1 minute. 304
A.6 An illustration of the procedure used to identify the *fairweather* cloud cover period. 307
A.7 Estimated mean cloud cover value $E\{N(t)\}$ (continuous line) and the smoothed function $E\{\widetilde{N(t)}\}$ (dashed line) as a function of the length of transition period. 308
A.8 Analytical (continuous line) and observed (circles) transition functions $J(t)$ corresponding to the estimated transition period lengths. . 308
A.9 An histogram of deviates $\varepsilon(t)$ in the cloud cover model and the corresponding probability density function (solid line) approximated with the *Beta* distribution. The cloud cover $N(t-1)$ for the month of *November* is given on a [0, 10] basis. 309
A.10 Components of incoming solar radiation on a slope: direct beam radiation at normal incidence, R_{Bn}, diffuse radiation, R_D, and diffuse and direct radiations reflected off by nearby terrain, R_R. The reflected contribution from a generic A location is shown as example. Sky view factor, S_{vf}, from A and shadow effects, S_h, in the represented landscape are also shown. The figure is adapted from *Dubayah and Loechel* (1997). 322
A.11 Horizon angle, H_ζ, for a direction ζ, adapted from *Dozier and Frew* (1990). 323
A.12 Digital Elevation Model (a), and sky-view factor, S_{vf}, (b) for the the *Versilia* watershed in Tuscany (Italy). 325
A.13 Shadow effect, S_h, (a) and terrain configuration factor, C_t, (b) for the the *Versilia* watershed in Tuscany (Italy). The shadow effect is calculated with sun height in the barycenter of the watershed, the 26 April 1982 at 8 am, local time. 325

List of Tables

2.1 The parameters of point Neyman-Scott Rectangular Pulse model. . . 14

2.2 Comparison between observed and simulated climatological indices of air temperature 33

2.3 Comparison between the observed and simulated mean of daily temperature amplitude ΔT_{day}, daily global shortwave radiation R_{sw}, and daily relative humidity U during rainy and rainless days. 55

3.1 Spatial resolution of some of the General Circulation Models which results were used in the IPCC 4AR. 62

3.2 General Circulation Models employed in the IPCC 4AR 82

4.1 Ratio of diffusivity, D, in air in comparison to heat diffusivity, from *Jones* (1983). 135

6.1 List of the parameters used in the simulations for each PFT. The values are assigned according to literature values (see Chapter 5) and are based on author personal judgement. 242

6.2 List of the parameters used to describe the hydrological properties in the simulations. 243

6.3 Synthetic experiment results, in terms of total evapotranspiration, ET, vegetation productivities, GPP, NPP, $ANPP$, soil moisture, θ, surface radiative temperature, T_s, net radiation, R_n, latent heat, λE, and sensible heat, H, for the different land covers. The wording D+G and D+E indicates deciduous trees with grass underneath, and a mixed wood of deciduous and evergreen plants, respectively. 245

7.1 Organization of dependent and independent factors of change in groups. Within each group factors of change are totally correlated, i.e., coefficient of correlation equal to one. Among different groups they are independent, i.e., correlation is equal to zero. 257

7.2 Determination coefficients, R^2, between the simulations at the point scale and spatially averaged in the distributed domain for the principal ecohydrological variables (column 1-2). Temporal averages of spatial standard deviations for the principal ecohydrological variables (column 3-4). The control and future scenarios are indicated with CTS and FUT, respectively. *) The standard deviations for the metrics of vegetation productivity are calculated separately for deciduous and evergreen species. These values are successively averaged using the Crown Area fractions as weights. Given the non-linearity of standard deviation operator the obtained values are not correct in absolute terms but are still useful for comparison. 280

A.1 The values of coefficients in equations (A.61) - (A.63) (from *Slingo* (1989)). 321

C.1 List of parameters used in "Tethys". 332

D.1 List of parameters used in "Chloris". 335

List of Symbols

α Attenuation coefficient for undercanopy resistance [−], page 134

α Parameter of the infiltration capacity computation [−], page 175

α Parameter of the theoretical derivation of the variance $VAR_{Pr}(h)$, page 81

α Relative humidity of air at the height z_{ow} [−], page 140

α Shape parameter of the Gamma distribution of rainfall intensity [−], page 14

α' Attenuation coefficient for leaf boundary layer conductance [−], page 136

α^{FUT} Shape parameter of the Gamma distribution of rainfall intensity for future climate conditions [−], page 57

α_{sno}^{M} Maximum value for the albedo of the snow [−], page 110

α_{sno}^{m} Minimum value for the albedo of the snow [−], page 110

α_1 Parameter of the force-restore method, page 123

α_Λ Leaf and stem reflectances [−], page 108

α_J Shape parameter in the photosynthesis model [−], page 149

α_Λ Ångström turbidity parameter [−], page 38

α_{ce} Shape parameter in the photosynthesis model [−], page 151

$\alpha_{dry\,\Lambda}$ Albedo for dry soil, page 109

α_{ps} Shape parameter in the photosynthesis model [−], page 151

$\alpha_{s\Lambda}$ Diffuse albedos of the generic surface underneath the canopy [−], page 103

$\alpha_{s\Lambda}^{\mu}$ Direct beam albedos of the generic surface underneath the canopy [−], page 103

$\alpha_{sat\,\Lambda}$ Albedo for saturated soil, page 109

α_{sno} Albedo of the snow [−], page 110

$\alpha_{soil,\Lambda}$ Diffuse ground albedo [−], page 109

$\alpha_{soil,\Lambda}^{\mu}$ Direct beam ground albedo [−], page 109

α_s Absorptivity of a generic surface s [−], page 112

$\alpha_{wat,\Lambda}$ Water albedo [−], page 110

$\bar{\mu}$ Average inverse diffuse optical depth per unit leaf and stem area [−], page 106

$\bar{N}$ Number of Monte Carlo iterations, page 257

β Fraction of the bulk transfer of water vapor between the air trapped in the soil pores close to the water and the roughness height [−], page 140

β Parameter for the computation of undercanopy resistance [−], page 134

β Parameter to take into account the possible dependence between X_i and Y_i, page 69

β^{-1} Mean waiting time for cell origins after the origin of the storm [h], page 14

β_Λ Upscatter parameters for diffuse radiation [−], page 106

β_e Effective turbidity coefficient, page 318

β_Q Quanta-to-energy converting factor [$\mu mol\, photons\ J^{-1}$], page 149

β_R Soil moisture stress factor [−], page 151

β_T Site slope [rad], page 42

$\beta_{0,\Lambda}$ Upscatter parameters for direct beam radiation [−], page 106

β_Λ Ångström turbidity parameter [−], page 38

β_{LO} Prescribed threshold on moisture stress for vegetation growth beginning [−], page 216

$\beta_{R,M}$ Moisture stress measure for vegetation growth beginning [−], page 216

$\check{p}$ Rejection threshold for difference in annual precipitation series [%], page 17

χ_L Departure of leaf angles from a spherical angle distribution [−], page 108

Δe Vapor pressure deficit [Pa], page 46

ΔGMT Time difference between the local time zone and Greenwich Mean Time [h], page 311

ΔS Entropy factor [$kJ\ mol^{-1}\ K^{-1}$], page 149

ΔT Variation of mean monthly temperature from CTS and FUT scenario [$^\circ C$], page 57

ΔT_{day} Daily temperature amplitude [$^\circ C$], page 56

Δt_{SL} Time difference between the standard and local meridian [h], page 311

Δ Parameter of ground albedo, page 109

δ Leaf boundary layer thickness $[mm]$, page 136

δ Solar declination $[rad]$, page 30

δ Upper soil thickness $[mm]$, page 123

$\Delta\rho$ Maximum change in bulk density at the soil surface $[kg\ m^{-3}]$, page 179

$\Delta\rho^*$ Maximum value reached after a long exposure to rainfall of $\Delta\rho$ $[kg\ \ m^{-3}]$, page 179

Δ_0 Empirical coefficient that express the value of vapor pressure deficit at which $f(\Delta e) = 0.5$ $[Pa]$, page 153

ϵ Intrinsic quantum efficiency $[\mu molCO_2\ \mu mol^{-1}\, photons]$, page 149

ϵ Parameter of the theoretical derivation of the variance $VAR_{Pr}(h)$, page 81

ϵ_{cs} Clear sky emissivity $[-]$, page 111

ϵ_s Emissivity of a generic surface s $[-]$, page 112

η Decay rate of distribution of the root biomass $[mm^{-1}]$, page 99

$\eta(i)$ Random deviate of annual precipitation, page 17

$\eta(t)$ Random deviate of the stochastic component of wind speed, page 51

η^{-1} Mean duration of the cell $[h]$, page 14

η_{cr} Parameter depending on soil-rainfall characteristics $[mm^2\ J^{-1}]$, page 179

γ Coefficient controlling the transition function of the cloud process $[h^{-1}]$, page 25

γ Daily angle, page 37

γ Parameter of the microcanonical model, page 302

Γ^* CO_2 compensation point $[Pa]$, page 149

γ_n Skewness of $\eta(i)$, page 17

γ_n Skewness of $\eta(t)$, page 51

γ_{cr} Characteristic parameter of the soil rainfall interaction $[mm^{-1}]$, page 179

γ_{dW_S} Skewness the stochastic component of wind speed, page 51

$\gamma_{h,l}$ Second moment of Y_h in the NSRP model, page 14

$\gamma_{P_{yr}}$ Skewness of annual precipitation, page 17

$\gamma_{P_{yr}}^{FUT}$ Skewness of annual precipitation for future climate conditions, page 57

$\hat{\alpha}$ Humidity equilibrium value for a soil water content θ_e [−], page 140

$\hat{f}_i$ Observed statistical properties or moments, page 15

κ Parameter for units conversion [$g\,C\ s\ \mu mol\,CO_2^{-1}\ day^{-1}$], page 200

κ Parameter of the microcanonical model, page 302

κ Decay parameter for the fraction of the PFT area occupied by leaves and stems projected in the vertical direction [−], page 169

$\kappa(h)$ Skewness of Y_h in the NSRP model, page 15

λE Latent heat [$W\ m^{-2}$], page 100

Λ Obukhov length [m], page 128

λ Latent heat of vaporization [$J\ kg^{-1}$], page 119

λ Memory of the upstream deviations in the calculation of flow directions, page 95

λ Scale the random cascade [−], page 300

$\Lambda 1$ First band *UV/VIS* of shortwave radiation, page 37

$\Lambda 1_e$ Effective wavelength for the entire band $\Lambda 1$, page 316

$\Lambda 2$ Second band *NIR* of shortwave radiation, page 37

$\Lambda 2_e$ Effective wavelength for the entire band $\Lambda 2$, page 316

$\lambda\,, = 1\,, 2\,, 3\,, 4$ Spectral bands of the *Slingo* (1989) model, page 40

λ^{-1} Mean storm origin arrivals [h], page 14

λ_f Latent heat of melting [$J\ kg^{-1}$], page 119

λ_s Latent heat of sublimation [$J\ kg^{-1}$], page 119

λ_s Soil heat conductivity [$J\ K^{-1}\ m^{-1}\ s^{-1}$], page 123

λ_{dry} Thermal conductivity of dry soil [$W\ m^{-1}\ K^{-1}$], page 123

λ_{sat} Thermal conductivity of saturated soil [$W\ m^{-1}\ K^{-1}$], page 123

λ_{soil} Thermal conductivity of solid soil [$W\ m^{-1}\ K^{-1}$], page 123

λ_{wat} Thermal conductivity of liquid water [$W\ m^{-1}\ K^{-1}$], page 123

$\mathcal{C}$ Fitting parameter of soil seal effect [$m^3\ kg^{-1}$], page 179

$\mathcal{N}$ Gaussian distribution, page 69

μ Cosine of the sun zenith angle [−], page 106

μ Parameter for the computation of aerodynamic resistance [−], page 131

μ_c Mean number of cell per storm [−], page 14

μ_c^{FUT} Mean number of cell per storm for future climate conditions [−], page 57

μ_h Mean of Y_h in the NSRP model, page 14

ω_1 Diurnal frequency $[s^{-1}]$, page 123

ω_Λ Scattering coefficient of phytoelements [−], page 106

ω_i Weights in the objective function, page 15

ω_Λ Single scattering albedo [−], page 37

ω_{grw} Growth respiration fraction [−], page 200

$\overline{\mu}$ Expected value of the PDF in the control scenario, page 70

$\overline{\nu}$ Expected value of the PDF for the future scenario, page 70

$\overline{d\Delta e}$ Mean of the stochastic component of vapor pressure deficit $[Pa]$, page 46

$\overline{dT}_h$ Average of the stochastic component of air temperature $[°C]$, page 30

$\overline{dW_s}$ Mean of the stochastic component of wind speed $[m\ s^{-1}]$, page 51

$\overline{K_i}$ Unsaturated conductivity averaged from the layer i and $i+1$ $[mm\ \ h^{-1}]$, page 185

$\overline{P_{atm}}$ Mean of the atmospheric pressure $[mbar]$, page 53

$\overline{P}_{yr}$ Average annual precipitation $[mm]$, page 17

$\overline{P}_{yr}^{FUT}$ Average annual precipitation for future climate conditions $[mm]$, page 57

$\overline{S}$ Mean of long-term precipitation statistics, page 72

$\overline{u}$ Intercepted snow unloading rate $[s^{-1}]$, page 165

$\overrightarrow{R_{tot}}$ Routed part of R_{tot} $[mm]$, page 191

Φ Local latitude $[rad]$, page 30

Φ Phenology state $[1, ..., 4]$, page 214

Φ' Local longitude $[angular\ degree]$, page 311

$\Phi(h)$ Probability that an arbitrary interval of length h is dry, page 14

Φ_L Leaf water potential $[kPa]$, page 151

ϕ_1 Parameter for the estimation of $G(\mu)$ [−], page 108

ϕ_2 Parameter for the estimation of $G(\mu)$ [−], page 108

$\Psi(\theta)$ Soil water potential $[mm]$ or $[kPa]$, page 181

Ψ_e Air entry bubbling pressure $[kPa]$ or $[mm]$, page 186

ψ_h Non-dimensional stability function for heat [−], page 128

ψ_m Non-dimensional stability function for momentum [−], page 128

ψ_w Non-dimensional stability function for water vapor [−], page 128

Ψ_{ss} Soil water potential at the begin of stomatal closure $[kPa]$, page 99

Ψ_{wp} Soil water potential at the complete stomatal closure $[kPa]$, page 99

$\rho(h)$ Lag-1 autocorrelation of Y_h in the NSRP model, page 15

ρ_a Air density $[kg\, m^{-3}]$, page 118

ρ_d Bulk density of soil $[kg\ m^{-3}]$, page 173

ρ_e Density threshold for water holding capacity of the snowpack $[kg\, m^{-3}]$, page 166

ρ_g Ground albedo referring to a large area of 5-50 $[km]$ radius surrounding the point of interest, page 38

ρ_m Lag-1 autocorrelation function of correlated deviation in cloud cover simulation, page 25

ρ_w Density of water $[kg\ m^{-3}]$, page 124

ρ_{cr} Bulk density of the seal $[kg\ m^{-3}]$, page 179

$\rho_{csB,\Lambda}$ Cloud albedo, which is different for direct beam [−], page 41

$\rho_{csD,\Lambda}$ Cloud albedo, incident diffuse radiation fluxes [−], page 41

$\rho_{d\Delta e}$ Lag-1 autocorrelation of the stochastic component of vapor pressure deficit [−], page 46

ρ_{dT} Lag-1 autocorrelation of the stochastic component of air temperature, page 30

ρ_{dW_s} Lag-1 autocorrelation of the stochastic component of wind speed [−], page 51

$\rho_{heaw,a}$ Heartwood carbon density $[g\, C\ m^{-3}]$, page 334

$\rho_{P_{atm}}$ Lag-1 autocorrelation of the atmospheric pressure [−], page 53

$\rho_{P_{yr}}$ Lag-1 autocorrelation of annual precipitation, page 17

$\rho_{Pr}(h)$ Lag-1 autocorrelation of precipitation at time aggregation period $[h]$, page 65

$\rho_{s,\Lambda}$ Sky albedo [−], page 38

ρ_{sapw} Sapwood carbon density $[g\,C\,m^{-3}]$, page 334

ρ_{sno} Snow density $[kg\,m^{-3}]$, page 166

ρ'_{sno} Intermediate value of snow density $[kg\,m^{-3}]$, page 168

ρ^{M}_{sno} Maximum of relative density of snow $[kg\,m^{-3}]$, page 168

ρ^{M1}_{sno} Maximum density allowed for snow in melting conditions $[kg\,m^{-3}]$, page 168

ρ^{M2}_{sno} Maximum density allowed for snow in freezing conditions $[kg\,m^{-3}]$, page 168

ρ^{new}_{sno} Density of fresh snow $[kg\,m^{-3}]$, page 168

ρ_{ss} Solid soil density $[kg\,m^{-3}]$, page 173

σ Parameter of canopy radiative transfer model, page 108

σ Stefan-Boltzmann constant $[W\,m^{-2}\,K^{-4}]$, page 30

$\sigma(T_{mon})$ Standard deviation of long-term average monthly temperature, page 72

σ_i Parameter of the theoretical derivation of the variance $VAR_{Pr}(h)$, page 81

σ^2_M Variance of cloud cover in the "fair weather region, page 25

σ^2_m Variance of correlated deviation in cloud cover simulation, page 25

$\sigma_{d\Delta e}$ Standard deviation of the stochastic component of vapor pressure deficit $[Pa]$, page 46

$\sigma_{dT,h}$ Standard deviation of the stochastic component of air temperature $[°C]$, page 30

σ_{dW_s} Standard deviation of the stochastic component of wind speed $[m\,s^{-1}]$, page 51

$\sigma_{P_{atm}}$ Standard deviation of the atmospheric pressure $[mbar]$, page 53

$\sigma_{P_{yr}}$ Standard deviation of annual precipitation $[mm]$, page 17

$\sigma^{FUT}_{P_{yr}}$ Standard deviation of annual precipitation for future climate conditions $[mm]$, page 57

τ Fundamental diurnal period $[s]$, page 123

τ Momentum flux $[kg\,m^{-1}\,s^{-2}]$, page 128

$\tau(q)$ Characteristic function of the scaling behavior, page 300

τ_1 Parameter for the computation of the albedo and density of the snow $[s]$, page 110

τ_Λ Leaf and stem transmittances $[-]$, page 108

τ_a Parameter for the computation of the albedo of the snow $[-]$, page 110

τ_f Parameter for the computation of the albedo and density of the snow [−], page 110

τ_N Cloud optical thickness [−], page 42

$\tau_S(t)$ Hour angle of the Sun $[rad]$, page 311

$\tau_{a\Lambda}$ Spectral aerosol optical depth [−], page 37

θ Inflation-deflation parameter in the multi-model ensemble approach, page 69

θ Scale parameter of the Gamma distribution of rainfall intensity $[mm\ h^{-1}]$, page 14

θ Volumetric soil water content [−], page 181

$\theta(z_d)$ Values of soil water content at different depths [−], page 173

θ^* Potential temperature scale $[K]$, page 128

θ^{FUT} Scale parameter of the Gamma distribution of rainfall intensity for future climate conditions $[mm\ h^{-1}]$, page 57

θ_1 Volumetric water content of the first layer, page 109

θ_a Potential temperature of air at the reference height $[K]$, page 127

θ_d Soil volumetric water content averaged at the dampening depth d [−], page 123

θ_e Soil water content averaged in the portion of soil interested by the evaporation process [−], page 140

θ_s Potential temperature at the surface $[K]$, page 127

θ_{33} Soil water content at -33 $[kPa]$ [−], page 186

θ_{fc} Soil water content at the field capacity [−], page 186

θ_F Water content of the layer of soil interested by infiltration [−], page 175

θ_{hy} Residual or hygroscopic soil water content [−], page 186

θ_R Soil water content available for the roots [−], page 147

θ_{sat} Soil water content at saturation [−], page 186

θ_{ss} Soil moisture content at the begin of stomatal closure [−], page 151

θ_{wp} Soil moisture content at the complete stomatal closure [−], page 151

$\tilde{\gamma}$ Parameter of the exponential decay of the frequency of non-precipitation, page 81

$\tilde{\omega_\lambda}$ Single scatter albedo of cloud optical properties, page 319

$\tilde{f}$ Scaling parameter controlling the rate of decline of K_v with depth $[mm^{-1}]$, page 187

$\varepsilon(i)$ Standard normal deviate, page 17

$\varepsilon(t)$ Normal random deviates, Beta distributed random deviates in the cloud component, page 25

ε_{al} Tuning parameter for carbohydrate reserve allocation $[0-1]$, page 206

$\varphi_{S,T}$ Local solar illumination angle $[rad]$, page 324

ς Coefficient controlling the transition function of the cloud process $[h^{-1}]$, page 25

ς_p Canopy-leaf contact area per unit area of ground $[-]$, page 165

$\vec{x}$ Position, page 42

$\widehat{\Delta e}$ Deterministic component of vapor pressure deficit $[Pa]$, page 46

$\widehat{r_b}$ Leaf boundary resistance for unit of *Crown Area* $[s\ m^{-1}]$, page 137

$\widehat{r_s}$ Canopy level stomatal resistance $[s\ m^{-1}]$, page 153

$\widehat{W_s}$ Deterministic component of wind speed $[m\ s^{-1}]$, page 51

$\widetilde{E\{N(t)\}}$ Smoothed mean cloud cover $[-]$, page 309

$\widetilde{f_l}$ Preliminary allocation fraction to leaves-grasses $[-]$, page 206

$\widetilde{f_r}$ Preliminary allocation fraction to fine roots $[-]$, page 206

$\widetilde{f_s}$ Preliminary allocation fraction to living sapwood $[-]$, page 206

$\widetilde{PAR}_{Bn}$ direct normal PAR $[W\ m^{-2}]$, page 42

$\widetilde{PAR}_D$ diffuse PAR $[W\ m^{-2}]$, page 42

$\widetilde{R}_{Bn,\Lambda}$ Direct beam radiation at normal incidence for cloudy sky conditions $[W\ m^{-2}]$, page 40

$\widetilde{R}_{D,\Lambda}$ Total diffuse radiation for cloudy sky conditions $[W\ m^{-2}]$, page 41

$\widetilde{R}_{Dd,\Lambda}$ Backscattered radiation for cloudy sky conditions $[W\ m^{-2}]$, page 41

$\widetilde{R}_{Dp,\Lambda}$ Incident diffuse radiation for cloudy sky conditions $[W\ m^{-2}]$, page 41

$\widetilde{R}_{Gn,\Lambda}$ Global radiation at normal incidence for cloudy sky conditions $[W\ m^{-2}]$ $[W\ m^{-2}]$, page 41

$\widetilde{T}(t)$ Deterministic component of air temperature $[^{\circ}C]$, page 30

Ξ Broad vegetation category identifier, page 199

ξ_h Third moment of Y_h in the NSRP model, page 14

ζ_S Solar azimuth $[rad]$, page 37

ζ_T Site aspect $[rad]$, page 42

ζ_{cr} Parameter depending on soil-rainfall characteristics $[mm^2\ J^{-1}]$, page 179

A Parameter of the soil water retention curve $[kPa]$, page 186

a Beta probability distribution parameter, page 25

a Empirical coefficient for leaf boundary layer computation $[m\ s^{-1/2}]$, page 136

a Empirical parameter linking A_{nC} to g_{s,CO_2} $[-]$, page 153

a Parameter of the prior distribution of λ_i, page 70

$a(T)$ Parameter of the microcanonical model $[-]$, page 302

A^* Gross assimilation rate for unit canopy before accounting for moisture stress $[\mu mol\ \mathrm{CO_2}\, m^{-2}\, s^{-1}]$, page 151

a_0 Parameter of the microcanonical model, page 302

A_B Single limiting factor of belowground resource availability $[-]$, page 206

A_C Gross photosynthetic rate $[\mu mol\, CO_2\ s^{-1}\ m^{-2}]$, page 149

A_H Limiting factor of soil moisture availability $[-]$, page 206

a_i Regression coefficient for the deterministic component of vapor pressure deficit, page 46

A_L Limiting factor of light availability $[-]$, page 206

A_N Limiting factor of nitrogen availability $[-]$, page 206

a_r Anisotropy factor $[-]$, page 189

a_T Area of the basic element per unit contour length that drains through the location $[mm]$, page 190

$A_{B,\lambda}$ Cloud diffuse reflectivity for direct beam incident radiation $[-]$, page 41

A_{cr} Critical age for leaf shed $[day]$, page 209

$A_{D,\lambda}$ Cloud diffuse reflectivity for diffuse incident radiation $[-]$, page 41

A_{max} Maximum photosynthetic capacity $[\mu mol\, CO_2\ s^{-1}\ m^{-2}]$, page 156

A_{nC} Net assimilation rate $[\mu mol\, CO_2\ s^{-1}\ m^{-2}]$, page 143

A_{NH} Soil humidity parameter $[-]$, page 206

A_{NT} Soil temperature parameter [−], page 206

Ag_L Leaf age [day], page 209

$ANPP$ Above-ground net primary production [$g\,C\,m^{-2}\,PFT\,day^{-1}$], page 213

B Parameter of the infiltration capacity computation [mm], page 175

b Beta probability distribution parameter, page 25

b Branching number [−], page 300

b Parameter of the prior distribution of λ_i, page 70

B_a Aerosol forward scattering factor [−], page 37

b_d Shape parameter reflecting the sensitivity of canopy to drought [−], page 211

b_i Regression coefficient in the deterministic component of air temperature, page 30

B_R Bowen ratio [−], page 244

$B_{R,\Lambda}$ Forward scattering fractions for Rayleigh extinction [−], page 37

$bare$ Subscript of the bare soil surfaces, page 100

C Parameter for carbohydrate reserve allocation, page 206

C Random number of cells in NSRP model [−], page 14

$c(t)$ Dimensionless snow unloading coefficient [−], page 165

c^R Minimum specific water holding capacity coefficient of the snowpack [−], page 166

c^R_{max} Maximum specific water holding capacity coefficient of the snowpack [−], page 166

C_1 General coefficient of the force-restore method [$m^2\,K\,J^{-1}$], page 123

C_2 General coefficient of the force-restore method [s^{-1}], page 123

c_a Atmospheric CO_2 concentration [Pa], page 153

C_d Drag coefficient [−], page 331

C_h Bulk transfer coefficient for heat, Stanton number [−], page 127

c_h Parameter for the computation of aerodynamic resistance [−], page 131

c_i Partial pressure of intercellular CO_2 [Pa], page 149

c_i Regression coefficient for the deterministic component of wind speed, page 51

c_i Specific heat of ice [$J\,kg^{-1}\,K^{-1}$], page 124

C_p Specific heat of air at a constant pressure $[J\,kg^{-1}\,K^{-1}]$, page 118

C_s Non-dimensional aerodynamic conductance $[-]$, page 134

c_s CO_2 concentration at the leaf surface $[Pa]$, page 153

C_t Terrain configuration factor $[-]$, page 324

$C_v(h)$ Coefficient of variation of Y_h in the NSRP model, page 15

$C_v(S)$ Coefficient of variation of long-term average precipitation statistics, page 72

c_w Specific heat of water $[J\ kg^{-1}\ K^{-1}]$, page 124

c_{ac} Canopy space CO_2 concentration $[Pa]$, page 153

C_{bare} Fraction of land cover occupied by bare soil areas $[-]$, page 96

C_{crown} Fraction of a basic computational element area occupied by one (or two, in case of vertical composition) *PFTs* named *Crown Areas* $[-]$, page 99

C_{flfr} Flower and fruit carbon pool $[g\,C\,m^{-2}\,PFT]$, page 199

C_{fol} Fraction of the PFT area occupied by leaves and stems projected in the vertical direction $[m^2\ vegetated\ area\ m^{-2}\ \ PFT\,area]$, page 169

$C_{heaw,a}$ Aboveground heartwood carbon pool $[g\,C\,m^{-2}\,PFT]$, page 334

C_{heaw} Heartwood carbon pool $[g\,C\,m^{-2}\,PFT]$, page 199

$C_{hydr,a}$ Aboveground carbohydrate reserve carbon pool $[g\,C\,m^{-2}\,PFT]$, page 334

C_{hydr} Carbohydrate reserve carbon pool $[g\,C\,m^{-2}\,PFT]$, page 199

C_{leaf} Green aboveground biomass (leaves or grass) carbon pool $[g\,C\ \ m^{-2}\,PFT]$, page 199

C_n Neutral transport coefficient $[-]$, page 131

C_{rock} Fraction of land cover occupied by rock covered areas $[-]$, page 96

C_{root} Fine roots carbon pool $[g\,C\,m^{-2}\,PFT]$, page 199

$C_{sapw,a}$ Aboveground sapwood carbon pool $[g\,C\,m^{-2}\,PFT]$, page 334

C_{sapw} Living sapwood carbon pool $[g\,C\,m^{-2}\,PFT]$, page 199

C_{sno} Logic operator for presence or absence of snow $[0/1]$, page 96

C_s Fractions of a generic land cover surface s $[-]$, page 104

C_{urb} Fraction of land cover occupied by urban areas $[-]$, page 96

C_{veg} Fraction of land cover occupied by vegetated areas $[-]$, page 96

C_{wat} Fraction of land cover occupied by water [−], page 96

cr Subscript correspondent to a parameter modified by the seal effect, page 179

cv_s Soil volumetric heat capacity $[J\ K^{-1}\ m^{-3}]$, page 123

cv_{soil} Volumetric heat capacity of soil solid $[J\ K^{-1}\ m^{-3}]$, page 123

cv_{wat} Volumetric heat capacity of water $[J\ K^{-1}\ m^{-3}]$, page 123

D Average wood trunk diameter $[m]$, page 334

D Molecular diffusion coefficient $[m^2\ s^{-1}]$, page 136

d Dampening depth $[mm]$, page 123

d Zero-plane displacement $[m]$, page 125

$D(\theta)$ Unsaturated water diffusivity $[mm^2\ h^{-1}]$, page 181

$d\Delta e(t)$ Stochastic component of vapor pressure deficit $[Pa]$, page 46

d_e Depth of soil interested by the evaporation process $[mm]$, page 140

d_{cold} Linear coefficient for foliage loss due to cold temperature $[day^{-1}\ {}^{\circ}C^{-1}]$, page 211

d_{cr} Seal thickness $[mm]$, page 179

d^*_{cr} Maximum value reached after a long exposure to rainfall of d_{cr} $[mm]$, page 179

$d_{d\,max}$ Maximum turnover rate induced by the drought $[day^{-1}]$, page 211

$d_{leaf,a}$ Turnover rate of green aboveground biomass due to leaf age $[day^{-1}]$, page 209

$d_{leaf,c}$ Turnover rate of green aboveground biomass due to cold stress $[day^{-1}]$, page 209

$d_{leaf,d}$ Turnover rate of green aboveground biomass due to drought stress $[day^{-1}]$, page 209

d_{leaf} Typical leaf dimension $[cm]$, page 99

$D_{LH,SE}$ Prescribed threshold on day length for senescence beginning $[h]$, page 216

D_{LH} Daily length $[h]$, page 37

d_{MG} Number of days of maximum growth $[day]$, page 216

d_{root} Turnover rate of fine roots $[day^{-1}]$, page 209

d_{sapw} Living sapwood to heartwood conversion rate $[day^{-1}]$, page 209

$d_{w,sno}$ Fraction of the canopy covered by snow [−], page 165

$d_{z,F}$ Thickness of the layer of soil interested by infiltration $[mm]$, page 175

$D_{z,i}$ Positive distance between the layer center and the precedent layer center $[mm]$, page 181

$d_{z,i}$ Thickness of soil layer i $[mm]$, page 181

dQ Net energy flux input to the snowpack $[W\ m^{-2}]$, page 162

Dr_d Dripping from canopy $[mm\ h^{-1}]$, page 171

Dr_s Canopy drainage from saturation excess $[mm\ h^{-1}]$, page 171

$Dr_{H_v\ or\ L_v}$ Total drainage from a generic vegetation layer $[mm\ h^{-1}]$, page 169

dt Time step $[h]$ or $[s]$, page 162

$dT(t)$ Stochastic component of air temperature $[^{\circ}C]$, page 30

dW_s Stochastic component of wind speed $[m\ s^{-1}]$, page 51

dx Cell size $[m]$, page 191

E Evaporation from a bare ground surface $[kg\ m^{-2}\ s^{-1}]$ or $[mm\,h^{-1}]$, page 140

E_0 Ratio between the actual Earth-Sun distance and the mean Earth-Sun distance $[-]$, page 37

e_a Ambient vapor pressure $[Pa]$, page 46

E_K Rainfall cumulative kinetic energy $[J\ mm^{-2}]$, page 179

E_r Erosion rate $[mm\ h^{-1}]$ or $[kg\ h^{-1}\ m^{-2}]$, page 173

E_{bare} Evaporation flux from bare soil $[mm\ h^{-1}]$ or $[kg\ m^{-2}\ s^{-1}]$, page 119

$e_{f,i}$ Evaporative fraction $[-]$, page 181

E_g Evaporation flux from the ground underneath the vegetation $[mm\ h^{-1}]$ or $[kg\ m^{-2}\ s^{-1}]$, page 119

$E_{In,H_v\ or\ L_v}$ Evaporation flux from intercepted water in the canopy $[mm\ h^{-1}]$ or $[kg\ m^{-2}\ s^{-1}]$, page 119

$E_{In_{S_{WE}}}$ Sublimation/evaporation from intercepted snow $[mm\ h^{-1}]$, page 165

$E_{Pr}(h)$ Mean of precipitation at time aggregation period $[h]$, page 65

e_{rel} Relative photosynthetic efficiency $[-]$, page 147

e_{sat} Vapor pressure at saturation $[Pa]$, page 46

$E_{sno,f\ or\ s}$ Evaporation/sublimation flux from snow in open surface and snow under the vegetation $[mm\ h^{-1}]$ or $[kg\ m^{-2}\ s^{-1}]$, page 119

E_{wat} Evaporation flux from water surfaces $[mm\ h^{-1}]$ or $[kg\ m^{-2}\ s^{-1}]$, page 119

ET Total evapotranspiration $[mm\ yr^{-1}]$, page 244

F Depth of water infiltrated in the soil $[mm]$, page 175

$f(\diamond)$ Logit-like transformation, page 65

f^2 Correction to the bulk Richardson number computation [−], page 131

f_f Final allocation fraction to fruit and flowers [−], page 206

f_h Final allocation fraction to carbohydrate reserves [−], page 206

f_i Theoretical statistical properties or moments, page 15

f_l Final allocation fraction to green aboveground [−], page 206

F_N Factor to scale photosynthesis from leaf to canopy level [−], page 145

f_r Final allocation fraction to fine roots [−], page 206

f_s Final allocation fraction to living sapwood [−], page 206

f_v Fraction of stem and branches that can be regarded as prevalently vertical [−], page 334

F_Λ Correction factor to compensate for multiple scattering effects [−], page 37

F_{cla} Fraction of clay in the soil [−], page 189

F_{obj} Objective function, page 15

F_{san} Fraction of sand in the soil [−], page 189

G Heat flux in the ground $[W\ m^{-2}]$, page 123

G Net capillary drive $[mm]$, page 175

g Gravitational acceleration $[m\ s^{-2}]$, page 128

g Subscript of ground underneath the vegetation, page 100

$G(\mu)$ Relative projected area of phytoelements in direction μ [−], page 106

$g(T)$ Respiration temperature dependence [−], page 202

g_0 Cuticular conductance or minimum stomatal conductance $[\mu mol\, CO_2\ m^{-2}\, leaf\ s^{-1}]$, page 153

g_b Boundary layer conductance $[m\ s^{-1}]$, page 136

g_c Interception exponential decay parameter $[mm^{-1}]$, page 171

g_s Stomatal conductance $[m\ s^{-1}]$, page 147

g_λ Asymmetry parameter of cloud optical properties, page 319

$g_{s,max}$ Maximum stomatal conductance $[m\ s^{-1}]$, page 147

GPP Gross primary production $[g\,C\ m^{-2}\,PFT\ day^{-1}]$, page 200

H Sensible heat $[W\ m^{-2}]$, page 100

h Rainfall aggregation period $[h]$, page 13

H_a Activation energy $[kJ\ mol^{-1}]$, page 149

H_c Canopy height $[m]$, page 99

H_d Deactivation energy $[kJ\ mol^{-1}]$, page 149

H_i Horton index, page 272

h_S Solar height $[rad]$, page 30

H_v Subscript of *High-vegetation* layer, page 99

$h_{1,\dots,10}$ Parameters of canopy radiative transfer model, page 108

H_ζ Horizon angle $[rad]$, page 324

$I\downarrow_\Lambda$ Downward diffuse fluxes per unit incident diffuse radiation $[-]$, page 103

$I\downarrow_\Lambda^\mu$ Downward diffuse fluxes per unit incident direct beam radiation $[-]$, page 103

$I\uparrow_\Lambda$ Upward diffuse fluxes per unit incident diffuse radiation $[-]$, page 103

$I\uparrow_\Lambda^\mu$ Upward diffuse fluxes per unit incident direct beam radiation $[-]$, page 103

$I_{\Lambda,abs}^\mu$ Direct beam fluxes absorbed by a general layer of vegetation per unit incident flux $[-]$, page 103

I_f Actual infiltration rate $[mm\ h^{-1}]$, page 176

I_f^C infiltration capacity $[mm\ h^{-1}]$, page 175

$I_{\Lambda,abs}$ Diffuse fluxes absorbed by a general layer of vegetation per unit incident flux $[-]$, page 103

In Intercepted water in the canopy $[mm]$, page 171

In' First update of intercepted water in the canopy $[mm]$, page 171

In^M Maximum interception, or canopy storage capacity $[mm]$, page 170

$In_{S_{WE}}$ Snow water equivalent of intercepted snow in the *high-vegetation* layer $[mm]$, page 162

$In'_{S_{WE}}(t)$ Intercepted snow before unloading $[mm]$, page 165

$In^{b}_{S_{WE}}$ Snow water equivalent of intercepted snow before accounting for melting $[mm]$, page 162

$In^{M}_{S_{WE}}$ Maximum canopy snow interception capacity $[mm]$, page 165

$In^{N}_{S_{WE}}$ New intercepted snow $[mm]$, page 162

J Smooth minimum between J_m and $PPFD$ $[\mu mol\, CO_2\ s^{-1}\ m^{-2}]$, page 149

$J(t)$ Transition function of the cloud process between the boundary of a storm period $[-]$, page 25

J_1 Cloud cover of the first hour after a storm and of the last hour of an inter-storm $[0-1]$, page 25

J_c Limit of assimilation rate due to the efficiency of the photosynthetic enzyme system (Rubisco-limited) $[\mu mol\, CO_2\ s^{-1}\ m^{-2}]$, page 149

J_e Limit of assimilation rate due to the amount of PAR captured by the leaf chlorophyll $[\mu mol\, CO_2\ s^{-1}\ m^{-2}]$, page 149

J_p Smoothed minimum of J_c and J_e $[\mu mol\ \mathrm{CO}_2\ m^{-2}\ s^{-1}]$, page 151

J_s Limit of assimilation rate due to the capacity of the leaf to export or utilize the products of photosynthesis, or PEP-carboxylase $[\mu mol\, CO_2\ s^{-1}\ m^{-2}]$, page 149

$J_{Day,LO}$ Maximum Julian day for leaf onset, page 216

J_{Day} Julian Day, page 37

J_{max} Canopy maximum electron transport capacity at $25°C$ $[\mu mol\, Eq\ s^{-1}\ m^{-2}]$, page 145

J^{L}_{max} Maximum electron transport capacity at $25°C$ at leaf scale $[\mu mol\, Eq\ s^{-1}\ m^{-2}]$, page 145

J_m Maximum electron transport capacity at canopy scale after accounting for temperature dependence $[\mu mol\, Eq\ s^{-1}\ m^{-2}]$, page 149

k Von Karman constant $[-]$, page 128

$K(\Lambda)$ Fractions of solar irradiance at the top of atmosphere in each band (*Gueymard*, 2008), page 40

$k(\lambda)$ Fractions of solar irradiance at the top of atmosphere in each band (*Slingo*, 1989), page 40

$K(\theta)$ Unsaturated hydraulic conductivity $[mm\ h^{-1}]$, page 181

$K(t)$ Cloud attenuation factor $[-]$, page 30

K_c Interception drainage rate coefficient $[mm\ h^{-1}]$, page 171

K_c Michaelis-Menten constant for CO_2 $[Pa]$, page 149

K_e Kersten number, page 123

K_h Eddy turbulent diffusivity of heat $[m^2\, s^{-1}]$, page 127

K_m Eddy turbulent diffusivity of momentum $[m^2\, s^{-1}]$, page 128

K_N Canopy nitrogen decay coefficient $[-]$, page 145

K_N Correction for the cloudiness in the atmospheric long-wave radiation calculation $[-]$, page 30

K_o Michaelis-Menten constant for O_2 $[Pa]$, page 149

k_s Soil heat diffusivity $[m^2\ s^{-1}]$, page 123

K_v Unsaturated conductivity in the normal direction to the slope $[mm\ \ h^{-1}]$, page 186

$k_{1,\ldots,4}$ Allometric constants, page 334

K_{bot} Conductivity of the bedrock $[mm\ h^{-1}]$, page 190

K_{det} Soil detachability coefficient $[g\ J^{-1}\ ]$, page 173

$K_{E,LD}$ Specific kinetic energy of the leaf and stem drainage $[J\ m^{-2}\ mm^{-1}]$, page 173

$K_{E,TR}$ Specific kinetic energy of rainfall reaching the ground $[J\ m^{-2}\ mm^{-1}]$, page 173

K_{ero} Erodibility factor $[kg\ h\ J^{-1}\ mm^{-1}]$, page 173

K_E Total flux of kinetic energy $[J\ m^{-2}\ h^{-1}]$, page 173

K_e Constant light extinction coefficient $[-]$, page 206

K_h Unsaturated conductivity in the parallel direction to the slope $[mm\ \ h^{-1}]$, page 189

K_{opt} Optical depth of direct beam per unit leaf and stem area $[-]$, page 103

$K_{s\,v}$ Vertical saturated hydraulic conductivity $[mm\ h^{-1}]$, page 186

L Generic leakage flux $[mm\ h^{-1}]$, page 181

$L(z)$ Leaf area index varying with height $[-]$, page 137

$L\downarrow$ Incoming long-wave radiation $[W\ m^{-2}]$, page 111

$L\uparrow$ Outgoing long-wave radiation $[W\ m^{-2}]$, page 111

L_v Subscript of *Low-vegetation* layer, page 99

L_{abs} Absorbed longwave radiation [$W\ m^{-2}$], page 100

L_{atm} Incoming atmospheric long-wave radiation [$W\ m^{-2}$], page 30

L_{kb} Leakage between the vadose zone and the underneath bedrock, recharge to deep aquifers [$mm\ h^{-1}$], page 185

LAI Leaf area index [$m^2\ leaf\ area\ m^{-2}\ ground\,area$], page 99

LAI_{min} Minimum leaf area index for considering vegetation completely defoliated [−], page 217

$M(\lambda, q)$ Statistical moment in the random cascade, page 300

$m(t)$ Stationary sequence of correlated deviation in cloud cover simulation $[0-1]$, page 25

m' Reference air mass [−], page 37

M_0 Mean cloud cover in the "fair weather region $[0-1]$, page 25

m_A Aerosol extinction air mass [−], page 316

M_B Reduction factor for direct PAR [−], page 42

M_f Turnover of fruit and flowers [$g\,C\ m^{-2}\,PFT\ day^{-1}$], page 213

m_f Parameter controlling the rate of decline of K_v with depth [mm], page 187

M_G Reduction factor for global PAR [−], page 42

m_O Ozone absorption air mass [−], page 316

m_R Rayleigh (molecular) scattering and uniformly mixed gases absorption air mass [−], page 316

m_W Water vapor absorption air mass [−], page 316

N Cloud cover, i.e., fraction of the celestial dome occupied by clouds $[0-1]$, page 25

n Level of subdivision in the random cascade [−], page 300

n Manning roughness coefficient [$s\ m^{-1/3}$], page 191

n Number of possible land cover surfaces, page 100

n_c Number of *Crown Areas*, page 99

N_f Foliage carbon-nitrogen C:N mass ratio [$g\,C\ g\,N^{-1}$], page 202

N_r Fine root carbon-nitrogen C:N mass ratio [$g\,C\ g\,N^{-1}$], page 202

N_s Living sapwood carbon-nitrogen C:N mass ratio [$g\,C\ g\,N^{-1}$], page 202

n_T Number of prognostic temperatures, page 115

N_{LAI} New leaf area onset in a time step dt [m^2 $leaf$ $area$ m^{-2} PFT $area$], page 217

n_{mod} Number of considered GCMs, page 69

$NDVI$ *Normalized Difference Vegetation Index* [−], page 104

NPP Net primary production [$g\,C\,m^{-2}\,PFT\,day^{-1}$], page 200

O_i Partial pressure of O_2 [Pa], page 149

p Random probability, page 257

P_r Precipitation intensity [$mm\ h^{-1}$], page 160

P_x Probability of weights that are not 0 or 1, page 300

P_{01} Probability of weights that are equal to 0 or 1, page 300

$P_{01}(T)$ Parameter of the microcanonical model [−], page 302

P_{01}^0 Parameter of the microcanonical model, page 302

$P_{atm,0}$ Reference atmospheric pressure [Pa], page 153

P_{atm} Atmospheric pressure [$mbar$] or [Pa], page 53

P_{orgC} Percentage of organic carbon content in the soil [%], page 189

P_{org} Percentage of organic material in the soil [%], page 189

$P_{r,fol}$ Precipitation reaching the vegetated surface [$mm\ h^{-1}$], page 169

$P_{r,H_v\,or\,L_v}$ Precipitation reaching the vegetated surface from a generic vegetation layer [$mm\ h^{-1}$], page 169

$P_{r,LD}$ Drainage from leaves and stems that reach the ground [$mm\ h^{-1}$], page 173

$P_{r,liq}$ Intensity of liquid rain precipitation [$mm\ h^{-1}$] or [$m\ s^{-1}$], page 124

$P_{r,sno}$ Intensity of snow precipitation [$mm\ h^{-1}$] or [$m\ s^{-1}$], page 124

$P_{r,TR}$ Free throughfall [$mm\ h^{-1}$], page 173

$P_{r,u,sno}$ Snow precipitation that reach the ground [mm], page 162

PAR_B Incoming direct beam *Photosynthetically Active Radiation* [$W\ m^{-2}$], page 104

PAR_D Incoming diffuse *Photosynthetically Active Radiation* [$W\ m^{-2}$], page 104

PAR_{abs} Absorbed *Photosynthetically Active Radiation* [$W\ m^{-2}$], page 104

$PPFD$ Photosynthetic photon flux density [$\mu mol\,CO_2\ s^{-1}\ m^{-2}$], page 149

Pr Neutral turbulent Prandlt number [−], page 128

Q Surface discharge $[mm\ h^{-1}]$, page 191

q Moment order [−], page 300

$q(t)$ Scaled incoming long-wave radiation $[W\ m^{-2}]$, page 30

q^* Specific humidity scale [−], page 128

q_a Specific humidity of the air at the reference height [−], page 120

q_i Vertical outflow from a layer i $[mm\ h^{-1}]$, page 181

q_s Specific humidity of air at the height z_{ow} [−], page 140

Q_v Incoming heat with precipitation $[W\ m^{-2}]$, page 100

Q_{fm} Heat releases from melting (negative) or freezing (positive) of the liquid water content held by the snow $[W\ m^{-2}]$, page 162

q_{ins} Total influx of water to the soil $[mm\ h^{-1}]$, page 175

$Q_{l,in}$ Incoming subsurface lateral fluxes $[mm\ h^{-1}]$, page 181

$Q_{l,out}$ Outgoing subsurface lateral fluxes $[mm\ h^{-1}]$, page 181

q_{runon} Runon flux $[mm\ h^{-1}]$, page 175

$q_{sat}(T_s)$ specific humidity at saturation [−], page 120

Q_{sub} Baseflow flux $[mm^3\ h^{-1}]$, page 190

R Universal gas constant $[J\ mol^{-1}\ K^{-1}]$, page 149

$r(t)$ Function of the solar height h_S, page 30

R^2 Determination coefficient, page 222

R_0 Rainfall pulse $[mm]$, page 300

R_0 Solar constant $[W\ m^{-2}]$, page 37

R_0 “Fair weather region, page 25

R'_0 Extraterrestrial radiation $[W\ m^{-2}]$, page 37

R_A Autotrophic respiration $[g\,C\ m^{-2}\,PFT\ day^{-1}]$, page 200

r_a Aerodynamic resistance $[s\,m^{-1}]$, page 125

r_b Leaf boundary layer resistance $[s\,m^{-1}]$, page 125

R_D Saturation excess runoff $[mm\ h^{-1}]$, page 189

R_d Gas constant for water vapor [$J\ kg^{-1}\ K^{-1}$], page 140

R_d Leaf (dark) respiration at the leaf level [$\mu mol\ CO_2\ m^{-2}\ s^{-1}$], page 151

r_e Effective radius of cloud-droplet size distribution [μm], page 319

R_g Growth respiration [$g\,C\ m^{-2}\,PFT\ day^{-1}$], page 200

R_H Infiltration excess runoff [$mm\ h^{-1}$], page 176

R_m Maintenance respiration [$g\,C\ m^{-2}\,PFT\ day^{-1}$], page 200

r_1 Undercanopy aerodynamic and sublayer non-dimensional resistance [−], page 134

r_2 Undercanopy aerodynamic and sublayer non-dimensional resistance [−], page 134

R_{abs} Absorbed shortwave radiation [$W\ m^{-2}$], page 100

r_{ah} Aerodynamic resistances to heat flux [$s\,m^{-1}$], page 127

r_{am} Aerodynamic resistances to momentum [$s\,m^{-1}$], page 127

r_{aw} Aerodynamic resistances to water vapor [$s\,m^{-1}$], page 127

$R^T_{B,\Lambda}$ Direct beam radiation at the ground surface with topographic effects [$W/;m^{-2}$], page 324

$R_{Bn,\Lambda}$ Direct beam radiation at normal incidence for clear sky [$W\ m^{-2}$], page 37

$R_{D,\Lambda}$ Total diffuse radiation for clear sky conditions [$W\ m^{-2}$], page 38

$R^T_{D,\Lambda}$ Diffuse radiation at the ground surface with topographic effects [$W/;m^{-2}$], page 324

R_{dC} Dark respiration [$\mu mol\,CO_2\ s^{-1}\ m^{-2}$], page 143

$R_{Dd,\Lambda}$ Backscattered radiation for clear sky conditions [$W\ m^{-2}$], page 38

$R_{Dp,\Lambda}$ Incedent diffuse radiation for clear sky [$W\ m^{-2}$], page 37

$R_{Gn,\Lambda}$ Global radiation at normal incidence for clear sky conditions [$W\ \ m^{-2}$], page 38

R_{hy} Hydraulic radius [mm], page 191

r_i Fraction of the root biomass contained in the soil layer i [−], page 181

r_{jv} Scaling factor between J_{max} and V_{max} [$\mu mol\,Eq\ \mu mol\,CO_2^{-1}$], page 151

R_{ltr} Maximum leaf-to-root or shoot-to-root ratio [−], page 208

R_{mF} Foliage maintenance respiration [$g\,C\ m^{-2}\,PFT\ day^{-1}$], page 200

R_{mH} Carbohydrate reserve maintenance respiration [$g\,C\ m^{-2}\,PFT\ day^{-1}$], page 200

R_{mR} Fine roots maintenance respiration $[g\,C\,m^{-2}\,PFT\,day^{-1}]$, page 200

R_{mS} Living sapwood maintenance respiration $[g\,C\,m^{-2}\,PFT\,day^{-1}]$, page 200

r_m Respiration rate coefficient on a $10°C$ base $[g\,C\,g\,N^{-1}\,day^{-1}]$, page 202

r_{nir} Near-infrared reflectances $[-]$, page 104

R_n Net radiation $[W\,m^{-2}]$, page 100

$R^T_{R,\Lambda}$ Reflected radiation at the ground surface with topographic effects $[W/;m^{-2}]$, page 324

R_{ref} Total shortwave radiation reflected $[W\,m^{-2}]$, page 100

$r_{s,min}$ Minimum stomatal resistance $[s\,m^{-1}]$, page 156

r_{soil} Soil resistance $[s\,m^{-1}]$, page 125

$R_{sw,n}$ Global shortwave radiation at normal incidence $[W\,m^{-2}]$, page 41

R_{sw} Global shortwave radiation $[W\,m^{-2}]$, page 41

r_s Stomatal resistance $[s\,m^{-1}]$, page 125

r_{t1} Measure of the inverse of the reduction of turbulence by the canopy $[-]$, page 134

r_{t2} Measure of the inverse of the reduction of turbulence by the canopy $[-]$, page 134

R_{tot} Runoff depth in a basic computational element $[mm]$, page 191

r_{vis} Visible reflectances $[-]$, page 104

Ri_B Bulk Richardson number $[-]$, page 131

RUE Long-term rain use efficiency $[gCm^{-2}mm^{-1}]$, page 276

S Statistical property of precipitation, page 65

s Subscript of generic surface (e.g., *high-vegetation*, (H_v), *low-vegetation*, (L_v), bare soil *bare*, ground, g, water, *wat*, snow, *sno*), page 100

$s(t)$ Function of the solar height h_S, page 30

s_1 Parameter of canopy radiative transfer model, page 108

s_e Effective saturation of soil $[-]$, page 186

$S_h(\vec{x},t)$ Shadow effect $[-]$, page 42

S_m Snow water equivalent converted to water $[mm]$, page 162

S_{dep} Snow depth $[m]$, page 168

S_{fl} Energy gradient of the flow $[-]$, page 191

S_{LAI} Specific leaf area of biomass $[m^2\, LAI\, g\, C^{-1}]$, page 199

S_{leaf} Tissue turnover of green aboveground biomass to litter $[g\, C\, m^{-2}\, PFT\, day^{-1}]$, page 209

S_{m1} Snowmelt in the snowpack at the ground $[mm]$, page 162

S_{m2} Snowmelt in the intercepted snowpack $[mm]$, page 162

$S_{p,In}$ Specific water retained by a vegetated area $[mm\, m^2\, PFT\, area\, m^{-2}\, leaf\, area]$, page 170

S_{root} Tissue turnover of fine roots biomass to litter, $[g\, C\, m^{-2}\, PFT\, day^{-1}]$, page 209

S_{sapw} Sapwood biomass that is converted into heartwood biomass $[g\, C\, m^{-2}\, PFT\, day^{-1}]$, page 209

S^b_{WE} snow water equivalent of ground snowpack before accounting for melting $[mm]$, page 162

SAI Stem area index $[m^2\, stem\, area\, m^{-2}\ \ ground\, area]$, page 99

$SKE_{Pr}(h)$ Skewness of precipitation at time aggregation period $[h]$, page 65

sno Subscript of the snow covered surfaces, page 100

sno, f Subscript for snow under the vegetation, page 117

sno, v Subscript for snow in an open surface, page 117

$Sp_{sno,In}$ Maximum snow load per unit of stem and leaf area $[kg\, m^{-2}]$, page 165

Sp_{wc} Water content in the snowpack $[mm]$, page 166

Sp^M_{wc} Maximum water holding capacity of the snowpack $[mm]$, page 166

T Generic transpiration flux $[mm\, h^{-1}]$, page 181

T Time scale $[h]$, page 300

t Time, page 13

$T(t)$ Air temperature $[^\circ C]$, page 30

t_0 Time at which inter-storm period begins $[h]$, page 25

t_b Length of the inter-storm period $[h]$, page 25

T_d Ground temperature at a certain dampening depth d $[^\circ C]$, page 123

T_f Freezing temperature $[K]$, page 153

T_g Temperature of bare ground $[^\circ C]$ or $[K]$, page 115

$T_g(z_d, t)$ Soil temperature at any time and profile depth $[^\circ C]$, page 123

T_m Average value of air temperature between sea level and Z_{ref} $[K]$, page 316

T_R Length of the post-storm transition period after which the cloud cover process can be considered stationary $[h]$, page 25

t_R Time needed to move the water from a basic computational element to downstream elements $[s]$, page 191

T_s Temperature of a generic surface $[^\circ C]$ or $[K]$, page 115

T_v Temperature of vegetation (leaf temperature) $[^\circ C]$ or $[K]$, page 115

T_ρ PFT population density $[number\,of\,individuals\ \ m^{-2}\,ground]$, page 334

$T_{a,\Lambda}$ Aerosol extinction transmittance $[-]$, page 37

t_{aft} Forward difference between the standard time and the limits of integration of the sun variables $[h]$, page 311

$T_{as,\Lambda}$ Aerosol scattering transmittance $[-]$, page 37

T_a Air temperature at the reference height z_{atm}, $[^\circ C]$ or $[K]$, page 30

$T_{B,\lambda}$ Cloud transmissivity for direct beam flux $[-]$, page 40

t_{bef} Backward difference between the standard time and the limits of integration of the sun variables $[h]$, page 311

T_{cold} Temperature threshold for foliage loss $[^\circ C]$, page 211

$T_{DB,\lambda}$ Cloud diffuse transmissivity for direct radiation $[-]$, page 41

$T_{DD,\lambda}$ Cloud diffuse transmissivity for incident diffuse radiation $[-]$, page 41

T_{dew} Dew point temperature $[^\circ C]$, page 47

t_{DO} Time when the dormant state begins., page 214

$T_{g,\Lambda}$ Uniformly mixed gas absorption transmittance $[-]$, page 37

$T_{H\,rise}$ Local time of sunrise $[local\ hour]$, page 30

$T_{H\,set}$ Local time of sunset $[local\ hour]$, page 30

$T_{H_v\,or\,L_v}$ Transpiration flux from vegetation $[mm\ h^{-1}]$ or $[kg\ m^{-2}\ s^{-1}]$, page 119

$T_{is\,\max}$ Maximum length of the interstorm period $[h]$, page 309

T_{is} Length of the interstorm period $[h]$, page 309

T_{max} Threshold temperature above which all precipitation is rain $[°C]$, page 160

T_{min} Threshold temperature below which all precipitation is in the form of snow $[°C]$, page 160

T_{mon} Monthly temperature $[°C]$, page 57

$T_{n,\Lambda}$ Nitrogen dioxide absorption transmittance $[-]$, page 37

$T_{o,\Lambda}$ Ozone absorption transmittance $[-]$, page 37

$T_{R,\Lambda}$ Rayleigh scattering transmittance $[-]$, page 37

$T_{r,i}$ Total transmissivity of the layer i $[mm^2\ h^{-1}]$, page 190

T_{rad} Radiative temperature $[K]$, page 111

T_{rC} Carbohydrate translocation rate $[g\,C\ m^{-2}\,PFT\ day^{-1}]$, page 208

T_{ref} Reference temperature $[K]$, page 149

$T_{s,LO}$ Prescribed threshold temperature for vegetation growth beginning $[°C]$, page 216

$T_{s,M}$ Average soil temperature of the preceding 30 days $[°C]$, page 216

t_{SE} Time when the senescence state begins., page 214

t_{sls} Time since last snowfall $[s]$, page 165

$T_{v,shd}$ Temperature of shadowed leaves $[°C]$ or $[K]$, page 115

$T_{v,sun}$ Temperature of sunlit leaves $[°C]$ or $[K]$, page 115

$T_{w,\Lambda}$ Water vapor absorption transmittance $[-]$, page 37

Tr_l Carbohydrate translocation rate to green aboveground $[g\,C\ m^{-2}\,PFT\ day^{-1}]$, page 208

Tr_r Carbohydrate translocation rate to fine roots $[g\,C\ m^{-2}\,PFT\ day^{-1}]$, page 208

U Flow velocity $[m\ s^{-1}]$, page 191

U Relative humidity $[-]$, page 47

u^* Friction velocity $[m\ s^{-1}]$, page 128

u_a Wind speed at the reference height $[m\,s^{-1}]$, page 127

u_n Nitrogen dioxide amounts in the atmospheric column $[cm]$, page 38

u_o Ozone amounts in the atmospheric column $[cm]$, page 38

$U_{In_{S_{WE}}}$ Unloading from the intercepted snow $[mm]$, page 162

V_{max} Canopy maximum Rubisco capacity at $25°C$ [$\mu mol\, CO_2\ s^{-1}\ m^{-2}$], page 145

V_{max}^{L} Maximum Rubisco capacity at $25°C$ at leaf scale [$\mu mol\, CO_2\ s^{-1}\ m^{-2}$], page 145

V_m Maximum Rubisco capacity at canopy scale after accounting for temperature dependence [$\mu mol\, CO_2\ s^{-1}\ m^{-2}$], page 149

V_{tree} Volume of wood of a representative tree [$m^3\ ,\ number\, of\, individuals^{-1}$], page 334

$VAR_{Pr}(h)$ Variance of precipitation at time aggregation period [h], page 65

W Cascade weight [$-$], page 300

w Precipitable water in atmospheric column [cm], page 316

W_m Dead wood turnover to litter [$g\, C\ m^{-2}\, PFT\ day^{-1}$], page 213

W_r Water released from the snowpack [mm], page 166

W_s Wind speed [$m\ s^{-1}$], page 51

w_{ch} Width of the stream rectangular section [m], page 191

$W_{TR,i}$ Upward flux of water from layer i [$mm\ h^{-1}$], page 189

W_x Weights that are not 0 or 1, page 300

wat Subscript of the water covered surfaces, page 100

WUE Hourly water use efficiency [$\mu mol\, CO_2\ s^{-1}\ m^{-2}$]/[$mm\ h^{-1}$], page 156

WUE Long-term water use efficiency [$gCm^{-2}mm^{-1}$], page 276

X Rainfall intensity [$mm\ h^{-1}$], page 14

X_0 Likelihood of the long-term observations in the control scenario, page 69

X_i Averages of the realizations of GCMs into the control scenario, page 69

Y Intensity of precipitation, page 13

y Flow depth [mm], page 191

$Y(t)$ Hourly temperature change [$°C$], page 313

Y_h Aggregated rainfall depth, page 13

Y_i Averages of the realizations of GCMs into the future scenario, page 69

z_d Depth into the soil [mm], page 99

z_{atm} Reference height [m], page 125

Z_{Kv} Maximum depth for hydraulic conductivity decline [mm], page 187

z_{oh} Roughness length for heat flux $[m]$, page 127

z_{om} Roughness length for momentum $[m]$, page 125

z_{ow} Roughness length for water vapor flux $[m]$, page 127

Z_{ref} Reference elevation $[m]$, page 316

$Z_{root}(z_d)$ Root profile $[-]$, page 99

Z_R Rooting depth $[mm]$, page 99

$Z_{s,i}$ Depth from the surface to the layer upper boundary $[mm]$, page 181

Z_{wt} Shallow water table depth $[mm]$, page 185

$\beta^{FUT^{-1}}$ Mean waiting time for cell origins after the origin of the storm for future climate conditions $[h]$, page 57

$\eta^{FUT^{-1}}$ Mean duration of the cell for future climate conditions $[h]$, page 57

$\lambda^{FUT^{-1}}$ Mean storm origin arrivals for future climate conditions $[h]$, page 57

$\lambda_0{}^{-1}$ Variance of the average observations in the control scenario, page 69

$\lambda_\circ$ Pore-size distribution index of soil $[-]$, page 186

$\lambda_i{}^{-1}$ Variances of the average of control and future scenario realizations of GCMs, page 69

$\widehat{Sp}_{sno,In}$ Specie specific value of maximum snow load per unit of stem and leaf area $[kg\,m^{-2}]$, page 165

LWP Liquid water path $[g\ m^{-2}]$, page 40

LWP_R Reference value of LWP for overcast condition $[g\ m^{-2}]$, page 42

$r_a{}'$ Undercanopy resistance $[s\,m^{-1}]$, page 125

$R_{dif,\Lambda}$ Diffuse shortwave radiation $[W\ m^{-2}]$, page 100

$R_{dir,\Lambda}$ Direct beam shortwave radiation $[W\ m^{-2}]$, page 100

$S_{vf}(\vec{x})$ Sky view factor $[-]$, page 42

S_{WE} Snow water equivalent of the ground snowpack $[mm]$, page 162

$z_{oh}{}'$ Undercanopy roughness length $[m]$, page 134

List of Acronyms

4AR Fourth Assessment Report

AOD Aerosol Optical Depth

ANN Artificial Neural Network

ANPP Above-Ground Net Primary Production

AR Autoregressive

ARFIMA Autoregressive Fractionally Integrated Moving Average

ARS Agriculture Research Service

AWE-GEN Advanced Weather Generator

CCA Canonical Correlation Analysis

CTS Control Scenario

DEM Digital Elevation Model

DTM Digital Terrain Model

EEA Environmental European Agency

ETCCDMI Expert Team on Climate Change Detection, Monitoring and Indices

FUT Future Scenario

GCM General Circulation Models

GDD Growing Degree-Days

GDP Gross Domestic Product

GPP Gross Primary Production

GWD Geostrophic Wind Direction

IPCC Intergovernmental Panel on Climate Change

LAI Leaf Area Index

LAM Limited Area Model

LWP Liquid Water Path

MCMC Markov Chain Monte Carlo

MKP Mandelbrot-Kahane-Peyriere

MODIS Moderate Resolution Imaging Spectroradiometer

NASA National Aeronautics and Space Administration

NDVI Normalized Difference Vegetation Index

NIR Near Infrared

NPP Net Primary Production

NSRP Neyman-Scott Rectangular Pulse

PAR Photosynthetically Active Radiation

PCMDI Program for Climate Model Diagnosis and Intercomparison

PFT Plant Functional Type

REA Reliability Ensemble Average

RCM Regional Climate Model

RUE Rain Use Efficiency

SAI Stem Area Index

SLP Sea Level Pressure

SRES Special Report on Emissions Scenarios

TAR Third Assessment Report

$T\&C$ Tethys and Chloris

TIN Triangulated Irregular Networks

USDA United States Department of Agricultural

UV/VIS Ultraviolet/Visible

UNEP United Nations Environment Programme

WMO World Meteorological Organization

WUE Water Use Efficiency

Chapter 1

INTRODUCTION

1.1 Scope of research

Natural ecosystems, environments and water resources should be considered a collective good whose preservation is fundamental for the entire society and for a sustainable development. Hydrological and ecological systems present strict linkages with land-use related economic activity. Furthermore, ecosystems at the same time are controlled and exert a control on climate. Many studies indicate that vegetation responds dynamically to climate variability and feeds back to significantly impact land atmosphere interactions and climate predictions (*Bonan*, 1995; *Foley et al.*, 2000; *Chapin III et al.*, 2008; *Bonan*, 2008). Climate, in turn, affects globally the society. The necessity to enhance our capability to forecast environmental changes and the consequences of such changes is unquestionable (*Clark et al.*, 2001; *Scholze et al.*, 2006; *Chapin III et al.*, 2008; *Tang and Bartlein*, 2008), although this is far from be a trivial task (*Wagener*, 2007). There is a growing evidence of recent climate change impacts in ecology and hydrology (*IPCC*, 2007b). For instance, both flora and fauna spanning an array of ecosystems and organizations hierarchies from species to the community level are expected to experience changes (*Walther et al.*, 2002).

Investing efforts on the interdisciplinary studies that involves hydrology, ecology, climatology, soil, and plant sciences, has been regarded very positively (*Bond*, 2003). Forecasting and assessing possible ecosystems changes requires a multi-disciplinary vision. The scientific scope of the thesis is the analysis of the interaction between vegetation dynamics and hydrologic cycle, when climate disturbances take part in the alteration of system boundary conditions. The interrelationship between water cycle and vegetation is governed by numerous processes. The latter processes involve multiple mechanisms (biotic, abiotic, mechanical, chemical), media (soil, water, air, plant tissues), spatial scales (biological cell to global Earth), and temporal scales (seconds to centuries) that are typically addressed in different fields of science. Efforts to merge different scientific backgrounds worldwide are on the way. In the last ten years, a new discipline called "ecohydrology" devoted at the investigation of the coupled dynamics of hydrologic cycle and vegetation has undergone significant

developments, gaining popularity (*Rodriquez-Iturbe et al.*, 1999; *Rodriguez-Iturbe*, 2000; *Rodriguez-Iturbe et al.*, 2001; *Eagleson*, 2002; *Bonan*, 2002; *Rodriguez-Iturbe and Porporato*, 2004). Along the directions mentioned above, this study attempts an interdisciplinary approach, developing opportune numerical tools to model eco-hydrological processes under different climates.

The coupled interaction between hydrological processes and vegetation dynamics is regarded as fundamental for enhancing the predictability of surface energy fluxes, subsurface moisture exchanges and hydrological components generally (*Tague*, 2009). Studying this interaction becomes more important in a changing climate, as non-stationarity in the system may induce changes that can amplify or reduce the feedbacks between hydrological and vegetation processes (*vanDijk*, 2004).

The description of a system where climate, hydrology, vegetation and other components influence each other dynamically for long periods require the entire Earth as study domain. For such a scope General Circulation Models, better if refined with hydrological, oceanic, bio-geochemical sub-models are used for long-term investigations of climate variability. In this scope, climate models have recently started to include and refine their dynamic vegetation components (*Foley et al.*, 2000; *Levis et al.*, 2004; *Bonan*, 2008). In one hand this allows to better understand the impacts of long-term vegetation changes. Vegetation composition or behavior is, indeed, significant and can alter the Earth climate (*Kleidon et al.*, 2000; *Friedlingstein et al.*, 2006; *Alo and Wang*, 2008). On the other hand investigations led at the global scale, do not allow to inquire local dynamics behaviors of hydrological and vegetation processes. This study attempts to bridge this gap using information from global scale climate models and downscaling such information to the smaller scales. The objective is to transfer the relevant effects of climate fluctuations and changes to local ecohydrological systems. There are expected climatic behavior as climate warming and shift in the global precipitation patterns that will very likely affect the hydrological cycle and the vegetation dynamics. An important consequence could be related to the greater likelihood of extreme climate events as predicted by many climate models (*Tebaldi et al.*, 2006).

It is plausible that a different climate will induce a shift in dominant species, as well as increase in vegetation mortality, or conversely, create more favorable conditions for plant to growth. Such changes are influenced and, in turn, have a direct consequence in the hydrological budget, leading to a complex and interactive system. Local feedbacks can act in a way to dampen or boost effects of the global change. Therefore, there is an effective need to provide insights about plant and hydrology interactions under future climate conditions, not only at the Earth scale.

This thesis introduces new numerical-models and what can be defined as a "blueprint" to extend climate disturbances from climate models through local eco-hydrologic systems. Future climate is inferred from a stochastic downscaling technique based on the use of a weather generator. A multi-model ensemble of General Circulation Models (GCMs) realizations is used to compare statistical properties of present and future climate and to derive factors of change (Chapter 3). An advanced weather

generator (*AWE-GEN*) has been developed to reproduce a wide range of temporal scale in weather variables, from the high frequency hourly values to the low frequency inter-annual variability. The generator has been designed to simulate input variables for eco-hydrological models. Specifically, precipitation, cloudiness, air temperature, vapor pressure, shortwave incoming radiation, wind speed, and atmospheric pressure are simulated (Chapter 2). The weather generator includes the possibility to generate "future" climate, modifying its parametrization according to the stochastic downscaling described in Chapter 3.

The observed series, as well as the series of hydro-meteorological variables generated by AWE-GEN for the two climates, present and future, serve as input to a newly developed hydrological model (*Tethys*) coupled with a model of vegetation dynamics (*Chloris*). The hydrological model reproduces all essential components of hydrological cycle resolving the mass and energy budgets at the hourly scale (Chapter 4). The vegetation model parsimoniously parameterizes essential plant life-cycle processes, including photosynthesis, phenology, carbon allocation, and tissue turnover (Chapter 5). Few words must be spent to better explain the choice of the model names. Tethys (Greek: $T\eta\theta\acute{\upsilon}\varsigma$), in Greek mythology, was an archaic Titaness and aquatic sea goddess, daughter of Uranus and Gaia and she was both sister and wife of Oceanus. She was mother of the chief rivers of the world known to the Greeks. She was considered as an embodiment of the waters of the world, for these reasons Tethys has been regarded has the proper name for the hydrological model. Chloris (Greek: $X\lambda\omega\rho\iota\varsigma$), in Greek mythology, was a Nymph associated with spring, flowers and new growth, though different stories about this character exist. She was abducted by (and later married) Zephyr, the god of the west wind. Her Roman equivalent was the goddess Flora, that means "vegetation" and the chlorophyll involved in plant photosynthesis owes its name to the Greek Nymph. For this reason the vegetation dynamic model was named Chloris.

A validation of the coupled application of "Tethys" and "Chloris" is discussed in Chapter 6. The models are tested for different climates and vegetation types worldwide with the scope to assess the capability of the numerical tools to reproduce hydrologic and vegetation metrics. The results obtained are highly satisfactorily and a proof of concept of the proposed methodology is discussed in Chapter 7, for a specific case study in a semiarid desert shrub ecosystem. The proposed blueprint is applied to simulate the present (1961-2000) and future (2081-2100) hydrological regimes for the area of Tucson (Arizona, U.S.A.). A comparison of control and future scenarios is discussed in terms of changes in the hydrological balance components, energy fluxes, and vegetation productivity metrics. An appreciable effect of climate change is observed and its implication are discussed for point scale and distributed domains in Chapter 7. Finally, the major conclusions and possibilities offered by the study are summarized in Chapter 8.

1.2 Implications of the research in risk assessment and mitigation

The implications of this work for risk management and mitigation are multiple. Being mainly focused on hydrology and eco-hydrology issues, the implications of the study are important for water related risks, such as flood risk (*Plate*, 2002; *Raff et al.*, 2009), drought risk (*Middelkoop et al.*, 2001; *Lehner et al.*, 2006), and for ecological risks. Ecological and environmental risks are related to the potential for increased damage to or irreversible loss of unique and threatened ecosystems, changes on forest composition or widespread tree mortality (*Kelly and Goulden*, 2008; *Smith et al.*, 2009a; *vanMantgem et al.*, 2009; *Fensham et al.*, 2009).

Given the extension and complexity of the topic examined in the thesis, the research rather than encompassing all of the aspects of the risk management chain focuses only on the hazard determination part (Figure 1.1). The risk management is a process that involves different sets of actions, depending on the operators involved and on the stage of the analysis (*Plate*, 2002). Risk management can be extended from the narrow sense of managing an existing risk situation to a wider sense where methodologies that offer the possibility to reduce the risk and to plan systems are implemented (*Plate*, 2002). The stages of operational risk management include actions such as hazard determination, vulnerability analysis, planning disaster relief, early warning, disaster response, etc. (Figure 1.1). Not only engineers are involved in these processes, but many other experts as well as local communities and political decision makers.

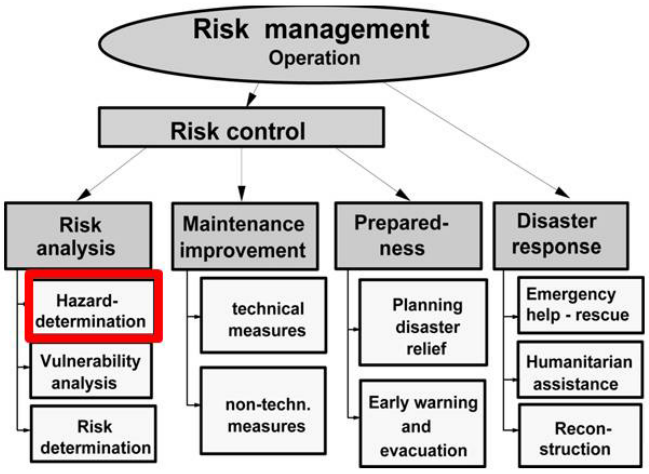

Figure 1.1: Stages of operational risk management, adapted from *Plate* (2002). Hazard determination in a changing climate is the aspect investigated in this research (red square).

Although many different risk management framework have been proposed, the determination of the hazard is always the preliminary step in order to establish solid bases for a comprehensive risk analysis. The determination of the hazard becomes much more important when non-stationarity has to be accounted for. Many water management system and flood protection measures developed throughout the world

have been designed and operated under the assumption of stationarity (*Milly et al.*, 2008). Stationarity is the notion that natural systems fluctuate within an unchanging envelope of variability. This is a foundational concept that permits design and management practices in water-resource engineering and ecology. It implies that any variable has a time-invariant probability density function, whose properties can be estimated from the observed record (*Milly et al.*, 2008). Nowadays, the growing human related pressure such as changes in land use or climate change have led to question the hypothesis of stationarity (*Milly et al.*, 2008; *Sivapalan and Samuel*, 2009). This implies a need for researches that identify patterns of changes, their uncertainties and transfer this information on the relevant environmental variables (*Porporato et al.*, 2006; *Sivapalan and Samuel*, 2009). There are studies that underline how climate change is going to affect risk evaluation and opening new challenging problems. For instance climate change can have important implications on flood risk evaluation (*Milly et al.*, 2002; *Hunt*, 2002; *Bronstert*, 2003; *Hamlet and Lettenmaier*, 2007; *Raff et al.*, 2009) or in risk-based planning of water resources management (*Middelkoop et al.*, 2001), such as the assessing of reservoir operations (*Brekke et al.*, 2009). Drought frequency alterations due to climate change can also affect ecological risks. Severe drought in moist tropical forests can exacerbate the risk of forest flammability and tree mortality (*Nepstad et al.*, 2004). Drought occurrence is also one of most widespread climate disasters affecting agricultural production (*Li et al.*, 2009). In this case the quantification of ecological risks is further complicated by the active role that crops or plants may play in a different climate. The expected consequences of climate change have also raised other reasons for concern with implications for non-conventional types of risks such as risk to unique and un-restorable systems, risks related to extreme weather events and uneven distribution of impacts across the Earth (*Smith et al.*, 2009a).

In this context, the thesis offers a methodology to estimate meteorological and ecohydrological variables in a non-stationary climate. The hazards that can be retrieved from such an analysis, e.g., extreme rainfall, flood frequency can be considered representative of *future* climate changed conditions and not of the past climate. This opens a wide set of opportunities in terms of risk analysis and risk management planning, since the possibility to generate future hazard scenarios allow to overcome the traditional risk analysis methodology based on historical observation. The price to pay to extend hazard quantification in the future is related to an increase of uncertainty. There can be situations where the increase in uncertainty can be dramatic. The possibility that the found uncertainty would be so large to question the practical implications of the research cannot be excluded a priori. However, few alternatives if any exist when the aim is to make long-term non-stationary predictions.

A number of studies have attempted to explicitly quantify the impact of climate change on flood and drought risks (*Lehner et al.*, 2006). The proposed methodology rather than focus on a quantification of changes in risk metrics, attempts to build a sound methodology to detect at the local spatial scale ecohydrological changes. Thus, although not inferred directly, the opportunity to determine the consequences

of hydrological variability in the severity and magnitude of flood, drought and ecological risks is embedded into the proposed method. This is particular important because there is a growing consensus that hydrological cycle is going to change (*IPCC*, 2007a; *Barnett et al.*, 2008) and that potentially significant adverse implications can result from these changes (*IPCC*, 2007a; *EEA*, 2007; *Bates et al.*, 2008).

Chapter 2

"AWE-GEN" AN HOURLY WEATHER GENERATOR

2.1 Introduction

Records of meteorological variables around the world are often very short, with substantial gaps and low spatial coverage. This creates a problem of data inadequacy in numerous applications. To overcome such problems, weather generators as the tools capable of generating consistent time-series of climatic variables have been proposed and used in the past (*Wilks and Wilby*, 1999). Specific motivations for using a weather generator can be found in several fields of science. These models have been significantly used in agricultural applications studies of crop sensitivity and productivity to climate realizations (*Semenov and Porter*, 1995; *Mavromatis and Hansen*, 2001; *Dubrovský et al.*, 2004). In water resource engineering, climate simulators were used to generate long time series of precipitation that are required for flood risk analysis or water resource evaluations (*Fowler et al.*, 2000; *Wheater et al.*, 2005). Other possible applications are related to the generation of inputs to hydrological models (e.g., *Rigon et al.*, 2006; *Ivanov et al.*, 2008a), ecosystem models, or in long-term land management and erosion studies (e.g., *Collins et al.*, 2004; *Istanbulluoglu et al.*, 2004). Sometimes the weather generators are employed also to replace missing data from recorded time-series.

The generation of meteorological variables in a weather generator is frequently based on empirical statistical models. In these cases, statistical properties and correlations among variables are inferred from observed data. Precipitation is the most important variable in weather generators. It is frequently modeled by using an approach of separating the process of precipitation occurrence from the problem of determining the precipitation amount (*Wilks*, 1999; *Wilks and Wilby*, 1999; *Srikanthan and McMahon*, 2001). Other climate variables, or their residuals, since the mean and variance are typically removed, are simulated by means of regression equations. The regression parameters are usually estimated differently for wet, dry, and transitional states. The time scales at which these variables are simulated can range from daily to annual. A number of well known models can be listed in the

category of empirical statistical approaches, such as the WGEN (*Richardson*, 1981; *Richardson and Wright*, 1984), the WXGEN model (*Sharpley and Williams*, 1990) used in the hydro-sedimentological SWAT model, the CLIGEN model (*Nicks et al.*, 1995) used in the hydro-sedimentological WEPP model, LARS-WG (*Semenov and Barrow*, 2002), ClimGen (*McKague et al.*, 2003), Met&Roll (*Dubrovský et al.*, 2004).

A physically consistent approach to generate meteorological variables is to directly use dynamic meteorological models, that solve the non-linear partial differential equations governing the dynamics of the atmosphere (*Cox et al.*, 1998). While being attractive, this approach has been mainly used for weather forecasting but not for long-term weather realizations, given the computational feasibility constrains of such simulations.

A third intermediate approach can be defined as the jointly use of empirical statistical relations and physically-based methods. In essence, the approach adopts stochastic models using some description of the underlying physical phenomena of the process, such as a simulation of rain cells and clustering, the cloudiness dependence on precipitation, the dependence of temperature on long- and short-wave radiation, etc. This third approach has received particular attention in rainfall modeling but it has been almost neglected in the implementation of complete climate simulators. A recent effort to fill this gap was undertaken by *Ivanov et al.* (2007), based on the earlier developed methodology of *Curtis and Eagleson* (1982), who proposed a weather generator at the hourly scale. While a number of variables are simulated stochastically, the approach attempts to preserve the underlying physical relations among them. The use of causal physical relationship within a weather generator allows to simulate finer temporal scale (hourly or minute). Using an empirical statistical weather generator for the same purpose is more difficult since statistical correlations become more complex to model at shorter time scale.

Wilks and Wilby (1999) underlined that testing a weather generator in attempt to only reproduce the mean climate, for the way itself in which weather generators are realized, is somewhat naive. The real challenge is in reproducing higher order moments, correlations among the variables, and low and high frequency properties such, as extreme events and inter-annual variability. The latest efforts to test and improve weather generators are directed towards these directions (*Wilks*, 1999; *Hansen and Mavromatis*, 2001; *Kyselý and Dubrovský*, 2005; *Fowler et al.*, 2005; *Kilsby et al.*, 2007). A comparison between inter-annual variability of observed and simulated data is a crucial test of reliability of a weather generator. For instance, it has been noticed previously that a common characteristic of weather generators is underestimation of the inter-annual variability (*Wilks*, 1989, 1999; *Wilks and Wilby*, 1999; *Srikanthan and McMahon*, 2001; *Kyselý and Dubrovský*, 2005). Several studies attempted to quantify this underestimation sometimes referred to as "overdispersion" (*Katz and Parlange*, 1998; *Wilks*, 1999). The random generation of numbers produce in the realizations a smaller variance than that of the corresponding observed data. *Wilks and Wilby* (1999) suggest that a possible explanation for the missing variance is that climate statistics change somewhat in the real world from year to year. A

simple weather generator, with the underlining assumption of stationarity, cannot capture such a variation. In order to capture such a behavior, the model internal parameters should change in time, thus violating the stationarity assumption.

The issue of under-predicting inter-annual variability and extremes is the most difficult challenge for weather generators. Especially when a weather generator is used for simulation of future scenarios, both low and high frequency statistics should be tested (*Kyselý and Dubrovský*, 2005; *Semenov*, 2008). The capability of such models to reproduce extremes is related to the internal structure of the model. On the other hand, the capability to generate inter-annual variability is introduced by conditioning the model with external information. A common approach is to link parameters of the weather generator to some properties of large-scale atmospheric circulation. For instance, different sets of weather generator parameters can be used for different ranges of values assumed by large-scale atmospheric properties. Several climate characteristics have been used for this scope: the mean monthly sea level pressure (SLP) (*Katz and Parlange*, 1993); the geostrophic wind direction (GWD) (*Kiely et al.*, 1998); the air masses provenance (*Wallis and Griffiths*, 1997); the objective Lamb weather type of atmospheric circulation (*Fowler et al.*, 2000); and the low-frequency realizations of monthly variable such as precipitation (*Wilks*, 1989) or temperature (*Hansen and Mavromatis*, 2001; *Kyselý and Dubrovský*, 2005).

The possibility to condition models externally allows one to use a weather generator when constructing climate change scenarios. The dependence of weather generator parameters on properties of large-scale atmospheric circulation links weather generators and General Circulation Models (GCMs). GCM realizations, in fact, can provide information about climate properties suitable to condition a weather generator. The GCM-predicted changes of large atmospheric patterns can therefore directly affect the weather generator parametrization and thus their realizations. *Wilks* (1992) pioneered the use of weather generator for climate change studies, and there is a recent evidence of a growing interest in such studies (*Semenov and Porter*, 1995; *Katz*, 1996; *Semenov and Barrow*, 1997; *Fowler et al.*, 2000, 2005; *Elshamy et al.*, 2006; *Kilsby et al.*, 2007; *Manning et al.*, 2009).

An hourly weather generator, AWE-GEN (Advanced WEather GENerator), is introduced in this work. The generator is capable of reproducing low and high-frequency characteristics of hydro-climatic variables and essential statistical properites of these variables. The weather generator employs both the physically-based and stochastic approaches and is a substantial evolution of the model presented by *Ivanov et al.* (2007). Enhancements of the original formulation are the following: a new formulation of the precipitation module based on the Poisson-Cluster process; a new formulation of the module simulating vapor pressure instead of dew point temperature; simulation of the daily cycle of wind speed; significant modifications of the shortwave radiation module, in particular the inclusion of explicit simulation of the photosynthetically active radiation; minor modifications of the cloudiness and air temperature components; and a new model to reproduce time-variability of the atmospheric pressure. An important capability for simulating the inter-annual vari-

ability of the precipitation process has been added. The capability to reproduce a wide set of statistics including extremes is also tested. Furthermore, a procedure to take into account non-stationary change of climate has been incorporated in the AWE-GEN framework. The procedure is based on a stochastic downscaling of GCM predictions. The variables simulated by the weather generator at hourly scale are precipitation, cloud cover, shortwave radiation with partition into various type and spectral bands, air temperature, vapor pressure, wind speed, and atmospheric pressure. These variables are typically necessary as inputs for ecological, hydrological, geomorphological, and crop-dynamics models.

Although I am aware of the possible inaccuracy related to the random number-generation (*Meyer et al.*, 2007), this problem has not been addressed herein. The random generator component available in *Matlab*© software is used.

2.2 Data and model validation

The performance of AWE-GEN has been tested to reproduce observations at several locations with different climates. The weather generator has been validated for 10 airport meteorological stations located in the USA: Tucson (Arizona), Muskegon (Michigan), Albuquerque (New Mexico), Boston (Massachusetts), Nashville (Tennessee), San Francisco (California), Chicago (Illinois), Miami (Florida), Philadelphia (Pennsylvania), Atlanta (Georgia) and one meteorological station in Italy (Firenze University). Time series of hourly meteorological variables ranging in duration from 8 to 40 year period were available for these stations. The data for the USA location have been downloaded by *Webmet* meteorological resources center (http://www.webmet.com/). The data for Firenze have been provided by the Tuscany Functional Center. It should be noted that given gaps or absence of some meteorological variable, the test has not been realized for all variables in every station. The results of weather generator performance are shown only for Boston (MA), where time series of 80 years are simulated starting with 18 years of observations. The accuracy of the results is very similar among all the stations. Information about the data are available in the Webmet web-site.

The precipitation component has been further tested for four stations in the Tuscany region (Italy): Arezzo, Camaldoli, Vallombrosa and Firenze Ximeniano (data from: Tuscany Functional Center). Twenty-five years at 20 minute resolution precipitation were available for these locations. This dataset for its particularly accuracy has been the object of previous studies to detect precipitation properties and developing rainfall models (*Becchi et al.*, 1994; *Veneziano and Iacobellis*, 2002; *Cowpertwait et al.*, 2002).

2.3 Precipitation

Existing weather generators emphasize precipitation as the primary variable of interest (*Wilks and Wilby*, 1999; *Srikanthan and McMahon*, 2001). The underlying

reason is that, due to the nature of coupling physical mechanisms, other hydro-climatic variables are affected directly or indirectly by the precipitation occurrence. Consequently, a correct reproduction of the precipitation regime influences all other weather variables. The use of models of stochastic precipitation has been addressed by the scientific community for many years, given their possible use in flood design, agricultural and ecological applications, etc. There is, indeed, a need of precipitation data across a range of time scales and for different purposes such as design of storm-water sewerage systems, flood hydrographs, and reservoir size. Among the first contributions in this field are worth to be mentioned the works of *LeCam* (1961); *Todorovic and Yevjevich* (1969); *Todorovic and Woolhiser* (1975); *Waymire and Gupta* (1981a,b,c); *Foufoula-Georgiou and Lettenmaier* (1987). The first models of rainfall were developed treating separately the rainfall occurrence and rainfall intensity models. Frequently, the occurrences of wet and dry states were simulated with the Markov chain and non-zero precipitation with statistical distributions such as the Exponential or the Gamma distribution. Although more complex, physically-based methods have been proposed, it is still common that weather generators use this approach to generate precipitation.

Generation of stochastic precipitation is mainly achieved with two methods: using models based on multifractality and Poisson-cluster models. Other approaches exist, but they have received less attention. The multifractal approach is based on observed scale invariance of the precipitation process, called multifractality. Multifractality implies that the rainfall process looks statistically the same at small and large scales, except for simple transformations (*Veneziano and Iacobellis*, 2002). The number of models that use multifractal scaling of rainfall has grown in the past decade, as testified from the literature: *Koutsoyiannis et al.* (1998); *Veneziano and Furcolo* (2002); *Veneziano et al.* (2002, 2006). This typology is considered here only in the scope of rainfall disaggregation. Multifractality theory is at the base of many rainfall disaggregation models (*Onof et al.*, 2005; *Gaume et al.*, 2007). Insights on multifractality and rainfall disaggregation techniques are provided in Appendix A.1 in the scope of describing a method to disaggregate rainfall from hourly to five minute intervals.

In AWE-GEN, the method based on the Poisson-cluster model is used to simulate rainfall (*Onof et al.*, 2000). The development of the Poisson-cluster models has began with *Rodriguez-Iturbe et al.* (1987) and *Rodriguez-Iturbe and Eagleson* (1987) and was further developed by *Rodriguez-Iturbe et al.* (1988), *Entekhabi et al.* (1989) and *Cowpertwait* (1991); *Cowpertwait et al.* (1996). Both Neyman-Scott and Bartlett-Lewis types were used as stochastic point process. These two are different types of Poisson processes of storm origins. In Poisson processes each storm has associated a random number of rectangular pulse (cells) with random intensity and duration. Different cells and storms may overlap to produce the total hyetograph. At any time the rainfall is the sum of the cells active at that time, eventually belonging to different storms. The difference between the Neyman-Scott and the Bartlett-Lewis types, is concentrated in the method of cell origin displacement within a storm. In

the Neyman-Scott model process the time between storm origin and origin of each cell is considered as a random variable. Conversely, in the Bartlett-Lewis model, the time between cell origin is considered to be a random variable. A schematic representation of the two models is shown in Figure: 2.1.

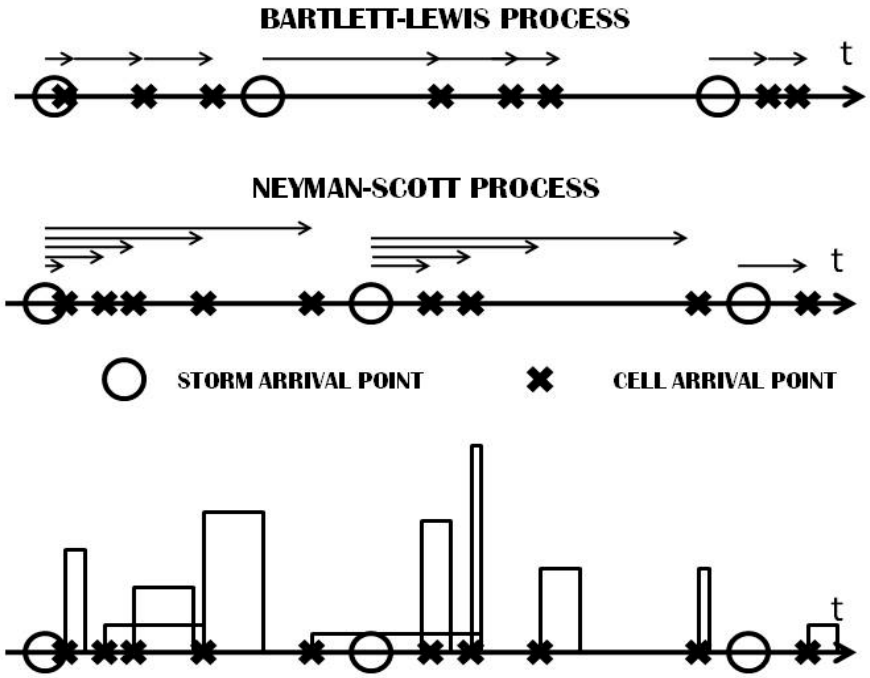

Figure 2.1: Schematic representation of Neyman-Scott and Bartlett-Lewis models with rectangular pulses.

Poisson-cluster models development has continued, over the years, extending the models into two-dimensional space, in order to provide a framework for modeling multi-site and spatio-temporal rainfall data (*Cowpertwait*, 1995; *Northrop*, 1998; *Cowpertwait et al.*, 2002; *Wheater et al.*, 2005; *Cowpertwait*, 2006; *Leonard et al.*, 2008). Another improvement has been introduced explicitly calculating the theoretical function of the third moment of the rainfall process, in order to better fit the extreme values (*Cowpertwait*, 1998; *Cowpertwait et al.*, 2002). The process has been also generalized allowing convective and stratiform rain cells to occur (*Cowpertwait*, 1994). This purpose was reached overlapping two rectangular pulse models, thus enhancing the capability of the model in reproducing finer structure of the rainfall process (*Cowpertwait*, 2004; *Cowpertwait et al.*, 2007).

Reliability of the Poisson-cluster models has been confirmed by a comparative analysis of its performance with numerous observed time series of precipitation. The model has demonstrated the capability to fit the essential characteristics of the precipitation process at a large number of time scales, including extreme events (*Cowpertwait*, 1991; *Cowpertwait et al.*, 1996; *Cowpertwait*, 1998; *Onof et al.*, 2000; *Cowpertwait et al.*, 2002; *Burton et al.*, 2008).

2.3.1 Neyman-Scott Rectangular Pulse model

The total intensity of precipitation $Y(t)$ of the Neyman-Scott Rectangulr Pulse (*NSRP*) model is the sum of the overlapping cells at any time t. This statement could be expressed formally with equation (2.1):

$$Y(t) = \int_{u=0}^{\infty} X_{t-u}(u) dN(t-u)\,, \tag{2.1}$$

where $dN(t-u)$ is 1 if there is a cell at the time $t-u$ and 0 otherwise, and $X_{t-u}(u)$ is the intensity at time t owing to a cell with origin at $t-u$. Given the characteristic of the rainfall measurements, rainfall data are available in aggregated form. Therefore, theoretical derivations of the statistical properties of the aggregated process $Y_h^{(i)}$ are needed to estimate the parameters of the model. The aggregated rainfall depth in the i^{th} interval of arbitrary length h is:

$$Y_h^{(i)} = \int_{(i-1)h}^{ih} Y(t) dt\,. \tag{2.2}$$

Under the hypothesis of stationarity the n^{th} moment of the process is $E\{(Y_h^{(i)})^n\} = E\{(Y_h^{(j)})^n\}$ and the indexes i and j could be omitted (*Cowpertwait*, 1998). The theoretical properties of a Neyman-Scott rectangular pulse model for a single site were derived up to the second order moments of Y_h by *Rodriguez-Iturbe et al.* (1987). The probability that an arbitrary interval of length h is dry was derived by *Cowpertwait* (1991) and the third moment was successively derived by *Cowpertwait* (1998). The theoretical expressions for the statistical properties of the *NSRP* model are a function of the distribution chosen for the random processes within the model.

The Neyman-Scott Rectangular Pulse (NSRP) method used to generate the internal structure of precipitation process in AWE-GEN is primarily based on the approach of *Cowpertwait* (1998); *Cowpertwait et al.* (2002); *Cowpertwait* (2004). The storm time origin occurs as a Poisson process with the rate λ $[h^{-1}]$, a random number of cells C is generated for each storm according to the geometrical distribution with the mean μ_c $[-]$. Cell displacement from the storm origin is assumed to be exponentially distributed with the mean β^{-1} $[h]$. A rectangular pulse associated with each precipitation cell has an exponentially distributed life time with the mean η^{-1} $[h]$ and intensity X $[mm\ h^{-1}]$. The latter is distributed according to the Gamma distribution with the parameters α and, θ. X must be positive and its probability density function is:

$$P(X) = \frac{X^{\alpha-1} e^{-X/\theta}}{\Gamma(\alpha)\ \theta^{\alpha}}\,. \tag{2.3}$$

An overview of the *NSRP* parameters is provided in table 2.1. The distributions adopted for the random process within the *NSRP* model fully define the statistical properties of the aggregated process $E\{Y_h\}$ over an arbitrary time-scale h (*Cowpert-*

wait, 1998). The mean is:

$$\mu_h = E\{Y_h\} = \lambda \mu_c E\{X\} h/\eta\,, \tag{2.4}$$

and the second moment is:

$$\begin{aligned}\gamma_{h,l} &= COV\{Y_h^i, Y_h^{i+l}\} = \lambda\eta^{-3} A(h,l)[2\mu_c E\{X^2\} + [E\{X\}]^2\beta^2 E\{C^2 - C\}/(\beta^2 - \eta^2)] \\ &\quad -\lambda[E\{X\}]^2 B(h,l) E\{C^2 - C\}/[\beta(\beta^2 - \eta^2)]\,,\end{aligned} \tag{2.5}$$

where $A(h,l)$ and $B(h,l)$ are defined in *Cowpertwait* (1998) (see Appendix A.2). The moments of the rainfall intensity for the Gamma distribution are $E\{X^n\} = \theta^n\Gamma(\alpha + n)/\Gamma(\alpha)$; and for the geometric distribution with mean equal to μ_c are $E\{C^2 - C\} = 2\mu_c(\mu_c - 1)$ and $E\{(C^2 - C)(C - 2)\} = 6\mu_c(\mu_c - 1)^2$. The third moments $\xi_h = E\{[Y_h - E\{Y_h\}]^3\}$ is also defined in *Cowpertwait* (1998) (see Appendix A.2). The probability that an arbitrary interval of length h is dry $\Phi(h) = P(Y_h = 0)$ is taken from *Cowpertwait* (1991) and *Cowpertwait et al.* (1996) with some modifications to make use of the geometrical distribution rather than the Poisson distribution in the generation of the random number of cells within a storm (see Appendix: A.2).

Table 2.1: The parameters of point Neyman-Scott Rectangular Pulse model.

Parameter	**Explanation**
λ	1/(mean storm origin arrivals) $[h^{-1}]$
β	1/(mean waiting time for cell origins after the origin of the storm) $[h^{-1}]$
η	1/(mean duration of the cell) $[h^{-1}]$
μ_c	Mean number of cell per storm $[-]$
α	Shape parameter of the Gamma distribution of rainfall intensity $[-]$
θ	Scale parameter of the Gamma distribution of rainfall intensity $[mm\ h^{-1}]$

2.3.2 Parameter fitting procedure

The utilized model has six unknowns and, thus, at least six equations are required in order to estimate these parameters. An exact estimation of the six parameters would need six statistical properties or moments $\hat{f}_i$ inferred from the observed data. The $\hat{f}_i$ should be successively compared with the statistical properties obtained from the theoretical expressions used in the *NSRP* model f_i. I.e., theoretically the following equation should be verified:

$$f_i(\lambda, \beta, \eta, \mu_c, \alpha, \theta) = \hat{f}_i\,. \tag{2.6}$$

From equation (2.4) and the equation for the first moment $E\{X\}$, one of the six parameters could be expressed in terms of the mean $E\{Y_h\}$ and the remaining parameters. Usually, θ is derived as a function of the other parameters (*Cowpertwait*,

1998; *Cowpertwait et al.*, 2002, 2007):

$$\theta = \frac{\eta \, E\{Y_h\}}{\alpha \, \lambda \, \mu_c \, h} \, . \tag{2.7}$$

Including equation (2.7) the problem reduces to the estimation of only five parameters. Rather than fitting exactly the parameters of the model, it is more desirable to use a wider set of statistical properties (for example $m > 5$) and find the best approximate solution. This solution allows to better reproduce a larger set of statistical properties instead of exactly reproducing few. In order to achieve this purpose, an objective function F_{obj} is defined following the procedure proposed by *Cowpertwait* (2006); *Cowpertwait et al.* (2007):

$$F_{obj} = \sum_{i=1}^{m} \omega_i \left[\left(1 - \frac{\hat{f}_i}{f_i} \right)^2 + \left(1 - \frac{f_i}{\hat{f}_i} \right)^2 \right] , \tag{2.8}$$

where ω_i are the weights in the objective function to emphasize the importance of certain statistical properties over the others. The choice of the m statistical properties, of $\hat{f}_i$, and of the weights ω_i into the objective function depends on the primary scope of the rainfall model. In the weather generator context, $\hat{f}_i$ are selected such that allow the model to fit a wide set of statistical properties without emphasizing any one in particular. After having carried out a large number of tests using available data, the four following properties were selected: the coefficient of variation $C_v(h) = \sqrt{\gamma_{h,0}}/\mu_h$; the lag-1 autocorrelation $\rho(h) = \gamma_{h,1}/\gamma_{h,0}$; the skewness $\kappa(h) = \xi_h/\gamma_{h,0}^{3/2}$; and the probability that an arbitrary interval of length h is dry, $\Phi(h)$. The utilized fitting procedure assumes that rainfall time series are available as the coarsest temporal resolution of 1 hour. It specifically uses the statistical properties of the rainfall process at four different time scales h: 1, 6, 24, and 72 hours. The weights ω_i are taken equal to "1" for all statistical properties and for the four different aggregation times. Totally, $m = 16$ statistical properties of rainfall observations are used to fit the five parameters $(\lambda, \beta, \eta, \mu_c, \alpha)$ and $E\{Y_1\}$ is finally used to estimate θ. Given the high non-linearity in the parameter functions, the automated procedure should be well constrained to avoid unrealistic values of the parameters (e.g., *Cowpertwait* (1998)). The adopted feasible regions are taken from *Cowpertwait* (1998): $0.0001 < \lambda < 0.05$; $0.01 < \beta < 0.99$; $1 < \mu_c < 80$; $0.5 < \eta < 30$; $0.1 < \alpha < 20$; in comparison to the original formulation, the regions of validity for η, μ_c, and α are restricted to reduce the tendency of the optimization procedure toward the boundaries. Overall, the simplex method (*Nelder and Mead*, 1965) is used as a minimization method for the imposed objective function. The method has been previously employed with good performance also in terms of its convergence characteristics (*Cowpertwait*, 1998; *Cowpertwait et al.*, 2007). In order to take into account the seasonality of site climatology, the parameters can be estimated on a monthly basis, i.e., six parameters for each months need to be inferred to completely define the *NSRP* model.

2.3.3 Low-frequency properties of the rainfall process

Previous efforts of validation of the *NSRP* model at larger time intervals, for instance at the yearly time scales, have indicated that the variance of the simulated process was smaller than the one inferred from observed data. As already stated in the introduction, due to their nature the conventional weather generator techniques often fail to capture entirely inter-annual variability (*Wilks and Wilby*, 1999). This observation is related to the underlying assumption of stationarity of precipitation process. This underestimation of inter-annual variability can be problematic for numerous applications in hydrology or when climate change scenario needs to be explicitly introduced. *Kilsby et al.* (2007) highlight that this problem is present not only in the framework of weather generators but in the physically-based climate models as well. Attempts to resolve this issue have typically conditioned externally the parameters of the rainfall models using climate characteristics, such as monthly statistic (*Wilks*, 1989) or indices of large-scale circulation (*Kiely et al.*, 1998). These approaches have been especially applied with Markov chain or renewal process of precipitation. However, examples to link *NSRP* to patterns of large-scale circulation also exist (*Fowler et al.*, 2000, 2005). The external conditioning allows one to produce realizations for non-stationary climates. For instance information about climate change can be introduced when "future" evolution of large-scale circulation patterns can be inferred from climate models.

In this study, to introduce the capability for reproducing low-frequency properties of the precipitation process, the total annual precipitation generated with the *NSRP* model is selected externally, on the basis of an annual precipitation model, as explained later in this section. Following this approach, the variance and autocorrelation properties of precipitation process at the annual scale are preserved. However, this does not assure the preservation of monthly variance of precipitation. This is a little counter-intuitive but preserving the monthly variance does not reflect on preserving also the annual variance. This statement has been numerically verified using an autoregressive model AR(1) to reproduce monthly time series of precipitation (after removing seasonality). The preservation of the annual variance, without preservation of the monthly one may induce a theoretical error. For instance, extremely drought years may be obtained with a uniformly lower amount of precipitation in all of the months rather than due to a drastic reduction of rainfall in a few months and vice-versa for extremely wet years. This artifact may become larger as the difference between the simulated variance of monthly precipitation and the observed one increases. Fortunately, the "overdispersion" at monthly scale is generally limited and the model errors due to the utilized methodology are thus negligible, as shown in the following analysis. Furthermore, it can be argued that inter-annual variability of precipitation is the the preferred property to be preserved for most agricultural, ecological, and hydrological applications.

Markov-type models have been commonly used to reproduce annual time series of precipitation (*Srikanthan and McMahon*, 1982, 2001), although they neglect the

long term persistency of the process (*Koutsoyiannis*, 2003a). In this study the inter-annual variability of precipitation is simulated using an autoregressive order-one model, AR(1), with the skewness modified through the Wilson-Hilferty transformation (*Wilson and Hilferty*, 1931; *Fiering and Jackson*, 1971):

$$P_{yr}(i) = \overline{P}_{yr} + \rho_{P_{yr}}(P_{yr}(i-1) - \overline{P}_{yr}) + \eta(i)\sigma_{P_{yr}}\sqrt{1-\rho_{P_{yr}}^2}\,, \tag{2.9}$$

where $\overline{P}_{yr}$ $[mm]$ is the average annual precipitation, $\sigma_{P_{yr}}$ $[mm]$ is the standard deviation, and $\rho_{P_{yr}}$ is the lag-1 autocorrelation of the process. The term $\eta(i)$ represents the random deviate of the process and is skewed according the Wilson-Hilferty transformation:

$$\eta(i) = \frac{2}{\gamma_n}\Big(1 + \frac{\gamma_n\,\varepsilon(i)}{6} - \frac{\gamma_n^2}{36}\Big)^3 - \frac{2}{\gamma_n}\,, \tag{2.10}$$

where the skewness of $\eta(i)$ is $\gamma_\eta = (1-\rho_{P_{yr}}^3)\gamma_{P_{yr}}/(1-\rho_{P_{yr}}^2)^{1.5}$; $\gamma_{P_{yr}}$ is the skewness inferred from observations and $\varepsilon(i)$ is the standard normal deviate. The Wilson-Hilferty transformation is not exact. However, the lag-one autocorrelation and the coefficient of skewness of annual rainfall data are usually within the limits of validity of the transformation and thus no significant errors are introduced (*McMahon and Miller*, 1971).

In this research, as a first step the time series of annual precipitation, n years-long is generated once the parameters ($\overline{P}_{yr}$, $\sigma_{P_{yr}}$, $\rho_{P_{yr}}$, $\gamma_{P_{yr}}$) are determined from observations. The output of the *NSRP* model that captures intra-annual precipitation regime (the high-frequency properties) is coupled with the AR(1) model that reproduces precipitation inter-annual variability (the low-frequency properties) in the following manner. First, the *NSRP* model is used to simulate precipitation series at the hourly time scales. The obtained total precipitation is then compared with the annual value obtained with the autoregressive model (2.9). If the difference between the two values is larger than a certain percentage $\check{p}$ of the measured long-term mean annual precipitation, the simulated one-year long hourly series are rejected and a new series is generated. Once the difference between the two values is below the $\check{p}$ threshold, the simulated with the *NSRP* model time series of precipitation are accepted and considered representative for that year. The rejection threshold $\check{p}$ can be chosen according to the information about observational errors of annual precipitation. An illustrative example of convergence between the two methods is shown in Figure 2.2

Given the stationary nature of the *NSRP* model, the search of "suitable" years can be computationally exhaustive for locations characterized by a high variance of annual precipitation. This may happen in years that are characterized by precipitation strongly deviating from the average value. For instance, it can be the case when a very high variance of annual precipitation is recorded or when observed time series have limited duration. The short duration does lead to a larger variance and does not permit a correct evaluation of the internal parameters of the *NSRP*

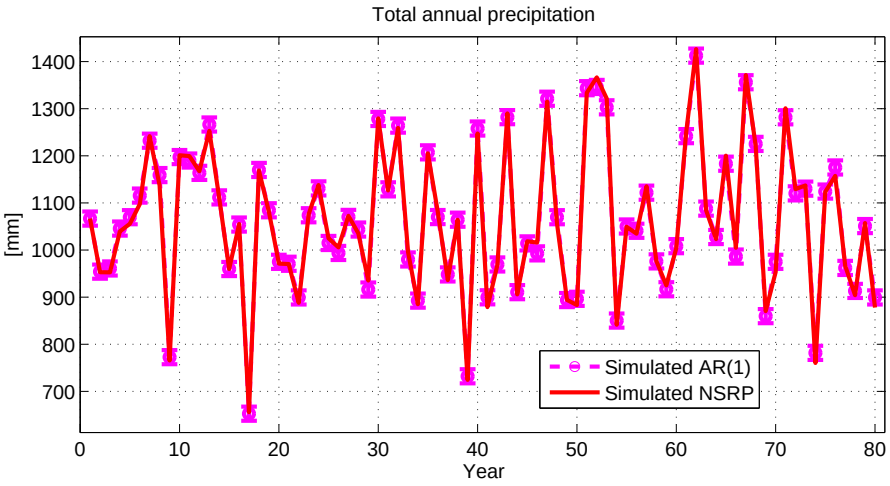

Figure 2.2: The annual precipitation simulated with the *NSRP* model (red line) after the external selection based on the AR(1) precipitation series (magenta dots) has been carried out. The vertical bars denote the $\check{p} = 2.5\%$ of the long-term average annual precipitation.

model. The computationally exhaustive search of "suitable" years is only related to time constrains, because although it is not easily demonstrable, it should be expected that some rare combination of random numbers in the *NSRP* model would reproduce total annual precipitation equal to the one produced by the annual model, AR(1). In order to reach the convergence in a reasonable computational time, an adjustment procedure similar to that proposed by *Kyselý and Dubrovský* (2005) is introduced after a pre-defined number of iterations without a satisfactory match between precipitation generated by AR(1) and annual total generated by *NSRP*. The simulation is stopped and annual precipitation of *difficult* years is generate applying a correction factor to the hourly precipitation series. In such cases, the hourly time series one year-long produced by the *NSRP* model are multiplied by a correction factor to match the precipitation simulated with the annual model. As concluded from numerous experiments carried out by the author, the above adjustments were found to be necessary only for a few years in a millennium, for stations with limited records of observational data.

Overall, the proposed procedure might somewhat alter the intra-annual structure of the rainfall process because of the correction factors and since the output of the *NSRP* model is sampled in a non-random fashion. *Kyselý and Dubrovský* (2005), justified such an adjustment with the fact that the magnitude of the correction is several times lower than the inter-diurnal or diurnal variability and consequently, the effect of the procedure is insignificant. For precipitation this statement can be questionable but note that the correction is applied in a very small fraction of years and only for locations characterized by a large inter-annual variability. The corrections are also minimized choosing among the rejected years simulated with the *NSRP* model, the ones with the total annual precipitation as closest as possible to the unmatched year simulated by the annual model.

Furthermore, it is argued that the drawbacks are minor with respect to the overall

capability of reproducing the inter-annual variability of precipitation process. The negligible effect of the procedure is demonstrated by the results obtained for precipitation statistics at shorter aggregation periods (shown in the result analysis). As results show, the adjustments are not appreciable in the internal structure of the precipitation and in the generation of extreme values. It has been further tested that results obtained for intra-annual precipitation enabling or disabling the adopted methodology of external selection are indistinguishable (results not shown).

When the most important statistical property to reproduce is inter-annual variability the proposed procedure could be enhanced using a generic ARFIMA(p, d, q) model instead of the AR(1). Without discussing the implication of using an ARFIMA model, the long-memory eventually present in the time series may be taken into account using such an approach (*Montanari et al.*, 1997; *Koutsoyiannis*, 2000, 2003a).

2.3.4 Results and validation

The capability of the model to reproduce the main statistics of the precipitation process at different aggregation periods is tested. The simulated mean, variance, lag-1 autocorrelation, skewness, frequency of non-precipitation, i.e. the probability that an arbitrary interval of length h is dry, and the transition probability from a wet-spell to another wet-spell are compared with observations at the monthly scale. The comparison is shown at the periods of aggregation of 1, 24 and 48 hours (Figure 2.3, 2.4 and 2.5).

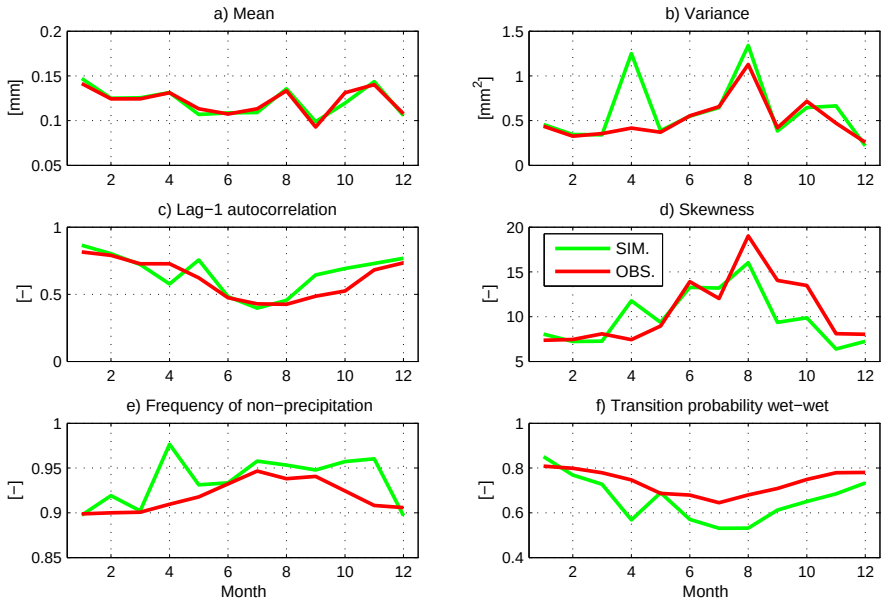

Figure 2.3: A comparison between observed (red) and simulated (green) monthly statistics of precipitation (mean, variance, lag-1 autocorrelation, skewness, frequency of non-precipitation, transition probability wet-wet), for the aggregation period of 1 hour.

Reproducing statistical properties different from the ones used in the calibration of precipitation parameters such as transition probability from wet-spells or all the

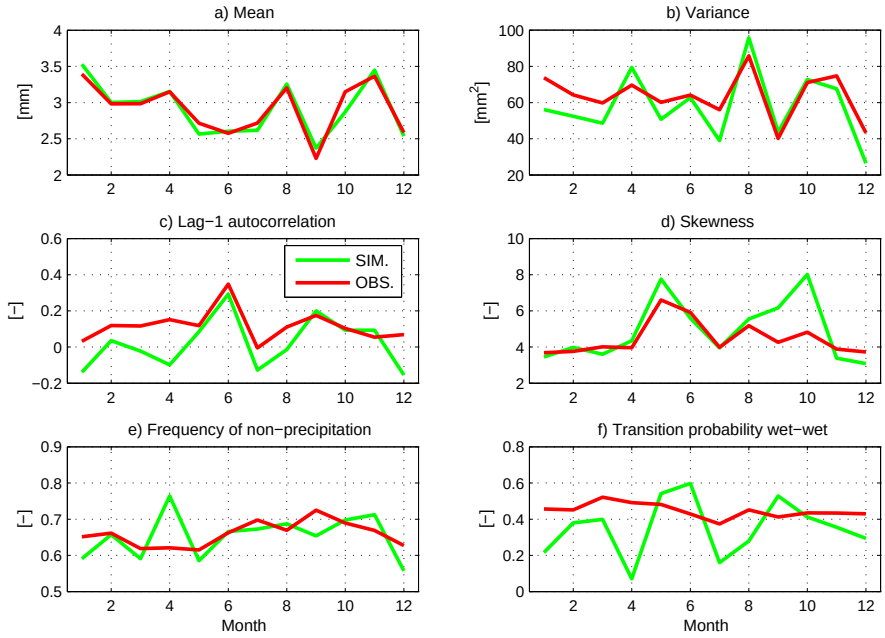

Figure 2.4: A comparison between observed (red) and simulated (green) monthly statistics of precipitation (mean, variance, lag-1 autocorrelation, skewness, frequency of non-precipitation, transition probability wet-wet), for the aggregation period of 24 hours.

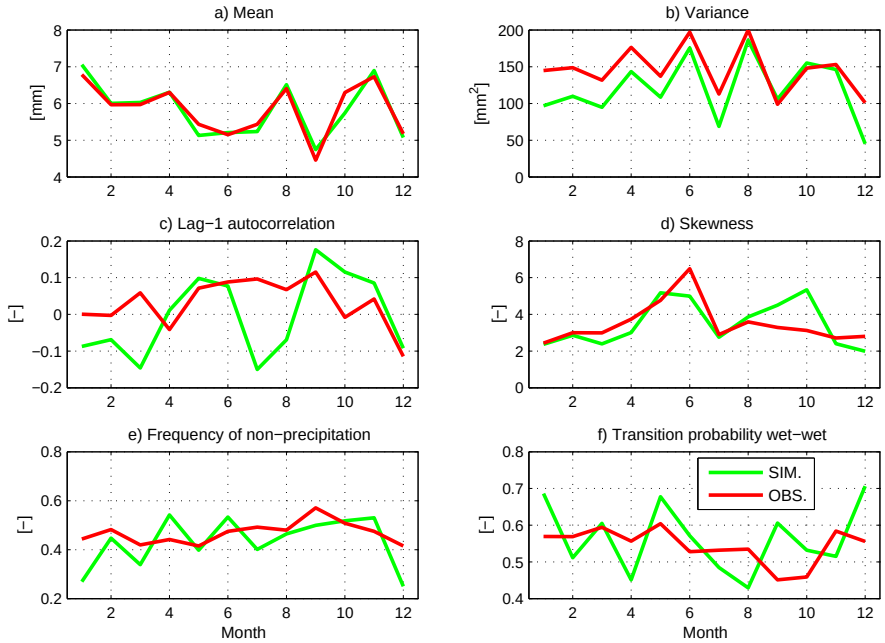

Figure 2.5: A comparison between observed (red) and simulated (green) monthly statistics of precipitation (mean, variance, lag-1 autocorrelation, skewness, frequency of non-precipitation, transition probability wet-wet), for the aggregation period of 48 hours.

statistics different from mean at aggregation of 48 [h] is particularly challenging. The results shown in Figure 2.5 for the 48 [h] aggregation period confirm that the statistical properties are also preserved at this time aggregation.
After the verification of statistics at short aggregation periods, the entire annual cycle of the rainfall process is checked in Figure 2.6. The simulated process perfectly preserves the mean but underestimates the monthly variance of observations, almost in every month. These differences are related to the poor skill of the *NSRP* model in reproducing, the low frequency variances as discussed in Section 2.3.3.

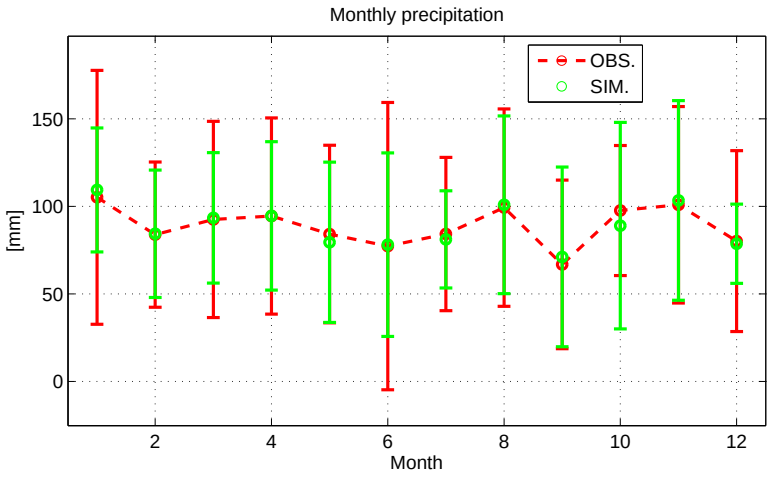

Figure 2.6: A comparison between observed (red) and simulated (green) monthly precipitation. The vertical bars denote the standard deviations of the monthly values.

The precipitation component must be checked to properly reproduce also extreme values including rainfall maxima and occurrences of dry and wet periods. The performance of the *NSRP* model with regards to the reproduction of the extreme values is influenced by its internal structure (probability distributions of random variables). Specifically, the distribution used to simulate the random intensity of the rainfall cell, X, directly affects the realizations of extremes. A Gamma probability distribution as previously tested by *Cowpertwait* (1998) is employed. Weibull and Mixed-Exponential probability distributions have been also tested and compared with the Gamma. Nonetheless, no appreciable differences have been observed. All of these probability distributions provide consistent results in terms of fitting of extreme values of precipitation intensity. The simulated and observed extreme precipitations for time aggregation periods of 1 hour and 24 hours are illustrated in Figures 2.7a and 2.7b. For all test locations, there is a good match between the simulated and observed values, especially for the return periods at up to 20-30 years. This is not appreciable for the location at Boston (Figure 2.7a,b), where only 18 years of observed values were available. For larger return periods, multiple simulations would be necessary to define the mean and confidence intervals of extreme precipitation and effectively corroborate the weather generator (*Semenov*, 2008). Cumulative probabilities associated with the data are estimated with the method of plotting position (*Cunnane*, 1978).

Extremes of dry spell and wet spell durations are generally poorly captured by the model, especially for dry climates. Simulations and observations sometimes differ also for return periods of less than one year. The results for Boston are illustrated in Figure 2.7c, where extreme dry spells are well simulated, while extreme wet spells, are slightly overestimated for return periods larger than 10 years (Figure 2.7d).

The fractions of total time that precipitation exceeds a certain depth are shown for different aggregation periods in Figure 2.8a. As seen, precipitation events with depth larger than 1 $[mm]$ are somewhat overestimated for aggregations periods longer than 48 $[h]$. Conversely, the fractions of time with precipitation depth larger than 20 $[mm]$ is slightly underestimated for the same aggregation periods. This is consistent given the preservation of precipitation average at each aggregation period. Errors of such type are almost unavoidable in the *NSRP* model, as parameterized in AWE-GEN. They might be related to the use of a single set of parameters to describe rainfall cells and clusters, that in the natural process are the result of different mechanisms, such as stratiform and convective rainfall. The use of *NSRP* models that overlap two different kind of cells (*Cowpertwait*, 2004; *Cowpertwait et al.*, 2007) might be used to reduce this error. The distribution of dry spell duration (Figure 2.8b) is usually represented reasonably well, although for temperate climates its mean is slightly underestimated. For Boston it is underestimated by 0.7 days, as confirmed from Figure 2.8b. In drier climates, the mean is usually preserved but the shape of the distribution can deviate from the observed one for intermediate dry spell durations. The distribution of the wet spell durations is generally captured by the weather generator with respect to the mean and the shape of the probability distribution (Figure 2.8c). This performance is realized whether the climate is dry or wet.

The errors seen in Figure 2.8a, are generally negligible. For example, the difference in the fraction of time precipitation depth exceed 1 $[mm]$ at aggregation time of 96 $[h]$ is typically around 0.1 but usually less than 0.05. These errors are acceptable and imply that only a small amount of rainfall is transferred from intense rainfall to drizzle. Errors in the representation of dry spell duration mean between 0.5 and 1.5 days are generally not desirable. It should be noted that this is usually the most difficult precipitation property to be simulated by the weather generator. This feature is important since the distribution of dry spell duration significantly affects the simulation of all other variables. Fortunately, it has been checked that although some inaccuracy can be appreciated, it does not influence the simulation performance of the other variables, as testified from the results in the following.

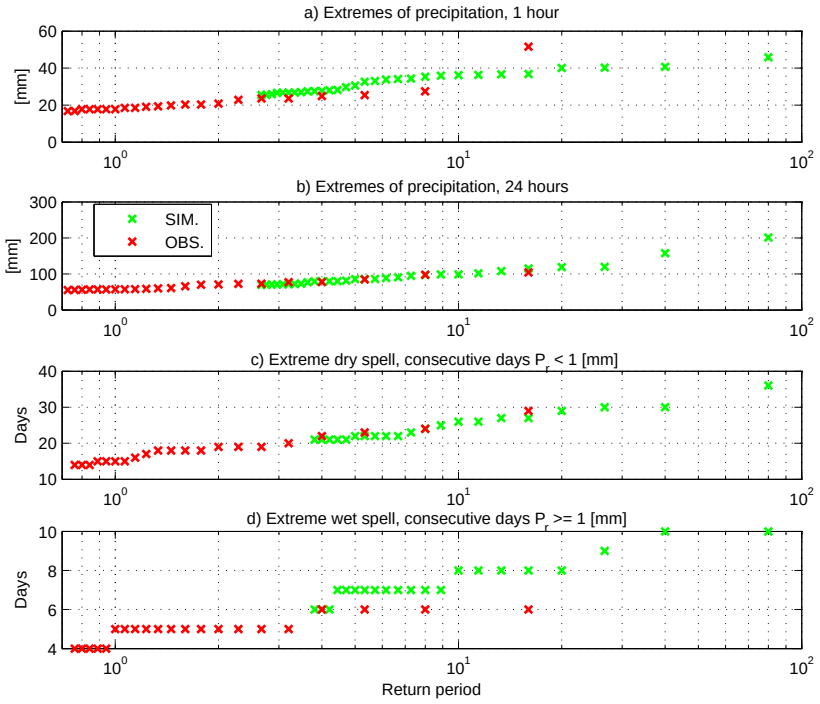

Figure 2.7: A comparison between the observed (red crosses) and simulated values of extreme precipitation (green crosses) at (a) 1-hour and (b) 24-hour aggregation periods; (c) extremes of dry and (d) wet spell durations. Dry/wet spell duration is the number of consecutive days with precipitation depth lower/larger than 1 $[mm]$.

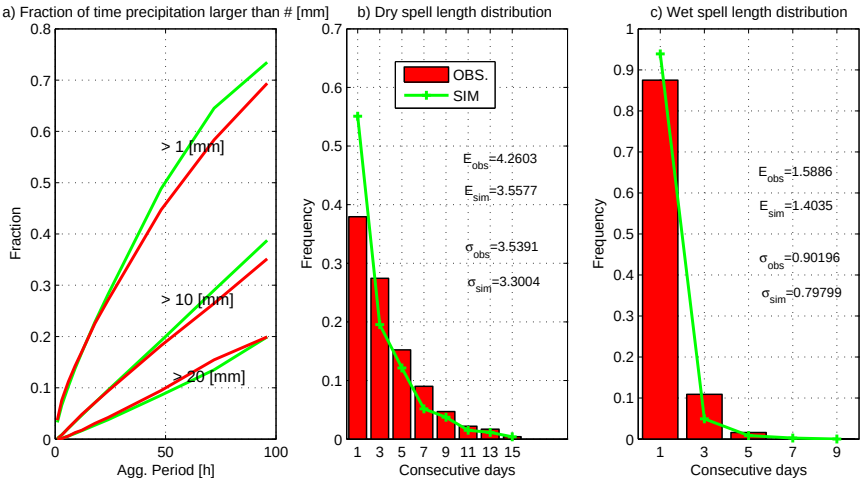

Figure 2.8: A comparison between observed (red) and simulated (green) fractions of time with precipitation larger than a given threshold $[1 - 10 - 20mm]$ at different aggregation periods (a). The same comparison for dry spell length distribution (b), i.e. consecutive days with precipitation depth lower than 1 $[mm]$ and for wet spell length distribution (c), i.e. consecutive days with precipitation depth larger than 1 $[mm]$. E_{obs} and σ_{obs} are the observed mean and standard deviation and E_{sim} and σ_{sim} are the simulated ones.

2.4 Cloud cover

Cloud cover is an important climatic variable directly affecting radiation fluxes and indirectly influencing air temperature and relative humidity. This variable is often neglected in empirical statistical weather generators (*Richardson*, 1981; *Semenov et al.*, 1998; *Parlange and Katz*, 2000). Commonly, weather generators simulate variables dependent on cloud cover, such as air temperature, on the basis of precipitation occurrence, e.g., dry and wet states. The latter are only weak implicit proxies for the process of cloud cover, that is not explicitly included. In simulations of the hydrological cycle and energy budget, the cloud cover is often assumed constant or its definition is oversimplified. This is a theoretically incorrect assumption incompatible with the high-frequency variation of cloud cover and its effect on shortwave radiation fluxes. In some applications, such as modeling of snowpack or vegetation dynamics, this assumption can lead to unrealistic results. The cloud cover simulated in AWE-GEN is based on the framework first developed by *Curtis and Eagleson* (1982) and further modified by *Ivanov et al.* (2007).

2.4.1 Model

Cloud cover $N(t)$ is the fraction of the celestial dome occupied by clouds. It can be measured in oktas $[0-8]$ or in cloud fraction $[0-1]$, where 0 signifies clear sky conditions and 1 is used to describe complete overcast conditions (*Muneer et al.*, 2000). The fraction notation will be used in the following. In the model of *Ivanov et al.* (2007), $N(t)$ $[-]$ is considered to be a random variable that has different dynamics during intra-storm and inter-storm periods. During an intra-storm period, i.e. the hours with precipitation different from zero, the value of cloudiness is assumed to be equal to 1. During an inter-storm period, the existence of the "fair weather" region, R_0, is assumed. The region is sufficiently distant from storms, thus the cloud cover can be assumed stationary and fully characterized by the first two statistical moments: the mean $E\{N(t)\}_{t\in R_0} = M_0$ and the variance $VAR\{N(t)\}_{t\in R_0} = \sigma_M^2$ of the process. The length of the post-storm transition period after which the cloud cover process can be considered stationary is indicated with T_R $[h]$. The second assumption is that the transition of the cloud process between the boundary of a storm period and the fair-weather takes place through an exponential function $J(t)$. The latter is characterized by two coefficients controlling the transition rates, ς and γ $[h^{-1}]$, and by the average cloud cover of the first hour after a storm and of the last hour of an inter-storm: J_1. The expression for the cloudiness becomes:

$$N(t) = M_0 + \big(J_1 - M_0\big)\big(1 - J(t)\big) + m(t)J(t)\,, \tag{2.11}$$

where $m(t)$ is the stationary sequence of correlated deviation with $E\{m(t)\} = 0$; $VAR\{m(t)\} = \sigma_m^2$ and autocorrelation function $\rho_m(l)$ (where l is the lag). The time varying conditional expectation and variance of cloud cover under this assumption

have been estimated from *Curtis and Eagleson* (1982):

$$E\{N(t)\}_{t\in t_b} = M_0 + \big(J_1 - M_0\big)\big(1 - J(t)\big) \;, \tag{2.12}$$

$$VAR\{N(t)\}_{t\in t_b} = \sigma_m^2 J(t)^2 \,. \tag{2.13}$$

The stationary sequence of correlated deviation $m(t)$ is modeled through an AR(1) model where the random deviates $\varepsilon(t)$ are distributed following a Beta probability distribution with parameter a and b and evaluated with the same procedure of lower and upper bound constraining proposed by *Ivanov et al.* (2007). The a and b parameters are estimated on the basis of the of the discretized cloudiness [0:0.1:1] at the step before $N(t-1)$ and therefore are in total eleven parameters. The procedure proposed by *Ivanov et al.* (2007) allows to use a different distribution of the correlated deviation $m(t)$ function of the cloudiness $N(t-1)$. This has been shown to improve significantly the results of the model in comparison to a fixed distribution for $\varepsilon(t)$, as used in *Curtis and Eagleson* (1982). The AR(1) model for $m(t)$ can be expressed as follows:

$$m(t) = \rho_m m(t-1) + \varepsilon(t)\sigma_m\sqrt{1-\rho_m^2} \,. \tag{2.14}$$

The transition function is calculated with the same expression defined by *Ivanov et al.* (2007):

$$J(t) = \big(1 - e^{-\varsigma(t-t_0)}\big)\big(1 - e^{-\gamma(t_0+t_b-t)}\big) \,, \tag{2.15}$$

where t_0 is the time at which inter-storm period begins and t_b is the length of the inter-storm period. The decay coefficients ς and γ are taken equal and are calculated with the procedure proposed by *Curtis and Eagleson* (1982). Assuming symmetry for the transition period, the second term of equation (2.15) can be neglected. Further, equation (2.15) can be reduced to $0.99 = \big(1 - e^{-\varsigma(T_R)}\big)$, when $t_0 = 0$ and $J(t) = 0.99$ for $t = T_R$. It follows that $\gamma = \varsigma = 4.61/T_R$.

The differences with the formulation of *Ivanov et al.* (2007) include the relaxation of the requirements of the minimum length of inter-storm period between two successive precipitation events; and the explicit computation of cloudiness in the first hours following and preceding rainfall spells J_1, instead of using a theoretical value equal to 1.

The parameters required for the model are estimate monthly and are: M_0, σ_m^2, $\rho_m(1)$, $\gamma = \varsigma$, J_1, and eleven values of a and b. The procedure for the parameter estimation follows that of *Curtis and Eagleson* (1982) and *Ivanov et al.* (2007), with some modifications (see Appendix A.3). First, the threshold value T_R of the transition period is determined to identify the fair-weather region, i.e., the region where $N(t)$ is stationary. Once the fair-weather region is identified the parameters M_0, σ_m^2, $\rho_m(1)$, $\gamma = \varsigma$, J_1 are easily evaluated with conventional techniques. The value of the first hour of the transition period J_1 is obtained as the average of all the first and last hours of the inter-storm periods. The empirical random deviate $\varepsilon(t)$

are estimated for fair weather region considering that when $t \in R_0$ the transition function $J(t) = 1$ and equation 2.11 reduces to $N(t) = M_0 + m(t)$. a and b are finally evaluated from $m(t)$ as a function of the discretized cloudiness [0:0.1:1] at the step before $N(t-1)$. This procedure might be regarded as over-parameterized. However, the complexity of the approach is required by the difficulty of simulating a stochastic process such as cloud cover. When time series of hourly cloudiness are available, the identification of all parameters is computationally efficient.

2.4.2 Results and validation

A comparison between the observed and simulated monthly distributions of cloud cover is shown in Figure 2.9 for the fair-weather period. The weather generator performs generally well, in reproducing both the shape of the probability density function and the seasonality of the process. A less than perfect agreement was noticed for few locations for summer months. This shortcoming was first noted by *Ivanov et al.* (2007) and is related to the non-stationarity in the cloudiness process when passing of atmospheric precipitation systems do not necessarily result in rainfall at a given location. The non stationarity of cloud cover occurrence in such periods can not be identified from the weather generator and consequently biases in the mean value are produced. The shape of probability density functions of total cloud cover are also well reproduced by AWE-GEN (Figure: 2.10). The differences between the simulated and observed mean cloud cover are generally less than 0.05, although sometimes discrepancies around 0.1 are appreciable. This holds true also for other tested locations. The performance of simulating the total cloudiness is not as satisfying as the one obtained for the fair-weather period. This is due to a higher difficulty of reproducing the transition regions.

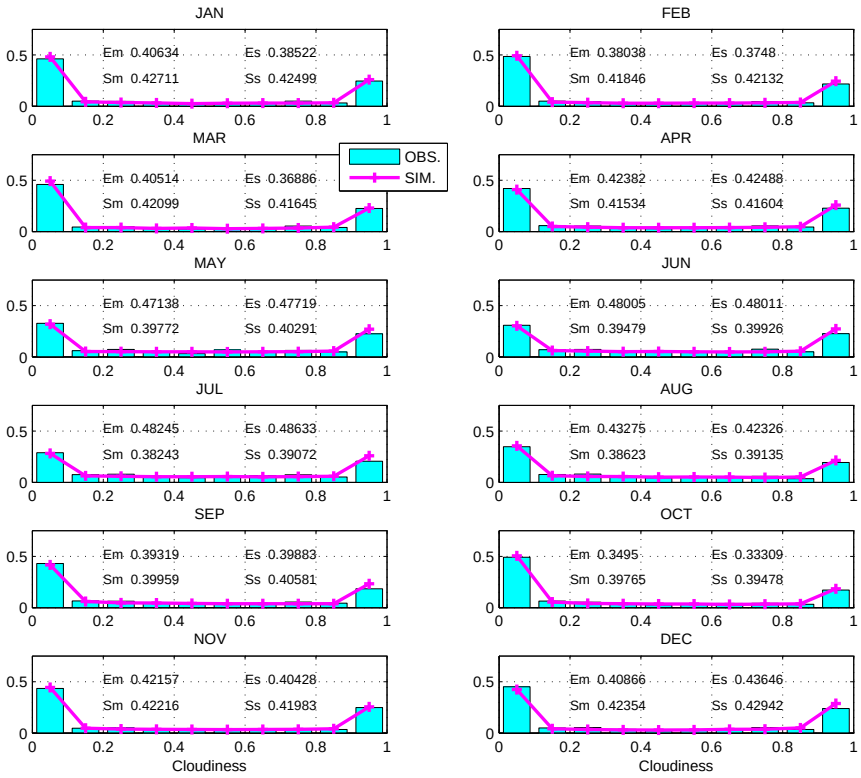

Figure 2.9: A comparison between the observed (cyan) and simulated (magenta) fair weather cloud cover distribution for every month. E_{obs} and σ_{obs} are the observed mean and standard deviation and E_{sim} and σ_{sim} are the simulated ones.

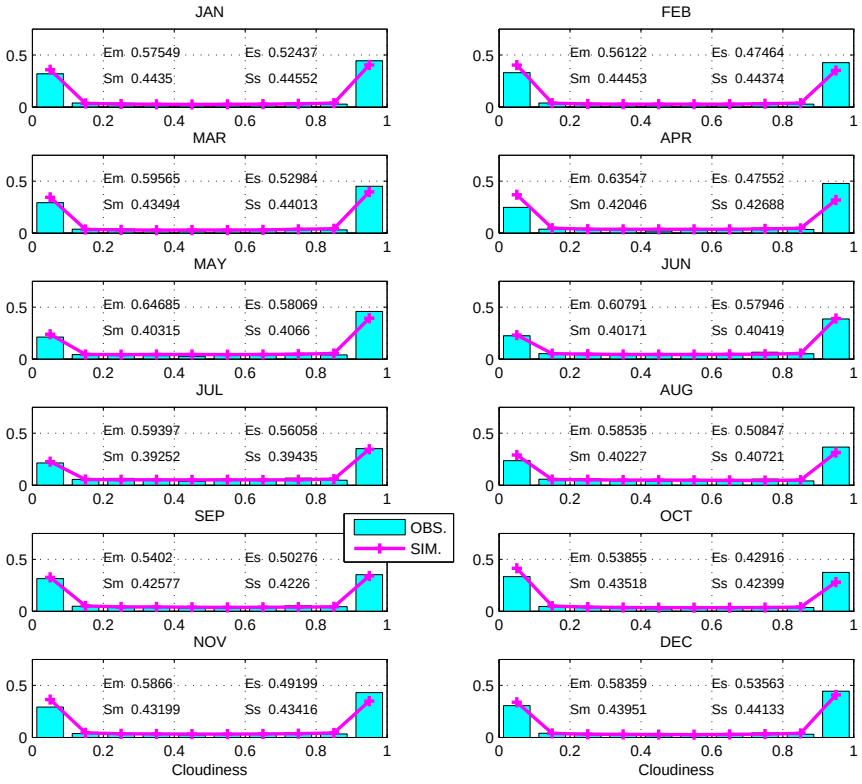

Figure 2.10: A comparison between the observed (cyan) and simulated (magenta) total cloud cover distribution, for every month. E_{obs} and σ_{obs} are the observed mean and standard deviation and E_{sim} and σ_{sim} are the simulated ones.

2.5 Air temperature

In weather generators, air temperature is commonly simulated at the daily scale, implying the generation of only maximum and minimum temperature or, alternatively, the temperature mean and its daily range (*Richardson*, 1981; *Semenov et al.*, 1998; *Wilks and Wilby*, 1999; *Parlange and Katz*, 2000). Typically, air temperature or its residuals are simulated through multi-regression equations between air temperature and other variables. Air temperature can be included to take into account the autocorrelation process. Consequently the effects of climate variables such as cloudiness, are considered only indirectly, i.e., in the use of different parameterizations or equations for wet or dry states. Although such an approach can reproduce the mean and the variance accurately, it is not suitable for applications that require information on intra-daily air temperature variation. For these reasons, a mixed physics-based stochastic approach was developed by *Curtis and Eagleson* (1982) and later enhanced by *Ivanov et al.* (2007). This work utilizes the same approach with some further improvements.

2.5.1 Model

The generation of air temperature $T(t)$ $[^{\circ}C]$ is simulated as the sum of a stochastic component $dT(t)$ $[^{\circ}C]$ and a deterministic component $\widetilde{T}(t)$ $[^{\circ}C]$:

$$T(t) = \widetilde{T}(t) + dT(t)\,. \tag{2.16}$$

The deterministic component of air temperature $\widetilde{T}(t)$ is assumed to be directly related to the underlying physical processes such as the divergence of radiative and eddy heat fluxes. More specifically the deterministic time-gradient of temperature $d\widetilde{T}(t)/dt$ is a function of the air temperature itself and of the incoming long-wave radiation. It is further related through two functions to the Sun's hourly position and site geographic location (*Curtis and Eagleson*, 1982; *Ivanov et al.*, 2007). Thus the deterministic component $\widetilde{T}(t)$ is expressed as follows:

$$\frac{d\widetilde{T}(t)}{dt} \;=\; b_0 - b_1\widetilde{T}(t) + b_2K(t)s(t) + b_3K(t)r(t) + b_4q(t)\,, \tag{2.17}$$

where b_i ($i = 0,\ 1,\ \ldots,\ 4$) are the five regression coefficient of the model, $q(t) = L_{atm}/1000$ $[W\ m^{-2}]$ is a scaled incoming long-wave radiation L_{atm} $[W\ m^{-2}]$, and $K(t) = 1 - 0.75N^{3.4}$ $[-]$ is the cloud attenuation factor defined by *Kasten and Czeplak* (1980). The longwave radiation L_{atm} $[W\ m^{-2}]$ is modeled using the air temperature:

$$L_{atm} \;=\; K_N(N)\sigma T_a^4\,, \tag{2.18}$$

where T_a $[K]$ is the air temperature at the reference height z_{atm} (chapter: 4), $\sigma = 5.670410^{-8}$ $[W\ m^{-2}\ K^{-4}]$ is the Stefan-Boltzmann constant; and $K_N(N) = 1 + 0.17N^2$ is the correction for the cloudiness N $[-]$ (*TVA*, 1972). $r(t)$ $[-]$ and $s(t)$ $[-]$

are functions of the solar height h_S $[rad]$ defined by *Curtis and Eagleson* (1982):

$$\begin{aligned} s(t) &= sin(\delta)sin(\Phi) - cos(\delta)cos(\phi)cos(\frac{\pi t}{12})\,, \quad T_{H\,rise} \le t \le T_{H\,set}\,, \\ s(t) &= 0\,, \qquad\qquad \text{otherwise}\,, \\ r(t) &= \frac{ds(t)}{dt} = \frac{\pi}{12}cos(\delta)cos(\Phi)sin(\frac{\pi t}{12})\,, \quad T_{H\,rise} \le t \le 12\,, \\ r(t) &= 0\,, \qquad\qquad \text{otherwise}\,, \end{aligned} \tag{2.19}$$

where t is the local hour, δ $[rad]$ is the solar declination, Φ $[rad]$ is the local latitude, $T_{H\,rise}$ $[local\ hour]$ is the local time of sunrise and $T_{H\,set}$ $[local\ hour]$ is the local time of sunset. For details on the calculation of these quantities see the Appendix A.4. The factors $r(t)$, $s(t)$ and $q(t)$ are subjected to modification daily and seasonally and they explain the deterministic variation of air temperature. The differential equation $d\widetilde{T}(t)/dt = f\big(\widetilde{T}(t), s(t), r(t), q(t), K(t)\big)$ is solved each day to compute the deterministic cycle of air temperature $\widetilde{T}(t)$ once the initial value of deterministic temperature $\widetilde{T}(t-1)$ is provided. *Curtis and Eagleson* (1982) provide a solution method of equation (2.17) summarized in Appendix A.5.

The stochastic temperature component $dT(t) = T(t) - \widetilde{T}(t)$, is estimated through an autoregressive model AR(1). At the hourly scale, the random deviate of temperature exhibits a significant dependence in the hour of the day. Differences are noticeable in the statistics of $dT(t)$ for different phases of the day: morning, midday, afternoon, evening, and night. The stochastic component is particularly important for the determination of extreme of air temperature, such as minimum and maximum temperatures. Consequently, the average of the stochastic component $\overline{dT}_h$, and its standard deviation $\sigma_{dT,h}$ are estimated differently for each hour of the day $h \in [0, \ldots, 23]$. Note that this is an improvement in comparison to the original models of *Curtis and Eagleson* (1982) and *Ivanov et al.* (2007).

$$dT(t) = \overline{dT}_h + \rho_{dT}\big(dT(t-1) - \overline{dT}_h\big) + \varepsilon(t)\sigma_{dT,h}\sqrt{(1-\rho_{dT}^2)}\,, \tag{2.20}$$

where $\varepsilon(t)$ are the standard normal deviate, ρ_{dT} is the lag-1 autocorrelation of the process. The average $\overline{dT}_h$ and the standard deviation $\sigma_{dT,h}$ of $dT(t)$ depend on the hour of the day.

The coefficients and the parameters used to estimate the deterministic and stochastic components are evaluated at the monthly scale. *Ivanov et al.* (2007) describe the procedure for estimation of the coefficients (see Appendix A.6). Once the regression coefficients are determined, the parameters $\overline{dT}_h$, $\sigma_{dT,h}$, and ρ_{dT} are estimated from $dT(t)$ using conventional techniques. A constrain on $\rho_{dT} < 0.96$ is required to avoid numerical instability. Otherwise, combinations of random numbers can lead to unrealistic values of temperature.

2.5.2 Results and validation

The assessment of the performance of an hourly weather generator should not be limited to the daily means, especially for the air temperature process. The reproduction of the daily cycle and minimum and maximum temperatures is indeed fundamental for evaluating its capability. Figure 2.11 shows the seasonal variation of mean air temperature and its standard deviation at the two aggregation periods of 1 hour and 24 hours. The observed values are reproduced almost perfectly. Note that the mean does not change with aggregation period. The seasonal variability of daily maximum and minimum air temperatures including standard deviations are illustrated in Figure 2.12. These quantities are well captured by the weather generator, although the variances can be slightly overestimated or underestimated. The daily cycle and the probability density function of air temperature are also well reproduced, as shown in Figure 2.13.

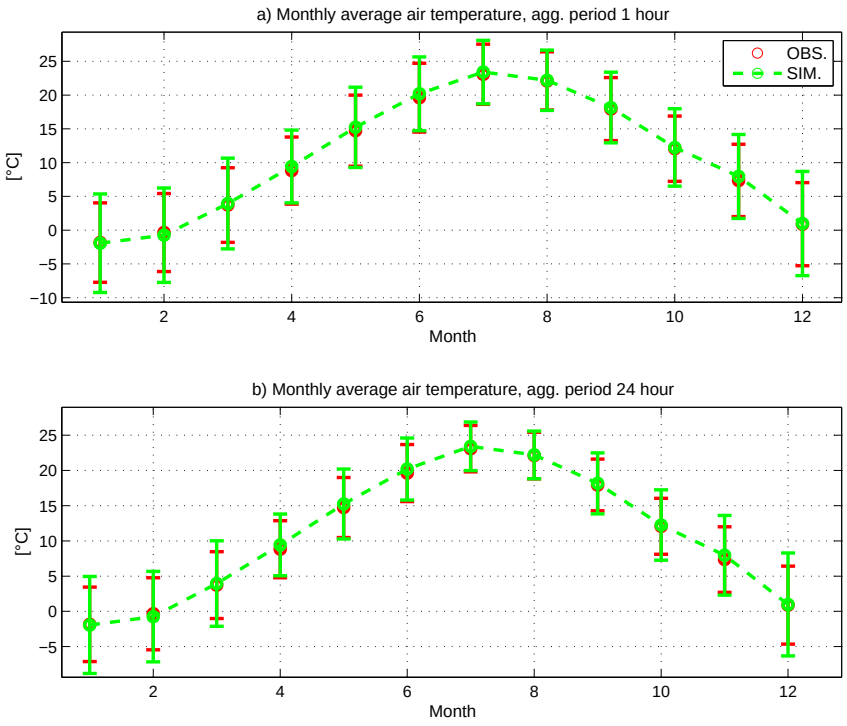

Figure 2.11: A comparison between the observed (red) and simulated (green) average air temperature for every month, aggregation periods of 1 $[h]$ (a) and 24 $[h]$ (b). The vertical bars denote the standard deviations.

Air temperature extremes at different return periods are reproduced satisfactorily, though overestimation or underestimation are often present both for minimum and maximum temperature. As seen in Figure 2.14 extremes of daily temperature (24 hour aggregation period) are generally reproduced better than hourly values. Nonetheless errors around 2-4 $[°C]$ for return periods of more than 10 years are not unusual. This shortcoming can be considered fairly insignificant for most hy-

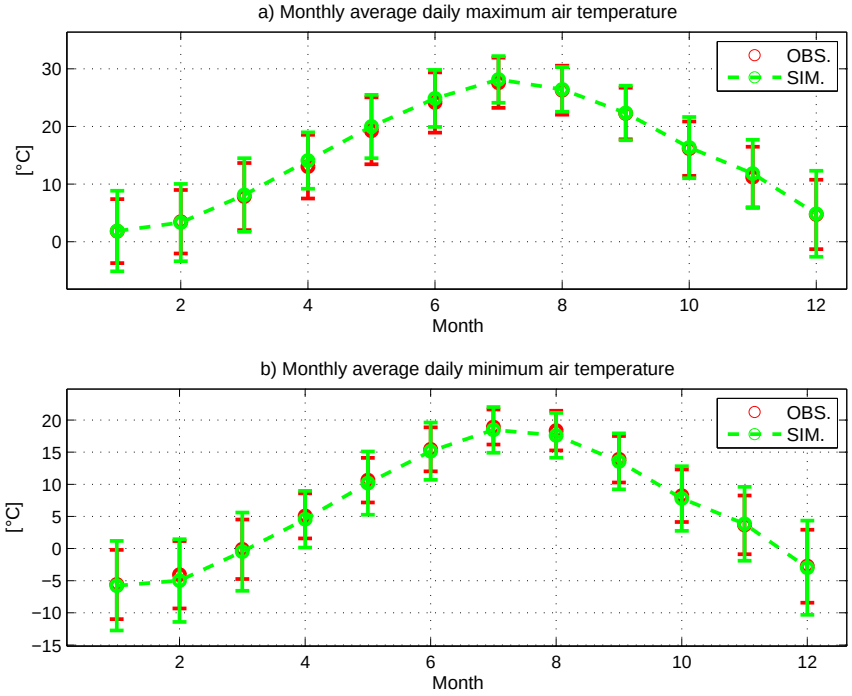

Figure 2.12: A comparison between the observed (red) and simulated (green) daily maximum (a) and minimum (b) air temperature for every month. The vertical bars denote the standard deviations.

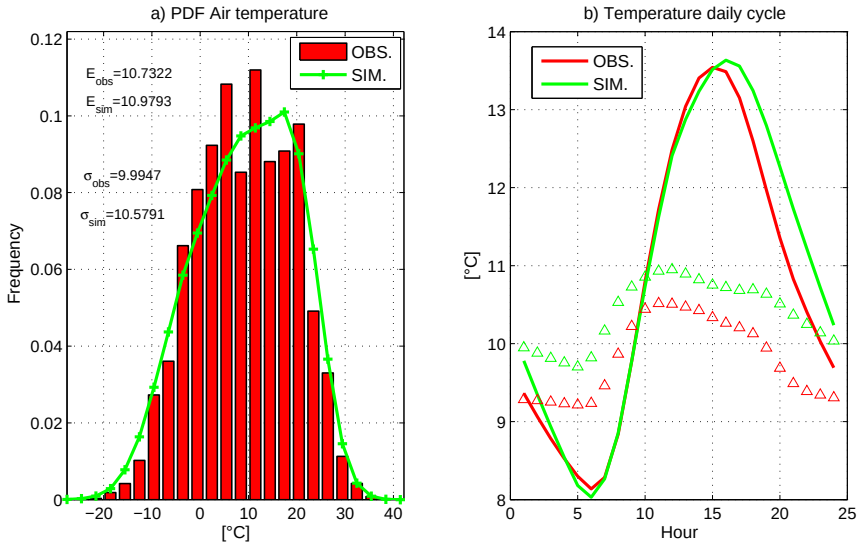

Figure 2.13: A comparison between the observed (red) and simulated (green) air temperature distribution (a) and average daily cycle (b). The triangles are the standard deviations for every day hour, E_{obs} and σ_{obs} are the observed mean and standard deviation and E_{sim} and σ_{sim} are the simulated ones.

drological applications. Some problems might arise only when the introduction of temperature thresholds for plant mortality or other natural processes is required.

The occurrence of heat and cold waves, i.e. the number of consecutive days with air temperature higher than the 90th percentile (heat wave) or lower than the 10th percentile (cold wave) are poorly represented (Figure 2.15). There are differences in the accuracy of the results among the tested stations but generally, the temperature wave occurrence is underestimated. In order to simulate these climatic characteristics correctly, information about larger patterns of the atmospheric circulation is required. Obviously, a point scale weather generator cannot capture such features. Fortunately, the simulation of extreme heat and cold waves can be assumed to have a minor influence for numerous ecological and hydrological applications. Thus, this shortcoming of AWE-GEN is acceptable in such applications. The estimation of heat and cold waves might be significant when climate change impacts on human health are required (*Rebetez et al.*, 2006). For such reasons, the occurrence of heat and cold waves is often emphasized by climatologists (*Alexander et al.*, 2006; *Tebaldi et al.*, 2006).

An analysis has been also performed for four indices of air temperature as defined in the "Expert Team on Climate Change Detection, Monitoring and Indices" (*ETCCDMI*) (http://cccma.seos.uvic.ca/ETCCDMI/list_27_indices.shtml). These four indices allow an evaluation of the weather generator from a climatologist perspective. Specifically, results are compared between observation and simulations for icing days (days with $T_{max} < 0$ [$^{\circ}C$]), summer days (days with $T_{max} > 25$ [$^{\circ}C$]), frost days (days with $T_{min} < 0$ [$^{\circ}C$]) and tropical nights (days with $T_{min} > 20$ [$^{\circ}C$]). As shown in Table 2.2, AWE-GEN is able to reproduce such indices confirming its overall skill.

Table 2.2: Comparison between observed and simulated climatological indices of air temperature

	Observed fraction	**Simulated fraction**
Icing days	0.080	0.091
Summer days	0.198	0.207
Frost days	0.254	0.272
Tropical nights	0.078	0.070

The inter-annual variability of air temperature is neglected in this version of AWE-GEN. This is related to the difficulties in finding a proper external conditioning to reproduce low-frequency of the air temperature process. However, the simulated mean annual temperature process presents a certain variance. In fact, random number generation and the influence of precipitation in the deterministic component of air temperature produce, a variation of mean annual temperature from year to year. However, the simulated variance of the process is somewhat lower than the observed one. This underestimation is related to the same "overdispersion" reason discussed in the annual precipitation occurrence (Section 2.1). Nevertheless, for several tested locations, the annual variance is only slightly underestimated and for

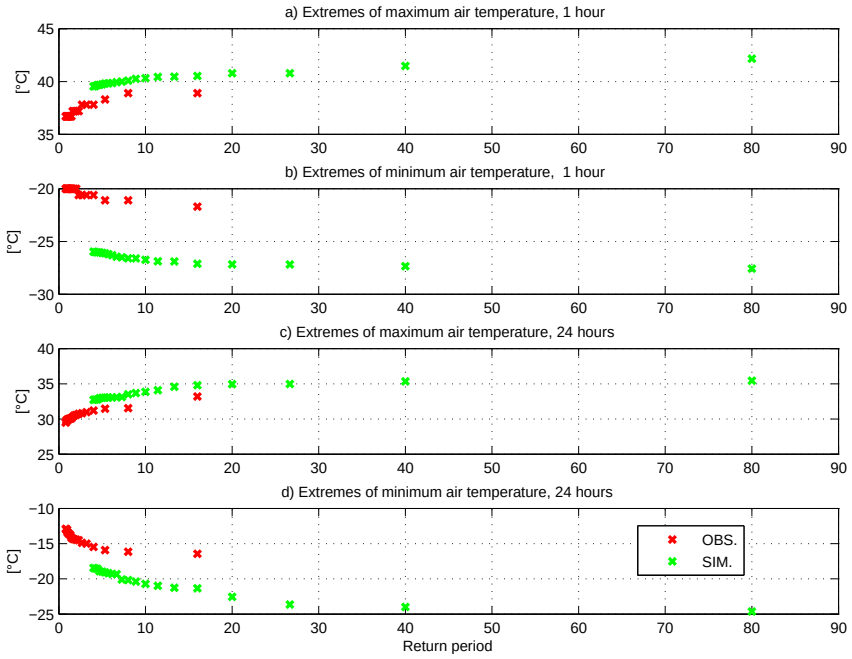

Figure 2.14: A comparison between the observed (red) and simulated (green) extremes of air temperature. a) Maxima of hourly temperature. b) Minima of hourly temperature. c) Maxima of daily temperature. d) Minima of daily temperature.

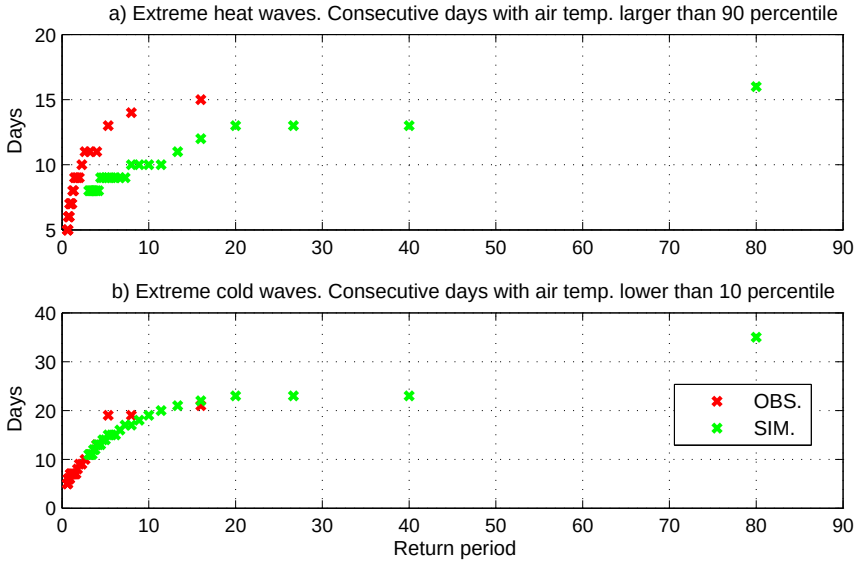

Figure 2.15: A comparison between the observed (red) and simulated (green) occurrence of heat (a) and cold (b) waves, i.e. consecutive days with temperature higher than the 90 percentile or lower than 10 percentile.

typical applications the mismatch between the simulated and natural process can be neglected.

2.6 Shortwave incoming radiation

A correct estimation of the shortwave radiation is important because it represents the main source of incoming energy in the land-surface systems, directly affecting several ecological and hydrological processes. In weather generators, radiation is commonly estimated through regression with other variables (*Richardson and Wright*, 1984; *Parlange and Katz*, 2000). The likely reason for such an approach is a conventional lack of methodology for direct estimation of cloudiness. However, once the site geographic location and cloudiness are known, several deterministic models with different degrees of complexity can be used to calculate the incoming shortwave radiation for clear-sky and overcast conditions (*Gueymard*, 1989; *Freidenreich and Ramaswamy*, 1999; *Muneer et al.*, 2000; *Gueymard*, 2001, 2008; *Ineichen*, 2006). These methods recur to a large use of empirical coefficients to determine the atmospheric transmittances and the scattering fractions for direct and diffuse shortwave radiation. In this study, the incoming shortwave radiation is estimated with the model *REST2* developed by *Gueymard* (2008) for clear sky conditions. The parameterizations of *Stephens* (1978) and *Slingo* (1989) are used to compute transmittances for arbitrary cloudy conditions. This approach follows mainly the one proposed by *Ivanov et al.* (2007), improving the clear sky component where the model of *Gueymard* (1989) is substituted with the more recent model of *Gueymard* (2008). In hydrological applications only global shortwave radiation component is usually considered, yet recent solar radiation models offer the convenience of shortwave flux computation in multiple-bands (*Freidenreich and Ramaswamy*, 1999; *Gueymard*, 2001). The partition of the incoming energy into different spectral bands could be useful for several purposes such as ecological or eco-hydrological simulations that require the photosynthetically active radiation, *PAR*, as input. Moreover using a multi-band approach allows one to minimize the overlapping effect between water vapor and gas, making the transmittance modeling more reliable (*Freidenreich and Ramaswamy*, 1999). The clear sky radiation component in AWE-GEN, considers two bands Λ: the ultraviolet/visible, *UV/VIS*, band with wavelengths $[0.29 - 0.70\ \mu m]$ and the near infrared, *NIR*, band with wavelengths $[0.70 - 4.0\ \mu m]$ (*Gueymard*, 2008). In the first band, ozone, nitrogen dioxide absorption, and Rayleigh scattering are concentrated; the absorption by water vapor and uniformly mixed gases is mainly concentrated in the second band.

The two-band model is a compromise between more complex formulations adopted in General Circulation Models and simple broadband approaches. This compromise allows one to compute explicitly the *PAR* without requiring a parametrization that is computationally infeasible in common applications of weather generators.

According to *Gueymard* (2008) the extraterrestrial radiation R_0' is partitioned in the fractions of 0.4651 in the *UV/VIS* band, and 0.5195 in the *NIR* band. The extraterrestrial radiation R_0' can be obtained starting with the value of the solar constant $R_0 = 1366.1\ [W\ m^{-2}]$, as suggested by *Darula et al.* (2005). This value is corrected to take into account the ratio between the actual Earth-Sun distance and

the mean Earth-Sun distance $R'_0 = E_0\ R_0\ [W\ m^{-2}]$. The correction factor E_0 [−] was derived by *Iqbal* (1983) as a function of the daily angle $\gamma = 2\pi(J_{Day} - 1)/365$:

$$\begin{aligned} E_0 &= 1.00011 + 0.034221\cos\gamma + 0.00128\sin\gamma \\ &\quad +0.000719\cos 2\gamma + 0.000077\sin 2\gamma\,, \end{aligned} \tag{2.21}$$

where J_{Day} is the Julian Day. The equations to calculate the instantaneous values of other variables used in the radiation computation, such as the solar altitude, h_S $[rad]$, solar azimuth, ζ_S $[rad]$, solar declination, δ $[rad]$, sunrise local time, $T_{H\,rise}$ $[local\ hour]$, sunset local time, $T_{H\,set}$ $[local\ hour]$, and daily length, D_{LH} $[h]$, are defined in the Appendix A.4. The equations are mainly drawn from *Iqbal* (1983) and *Eagleson* (2002).

2.6.1 Direct and diffuse radiation for clear sky conditions

When extraterrestrial radiation enters the atmosphere, it is attenuated by Rayleigh scattering $T_{R,\Lambda}$ [−], uniformly mixed gas absorption $T_{g,\Lambda}$ [−], ozone absorption $T_{o,\Lambda}$ [−], nitrogen dioxide absorption $T_{n,\Lambda}$ [−], water vapor absorption $T_{w,\Lambda}$ [−], and aerosol extinction $T_{a,\Lambda}$ [−] (*Gueymard*, 1989, 2008). The equations to compute the transmittance terms $T_{X,\Lambda}$ for both bands are given in *Gueymard* (2003, 2008) and in Appendix A.7.

The direct beam radiation at normal incidence $R_{Bn,\Lambda}$ $[W\ m^{-2}]$ is computed for the first band *UV/VIS* $\Lambda 1$, and for the second band *NIR* $\Lambda 2$:

$$R_{Bn,\Lambda 1} = 0.4651 R'_0 \prod_X T_{X,\Lambda 1}\ , \tag{2.22}$$

$$R_{Bn,\Lambda 2} = 0.5195 R'_0 \prod_X T_{X,\Lambda 2}\,. \tag{2.23}$$

Following the model of *Gueymard* (2008) the incedent diffuse irradiance $R_{Dp,\Lambda}$ $[W\ m^{-2}]$ on a perfectly absorbing ground (zero albedo) is defined in equation (2.24) where the prime indicate that the transmittances are calculated with a reference air mass $m' = 1.66$ [−].

$$\begin{aligned} R_{Dp,\Lambda} &= T_{o,\Lambda} T_{g,\Lambda} T'_{n,\Lambda} T'_{w,\Lambda} \Big[B_{R,\Lambda}\big(1 - T_{R,\Lambda}\big) T_{a,\Lambda}^{0.25} \\ &\quad + B_a F_\Lambda T_{R,\Lambda}\big(1 - T_{as,\Lambda}^{0.25}\big) \Big] R'_{0,\Lambda} \sin(h_S)\,, \end{aligned} \tag{2.24}$$

where h_S $[rad]$ is the solar altitude, $B_{R,\Lambda}$ [−] are the forward scattering fractions for Rayleigh extinction, B_a [−] is the aerosol forward scattering factor, and F_Λ [−] is a correction factor to compensate for multiple scattering effects and shortcomings of the simplified approach (*Gueymard*, 2008). The term $T_{as,\Lambda}$ [−] is the aerosol scattering transmittance function of the single scattering albedos, $\omega_{\Lambda 1}$ [−] and $\omega_{\Lambda 2}$ [−], and of the spectral aerosol optical depth, $\tau_{a\Lambda}$ [−] (*Gueymard*, 1989, 2008). For the parameterizations of the above quantities, see *Gueymard* (2008) and Appendix A.7.

Backscattered radiation $R_{Dd,\Lambda}$ $[W\ m^{-2}]$ must be added to the diffuse fluxes because of the interaction between the reflecting earth surface and the scattering layer of the atmosphere. This component is computed as follows (*Gueymard*, 2008):

$$R_{Dd,\Lambda} = \rho_g \rho_{s,\Lambda} \big(R_{Bn,\Lambda} \sin(h_S) + R_{Dp,\Lambda} \big) / \big(1 - \rho_{g,\Lambda} \rho_{s,\Lambda} \big) \,, \tag{2.25}$$

where ρ_g $[-]$ is the ground albedo referring to a large area of 5-50 $[km]$ radius surrounding the point of interest and $\rho_{s,\Lambda}$ $[-]$ is the sky albedo, which is described in *Gueymard* (2008) (Appendix: A.7). Finally, the total diffuse irradiance for clear sky conditions in each band is $R_{D,\Lambda} = R_{Dp,\Lambda} + R_{Dd,\Lambda}$ and the normal global irradiance is $R_{Gn,\Lambda} = R_{Bn,\Lambda} + R_{D,\Lambda}$.

The parameters required for the clear sky radiation model of *Gueymard* (2008) are the ozone u_o $[cm]$ and nitrogen dioxide u_n $[cm]$ amounts in the atmospheric column, the single scattering albedos $\omega_{\Lambda 1}$ $[-]$ and $\omega_{\Lambda 2}$ $[-]$, the surrounding ground albedo ρ_g $[-]$, and the Ångström turbidity parameters α_Λ $[-]$ and β_Λ $[-]$ from which the spectral aerosol optical depth $\tau_{a\Lambda}$ can be obtained trough the Ångström equation:

$$\tau_{a\Lambda} = \beta_\Lambda \Lambda^{-\alpha_\Lambda} \,. \tag{2.26}$$

In the two band model, the wavelength Λ is substituted by an effective wavelength Λ_e for each of the two bands. Further α_Λ and β_Λ are taken equal for the two band (*Gueymard*, 1989, 2008). These parameters are not commonly available for a typical application of the weather generator. Nonetheless, the ranges of variation of several of these parameters are limited. In most cases typical values can be assumed. The value of the single scattering albedo ω_Λ is typically constrained between 0.75-0.98 for most applications (*Russell et al.*, 2002); *Gueymard* (2008) suggests to adopt a value of $\omega_{\Lambda 1} = 0.92$ and a value $\omega_{\Lambda 2} = 0.84$ when no-information is available. The ozone, u_o, and the nitrogen dioxide, u_n, amounts have a minimal influence in the overall process and constant values of 0.35 $[cm]$ and 0.0002 $[cm]$, respectively, are assumed in the weather generator. The surrounding ground albedo ρ_g $[-]$ depends on the location but for snow-free region its value is typically between 0.1 and 0.25. The contribution of backscattered radiation is very small (*Gueymard*, 2008) and may become important only in snow-covered region, where ρ_g can reach the values of 0.7-0.85. The Ångström turbidity parameters α and β require a more detailed discussion. These parameters, especially β, have a strong effect in determining the clear sky irradiance. Suitable values of α and β can be derived from the spectral irradiance measurement, typically Aerosol Optical Depth (AOD) from n discrete bands using a linearization of Ångström equation (2.26) (*Gueymard*, 2008). The development of various sun-photometric ground networks, especially AERONET (http://aeronet.gsfc.nasa.gov/) (*Holben et al.*, 1998) has provided a large data archive of measured AOD and other atmospheric states with a world-wide coverage. The possible values that the Ångström turbidity α can assume are 1.3±0.5. The parameter β, on the other hand, can vary several orders of

magnitude reflecting sky conditions, from nearly zero (0.001 or less) for clear sky to 0.5 for very hazy conditions (*Chaiwiwatworakul and Chirarattananon*, 2004). When site-specific values of α and β are not available, the weather generator uses reference values: 1.3 for α (*Gueymard*, 1989) and β is calibrated to fit the average monthly clear sky radiation.

An example of the performance obtained with the model of *Gueymard* (2008) for clear sky condition is shown in Figure 2.6.1, where global, direct and diffuse broadband shortwave radiation are compared with the observations. The daily cycles of the clear sky shortwave radiation are reproduced satisfactorily for the different components, although midday differences typically in the order of $[10-20]$ $[W\ m^{-2}]$ are detectable. Generally, the results tend to underestimate the peaks of direct and diffuse radiation. Differences in the average monthly values are somewhat smaller.

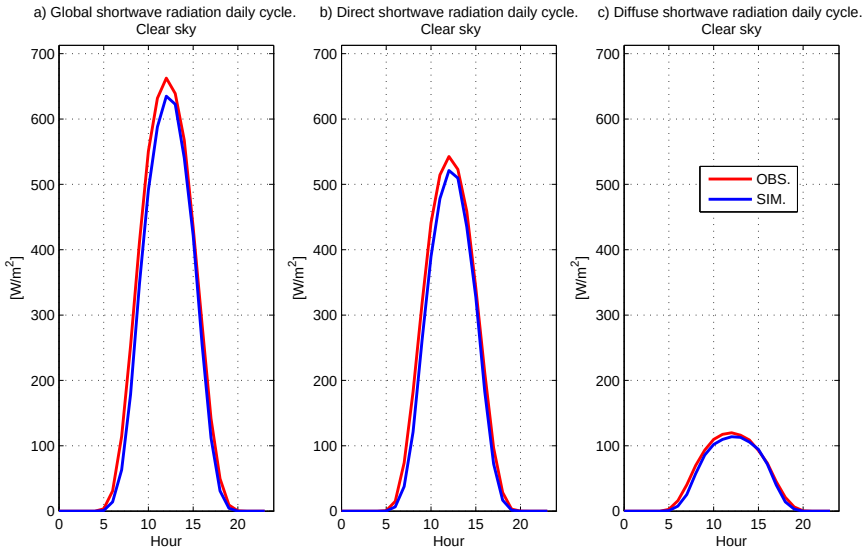

Figure 2.16: A comparison between the observed (red) and simulated (blue) daily cycle of global (a), direct (b) and diffuse (c) shortwave radiation for clear sky condition.

2.6.2 Direct and diffuse radiation for overcast conditions

Relative fluxes for cloudy conditions need to be addressed, after clear sky radiation fluxes are reproduced satisfactorily. Typically, in hydrological applications empirical equations relating the total cloud cover N $[-]$ to the ratio between clear sky and total or partially overcast radiation were used to account for clouds effects (*Kasten and Czeplak*, 1980; *Becker*, 2001). Radiative properties of clouds are related to their type and structure. The latter should be taken into account through some parametrization. The approach described in *Ivanov et al.* (2007) is also employed in AWE-GEN and uses the models developed by *Stephens* (1978) and *Slingo* (1989). These approaches argue that radiative properties of clouds are mainly related to the total vertical liquid water path LWP $[g\ m^{-2}]$, which remains almost constant for clouds with the same broadband optical thickness (*Stephens*, 1978). Specifically

Slingo (1989) simplified a multi-band cloud transmittance model to include only four wavelength bands, making the application suitable for weather generator purposes. This model parameterizes cloud transmittances for diffuse $R_{D,\Lambda}$ and normal direct beam $R_{Bn,\Lambda}$ clear sky fluxes, considering the latter normally incident on top of the clouds. *Slingo* (1989) accounted for four spectral bands λ, one in *UV/VIS* and three in *NIR* wavelength intervals: $[0.25-0.69\mu m], [0.69-1.19\mu m], [1.19-2.38\mu m], [2.38-4.0\mu m]$. The four band approach of *Slingo* (1989) can be transferred into the two band of *Gueymard* (2008) considering that the first bands of the two model *UV/VIS* almost coincide $\Lambda 1 \simeq \lambda 1$ and the second band $\Lambda 2$ is the sum of the other three bands $\Lambda 2 = \lambda 2 + \lambda 3 + \lambda 4$. The fluxes in the ultraviolet/visible, *UV/VIS*, band with wavelengths $[0.29 - 0.70\mu m]$, $\Lambda 1$, are therefore obtained from the first band of *Slingo* (1989) model and the fluxes in the near infrared, *NIR*, band with wavelengths $[0.70 - 4.0\mu m]$, $\Lambda 2$, are obtained by adding the values for the three bands (*Ivanov et al.*, 2007). The direct normal irradiance in each band $\lambda\,, = 1\,, 2\,, 3\,, 4$ for cloudy conditions $\widetilde{R}_{Bn,\Lambda}$ $[W\ m^{-2}]$ is estimated as a linear combination of the fluxes from clear and cloudy fractions of the sky (*Slingo*, 1989):

$$\widetilde{R}_{Bn,\Lambda} = R_{Bn,\Lambda}\Big[(1-N) + T_{B,\lambda}N\Big]\frac{k(\lambda)}{K(\Lambda)}\,, \tag{2.27}$$

where $T_{B,\lambda}$ $[-]$ is the cloud transmissivity for direct beam flux in band λ, $k(\lambda)$ are the respective fractions of solar irradiance at the top of atmosphere in each band for *Slingo* (1989), [0.460 0.326 0.181 0.033] and $K(\Lambda)$ are the respective fractions of solar radiation in the model of *Gueymard* (2008) [0.4651 0.5195]. Further details of the parametrization can be found in the auxiliary material of *Ivanov et al.* (2007) and in Appendix A.8 of this work.

The diffuse radiative fluxes for cloudy conditions can result from the diffuse clear sky fraction and from the direct radiation incident on the clouds. The incident component of diffuse radiation in each band $\lambda\,, = 1\,, 2\,, 3\,, 4$ for cloudy conditions $\widetilde{R}_{Dp,\Lambda}$ $[W\ m^{-2}]$ is estimated as a linear combination of the fluxes from clear and cloudy fractions of the sky (*Slingo*, 1989):

$$\widetilde{R}_{Dp,\Lambda} = (1-N)R_{Dp,\Lambda} + N\Big[T_{DB,\lambda}R_{Bn,\Lambda} + T_{DD,\lambda}R_{Dp,\Lambda}\Big]\frac{k(\lambda)}{K(\Lambda)}\,, \tag{2.28}$$

where $T_{DB,\lambda}$ $[-]$ and $T_{DD,\lambda}$ $[-]$ are the diffuse transmissivity for direct and incident diffuse radiation, respectively. The backscattered contribution under a cloudy sky $\widetilde{R}_{Dd,\Lambda}$ $[W\ m^{-2}]$ is computed accounting for the effects of cloud transmittance:

$$\begin{aligned}\widetilde{R}_{Dd,\Lambda} &= \big[\rho_g\rho_{csB,\Lambda}/\big(1-\rho_{g,\Lambda}\rho_{csB,\Lambda}\big)\big]\,\widetilde{R}_{Bn,\Lambda}\sin(h_S) \\ &\quad + \big[\rho_g\rho_{csD,\Lambda}/\big(1-\rho_{g,\Lambda}\rho_{csD,\Lambda}\big)\big]\,\widetilde{R}_{Dp,\Lambda}\,.\end{aligned} \tag{2.29}$$

The equation 2.29 has the same expression as 2.25, with the difference that the sky albedo for overcast or partially overcast conditions depends on the cloud albedo, which is different for direct beam $\rho_{csB,\Lambda}$ $[-]$ and diffuse radiation $\rho_{csD,\Lambda}$ $[-]$. The

albedos $\rho_{csB,\Lambda}$ and $\rho_{csD,\Lambda}$ are estimated as a linear combination of clear sky albedo ρ_s [−] and diffuse reflectivity for direct and diffuse incident radiation $A_{B,\lambda}$ [−], $A_{D,\lambda}$ [−]:

$$\rho_{csB,\Lambda} = (1-N)\rho_{s,\Lambda} + NA_{B,\lambda}\frac{k(\lambda)}{K(\Lambda)} \,, \tag{2.30}$$

$$\rho_{csD,\Lambda} = (1-N)\rho_{s,\Lambda} + NA_{D,\lambda}\frac{k(\lambda)}{K(\Lambda)} \,, \tag{2.31}$$

where the diffuse reflectivity for direct beam and diffuse incident radiation $A_{B,\lambda}$, $A_{D,\lambda}$ are defined in *Slingo* (1989) (Appendix A.8) and are considered to be an approximation of cloud albedo.

The total diffuse radiation for cloudy sky is therefore: $\widetilde{R}_{D,\Lambda} = \widetilde{R}_{Dp,\Lambda} + \widetilde{R}_{Dd,\Lambda}$. The final value of the global radiation in each band Λ is $\widetilde{R}_{Gn,\Lambda} = \widetilde{R}_{Bn,\Lambda} + \widetilde{R}_{D,\Lambda}$. For an arbitrary sky condition global normal shortwave radiation is indicated as $R_{sw,n}$ [$W\ m^{-2}$], where $R_{sw,n} = \sum_\Lambda \widetilde{R}_{Gn,\Lambda}$, if $N > 0$, and $R_{sw,n} = \sum_\Lambda R_{Gn,\Lambda}$, if $N = 0$.

The described model requires cloud cover fractions and the cloud optical thickness τ_N [−], which is essential for the description of the radiative properties of clouds (*Stephens*, 1978). The thickness τ_N can be approximately parameterized in terms of the liquid water path, LWP (*Stephens*, 1978). The cloudy sky condition is assumed to be characterized by a certain amount of $LWP(N)$ [$g\ m^{-2}$], which is estimated from a reference value of LWP for overcast conditions LWP_R [$g\ m^{-2}$] (*Ivanov et al.*, 2007):

$$LWP(N) = LWP_R\, N \,. \tag{2.32}$$

From equation (2.32), it follows that LWP varies from 0, when $N = 0$, to LWP_R ($N = 1$). Note that the exponential dependence of LWP on cloudiness N in *Ivanov et al.* (2007) has been replaced with a linear one, which leads to the relationship $R_{sw,n}(N)/R_{sw,n}(0)$ that better matches observations (*Kasten and Czeplak*, 1980). By evaluating different LWP_R for different months, this parametrization allows one to take into account the seasonal differences in cloud properties. In some circumstances LWP measurements or estimations could be also available and may be used directly.

The output of the radiation component of the weather generator contains the direct and diffuse radiation fluxes for the ultraviolet/visible *UV/VIS* band [$0.29 - 0.70\mu m$] and the near infrared *NIR* band [$0.70 - 4.0\mu m$]. As stated previously, the photosynthetically active radiation (*PAR*) may be important in several applications. The *PAR* radiation is the spectral range of solar light between 0.40 [μm] and 0.70 [μm]. This range does not coincide perfectly with the first radiation band *UV/VIS*. Reduction factors between the first radiation band and PAR are adopted (equations 2.33 and 2.34), as proposed by *Gueymard* (2008). The reduction factors, M_B [−] and M_G [−], are considered valid also for cloudy conditions, although the original formulation of *Gueymard* (2008) was proposed only for clear sky conditions. This

assumption should not introduce significant errors since the reduction factors depend only on Ångström turbidities, and on the air mass of aerosol extinction and of Rayleigh scattering. These factors are not expected to be modified under cloudy conditions.

$$\widetilde{PAR}_{Bn} = \widetilde{R}_{Bn,\Lambda 1}\, M_B \ , \tag{2.33}$$

$$\widetilde{PAR}_{D} = \widetilde{R}_{Gn,\Lambda 1}\, M_G - \widetilde{PAR}_{Bn} \, , \tag{2.34}$$

where $\widetilde{PAR}_{Bn}$ $[W\ m^{-2}]$ and $\widetilde{PAR}_{D}$ $[W\ m^{-2}]$ are the direct beam PAR at normal irradiance and the diffuse PAR, respectively. The parametrization for the two reduction factors M_B and M_G can be found in *Gueymard* (2008) and in Appendix A.7. The same equations are used for clear sky condition.

The spatial distribution of solar radiation over a surface is function of the surface geometry, i.e. of the local topography. Site slope β_T $[rad]$ and aspect ζ_T $[rad]$ can alter the daily distribution of incoming energy at the ground. Furthermore, the reflection and shadow effects of the surrounding terrain can strongly influence radiation fluxes. Obviously, the terrain effects are site-specific and are not accounted for in the weather generator. For a flat unobscured surface the only applicable adjustment is to multiply the $\widetilde{R}_{Bn,\Lambda}$ by the sine of the solar altitude h_S: $\widetilde{R}_{B,\Lambda} = \widetilde{R}_{Bn,\Lambda} \sin(h_S)$ in order to obtain the flux density for unit surface area. The same holds for clear sky condition. When local topographic effects are non-negligible, $\sin(h_S)$ is substituted by a function of β_T and ζ_T (Appendix A.9). When the remote shading effect becomes important, the sky view factor $S_{vf}(\vec{x})$ and the shadow effect $S_h(\vec{x}, t)$ function at the position $\vec{x}$ and the local time t, should be introduced (*Olseth et al.*, 1995; *Kumar et al.*, 1997; *Dubayah and Loechel*, 1997; *Rigon et al.*, 2006; *Ivanov et al.*, 2007). Although topography effects cannot be accounted for directly by the weather generator, insights on the topographic effects on solar radiation are provided in Appendix A.9.

2.6.3 Results and validation

In all simulations, the stations are considered to be located on a flat surface, without topography-induced shadow or obstruction effects. The β Ångström turbidity parameter is calibrated monthly to fit the average value of global, direct, and diffuse clear sky radiation. The reference value of the liquid water path LWP_R is successively calibrated to fit the global, direct, and diffuse shortwave radiation for all sky conditions. The results obtained are shown in Figures 2.17, 2.18, and 2.19. The monthly average of shortwave radiation (Figure 2.17) is simulated properly, with occasional differences of 5-15 $[W\ m^{-2}]$. Such differences could be related to the higher frequency variability of parameters such as β Ångström turbidity or LWP_R. Weekly or daily variabilities of these parameters are not captured in AWE-GEN, as the relevant parameters are calibrated at the monthly scale. There is also an effect of error propagation from the simulation of the cloud process, that can make the results worsen. Daily cycles of shortwave radiation are reproduced satisfactorily

for different components (Figure 2.18), although biases are present during mid-day hours for several stations. The weather generator tends to overestimate direct radiation and underestimate diffuse radiation, as shown in Figure 2.18 for Boston. However, it should be noted that the opposite holds true sometimes. Annual cycles of global radiation for different hours of local time are simulated very well, except for small deviations at the sunrise and sunset hours (Figure 2.19). This mismatch can be related to the reflection of beam radiation inducing radiative fluxes before sunrise and after sunset or to the measurement errors that are very likely to occur at low radiation density.

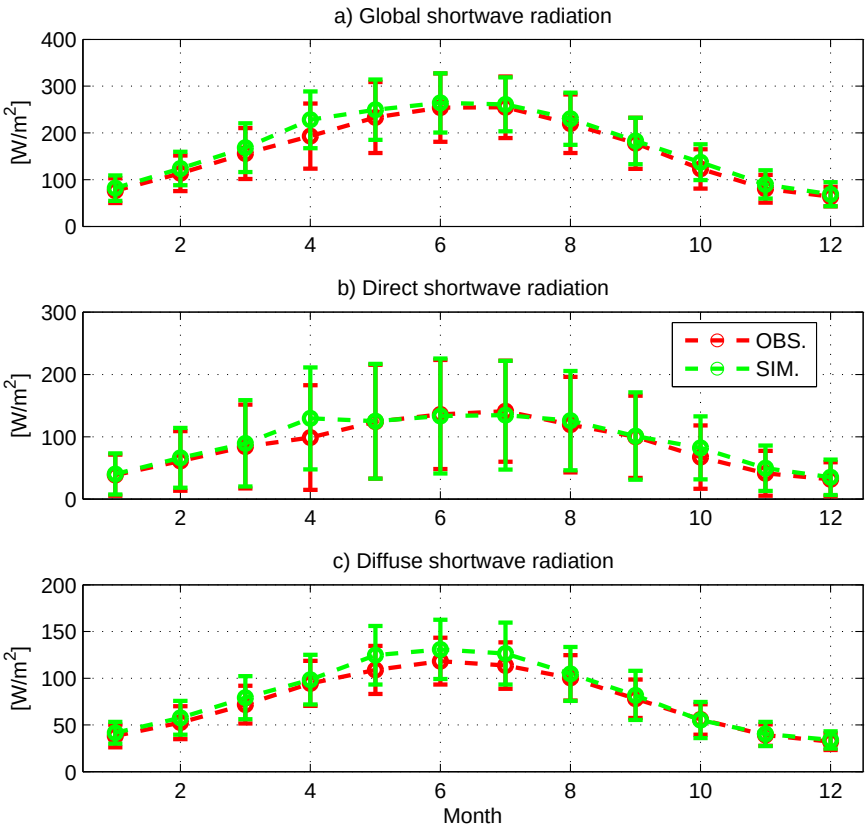

Figure 2.17: A comparison between the observed (red) and simulated (green) mean monthly shortwave radiation. a) Global radiation. b) Direct beam radiation. c) Diffuse radiation. The vertical bars denote the standard deviations of the monthly values.

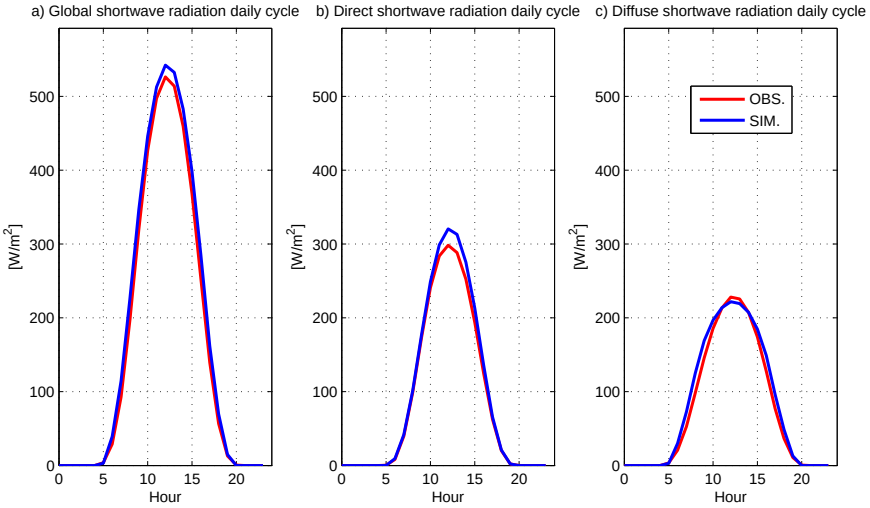

Figure 2.18: A comparison between the observed (red) and simulated (blue) daily cycle of global (a), direct (b) and diffuse (c) shortwave radiation for all sky conditions.

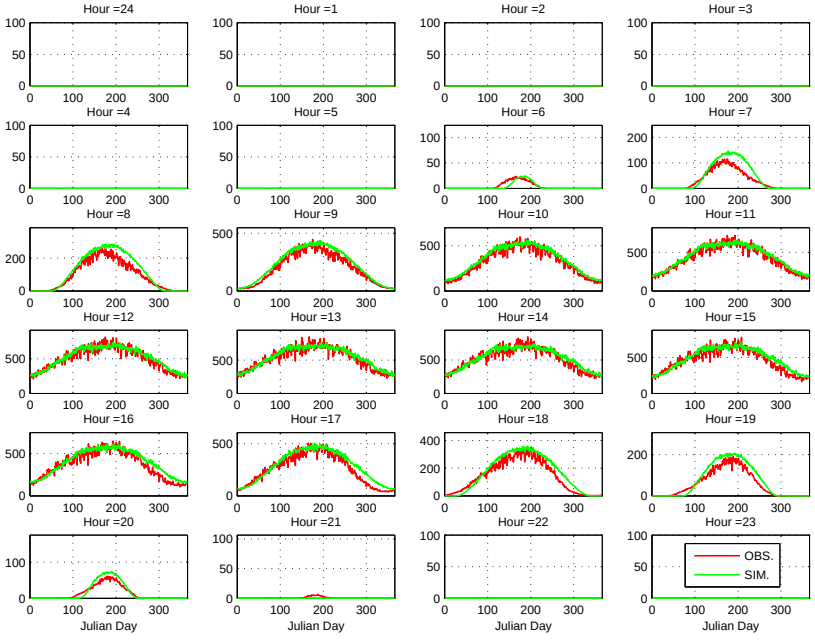

Figure 2.19: A comparison between the observed (red) and simulated (green) annual cycle of global shortwave radiation for different local time hours. The global shortwave fluxes are expressed in $[W\ m^{-2}]$.

2.7 Vapor pressure

Given the importance of vapor pressure for several hydrological and ecological applications, it needs to be included as one of the simulated variables. This variable is not commonly simulated by weather generators (*Semenov et al.*, 1998). Some weather generators include relative humidity (*Sharpley and Williams*, 1990; *McKague et al.*, 2003) or dew point temperature (*Parlange and Katz*, 2000; *Ivanov et al.*, 2007). Relative humidity or dew point temperature are generally estimated with a multi-regressive analysis (*Parlange and Katz*, 2000). An attempt to introduce a more physically-based approach was done by considering that dew point temperature is almost constant during the day time and has the tendency to come into equilibrium with nightly minimum temperatures (*Kimball et al.*, 1997). *Kimball et al.* (1997) pointed out that in arid and semiarid climate the dew point temperature could differ from nightly minimum temperature and proposed an empirical model to take into account these adjustments. A modified version of the same model was used to simulate dew point temperature by *Ivanov et al.* (2007). Typically, a daily or longer time step is used to simulate dew point temperature. *Curtis and Eagleson* (1982) proposed a multi-regressive model to simulate hourly dew point temperature for cases when its cross-correlation with other variables is non-negligible. While the conversion of relative humidity or dew point temperature into vapor pressure is mathematically straightforward, it involves non-linearity. Because of that, accurate simulations of dew point temperature or relative humidity do not necessary imply a good fit for vapor pressure. Dew point or relative humidity outputs of weather generators should be checked before asserting their suitability for applications that require vapor pressure.

2.7.1 Model

This study approaches the simulation of air humidity via the simulation of vapor pressure deficit Δe $[Pa]$, i.e., the difference between the vapor pressure at saturation e_{sat} $[Pa]$, and the air ambient vapor pressure e_a $[Pa]$, where $e_{sat} = 611 \exp[17.27\, T_a/(237.3 + T_a)]$ $[Pa]$ (with T_a $[^\circ C]$) is a well known expression (*Dingman*, 1994). Following *Bovard et al.* (2005), who noted a correlation between vapor pressure deficit Δe and PAR during daylight time, correlations of vapor pressure deficit Δe with shortwave radiation and temperature have been analyzed in this study. The vapor pressure deficit Δe shows a strong correlation with air temperature and a weaker correlation with global shortwave radiation lagged by several hours. Specific humidity and vapor pressure e_a remain almost constant throughout the day, especially in dry climates. Therefore variations of Δe and relative humidity U $[-]$ are well explained by the diurnal cycle of air temperature. Specifically, there is a positive relation between the daily cycle of air temperature and the daily cycle of vapor pressure deficit. The assumption is primarily valid when the atmosphere is stable and exchanges between air masses with different characteristics are limited.

In order to simulate vapor pressure, a similar model framework as for the case of

air temperature is used: Δe is simulated as the sum of the deterministic component, $\widehat{\Delta e}$ $[Pa]$ and the stochastic component, $d\Delta e$ $[Pa]$:

$$\Delta e(t) = \widehat{\Delta e}(t) + d\Delta e(t)\,. \tag{2.35}$$

The deterministic component of vapor pressure deficit is related to air temperature through a cubic function, which is essentially an approximation of the commonly used exponential relation between T_a $[^\circ C]$ and e_{sat}. From observational data, a non-negligible correlation was also detected with global shortwave radiation R_{sw} $[W\ m^{-2}]$ at lag one and two hours. The influence of solar radiation is generally minor, but it becomes important when air temperature effects are secondary. The deterministic component Δe is calculated with the equation:

$$\widehat{\Delta e}(t) = a_0 + a_1 T_a^3(t) + a_2 R_{sw}(t-1) + a_3 R_{sw}(t-2)\,, \tag{2.36}$$

where a_i ($i = 0,\ 1,\ \ldots,\ 3$) are the regression coefficients. The deterministic component $\widehat{\Delta e}$ usually shows a minor variance, when compared with the $\Delta e(t)$. The residuals $d\Delta e(t)$, that constitute the stochastic component of vapor pressure deficit, are modeled with the AR(1) approach in a similar fashion as for other variables:

$$d\Delta e(t) = \overline{d\Delta e} + \rho_{d\Delta e}\big(d\Delta e(t-1) - \overline{d\Delta e}\big) + \varepsilon(t)\sigma_{d\Delta e}\sqrt{(1-\rho_{d\Delta e}^2)}\,, \tag{2.37}$$

where $\overline{d\Delta e}$ is the average of vapor pressure deficit deviations, $\sigma_{d\Delta e}$ is the standard deviation and $\rho_{d\Delta e}$ is the lag-1 autocorrelation of the process, and $\varepsilon(t)$ are the standard normal deviate. Finally, the atmospheric vapor pressure e_a is calculated as the difference between e_{sat} and $\Delta e(t)$. It may be possible that the value of e_a calculated with the proposed procedure will assume values larger than e_{sat} and smaller than 0. Because of that, such values are simply corrected and assigned to the boundary values 0 and e_{sat}. This approximation might introduce a bias in the e_a values toward the limits. Nonetheless, this shortcoming is expected to slightly affect hydrological or ecological applications and furthermore could be corrected in future versions of the model.

The parameters of the deterministic component a_i ($i = 0,\ 1,\ \ldots,\ 3$) are estimated on a monthly basis using conventional regression techniques, for example, the least square approach. The parameters of the stochastic component $\overline{d\Delta e}$, $\sigma_{d\Delta e}$ and $\rho_{d\Delta e}$ are evaluated using the time series of $d\Delta e(t)$ after removing the deterministic component from the observed series of Δe.

2.7.2 Results and validation

The performance of AWE-GEN in simulating metrics of air humidity is evaluated by investigating several statistical properties of vapor pressure, e_a $[Pa]$, relative humidity, U $[-]$, and dew point temperature, T_{dew} $[^\circ C]$. The capability of the model to reproduce the first two moments of vapor pressure at the time aggregation

periods of 1 hour and 24 hours is shown in Figure 2.20. Overall the performance is quite remarkable. The vapor pressure probability density function (Figure 2.21b) is also well simulated. In hydrologic applications, the simulation of the daily cycle of relative humidity is an important feature that affects evaporation flux estimation. In Figure 2.21a, the comparison between simulations and observations highlights a good overlap of the daily cycles, especially during day-time hours.

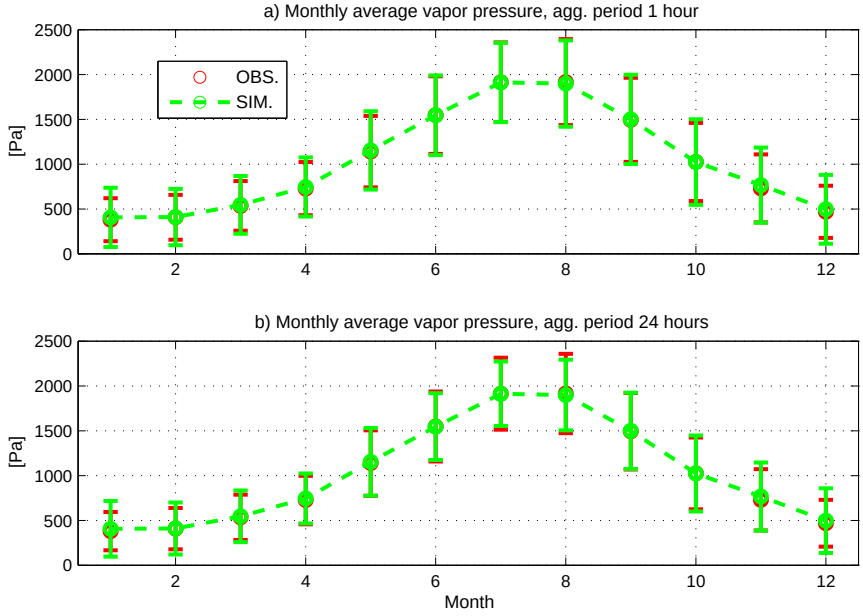

Figure 2.20: A comparison between the observed (red) and simulated (green) mean monthly vapor pressure for 1 $[h]$ (a) and 24 $[h]$ (b) aggregation time periods. The vertical bars denote the standard deviations of the monthly values.

The fitting of the probability density functions of relative humidity, U, and dew point temperature, T_{dew}, are shown in Figure 2.22. AWE-GEN also satisfactorily reproduces these quantities. The relative humidity probability density in the upper and lower limits of the feasible range is overestimated. This holds true for several locations and is due to the overshot approximation. PDF shape differences in the tails of the T_{dew} distributions are rather frequent due to non-linearities in the transformation of e_a to T_{dew}. The seasonality of mean relative humidity and its variance are also well captured (Figure 2.23), with only a slight underestimation of the 24 hours variance, especially in dry climates. Conversely, the dew point temperature is poorly simulated. The monthly variances simulated by AWE-GEN are usually larger than the observed ones (Figure 2.24a). This holds true for all the analyzed metrics of daily dew point temperature, i.e., mean, maximum, and minimum. Furthermore, the mean of daily maximum and minimum dew point temperature are typically overestimated and underestimated, respectively (Figure 2.24). Shortcomings in reproducing dew point temperature should be not an issue in many applications, since vapor pressure, e_a, and relative humidity, U, are typically required. When T_{dew} is the variable of interest, the above limitations may become important and the

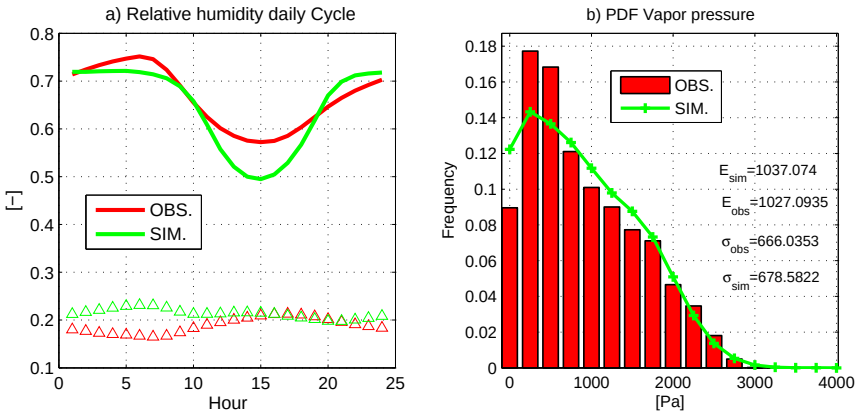

Figure 2.21: A comparison between the observed (red) and simulated (green) relative humidity daily cycle (a) and vapor pressure probability density function (b). The triangles in (a) represent the daily cycle of relative humidity standard deviation. E_{obs} and σ_{obs} are the observed mean and standard deviation and E_{sim} and σ_{sim} are the simulated ones.

suitability of simulated T_{dew} values must be checked according to the scope of the study.

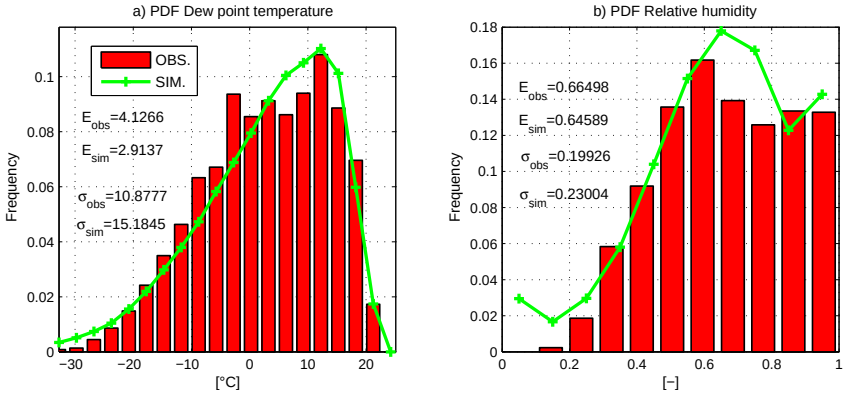

Figure 2.22: A comparison between the observed (red) and simulated (green) dew point temperature (a) and relative humidity (b) probability density functions. E_{obs} and σ_{obs} are the observed mean and standard deviation and E_{sim} and σ_{sim} are the simulated ones.

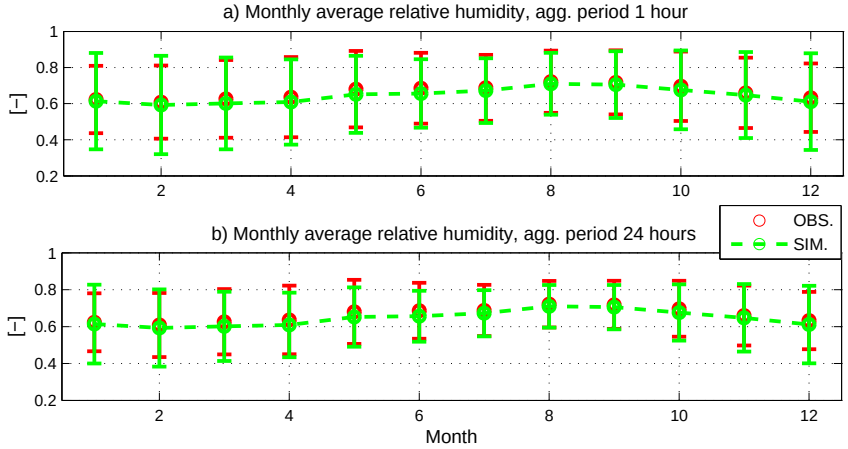

Figure 2.23: A comparison between the observed (red) and simulated (green) mean monthly relative humidity for aggregation periods of 1 hour (a) and 24 hours (b). The vertical bars denote the standard deviations of the monthly value.

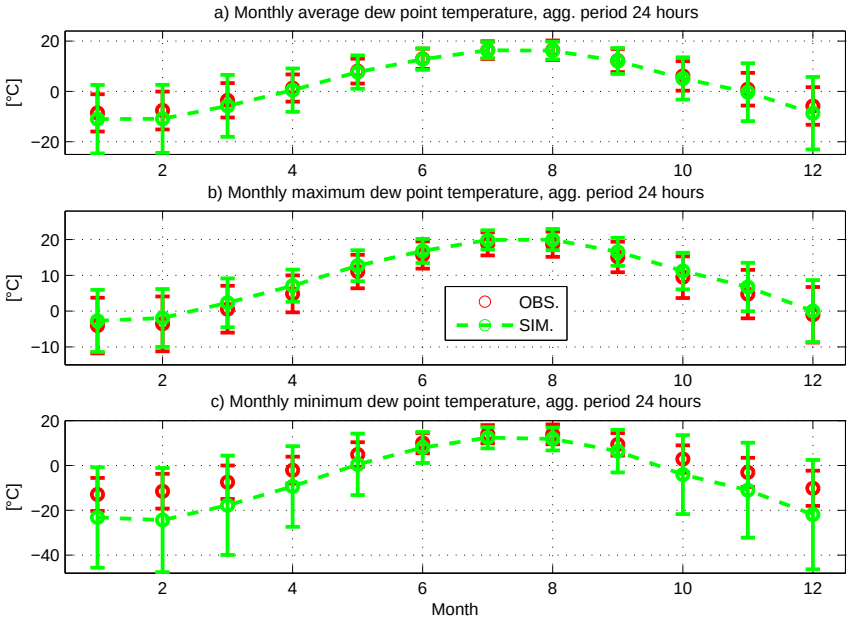

Figure 2.24: A comparison between the observed (red) and simulated (green) monthly dew point temperature for aggregation periods of 24 hours. a) Mean dew point temperature. b) Maximum dew point temperature. c) Minimum dew point temperature. The vertical bars denote the standard deviations of the monthly value.

2.8 Wind speed

Several studies highlight that cross-correlation between wind speed and other variables is typically very weak (*Curtis and Eagleson*, 1982; *Parlange and Katz*, 2000; *Ivanov et al.*, 2007) and thus wind speed is usually modeled as an independent variable. Nevertheless, in some locations wind speed exhibits a marked daily cycle and therefore the assumption of independence may need to be questioned. The inclusions of correlations among wind speed and other variables can be important because it allows the generator to capture wind speed intra-daily variations. The daily cycle of wind speed may affect the estimation of quantities such as the sensible and latent heat and is often required in hydrological and eco-hydrological modeling. The wind speed daily cycle is mainly related to the turbulent fluxes occurring in the surface boundary layer that are enhanced during the day-time by the the dissipation of sensible heat. The wind daily cycle is thus more pronounced in dry climates where the Bowen ratio is higher. Starting with this physical concept, the relation between the global solar radiation and wind speed has been investigated. It was found that the maximum correlation between the two cycles is usually shifted by several hours, possibly because of the different thermal properties of the ground surface and air. Correlation between different lags of global solar radiation and wind speed have been checked. The assumption of correlation between radiation and wind speed may become invalid for sites with strongly advective regime, e.g., when a site is located in a sea proximity, where the differential heating of surface affects the average daily cycle through sea breeze. Therefore, the weather generator is not expected to yield robust results for such locations that may present very complex daily cycles.

2.8.1 Model

The correlation coefficients found between wind speed W_s $[m\ s^{-1}]$ and time shifted global solar radiation R_{sw} $[W\ m^{-2}]$ are usually very small, however they are significant enough to induce a daily cycle in the wind speed component. Similarly to previously discussed approaches, the method adopted here to simulate the wind speed, W_s $[m\ s^{-1}]$, is based on representing the process as a sum of the deterministic $\widehat{W_s}$ and the stochastic component dW_s:

$$W_s(t) = \widehat{W_s}(t) + dW_s(t)\,. \tag{2.38}$$

The deterministic component $\widehat{W_s}(t)$ relates the wind speed to the incident global shortwave radiation R_{sw}. The correlation is shifted by several hours and the shift strongly depends on the site location. Lags up to three hours of R_{sw} are used to calculate the deterministic component of wind speed:

$$\widehat{W_s}(t) = c_0 + c_1 R_{sw}(t) + c_2 R_{sw}(t-1) + c_3 R_{sw}(t-2) + c_4 R_{sw}(t-3)\,, \tag{2.39}$$

where c_i $(i = 0,\ 1,\ \ldots,\ 4)$ are the regression coefficients. The stochastic component $dW_s(t) = W_s(t) - \widehat{W_s}(t)$ is modeled with the autoregressive AR(1) model including

the Wilson-Hilferty transformation (*Wilson and Hilferty*, 1931; *Fiering and Jackson*, 1971). This transformation is necessary to represent the generally positive skewness exhibited by hourly wind speed data. The overall distribution of wind speed is indeed positively skewed and the Weibull distribution has been often used to model it (*Takle and Brown*, 1978; *Deaves and Lines*, 1997). The stochastic component dW_s becomes:

$$dW_s(t) = \overline{dW_s} + \rho_{dW_s}\big(dW_s(t-1) - \overline{dW_s}\big) + \eta(t)\sigma_{dW_s}\sqrt{(1-\rho_{dW_s}^2)}\,, \qquad (2.40)$$

where $\overline{dW_s}$ is the average wind speed deviation, σ_{dW_s} is the standard deviation, and ρ_{dW_s} is the lag-1 autocorrelation of the process. The term $\eta(t)$ represents the random deviate of the process and is skewed according to the Wilson-Hilferty transformation:

$$\eta(t) = \frac{2}{\gamma_n}\Big(1 + \frac{\gamma_n \varepsilon(t)}{6} - \frac{\gamma_n^2}{36}\Big)^3 - \frac{2}{\gamma_n}\,, \qquad (2.41)$$

where the skewness of $\eta(t)$ is $\gamma_n = (1-\rho_{dW_s}^3)\gamma_{dW_S}/(1-\rho_{dW_s}^2)^{1.5}$; γ_{dW_s} is the skewness of the data, and $\varepsilon(t)$ are the standard normal deviate.

The proposed approach remains valid also when the wind speed is an independent process; in this case the simulation will be dominated by the stochastic component, producing consistent results.

The parameters c_i ($i = 0, 1, \ldots, 4$) of the deterministic component are estimated with conventional regression techniques. The parameters of the stochastic component $\overline{dW_s}$, σ_{dW_s}, ρ_{dW_s}, and γ_{dW_S} are evaluated from the time series of $dW_s(t)$ after removing the deterministic component from the observed series of W_s. Wind speed generally does not present marked differences throughout the year, therefore the parameters are derived and assumed to be valid for all months.

2.8.2 Results and validation

The probability density function of wind speed is well captured in AWE-GEN as well as are the first two statistical moments of the process (Figure 2.25a). The wind speed daily cycle is reproduced correctly (Figure 2.25b) for almost all of the analyzed stations, and surprisingly also for stations located near sea. Nonetheless, it would not be surprising if the weather generator would perform poorly in some cases. The weather generator is unable to reproduce extremes, as seen in Figure 2.26. The hourly and daily extremes of wind speed are strongly underestimated, even for return periods lower than one year. This is not a problem for ecological or hydrological purposes. However, AWE-GEN cannot be used to generate meteorological forcing for structural design purposes that require wind extremes.

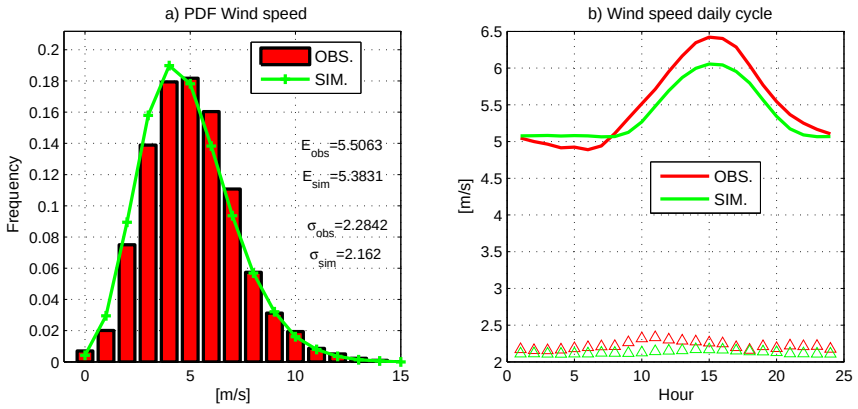

Figure 2.25: A comparison between the observed (red) and simulated (green) wind speed probability density function (a) and daily cycle of wind speed (b). E_{obs} and σ_{obs} are the observed mean and standard deviation and E_{sim} and σ_{sim} are the simulated ones.

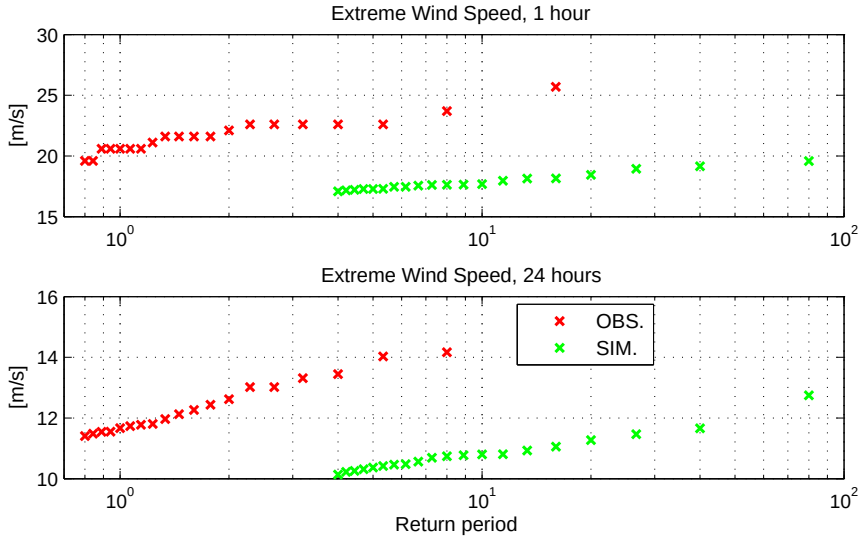

Figure 2.26: A comparison between the observed (red) and simulated (green) extremes of wind speed at aggregation periods of 1 hour (a) and 24 hours (b).

2.9 Atmospheric pressure

The atmospheric pressure P_{atm} $[mbar]$ is generally neglected in weather generators given its relatively low impact on hydrological and ecological processes. However, P_{atm} is useful in many non-linear equations describing physical phenomena, such as evaporation. This observation implies that using a constant value of atmospheric pressure is theoretically incorrect. In AWE-GEN, a simple autoregressive model AR(1) is employed with parameters estimated to be valid for the entire year, thus neglecting the seasonal distribution of this variable.

$$P_{atm}(t) = \overline{P_{atm}} + \rho_{P_{atm}} \left(P_{atm}(t-1) - \overline{P_{atm}} \right) + \varepsilon(t) \sigma_{P_{atm}} \sqrt{(1 - \rho^2_{P_{atm}})}, \quad (2.42)$$

where $\overline{P_{atm}}$ is the average atmospheric pressure, $\sigma_{P_{atm}}$ is the standard deviation, $\rho_{P_{atm}}$ is the lag-1 autocorrelation of the process, and $\varepsilon(t)$ are the standard normal deviate. The shape of the atmospheric pressure distribution is perfectly reproduced as well as are the main statistics (Figure 2.27).

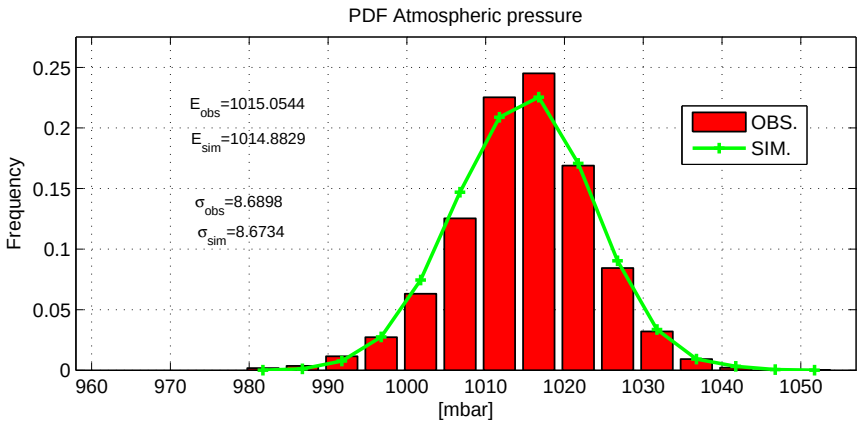

Figure 2.27: A comparison between the observed (red) and simulated (green) atmospheric pressure probability density function. E_{obs} and σ_{obs} are the observed mean and standard deviation and E_{sim} and σ_{sim} are the simulated ones.

The parameters of the model $\overline{P_{atm}}$, $\sigma_{P_{atm}}$ and $\rho_{P_{atm}}$ are evaluated from the time series of $P_{atm}(t)$ with conventional procedure.

2.10 Covariance between variables

The use of an intermediate physically-stochastic weather generator allows one to take into account mechanistic dependence between the meteorological variables, e.g precipitation vs cloudiness and, at the same time, directly introduces statistical correlations, e.g., vapor pressure vs temperature. Figure 2.28 illustrates a qualitative comparison of the interdependence between different variables. Precipitation occurrence affects cloud cover realizations, the latter process controls solar radiation and daily temperature range. Consequently, solar radiation and air temperature influence vapor pressure and wind speed calculation, generating a cascade of causal feedbacks that, starting from precipitation, affect all of the other variables.

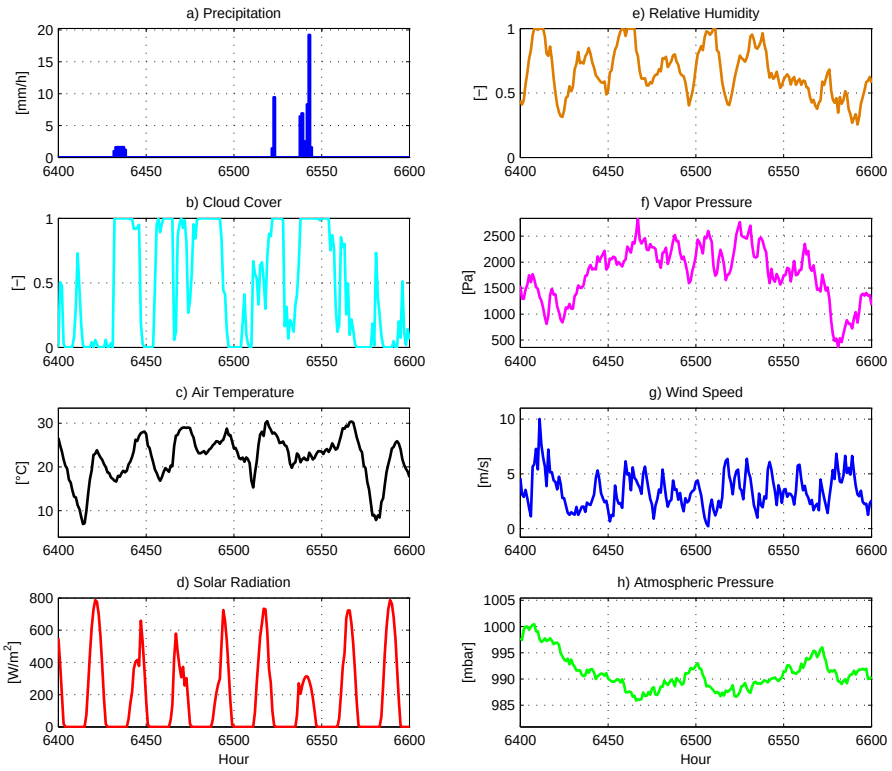

Figure 2.28: Simulated hourly values of hydro-meteorological variables with AWE-GEN: a.) precipitation; b.) cloud cover, c.) air temperature, d.) global shortwave radiation, e.) relative humidity, f.) vapor pressure, g.) wind speed, and h.) atmospheric pressure.

An explicit analysis of cross-correlation between climate variables is provided here. In Figure 2.29 a comparison between the observed and simulated mean monthly cloudiness and the number of wet days is shown. The interdependence between these two variables is generally captured in AWE-GEN but it cannot be appreciated for the discussed location. The performance in reproducing such a feature is well discernable for climates with a strong cloud cover seasonality, such as the climate corresponding to the location of San Francisco. Table 2.3 is a synthesis of the mean values of

Table 2.3: Comparison between the observed and simulated mean of daily temperature amplitude ΔT_{day}, daily global shortwave radiation R_{sw}, and daily relative humidity U during rainy and rainless days.

Variable	**Rain days**		**Rainless days**	
	Measured	Simulated	Measured	Simulated
$\Delta T_{day}[°C]$	6.8	8.0	8.4	9.0
$R_{sw}[W\ m^{-2}]$	111	143	181	186
$U[-]$	0.80	0.65	0.61	0.64

daily temperature amplitude, ΔT_{day}, the daily global shortwave radiation, R_{sw}, and the daily relative humidity, U, during rainy and rainless days. AWE-GEN tends to overestimate daily temperature amplitude for rainy days and to underestimate the relative humidity during rainy days. These shortcoming are a consequence of the structure of the weather generator that only implicity accounts for the influence of rainy hours in air temperature simulation. Cloud attenuation coefficient $K(t)$ and long-wave incoming radiation L_{atm} are the only variables connecting T_a to N. Moreover, this linkage is explicitly accounted for at the hourly and not at the daily scale. These dependencies in humid temperate climate such as the one characterize of Boston area cannot fully explain the marked difference in ΔT_{day} between rainy and rainless days. Also the underestimation of daily relative humidity, U, in rainy days can be explained by the same reasons and it is furthermore affected by the error on daily temperature amplitude.

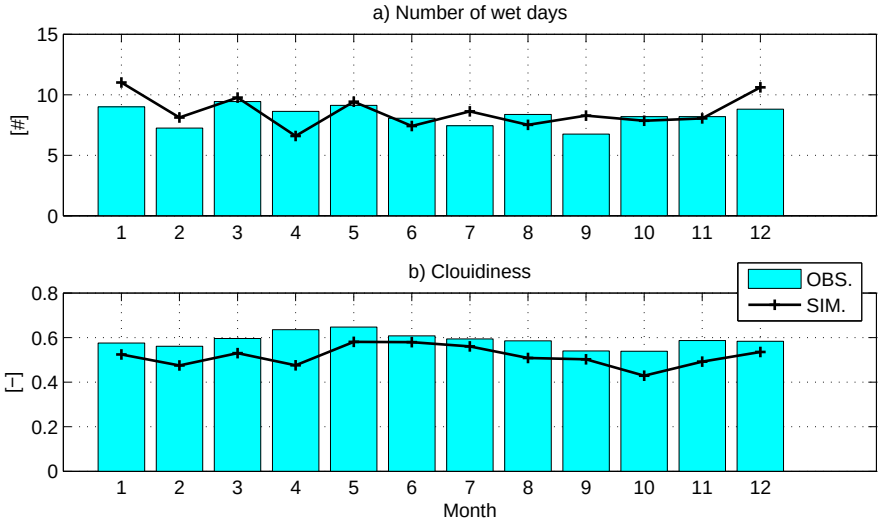

Figure 2.29: A comparison between the observed (cyan) and simulated (black) monthly number of wet days (a) and cloud cover (b).

Figure 2.30 shows an overview of cross-correlations at the daily scale between some of the variables. The principal cross-correlations are captured at lag-0. The hourly weather generator, unlike the empirical statistical weather generator, reproduces the cross correlation between climate variables only implicity, especially at the daily time scale. Although overall some differences can be noted, the results are considered

quite satisfactory in this sense.

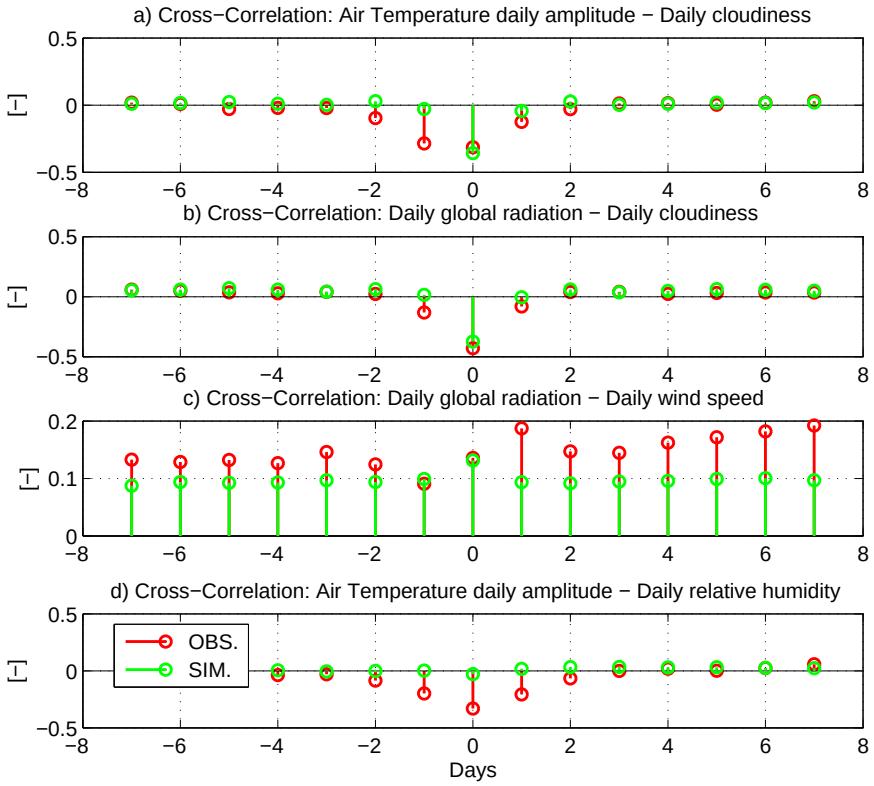

Figure 2.30: A comparison between the observed (red) and simulated (green) cross-correlation between: daily temperature amplitude and cloudiness (a), global solar radiation and cloudiness (b), global solar radiation and wind speed (c), and global solar radiation and relative humidity (d).

2.11 Application of AWE-GEN in climate change studies

The developed weather generator can be also used for climate change studies. There is the possibility to parameterize AWE-GEN on the basis of climate statistics that are not calculated from observations but are derived from a methodology of stochastic downscaling. A detailed discussion about the use of the weather generator for the simulation of future climate scenarios, as inferred from climate models, can be found in Chapter 3. Briefly, the stochastic downscaling procedure derives distributions of factors of change for several climate statistics from a multi-model ensemble of outputs of General Circulation Models (GCM) using a Bayesian approach. The methodology infers factors of change for precipitation and air temperature statistics, comparing realizations of climate models for two intervals of time. The two investigated periods are usually representing 20-40 years of simulated present climate conditions and 20-40 years of simulated future climate conditions. The factors of change are subsequently applied to the statistics derived from the observations to calculate statistics representative of the future climate conditions. Once all the statistical properties are calculated for the future climate, these are used to re-evaluate the parameters of the weather generator. A new set of modified parameters of AWE-GEN is estimated. AWE-GEN is then used to simulate a scenario corresponding to future climate conditions (see Chapter 3).

For several reasons explained in Chapter 3 the methodology is able to modify only a limited number of AWE-GEN parameters. Specifically, a new set of precipitation parameters: λ^{FUT}, β^{FUT}, η^{FUT}, μ_c^{FUT}, α^{FUT}, θ^{FUT} can be calculated as final result of the stochastic downscaling procedure. Corrections are also provided for the inter-annual variability of precipitation re-estimating $\overline{P}_{yr}^{FUT}$, $\sigma_{P_{yr}}^{FUT}$, $\gamma_{P_{yr}}^{FUT}$, and new parameters $\Delta T = T_{mon}^{FUT} - T_{mon}^{OBS}$ are introduced to account for changes in the air temperature. The new parameters ΔT_i $i = 1, ..., 12$ represent the variation of mean monthly temperature, T_{mon}, between the present and estimated future climate conditions (Chapter 3) and can be used by AWE-GEN during the simulation of the the air temperature component. Note that precipitation and air temperature affects directly or indirectly all the other variables due to the imposed linkages within the weather generator. In such a way the information about the climate change can be also transferred to variables not directly accounted for in the downscaling.

Finally, the new parameter set is required by AWE-GEN to simulate the time series of meteorological variables for the *future* climate. The time series of meteorological variables simulated with this procedure are considered to represent at hourly time scale the most probable expression of future climate for a given location (see Chapter 3 for details). The method is sufficiently generic to be applied to any future scenarios from simulations obtained with any arbitrary group of global or regional climate models. For these reasons the proposed procedure can be regarded as a powerful tool for climate change study at the local scale.

Chapter 3

DOWNSCALING AND MULTI-MODEL ENSEMBLE

3.1 Introduction

The importance of climate change science for society has been emphasized in many studies and many discussions about its impacts have been already carried out not only among scientists. A detailed discussion on climate change causes and implications is out of the scope of this work and thus is not provided. The interested reader can easily refer to the large body of literature on this subject. The primary up-to-date reference on climate change science is the Fourth Assessment Report (4AR) of the Intergovernmental Panel on Climate Change IPCC (*IPCC*, 2007a). It provides the definition of the scientific basis for climate change, as well as the possible impacts, adaptation, and mitigation strategies. The Intergovernmental Panel on Climate Change (IPCC) is a scientific intergovernmental body, that includes scientists from around the world, challenged to evaluate the risk of climate change caused by human activity. The panel was established in 1988 by the World Meteorological Organization (WMO) and the United Nations Environment Programme (UNEP), two organizations of the United Nations. The IPCC in 2007 received the Nobel Peace Prize *"for their efforts to build up and disseminate greater knowledge about man-made climate change, and to lay the foundations for the measures that are needed to counteract such change"*, quoting the official motivation of the nobel prize web-site.

Climate change has potentially significant adverse implications on the hydrological cycle and water resources. Numerous efforts have been devoted to studying these implications. Special technical reports on water resources were issued by the Environmental European Agency (*EEA*, 2007) and the IPCC (*Bates et al.*, 2008). These reports highlight several emergencies that the community will have to face in the future to cope with a changing climate. Research on climate change impacts on the hydrological cycle and the possible feedbacks between hydrological and vegetation systems are urgently needed, in order to understand and quantify these anticipated changes. Several studies have already attempted the investigation of implications in

hydrology of climate change at the local or regional scales (*Müller-Wohlfeil et al.*, 2000; *Burlando and Rosso*, 2002; *vanRheenen et al.*, 2004; *Wood et al.*, 2004; *Christensen et al.*, 2004; *Merritt et al.*, 2006; *Leander and Buishand*, 2007; *Salathé et al.*, 2007; *Bavay et al.*, 2009; *Boé et al.*, 2009; *Chiew et al.*, 2009; *Vivoni et al.*, 2009) or the quantification of non-stationarity in the recorded time series of hydrological variables (*Brunetti et al.*, 2001a,b; *Groisman et al.*, 2004; *Hamlet et al.*, 2007).

Analyzing scientific studies on climate change, two prevalent approaches can be identified. The first one is the development and application of *General Circulation Models*, aimed at forecasting climate evolution in the next decades or centuries by means of simulations. These simulations could be eventually downscaled to infer knowledge at a local scale. The second approach concerns the analysis of long-range data series in order to ascertain whether signals of climatic change related to the increasing greenhouse effect can already be detected. The first approach is followed here. A stochastic downscaling procedure coupled with the weather generator described in Chapter 2 is presented in the following.

3.2 Stochastic downscaling

Information about future climate and its change is usually inferred from *General Circulation Models* (or *Global Climate Models*) commonly indicated with the acronym GCMs. Only models whose spatial domain is the entire Earth may be used to predict the effects of the enhancement of greenhouse gases in the atmosphere. GCMs are, in fact, complex numerical tools able to simulate globally the climate system of the Earth. Recent versions of GCMs together with the classical four components: atmosphere, oceans, land surface and sea-ice include also descriptions of the biological and biogeochemistry cycles (*Treut et al.*, 2007; *Bonan*, 2008). These tools have become essential in studying climate change (*Prudhomme et al.*, 2002; *Wilby et al.*, 2002; *Burlando and Rosso*, 2002; *Schmidli et al.*, 2006) and their realizations of climatic variables represent the basis of our current knowledge about future climate. It must be noted, however, that there is a disagreement with regards to the reliability of GCMs skill to reproduce much more than global averages of climatic variables within the Earth system. Recent studies point to the limited skill of GCMs to match even roughly the local observations (*Koutsoyiannis et al.*, 2008) and cast shadows on the level of credibility of these models (*Frank*, 2008). Nonetheless, other researches confirm that despite caveats and large uncertainties present (*Rial et al.*, 2004; *Bony et al.*, 2006; *Räisänen*, 2007; *Knutti*, 2008), climate model projections provide valuable insights and information about future climate and GCMs are suitable tools for making predictions (*Hayhoe et al.*, 2007; *Räisänen*, 2007; *Reichler and Kim*, 2008; *Knutti*, 2008). Note that since GCMs realizations are the foundation of any climate change prediction study, questioning the reliability of GCMs means questioning the overall possibility of making inferences about future climate and consequently whatever scientific discussion about climate change predictions must be looked as biased from the beginning. The opinion of the author is that while

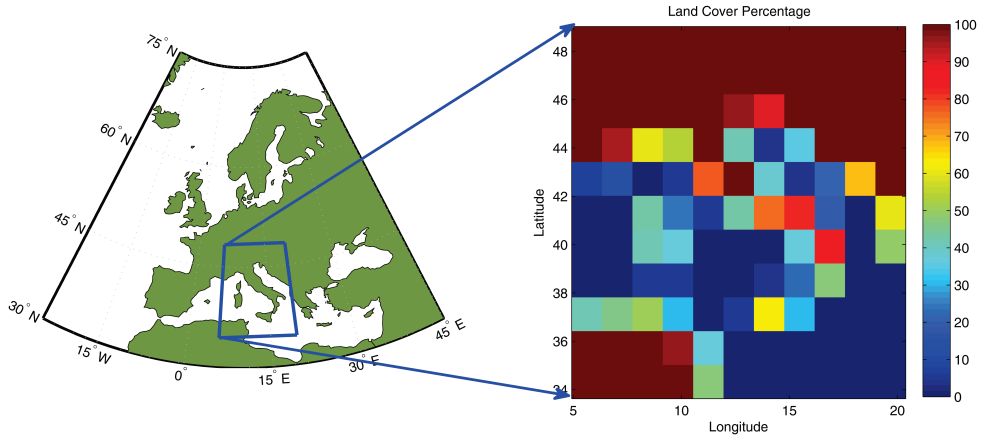

Figure 3.1: Representation of the partition between land cover (100%) and sea cover (0%) in CCSM-3.0, for the Italian region.

climate models provide information that may not be exact in the absolute sense, yet due to their physically-based nature and their global scale of application, they still provide a robust prediction of a tendency, or at least they identify the emergence of a climate change signal. For these reasons, in this study GCM predictions are used in a differential sense and the climate change information is inferred from an ensemble of climate models (see details in Section 3.2.2 and 3.2.3). Nonetheless, the possibility that model artifacts can undermine the credibility of the study could not be totally dismissed but currently few alternatives, if any, are available.

GCMs have an important drawback, because the commonly used spatial resolutions are too coarse to be used directly in local studies. A brief overview of the spatial resolutions adopted by some of the GCMs that were used in the IPCC 4AR is provided in table 3.1. In order to emphasize this notion, Figure 3.1 shows how the partition between land cover and sea cover for the Italian region is represented in one of the GCMs with finer spatial resolution (CCSM-3.0). Such a mismatch between GCMs basic computational units and the spatial resolution required for local scale studies is apparent. Hydrological or eco-hydrological models, as well as mesoscale meteorological models, require information at finer spatial resolutions. This creates a "gap" between the scale of GCM predictions and actual applications (*Fowler et al.*, 2007). Bridging this gap represents one of the most challenging problems for the assessment of impacts of climate change, including the application of climate change scenarios to hydrological models (*Fowler et al.*, 2007). Recently, a considerable scientific effort has focused on the development of techniques known as *downscaling* that would allow to extend GCM forecasts to smaller scales. A large interest of scientific community on development and evaluation of downscaling techniques remarks how much these methods are required and considered useful in climate change studies (*Wilby et al.*, 2002; *Burlando and Rosso*, 2002; *Wood et al.*, 2004; *Varis et al.*, 2004; *Xu et al.*, 2005; *Schmidli et al.*, 2006). Comprehensive reviews on the subject are provided by *Prudhomme et al.* (2002) and recently by *Fowler et al.* (2007).

The principal downscaling techniques may be grouped in two categories, "dy-

Table 3.1: Spatial resolution of some of the General Circulation Models which results were used in the IPCC 4AR.

Model	**N° of Lat. cells**	**N° of Long. cells**	**Lat. grid dimension**
MIROC3.2(hires)	160	320	1.12°
INGV-SXG	160	320	1.12°
CCSM-3.0	128	256	1.4°
ECHAM-5	96	192	1.87°
CSIRO-Mk3.5	96	192	1.87°
GFDL-CM2.1	90	144	2.5°
CGCM3.1(T63)	64	128	2.81°
CNRM-CM3	64	128	2.81°
PCM	64	128	2.81°
MIROC3.2(medres)	64	128	2.81°
IPSL-CM4	72	96	3.75°
GISS-ER	46	72	5.0°

namic" downscaling and "statistical" downscaling. Dynamic downscaling indicates the use of GCMs outputs as input to finer resolution climate models, such as the regional climate models (RCMs) or limited area models (LAMs). Given appropriate boundary condition these models are able to reproduce more reliable characteristics of local climate and preserve the physical processes involved in the climate dynamics. As a drawback, dynamic downscaling requires large computational resources and is subject to similar problems and uncertainties present in GCM applications. The second technique is to use statistical downscaling, where the fundamental idea is to find a functional relationship between one or more variables of GCM outputs (predictors) and some observed climate variable of the analyzed area (predictands). A common subdivision is to distinguish between three different types of statistical downscaling (*Varis et al.*, 2004; *Fowler et al.*, 2007):

1. Transfer functions;
2. Weather typing schemes;
3. Weather generators (WGs).

Transfer functions downscaling type refers to statistic techniques of correlation. The simplest approach is to use a multiple linear regression but also the canonical correlation analysis (CCA)(*von Storch et al.*, 1993) or artificial neural networks (ANN) (*Cannon and Whitfield*, 2002) can be used. All of these approaches are employed to define linkages between predictors and predictants. Weather typing schemes is the type of downscaling in which relationships between atmospheric circulation patterns and local climate are investigated. The method consists in relating empirically defined weather classes or atmospheric synoptic indices to characteristics of the local climate (e.g., local precipitation). Modifications in weather classes or atmospheric indices derived from climate models are thus transferred to local or regional climate (*Varis et al.*, 2004). Finally, weather generators are employed to downscale GCM

realizations. A wider description of the capability of weather generator tools is provided in Chapter 2. In the downscaling realized with weather generators, a common approach is to modify the parameters of the latter using inferences from GCM outputs. The newly parameterized generators are successively applied to simulate time series for a *"future"* climate. Henceforth, this type of downscaling is referred to as "stochastic downscaling", given the predominantly stochastic nature of the underlying relationships used in weather generators. This connotation further helps to distinguish this approach from other types of "statistical" downscaling techniques (*Fowler et al.*, 2007).

3.2.1 Methodology

A stochastic downscaling that utilizes the weather generator described in Chapter 2 is presented in the following. GCM realizations are used to derive factors of change for several statistics of hydro-climatic variables by comparing a specific control scenario with a specific future scenario. The control scenario (CTS) is a period of time when both observations and climate model simulations are available; while in the future scenario (FUT) only model simulations are available. The term *factor of change* expresses the difference between statistics of climate variables computed for the two scenario periods. The factor of change can be a product factor, when the ratio between statistics for FUT and CTS scenarios is computed; or it can be an additive factor (or "delta-change"), when the algebraic difference between FUT and CTS scenario statistics is calculated. Using the factors of change can be considered to be the simplest method in using the GCM-scale projections (*Prudhomme et al.*, 2002; *Fowler et al.*, 2007). The attractive feature of the presented approach is in the possibility to apply these factors of change not only to long-term means but also to higher order statistics and different aggregation intervals, allowing one to also account for seasonality. A pioneer work in this direction was realized by (*Bouraoui et al.*, 1999) and recently, *Kilsby et al.* (2007) have extended the use of factors of change to several precipitation statistics as well as to other hydro-climatic variables parameterizing a daily weather generator. Accounting for higher order statistic and seasonality leads to a strong enhancement of the downscaling technique capabilities, especially for such a variable as precipitation. The estimated factors of change can be employed to re-parameterize AWE-GEN. The latter can be subsequently used to simulate time series of hydro-climatic variables for future climate scenarios.

The proposed methodology infers climate change information by a) inferring changes of climate statistics from GCM (or RCM) simulations only, and b) applying them directly to the statistics of observed variables. A possible discrepancy between GCM outputs and observations is therefore by-passed. Certainly, time series obtained at a single station may be quite different as compared to a climate model output. This is due to both the mismatch in the spatial scale and the averaging aspect of a large-scale model that cannot reproduce microclimatic conditions. By-passing the differences between GCM outputs and observations implies that the factors of change computed as difference or ratio between CTS and FUT scenarios are applied directly to the

station observations in order to generate future climate through the weather generator. Such an approach implicitly assumes that the bias between the true climate and the climate reproduced with a GCM model will be maintained unchanged in the future. Furthermore, it also assumes that the empirical statistical relationships used in the weather generator and based on the hypothesis of climate stationary will hold true in future as well. This latter assumption can be relaxed for components such as precipitation that are fully stochastic. Obviously, these assumptions cannot be proven to be right or false but should be rather accepted as a necessary compromise in attempt to infer implications of climate change at the local scale. Furthermore, these assumptions can be considered equivalently acceptable compared to explicit or implicit assumptions made in other downscaling methodologies (*Fowler et al.*, 2007).

3.2.2 Factors of change

Factor of changes may theoretically be applied to every statistic of hydro-meteorological variables simulated by climate models. In the presented approach of stochastic downscaling only precipitation and air temperature are directly considered because of practical and computational reasons. These variables are the two principal hydro-meteorological states strongly affecting the hydrological cycle. Once the factors of change are introduced into AWE-GEN, other variables might be affected as a result of the imposed linkages (Chapter 2).

The product factors of change might be also applied to vapor pressure e_a, incoming shortwave radiation R_{sw}, cloudiness N, wind speed W_s, and atmospheric pressure P_{atm}. Among these, e_a is one of the important variables of the hydrologic cycle and its predicted change might be non-negligible. Nonetheless, surface vapor pressure or, equivalently, specific humidity, is not among conventional outputs available from GCMs. Therefore a stochastic downscaling (see Section 3.2.3) for this variable has not been performed. The impact of future climate conditions in e_a will be accounted for by its deterministic component (2.7) that has a direct linkage to air temperature and an indirect coupling to changes in precipitation (through the shortwave radiation). Furthermore, the introduction of factors of change for the other climatic variables is not straightforward and it might partially delete causal relationships introduced by the generator. Due to these reasons, R_{sw}, N, W_s, and P_{atm} are also not explicitly modified in the weather generator simulations of future climate, though such modifications should be considered as a task in future applications of the framework. Similar to e_a, the variables R_{sw}, N, and W_s will be affected indirectly via the assumed linkages to precipitation and air temperature processes. For instance, shortwave radiation changes will reflect the changes in precipitation and cloudiness occurrence. This implies that simulated changes for R_{sw} might differ from the actual factors of change produced by climate models.

The factors of change for precipitation are calculated separately for each statistical property used to estimate weather generator parameters. Specifically mean, variance, skewness, frequency of no-precipitation and lag-1 autocorrelation at four

different time aggregation periods (h: 1-6-24-72 hours) are required. The product factors of change are derived for the following statistics: the mean $E_{Pr}(h)$, the variance $VAR_{Pr}(h)$, and the skewness $SKE_{Pr}(h)$, where h is the aggregation interval. The product factor is also applied to the frequency of non-precipitation $\Phi_{Pr}(h)$, following a logit-like transformation: $f(\Phi_{Pr}) = \Phi_{Pr}/(1-\Phi_{Pr})$, as proposed by *Kilsby et al.* (2007). This transformation allows to linearize Φ_{Pr} across a wide range of values, reducing inaccuracies in the computation of the product factor. The downscaling of the lag-1 autocorrelation $\rho_{Pr}(h)$ is neglected due to difficulties in finding a proper relationship for the factor of change of this statistic, and due to the weaker sensitivity of weather generator parameter computation to $\rho_{Pr}(h)$ variations. The general equation expressing the product factor of change for a statistical property S of precipitation at the time aggregation h is:

$$\frac{S(h)^{FUT}}{S(h)^{OBS}} = \frac{S(h)^{GCM,FUT}}{S(h)^{GCM,CTS}}\,, \tag{3.1}$$

where the superscripts FUT denotes the future scenario, OBS denotes observations, and CTS denotes the control scenario. The notation GCM implies a model (GCM or regional-scale) derived climatology. The sought statistical property of precipitation for future climate, S^{FUT}, is calculated from the observed statistics of present climate, S^{OBS}, and the product factor of change (right hand side of 3.1) computed using statistics derived from the control and the future scenarios, $S^{GCM,FUT}/S^{GCM,CTS}$, obtained from GCM outputs. In order to include the effects of intra-annual seasonality, the factors of change are calculated on a monthly basis.

Low-frequency effects are important in the detection of climate change impacts, especially when long-term variations in the occurrence and duration of drought or wet periods are likely to be encountered. As discussed in Chapter 2, AWE-GEN is capable of taking into account such features of precipitation regime. Therefore, the statistical properties describing the inter-annual variability of precipitation are also downscaled using the derived factors of change from GCM realizations, as discussed in the following. Specifically, once the downscaling is carried out for the mean precipitation at finer aggregation intervals and realized independently for each month, the total annual precipitation $\overline{P}_{yr}^{FUT}$ is consequently obtained as the sum of modified monthly precipitation. Note that given the linearity of mean operator $\overline{P}_{yr}^{FUT}$ is the mean annual precipitation. This ensures a perfect correspondence between the mean simulated at the hourly scale for the future and the mean $\overline{P}_{yr}^{FUT}$ simulated by the autoregressive model. The application of independent factors of change on a monthly basis, however, has a not immediately apparent implication: $\overline{P}_{yr}^{FUT}$ may not be exactly equal to $\overline{P}_{yr}^{OBS} \cdot [\overline{P}_{yr}^{GCM,CTS}/\overline{P}_{yr}^{GCM,FUT}]$ where the expression in the brackets is the factor of change estimated at the annual scale. In other words the ratio $\overline{P}_{yr}^{GCM,CTS}/\overline{P}_{yr}^{GCM,FUT}$ may not be exactly equal to the ratio $\overline{P}_{yr}^{OBS}/\overline{P}_{yr}^{FUT}$. This outcome is due to the fact that applying the factors of change at the monthly scale is different from applying a factor of change at the annual scale (a single factor

of change). However, in order to account for seasonality and to be coherent with the factors of change calculated at the aggregation periods smaller than 1 year, $\overline{P}_{yr}^{FUT}$ is used as the mean annual precipitation of the FUT scenario.

Besides mean precipitation, other two statistical properties of annual precipitation must be downscaled explicitly using equation (3.1): the coefficient of variation and the skewness. The downscaling of the former is necessary in order to introduce changes in the variance of the precipitation annual time series. It is necessary to compute a factor of change for the coefficient of variation and not directly for the variance because of the exactness of the ratio $\overline{P}_{yr}^{GCM,CTS}/\overline{P}_{yr}^{GCM,FUT}$ is not generally guaranteed, as explained above. The autocorrelation property of annual precipitation process, AR(1) model, is not directly downscaled. The value inferred from observations is kept for simulations of future climate. This approximation is due to the same difficulties in downscaling ρ_{Pr} mentioned above.

The factors of change are also derived for air temperature. An additive factor is applied to the mean monthly temperature T_{mon}:

$$T_{mon}^{FUT} = T_{mon}^{OBS} + \left(T_{mon}^{GCM,FUT} - T_{mon}^{GCM,CTS}\right). \tag{3.2}$$

Correcting only the mean does not permit to infer changes of higher order statistics and thus to capture the possible changes in the daily cycle or frequency of extremes. This limitation is related to the procedure used in the estimation of the parameters of the air temperature model. Nevertheless, in many cases intra-daily changes can be considered to have a fairly minor effect on the hydrological dynamics, though there might be applications where this does not hold true. The monthly corrections $\Delta T = T_{mon}^{GCM,FUT} - T_{mon}^{GCM,CTS}$ are taken into account by the AWE-GEN air temperature component that produce time series of T_a at the hourly scale (see Section 2.5.1 and 2.11).

3.2.3 Multi-model ensemble approach to predict future conditions

The proposed stochastic downscaling procedure requires several factors of change, that can be obtained from realizations of one or more climate models. This study uses predictions obtained from General Circulation Models but the same methodology can be extended to outputs of Regional Climate Models without loss of generality. A non-arbitrary choice of any particular climate model or a group of climate models is challenging. It has been repeatedly demonstrated that different models produce different results and not a single model has the best performance when a variety of metrics are taken into account (*Lambert and Boer*, 2001; *Tebaldi et al.*, 2004; *Knutti*, 2008). Fortunately, recent projects, such as the Coupled Model Intercomparison Project phase 3 (CMIP3)(*Meehl et al.*, 2007a), have provided open access to an unprecedented set of global climate model experiments with projections for twentieth and twenty-first century climate. This has enlarged the possibility of choice among models allowing multi-model ensemble studies (*Meehl et al.*, 2007a). The approaches to circumvent the difficulty in quantifying model projections and

thus provide insights on climate change related problems can be grouped in three categories. The first approach is to use a single climate model outputs, the second is to ignore characteristics of model performance altogether and simply average model outputs (*IPCC*, 2001; *Coppola and Giorgi*, 2009), the third approach is to provide weighted averages of model results. This study benefits from recent developments in probabilistic multi-model ensembles (*Tebaldi and Knutti*, 2007) and it falls in the third category.

Various multi-model ensemble and probabilistic approaches to the analysis of climate projections have been recently proposed, such as the Reliability Ensemble Average (REA) (*Giorgi and Mearns*, 2003), and Bayesian methods (*Tebaldi et al.*, 2004; *Greene et al.*, 2006; *Furrer et al.*, 2007; *Smith et al.*, 2009b; *Tebaldi and Sansó*, 2009). See *Tebaldi and Knutti* (2007) for a detailed review. The underlying idea is that a performance forecast can be improved by weight-averaging or combining results from multiple models. This has been demonstrated to be particularly applicable for GCM performance with respect to the past climate (*Jun et al.*, 2008; *Reichler and Kim*, 2008), indicating that model biases are partially random. This assumption is, indeed, related to the fact that random errors tend to cancel out and thus the prediction uncertainty decreases as the number of models grows (*Tebaldi and Knutti*, 2007). Nonetheless, there are numerous issues that must be considered when constructing a multi-model climate projection depending on whether a multi-model ensemble is realized in the form of probability distributions or simple averages and measures of variability across involved models (*Tebaldi and Knutti*, 2007). These issues could be the substantial lack of independence between models, the effort put in model tuning and the overall problem that forecasts cannot be verified or disproved (*Tebaldi and Knutti*, 2007). Other important shortcomings inherent to models include sensitivity to initial and boundary conditions, structural and parameter uncertainties, and simplifications of physical principles. All these issues combined contribute to increase uncertainty in climate projections. Nonetheless, there is a certain confidence that models do provide reliable projections of climate change or, at least, that the uncertainty is reasonably well captured by the variation among different models (*Räisänen*, 2007; *Knutti*, 2008). *Räisänen* (2007) underlines that the variation of climate change between different models is probably the most meaningful measure of uncertainty that is presently available, although, this measure is more likely to underestimate than overestimate the actual uncertainty. This last statement is reflected in a disagreement of uncertainty bounds produced by the different methods of multi-model ensembles (*Tebaldi and Knutti*, 2007).

It could be argued that the multi-model ensemble approach producing probability density functions (PDFs) of changes for a certain variable may be questionable and imply too much certainty. The author strongly agrees with the notion expressed by *Knutti* (2008), who asserts that the problem is rather in objective interpretation of these PDFs than in questioning whether they should be constructed in the first place. Indeed, PDFs provide an indication of which outcome is more likely or stated

differently, which confidence bounds are more plausible than others and they overall provide indications about uncertainty (*Knutti*, 2008). It would be erroneous to interpret the calculated PDFs, as the effective probability of certain realizations in the future and their means as the "future climate". It should be noted that the alternative is to not have uncertainty metrics at all, e.g., use simple average of models, or to abandon the idea of future climate predictability. The latter, might became a very risky position, in the framework of climate change science, because once we will be able to have highly certain projections, it is likely to be too late to undertake any action. Thus, as stated by *Knutti* (2008), the communication of climate projections, their uncertainties, and caveats is crucial and certainly worth of attention and discussion.

The multi-model ensemble approach realized in this study follows that of *Tebaldi et al.* (2005), who proposed a Bayesian statistical model. The model combines information from several GCMs and observations to determine the probability density functions (PDFs) of future changes for a certain climatic variable at the regional scale. In the Bayesian framework, all uncertain quantities are modeled as random variables, with a priori probability distributions. The assumptions include the specification of conditional distributions for the data (likelihood), given the parameters and the prior distributions for all the parameters used in the Bayesian framework. Following the Bayes' theorem, prior distributions and likelihood are combined into posteriori distributions of the parameters. The objective of such a procedure is to capture the posterior distributions of the product or additive factors of change. *Tebaldi et al.* (2005) assume Gaussian distributions for regionally averaged realizations of GCMs into the control scenario X_i and into the future scenario Y_i with $i = 1, ..., n_{mod}$, n_{mod} is the number of considered GCMs:

$$X_i \sim \mathcal{N}(\mu, {\lambda_i}^{-1}), \tag{3.3}$$

$$Y_i \sim \mathcal{N}(\nu, (\theta\lambda_i)^{-1}), \tag{3.4}$$

where $\mathcal{N}(\mu, \lambda^{-1})$ indicates a Gaussian distribution with mean μ and variance λ^{-1}. The variable μ and ν represent the *"true"* values of control scenario and future climate for a certain variable of interest in a specific region. The parameters λ_i are the reciprocal of the variance. Note that the latter quantities are not observable variables but are parameters in the Bayesian framework, and posterior distributions are derived for them as well as for the means μ and ν. Posterior distributions of product, ν/μ, or additive, $\nu - \mu$, factors of change can be easily calculated as well. To allow for the possibility that Y_i has a different precision from X_i an additional parameter θ is introduced. This parameter is called inflation-deflation and is common to all the GCMs. The parameter θ represents the relative weight of future realizations of GCMs compared with control scenario realizations, allowing to account for different accuracy in the two periods. A further parameter β, common to all GCMs, is introduced to take into account the possible dependence between X_i and Y_i, these quantities are linked through a linear regression equation or, equivalently, they can

be assumed jointly normal distributed. Further information about the Bayesian approach assumptions are provided in *Tebaldi et al.* (2005). The likelihood of the observations, X_0, in the control scenario is assumed to be Gaussian distributed with the same mean μ of equation 3.3 and variance ${\lambda_0}^{-1}$:

$$X_0 \sim \mathcal{N}(\mu, {\lambda_0}^{-1}) . \tag{3.5}$$

The parameter λ_0 represents a measure of the natural variability of a given climatic process. For example, if X_0 represents average air temperature observed in a certain number of years, n, over a region, then ${\lambda_0}^{-1}$ is the variance of this average. Obviously, the parameter λ_0 is impossible to determine given the uniqueness of climate realizations, which does not permit having numerous long-term averages of the same climate process to estimate the corresponding variance. Ultimately, ${\lambda_0}^{-1}$ might be calculated using the ergodicity hypothesis, if a long record of observations is available. *Giorgi and Mearns* (2002), for example, calculate natural variability (standard deviations) for 30-year averaged air temperature, for summer and winter periods. They estimate them as the difference between the maximum and minimum values of 30-year moving average series of twentieth century using observed detrended air temperature series. However, the determination of λ_0 is indeed a difficult problem. In this study, it is expressed in terms of standard deviation or coefficient of variation metrics and the sensitivity of the multi-model ensemble to λ_0 has been carried out to justify the choice of particular values used in the downscaling. Further details are provided later in the text (Section 3.2.4).

The a priori assumed distributions for the parameters $\mu, \nu, \theta, \beta, \lambda_i$ are chosen to be uninformative as much as possible, e.g. the Uniform distribution over $[0, +\infty)$ or $(-\infty, +\infty)$, or the Gamma distribution with mean 1 and variance 1000. Specifically, the Gamma distribution is adopted for each λ_i and θ. Uniform distributions are assumed for μ, ν, and β.

Given the nature of the prior distributions adopted, the posterior distributions of the parameters are too complex to be obtained analytically and only empirical estimates of the posterior distributions can be realized. Markov Chain Monte Carlo, (MCMC), method is used to estimate the posterior distributions. Details on the method can be found in the appendix of *Tebaldi et al.* (2005) and in Appendix B.1. Some statistical properties of the posterior distributions can be directly calculated, highlighting the nature of the method. For instance the mean and the variance of μ

and ν (calculated with $\beta = 0$ for simplicity) are:

$$\overline{\mu} \approx \Big(\sum_{i=0}^{n_{mod}} \lambda_i X_i\Big) / \Big(\sum_{i=0}^{n_{mod}} \lambda_i\Big), \tag{3.6}$$

$$\sigma^2(\mu) \approx \Big(\sum_{i=0}^{n_{mod}} \lambda_i\Big)^{-1}, \tag{3.7}$$

$$\overline{\nu} \approx \Big(\sum_{i=1}^{n_{mod}} \lambda_i Y_i\Big) / \Big(\sum_{i=1}^{n_{mod}} \lambda_i\Big), \tag{3.8}$$

$$\sigma^2(\nu) \approx \Big(\theta \sum_{i=1}^{n_{mod}} \lambda_i\Big)^{-1}. \tag{3.9}$$

Equations (3.6)-(3.9), highlight that the parameters λ_i can be interpreted as the weights that each model has in the calculation of a certain climate variable. The parameters λ_i are measures of model reliability and accuracy in simulating present and future climate. The posterior means of λ_i are:

$$\overline{\lambda_i} \approx \frac{a+1}{b + \frac{1}{2}\Big[(X_i - \overline{\mu})^2 + \theta(Y_i - \overline{\nu})^2\Big]}, \tag{3.10}$$

where $a = b = 0.001$ are parameters of the prior distributions that are negligible in the overall procedure. The quantities $(X_i - \overline{\mu})$ and $(Y_i - \overline{\nu})$ represent the *bias* and the *convergence* criteria, respectively. The *bias* measures the difference between the GCMs simulations X_i and the best approximation of the truth $\overline{\mu}$. Note that if $\lambda_0 \approx \infty$, i.e. there is no natural variability, the *bias* criterion measures the difference from the observation $\overline{\mu} = X_0$. Conversely, when a large natural variability can be hypothesized, $\lambda_0 \approx 0$, i.e., the *bias* criterion measures the distance between the "consensus" estimate in the control scenario. In the last case, the criterion can be interpreted as a convergence between models in the control scenario. The proper *convergence* criterion $(Y_i - \overline{\nu})$, instead, measures the distance between the GCMs simulations and the "consensus" estimate $\overline{\nu}$ of future realizations. Note that for each statistic $\overline{\nu}$ represents the expected value of the PDF for the future.

A multi-model ensemble approach of inference is used for all statistical properties of climatic variables that are part of stochastic downscaling, i.e., the mean, $E_{Pr}(h)$, the variance, $VAR_{Pr}(h)$, the transformed frequency of non-precipitation, $f(\Phi_{Pr}(h))$, and the skewness, $SKE_{Pr}(h)$, of fine-scale precipitation (for each month), the coefficient of variation and the skewness of annual precipitation, $\overline{Pr_{yr}}$, and the mean monthly air temperature. For all of the above properties, the posterior probability density functions (PDFs) of product factors of change, ν/μ, are calculated. Posterior distributions of additive factors of change, $(\nu - \mu)$, are calculated for the twelve average monthly air temperature T_{mon}.

Long-term statistics of present climate X_0 are calculated from observed values based on point measurements, which therefore represent a much smaller area as compared to a typical GCM grid cell size. The difference between observations,

expressed through X_0, and climate model realizations is accounted for by the *bias* criterion used to weight different GCM realizations in getting proper downscaling information. This implies that the shape of the probability density functions of the factors of change is somewhat dependent on the observed climate X_0. For two locations in the same area, the factors of change may thus differ even when exactly the same climate models are used in the downscaling. The original multi-model ensemble procedure (*Tebaldi et al.*, 2005) compares GCM realizations with the average climate observed over an entire GCM grid cell. The use of point measurements is not expected to appreciably modify the procedure since in this case the weights assigned to specific GCMs are influenced by their capability to fit the climate of a specific location, rather than the climate of an entire grid cell.

3.2.4 Application of the multi-model ensemble approach

Realizations from eight GCMs, for a specific carbon dioxide emission scenario, have been chosen for the current study. A description of the models, emission scenarios and the underlying motivations for this choice are discussed in Section 3.3.

The developed method is applied for the location of meteorological station in the Tucson airport (110.91 W, 32.21 N; elevation 728 [m *a.s.l.*]), where observations are available from 1961 through 2000. This period thus represents the interval of the control scenario, for which both observations and climate models simulations can be used. The future climate scenario is based only on GCM projections for the period of 2081-2100.

The GCMs realizations are taken as representative of the analyzed area. An analysis of the sensitivity of climate model outputs with respect to a given location has been performed. The goal was to ascertain that the found differences were not due to the choice of a particular grid cell. Given the large size of GCM grid cells, the analysis has been restricted to 25 grid cells centered around a cell containing the case study location. This effectively corresponds to an area with a radius of 500-1000 [km], with the point of interest located in the center. The differences among the factors of change simulated by the same climate model in neighboring cells have been checked for several world-wide locations. It was noticed, that GCM outputs are spatially self-consistent, i.e., for the same GCM the differences between the factors of change in neighboring cells are very small as compared to the differences among multiple GCMs for this same location. Furthermore, if an ensemble is composed of GCM outputs for 25 cells centered around the area of interest, the factors of change for the central cell are almost always very close to the ensemble mean. This implies that the deviations from the mean are predominantly due to the spatial gradient of climate change, as predicted by a specific GCM, rather than due to random biases. Consequently, this study uses outputs of GCMs corresponding to the grid cell that was identified as closest to the location of interest. Note that the above would be also the simplest choice to make if any sensitivity was performed.

A further explanation is necessary to justify values adopted in this study for λ_0, which represents a measure of the variance (or inverse of the variance, to be precise)

of the mean of a long-term climatic process. Given the high uncertainty of this parameter, no rigorous methodology exists for its estimation. One approach for monthly air temperature is described by *Giorgi and Mearns* (2002). Therefore, values for the parameter λ_0 have been hypothesized such that they were within a physically realistic interval. The sensitivity of the posterior distributions of the factors of change for temperature and precipitation has been checked for a range of λ_0 values.

Specifically, in estimating air temperature for the CTS scenario, the parameter λ_0 has been estimated assuming a *"known"* value of standard deviation $\sigma(T_{mon})$, i.e., $\lambda_0 = 1/\sigma(T_{mon})^2$. The tested interval of $\sigma(T_{mon})$ was $[0.05 \div 3]$ $[^\circ C]$. This interval is much broader as compared to the values of $\sigma(T_{mon})$ in the $0.25 \div 1.75$ $[^\circ C]$ interval used by *Giorgi and Mearns* (2002) and *Tebaldi et al.* (2005). In terms of precipitation process, the parameter λ_0 for all of the statistics S of precipitation calculated for the 40 years of CTS scenario has been estimated assuming *"known"* coefficients of variation $C_v(S)$, such that $\lambda_0 = 1/(C_v(S)\,\overline{S})^2$. Values of $C_v(S)$ varying from 0.001 to 0.5 $[-]$ have been tested. Figure 3.2 illustrates the dependence of the mean and the 10-90 percentile intervals for average temperature (the month of April) and the mean and the variance of precipitation at the 24-hour aggregation period. Figure 3.3 shows the same analysis for the month of July. As seen in the figures, the uncertainty bounds of the posterior PDFs estimated for the factors of change are affected by the chosen natural variability. This is especially true for higher order precipitation statistics. The increase or decrease of uncertainty, i.e., wider or narrower vertical bars in Figure 3.2 and 3.3, do not have a clear tendency and overall depend on the analyzed statistic and month. It can be also noticed that the means of the PDFs are relatively constant over a large range of natural variability metric values. The mean changes appreciably only for very large or very small values of these metrics. It should be further noticed that if the analysis is limited to narrower, more plausible, intervals, such as $C_v(S) = 0.05 \div 0.15$ and $\sigma(T_{mon}) = 0.5 \div 1.0$, the spread of the posterior PDFs of factors of change remains fairly constant. Because of this low sensitivity, fixed values of $C_v(S) = 0.075$ and $\sigma(T_{mon}) = 0.65$ $[^\circ C]$ were used in this work to determine the posterior distributions of the factors of change in the Bayesian multi-model ensemble.

In the successive step, the posterior distributions of the factors of change are calculated for the analyzed statistics using the Bayesian multi-model ensemble approach (Section 3.2.3).

Figure 3.4a illustrates the posterior probability density functions of average temperature in September using simulations of the CTS and FUT scenarios. The means of September temperature based on individual simulations by eight models for the periods of 1961-2000 and 2081-2100 are also shown along with the mean temperature estimated from 1961-2000 observations. Note that while observations are available for the period of 1961-2000, the employed Bayesian approach allows the estimation of the PDF of the mean September temperature (CTS scenario) based on observation and GCM simulations. A comparison with the observed mean provides both

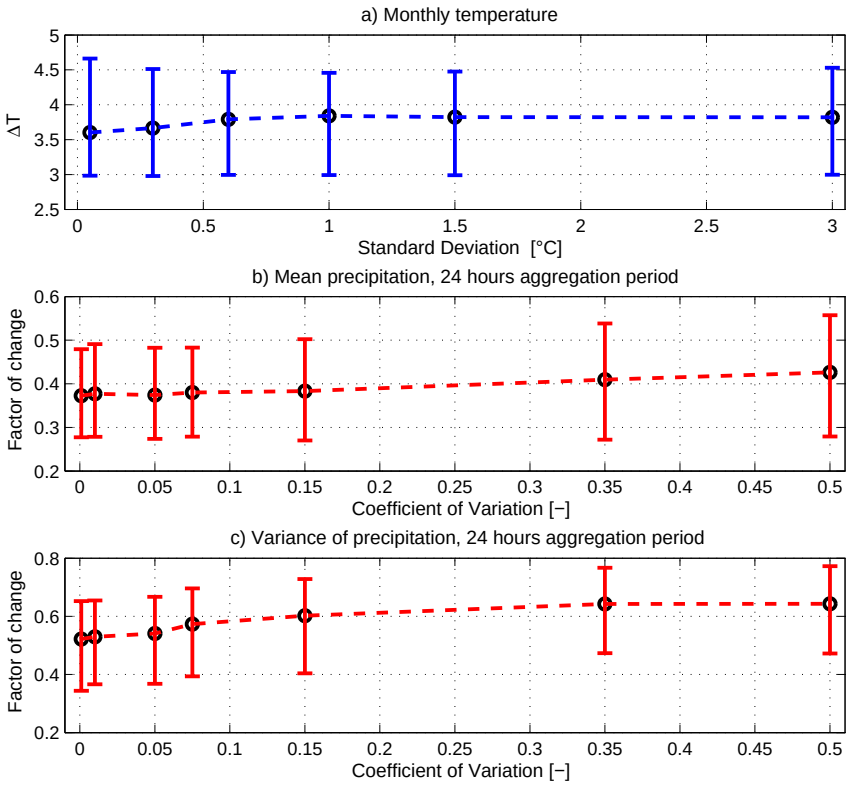

Figure 3.2: The subplots illustrate sensitivities of the computed probability density functions of the factors of change with respect to the metrics of natural variability (the parameter λ_0 in text). These are expressed using either the standard deviation of monthly temperatures (subplot (a)) or the coefficient of variation for precipitation statistics (subplots (b) and (c)). The presented analysis is for the location of Tucson, the month of April a.) Sensitivity of the factor of change for mean monthly temperature; the circles denote the mean of the posterior PDFs and the vertical bars give the 10-90 percentile intervals of the PDF. b.) The factor of change for mean precipitation at the aggregation period of 24 hours; the circles denote the mean of the PDFs and the vertical bars give the 10-90 percentile intervals of the PDF. c.) The factor of change for precipitation variance at the aggregation period of 24 hours; the circles denote the mean of the PDFs, and the vertical bars give the 10-90 percentile intervals of the PDF.

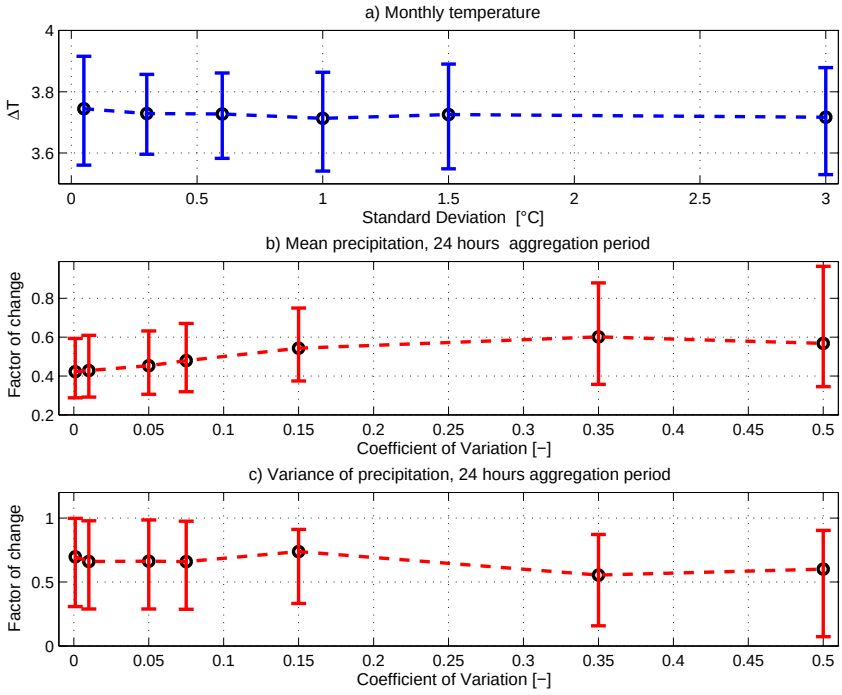

Figure 3.3: Same as Figure 3.2 for the month of July.

quantitative and qualitative metrics of GCM performance. Figure 3.4b shows the posterior PDF of the additive factor of change, $\Delta T = \nu - \mu$, together with the factors of change predicted by the individual models. Figure 3.4c illustrates the probability density functions of the total precipitation in September, analogous to those shown in Figure 3.4a. Figure 3.4d shows the PDFs of the product factor of change, $FC = \nu/\mu$, for the total precipitation in September as well as the factors of change predicted by the individual models. Figure 3.5 shows the same analysis of Figure 3.4 for the month of February. Note that sometimes the values that the variables assume in the posterior PDF are outside the range of variability expressed by single climate model realizations, e.g., Figure 3.5c. This outcome can be surprising, since one can expect that μ and ν are simply weighted averages of climate model realizations. This is not exactly true because of the parameter β. As said, this parameter takes into account the dependence between GCM realizations in the CTS and FUT scenarios through a linear regression equation. Such a dependence can effectively force μ and ν to assume values outside the intervals predicted by single GCMs (for details refer to (*Tebaldi et al.*, 2005) and Appendix B.1).

Factors of change, including the mean, and the 10-90 percentile intervals calculated for several precipitation statistics at the aggregation period of 24 and 96 hours are shown in Figure 3.6 and Figure 3.7. As seen, the uncertainty present in the estimation of the factors of change for precipitation statistics is very high with a tendency to increase for higher order statistics. The uncertainty is also strongly related to seasonality, since in some months model predictions tend to provide a

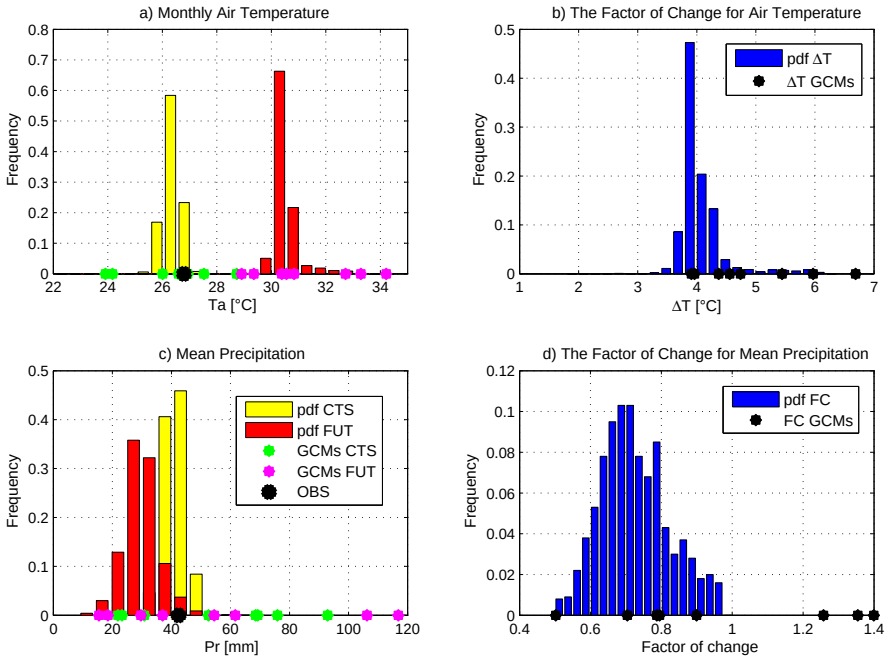

Figure 3.4: The posterior probability density functions (PDF) obtained from the multi-model ensemble for the location of Tucson airport, the month of September. a.) The PDF of mean September temperature for the CTS (yellow bars) and the FUT (red bars) scenarios. Also shown are the observation (OBS) and results from the individual models for the CTS (green dots) and FUT (magenta dots). b.) The PDF of the additive factor of change for air temperature, $\Delta T = \nu - \mu$, (blue bars) and predictions by the individual models (black dots). c.) The PDF of mean September precipitation for the CTS (yellow bars) and the FUT (red bars) scenarios. Also shown are the observation (OBS) and results from the individual models for the CTS (magenta dots) and FUT (green dots). d.) The PDF of the product factor of change for precipitation, $FC = \nu/\mu$, (blue bars) and predictions by the individual models (black dots).

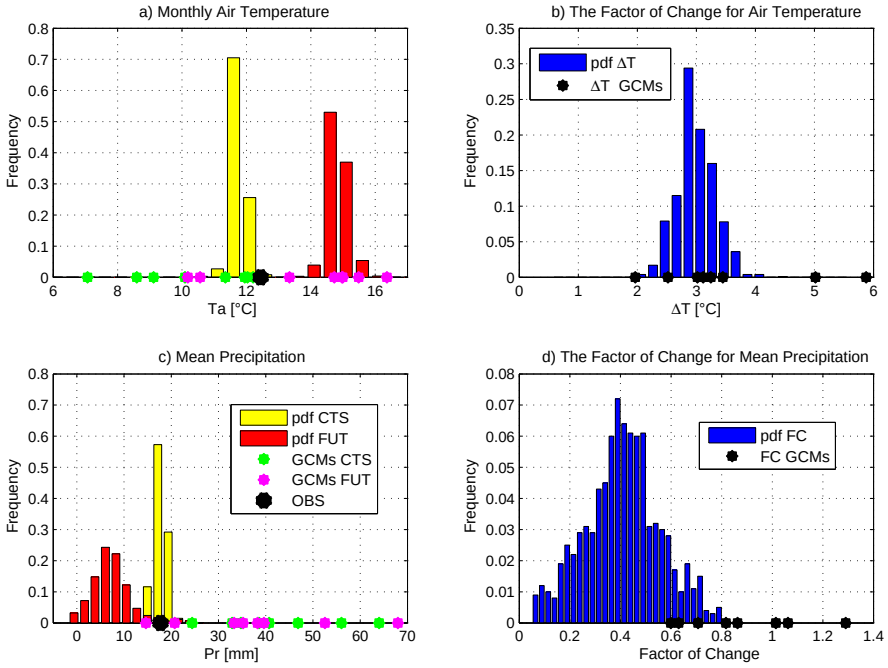

Figure 3.5: Same as Figure 3.4 for the month of February.

more accurate estimation than in others.

It should be noted that the multi-model ensemble approach allows the computation of PDFs for the factors of change only. In order to transfer the information contained in the factors of change to the magnitudes of meteorological variables, it is necessary to use a weather generator. Theoretically, at this stage the weather generator must account for the entire PDF of each of the factors of change. This would require the use of Monte Carlo-type simulations and the specification of covariance between the factors of change for precipitation statistics and the covariance between precipitation and temperature. In such an approach, the factors of change for each statistic would be extracted randomly (accounting for the covariances) and each set of the factors of change would be used for a single weather generator simulation. This approach contains high uncertainties because of the assumption on mutual correlations between the factors of change and implies a much more significant computational burden. However, it is used in Chapter 7 where details about the assumptions and the methodology are provided. In this section, only the mean of the PDFs for every factor of change is used to illustrate a simple application of the procedure. Therefore, in the presented case study the weather generator is re-parameterized using only the mean of each factor of change PDF. The results can thus be considered as the "most likely" expression of the future climate at the location of Tucson airport, as inferred from the group of climate models and the proposed methodology.

The power of providing the uncertainty contained in the PDF of a given factor of change is illustrated in Figure 3.8. The 10-90 percentile intervals inferred from the

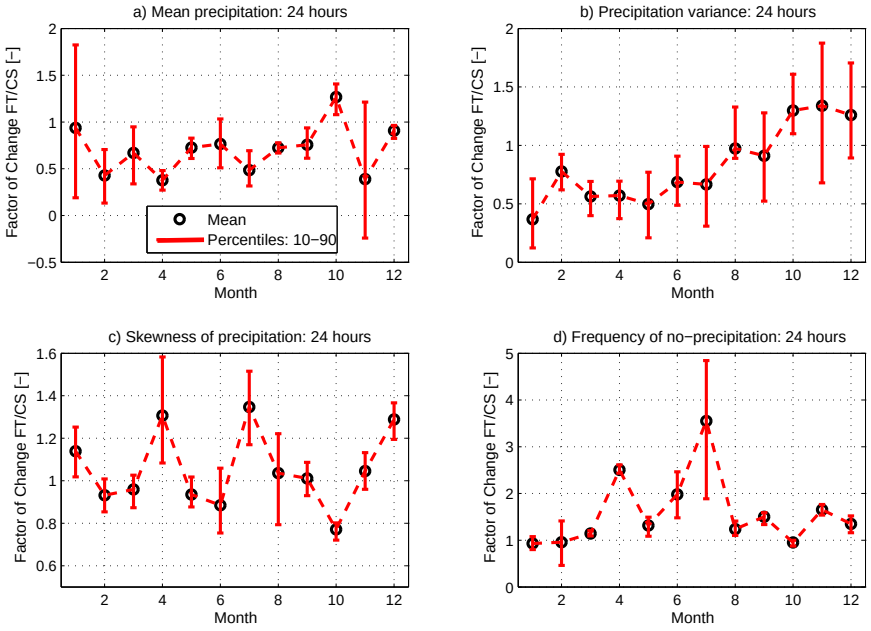

Figure 3.6: The factors of change estimated for different precipitation statistics at the aggregation interval of 24 hours. The mean (black circles) and the 10-90 percentile intervals (red lines) are computed from the posterior PDFs of these statistics. a.) Mean precipitation. b.) Variance of precipitation. c.) Skewness of precipitation. d.) Logit transformed frequency of no-precipitation.

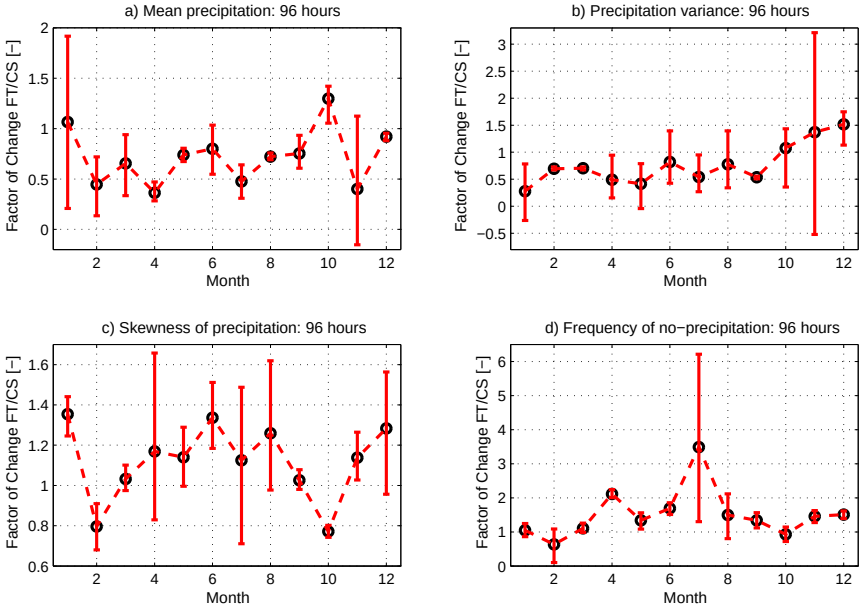

Figure 3.7: Same as Figure 3.6 for aggregation periods of 96 hours.

monthly posterior distributions of the factors of change for the FUT scenario are plotted along with the annual cycles of air temperature and precipitation (Figure 3.8a-c). This is possible once the independence of mean air temperature and mean precipitation is assumed. As seen, the uncertainty bounds for the air temperature changes (Figure 3.8b) are generally less than 1 $[^{\circ}C]$, with a maximum of ≈ 1.5 $[^{\circ}C]$ in April. Thus, the prediction of an increase of air temperature can be regarded as very likely. The magnitude of this change is around $3.5 \div 4.5$ $[^{\circ}C]$, with larger values in the second half of the year, i.e., June through December.

Figure 3.8c shows the annual cycle of observed precipitation along with the mean predicted future precipitation, that also includes the 10-90 percentile intervals. As seen, the relative uncertainty for precipitation prediction is much higher than for air temperature. For instance, for the month of January the 10-90 percentile interval may indicate both a reduction and an increase in precipitation. Nonetheless, for most months the confidence about the sign of the future change is much higher. A reduction of precipitation annual total can be inferred from these results. Significant decreases are predicted for April, July and November, the uncertainty is however quite large for the fall and winter months.

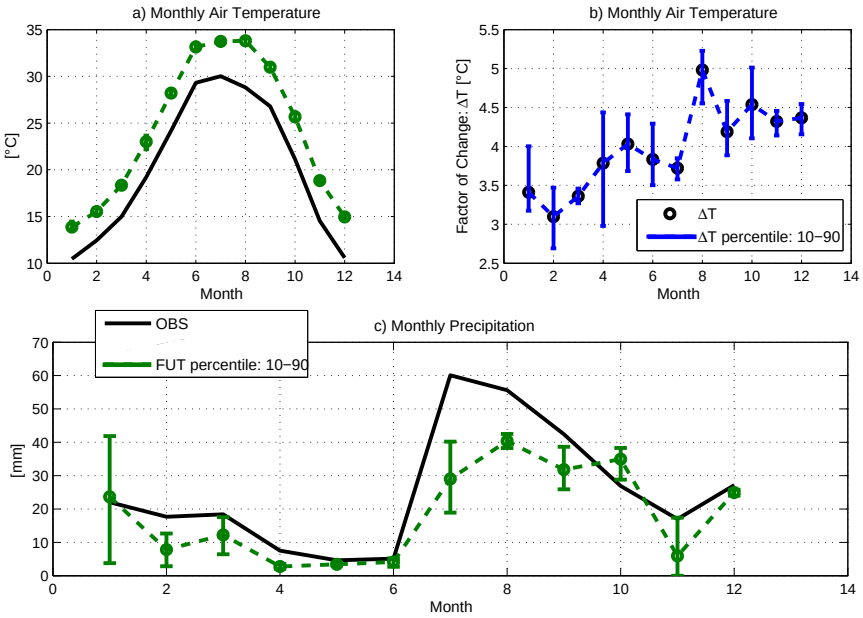

Figure 3.8: The effect of the factors of change on the annual cycles of monthly temperature and precipitation for the location of Tucson airport. a.) The observed mean monthly temperature for the period 1961-2000 (black line); the predicted mean monthly air temperature (green dashed line) and the 10-90 percentile intervals (vertical bars, cannot be seen for all months because of the small magnitude) computed from the posterior distributions of the factors of change applied to the observed cycle. b.) The mean monthly temperature change (black dots) and the 10-90 percentile bounds (blue vertical bars). c.) The observed mean monthly precipitation for the period 1961-2000 (black line); the predicted mean monthly precipitation (green dashed line) and the 10-90 percentile intervals (vertical bars) computed from the posterior distributions of the factor of changes applied to the observed cycle.

3.2.5 Extension of precipitation statistics to finer time scales

Usually, GCM realizations are only available at the daily or larger aggregation intervals. An overview of availability of GCM outputs used in the 4AR of the IPCC, can be found on the web-site of the Program for Climate Model Diagnosis and Intercomparison (PCMDI); (http://www-pcmdi.llnl.gov/ipcc/about_ipcc.php). Precipitation time series aggregated over the 24-hour period are used here to preserve the possibility of choice among many models. Since, several statistics of precipitation in the weather generator are required at the aggregation intervals of 1 hour and 6 hours, a methodology to infer the factors of change for these periods is necessary. The extension to shorter time scales is straightforward for the mean, i.e., given the linearity of the mean operation, the factors of change are equal at each aggregation period. This is the reason why it is possible to obtain monthly values of mean *future* precipitation, calculated, for instance, with the factor of change at 24 hours aggregation period (Figure 3.8).

The extension to shorter time scales is not such a trivial task for the other statistical properties, such as the variance $VAR_{Pr}(h)$, the frequency of non-precipitation $\Phi_{Pr}(h)$, and the skewness $SKE_{Pr}(h)$. In order to infer VAR_{Pr} at 1 hour and 6 hours aggregation intervals, the theoretical derivation of *Marani* (2003, 2005) is applied. *Marani* (2005) has extensively tested three formulations of $VAR_{Pr}(h)$ using several rainfall datasets from stations world-wide. It was noticed that equation (3.11) produced the best fitting for the aggregation intervals varying between 15 minutes and 96 hours:

$$VAR_{Pr}(h) = \begin{cases} 2\sigma_i^2 \frac{\epsilon}{\alpha}\left[\frac{\epsilon}{\alpha}\left(e^{-\frac{\alpha h}{\epsilon}} - 1\right) + h\right] & \text{if } h \le \epsilon\,, \\ 2\sigma_i^2 \left[\frac{\epsilon^\alpha e^{-\alpha}}{(1-\alpha)(2-\alpha)} h^{2-\alpha} + \frac{\epsilon}{\alpha}\left(1 - \frac{e^{-\alpha}}{1-\alpha}\right)h + \frac{\epsilon^2}{\alpha^2}\left(e^{-\alpha} - 1\right) + 2\frac{\epsilon^2 e^{-\alpha}}{\alpha(2-\alpha)}\right] & \text{if } h \ge \epsilon\,, \end{cases} \tag{3.11}$$

where σ_i^2, ϵ, and α are parameters of (3.11) estimated from the variance $VAR_{Pr}^{FUT}(h)$ at different aggregation periods equal to or larger than one day: $h = 24\,, 48\,, 72$, and, 96 hours. The values of $VAR_{Pr}^{FUT}(h)$ are thus calculated once $VAR_{Pr}^{OBS}(h)$ and the factors of change for precipitation variance are known at the aggregation periods $h \ge 24$ hours.

Equation (3.11)along with the Bartlett-Lewis rainfall stochastic model was used to generate hourly sequences of precipitation and small-scale variability uniquely from observed daily statistics (*Marani and Zanetti*, 2007). A complete description of the theoretical background of (3.11) can be found in *Marani* (2003, 2005).

The extension to 1-hour and 6-hour aggregation periods of the frequency of non-precipitation $\Phi_{Pr}(h)$ is realized through an exponential function (3.12), that links $\Phi_{Pr}(\ge 24)$ to $\Phi_{Pr}(< 24)$, given that $\Phi_{Pr}(0) = 1$, by definition:

$$\Phi_{Pr}(h) = e^{-\tilde{\gamma} h}\,. \tag{3.12}$$

The exponential decay of the frequency of non-precipitation, $\Phi_{Pr}(h)$, has been

observed in practically all of the analyzed time series. The parameter $\tilde{\gamma}$ is estimated from $\Phi_{Pr}(24)^{FUT}$ and $\Phi_{Pr}(48)^{FUT}$. The values of $\Phi_{Pr}(h)^{FUT}$ are calculated from the observed $\Phi_{Pr}(h)^{OBS}$ using the factors of change FC for logit transformed frequency of non-precipitation $FC[f(\Phi(h))]$. This operation requires the use of the inverse of the logit transformation, $f^{-1}\{\diamond\}$: $\Phi_{Pr}(h)^{FUT} = f^{-1}\{FC[f(\Phi(h))] \cdot f(\Phi_{Pr}(h)^{OBS})\}$. Since the fitting of $\Phi_{Pr}(h < 24)$ is carried out with two values of $\Phi_{Pr}(h \geq 24)$, e.g., at 24 and 48 hours, $\tilde{\gamma}$ is determined using the least squares method.

Skewness $SKE_{Pr}(h)$ is not extended to 1-hour and 6-hour aggregation periods since no suitable relationship was found for this statistic. The factors of change for 1-hour and 6-hour skewness are taken equal to one. This implies that the values obtained from observations are employed for generating future scenarios.

Once all the statistical properties are calculated for the future climate, a new set of modified parameters of AWE-GEN is estimated. AWE-GEN can then be used to simulate a scenario corresponding to future climate conditions.

3.3 General Circulation Models (GCMs) and scenarios

In this section the accessibility to General Circulation Models realizations for different carbon dioxide concentration scenarios is discussed and the underlining reasons for the chosen subset of models are provided. A principal reference for GCMs applications and scenario definition is the IPCC 4AR (*IPCC*, 2007a). Specifically in the Chapters VIII (*Randall et al.*, 2007) and X (*Meehl et al.*, 2007b) of the Working Group I, climate models are evaluated and their projections discussed. The General Circulation Models used in the IPCC 4AR are 25 in total including different versions of same climate models. An overview is presented in table 3.3.

Future emissions and scenario definitions remained unchanged between the Fourth Assessment Report (4AR) issued in 2007 and the Third Assessment Report (TAR) of Intergovernmental Panel on Climate Change, issued in 2001. Conversely the climate models of the 4AR are a generation younger and evolved versions of the ones of TAR. A complete description of the specific emission scenarios used in TAR and 4AR is described in the Special Report on Emissions Scenarios (SRES) published by IPCC in 2000 (*IPCC*, 2000).

Since projections of climate change heavily depend upon future human activity, climate models are run assuming scenarios. There are 40 different scenarios, each making different assumptions for future greenhouse gas pollution, land-use and other driving forces. Assumptions about future technological development as well as the future economy are also made for each scenario. Most include an increase in the consumption of fossil fuels and Gross Domestic Product (GDP) all around the world, though there is some argument about the validity of these assumptions. Several limits to growth appear, in fact, to be neglected or misunderstood. For instance, the maximum in oil consumption, named *peak oil* (*Brandt and Farrell*, 2007; *Kharecha and Hansen*, 2008). Nevertheless, the scenarios proposed in *IPCC* (2000) have been

Table 3.2: General Circulation Models employed in the IPCC 4AR

Originating Group(s)	**Country**	**Model ID**
Beijing Climate Center	China	BCC-CM1
Bjerknes Centre for Climate Research	Norway	BCCR-BCM2.0
National Center for Atmospheric Research	USA	CCSM3
Canadian Centre for Climate Modelling & Analysis	Canada	CGCM3.1(T47)
Canadian Centre for Climate Modelling & Analysis	Canada	CGCM3.1(T63)
Mto-France / Centre National de Recherches Mtorologiques	France	CNRM-CM3
CSIRO Atmospheric Research	Australia	CSIRO-Mk3.0
CSIRO Atmospheric Research	Australia	CSIRO-Mk3.5
Max Planck Institute for Meteorology	Germany	ECHAM5/MPI-OM
Meteorological Institute of the University of Bonn, Meteorological Research Institute of KMA, and Model and Data group	Germany Korea	ECHO-G
LASG / Institute of Atmospheric Physics	China	FGOALS-g1.0
US Dept. of Commerce- NOAA- Geophysical Fluid Dynamics Laboratory	USA	GFDL-CM2.0
US Dept. of Commerce- NOAA- Geophysical Fluid Dynamics Laboratory	USA	GFDL-CM2.1
NASA Goddard Institute for Space Studies	USA	GISS-AOM
NASA Goddard Institute for Space Studies	USA	GISS-EH
NASA Goddard Institute for Space Studies	USA	GISS-ER
Instituto Nazionale di Geofisica e Vulcanologia	Italy	INGV-SXG
Institute for Numerical Mathematics	Russia	INM-CM3.0
Institut Pierre Simon Laplace	France	IPSL-CM4
Center for Climate System Research (The University of Tokyo), National Institute for Environmental Studies, and Frontier Research Center for Global Change (JAMSTEC)	Japan	MIROC3.2(hires)
Center for Climate System Research (The University of Tokyo), National Institute for Environmental Studies, and Frontier Research Center for Global Change (JAMSTEC)	Japan	MIROC3.2(medres)
Meteorological Research Institute	Japan	MRI-CGCM2.3.2
National Center for Atmospheric Research	USA	PCM
Hadley Centre for Climate Prediction and Research Met Office	UK	UKMO-HadCM3
Hadley Centre for Climate Prediction and Research Met Office	UK	UKMO-HadGEM1

used worldwide in climate change studies and are considered to cover a broad spectrum of possible future emission and economy projections. The emission scenarios of *IPCC* (2000) are organized into families, which contain scenarios that are similar to each other in some respects. IPCC assessment report projections for the future are made in the context of a specific scenario family. Specifically the considered family are four and the quoted *IPCC* (2000) description is provided in the following:

- The **A1** storyline and scenario family describes a future world of very rapid economic growth, global population that peaks in mid-century and declines thereafter, and the rapid introduction of new and more efficient technologies. Major underlying themes are convergence among regions, capacity building, and increased cultural and social interactions, with a substantial reduction in regional differences in per capita income. The A1 scenario family develops into three groups that describe alternative directions of technological change in the energy system. The three A1 groups are distinguished by their technological emphasis: fossil intensive (A1FI), non-fossil energy sources (A1T), or a balance across all sources (A1B).

- The **A2** storyline and scenario family describes a very heterogeneous world. The underlying theme is self-reliance and preservation of local identities. Fertility patterns across regions converge very slowly, which results in continuously increasing global population. Economic development is primarily regionally oriented and per capita economic growth and technological change are more fragmented and slower than in other storylines.

- The **B1** storyline and scenario family describes a convergent world with the same global population that peaks in midcentury and declines thereafter, as in the A1 storyline, but with rapid changes in economic structures toward a service and information economy, with reductions in material intensity, and the introduction of clean and resource-efficient technologies. The emphasis is on global solutions to economic, social, and environmental sustainability, including improved equity, but without additional climate initiatives.

- The **B2** storyline and scenario family describes a world in which the emphasis is on local solutions to economic, social, and environmental sustainability. It is a world with continuously increasing global population at a rate lower than A2, intermediate levels of economic development, and less rapid and more diverse technological change than in the B1 and A1 storylines. While the scenario is also oriented toward environmental protection and social equity, it focuses on local and regional levels.

The emission scenarios considered in the 4AR are only a subset of the forty defined on the Special Report on Emissions Scenarios and they include the scenario A2, A1B and B1 (*Meehl et al.*, 2007b). This subset of the SRES marker scenarios is the same used in the TAR and they represent "low" (B1), "medium" (A1B) and "high" (A2) forecasts, with respect to the prescribed concentrations of greenhouse gases and the

resulting radiative forcing (*Meehl et al.*, 2007b). The B1 is the closer to the low end of the range of CO_2 emission projections, (CO_2 concentration of about 550 [*ppm*] by 2100), the A2 is closer to the high end of the range (CO_2 concentration of about 850 [*ppm*] by 2100) and the A1B is almost in the middle of the range (CO_2 concentration of about 700 [*ppm*] by 2100). *Meehl et al.* (2007b) specify that the choice was made solely due to the limited computational resources for multi-model simulations and thus does not imply any preference or qualification of these three scenarios over the others. However, they clarify that qualitative conclusions derived from the three chosen scenarios are in most cases also valid for others defined by SRES.

In order to present a proof-of-concept case and due to constraints in computational resources, only a single CO_2 emission scenario, the A1B scenario is used in the study. The A1B scenario is an intermediate case between the B1 and A2 and it should supposedly provide an intermediate effect of climate change, that approximately corresponds to the median curve of global temperature increase among all considered scenarios in the 4AR (*IPCC*, 2007a). Moreover realizations for this scenario are available from almost all GCMs used in the 4AR of the IPCC (www-pcmdi.llnl.gov/ipcc/about_ipcc.php). In the opinion of the author, A1B emission scenario is also the most plausible among the proposed ones.

As anticipated in Section 3.2.3, among the 25 General Circulation models that were used in IPCC 4AR (*Meehl et al.*, 2007a,b), only a subset of eight models was used in a case study of the multi-model ensemble and stochastic downscaling. General Circulation Model realizations were obtained from the dataset compiled in the World Climate Research Programme's (WCRP's), Coupled Model Intercomparison Project phase 3 (CMIP3) (*Meehl et al.*, 2007a). The selection of models was based on two criteria: data availability (availability of daily precipitation time series as the principal constraint) and a relative independence among the models. The reasons underlying the first criterion are obvious, the latter criterion is a consequence of one of the requirements for using the multi-model ensemble approach, which is the mutual independence between model realizations. Climate models developed by different groups around the world can be assumed to be independent to a certain extent; nevertheless, they can share components or have similar theoretical arguments for their parameterizations (*Tebaldi and Knutti*, 2007). In order to preserve the relative independence among models, when multiple or updated versions of the same climate model were available, only a single version of such a GCM was used. The same discrimination was realized, for different models provided by the same originating group or for models that borrow many components by other ones. On the basis of the above criteria the following models are used in this work: CCSM3, CGCM3.1(T63), CSIRO-Mk3.5, ECHAM5-MPI-OM, GFDL-CM2.1, INGV-SXG, IPSL-CM4, and MIROC3.2(medres) (Table 3.3).

An illustration of the relative performance of eight GCMs in terms of monthly precipitation and temperature is provided in Figures 3.9 and 3.10. The large spread exhibited by GCM outputs underlines inherent uncertainties in climate model predictions. This is especially true for precipitation, where the monsoon season is poorly

captured (Figure 3.10a) by majority of the models and the factors of change are substantially different among the models (Figure 3.10c). Air temperature is generally simulated better (Figure 3.9a) and although the GCM projections are different to a certain extent, all of the factors of change are positive and their relative differences are contained within 2 [$^{\circ}C$] intervals for most months (Figure 3.9c).

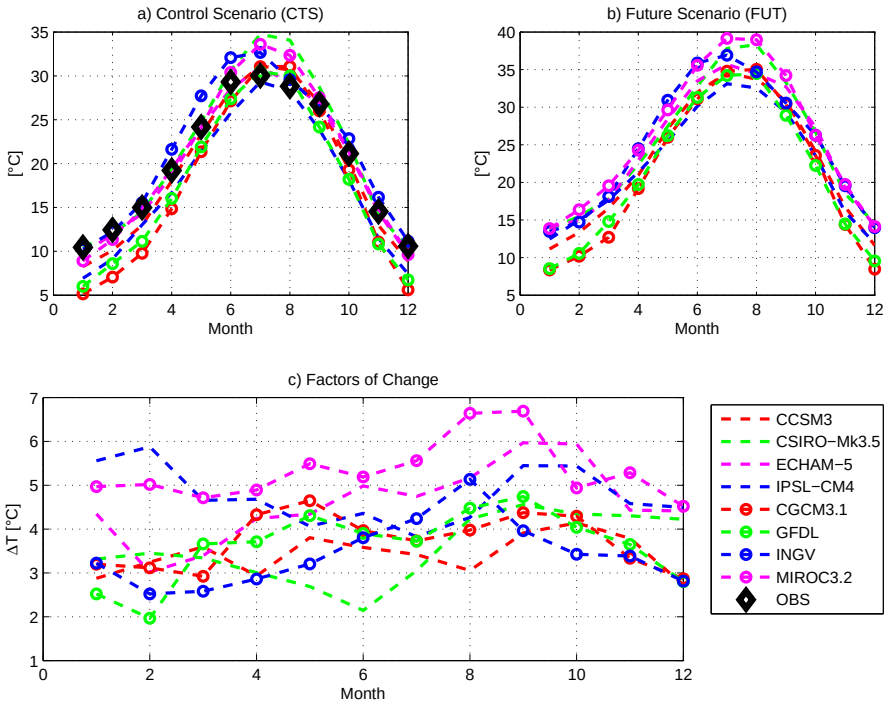

Figure 3.9: The time series of mean monthly temperature calculated from eight GCMs: CCSM3, CGCM3.1(T63), CSIRO-Mk3.5, ECHAM5-MPI-OM, GFDL-CM2.1, INGV-SXG, IPSL-CM4, and MIROC3.2(medres) for the location of Tucson airport, including observations (OBS). a) Control scenario (CTS) 1961-2000. b) Future scenario (FUT), 2081-2100. c) Additive factors of change for mean monthly temperature.

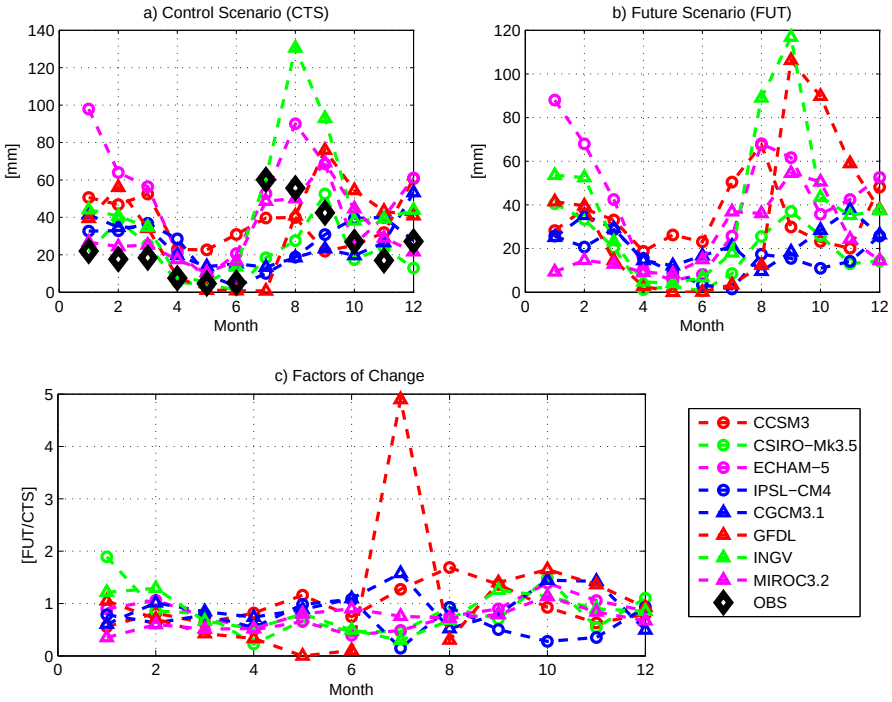

Figure 3.10: The time series of total monthly precipitation calculated from eight GCMs: CCSM3, CGCM3.1(T63), CSIRO-Mk3.5, ECHAM5-MPI-OM, GFDL-CM2.1, INGV-SXG, IPSL-CM4, and MIROC3.2(medres) for the location of Tucson airport, including observations (OBS). a) Control scenario (CTS) 1961-2000. b) Future scenario (FUT), 2081-2100. c) Multiplicative factors of change for monthly precipitation.

Chapter 4

"TETHYS" A HYDROLOGICAL MODEL

4.1 Introduction

The history of numerical hydrological modeling dates back almost half century (*Todini*, 2007), when one of the most famous models the "*Stanford Watershed Model*" (*Crawford and Linsley*, 1966) was implemented. In the successive years conceptual (*Beven and Kirkby*, 1979) and physically based distributed model (*Abbott et al.*, 1986a,b) have been developed. Recently, important advances have regarded the inclusion of topographic (*Rigon et al.*, 2006) and vegetation feedbacks (*Ivanov et al.*, 2008a) within physical based distributed models.

While presenting a new model two questions naturally arise: *why is there a need to develop a new hydrological modeling tool?* and *what is new in this tool?*. These questions require a prompt answer. The primary scope of the study was to investigate the interactive vegetation-hydrology dynamics including snow effects. For such a purpose most of the available models were unadapt, because they do not directly model all the mentioned components. Commonly, vegetation is considered to be static or is externally prescribed. Several assumptions made in current hydrological models appear to be unrealistic, when the primary purpose is to consider the mutual interaction between water fluxes and vegetation dynamics. Moreover, there is a long tradition in hydrological modeling to treat accurately flow-routing components when compared to energy mediated soil-moisture fluxes. The opposite holds true in land surface modeling emphasizing the need for tools that attempt to simulated both with the same accuracy. Furthermore, the possibility to modify components or to adapt the model for a specific problem or location is often limited or even impossible in commercial and generally available models. This issue is very important when the capability to control the processes and to obtain not standard outputs is required.

Given these considerations, a new model "Tethys" has been developed. Its scope is to be a flexible and easily controllable tool able to model the hydrological cycle and emphasize its interaction with vegetation. Another motivation has been the will

to reduce the computational requirements, simplifying when possible, the numerical schemes. Among the most important assumptions can be listed: the use of a single prognostic surface temperature (Section: 4.2.5) and the use of an unsaturated soil component where capillarity effects are neglected (Section: 4.7.3). These assumptions are discussed in the following and imply several numerical simplifications.

The presented model has been clearly influenced from the physical processes accounted for and conceptualized within numerous existent models developed by the hydrological and land surface modeling communities. The principal references to which "Tethys" is inspired are: *tRIBS-VEGGIE* (*Garrote and Bras*, 1995; *Ivanov et al.*, 2004a,b; *Ivanov*, 2006; *Vivoni et al.*, 2007; *Ivanov et al.*, 2008a), *GEOTOP* (*Bertoldi et al.*, 2006b; *Rigon et al.*, 2006), *DHVSM* (*Wigmosta et al.*, 1994), *RHESSys* (*Band et al.*, 1993; *Mackay and Band*, 1997; *Tague and Band*, 2004), *CLM* (*Bonan*, 1996; *Oleson et al.*, 2004), *SiB* (*Sellers et al.*, 1986, 1996b), *ISBA* (*Noilhan and Planton*, 1989; *Noilhan and Mafhouf*, 1996), *ECMWF* (*Viterbo and Beljaars*, 1995), *MOBIDIC* (*Campo et al.*, 2006), *TOPKAPI* (*Ciarapica and Todini*, 2002), *SHETRAN* (*Ewen et al.*, 2000), *KINEROS* (*Smith et al.*, 1995).

The coupled model of energy and water budgets at the element scale is introduced in this Chapter. A description is provided of the conceptual assumptions and the mathematical formulation of the energy and moisture fluxes, including radiation exchanges, sensible, latent, and ground heat fluxes, snow hydrology dynamics, water fluxes passing through two vegetation layers. Unsaturated and saturated dynamics within a multi-layer soil up to the bedrock interface are also accounted for. An entire section is dedicated to the analysis of the resistances between the ground surface and the surface boundary layer, underlining the hypothesis behind this theoretical framework and the sensitivity of energy and moisture fluxes to the proposed schemes. The interaction between hydrological fluxes and states and vegetation structure of different plant species that can be present within a given element is particularly emphasized. For instance, the model explicitly includes the interaction between snow, radiation, and vegetation effects; furthermore, the *Leaf Area Index* (LAI) and the biophysical processes of stomatal closure and photosynthesis are time dependent, providing dynamic feedbacks between water fluxes and vegetation. In this regard, "Tethys" exchanges state variables with the vegetation dynamic model "Chloris", presented in Chapter 5. Therefore, "Tethys" can be fully considered an eco-hydrological model (*Bonan*, 1995; *Rodriquez-Iturbe et al.*, 1999; *Arora*, 2002; *Daly and Porporato*, 2005).

The formulation proposed in the following deals mainly with the element scale. Nonetheless, insights about its extension at larger watershed scales is discussed. Note that the effects at larger scale, e.g. watershed, are the combined effects of the superposition of the hydrological processes, at the plot, or hillslope scale.The spatial interactions are introduced through boundary conditions, i.e. the possible connections with neighbor elements. The principal state variables are the soil moisture content distributed with depth that directly or indirectly control all the energy fluxes. Soil moisture can be strongly affected by lateral moisture exchange. Conse-

quently, in order to extend the model to watershed scale, this effect is included. As a consequence, a quasi-three-dimensional domain is obtained, where lateral moisture transfers could influence the spatio-temporal variability of states.

Physically-based equations or conceptualization of physical processes are used in the implementation of "Tethys" components. Therefore, the model is essentially physically based and mechanistic driven, although the introduction of empirical equations or coefficients has been often necessary. "Tethys" includes the state-of-art process understanding and modeling of hydrological, energy exchange, and vegetation dynamic phenomena, having as constraint the underlying lack of knowledge of several natural process and the uncertainties in boundary conditions. It must be remarked that the state-of-art process understanding is related to the author knowledge, perception and preferences, leading to an unavoidable model subjectivity.

For its structure "Tethys" can be partially seen to belong to the old blueprint on physically based models proposed by *Freeze and Harlan* (1969) or *Loague et al.* (2006), rather than the newer proposed by *Beven* (2002); *Sivapalan* (2003); *McDonnell et al.* (2007), and *Troch et al.* (2008). In the latter is hoped for the introduction of representative elementary watershed (*Reggiani and Schellekens*, 2003) as basic hydrological unit or syntheses between process understanding at local scales and conceptual modeling at watershed scale. However, these novel philosophical considerations and the directions proposed in the mentioned references are also taken into account in the model development and as warnings of possible shortcomings and deficiencies of the proposed tool. I'm, indeed, aware of issues, such as, significant watershed and sub-watershed heterogeneities; immobile storage and preferential flows; scaling behaviors that imply inadequacy of the physical scheme adopted at element scale; equifinality in the parameters determination; etc. (*Beven*, 2001; *McDonnell*, 2003; *Beven*, 2006; *McDonnell et al.*, 2007). Notwithstanding, investing efforts in developing a mechanistic model, that attempts to reproduce our understanding of the natural processes, avoiding, when possible, simplified conceptualizations, is still, in my opinion, the best way to face the hydrological modeling challenge.

4.1.1 Model overview

The model simulates the energy and water balances of both vegetated and non-vegetated surfaces that can occupy simultaneously a given element, including snow cover. In a domain of study, the dynamics of each computational element are simulated separately. The spatial interaction is introduced by considering the surface and subsurface moisture transfers between elements, this affects the soil moisture state, that in turn affects the local dynamic via the coupled energy-water interactions.

The processes that interact each other in a dynamic fashion creating a coupled vegetation-hydrology system are numerous as reported in Figure 4.1 with a flow chart, and in Figure 4.2 with a cartoon. These processes are enumerated briefly:

- ◇ **Model Components**

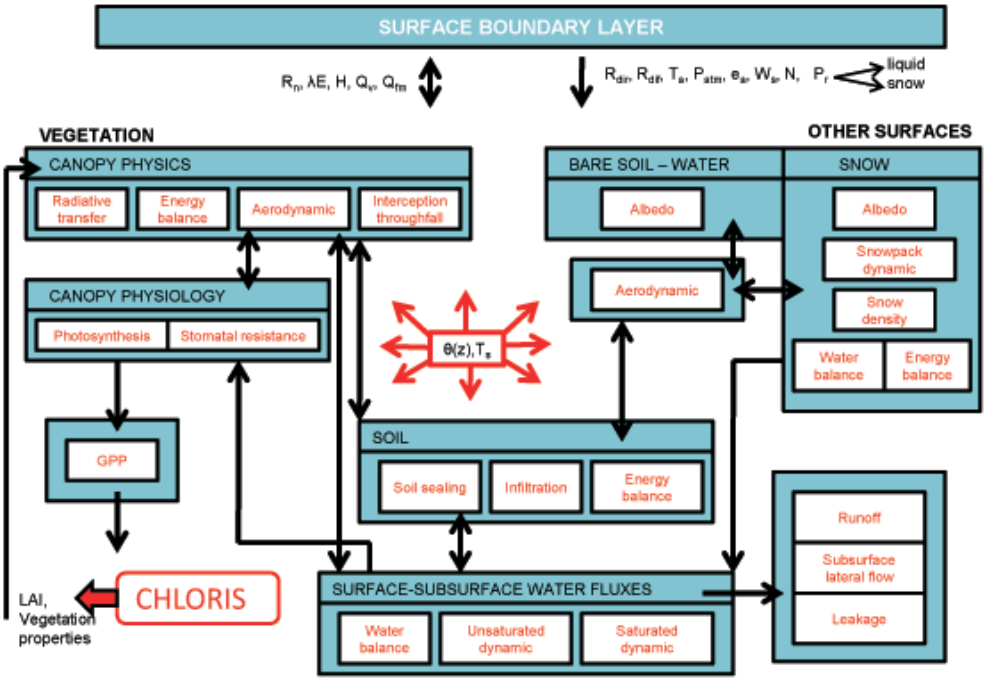

Figure 4.1: Components of "Tethys" showing the coupling between hydrological, energy, and biochemical processes. The model is forced with atmospheric inputs and it returns to the atmosphere energy and mass fluxes. All the components and symbols are detailed in the text.

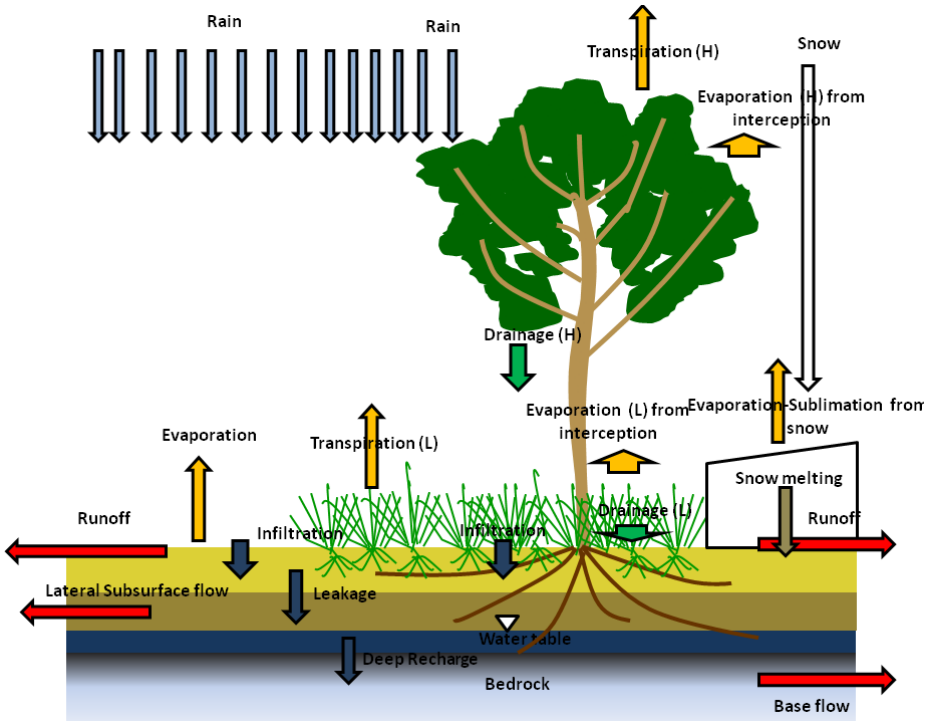

Figure 4.2: A visual scheme of the components included in the hydrological and energy balance schemes.

- absorption, reflection, and transmittance of solar shortwave radiation and atmospheric longwave radiation (Section: 4.2);
- sensible and latent heat fluxes, partition of latent heat into evaporation and transpiration, ground heat flux and incoming heat with precipitation (Section 4.3);
- resistance scheme for water and energy fluxes, including aerodynamic resistance, leaf boundary layer resistance, soil resistance and stomatal physiology (Section 4.4), this part is highly coupled with the vegetation model described in Chapter 5;
- snow hydrology component, including snowpack energy balance, snowmelt, and snow interception (Section 4.5);
- interception, throughfall, stem flow, and splash erosion (Section 4.6);
- infiltration, soil sealing, water movement into a multi-layer soil including unsaturated and saturated zone dynamics, and runoff formation (Section 4.7).
- surface flow routing (Section 4.8).

The model operates at an *hourly* time scale due to numerical requirements. The only components that are allowed to operate at finer time resolution are the one related to subsurface and surface water dynamic (Section 4.7 and 4.8). The differential equations governing the subsurface water dynamics are solved with an adaptive variable time step. Infiltration, soil sealing, and erosion components can be forced disaggregating rainfall at the 5 $[min]$ time scale, with the rainfall disaggregator described in Appendix A.1. Finally surface flow routing uses 2 $[s]$ of internal time step. In future versions the possibility to introduce more flexible computation time grids is suggested.

4.1.2 Basic computational element

Basic computational element refers to the smallest element for which the model computes the energy and water fluxes. The basic computational element is characterized by a topographic representation, where the element is drawn from the wider watershed representation and interacts with the neighbors elements. The basic element is further characterized by a land cover composition in which are schematized the possible fractions of land use.

Topographic representation

In a distributed watershed model, topography is typically represented utilizing a number of elementary computational structures (*Kampf and Burges*, 2007). These structures are here referred as *Basic computational elements*. *Basic computational elements* can be defined using criteria such as topography, land surface characteristics or hydrological functionality. They can be represented in different ways, such as sub-watersheds, contour-based streamtubes, triangulated irregular networks (TIN),

or grid domains (*Kampf and Burges*, 2007). Each of these elements is a separate unit connected with topological or hierarchical relationships to the others.

In distributed hydrology, regular square grid representing elevation known as Digital Elevation Model (DEM), or Digital Terrain Model (DTM) have been widely used to represent the watershed topography in the last couple of decades (*O'Callaghan and Mark*, 1984; *Abbott et al.*, 1986b; *Quinn et al.*, 1991; *Wigmosta et al.*, 1994; *Beven and Freer*, 2001; *Bertoldi et al.*, 2006b). Regular grid on the form of DEM are the most used elementary computational structures. Alternative approaches are offered by the TIN data structure, that is a piece-wise linear interpolation of a set of points that results in a group of non-overlapping triangular elements of varying dimensions (*Kampf and Burges*, 2007). The TIN has some advantage in comparison to the grid representation, for instance, the multiple resolution offered by the irregular domain and the preservation of linear features such as channels. The construction of a triangular irregular network model for distributed hydrologic modeling has been detailed by *Tucker et al.* (2001), and *Vivoni et al.* (2004). Hydrologic models based on triangular elements to represent topography are well documented in the literature (*Ivanov et al.*, 2004a; *Vivoni et al.*, 2005). Other less conventional techniques to delineate the computational elements have been also proposed (*Menduni et al.*, 2002).

The topographic representation in "Tethys" is based on the DEM regular square grid (Figure 4.3a and Figure 4.4 left). This solution is the most conventional and simple. The use of a grid cell as basic computational element in distributed hydrological modeling can present some caveats, and certainly it is not a parsimonious computational choice. Nevertheless, the wide use of grid representations in literature makes it appealing because the pro and cons of the methodology are well known. Furthermore, algorithms to retrieve topographic and hydrologic features from DEM are easily available (*Schwanghart and Kuhn*, 2010). For instance, cell slope, aspect, curvature can be routinely computed from a DEM representation as illustrated in Figure 4.3. The same consideration holds true for the computation of terrain parameters affecting solar radiation (Appendix A.9) or important hydrologic characteristic such as flow direction (Figure 4.4 right). Adopting different *basic computational elements* would require the develop of proper routines for each of these characteristics and it is clearly beyond the scope of this study.

An important topographic characteristic for hydrological analysis is the delineation of the flow directions. Numerous methods have been proposed and a substantial body of literature has dealt with this issue (*O'Callaghan and Mark*, 1984; *Quinn et al.*, 1991; *Tarboton and Rodriguez-Iturbe*, 1991; *Costa-Cabral and Burges*, 1994; *Tarboton*, 1997; *Orlandini et al.*, 2003; *Seibert and McGlynn*, 2007; *Orlandini and Moretti*, 2009). Surface flow paths can be obtained from gridded elevation data by connecting grid cell centers along predetermined flow directions. Unfortunately, computing flow directions requires some DEM pre-processing exercise. All DEMs present some spurious errors commonly referred to as sinks, depressions and pits (*Grimaldi et al.*, 2007). Natural or artificial depressions and flat areas within a

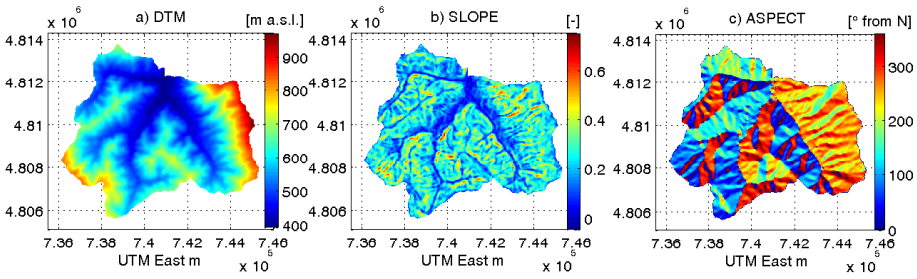

Figure 4.3: Representation of topographic attributes using a regular square grid. a.) Digital Elevation Model. b.) Slope fraction [−] calculated with the maximum steepness method. c.) Aspect in angular degree [°] from North. All the attributes refer to the Cerfone creek watershed in Tuscany (Italy).

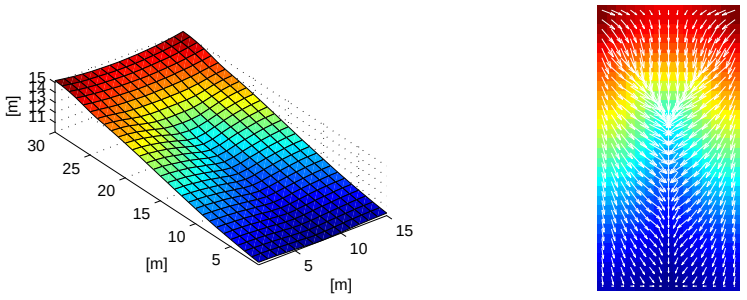

Figure 4.4: Representation of topographic and hydrological features for a small zero-order catchment, i.e., Digital Elevation Model (left panel) and arrows outlining the flow directions (right panel). The domain is the one of the Biosphere 2 Hillslope Experiment (*Hopp et al.*, 2009).

DEM are critical in the computation of the flow directions (*Nardi et al.*, 2008). The absence of slope, indeed, does not allow to directly identify the direction of flow and generates problem to all the flow routing algorithm that are topographically based (e.g. kinematic routing) as the one adopted in "Tethys" (Section 4.8). Methods to assign flow directions without modifying the DEM and computing a positive slope have been proposed, see *Nardi et al.* (2008) for a review. This method usually generates unrealistic banded effects of flow lines following straight, parallel directions and cannot be used for slope based routing. Other methods modify the DEM to enforce a positive gradient to the flat surface in order to allow the flow to propagate from higher to lower terrain (*Nardi et al.*, 2008). For instance, *Orlandini et al.* (2003) use a recursive procedure to raise the elevations of the cells located in flat or depressed areas so as to ensure a drainage direction with a small positive slope (downward) for all the cells of the catchment. Another methodology is the PEM4PIT (physical erosion model for pit removal), based on the implementation of a landscape equilibrium model to modify the original surface (*Grimaldi et al.*, 2007). In "Tethys" the method of *Orlandini et al.* (2003) is used in order to pre-process the DEM and allow the computation of flow directions. The flow directions are commonly determined using single and multiple flow direction algorithms (*Nardi et al.*, 2008; *Orlandini and Moretti*, 2009). The difference lays in the partition of the flow from the upslope cell to the neighboring cells with a lower elevation. In single flow direction methods all the flow is concentrated toward a single cell, when multiple flow direction are considered the flow is subdivided among several cells, at least two.

The simplest flow direction method is called D-8 and identify a single flow direction in one of the eight adjacent cells. The receiving cell is the one for which the steepest slope is calculated (*O'Callaghan and Mark*, 1984). From an extensive review of literature work *Nardi et al.* (2008) conclude that single flow direction methods are incapable to efficiently simulate flow on hillslope and that multiple flow direction methods cannot accommodate concentrated channel flow. Multiple drainage directions are questioned to often produce an excessive dispersion of flow, which may be inconsistent with the physical drainage (*Orlandini et al.*, 2003). In this respect, single drainage direction methods being non-dispersive appear preferable. A reasonable compromise between the simplicity of the single flow method and the sophistication introduced in more recent multi-flow formulations has been proposed by *Tarboton* (1997). The multi-flow method of *Tarboton* (1997), usually named D-infinity, estimates flow direction by approximating the topographic surface using the eight adjacent triangular facets. The flow direction is identified with an angular measure. In the D-infinity model, the dispersion is minimized since the flow will be apportioned between at most two receiving cells. A more recent single flow direction method has been proposed by *Orlandini et al.* (2003). The scheme is still based on the eight-triangular facet of D-infinity. Nevertheless, in order to provide a more conservative drainage patterns the method approximates the flow direction to the facet edge that minimizes the cumulative lateral transversal deviation, or the cumulative least angular deviation measured along the path on a predefined number

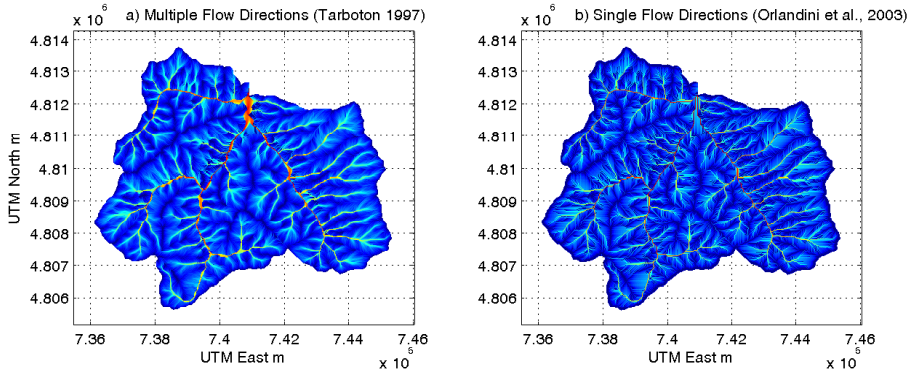

Figure 4.5: Maps of flow accumulation, i.e. upslope area according to the calculated flow directions. a.) D-infinity *Tarboton* (1997) method. b.) Single flow method of *Orlandini et al.* (2003) using lateral transversal deviation with $\lambda = 0$. The domain is the Cerfone creek watershed in Tuscany (Italy).

of antecedent steps. The method account for the memory of the upstream deviations trough a λ coefficient. For $\lambda = 1$, full memory of the upstream deviations is retained. For $0 < \lambda < 1$, the upstream deviations are dampened proceeding downstream (see *Orlandini et al.* (2003) for details). The least angular deviation method with $\lambda = 0$ reproduces the classical D-8 method. Flow directions in "Tethys" can be estimated with the two methods introduced above: the multi-flow of *Tarboton* (1997) and the single flow of *Orlandini et al.* (2003). The flow direction matrix is successively used in the Section 4.8 to route the surface water flow. Maps of flow accumulation, i.e. upslope area according to the calculated flow directions, are shown in Figure 4.5. The difference among the two method is evident, with the multiple flow producing an unrealistic dispersion of the flow near the outlet. Recently a combination of single and multiple flow directions in a morphologically significant manner has been proposed and will be considered to delineate flow directions in future version of "Tethys" (*Orlandini and Moretti*, 2009).

A further topographic characteristic required for flow routing modeling is the distinction between cells that belong or do not to the channel network. This distinction that leads to the delineation of the channel network can be easily made when geographical information about the stream positions are available. Methodologies to identify the channel network directly from DEM have been also provided (*Montgomery and Dietrich*, 1988, 1989). The simplest method is to set a threshold on the contributing area, i.e, identify a channel cell when the flow accumulation is larger than a given value (Figure 4.5). When no information on the position of the channels is available, such a method is used in "Tethys".

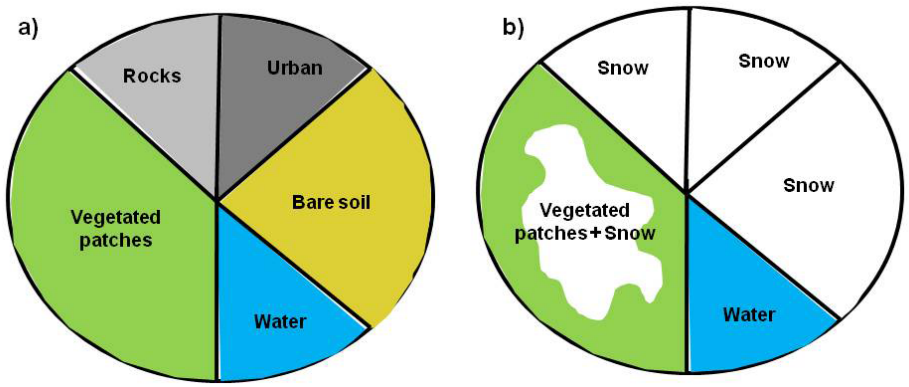

Figure 4.6: An illustration of the land cover composition of a general *basic computational element*. (a) The area is subdivided into vegetated, bare soil, water, urban, and rock covered, surfaces. (b) The presence of snow $C_{sno} = 1$ alters the composition.

Land cover composition

Within a basic computational element, "Tethys" can account for up to six different land covers: vegetated areas, bare soil areas, expanses of water, urban areas, and rock covered areas. Besides, the model computes the presence or absence of snow that can interact with the other surfaces. The underlaying assumption is that when snow is present at the ground it covers all the other surfaces, excluding expanses of water and vegetated areas. Water surfaces are not allowed to hold snow, though they are allowed to freeze. The interaction between vegetated areas and snow is taken into account in a more complex fashion. This includes interception of snow by the canopies (Section: 4.5.3) and modifications of the adopted parametrization schemes as a function of relative height between snow and plants. Further details are provided later in this Chapter. A graphic representation of the possible land covers within a basic element is shown in Figure 4.6. Fractions of land cover are indicate with the following symbols: C_{veg}, C_{bare}, C_{wat}, C_{urb}, and C_{rock} [−], where the symbols represent respectively the fraction occupied by vegetated, bare soil, water, urban, and rock covered, areas. The presence or absence of snow is indicated with a logic operator: C_{sno} [−], that assumes value 1 in presence of snow and 0 otherwise. Obviously, it follows that $C_{veg} + C_{bare} + C_{wat} + C_{urb} + C_{rock} = 1$.

In order to simplify the model development and description the possibility to include rock covered surfaces and urban areas is disabled in this first version of "Tethys". Land cover composition reduces to only four different types. Since the principal interest lays in the investigation of vegetation dynamics, neglecting rock covered surfaces and urban areas is not considered a significant limitation for this study. In future versions of the model, the inclusion of these two land cover components is instead recommended. The representation of an urban hydrology component is regarded with growing interest from the scientific community as testified by numerous recent studies (*Dupont and Mestayer*, 2006; *Rodriguez et al.*, 2008; *Oleson et al.*, 2008a).

Vegetation composition and attributes

The vegetated fraction, C_{veg}, of the basic computational elements can include one or more vegetation types. The model provides an horizontal and vertical composition of vegetation patches. Each vegetation patch can be composed of a single vegetation specie or more often of multiple vegetation species. In the second case, it is assumed to deal with multiple vegetation species as single Plant Functional Types (*PFTs*) (*Bonan et al.*, 2002). Adopting a single *PFT* for vegetation species that share life form (tree, shrub, grass), vegetation physiology (e.g., leaf optical properties, stomatal physiology, leaf photosynthetic characteristics) and structural attributes (e.g., height, leaf dimension, roughness length, root profile) is a common assumption made in many dynamics vegetation models to reduce the computational complexity of the problem. When large computational resources are available, the absence of an upper limit to the number of *PFTs* that can be included into the model allows a complete vegetation species differentiation.

The horizontal land cover composition of "Tethys" is presented in Figure 4.7. A bare soil area and areas cover by different vegetation patches named *Crown Areas* are included. The fractions of the *Crown Areas* are represented with the symbol C_{crown} $[-]$. The number n_c of *Crown Areas* depends on the specific element, and their sum correspond to the total vegetated area $\sum_{i=1}^{n_c} C_{crown} = C_{veg}$. *Crown Area* refers, herein, to the area occupied by one or two different *PFTs* and may be limited by the area actually occupied by the vegetation structure for grass and shrub species, or to the area below the crown for tree species. The n_c fractions C_{crown} of a basic computational element occupied by vegetation and the fraction occupied by bare soil are inputs of the model and should be defined, a priori. Each *Crown Area* or bare soil fraction is used to weight its relative contribution to the element-scale flux values. This partition is very important since strongly affect the estimation of the surface water and energy fluxes (Section: 4.3). In a fully dynamics vegetation model these fractions are subject to changes due to species competition and mortality. In the vegetation model "Chloris" coupled to "Tethys" species competition is neglected, thus *Crown Areas* fractions are constant during the entire simulation (see Chapter 5).

The vertical composition is realized within each *Crown Area*. The latter can include at the most two different *PFTs*, one for the upper canopy, henceforth named *High-vegetation* (H_v) layer and one for the lower canopy, henceforth named *Low-vegetation* (L_v) layer. Different *Crown Areas* may share one *PFT* as shown in Figure 4.8. For instance when the same grass specie appears in an isolated vegetated patch and below a cluster of trees. In this case the same *PFT* belonging to two different *Crown Areas* has the same vegetation parameters, but different dynamics. In fact, energy fluxes and photosynthetic activity can be influenced by the other *PFT* that occupies the same *Crown Area*.

It should be remarked that considering explicitly a vertical composition of vegetation is far to be common in climate and eco-hydrological modeling, and few examples

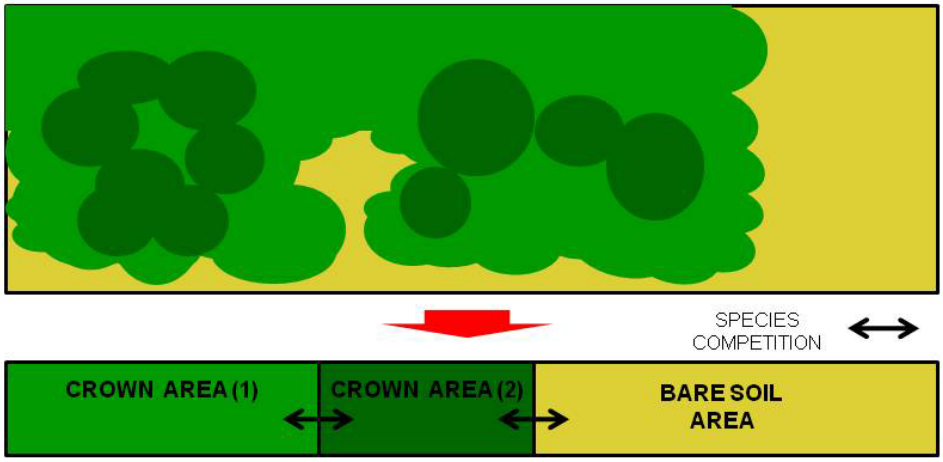

Figure 4.7: An illustration of vegetation representation at the element scale. The area is subdivided into patches of bare soil, and patches of vegetation (*Crown Areas*) that may included up two *PFTs*, one denoting the upper canopy (High-vegetation H_v) and one the lower canopy (Low-vegetation L_v). Note that species competition is not enabled in this version of the model.

are available, e.g., *IBIS* model (*Foley et al.*, 1996). This composition, indeed, significantly complicates the radiation, energy and water transfer schemes.

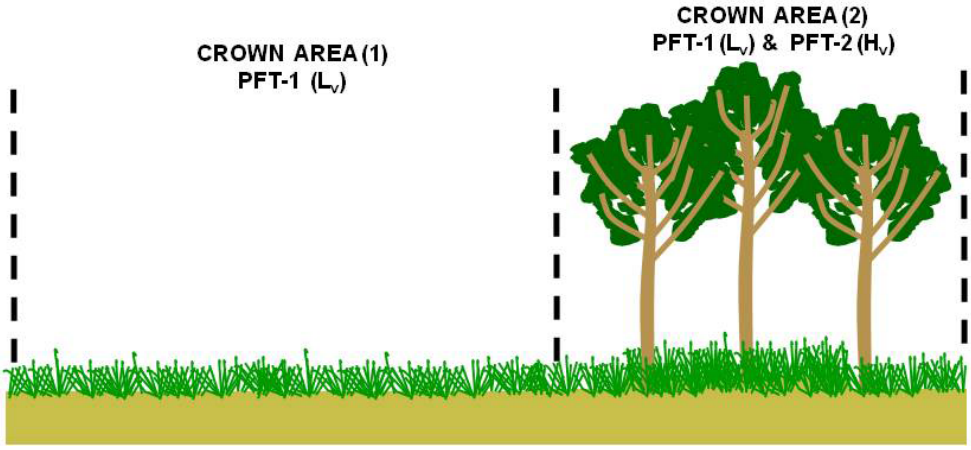

Figure 4.8: An illustration of the vertical composition of vegetation at the element scale.

The vegetation attributes necessary in the description of the hydrological part of the model are introduced in the following. Leaf and stem area index, LAI $[m^2\ leaf\ area\ m^{-2}\ ground area]$, SAI $[m^2\ stem\ area\ m^{-2}\ \ ground area]$ represent the projections perpendicular to the the terrain of the area occupied by leaves and by the stem structure respectively. LAI and SAI are usually expressed at the *Crown Area* level, i.e. LAI $[m^2\ leaf\ area\ m^{-2}\ \ PFT area]$ and SAI $[m^2\ stem\ area\ m^{-2}\ PFT area]$, where the PFT area, in this case corresponds to the *Crown Area*. The quantities at the element scale are obtained multiplying for the relative *Crown Area* fractions C_{crown}. In the text when the units of measurement

for LAI and SAI are not specified, they must be considered referred to the *Crown Area* level.

The canopy height, H_c $[m]$, represents the distance between the ground surface and the top of the canopy. The quantity d_{leaf} $[cm]$ is the typical leaf dimension. The quantities Ψ_{ss} $[kPa]$ and Ψ_{wp} $[kPa]$ are the soil potential at the begin of stomatal closure and at the complete stomatal closure, commonly named wilting point. Finally, the root profile, $Z_{root}(z_d)$ $[-]$, is introduced, with root profile is to be intended the profile of fine root responsible for water uptake. Since usually no differentiation is made between fine and coarse root profiles, an exponential root density profile is used for each PFT (*Jackson et al.*, 1996) (equation 4.1), though more complex and time-varying root profile representations exist (*Feddes et al.*, 2001; *Schenk and Jackson*, 2002; *Arora and Boer*, 2003).

$$Z_{root}(z_d) \quad = \quad 1 - e^{-\eta z_d}\,, \tag{4.1}$$

where z_d $[mm]$ is the depth, positive downward and η $[mm^{-1}]$ is the decay rate of distribution of the root biomass with the soil depth. The parameter η depends on the vegetation type and can be estimated once the rooting depth Z_R $[mm]$ is known. The rooting depth is typically defined as the depth that contains 95% of the root biomass, but for simplicity the 95.02% is used, in such a way the term η becomes $\eta = 3/Z_R$. This equality can be easily demonstrated integrating the root profile up to the Z_R (*Arora and Boer*, 2003).

Although all the described attributes of vegetation are dynamics component (time-varying) only the LAI time-variations are accounted for. The other attributes are assumed to be constant and they must be specified as model inputs for each PFT. Time-invariant vegetation properties can be obtained from literature: for instance *Jackson et al.* (1996) provide a comprehensive study of the root distributions for a variety of species. *Bonan* (1996) provides typical values of leaf dimension for various plant types. *White et al.* (2000) provide values of soil potential at the begin of stomatal closure and at the wilting point. *Levis et al.* (2004) suggest that the stem area index SAI may be taken as 25% of the maximum LAI for trees and 5% of average LAI for grasses, although these values seems very large in comparison to other estimates. Finally, canopy height H_c is a characteristic easily determinable that depends on the PFT and on the specific location. Further details about vegetation structure, composition, and process dynamics are described in Chapter 5.

4.2 Radiative fluxes

The components necessary to estimate the net radiation at element scale are described in this section. The net radiation R_n $[W\ m^{-2}]$ is given by the sum of the absorbed shortwave R_{abs} $[W\ m^{-2}]$ and absorbed longwave fluxes L_{abs} $[W\ m^{-2}]$. R_n and the incoming heat with precipitation Q_v are successively partitioned into sensible heat H and latent heat λE within the energy balance (Section: 4.3).

In the description of the model components a distinction between vegetated and non-vegetated surfaces is made. The presence of vegetation with its canopy structure and spatial distribution of leaf area significantly affects the radiation regime and the computation of mass and energy exchange between a vegetated patch and the atmosphere.

4.2.1 Shortwave fluxes

At the element scale, the incoming solar radiation is partitioned first into direct beam R_{dir} $[W\ m^{-2}]$ and diffuse radiation R_{dif} $[W\ m^{-2}]$. The direct beam and diffuse fluxes are further partitioned into two different bands the ultraviolet/visible (UV/VIS) $\Lambda 1$ $[0.29 \div 0.70\ \mu m]$ and the near-infrared (NIR) $\Lambda 2$ $[0.70 \div 4.0\ \mu m]$ wavebands. A detailed discussion on incoming shortwave radiation is presented in Section 2.6. The remote topographic effects, such as, sky view factor S_{vf} $[-]$ and shadow effect S_h $[-]$ are considered to be already accounted for in the calculation of R_{dir} and R_{dif} (Appendix A.9).

The shortwave incoming energy is conserved. This means that the shortwave radiation flux should be absorbed or reflected by vegetation, soil or other land cover components. The conservation of global shortwave radiation could be described formally through equation 4.2:

$$\sum_{\Lambda} [R_{dir,\Lambda} + R_{dif,\Lambda}] \quad = \quad R_{abs,H_v} + R_{abs,L_v} + R_{abs,g} + \sum_{s=1}^{n} R_{abs,s} + R_{ref}\ , \quad (4.2)$$

where R_{abs,H_v}, R_{abs,L_v}, $R_{abs,g}$, $R_{abs,s}$ $[W\ m^{-2}]$ are the shortwave radiation fluxes absorbed by *high-vegetation*(H_v), *low-vegetation* (L_v), ground underneath the vegetation and other possible n surfaces (e.g. bare soil, water, snow). R_{ref} $[W\ m^{-2}]$ represents the total shortwave energy reflected, its value depends on land cover composition and more specifically on the albedos of the surfaces facing the sky.

Vegetated surface

For a vegetated surface, in the most general case, the shortwave radiation is considered to impact the *high-vegetation* canopy (H_v) and to transfer first through the *high-vegetation* and than through the *low-vegetation* (L_v) layer, ultimately reaching the ground as shown in Figure 4.10.

The direct beam, $I^{\mu}_{\Lambda,abs}$ $[-]$, and diffuse, $I_{\Lambda,abs}$ $[-]$, fluxes in the two wavebands absorbed by a general layer of vegetation per unit incident flux are described by the equations (4.3)-(4.4) and in Figure 4.9. The superscript μ indicates the direct beam component.

$$I^{\mu}_{\Lambda,abs} \quad = \quad 1 - I\uparrow^{\mu}_{\Lambda} - (1-\alpha_{s\Lambda}) I\downarrow^{\mu}_{\Lambda} - (1-\alpha^{\mu}_{s\Lambda}) e^{-K_{opt}[LAI+SAI]}\ , \quad (4.3)$$

$$I_{\Lambda,abs} \quad = \quad 1 - I\uparrow_{\Lambda} - (1-\alpha_{s\Lambda}) I\downarrow_{\Lambda}\ , \quad (4.4)$$

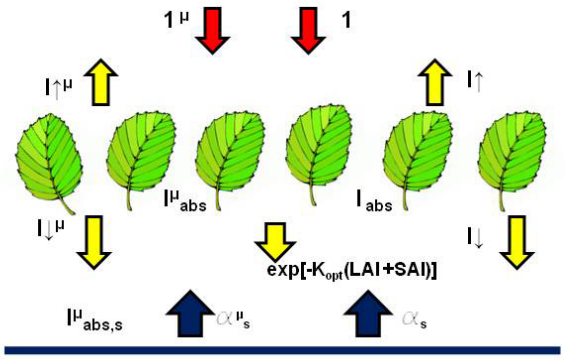

Figure 4.9: A schematic diagram of the beam and diffuse solar radiation absorbed, transmitted, and reflected by a general layer of vegetation with and underneath surface s. The scheme is valid for both the wavebands $\Lambda 1$ and $\Lambda 2$.

The terms $I\uparrow_{\Lambda}^{\mu}$ and $I\uparrow_{\Lambda}$ $[-]$ are the upward diffuse fluxes per unit incident direct beam and diffuse flux. $I\downarrow_{\Lambda}^{\mu}$ and $I\downarrow_{\Lambda}$ $[-]$ are the downward diffuse fluxes per unit incident direct beam and diffuse radiation. $e^{-K_{opt}(LAI+SAI)}$ $[-]$ is the direct beam flux transmitted through a general canopy per unit incident flux that is approximated through the Beer's law (*Monsi and Saeki*, 2005), where LAI $[m^2\ leaf\ area\ m^{-2}\ PFT\ area]$ is the leaf area index, SAI $[m^2\ stem\ area\ m^{-2}\ \ PFT\ area]$ is the stem area index and K_{opt} $[-]$ is the optical depth of direct beam per unit leaf and stem area. Upward fluxes $I\uparrow_{\Lambda}^{\mu}$, $I\uparrow_{\Lambda}$ $[-]$, downward fluxes $I\downarrow_{\Lambda}^{\mu}$ and $I\downarrow_{\Lambda}$ and, K_{opt} are calculated through a canopy radiative transfer scheme (Section: 4.2.2). All these quantities are function of the two canopy layers H_v and L_v (section: 4.1.2), since they depends on canopy type and structure. $\alpha_{s\Lambda}^{\mu}$ and $\alpha_{s\Lambda}$ $[-]$ are the direct beam and diffuse albedos of the general surface underneath the canopy that can be represented by *low-vegetation*, bare ground or snow (Section: 4.2.2).

The total solar radiation absorbed by *high-vegetation* R_{abs,H_v} $[W\ m^{-2}]$ is obtained as follows:

$$R_{abs,H_v} = \sum_{\Lambda}\left[R_{dir,\Lambda}I_{\Lambda,abs}^{\mu}(H_v) + R_{dif,\Lambda}I_{\Lambda,abs}(H_v)\right]. \tag{4.5}$$

The terms $I\uparrow_{\Lambda}^{\mu}$ and $I\uparrow_{\Lambda}$ in the equations (4.3)-(4.4) are multiplied by the sky view factor S_{vf} to take into account the eventual smaller portion of sky available to reflect the radiation. The underneath albedos becomes $\alpha_{s\Lambda}^{\mu} = I\uparrow_{\Lambda}^{\mu}(L_v)$ and $\alpha_{s\Lambda} = I\uparrow_{\Lambda}(L_v)$.

The equation for shortwave solar radiation absorbed by *low-vegetation* R_{abs,L_v} $[W\ m^{-2}]$ is similar to the previous one, whit different downward incoming fluxes and different albedos. The direct beam and diffuse radiation fluxes are modified by the passage through the *high-vegetation* layer and the albedos are relative to the surface underneath the *low-vegetation* layer, e.g., bare soil or snow.

$$R_{abs,L_v} = \sum_{\Lambda}\left[R_{dir,\Lambda,H_v}I_{\Lambda,abs}^{\mu}(L_v) + R_{dif,\Lambda,H_v}I_{\Lambda,abs}(L_v)\right], \tag{4.6}$$

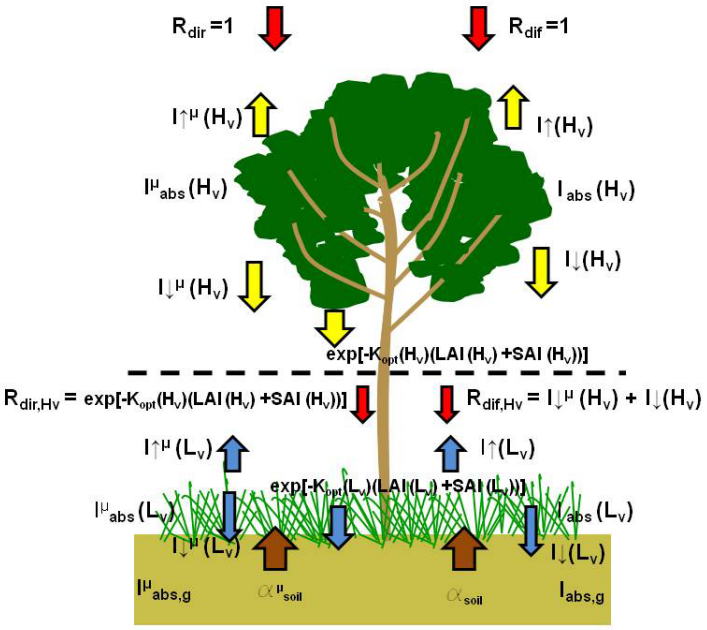

Figure 4.10: A schematic diagram of the beam and diffuse solar radiation absorbed, transmitted, and reflected by high-vegetation, low-vegetation, and under-canopy ground. In this case the underneath surface is bare ground $s = g$, with albedos $\alpha^{\mu}_{soil,\Lambda}$-$\alpha_{soil,\Lambda}$. The scheme is valid for both the wavebands $\Lambda 1$ and $\Lambda 2$.

where R_{dir,Λ,H_v} and R_{dif,Λ,H_v} are the direct beam and diffuse radiation transmitted by the upper vegetation layer (H_v) and $I^{\mu}_{\Lambda,abs}(L_v)$, $I_{\Lambda,abs}(L_v)$ are estimated from (4.3)-(4.4) with $\alpha^{\mu}_{s\Lambda}$ and $\alpha_{s\Lambda}$ relative to soil or snow covers (Section 4.2.2).

$$R_{dir,\Lambda,H_v} = R_{dir,\Lambda}\left[e^{-K_{opt}(H_v)[LAI(H_v)+SAI(H_v)]}\right] \tag{4.7}$$

$$R_{dif,\Lambda,H_v} = R_{dir,\Lambda} I\downarrow^{\mu}_{\Lambda}(H_v) + R_{dif,\Lambda} I\downarrow_{\Lambda}(H_v). \tag{4.8}$$

The solar radiation flux absorbed by the under-canopy layer $R_{abs,s}$ $[W\ m^{-2}]$ that, repeatedly, could be bare ground or snow is:

$$R_{abs,s} = \sum_{\Lambda}\Big[R_{dir,\Lambda,H_v} e^{-K_{opt}(L_v)[LAI(L_v)+SAI(L_v)]}(1-\alpha^{\mu}_{s\Lambda}) + [R_{dir,\Lambda,H_v} I\downarrow^{\mu}_{\Lambda}(L_v) + R_{dif,\Lambda,H_v} I\downarrow_{\Lambda}(L_v)](1-\alpha_{s\Lambda})\Big]. \tag{4.9}$$

The scheme provided in Figure 4.10 summarizes the complete case with two vegetation layers, although in many occasions only one of the two can be present. In the latter case the radiative transfer scheme reduces at a single vegetation layer, such as in *Ivanov et al.* (2008a).

The presence of snow in the canopies, as already stated, modifies the canopy radiative transfer scheme (see Section: 4.2.2). Besides, the presence of snow at the ground also alters the underneath albedo. The equations (4.3)-(4.4) are dynamically modified to take into account the current underneath albedo. Bare ground, $\alpha^{\mu}_{soil,\Lambda}$-$\alpha_{soil,\Lambda}$, or low vegetation, $I\uparrow^{\mu}_{\Lambda}(L_v)$-$I\uparrow_{\Lambda}(L_v)$, albedos are eventually substituted

with the snow albedos, $\alpha^{\mu}_{snow,\Lambda}$-$\alpha_{snow,\Lambda}$. Such modifications are a function of the relative difference of height between snowpack and canopies as illustrated in Figure 4.11.

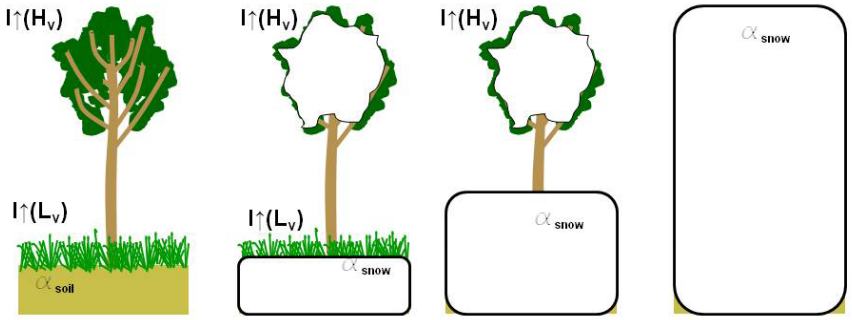

Figure 4.11: Interaction between snow depth and vegetation height used to determine the values of the albedos. The fourth scheme, with *high vegetation* completely covered by snow is not taken into account into "Tethys". The schemes are valid for both the wavebands $\Lambda 1$ and $\Lambda 2$ and for direct beam (μ) and diffuse radiation.

In analogy to what done for shortwave radiation, the absorbed *Photosynthetically Active Radiation*. PAR_{abs} $[W\ m^{-2}]$. is calculated taking into account the direct beam, $I^{\mu}_{vis,abs}$, and diffuse, $I_{vis,abs}$ $[-]$, fluxes absorbed by the vegetation canopies per unit incident flux in the ultraviolet/visible waveband $[0.29 \div 0.70\ \mu m]$. This band does not overlap perfectly with the *Photosynthetically Active Radiation* band $[0.40 \div 0.70\ \mu m]$. Nonetheless, errors coming from the use of the absorbed fractions in the visible waveband are considered negligible in comparison to other uncertainties.

$$PAR_{abs} = (PAR_B I^{\mu}_{vis,abs} + PAR_D I_{vis,abs}) \frac{LAI}{LAI + SAI}, \tag{4.10}$$

where PAR_B and PAR_D are the incoming *Photosynthetically Active Radiation* to the canopy, once shadow effect, S_h, and sky view factor, S_{vf}, are already accounted for (see Section: A.9). Note that when the scheme includes the two vegetation layers, PAR_B and PAR_D for the *low-vegetation* layer (L_v) are obtained accounting for the transmission through the upper layer as done for total shortwave in the equations (4.7)-(4.8). Equation 4.10 assumes that leaves absorb $\frac{LAI}{LAI+SAI}$ of the radiation absorbed by the vegetation.

The visible and near-infrared reflectances, r_{vis} and r_{nir} $[-]$, are estimated only for the upper vegetation layer. When both vegetation layers are present this is H_v:

$$r_{\Lambda} = \frac{R_{dir,\Lambda}[S_{vf} I \uparrow^{\mu}_{\Lambda} (H_v)] + R_{dif,\Lambda}[S_{vf} I \uparrow_{\Lambda} (H_v)]}{R_{dir,\Lambda} + R_{dif,\Lambda}}. \tag{4.11}$$

Using the visible and near-infrared reflectances is possible to calculate the *Normalized Difference Vegetation Index* (NDVI) for a specific *Crown Area*: $NDVI = \frac{r_{nir} - r_{vis}}{r_{nir} + r_{vis}}$.

Generally, variables estimated separately for each different land cover of a given

basic element can be expressed as quantities averaged at the element-scale. The latter are composed through a linear combination of the relative contributions (proportional to the corresponding fractional areas) of all the land covers within a basic element. The contribution of the vegetated fraction is in turn obtained as a linear combination of all the *Crown Areas*. The element-scale quantity of the *Normalized Difference Vegetation Index*, $\overline{NDVI}$, previously estimated at the *Crown Area* scale, can be obtained as:

$$\overline{NDVI} = \frac{\bar{r}_{nir} - \bar{r}_{vis}}{\bar{r}_{nir} + \bar{r}_{vis}}, \tag{4.12}$$

with:

$$\bar{r}_{\Lambda} = \frac{R\uparrow_{veg} + R\uparrow_{s}}{R_{dir,\Lambda} + R_{dif,\Lambda}}, \tag{4.13}$$

$$R\uparrow_{veg} = \sum_{i=1}^{n_c}\Big\{C_{crown,i}\Big(R_{dir,\Lambda}[S_{vf}I\uparrow_{\Lambda}^{\mu}(H_v,i)] + R_{dif,\Lambda}[S_{vf}I\uparrow_{\Lambda}(H_v,i)]\Big)\Big\}, \tag{4.14}$$

$$R\uparrow_{s} = \sum_{s=1}^{n}\Big\{C_s\left[(S_{vf}\alpha_{s\Lambda}^{\mu})R_{dir,\Lambda} + (S_{vf}\alpha_{s\Lambda})R_{dif,\Lambda}\right]\Big\}, \tag{4.15}$$

where C_{crown} $[-]$ are the fractions of the n_c *Crown Areas*, C_s $[-]$ are the fractions of the n possible surfaces different from vegetation, s, and $\alpha_{s\Lambda}^{\mu}$ and $\alpha_{s\Lambda}$ are the albedos for beam and diffuse radiation of a generic s surface. The element-scale quantities may be useful for model verification/calibration, e.g., the $NDVI$ values estimated using (4.12) can be used to relate the model output to observations from remote sensing platforms (*Myneni et al.*, 2002).

Non-vegetated surface

The total shortwave radiation flux absorbed by a general non vegetated surface, s, such as bare soil, water, or snow in an open field is:

$$R_{abs,s} = \sum_{\Lambda}\left[R_{dir,\Lambda}(1 - S_{vf}\alpha_{s\Lambda}^{\mu}) + R_{dif,\Lambda}(1 - S_{vf}\alpha_{s\Lambda})\right], \tag{4.16}$$

where $\alpha_{s\Lambda}^{\mu}$ and $\alpha_{s\Lambda}$ are the albedos for beam and diffuse radiation of a generic surface s.

4.2.2 Surface albedos

Four types of land covers can be considered within a computational element: vegetated, bare soil, snow, and water, covered areas (see Section: 4.1.2). The vegetation albedos are parameterized recurring to a canopy radiative transfer scheme, where biophysical properties of a vegetation type are considered (e.g., leaf and stem reflectances and transmittances, leaf orientation, canopy total biomass, etc.). Ground albedo that is needed for isolated patches of bare soil or for bare soil under the canopy

is parameterized based on the soil surface moisture content. The snow albedo is a function of the snow age and of the thermodynamic condition of the snow, e.g., freezing or melting conditions. The water albedo is parameterized based on solar altitude.

Canopy radiative transfer scheme

The introduction of a canopy radiative transfer scheme is necessary in order to define the albedos of a vegetated surface. The canopy radiative transfer scheme provides, indeed, the variables $I\uparrow_{\Lambda}^{\mu}$, $I\uparrow_{\Lambda}I\downarrow_{\Lambda}^{\mu}$, $I\downarrow_{\Lambda}$, and K_{opt} required in the shortwave energy balance of vegetated surfaces (Section 4.2.1). The first assumption about radiation transfer in a canopy were made by *Monsi and Saeki* in 1953 (*Monsi and Saeki*, 2005) where the Beer's law was used for radiation transmission. Successively more complete models have been proposed recognizing the importance of subdividing total radiation in direct beam and diffuse components and in two wavebands: ultraviolet/visible (*UV/VIS*) and near-infrared *NIR* (*Goudriaan*, 1977; *Spitters et al.*, 1986).

In "Tethys" the radiative transfer for vegetation canopies is calculated using the two-stream approximation (*Dickinson*, 1983; *Sellers*, 1985; *Dai et al.*, 2004). The two-stream approximation has been applied in several land surface schemes, ecological and hydrological models (*Sellers et al.*, 1986, 1996b; *Bonan*, 1996; *Dai et al.*, 2004; *Oleson et al.*, 2004; *Ivanov et al.*, 2008a). The two-stream approximation has been shown to perform better than the Goudriaan's radiation model and the Beer's law even when two different extinction coefficients for diffuse and direct radiation are used (*Wang*, 2003). The derivation of the governing equations for the two-stream model is based on the assumption that the incident sky diffuse radiation and the scattered radiation in the canopy are all isotropic in inclination, that the vertical structure of the canopy is uniform and that the optical properties of the adaxial and abaxial leaf surfaces are the same (*Dai and Sun*, 2006). Therefore, there are cases in which the two-stream model is not applicable, especially when the vertical structure of the canopy is not uniform (*Dai and Sun*, 2006). For such a reason canopy transfer models including multi-layer schemes have been proposed as testified from numerous recent references (*Hanan*, 2001; *Zhao and Qualls*, 2005; *Dai and Sun*, 2006; *Tian et al.*, 2007; *Dickinson*, 2008). The drawback of multi-layers methods is related to computational requirements (*Sellers et al.*, 1992a). The two-stream approximation is, thus, considered a compromise between physical process representation and computational feasibility. Moreover, a comparison between a two-stream approximation model and a more complex multi-layer model has shown differences of absorbed fluxes negligible for hydrological applications (*Dai and Sun*, 2007).

The two-stream approximation equations are:

$$-\bar{\mu}\frac{dI\uparrow}{d(LAI+SAI)} + [1-(1-\beta)\omega]I\uparrow - \omega\beta I\downarrow = \omega\bar{\mu}K_{opt}\beta_0 e^{-K_{opt}(LAI+SAI)}\,, \quad (4.17)$$

$$\bar{\mu}\frac{dI\downarrow}{d(LAI+SAI)} + [1-(1-\beta)\omega]I\downarrow - \omega\beta I\uparrow = \omega\bar{\mu}K_{opt}(1-\beta_0)e^{-K_{opt}(LAI+SAI)}\,, \quad (4.18)$$

where $I\uparrow$ and $I\downarrow$ $[-]$ are the upward and downward diffuse radiative fluxes per unit incident flux, $K_{opt} = G(\mu)/\mu$ $[-]$ is the optical depth of direct beam per unit leaf and stem area, μ is the cosine of the zenith angle of the incident beam or equivalent the sine of the solar altitude $\mu = \sin(h_S)$ (where h_S $[rad]$ is the solar altitude, see Appendix A.4), $G(\mu)$ $[-]$ is the relative projected area of phytoelements in direction μ, $\bar{\mu}$ $[-]$ is the average inverse diffuse optical depth per unit leaf and stem area, ω $[-]$ is the scattering coefficient of phytoelements, β and β_0 $[-]$ are the upscatter parameters for diffuse and direct beam radiation, respectively. The optical parameters $G(\mu)$, $\bar{\mu}$, ω, β, and β_0 are calculated based on work of *Sellers* (1985) [see also *Oleson et al.* (2004)].

Once vegetation optical properties, the direct beam albedo, $\alpha^{\mu}_{s\Lambda}$, and diffuse albedo, $\alpha_{s\Lambda}$, of the surface, s, underneath the vegetation are known, the equations (4.17)-(4.18) can be solved. This allows to calculate the fluxes, considering a unit of incident radiation, absorbed by the vegetation, reflected by the vegetation, and transmitted through the vegetation for direct and diffuse radiation and for ultraviolet/visible $[0.29 \div 0.70\ \mu m]$ and near-infrared $[0.70 \div 4.0\ \mu m]$ wavebands. The surface s underneath the *high-vegetation* (H_v) layer in case of a vertical composite vegetation is another vegetated surface. In this case, the albedos are obtained using the two-stream approximation in the *low-vegetation* layer (L_v).

The relative projected area of leaves and stems in the direction μ, $G(\mu)$ was provided by fitting a nonlinear expression from *Goudriaan* (1977) once the value of χ_L is given:

$$G(\mu) = \phi_1 + \phi_2\mu\,, \quad (4.19)$$

where $\phi_1 = 0.5 - 0.633\chi_L - 0.33\chi_L^2$ and $\phi_2 = 0.877(1-2\phi_1)$ for $-0.4 < \chi_L < 0.6$. χ_L is an empirical parameter related to the leaf angle distribution (*Ross*, 1975). χ_L represents the departure of leaf angles from a spherical angle distribution and equals $+1$ for horizontal leaves, 0 for a spherical leaf angle distribution, and -1 for vertical leaves. The leaf angle distribution is a key parameter to characterize canopy structure and plays an important role in controlling energy and mass transfer in the soil-vegetation-atmosphere continuum (*Wang et al.*, 2007a). Insights and a recent review of leaf angle parameterizations can be found in *Wang et al.* (2007a), where the authors show that the *Ross-Goudriaan* approach as applied in "Tethys" is valid and comparable with other methods. The average inverse diffuse optical depth per

unit leaf and stem area $\bar{\mu}$ is:

$$\bar{\mu} = \int_0^1 \frac{\mu}{G(\mu)} d\mu = \frac{1}{\phi_2}\left[1 - \frac{\phi_1}{\phi_2}\ln\left(\frac{\phi_1+\phi_2}{\phi_1}\right)\right], \tag{4.20}$$

This integral is based on the assumptions: $\phi_1 \neq 0$ and $\phi_2 \neq 0$. There might be situations when ϕ_1 or ϕ_2 could be zero, consequently the integral (4.20) is no longer valid and *Dai et al.* (2004) provide supplementary solutions as follows:

$$\bar{\mu} = 1/0.877 \text{ if } \phi_1 = 0 \tag{4.21}$$

$$\bar{\mu} = 1/[2\phi_1] \text{ if } \phi_2 = 0 \tag{4.22}$$

The optical parameters of vegetation, ω, β, and β_0 vary with wavelength (Λ) and are defined as:

$$\begin{aligned} \omega_\Lambda &= \omega_\Lambda^{veg}, \\ \omega_\Lambda\beta_\Lambda &= \omega_\Lambda^{veg}\beta_\Lambda^{veg}, \\ \omega_\Lambda\beta_{0,\Lambda} &= \omega_\Lambda^{veg}\beta_{0,\Lambda}^{veg}. \end{aligned} \tag{4.23}$$

For vegetation, $\omega_\Lambda^{veg} = \alpha_\Lambda + \tau_\Lambda$. α_Λ [$-$] is a weighted combination of the leaf and stem reflectances ($\alpha_\Lambda^{leaf}, \alpha_\Lambda^{stem}$):

$$\alpha_\Lambda = \alpha_\Lambda^{leaf} w_{leaf} + \alpha_\Lambda^{stem} w_{stem}, \tag{4.24}$$

where $w_{leaf} = LAI/(LAI + SAI)$ and $w_{stem} = SAI/(LAI + SAI)$. τ_Λ [$-$] is a weighted combination of the leaf and stem transmittances ($\tau_\Lambda^{leaf}, \tau_\Lambda^{stem}$):

$$\tau_\Lambda = \tau_\Lambda^{leaf} w_{leaf} + \tau_\Lambda^{stem} w_{stem}. \tag{4.25}$$

The upscatter for diffuse radiation is:

$$\omega_\Lambda^{veg}\beta_\Lambda^{veg} = \frac{1}{2}\left[\alpha_\Lambda + \tau_\Lambda + (\alpha_\Lambda - \tau_\Lambda)\left(\frac{1+\chi_L}{2}\right)^2\right] \tag{4.26}$$

and the upscatter for direct beam radiation is:

$$\omega_\Lambda^{veg}\beta_{0,\Lambda}^{veg} = \frac{1+\bar{\mu}K_{opt}}{\bar{\mu}K_{opt}} a_s(\mu)_\Lambda, \tag{4.27}$$

where the single scattering albedo is:

$$\begin{aligned} \alpha_s(\mu)_\Lambda &= \frac{\omega_\Lambda^{veg}}{2}\int_0^1 \frac{\mu G(\mu)}{\mu G(\mu) + \mu G(\mu)} d\mu \\ &= \frac{\omega_\Lambda^{veg}}{2}\frac{G(\mu)}{\mu\phi_2 + G(\mu)}\left[1 - \frac{\mu\phi_1}{\mu\phi_2 + G(\mu)}\ln\left(\frac{\mu\phi_1 + \mu\phi_2 + G(\mu)}{\mu\phi_1}\right)\right]. \end{aligned} \tag{4.28}$$

The upward diffuse fluxes per unit incident direct beam and diffuse flux, i.e., the

vegetated surface albedos are:

$$I\uparrow_{\Lambda}^{\mu} = \frac{h_1}{\sigma} + h_2 + h_3\,, \tag{4.29}$$

$$I\uparrow_{\Lambda} = h_7 + h_8\,. \tag{4.30}$$

The downward diffuse fluxes per unit incident direct beam and diffuse radiation, respectively, are:

$$I\downarrow_{\Lambda}^{\mu} = \frac{h_4}{\sigma}e^{-K_{opt}(LAI+SAI)} + h_5 s_1 + \frac{h_6}{s_1}\,, \tag{4.31}$$

$$I\downarrow_{\Lambda} = h_9 s_1 + \frac{h_{10}}{s_1}\,. \tag{4.32}$$

The estimation of parameters h_1 to h_{10}, σ, and s_1, strictly for $\sigma \neq 0$, follows *Sellers* (1985) and *Oleson et al.* (2004) and it is provided in the Appendix C.1. *Dai et al.* (2004) give also the parametrization for $\sigma = 0$ together with new expressions for $I\uparrow_{\Lambda}$ and $I\downarrow_{\Lambda}$.

With the presence of snow in the canopy, as intercepted snow, the optical parameters ω, β, and β_0 are determined as a weighted combination between the vegetation and intercepted snow parameters:

$$\begin{aligned}
\omega_{\Lambda} &= \omega_{\Lambda}^{veg}(1-d_{w,sno}) + \omega_{\Lambda}^{sno}(d_{w,sno})\,,\\
\omega_{\Lambda}\beta_{\Lambda} &= \omega_{\Lambda}^{veg}\beta_{\Lambda}^{veg}(1-d_{w,sno}) + \omega_{\Lambda}^{sno}\beta_{\Lambda}^{sno}(d_{w,sno})\,,\\
\omega_{\Lambda}\beta_{0,\Lambda} &= \omega_{\Lambda}^{veg}\beta_{0,\Lambda}^{veg}(1-d_{w,sno}) + \omega_{\Lambda}^{sno}\beta_{0,\Lambda}^{sno}(d_{w,sno})\,,
\end{aligned} \tag{4.33}$$

where $d_{w,sno}$ is the fraction of canopy covered by snow (see Section: 4.3.1). The value of ω_{Λ}^{sno}, β_{Λ}^{sno}, and $\beta_{0,\Lambda}^{sno}$ for intercepted snow are taken from the appendix B of *Sellers et al.* (1986).

The optical properties introduced, i.e., leaf and stem reflectances, $(\alpha_{\Lambda}^{leaf}, \alpha_{\Lambda}^{stem})$; leaf and stem transmittances, $(\tau_{\Lambda}^{leaf}, \tau_{\Lambda}^{stem})$, and the leaf angle distribution, χ_L, for different plant functional types and for VIS and NIR wavelengths were first provided by *Dorman and Sellers* (1989) and can be also found in *Oleson et al.* (2004) (page 28).

Ground albedo

The direct beam, $\alpha_{soil,\Lambda}^{\mu}$ [−], and diffuse, $\alpha_{soil,\Lambda}$ [−], ground albedos depend on soil color class and moisture content at the soil surface (*Dickinson et al.*, 1993):

$$\alpha_{soil,\Lambda}^{\mu} = \alpha_{soil,\Lambda} = (\alpha_{sat\ \Lambda} + \Delta) \leq \alpha_{dry\ \Lambda}\,, \tag{4.34}$$

where Δ [−] depends on the volumetric water content, θ_1 [−], of the upper layer of the soil column (see Section 4.7.3) through the equation: $\Delta = (0.11 - 0.40\,\theta_1) > 0$. The terms $\alpha_{sat\,\Lambda}$ and $\alpha_{dry\,\Lambda}$ [−] are the albedos for saturated and dry soil that depend in turn on color classes (assigned as in *Dickinson et al.* (1993), see also *Oleson et al.* (2004), page 30).

Since often the soil color class is unknown or its estimation is difficult, typical values: $\alpha_{sat,vis} = 0.11$, $\alpha_{dry,vis} = 0.22$, $\alpha_{sat,nir} = 0.225$ and, $\alpha_{dry,nir} = 0.45$ can be used. In the proposed approach the ground albedos are assumed to be independent of the type of incident radiation (direct beam or diffuse), while they can be different for different wavebands.

Snow albedo

A good parametrization of snow albedo is fundamental to simulate properly snowpack dynamics (Section: 4.5.2). The partition between reflected and absorbed shortwave energy of a surface covered by snow can vary of more than 50% regarding the condition of the snow. Snow albedo has been shown to depend on many factors, such as precipitation history, snow depth, radiation type, sun angle, wavelength, grain size and type, liquid water content of the snowpack, meteorological conditions, and air pollution effects (*Wiscombe and Warren*, 1980; *Aoki et al.*, 2003; *Mölders et al.*, 2008). For instance, only the presence of clouds can alter snow albedo by changing the proportion between direct beam and diffuse radiation. Another example is the influence of precipitation history, e.g., each snow event refreshes snow albedo in a different way, and consequently the penetration depth of incoming radiation can vary to some extent (*Wiscombe and Warren*, 1980). Given this multiple dependencies, modeling snow albedo is far from be a trivial task. *Pederson and Winther* (2005) comparing seven GCM snow albedo schemes realized that all the scheme proposed showed shortcomings.

In "Tethys" a simple scheme of snow albedo parametrization is preferred in comparison to complex ones (*Wiscombe and Warren*, 1980; *Melloh et al.*, 2002; *Gardner and Sharp*, 2010). The snow albedo parametrization follows the approach first proposed in the *ISBA* model by *Douville et al.* (1995). It includes snow age dependencies and it distinguishes between melting and freezing periods. Typically refrozen snow albedo is lower than fresh snow albedo due to metamorphism effects inside the snowpack, liquid water content, and impurity. Snow albedo of melting periods is parameterized with a decreasing exponential function in order to account for wet metamorphism. During cold days, a weak linear decrease function is imposed, according to the observational study of *Baker et al.* (1990). The snow albedos are assumed to be the same, independently of the type of incident radiation (direct beam or diffuse) and wavebands $\alpha^{\mu}_{sno,\Lambda} = \alpha_{sno,\Lambda} = \alpha_{sno}$:

$$\begin{aligned} \alpha_{sno}(t+dt) &= \alpha_{sno}(t) - \tau_a \frac{dt}{\tau_1}, && \text{if } T_s < 0, \\ \alpha_{sno}(t+dt) &= [\alpha_{sno}(t) - \alpha^m_{sno}] \exp\left(-\tau_f \frac{dt}{\tau_1}\right) + \alpha^m_{sno}, , && \text{if } T_s = 0, \end{aligned} \quad (4.35)$$

where $\tau_a = 0.008$ $[-]$, $\tau_f = 0.24$ $[-]$, and $\tau_1 = 86400$ $[s]$ are parameters proposed by *Douville et al.* (1995). $\alpha^m_{sno} = 0.5$ $[-]$ is the minimum allowed albedo of the snow and T_s $[^\circ C]$ is the snowpack temperature. When a new snowfall occurs the albedo of the snow, α_{sno}, is reset to a maximum value $\alpha^M_{sno} = 0.85$ $[-]$. Equation (4.35) gradually

decreases the albedo from the maximum of 0.85 to a minimum of 0.5 as the snow ages. In the original *ISBA* parametrization a snowfall was considered to refresh the albedo when a threshold value of $P_{r,sno} = 10$ $[mm\ h^{-1}]$ of snow water equivalent S_{WE} $[mm]$ was exceeded. It has been shown that the snow albedo modeling is very sensitive to this parameter, and that the original parametrization underestimates the snow albedo in periods with minor snow events (*Pederson and Winther*, 2005; *Mölders et al.*, 2008). For such a reason after testing the model in a mountain location in Idaho (USA)(see Section 6.4) snowfall intensity of $P_{r,sno} = 2.3$ $[mm\ h^{-1}]$ has been considered sufficient to refresh the snow albedo.

A more complete snow albedo parametrization is used in the *BATS* model (*Dickinson et al.*, 1993). Such a parametrization is derived from the work of *Wiscombe and Warren* (1980), where solar altitude, grain size and different types of incident radiation and wavebands are considered. The *BATS* parametrization that includes a larger number of dependencies has been also tested and compared with the scheme described above. The comparison carried out at the Reynolds Creek experimental watershed (Idaho) shows that the *BATS* parametrization does not provide better results than the one implemented in "Tethys".

Note, that when there is a snow mantle under a canopy, shadow effects induced by the surmounting vegetation and the modified surface reflectances due to snow albedos are properly accounted for in the model as shown in Figure 4.11. Therefore, the scheme used to calculate the shortwave radiation fluxes absorbed by the canopy and the underneath snowpack is consistent with the scope to model vegetation, energy and water interactions in cold environments. Nonetheless, the capability of the model is weakened by the use of a single surface temperature that does not permit to distinguish between different surfaces (Section 4.2.5). This implies that energy fluxes of the portion of uncovered vegetation are neglected when snow is present in a basic computational element (see Section 4.2.5 for further details).

Water albedo

Lake and wetland albedos are parameterized as in *Bonan* (1996). The beam direct albedos are considered function of the cosine of the solar zenith angle, μ, or equivalent of the sine of the solar altitude, h_S $[rad]$, $\mu = \sin(h_S)$:

$$\alpha^{\mu}_{wat,vis} = \alpha^{\mu}_{wat,nir} = 0.06(\mu^{1.7} + 0.15)^{-1}. \tag{4.36}$$

The diffuse albedos are instead constant $\alpha_{wat,\Lambda} = 0.06$. Consequently, the water surface albedos are assumed to be independent of the wavelengths, while they are influenced by the incident radiation (direct beam or diffuse).

4.2.3 Long-wave fluxes

The net absorbed long-wave radiation, L_{abs} $[W\ m^{-2}]$, is given by the difference between the incoming long-wave radiation, $L\downarrow$ $[W\ m^{-2}]$, and the outgoing long-wave radiation, $L\uparrow$ $[W\ m^{-2}]$. The outgoing long-radiation depends on the radiative

temperature of the surface, T_{rad} $[K]$, through the Stefan-Boltzmann law. At the Earth surface the incoming longwave radiation is the downward atmospheric radiation L_{atm}:

$$L_{abs} = S_{vf} L_{atm} - L\uparrow, \tag{4.37}$$

where L_{atm} $[W\ m^{-2}]$ is (*Bras*, 1990):

$$L_{atm} = \epsilon_{cs} K_N(N)\, \sigma T_a^4, \tag{4.38}$$

where T_a $[K]$ is the air temperature at the reference height z_{atm} (Section 4.4), $\sigma = 5.6704\ 10^{-8}$ $[W\ m^{-2}\ K^{-4}]$ is the Stefan-Boltzmann constant, S_{vf} $[-]$ is the sky view factor, $K_N(N) = 1 + 0.17N^2$ is the correction for the cloudiness N $[-]$ (*TVA*, 1972), and $\epsilon_{cs} = 0.70 + 5.95\ 10^{-5} e_a[\exp(1500/T_a)]$ is the clear sky emissivity, with e_a $[hPa]$ atmospheric vapor pressure, and T_a in $[K]$ (*Idso*, 1981). Different parameterizations are available in literature for humidity and clouds effects in incoming long-wave radiation (*Bras*, 1990; *Sugita and Brutsaert*, 1993; *Prata*, 1996; *Pirazzini et al.*, 2001; *Iziomon et al.*, 2003), nonetheless tests carried out on available data of measured downward radiation have led to use the above equations.

Vegetated surface

The long-wave radiation fluxes in the general case of two vegetation layers are:

$$L\uparrow_{H_v} = (1-\alpha_{H_v}) L\uparrow_{L_v} + \epsilon_{H_v}\sigma T_s^4, \tag{4.39}$$
$$L\downarrow_{H_v} = (1-\alpha_{H_v}) S_{vf} L_{atm} + \epsilon_{H_v}\sigma T_s^4, \tag{4.40}$$
$$L\uparrow_{L_v} = (1-\alpha_{L_v}) L\uparrow_{s} + \epsilon_{L_v}\sigma T_s^4, \tag{4.41}$$
$$L\downarrow_{L_v} = (1-\alpha_{L_v}) L\downarrow_{H_v} + \epsilon_{L_v}\sigma T_s^4, \tag{4.42}$$
$$L\uparrow_{s} = (1-\alpha_{s}) L\downarrow_{L_v} + \epsilon_{s}\sigma T_s^4, \tag{4.43}$$

where $L\downarrow_{H_v}$ and $L\downarrow_{L_v}$ are downward longwave radiation from high and low vegetation layers respectively. The fluxes $L\uparrow_{H_v}$, $L\uparrow_{L_v}$, $L\uparrow_s$ are the upward longwave radiation from high, low vegetation layers, and the surface s underneath the canopies. T_s $[K]$ is the prognostic surface temperature that is an unique value (see Section: 4.2.5). The parameters ϵ_{H_v}, and ϵ_{L_v} are the vegetation emissivities, and α_{H_v}, α_{L_v} are the vegetation absorptivities. Finally, ϵ_s is the emissivity of the surface underneath vegetation and α_s is the correspondent absorptivity.

According to the equations described above and to the scheme of Figure 4.12 the absorbed long-wave radiation in the two vegetation layers L_{abs,H_v}, L_{abs,L_v} $[W\ m^{-2}]$ and in the underneath surface $L_{abs,s}$ $[W\ m^{-2}]$ are:

$$L_{abs,H_v} = S_{vf} L_{atm} - L\downarrow_{H_v} - S_{vf} L\uparrow_{H_v} + L\uparrow_{L_v}, \tag{4.44}$$
$$L_{abs,L_v} = L\downarrow_{H_v} - L\downarrow_{L_v} - L\uparrow_{L_v} + L\uparrow_{s}, \tag{4.45}$$
$$L_{abs,s} = L\downarrow_{L_v} - L\uparrow_{s}\ . \tag{4.46}$$

In the case of a single vegetation layer the system of equations (4.39)-(4.43) reduces to a three equation system, as described in *Bonan* (1996) and *Ivanov et al.* (2008a).

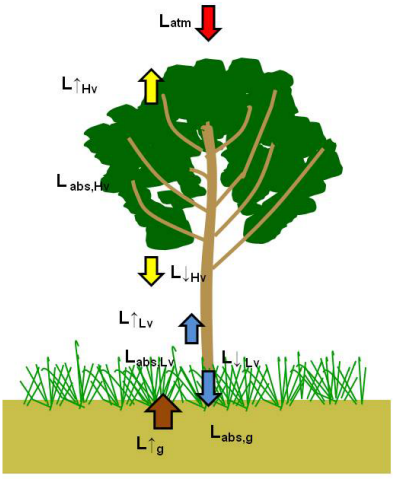

Figure 4.12: A schematic cartoon of long-wave radiation fluxes absorbed, transmitted, reflected, and emitted by vegetation and under-canopy surface. In the illustrated scheme the surface underneath the vegetation is bare ground ($s = g$). L_{atm} is the downward atmospheric longwave radiation flux, $L_v \downarrow_{(H_v)-(L_v)}$ are the downward longwave radiation fluxes from the vegetation canopies, $L \uparrow_g$ is the upward longwave radiation flux from the ground, and $L_v \uparrow_{(H_v)-(L_v)}$ are the upward longwave radiation fluxes from the canopies. L_{abs,H_v}, L_{abs,L_v}, $L_{abs,g}$ are the absorbed longwave radiation fluxes for high and low vegetation layers, and understory ground respectively.

In the above equations, it is assumed that leaves emit long-wave radiation from both sides. The scheme also assumes that a fraction $(1 - \alpha_{(H_v)-(L_v)})$ of long-wave radiation is transmitted through the canopy and the fraction $(1 - \alpha_s)$ of downward longwave radiation below the canopy is reflected by the underneath surface. The vegetation emissivity are assumed $\epsilon_v = 1 - e^{-(LAI+SAI)/\vec{\mu}}$, where LAI and SAI are the one-sided leaf and stem area indices and $\vec{\mu} = 1$ is the average inverse optical depth for longwave radiation (*Bonan*, 1996). The absorptivities, α_v, are taken equal to the emissivities, ϵ_v, and all these quantities depend on the vegetation layer H_v or L_v.

The presence of a snowpack with a certain depth modifies the long-wave radiation exchange. The changes due to the presence of snow are accounted for comparing the depth of the snow and the height of the plants in the low-vegetation layer. The scheme is similar to the one used to compute the effects of the snowpack in the shortwave radiation fluxes (Figure 4.11).

Non-vegetated surface

For a generic non-vegetated surface, s, the absorbed net long-wave radiation takes the form:

$$L_{abs,s} = \alpha_s \, S_{vf} L_{atm} - L\uparrow_s \,, \tag{4.47}$$

$$L\uparrow_s = S_{vf} \, \epsilon_s \sigma T_s^4 \,, \tag{4.48}$$

where α_s $[-]$ and ϵ_s $[-]$ are the absorptivity and the emissivity of the surface s,and T_s $[K]$ is the surface temperature (Section 4.2.5). Equation (4.47) assumes that the fraction $(1 - \alpha_s)$ of the atmospheric long-wave flux is reflected. Typical values of emissivity used in the model are: $\epsilon_{sno} = 0.97$ for snow, $\epsilon_{soil} = 0.96$ for bare soil, $\epsilon_{wat} = 0.96$ for water surfaces. The absorptivities, α_s, are taken equal to the emissivities ϵ_s.

4.2.4 Net radiation

The total net radiation, R_n $[W \ m^{-2}]$, absorbed at element scale is the weighted sum of the net radiation absorbed by the single land cover fractions, i.e. vegetated areas, bare soil areas, water and snow covered surfaces.

$$R_n = R_{n,H_v} + R_{n,L_v} + R_{n,soil} + R_{n,sno} + R_{n,wat} \,, \tag{4.49}$$

where R_{n,H_v}, R_{n,L_v}, $R_{n,soil}$ $[W \ m^{-2}]$ are the total net radiations absorbed by *high vegetation*, *low vegetation* layers, and by the ground in the entire basic computational element. The absorbed net radiation by snow and water surfaces at element scale are $R_{n,snow}$ and $R_{n,wat}$ $[W \ m^{-2}]$ respectively. The calculation of the different net radiation quantities is illustrated in the following:

$$R_{n,H_v} = [1 - C_{sno}] \sum_{i=1}^{n_c} \Big(C_{crown,i} [R_{abs,H_v,i} + L_{abs,H_v,i}] \Big) \,, \tag{4.50}$$

$$R_{n,L_v} = [1 - C_{sno}] \sum_{i=1}^{n_c} \Big(C_{crown,i} [R_{abs,L_v,i} + L_{abs,L_v,i}] \Big) \,, \tag{4.51}$$

$$\begin{aligned} R_{n,soil} = {} & C_{bare} [R_{abs,bare} + L_{abs,bare}] [1 - C_{sno}] \\ & + \sum_{i=1}^{n_c} \Big(C_{crown,i} [R_{abs,s,i} + L_{abs,s,i}] \Big) \,, \end{aligned} \tag{4.52}$$

$$R_{n,sno} = C_{sno} \Big[R_{abs,sno} + L_{abs,sno} \Big] \Big[1 - \sum_{i=1}^{n_c} C_{crown,i} - C_{wat} \Big] \,, \tag{4.53}$$

$$R_{n,wat} = C_{wat} [R_{abs,wat} + L_{abs,wat}] \,, \tag{4.54}$$

where the $C_{crown} \,, i = 1, ..., n_c$ $[-]$ represent the fractions occupied by vegetation patches, C_{bare} $[-]$ is the fraction occupied by bare soil, C_{wat} $[-]$ is the fraction occupied by water surfaces, and C_{sno} $[-]$ is a coefficient that assumes the value 1 in presence of snow and 0 otherwise (see Section 4.1.2). When snow is present, i.e. $C_{sno} = 1$, the net radiation absorbed by the vegetation layers is neglected, together

with the sensible heat emitted by the same layers. In other words, it is assumed that the net radiation absorbed by the snow-free vegetation is exactly counterbalanced by the sensible heat flux (see Section: 4.3.1). This simplification is related to the unique prognostic surface temperature used to solve the energy budget (Section 4.2.5). The subscript, s, may refer to the ground underneath the canopy, i.e. $s = g$ in equation (4.9) and (4.46), and consequently $R_{abs,g}$ and $L_{abs,g}$ are the shortwave and longwave fluxes absorbed by the ground. Otherwise, s may refer to the snowpack underneath the vegetation layers ($s = sno$ in equation (4.9) and (4.46)). Note that in this second case the net radiation absorbed by the snowpack below vegetated areas is computed. This quantity takes into account the radiation transfer through the vegetation structure and thus the vegetation shadow effect.

4.2.5 Single-temperature simplification

One of the most important approximation in "Tethys" is to assume a unique value of surface temperature T_s. This value represents an homogeneous surface radiative temperature and it is assigned to all the possible land covers within the basic computational element in absence of snow (Section 4.1.2).

When snow cover is present at the ground, T_s represents the snowpack temperature, thus the energy budget of snow-free vegetation surfaces is not explicitly resolved. This assumption implies that snow-free vegetation emits an amount of heat energy flux equivalent to the absorbed net radiation. The latent heat flux from vegetated surface with snow is considered negligible. Consequently, there is no need to track vegetation temperature in this case.

The single prognostic temperature simplification is related to the large computational efforts required to solve the energy budget for a multi-temperature scheme. Generally, the energy balance closure imposes the numerical solution of a system of highly non-linear equations which unknowns are the different prognostic T_j temperatures with $j = 1, ..., n_T$, where n_T is the number of prognostic temperatures accounted for in the model. The T_j may be dependent or independent according with the implementation of the resistance scheme. Even in the unrealistic case of independent T_j, a single non-linear energy balance equation must be solved n_T times. The use of an unique value of T_s, as proposed in Section 4.3.5, permits to reduce the system of equations to a single equation and thus to solve only once the energy balance. The reduction of the computational effort is remarkable.

In advanced models, multi-temperature schemes are typically implemented using two different temperatures, one for bare ground, T_g, and one for vegetation (leaf temperature), T_v, (*Braud et al.*, 1995; *Sellers et al.*, 1996b; *Anderson et al.*, 2000; *Oleson et al.*, 2004; *Ivanov et al.*, 2008a). Sometime a further differentiation between sunlit leaves, $T_{v,sun}$, and shadowed leaves, $T_{v,shd}$, temperatures is realized in land-surface schemes of biochemical models of photosynthesis (*Baldocchi and Harley*, 1995; *Wang and Leuning*, 1998; *Dai et al.*, 2004). Totally 3 prognostic temperatures must be used or even more in multi-layer vegetation schemes. When snow or other surface such as rocks or water are considered n_T can further increase making the energy

balance estimation particularly challenging and highly computational demanding. It should be noted that even the use of detailed models with three or more prognostic temperatures is still a coarse approximation of the real-world. Leaf temperature can also change of 3-4 [$^{\circ}C$] within the same leaf (*Stokes et al.*, 2006) and the temperature of bare ground below vegetation layers may be quite different with regards to the temperature of isolated patch of bare soil. Vegetation shadow effect may further induce important temperature differences within the canopy and in the surrounding. Given such a complex picture, the modeling exercise is subjected to large uncertainties that are only partially mitigated when two or three temperatures are adopted.

The use of a single T_s creates further limitations. For instance, all the components of absorbed net radiation are summarized in a single R_n (Section 4.3.5). Such simplification implies that for very dense canopies the net radiation absorbed by the leaves, may be counterbalanced by undercanopy ground evaporation or sensible heat, contrasting with the physical realization of the process. This shortcoming can be somehow mitigated by the control exerted by the undercanopy resistance r'_a (Section 4.4.2). Using a single T_s imposes also the use of a big-leaf model for photosynthesis, where T_v must be approximated with T_a (Section: 4.4.5). A more realistic "two big-leaves" model with a separation between $T_{v,sun}$ and $T_{v,shd}$ would probably produce better results (see also Section: 4.4.5).

Despite all the above limitations, in this first version of "Tethys" a single prognostic temperature T_s is considered adequate for the objective of the study. This assumption allows to speed up the computation of the energy balance. It further simplifies the computation of net radiation and photosynthesis, since there is no need to distinguish between sunlit and shadowed fractions of the canopy. The numerical solution of a multiple temperature scheme, with 7 different prognostic temperatures, and a "two big-leaves" canopy partition scheme have been already implemented within the code and can be turned on in successive versions.

4.3 Soil-vegetation-atmosphere mass and heat transfer scheme

In order to estimate sensible and latent heat fluxes between the ground surface and the atmospheric surface layer, the model uses the resistance analogy (*Garratt*, 1992; *Arya*, 2001; *Brutsaert*, 2005). Such a theoretical framework is commonly used in land surface schemes and hydrological models (*Sellers et al.*, 1986; *Choudhury and Monteith*, 1988; *Noilhan and Planton*, 1989; *Dickinson et al.*, 1993; *Ducoudré et al.*, 1993; *Viterbo and Beljaars*, 1995; *Braud et al.*, 1995; *Sellers et al.*, 1996b; *Noilhan and Mafhouf*, 1996; *Bonan*, 1996; *LoSeen et al.*, 1997; *Mengelkamp et al.*, 1999; *Cox et al.*, 1999; *Oleson et al.*, 2004; *Bertoldi et al.*, 2006b; *Ivanov et al.*, 2008a). For a remarkable summary of such an approach refer to *Sellers et al.* (1997). In this section the numerical scheme to estimate sensible, latent and, ground heat fluxes is presented postponing to the following Section 4.4 a detailed description of the

resistances and their computation. The description below provides the mathematical tools to estimate energy and water fluxes from both a generic non-vegetated surface, s, and several vegetated patches that can be contemporarily present within a given basic computational element.

4.3.1 Sensible heat

The conceptual diagram of sensible heat flux with resistances is described in Figure 4.13 for a snow free vegetated patch and in Figure 4.14 when snow is present and it covers the *low-vegetation*, (L_v), layer.

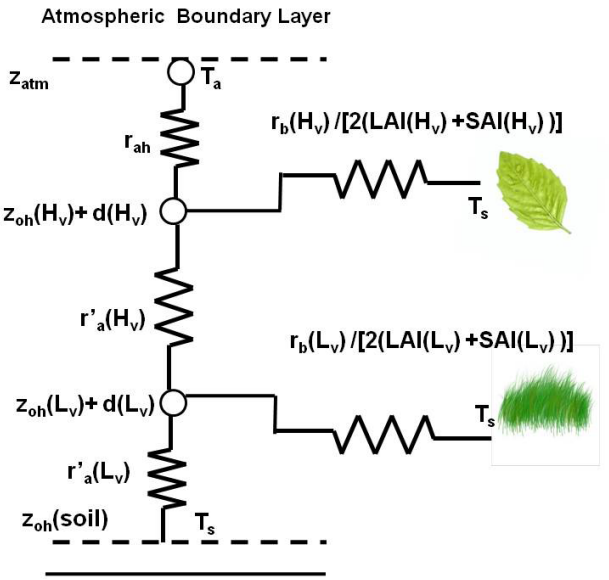

Figure 4.13: A conceptual diagram of sensible heat flux including resistances for a vegetated patch (*Crown Area*) without snow cover, for the definition of symbols refer to the text.

.

The sensible heat flux, H $[W\ m^{-2}]$, between the ground surface and the atmosphere surface layer at height z_{atm} is the weighted sum of the different land cover fractions. It is assumed that the heat stored by the vegetation is negligible. Thus the sensible heat flux at element scale is:

$$\begin{aligned} H \;=\; & \sum_{i=1}^{n_c}\left(C_{crown,i}[H_{H_v,i}+H_{L_v,i}+H_{g,i}]\right)+C_{bare}H_{bare}+C_{wat}H_{wat}+ \\ & \left[d_{w,sno}\sum_{i=1}^{n_c}\left(C_{crown,i}\left[LAI(H_{v,i})+SAI(H_{v,i})\right]\right)+\left(1-\sum_{i=1}^{n_c}C_{crown,i}-C_{wat}\right)\right]H_{sno,f}+ \\ & \sum_{i=1}^{n_c}\left(C_{crown,i}H_{sno,v,i}\right)\ , \end{aligned} \tag{4.55}$$

where H_{H_v}, H_{L_v}, and H_g $[W\ m^{-2}]$ are the sensible heat from *high-vegetation*, *low-vegetation* layers and from the ground underneath the vegetation. H_{bare}, H_{wat} $[W\ m^{-2}]$ are the sensible heat from bare soil and water surfaces respectively. $H_{sno,f}$

and $H_{sno,v}$ $[W\ m^{-2}]$ are the sensible heat from snow in an open space and under the vegetation respectively. Finally, the variable $d_{w,sno}$ $[-]$ is the fraction of *high-vegetation* covered by snow (Section: 4.3.1). The *low-vegetation* layer is assumed completely covered when there is snow, $C_{sno} = 1$, consequently the sensible heat flux from low-vegetation, H_{L_v}, is equal to zero and the flux $H_{sno,v}$ is computed.

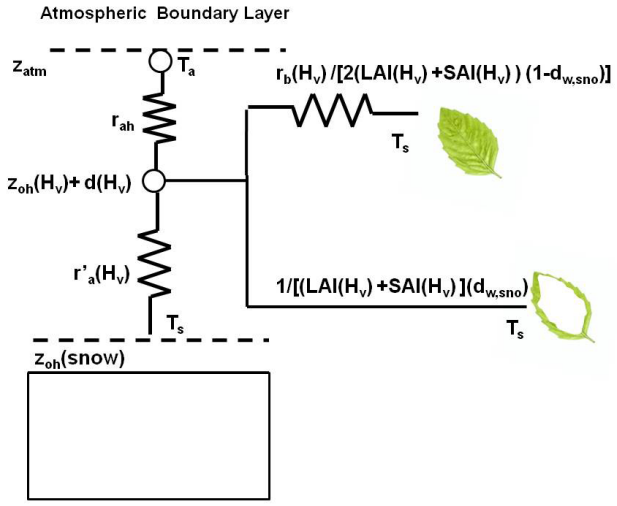

Figure 4.14: A conceptual diagram of sensible heat including resistances for a vegetated patch (*Crown Area*) in the presence of snow, for the definition of symbols refer to the text.

.

Vegetated surface

The sensible heat fluxes for different elements of a vegetated surface are estimated referring to the surface temperature T_s $[°C]$:

$$H_{H_v} = [1 - C_{sno}]\rho_a C_p \frac{(T_s - T_a)}{r_{ah} + \frac{r_b(H_v)}{2[LAI(H_v)+SAI(H_v)](1-d_{w,sno})}}, \quad (4.56)$$

$$H_{L_v} = [1 - C_{sno}]\rho_a C_p \frac{(T_s - T_a)}{r_{ah} + r_a{}'(H_v) + \frac{r_b(L_v)}{2[LAI(L_v)+SAI(L_v)]}}, \quad (4.57)$$

$$H_g = [1 - C_{sno}]\rho_a C_p \frac{(T_s - T_a)}{r_{ah} + r_a{}'(H_v) + r_a{}'(L_v)}, \quad (4.58)$$

$$H_{sno,v} = [C_{sno}]\rho_a C_p \frac{(T_s - T_a)}{r_{ah} + r_a{}'(H_v)}, \quad (4.59)$$

where T_s $[°C]$ is the homogeneous surface temperature, $C_p = 1005+[(T_a+23.15)^2]/3364$ $[J\,kg^{-1}\,K^{-1}]$ is the specific heat of air at a constant pressure, ρ_a $[kg\,m^{-3}]$ is the air density, r_{ah} $[s\ m^{-1}]$ is the aerodynamic resistance to heat flux, r_b and $r_a{}'$ $[s\ m^{-1}]$ are, respectively, the leaf boundary and undercanopy resistances function of the vegetation type $H_v - L_v$. Further details about resistances can be found in Section 4.4. Note that in equations (4.56)-(4.57) both side of the leaves are considered to emit sensible heat.

The term $d_{w,sno} = \min[1, In_{S_{WE}}/In^{M}_{S_{WE}}]$ $[-]$ is the fraction of high-vegetation covered by intercepted snow as parameterized by *Lee and Mahrt* (2004), where $In_{S_{WE}}$ $[mm]$ is the intercepted snow, and $In^{M}_{S_{WE}}$ $[mm]$ is the maximum intercepted snow (Section: 4.5.3). The logic operator C_{sno} $[-]$ is used to determine the presence or absence of snow.

When $C_{sno} = 1$ the sensible heat from uncovered vegetation is neglected. In such a case also the net radiation absorbed (Section: 4.2.4) is neglected for snow free vegetated areas. These two terms are assumed to be in balance and to provide a temperature of the canopy that may be different from the snowpack temperature and that remains unknown (Section: 4.2.5).

Non-vegetated surface

The sensible heat fluxes for other land cover types are estimated as:

$$H_{bare} = [1 - C_{sno}]\rho_a C_p \frac{(T_s - T_a)}{r_{ah}}, \tag{4.60}$$

$$H_{wat} = \rho_a C_p \frac{(T_s - T_a)}{r_{ah}}, \tag{4.61}$$

$$H_{sno,f} = [C_{sno}]\rho_a C_p \frac{(T_s - T_a)}{r_{ah}}. \tag{4.62}$$

4.3.2 Latent heat, evaporation and transpiration

The conceptual diagram of latent heat flux and related resistances is described in Figure 4.15 for a snow free vegetated patch.

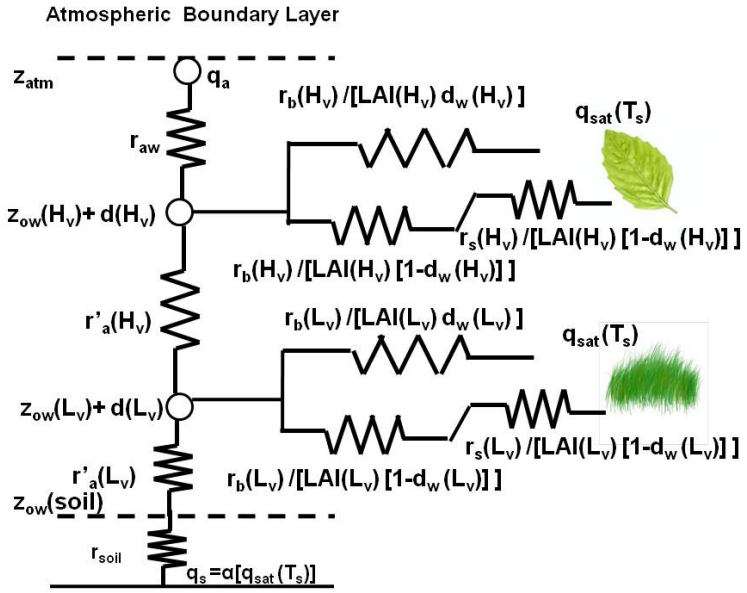

Figure 4.15: A conceptual diagram for latent heat including resistances in a vegetated patch (*Crown Area*) without snow cover, for the definition of symbols refer to the text.

.

The latent heat flux, λE $[W\ m^{-2}]$, between the ground surface and the atmosphere surface layer at height z_{atm} is the weighted sum of the different land cover fractions. It is assumed that the water vapor stored by the vegetation is negligible. Thus the latent heat flux at element scale is:

$$\begin{aligned}
\lambda E &= \lambda\Bigg[\sum_{i=1}^{n_c}\Big[C_{crown,i}\Big(T_{H_v,i}+T_{L_v,i}+E_{In,H_v,i}+E_{In,L_v,i}+E_{g,i}\Big)\Big]+ \\
&\quad C_{bare}E_{bare}+C_{wat}E_{wat}(T_s>0)\Bigg]+ \\
&\quad \lambda_s\Bigg[\Big(d_{w,sno}\sum_{i=1}^{n_c}\big(C_{crown,i}[LAI(H_{v,i})+SAI(H_{v,i})]\big)\Big)E_{sno,f}+ \\
&\quad \Big(1-\sum_{i=1}^{n_c}C_{crown,i}-C_{wat}\Big)E_{sno,f}+ \\
&\quad C_{wat}E_{wat}(T_s<0)+\sum_{i=1}^{n_c}\big(C_{crown,i}E_{sno,v,i}\big)\Bigg], \qquad (4.63)
\end{aligned}$$

where $\lambda = 1000[2501.3 - 2.361\ T_a]\ [J\ kg^{-1}]$ is the latent heat of vaporization, $\lambda_s = \lambda + \lambda_f$ is the latent heat of sublimation with $\lambda_f = 333700\ [J\ kg^{-1}]$ latent heat of melting. The terms T_{H_v}, T_{L_v}, and E_g $[kg\ m^{-2}\ s^{-1}]$ are the transpiration fluxes from *high-vegetation*, *low-vegetation* layers, and the evaporation flux from the ground underneath the vegetation. The terms E_{bare} and E_{wat} $[kg\ m^{-2}\ s^{-1}]$ are the evaporation fluxes from bare soil and water surfaces respectively. The terms $E_{sno,f}$ and $E_{sno,v}$, $[kg\ m^{-2}\ s^{-1}]$ are the total evaporation/sublimation fluxes from snow in an open space and under the vegetation respectively. Finally, the terms E_{In,H_v} and E_{In,L_v} $[kg\ m^{-2}\ s^{-1}]$ are the evaporation fluxes from intercepted water in the *high* and *low-vegetation* layers.

All the evaporation and transpiration terms are limited by the effective availability of water in the soil, in the snowpack and in the storages of interception.

Vegetated surface

The evaporations and transpiration fluxes from different elements of a vegetated surface are estimated once the specific humidity at saturation $q_{sat}(T_s)$ $[-]$ and the homogeneous surface temperature T_s $[^\circ C]$ are known:

$$T_{H_v} = [1-C_{sno}]\frac{\rho_a(q_{sat}(T_s)-q_a)}{r_{aw}+\frac{r_b(H_v)}{LAI(H_v)(1-d_{w,sno})(1-d_{w,H_v})}+\frac{r_s(H_v)}{LAI(H_v)(1-d_{w,sno})(1-d_{w,H_v})}}, \qquad (4.64)$$

$$T_{L_v} = [1-C_{sno}]\frac{\rho_a(q_{sat}(T_s)-q_a)}{r_{aw}+\frac{r_b(L_v)}{LAI(L_v)(1-d_{w,L_v})}+\frac{r_s(L_v)}{LAI(L_v)(1-d_{w,L_v})}}, \qquad (4.65)$$

$$E_g = [1 - C_{sno}] \frac{\rho_a(\hat{\alpha}\, q_{sat}(T_s) - q_a)}{r_{aw} + r_{soil} + r_a'(H_v) + r_a'(L_v)}\,, \tag{4.66}$$

$$E_{In,H_v} = [1 - C_{sno}] \frac{\rho_a(q_{sat}(T_s) - q_a)}{r_{aw} + \frac{r_b(H_v)}{LAI(H_v) d_{w,H_v}}}\,, \tag{4.67}$$

$$E_{In,L_v} = [1 - C_{sno}] \frac{\rho_a(q_{sat}(T_s) - q_a)}{r_{aw} + \frac{r_b(L_v)}{LAI(L_v) d_{w,L_v}} + r_a'(H_v)}\,, \tag{4.68}$$

$$E_{sno,v} = [C_{sno}] \frac{\rho_a(q_{sat}(T_s) - q_a)}{r_{aw} + r_a'(H_v)}\,, \tag{4.69}$$

where $q_a = 0.622 e_a/(P_{atm} - 0.378 e_a)$ $[-]$ is the specific humidity of the air at the reference height z_{atm} with e_a $[Pa]$ air vapor pressure, and P_{atm} $[Pa]$ atmospheric pressure. The terms $\hat{\alpha}$ $[-]$ and r_{soil} $[s\ m^{-1}]$ are the relative humidity in the soil pores and the soil resistance, which description is provided in Section 4.4.4.

The fraction of vegetation covered by intercepted water $d_w = \min(1, [In/In^M]^{2/3})$ $[-]$ is taken from *Deardorff* (1978), where In $[mm]$ is the intercepted water and In^M $[mm]$ is the maximum intercepted water (Section: 4.6.2). The variable d_w, In, and In^M are function of the vegetation type $H_v - L_v$.

When snow is present, $C_{sno} = 1$, it is assumed that the transpiration and evaporation fluxes from the uncovered vegetation are negligible. This assumption is generally true given the low temperatures and the low photosynthetic activity during cold months. The assumption might be violated at high-altitude climate where a snowpack at the ground may persist until late spring. In this case transpiration fluxes can became significant while snow is still present at the ground. Such a simplification is related to the single surface homogenous temperature, T_s, that does not allow an explicit solution of the energy budget for uncovered vegetation and snowpack (Section: 4.2.5).

Non-vegetated surface

The evaporation fluxes from non vegetated land cover types are estimated as:

$$E_{bare} = [1 - C_{sno}] \frac{\rho_a(\hat{\alpha}\, q_{sat}(T_s) - q_a)}{r_{aw} + r_{soil}}\,, \tag{4.70}$$

$$E_{wat} = \frac{\rho_a(q_{sat}(T_s) - q_a)}{r_{aw}}\,, \tag{4.71}$$

$$E_{sno,f} = [C_{sno}] \frac{\rho_a(q_{sat}(T_s) - q_a)}{r_{aw}}\,, \tag{4.72}$$

where all the symbols have been previously defined.

4.3.3 Ground heat

The flux of heat in the ground, G $[W\ m^{-2}]$, at any depth, z_d $[m]$, (definite positive upward) and time t $[s]$, once the coupling of water and heat transfer is neglected and a semi-infinite domain is considered, can be written as $G(z_d, t) = -\lambda_s \partial T_g/\partial z_d$. In these conditions the flux $G(z_d, t)$ can be generally calculated through the heat

diffusion equation (*Hu and Islam*, 1995; *Núnez et al.*, 2010):

$$cv_s \frac{\partial T_g}{\partial t} = \frac{\partial}{\partial z_d}\Big(-G(z_d,t)\Big)\,, \tag{4.73}$$

where $T_g(z_d,t)$ $[^\circ C]$ is the soil temperature at any time and profile depth, λ_s $[J\ K^{-1}\ m^{-1}\ s^{-1}]$ is the soil heat conductivity and cv_s $[J\ K^{-1}\ m^{-3}]$ is the soil volumetric heat capacity. For further details on heat transfer into soil refer to *Hillel* (1998). A local homogeneous terrain with λ_s and cv_s constant with depth and within the computational element is assumed (*Deardorff*, 1978; *Noilhan and Planton*, 1989; *Ivanov et al.*, 2008a). Equation 4.73 becomes:

$$\frac{\partial T_g}{\partial t} = k_s \frac{\partial^2 T_g}{\partial z_d^2}\,, \tag{4.74}$$

where $k_s = \lambda_s / cv_s$ $[m^2\ s^{-1}]$ is the soil heat diffusivity. A clarification is necessary for the definitions of soil temperature, since many definitions have been provided in literature, e.g. ground surface temperature, surface temperature, surface skin temperature (*Hu and Islam*, 1995). In the following ground temperature, T_g, refers to the average temperature of a certain soil layer and surface temperature, T_s, refers to the temperature at the interface between the ground and the atmosphere.

The partial differential equation (4.74) can be solved through finite-difference methods (*Cox et al.*, 1999; *Cichota et al.*, 2004; *Bertoldi et al.*, 2006b) once a time step and a space domain are defined. When the ground temperature profile, $T_g(z_d,t)$, is known, the heat flux $G(z_d,t) = -\lambda_s \partial T_g / \partial z_d$ at each depth and time is also known. The solution of the partial differential equation (4.74) generally requires a certain computational effort. For this reason approximate methods have been proposed to estimate $G(z_d,t)$ and especially the value of $G(0,t)$ at the interface between the land surface and the atmosphere (*Hu and Islam*, 1995; *Wang and Bras*, 1999). The "force-restore" method is used in "Tethys" among many possible simplified approaches (*Liebethal and Foken*, 2007; *Núnez et al.*, 2010). The "force-restore" method received a great popularity in hydrological and land surface schemes (*Dickinson*, 1988; *Noilhan and Planton*, 1989), because it essentially reduces the partial differential equation (4.73) into an ordinary differential equation for the variable ground temperature T_g of a soil slab with thickness δ. Note that when the thickness of the soil tend to zero $\lim_{\delta \to 0} T_g = T_s$, T_g coincides with the surface temperature T_s. In the force restore method the heat diffusion equation is solved in response to purely periodical forcing with diurnal frequency ω_1. Since different assumptions can be made with respect to the thickness of the soil slab δ, several force-restore methods exist (*Hu and Islam*, 1995). The generic force restore equation can be written as:

$$\frac{dT_s}{dt} = C_1 G - C_2 (T_s - T_d)\,, \tag{4.75}$$

where C_1 $[m^2\ K\ J^{-1}]$, and C_2 $[s^{-1}]$ are general coefficient of the force-restore method and T_d is the ground temperature at a certain dampening depth d. The coefficients

C_1 and C_2 depend on the upper soil thickness, δ, the soil volumetric heat capacity, cv_s, and the dampening depth of the diurnal temperature wave $d = (2k_s/\omega_1)^{1/2}$ $[m]$, where $\omega_1 = 2\pi/\tau$ $[s^{-1}]$ and $\tau = 86400$ $[s]$ are the fundamental frequency and period respectively.

Two versions of the force-restore method, i.e. *Deardorff* (1978) and *Lin* (1980) have been tested with data from a eddy-covariance station in a semiarid environment (Lucky-Hills, Arizona, see Section 6.2). The *Deardorff* (1978) force restore method assumes the limit case $\lim_{\delta\to 0} T_g = T_s$ and consequently $C_1 = 2/(cv_s d) = 2\sqrt{\pi/(\lambda_s cv_s \tau)}$ and $C_2 = \omega_1$. The *Lin* (1980) force restore assumes $T_s = 0.5(T_s + T_g)$, that gives $C_1 = (1/\alpha_1)[2/(cv_s d)]$ and $C_2 = (1/\alpha_1)\omega_1$, where $\alpha_1 = 1+\delta/d$. According with the better result obtained the method of *Deardorff* (1978) is implemented in "Tethys". Furthermore, this method does not depends on the upper soil thickness, that is equal to zero $\delta = 0$ and thus $T_g(\delta) = T_s$. The *Deardorff* (1978) method has been successfully applied in the *ISBA* land surface scheme (*Noilhan and Mafhouf*, 1996). The equations to compute the soil heat flux $G(0,t)$ at the interface becomes:

$$G(t) = \frac{1}{C_1}\Big[\frac{2\pi}{\tau}[T_s(t) - T_d(t)] + \frac{T_s(t) - T_s(t-1)}{dt}\Big]\,. \tag{4.76}$$

The temperature at the dampening depth, T_d, is updated with the equation: $dT_d/dt = (T_s - T_d)/\tau$ (*Noilhan and Planton*, 1989). Solving for $T_d(t)$ becomes:

$$T_d(t) = \frac{1}{1 + dt/\tau}\Big[T_d(t-1) + \frac{dt}{\tau}T_s(t)\Big]\,. \tag{4.77}$$

The volumetric heat capacity cv_s $[J\ K^{-1}\ m^{-3}]$ and the thermal conductivity λ_s $[J\ K^{-1}\ m^{-1}\ s^{-1}]$ depend on the soil type, on its water content, and eventually on the presence of an ice content (*Peters-Lidard et al.*, 1998; *Oleson et al.*, 2004). The model does not include the cycle of soil freezing and thawing and the water present in the soil pores is always considered in a liquid state, although this assumption might led to neglect important components of soil energy budget in cold climate as demonstrated by *Boone et al.* (2000). Only dependencies on soil moisture, θ $[-]$, and soil properties are thus considered. Such dependencies are taken from the Community Land Model 3.0 parametrization (*Oleson et al.*, 2004). The volumetric heat capacity cv_s is:

$$cv_s = cv_{soil}(1 - \theta_{sat}) + cv_{wat}\theta_d\,, \tag{4.78}$$

where cv_{soil} is the volumetric heat capacity of soil solid estimated from pedotransfer function (Section: 4.7.4) and $cv_{wat} = 4.186\ 10^6$ $[J\ K^{-1}\ m^{-3}]$ is the constant volumetric heat capacity of water. The variable θ_d is the soil moisture averaged from the dampening depth, d, to the surface. The thermal conductivity λ_s is from *Farouki*

(1981):

$$\begin{aligned} \lambda_s &= K_e\lambda_{sat} + (1 - K_e)\lambda_{dry} \quad \text{if } \theta_d/\theta_{sat} > 10^{-7} \ , \\ \lambda_s &= \lambda_{dry} \qquad \text{if } \theta_d/\theta_{sat} \leq 10^{-7} \ , \end{aligned} \tag{4.79}$$

where λ_{dry} $[W\ m^{-1}\ K^{-1}]$ is the thermal conductivity of dry soil (Section: 4.7.4), K_e is the Kersten number which is a function of the relative saturation $K_e = \ln(\theta_d/\theta_{sat}) + 1 \geq 0$ and $\lambda_{sat} = \lambda_{soil}^{1-\theta_{sat}}\lambda_{wat}^{\theta_{sat}}$ is the saturated thermal conductivity with λ_{soil} thermal conductivity of solid soil from pedotransfer function (Section: 4.7.4) and $\lambda_{wat} = 0.6$ $[W\ m^{-1}\ K^{-1}]$ thermal conductivity of liquid water.

Theoretically, the dampening depth, d, varies with the soil moisture content θ_d that in turn is calculated as the average soil moisture of the soil up to the dampening depth. This creates a complex non-linear interaction. However given the small range of variation of d, the dampening depth is calculated a priori considering a completely dry soil, i.e., $\theta_d = \theta_{hy}$ (See Section 4.7.4). The obtained value of d is then used for the entire simulation.

4.3.4 Incoming heat with precipitation

The incoming heat with precipitation, Q_v $[W\ m^{-2}]$, is usually not considered in hydrological model and land surface scheme (*Douville et al.*, 1995; *Ivanov et al.*, 2008a). Indeed, Q_v typically accounts for a negligible fraction of the energy balance and only during rainy or snowy periods. The incoming heat with precipitation is, instead, often computed when the energy budget of the snowpack is required, in this case its relative importance increases (*Bras*, 1990; *Wigmosta et al.*, 1994; *Tarboton and Luce*, 1996; *Essery et al.*, 1999; *Marks et al.*, 1999; *Williams and Tarboton*, 1999).

In order to estimate, Q_v, precipitation temperature must be known. In "Tethys" the temperature of rain is assumed to be the greater among air temperature, T_a $[^\circ C]$, and freezing point $T = 0$ $[^\circ C]$. The temperature of snow is assumed to be the lesser among air temperature and freezing point (*Tarboton and Luce*, 1996). Naturally, precipitation temperature may differ sensibly from the air temperature given its dependence on mesoscale meteorological patterns. However, the assumption of correspondence between air and precipitation temperature can be overall accepted and it does not require the knowledge of other variables such as the profile of temperature in the atmospheric boundary layer. The incoming heat with precipitation, Q_v $[W\ m^{-2}]$, is defined herein as the energy required to convert the precipitation to the temperature of the surface T_s $[^\circ C]$. When snow is present this becomes the temperature of the snow layer. This definition differs from what proposed by other authors (*Tarboton and Luce*, 1996) where the difference with the reference state $T = 0$ $[^\circ C]$ are considered. The variable Q_v is thus calculated as:

$$Q_v = c_w P_{r,liq}\ \rho_w\big[\max(T_a, 0) - T_s\big] + c_i P_{r,sno}\ \rho_w\big[\min(T_a, 0) - T_s\big] \ , \tag{4.80}$$

where $c_w = 4186$ $[J\ kg^{-1}\ K^{-1}]$ is the specific heat of water, $c_i = 2093$ $[J\ kg^{-1}\ K^{-1}]$

the specific heat of ice, $\rho_w = 1000$ $[kg\ m^{-3}]$ is the density of water and $P_{r,liq}$, $P_{r,sno}$ $[m\ s^{-1}]$ are the intensity of rain and snow respectively (see Section: 4.5.1).

4.3.5 Numerical solution for surface temperature

The prognostic surface temperature, T_s, is required in order to close the energy balance. As explained in Section 4.2.5 T_s is the only prognostic temperature considered and consequently T_s is the only unknown in the computation of energy fluxes. Incoming heat with precipitation, Q_v, net radiation, R_n, sensible heat, H, latent heat, λE, and ground heat flux, G, can be all calculated once T_s is known. Neglecting the heat stored by the vegetation canopy, the heat released by CO_2 fixation, and any lateral advective terms, the surface balance in absence of snow becomes:

$$R_n(T_s) - H(T_s) - \lambda E(T_s) - G(T_s) + Q_v(T_s) \quad = \quad 0\,. \tag{4.81}$$

Equation (4.81) is highly non-linear, for instance all the resistance terms r_{ah}, r_{aw}, r_{soil}, r_s theoretically depend on surface temperature T_s. The solution of (4.81) can be found only numerically, since no analytic solution exists. In "Tethys" the *matlab* command *fzero* is used to solve (4.81) . The algorithm, which was originated by T. Dekker, uses a combination of bisection, secant, and inverse quadratic interpolation methods. A *Fortran* version, upon which the *fzero* M-file is based, is in *Forsythe et al.* (1976). The closure of the energy balance in presence of snow is presented in Section 4.5.2, and also uses the *Matlab* command *fzero*.

4.4 Energy and mass transfer resistances

The parametrization of the vertical fluxes is based on the analogy with Ohm's law. Serial and parallel resistance terms are used to mediate the transfer of heat and water vapor between the land surface (vegetation, bare soil, snow, water) and the atmospheric surface layer. Five different types of resistance are accounted for: aerodynamic resistance, r_a, leaf boundary layer resistance, r_b, undercanopy resistance, $r_a{}'$, soil resistance, r_{soil}, and stomatal resistance, r_s. The resistances have dimensions of inverse of velocity $[s\,m^{-1}]$ and depend on many factors including surface roughness (e.g., canopy structure and leaf dimensions), wind speed, surface temperature, atmospheric stability, photosynthetic activity, etc.

An illustrative example of the assumption made with regards to the vertical profile of wind speed in case of a vegetated area is provided in Figure 4.16, where some important variable as reference height, z_{atm}, zero-plane displacement d, and roughness for momentum, z_{om}, are sketched and they will be use later in this section.

Note that often land surface and hydrological models neglect some or many resistance terms in order to simplify the entire scheme. For instance, the boundary leaf resistance concept has often be ignored, especially by the hydrological community (*Noilhan and Mafhouf*, 1996; *Bertoldi et al.*, 2006b; *Campo et al.*, 2006). In the well known Penmann-Monteith equation to estimate evapotranspiration only stom-

atal resistance and aerodynamic resistance are taken into account (*Dingman*, 1994; *Brutsaert*, 2005). It is possible to argue that other resistance terms are somehow embedded in r_a and r_s, though this is theoretically incorrect since nor r_a neither r_s consider at the same time vegetation characteristics and wind speed as required by r_b or ${r_a}'$. Furthermore, as it is shown in this section, the values assumed by different resistance terms are in many cases comparable. Consequently, any terms can be neglected without run the risk of oversimplifications or shortcomings.

Studies in the field of plant physiology pointed out that further resistance terms, such as the internal conductance to CO_2, that describe the movement of CO_2 from substomatal cavities to sites of carboxylation, or root, xylem, and leaf resistances that describe the resistance of different plant portions to the movement of water might play a role in the carbon and water fluxes and consequently in the latent heat flux (*Sperry et al.*, 2003; *Warren*, 2006; *Nobel*, 2009). However, adding these resistance would imply a complete characterization of the physiology of the plant and it is clearly beyond the scope of this study. The possible influence of the above mentioned resistances is completely neglected in "Tethys", or it is indirectly compensated by other parameters. For instance, neglecting the internal conductance to CO_2 can be compensated by an underestimation of biochemical parameters as maximum Rubisco capacity or maximum electron transport capacity (described later in this section) (*Warren*, 2006).

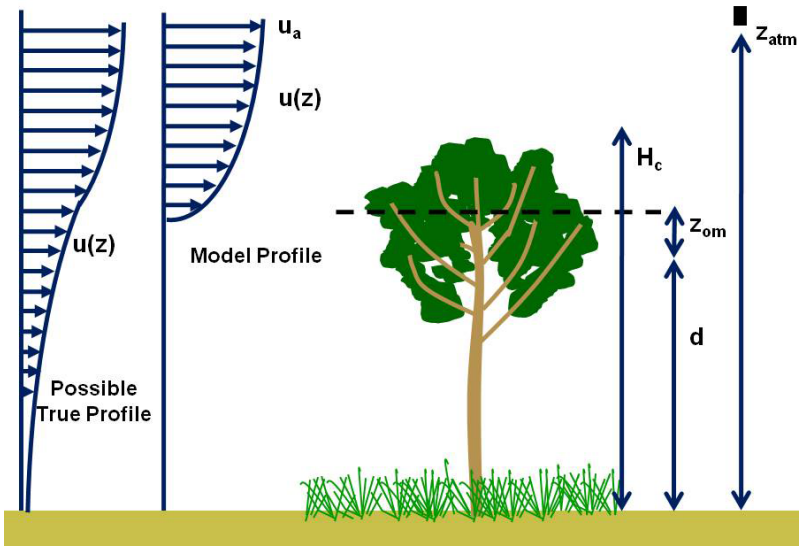

Figure 4.16: Illustration of the assumption made for the wind vertical profile between the land surface and the atmospheric surface layer, where $u(z)$ is the wind velocity, z_{atm} is the reference height, d is zero-plane the displacement, z_{om} is the roughness for momentum, and H_c is the canopy height.

4.4.1 Aerodynamic resistance

In order to obtain reliable estimations of sensible and latent heat fluxes an accurate parametrization of the aerodynamic resistance is necessary. The aerodynamic

resistance is a measure of the capability of the lower part of the atmospheric surface layer to oppose or expedite turbulent fluxes of momentum, sensible, and latent heat. In the following the derivation of the aerodynamic resistances to heat flux, r_{ah}, and to water vapor, r_{aw} are discussed. The latter terms are necessary in the computation of hydrological fluxes. The derivation of the aerodynamic resistance to momentum r_{am} is described in the Appendix C.2. The heat flux, H $[W\ m^{-2}]$, can be generally written as:

$$H = -\rho_a C_p K_h \frac{\partial \theta}{\partial z} \ , \tag{4.82}$$

where ρ_a $[kg\, m^{-3}]$ is the air density, $C_p = 1005 + [(T_a + 23.15)^2]/3364$ $[J\, kg^{-1}\, K^{-1}]$ is the specific heat of air at a constant pressure with T_a $[^{\circ}C]$ air temperature at a reference height z_{atm} $[m]$. The parameter K_h $[m^2\, s^{-1}]$ is the eddy diffusivity of heat and θ $[K]$ is the potential temperature. Once the position of the sink for heat is specified, defining the roughness length, z_{oh} $[m]$, and the zero-plane displacement, d $[m]$, the discrete expression for H becomes:

$$H = \rho_a C_p K_h \frac{(\theta_s - \theta_a)}{[z_{atm} - d - z_{oh}]} \ , \tag{4.83}$$

where θ_a and θ_s are the potential temperatures at the reference height and at the surface respectively. The eddy diffusivity, K_h, is a parameter highly variable and difficult to estimate due to the turbulent nature of the transfer. In the scientific literature a great effort has been carried out to found a functional relationship between heat flux and the gradient of temperature. Such a relationship embeds the turbulence and the stability structures of the atmospheric surface layer.

Rather than calculate K_h directly generally two other parameters are introduced, i.e. the aerodynamic resistance to heat transfer r_{ah} $[s\, m^{-1}]$ and the bulk transfer coefficient for heat C_h $[-]$, also called Stanton number. These three parameters are related each other from the relationships:

$$K_h/\partial z = C_h u_a = 1/r_{ah} \ , \tag{4.84}$$

where u_a is the wind speed at the reference height, z_{atm}, i.e. the height within the atmospheric surface layer (*Abdella and McFarlane*, 1996) where the meteorological variable are computed, see also Figure 4.16. The aerodynamic resistance can be expressed in term of heat flux by:

$$r_{ah} = \rho_a C_p \frac{(\theta_s - \theta_a)}{H} \, . \tag{4.85}$$

The determination of the aerodynamic resistance r_{ah} has been mainly solved with the Monin-Obukhov similarity theory (*Monin and Obukhov*, 1954; *Arya*, 2001). Starting from this theory many authors have proposed different parameterizations to estimate aerodynamic resistances to heat transfer (*Liu et al.*, 2007). These parameterizations can be differentiated in direct Monin-Obukohv similarity theory

application, empirical method and semi-empirical parameterizations. In "Tethys" the aerodynamic resistance can be calculated in two way, applying the complete Monin-Obukohv similarity theory or introducing a simplification. Such simplification has been proposed by *Mascart et al.* (1995) and has been applied in the *ISBA* model (*Noilhan and Mafhouf*, 1996). Simplified parameterizations may be necessary because solving the complete Monin-Obukohv similarity theory is highly computational demanding given the non-linearities and iterations involved in the problem. It is later shown in this section that the two methods provide fairly similar results in terms of r_{ah}.

According to the application of Monin-Obukhov similarity theory the fluxes of momentum, τ $[kg\ m^{-1}\ s^{-2}]$, sensible heat, H $[W\ m^{-2}]$, and water vapor, λE $[W\ m^{-2}]$, in the atmospheric surface layer, under the assumption of stationary and horizontally homogeneous conditions, are function of the friction velocity, u^* $[m\ s^{-1}]$, a potential temperature scale, θ^* $[K]$, and a specific humidity scale, q^* $[-]$:

$$\tau = \rho_a u^{*2}\,, \tag{4.86}$$

$$H = -\rho_a C_p u^* \theta^*\,, \tag{4.87}$$

$$\lambda E = -\lambda \rho_a u^* q^*\,, \tag{4.88}$$

where $\lambda = 1000[2501.3 - 2.361(T_a)]$ $[J\ kg^{-1}]$ is the latent heat of vaporization. The turbulent scaling quantities can be written as a function of the mean field variables (*Abdella and McFarlane*, 1996) using the integrated flux-profile relationship of *Dyer* (1974):

$$u^* = \frac{k u_a}{ln\left(\frac{z_{atm}-d}{z_{om}}\right) - \psi_m\left(\frac{z_{atm}-d}{\Lambda}\right) + \psi_m\left(\frac{z_{om}}{\Lambda}\right)}\,, \tag{4.89}$$

$$\theta^* = \frac{k Pr^{-1}(\theta_a - \theta_s)}{ln\left(\frac{z_{atm}-d}{z_{oh}}\right) - \psi_h\left(\frac{z_{atm}-d}{\Lambda}\right) + \psi_h\left(\frac{z_{oh}}{\Lambda}\right)}\,, \tag{4.90}$$

$$q^* = \frac{k Pr^{-1}(q_a - q_s)}{ln\left(\frac{z_{atm}-d}{z_{ow}}\right) - \psi_w\left(\frac{z_{atm}-d}{\Lambda}\right) + \psi_w\left(\frac{z_{ow}}{\Lambda}\right)}\,, \tag{4.91}$$

where $k = 0.4$ is the von Karman constant, Pr is the neutral turbulent Prandlt number, describing the ratio between the eddy diffusivity of momentum, K_m, and of heat, K_h, i.e. $Pr = K_m/K_h$ (*Grachev et al.*, 2007). The variables θ_s, and q_s are the potential temperature and specific humidity at the surface; z_{om}, z_{oh}, and z_{ow} $[m]$ are the roughness lengths for momentum, heat, and water vapor respectively; Λ $[m]$ is the Obukhov length and ψ_m, ψ_h, ψ_w $[-]$ are the non-dimensional integral stability function for momentum, heat, and water vapor respectively. Note that the apparent sinks for momentum, heat and water vapor are theoretically in three different positions, i.e. $z_{om} + d$, $z_{oh} + d$, and $z_{ow} + d$. The Obukhov length Λ is defined as:

$$\Lambda = \frac{u^{*2}\, T_a}{k\, g\, \theta^*} = \frac{-\rho_a C_p u^{*3} T_a}{k\, g\, H}\,, \tag{4.92}$$

where T_a $[K]$ is the air temperature at the reference height z_{atm} and $g = 9.81$ $[m\ s^{-2}]$ is the gravitational acceleration.

An insight must be provided for the aerodynamic and thermal dynamic roughness lengths z_{om}, z_{oh}, and z_{ow} that must be known a priori. Scalar roughness heights changes with surface characteristics, atmospheric flow, and thermal dynamic state of the surface (*Su*, 2002; *Zhao et al.*, 2008). Mechanistic models to evaluate z_{om}, z_{oh} together with the displacement height, d, have been proposed by different authors *Massman* (1997); *Su et al.* (2001). These models related z_{oh} to z_{om} through the Stanton number and are based on complex parameterizations including the derivation of functional forms to describe the vertical structure of the vegetation canopy in order to calculate the within-canopy turbulence profile. The application of similar schemes for different land cover conditions would require the specification of many parameters that are highly uncertain and very difficult to determine in the field. Such an approach does not match the scope of "Tethys". The roughness lengths and displacement height are calculated with the relationships proposed by *Brutsaert* (1982), where only the height of the vegetation (or a reference value for z_{om}) is required. The parametrization of *Brutsaert* (1982) has been widely used in hydrological models and land surface schemes (*Ivanov et al.*, 2008a). In case of vegetated surface the roughness are function of the canopy height H_c:

$$z_{om} = 0.123 H_c \ , \tag{4.93}$$

$$z_{oh} = z_{ow} = 0.1 z_{om} \ , \tag{4.94}$$

$$d = 0.67 H_c \, . \tag{4.95}$$

Other studies provide different parameterizations to link the roughness lengths z_{om}, z_{oh} to vegetation height, H_c, and Leaf Area Index, LAI, (*Raupach*, 1994; *Zeng and Wang*, 2007). Especially, the equations proposed by *Zeng and Wang* (2007) seem simple enough to be applied in hydrological model and will be considered for further improvements of "Tethys". Considerations about z_{ow} are rare since this parameter, as done in equation (4.94), is very often assumed to be equal to z_{oh}. A detailed classification of roughness length parameters for different land uses can be found in *Wieringa* (1993). In "Tethys" the following values are used $z_{om} = 0.003$ $[m]$ for bare soil, $z_{om} = 0.0002$ $[m]$ for water surfaces, and $z_{om} = 0.001$ $[m]$ for snow in a open field.

The Monin-Obukhov similarity theory implies the solution of the equations (4.85), (4.87), and (4.90) to calculate the aerodynamic resistance, r_{ah}, as:

$$\begin{aligned} r_{ah} = \ & \frac{Pr}{k^2 u_a} \Big[\ln\Big(\frac{z_{atm} - d}{z_{om}}\Big) - \psi_m\big(\frac{z_{atm} - d}{\Lambda}\big) + \psi_m\big(\frac{z_{om}}{\Lambda}\big) \Big] \cdot \\ & \Big[\ln\Big(\frac{z_{atm} - d}{z_{oh}}\Big) - \psi_h\big(\frac{z_{atm} - d}{\Lambda}\big) + \psi_h\big(\frac{z_{oh}}{\Lambda}\big) \Big] \, . \end{aligned} \tag{4.96}$$

Note that in windless condition, i.e. $u_a = 0$, the aerodynamic resistance $r_{ah} = \infty$, consequently there is no heat flux. In nature such a condition is unverified since a free convection can guarantee a certain transport also in calm condition (*Kondo*

and Ishida, 1997). However, free convective fluxes are negligible and $r_{ah} = \infty$ is assumed in the model. In neutral condition the integral stability functions $\psi_m(x)$, $\psi_h(x)$ are equal to zero and the neutral aerodynamic resistance to heat transfer takes the expression:

$$r_{ah} = \frac{1}{k^2 u_a}\Big[\ln\Big(\frac{z_{atm}-d}{z_{om}}\Big)\Big]\Big[\ln\Big(\frac{z_{atm}-d}{z_{oh}}\Big)\Big]\,, \tag{4.97}$$

and from equation (4.89), the wind profile in neutral condition is represented with the well known logarithmic form:

$$u_a = \frac{u^*}{k}\ln\Big(\frac{z_{atm}-d}{z_{om}}\Big)\,. \tag{4.98}$$

The Prandtl number in equation (4.96) is often assumed to be equal to 1 (*Noilhan and Mafhouf*, 1996; *van den Hurk and Holtslag*, 1997; *Liu et al.*, 2007), although other authors provide different values (*Mascart et al.*, 1995). Generally, the value of Pr is related to the flow and stability conditions and its correct determination is still problematic (*Grachev et al.*, 2007). For these reasons, a value $Pr = 1$ is used in "Tethys". For non neutral condition the form of the stability functions $\psi_m(x)$, $\psi_h(x)$ must be specified. The differentiation between stable and unstable condition is accounted for calculating the bulk Richardson number Ri_B (*Mascart et al.*, 1995; *Abdella and McFarlane*, 1996; *van den Hurk and Holtslag*, 1997) including the correction proposed by *Kot and Song* (1998) to take into account that z_{om} and z_{oh} are different:

$$Ri_B = f^2\,\frac{g(\theta_a-\theta_s)(z_{atm}-d)}{0.5(\theta_a+\theta_s){u_a}^2}\,, \tag{4.99}$$

where $f^2 = [1-z_{om}/(z_{atm}-d)]^2/[1-z_{oh}/(z_{atm}-d)]$ is the modification proposed by *Kot and Song* (1998). Boundary layer stable conditions provide a bulk Richardson number $Ri_B > 0$ that in turn gives $\theta_s < \theta_a$, $H < 0$, and $\Lambda > 0$. Conversely, for unstable condition the bulk Richardson number is $Ri_B < 0$ that in turn gives $\theta_s > \theta_a$, $H > 0$, and $\Lambda < 0$ (Figure 4.17).

The stability functions $\psi_m(\zeta)$, $\psi_h(\zeta)$ for unstable conditions were obtained from experimental data by *Businger et al.* (1971) (see also *van den Hurk and Holtslag* (1997)):

$$\psi_m(\zeta) = \ln\Big[\Big(\frac{1+x}{2}\Big)^2\Big(\frac{1+x^2}{2}\Big)\Big] - 2\arctan(x) + \pi/2\,, \tag{4.100}$$

$$\psi_h(\zeta) = 2\ln\Big[\Big(\frac{1+x^2}{2}\Big)\Big]\,, \tag{4.101}$$

$$x = (1-\gamma\zeta)^{1/4}\,, \tag{4.102}$$

where $\gamma = 16$ both for momentum and heat as suggested by *Dyer* (1974) when $k = 0.4$. For stable condition *Businger et al.* (1971) assumed that $\psi_m(\zeta)$, $\psi_h(\zeta)$ are linear function of the argument ζ. *Louis* (1979) and others argued that the

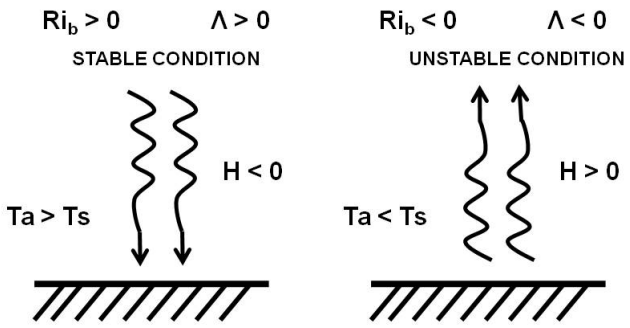

Figure 4.17: Signs of some quantity in case of stable or unstable conditions of the atmospheric surface layer. The potential temperatures, θ, are replaced with conventional temperatures T. This is possible since the reference height, z_{atm}, is relative close to the surface and changes in atmospheric pressure are negligible.

formulation of *Businger et al.* (1971) suppresses turbulent exchange too strongly, in particular under very stable conditions. The improved expression of *Beljaars and Holtslag* (1991) is adopted in "Tethys":

$$\psi_m(\zeta) = -\Big[a\zeta + b\Big(\zeta - \frac{c}{d}\Big)\exp(-d\zeta) + \frac{bc}{d}\Big]\,, \tag{4.103}$$

$$\psi_h(\zeta) = -\Big[\Big(1 + \frac{2a}{3}\zeta\Big)^{1.5} + b\Big(\zeta - \frac{c}{d}\Big)\exp(-d\zeta) + \Big(\frac{bc}{d} - 1\Big)\Big]\,, \tag{4.104}$$

where $a = 1$, $b = 0.667$, $c = 5$, and $d = 0.35$ are experimental coefficients. An iterative procedure hypothesizing a initial value of Λ is necessary to solve for r_{ah}. The Obukhov length, $\Lambda = f(u^*, \theta^*)$, is, indeed, a function of the friction velocity, $u^* = f(\Lambda)$, and of the potential temperature scale, $\theta^* = f(\Lambda)$, that in turn are functions of the Obukhov length Λ. The initial value of Λ is chosen once the stability conditions of the atmospheric surface layer are known. As stated previously, such a procedure requires a highly numerical effort, because of the iterations. For this reason empirical and semi-empirical approximation of the Monin-Obukhov similarity theory have been proposed (*Louis*, 1979; *Mascart et al.*, 1995; *Launiainen*, 1995; *Abdella and McFarlane*, 1996; *van den Hurk and Holtslag*, 1997), for a review see *Liu et al.* (2007). In "Tethys" together with the complete solution of the Monin-Obukhov similarity theory, the approximate solution proposed by *Mascart et al.* (1995) following the study of *Louis* (1979) and applied in the *ISBA* land surface scheme (*Noilhan and Mafhouf*, 1996) is implemented. This approach estimates the bulk transfer coefficient for heat $C_h = 1/(r_{ah}u_a)$. The coefficient C_h is expressed as a function of the neutral transport coefficient, C_n, and of an empirical equation, $F_h = f(Ri_B)$, function of the bulk Richardson number, Ri_B:

$$C_h = \frac{1}{r_{ah}u_a} = C_n F_h(Ri_B)\,, \tag{4.105}$$

where the terms C_n and $F_h(Ri_B)$ are:

$$C_n = \frac{k^2}{\ln\big[(z_{atm} - d)/z_{om}\big]^2}\,, \tag{4.106}$$

$$\begin{aligned} F_h(Ri_B) &= \Big[1 - \frac{15Ri_B}{1 + c_h\sqrt{|Ri_B|}}\Big]\Big[\frac{\ln[(z_{atm} - d)/z_{om}]}{\ln[(z_{atm} - d)/z_{oh}]}\Big] \quad \text{if } Ri_B \leq 0\,, \\ F_h(Ri_B) &= \Big[\frac{1}{1 + 15Ri_B\sqrt{1 + 5Ri_B}}\Big]\Big[\frac{\ln[(z_{atm} - d)/z_{om}]}{\ln[(z_{atm} - d)/z_{oh}]}\Big] \text{ if } Ri_B > 0\,, \end{aligned} \tag{4.107}$$

where c_h is calculate as follows:

$$c_h = 15{c_h}^* C_n\big[(z_{atm} - d)/z_{oh}\big]^{p_h}\left[\frac{\ln[(z_{atm} - d)/z_{om}]}{\ln[(z_{atm} - d)/z_{oh}]}\right]\,, \tag{4.108}$$

$${c_h}^* = 3.2165 + 4.3431\mu + 0.5360\mu^2 - 0.0781\mu^3\,, \tag{4.109}$$

$$p_h = 0.5802 - 0.1571\mu + 0.0327\mu^2 - 0.0026\mu^3\,, \tag{4.110}$$

where $\mu = \ln(z_{om}/z_{oh})$. Note that the expression of $F_h(Ri_B)$ in equation (4.107) for stable condition is slightly different from the one originally proposed by *Mascart et al.* (1995). In equation (4.107) the enhancements first described by *Louis et al.* (1982) and introduced by *Noilhan and Mafhouf* (1996) (page 157) are taken into account [see also *van den Hurk and Holtslag* (1997) (page 132)].

The aerodynamic resistance to water vapor, r_{aw}, that is necessary in the latent heat flux estimation is assumed to be equal to the aerodynamic resistance to heat flux r_{ah}. This assumption allows, in the other sections of the thesis, to use a single general aerodynamic resistance $r_a = r_{aw} = r_{ah}$. The approximation is very common and it is made by many existent land surface and hydrological models (*Viterbo and Beljaars*, 1995; *Sellers et al.*, 1996b; *Noilhan and Mafhouf*, 1996; *Bertoldi et al.*, 2006b; *Ivanov et al.*, 2008a). The rationale of the assumption is given by the negligible differences in term of water vapor and heat transfer in turbulent conditions. As a consequence of this assumption the equalities $z_{ow} = z_{oh}$ and $\psi_w(\zeta) = \psi_h(\zeta)$ are justified.

An illustrative example of the values assumed by aerodynamic resistance to heat flux, r_{ah}, once wind speed, u_a $[m\ s^{-1}]$, and instability (or stability) of the atmosphere, $T_s - T_a$ $[°C]$, are given, is shown in Figure 4.18. The two methods implemented in "Tethys" to calculate r_{ah} are compared in bare soil and vegetated conditions.

From Figure 4.18 it is possible to notice that the aerodynamic resistance for bare soil is much larger compared to vegetated areas. This effect growths as the height of the canopy becomes more relevant. A taller vegetation enhances the formation of turbulent eddies and thus the transfer of heat and water fluxes. Such an observation implies that for woody areas with tall trees other resistances, for example boundary leaf resistance r_b, might be dominant in comparison to r_{ah}. In Figure 4.18 can be also clearly observed the sudden effect of atmosphere stability that increases r_{ah} to very

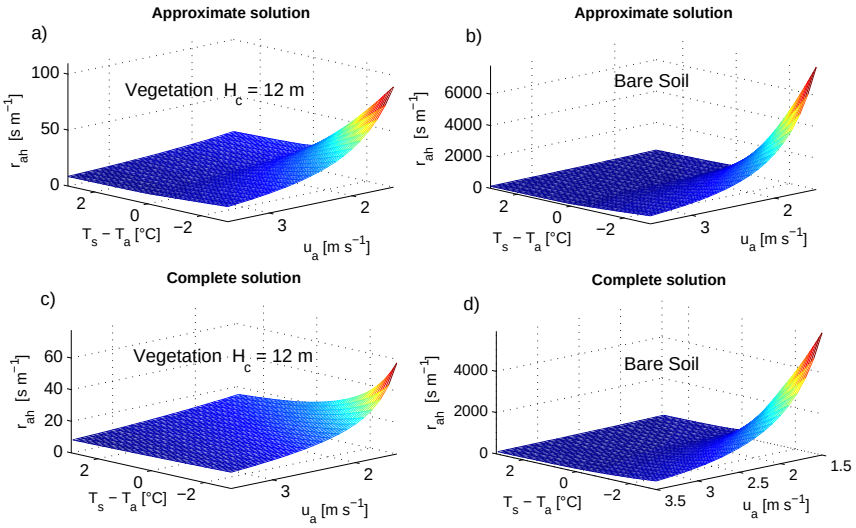

Figure 4.18: Aerodynamic resistance, r_{ah} $[s\ m^{-1}]$, sensitivity to wind speed at the reference height, u_a $[m\ s^{-1}]$, and instability of the atmosphere, $T_s - T_a$ $[°C]$, calculated with the complete solution of the Monin-Obukhov similarity theory (c) and (d), and with the approximation proposed by *Mascart et al.* (1995); *Noilhan and Mafhouf* (1996) (a) and (b), for a vegetated area with $H_c = 12$ $[m]$ (a) and (c), and for a bare soil area (b) and (d). A fixed $T_a = 15$ $[°C]$ is used.

high values when the wind speed is not sufficient to enhance the fluxes. Conversely, in unstable or windy condition r_{ah} is almost constant around a minimum value. The complete solution of the Monin-Obukhov similarity theory (Figure 4.18c and d) and the approximate solution proposed by *Mascart et al.* (1995); *Noilhan and Mafhouf* (1996) (Figure 4.18a and b) provide similar results. The approximate solution is generally more conservative providing lower values of r_{ah} for stable conditions and higher values for unstable conditions.

4.4.2 Undercanopy resistance

The aerodynamic resistance between the ground surface and the sink for momentum in the vegetation or between the two vegetation sinks for momentum (when two vegetation layers are present) is called undercanopy resistance $r_a{}'$ $[s\ m^{-1}]$. Such a resistance generally depends on the turbulence structure and stability of the roughness sublayer. Several detailed approaches to calculate the transfer of momentum in the roughness sublayer have been proposed (*Raupach*, 1989; *Massman*, 1997). However, as done for roughness length and displacement height simplified relationship are used to avoid excessive parameterizations. A first attempt to simply parameterize such resistance was done by *Choudhury and Monteith* (1988). They assumed an exponential profile of the eddy diffusivity, $K_h(z)$ $[m^2\ s^{-1}]$, in the canopy, omitting the effect of atmospheric stability within and below the canopy. Under such

assumptions the expression for $r_a{}'$ is:

$$r_a{}' = \frac{H_c}{\alpha K_h(H_c)}\left[e^{\alpha(1-z_{oh}{}'/H_c)} - e^{\alpha(1-(z_{oh}+d)/H_c)}\right] , \quad (4.111)$$

$$K_h(H_c) = u^* k(H_c - d) , \quad (4.112)$$

where $z_{oh}{}'$ $[m]$ is the undercanopy roughness height, d $[m]$ is the zero plane displacement, k $[-]$ is the Von Karman constant, H_c $[m]$ is the canopy height, u^* $[m\ s^{-1}]$ is the friction velocity from equation (4.98), and α $[-]$ is an attenuation coefficient. The superscript prime indicates the undercanopy quantities. The *Choudhury and Monteith* (1988) parametrization has received a certain popularity and has been adopted by other authors (*Shuttleworth and Gurney*, 1990; *Bonan*, 1996; *LoSeen et al.*, 1997; *Ivanov et al.*, 2008a). The value assigned to α is typically around 3. As pointed out by *Zeng et al.* (2005) such a parametrization can encounter problems for thick or very sparse canopy since it does not depend on the Leaf Area Index.

Recently *Zeng et al.* (2005), in order to improve the performance of the Community Climate System Model, provided two new formulations for $r_a{}'$ whit an explicit dependence on Leaf Area Index. Such an update was necessary to correct the excessive warm bias in ground temperature observed for simulations in a sparse canopy environment. Figure 4.19 shows the comparison between the behavior of $r_a{}'$ as a function of the LAI (*Zeng et al.*, 2005) and $r_a{}'$ calculated with different constant values of the attenuation coefficients α as proposed by *Choudhury and Monteith* (1988). Typical values of α around 2.5-3 correspond to canopy with LAI larger than 1.5, 2. The value of $r_a{}'$ is strongly sensitive to α. In order to be consistent with the physical process, the attenuation coefficient, α, is expected to decrease rather than remain constant as LAI becomes smaller and this is effectively captured by the parametrization of *Zeng et al.* (2005).

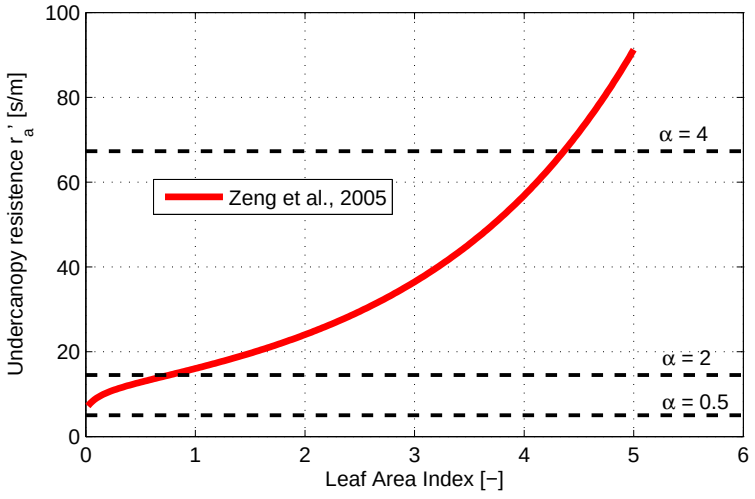

Figure 4.19: Undercanopy resistance, $r_a{}'$, function of the LAI in the parametrization proposed by *Zeng et al.* (2005) (red-line) and by *Choudhury and Monteith* (1988) with different values of the attenuation coefficient, α, (dashed black-lines). The $r_a{}'$ are calculated with a fixed $H_c = 12$ $[m]$ and $u_a = 5$ $[m\ s^{-1}]$.

Given the dependence of $r_a{}'$ on the LAI, the second of the two schemes proposed by *Zeng et al.* (2005) to parameterize the undercanopy resistance is adopted in "Tethys". *Zeng et al.* (2005) express the undercanopy resistance, $r_a{}'$, in terms of a non-dimensional aerodynamic conductance C_s $[-]$, where the relationship between the two quantities is $r_a{}' = 1/(C_s u^*)$ (*Zeng and Dickinson*, 1998). In order to calculate C_s two measures of the inverse of the reduction of turbulence by the canopy are defined as:

$$r_{t1} = \frac{H_c}{d(\beta + 0.1)}\Big[1 - e^{-\beta d/H_c}\Big]e^{\beta} \ , \tag{4.113}$$

$$r_{t2} = \frac{H_c}{\beta\, d}\Big[1 - e^{-\beta d/H_c}\Big]e^{\beta} \ , \tag{4.114}$$

where $\beta = 0.7LAI$ is a parameter defined by *Zeng et al.* (2005). The undercanopy aerodynamic and sublayer non-dimensional resistances are defined as:

$$r_1 = \frac{d}{k(H_c - d)} r_{t1} \ , \tag{4.115}$$

$$r_2 = r_{t2}^{0.45} \ln(z_{om}{}'/z_{oh}{}')/k \ , \tag{4.116}$$

where $z_{om}{}'$ and $z_{oh}{}'$ are the roughness lengths of the underneath surface for momentum and heat respectively. The underneath surface can be bare soil or the low vegetation layer. Finally, C_s is computed for any LAI as $C_s = 1/(r_1 + r_2)$.

Note that the value of $r_a{}'$ is obtained for neutral condition. This implies that when the stability of the atmosphere becomes significative $r_a{}'$ is underestimated. Nonetheless, such an approximation is expected to influence only marginally the final results. Simple corrections to account for stability conditions in C_s have been also proposed and can be implemented in future versions of "Tethys" (*Sakaguchi and Zeng*, 2009).

4.4.3 Leaf boundary resistance

Exchanges of water vapor, carbon dioxide, and heat between plants and atmosphere are also controlled from a thin layer of air between the leaf surfaces and the surrounding environment. It is observationally verified that the magnitude of temperature, wind velocity, water vapor, and CO_2 concentrations observed at the leaf surface and in the free atmosphere are rather different (*Vesala*, 1998). This a consequence of a significative gradient of these quantities within a thin air layer in correspondence of the leaf surface. This thin layer is referred as the leaf boundary layer and its thickness, δ $[mm]$, is defined as the distance from leaf surface where the flow velocity differs from the ambient value of only a small prescribed quantity (for instance 1%).

Rather than in the thickness of the leaf boundary layer, in eco-hydrological modeling the interest lays in the opposition that such a layer exerts to the transfer of mass and heat. The magnitude of this opposition is measured as leaf boundary resistance, r_b $[s\ m^{-1}]$. Oppositely, the enhancement of the transfers is measured as leaf bound-

ary layer conductance $g_b = 1/r_b$ $[m\ s^{-1}]$. In still air, the boundary leaf resistance is mainly related to molecular diffusion. Generally, the process is controlled by a diffusion coefficient, D, that changes according to the diffusion medium, e.g. air, CO_2, etc., the transferred quantity, e.g., water vapor, CO_2, momentum, and heat, and the turbulence conditions. Values of diffusivity, compared to the heat diffusivity were proposed by *Jones* (1983) and are tabulated in table 4.1.

Table 4.1: Ratio of diffusivity, D, in air in comparison to heat diffusivity, from *Jones* (1983).

Air Condition	Heat	Water vapor	CO_2	Momentum
Still Air (Molecular Diffusion)	1.0	1.12	0.68	0.73
Laminar	1.0	1.08	0.76	0.80
Turbulent	1.0	1.0	1.0	1.0

When turbulence increases mainly as a consequence of an augment of wind speed the transport in the leaf boundary layer becomes turbulent. In turbulent condition all the different quantities are transported equal efficiently (Table 4.1). The leaf boundary layer thickness growths in the direction of wind speed and the boundary layer nature evolves from diffusive to laminar to turbulent. Such an evolution is related to the convection condition present in the ambient around the leaf. Typically, in literature only laminar and turbulent states are considered (*Jones*, 1983). The transport through molecular diffusivity is confined to the sub-stomatal space in the leaf interior. Nevertheless, some author argues that in a thin sub-layer of the leaf boundary layer (Figure 4.20) the molecular diffusivity plays and important role and suggests to include this sub-layer in the determination of r_b (*Vesala*, 1998). An illustration of leaf boundary layer concept is provided in Figure 4.20.

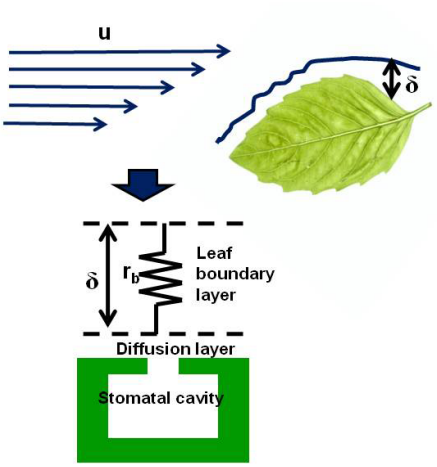

Figure 4.20: Illustration of leaf boundary layer concept. A leaf boundary layer with thickness, δ, surrounds the leaf creating a resistance, r_b, in the mass-energy transfer from the leaf surface-subsurface to the atmosphere. A diffusive sub-layer between the proper leaf boundary layer and the leaf surface seems plausible (*Vesala*, 1998), although it is not considered in "Tethys".

The leaf boundary resistance has been shown to depend on several factors, as leaf morphology (shape, size, roughness), leaf motion/orientation against the flow, and wind speed (*Jones*, 1983; *Schuepp*, 1993). Generally, the leaf boundary resistance, r_b, can be calculated empirically from mathematical models (*Schuepp*, 1993). For instance, a first approach was to approximate leaves through flat plates in laminar forced convection conditions. Nonetheless, given the heterogeneities in leaf shape and dimension, laboratory experiments were led to determine more suitable relationships for r_b as a function of leaf dimension and flow characteristics. The expression first proposed by *Jones* (1983) and used also by *Choudhury and Monteith* (1988) and *Shuttleworth and Gurney* (1990) is used:

$$g_b(z) = a[u(z)/d_{leaf}]^{1/2}\,, \tag{4.117}$$

where $g_b(z)$ $[m\ s^{-1}]$ is the mean one-sided bulk leaf boundary conductance, $g_b(z) = 1/r_b(z)$, the parameter d_{leaf} $[m]$ is the characteristic leaf dimension, often referred to as leaf width, and $a = 0.01$ $[m\ s^{-1/2}]$ is an empirical coefficient (*Choudhury and Monteith*, 1988). The wind profile, $u(z)$, within the canopy is assumed to follow an exponential function governed by an attenuation coefficient α' $[-]$:

$$u(z) = u(H_c)\exp[\alpha'(z/H_c - 1)]\,. \tag{4.118}$$

A specific value for the attenuation coefficient, $\alpha' = 3$, was proposed by *Choudhury and Monteith* (1988) after a sensitivity analysis. The coefficient α' controls the vertical gradient of wind speed along the canopy that in turn control the capacity of the process to enhance or prevent transfer at different canopy heights. In "Tethys" the coefficient α' is evaluated assuming a point equivalence between equation (4.118) used to compute the exponential wind speed profile within the canopy and the logarithmic wind profile above the sink of momentum (equation 4.98). The latter is assumed in order to calculate the aerodynamic resistance in atmospheric neutral condition (Section 4.4.1). Specifically, the two wind profiles are forced to produce the same value of wind velocity not only at the reference height z_{atm} $[m]$, as implicitly required by the equations, but also at the canopy height H_c $[m]$ (Figure 4.21a). Under such an assumption the attenuation coefficient α' becomes:

$$\alpha' = \ln[u_a/u(H_c)]/(z_{atm}/H_c - 1)\,, \tag{4.119}$$

where $u(H_c)$ is calculated from equation (4.98) once the friction velocity u^* is known imposing $u_a = u(z_{atm})$. Values of α' obtained under this assumption are similar to the range of values $\alpha' \approx 2 - 4$ proposed by *Choudhury and Monteith* (1988) or used by *Bonan* (1996); *Ivanov et al.* (2008a). With the proposed equation (4.119) the value assumed by α' decreases with the canopy height, as can be observed in Figure 4.21b. Such an outcome is consistent with the intuitive realization of the physical process, where a lower canopy is expected to exert a minor attenuation on wind speed.

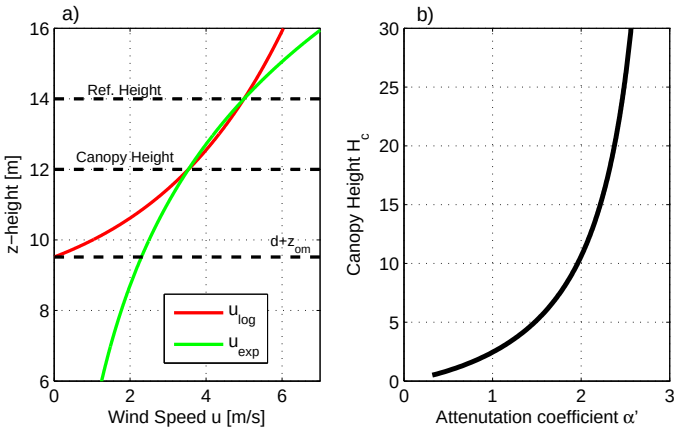

Figure 4.21: Illustration of the implications of equation (4.119) in the determination of α' $[-]$. a.) Logarithmic and exponential profile of wind speed forced to produce the same value of wind speed u at the canopy height H_c. b.) Values assumed by α' for different canopy heights.

Finally, the value of g_b must be integrated over the entire canopy. In order to realize this integration, a linear distribution of the Leaf Area Index, $L(z) = (LAI\ z)/H_c$, is assumed, where $L(z)$ is the leaf area index varying with height and H_c is the total height of the canopy (*Choudhury and Monteith*, 1988). The mean plant leaf boundary conductance g_b is:

$$g_b = \frac{\int_0^{LAI} g_b(z) dL'}{LAI} = \left(\frac{2a}{\alpha'}\right)\left(\frac{u(H_c)}{d_{leaf}}\right)^{1/2}\left[1 - e^{-\alpha'/2}\right] \ . \tag{4.120}$$

The mean one-sided resistance for unit leaf area is then $r_b = 1/g_b$ and for unit of *Crown Area* is:

$$\widehat{r_b} = 1/(g_b\ LAI)\,. \tag{4.121}$$

In the presented approach no attempt is made to distinguish between fluxes of vapor and heat in the determination of r_b. Slight differences due to the diffusion coefficients, in fact, are negligible across the laminar boundary layers of leaves, especially compared to other uncertainties (*Choudhury and Monteith*, 1988). Effects of stability conditions are also neglected in the evaluation of the wind speed profile. A sensitivity analysis of r_b $[s\ m^{-1}]$ to the leaf dimension d_{leaf} $[cm]$ and wind speed u_a $[m\ s^{-1}]$ is presented in Figure 4.22. The increase of r_b with larger leaf dimensions and with lower wind velocities is easily appreciable.

4.4.4 Soil resistance

Bare ground evaporation is computed within the quantities E_g and E_{bare} $[kg\ m^{-2}\ s^{-1}]$. These are controlled by atmospheric conditions, surface soil wetness and moisture transport below the soil surface. Simplifying, bare ground evaporation can be reduced to a combination of two physical processes (*Kondo et al.*, 1990; *Mahfouf and*

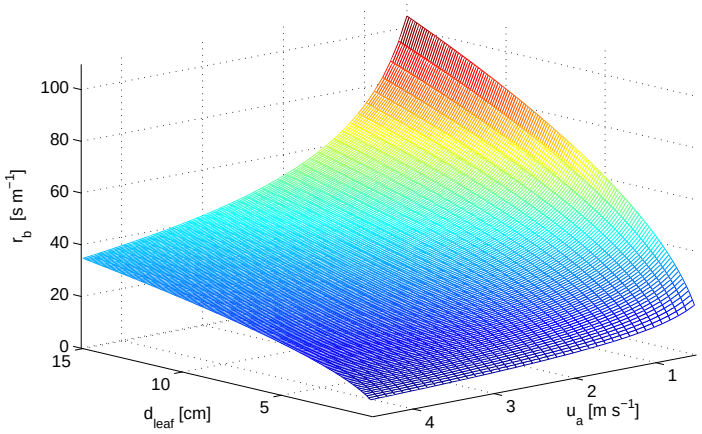

Figure 4.22: Sensitivity analysis of leaf boundary resistance, r_b $[s\ m^{-1}]$, to wind speed at the reference height, u_a $[m\ s^{-1}]$, and leaf dimension, d_{leaf} $[cm]$. The vegetation height is fixed to $H_c = 12$ $[m]$ and $LAI = 1$.

Noilhan, 1991; *He and Kobayashi*, 1998; *Wu et al.*, 2000). First, water vapor is transported mainly by molecular diffusion from the liquid surface in the soil pores to the immediately aboveground air, referred to as land surface. In the second process water vapor is carried from the land surface into the atmospheric surface layer by laminar or turbulent airflow (see Figure 4.23). The second process is characterized by the atmospheric resistance, r_a, and it has been described in Section 4.4.1. The first process is, instead, governed by a resistance exerted by the soil to the diffusion of water vapor. Such a resistance depends on the relative humidity adjacent to the free-water surface in the soil matrix, that in turn depends on the vertical and horizontal soil moisture profiles.

In dry conditions the relative humidity in the pores has a strong vertical gradient in the top few $[mm]$ of the soil. This gradient is inversely proportional to the diffusivity of water vapor, the latter is strongly dependent on soil texture and structure properties (*Kondo et al.*, 1990). A description of bare ground evaporation process with an explicit modeling of the water vapor diffusion process can be obtained only using a fine temporal step and dividing the soil in numerous layers in the top 5-10 $[cm]$ (*Camillo et al.*, 1983). Water vapor diffusion into the soil is governed by mass and heat transfer laws, producing a very complex and highly coupled three state system (*Saito et al.*, 2006; *Bittelli et al.*, 2008). Furthermore, non-linearities in governing equations and hydraulic properties of the soil lead to an elevated computational demand, prohibitive for large scale problems. For these reasons, simpler parameterizations have been proposed to relate soil evaporation E and soil moisture θ $[-]$. Empirical parameterizations are typically valid when the thickness of the top soil layer is in the order of few $[cm]$ (*Wu et al.*, 2000). Following the subdivision of *Kondo et al.* (1990) empirical parameterizations of the $E - \theta$ relationship can be distinguished in α, β, and threshold methods. These methods are briefly described

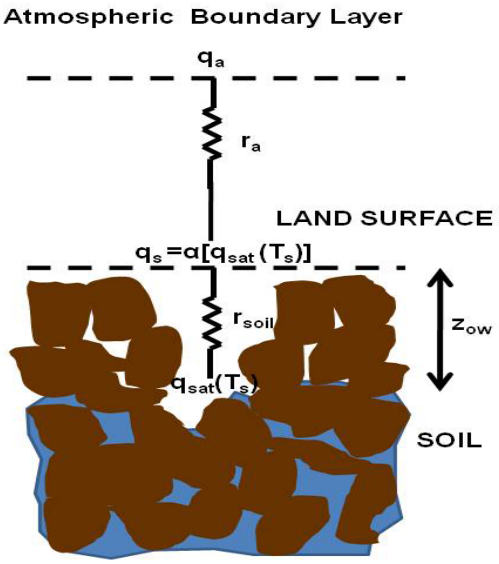

Figure 4.23: Illustration of the scheme assumed to describe soil resistance to evaporation. Both α and β methods are outlined in the figure. The scheme is drawn from *Mahfouf and Noilhan* (1991).

in the following.

Evaporation, E $[kg\ m^{-2}\ s^{-1}]$, from a bare ground surface (E_g or E_{bare} in "Tethys") can be generally written as:

$$E = \frac{\rho_a \beta [\alpha q_{sat}(T_s) - q_a]}{r_a}\,, \tag{4.122}$$

where ρ_a $[kg\ m^{-3}]$ is the air density, q_a $[-]$, and $q_{sat}(T_s)$ $[-]$ are the specific humidity at the reference height z_{atm}, and the specific humidity at saturation calculated using the surface temperature T_s. The term $\alpha = q_s/[q_{sat}(T_s)]$ represents the relative humidity of air at the height z_{ow}, with q_s specific humidity at the same height. The variable z_{ow} is the roughness height for water vapor, described in Section 4.4.1. The term $\beta = E/E_{pot}$ is the fraction of the bulk transfer of water vapor between the air trapped in the soil pores close to the water (considered at saturation $q = q_{sat}(T_s)$) and the specific humidity q_a at the reference height.

The α and β methods differ in the use of the α or the β parameter to calculate E. In the α method is specified a value for α and $\beta = 1$, conversely in the β method is β that is specified and $\alpha = 1$. Combinations of the two methods also exist. Analyzing the two methods, it is not clear which of the two is generally superior, although practically the β method seems to have had a larger popularity (*Kondo et al.*, 1990; *Wu et al.*, 2000). Another possibility to parameterize the $E - \theta$ relationship is to use the threshold methods. In this case evaporation occurs at the potential rate (determine by the atmospheric demand term) until the soil is no longer able to meet this demand and then becomes limited by supply (*Wetzel and Chang*, 1987). Comparative studies of different parameterizations of evaporation over bare ground can be found in literature (*Mahfouf and Noilhan*, 1991; *Wu et al.*, 2000). In "Tethys"

a β method is adopted as proposed by *Sellers et al.* (1992b) and successively used by *Sellers et al.* (1996b); *Ivanov et al.* (2008a), and *Oleson et al.* (2008b) for the recent updates of the Community Land Model. The β method is completed accounting for the relative humidity of the air adjacent to the pores.

The theoretical definition of the humidity equilibrium value $\hat{\alpha}(\theta_e)$, for a water content θ_e $[-]$, was provided by *Philip* (1957) by an exact thermodynamic relationship in terms of soil temperature close to the pores:

$$\hat{\alpha} = \exp\left[\frac{g\ \Psi\ (\theta_e)}{10^3\ R_d\ T_s}\right], \tag{4.123}$$

where $R_d = 461.5\ [J\ kg^{-1}\ K^{-1}]$ is the gas constant for water vapor, $g\ [m\ s^{-2}]$ is the gravitational acceleration, $T_s\ [K]$ is the surface temperature, and $\Psi(\theta_e)\ [mm]$ is the soil water potential of a certain portion of soil with depth $d_e\ [mm]$ interested by the evaporation process. In numerical models, the soil water potential, $\Psi(\theta_e)$, represents the water potential in the first layer of soil considered, typically in the order of few millimeters. It must be noticed that the theoretical definition of $\hat{\alpha}$ in the Philip equation (4.123) is not a truly α method (*Kondo et al.*, 1990; *Oleson et al.*, 2008b). The relative humidity value, $\hat{\alpha}$, should be considered correspondent to the air adjacent to the water in the soil pore and not at the roughness height z_{ow}. This slight difference between $\hat{\alpha}$ and α is often misunderstood in literature. Other authors have proposed empirical relationships, for proper α methods, calculated for different soil types and depths (*Noilhan and Planton*, 1989; *Jacquemin and Noilhan*, 1990; *Wu et al.*, 2000). In "Tethys", the relative humidity of the air adjacent to the pores, $\hat{\alpha}$, is calculated with equation (4.123).

The β method to parameterize the soil moisture effect on E has been frequently used in land surface and hydrological models (*Deardorff*, 1978; *Kondo et al.*, 1990; *Cox et al.*, 1999; *Albertson and Kiely*, 2001; *Laio et al.*, 2001). In analogy to the other resistances described in this section, the $\beta(\theta_e)$ $[-]$ parameter can be expressed as a resistance to bare ground evaporation process. The soil resistance term, r_{soil} $[s\ m^{-1}]$, is related to $\beta(\theta_e)$ through:

$$\beta = \frac{r_a}{r_a + r_{soil}}, \tag{4.124}$$

where $r_{soil}\ [s\ m^{-1}]$ represents the resistance encountered from the water vapor to move from the free water in the soil to the roughness height z_{ow} (Figure 4.23). The parametrization for soil resistance, $r_{soil} = f(\theta_e)$, is taken from *Oleson et al.* (2008b):

$$r_{soil} = \exp\left[8.206 - 4.255\left(\frac{\theta_e - \theta_{hy}}{\theta_{sat} - \theta_{hy}}\right)\right]. \tag{4.125}$$

The dependence of r_{soil} on the soil moisture θ_e is shown in Figure 4.24a. In order to compute the soil moisture θ_e $[-]$ is necessary to define a characteristic soil depth for the evaporation process $d_e\ [mm]$. Both α and β methods depend strongly on the thickness of the soil layer assumed to calculate the soil moisture θ_e (*Wu et al.*, 2000).

Nonetheless, the same or similar relationships have been often used for different soil depths. The term d_e is thus important for the computation of the values of $\hat{\alpha}$ and r_{soil}. Furthermore, in the described model, the capillary effects are neglected in the soil moisture dynamic (Section: 4.7.3). Consequently, for the bare ground case the characteristic soil depth of the evaporation process, d_e, also determines the portion of soil that provides water mass for the evaporation. In bare soil once capillarity effects are neglected, no other mechanism is able to move upward soil water except evaporation. Therefore, it becomes fundamental an appropriate assumption for the value to assign to d_e. A recent theoretical study points out that the characteristic depths of the evaporation process can be estimated as a balance between gravitational and viscous forces and they depend on soil type, especially on particle size (*Lehmann et al.*, 2008). As the soil becomes coarser the characteristic depth affecting porous media decreases. *Lehmann et al.* (2008) found values of metrics assimilable to d_e between 90 and 140 $[mm]$ for coarse and fine sand respectively and they provide an equation to relate the characteristic depth of the drying front and parameters of the soil water retention curve (see Section 4.7.4). This approach, although very interesting, lacks empirical confirmations. Consequently, the soil depth interested by evaporation, d_e, is considered a calibration parameter specified a priori in the simulation. The qualitative dependence on the soil type, as detected from *Lehmann et al.* (2008) can be maintained providing larger d_e for fine soil textures.

Further comments are necessary to describe the behavior of β calculated with equation (4.125). The value of β is strongly influenced by the aerodynamic resistance r_a, as shown in Figure 4.24b. Using typical values of r_a, β assumes values lower than 1 also when the soil moisture is not a limiting factor. Such an outcome is highly unrealistic and differs from other approaches (*Mahfouf and Noilhan*, 1991; *Laio et al.*, 2001). The parametrization of equation (4.125) leaves a residual soil resistance $r_{soil} = 52\ [s\ m^{-1}]$ also in completely wetted condition $\theta_e = \theta_{sat}$. The influence of this residual resistance becomes larger as r_a magnitude decreases. Although suspicious, equation (4.125) is used to parameterize r_{soil}. Unfortunately, the physical process of bare ground evaporation and drying front formation is still not completely understood (*Shokri et al.*, 2009) and many caveats can be found in the empirical parameterizations. A general concern in the use of different soil resistance schemes exists among modelers (*Ivanov* 2008, personal communication).

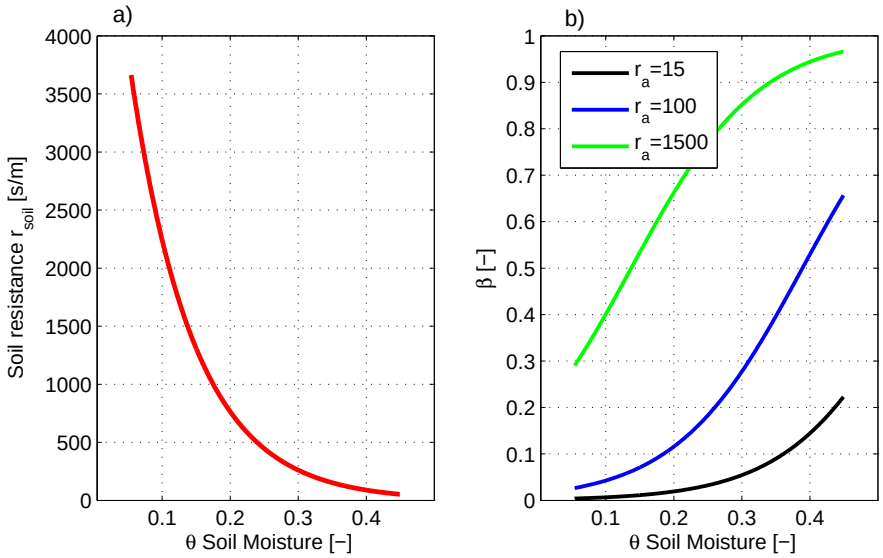

Figure 4.24: Values assumed by soil resistance r_{soil} and β parameter as a function of soil moisture, θ, for a sand loam soil. The graphs are obtained from equations 4.124 and 4.125.

4.4.5 Stomatal resistance and photosynthesis

In this Section the framework used to estimate stomatal resistance, r_s $[s\ m^{-1}]$, net assimilation rate, A_{nC} $[\mu mol\, CO_2\ s^{-1}\ m^{-2}]$, and dark respiration, R_{dC} $[\mu mol\, CO_2\ s^{-1}\ m^{-2}]$, is introduced . These quantities are calculated using a coupled model of photosynthesis and stomatal resistance. For computational reasons, simplification have been introduced in the biochemical model The conceptual assumptions to scale from unit leaf to unit canopy are also presented.

Canopy partition

In order to describe the fluxes of energy, water, and CO_2 across the vegetation is necessary to provide a partition of the canopy (*Dai et al.*, 2004). The scaling from what happens at the leaf-scale and what happens at the entire canopy scale, in terms of mass and energy fluxes is the results of several non-linear interactions. These interactions involve the energy absorbed, the leaf temperature, and the stomatal opening at different levels and fractions of the canopy. Processes, such as photosynthesis and transpiration depend non-linearly on absorbed solar radiation and temperature of leaves, and generally the entire radiative balance is affected by the canopy partition (*Sinclair et al.*, 1976). Seasonal and diurnal changes in solar zenith angle result in different exposures of canopy parts to sunlight and shadows, the canopy representation thus influences carbon uptake, transpiration, and energy partition. In scientific literature, canopy partition schemes have been mainly introduced within the modeling of photosynthesis and canopy radiative transfer processes. The existent approaches to make a partition of the canopy can be summarized in: "big-leaf" models: the canopy is considered as a single leaf, "two big-leaves" models: where the canopy is divided into sunlit and shaded leaves, and multi-layers models: where a complete description of the canopy structure is attempted.

The simplest approach is to model the canopy as a "big-leaf", where proper scaled quantities are used to calculate the fluxes over the entire canopy (*Farquhar*, 1989; *Sellers et al.*, 1996b; *Bonan*, 1996; *Friend et al.*, 1997; *Dickinson et al.*, 1998; *Oleson et al.*, 2004). The big-leaf models require assumptions about leaf properties along the vertical profile of the plant. Typically, the distribution of photosynthetic capacity of leaves is assumed to be in proportion with the profile of absorbed irradiance. The entire canopy photosynthesis is represented with the equations that describes single leaf photosynthesis (*Sellers et al.*, 1992a). This assumption is an analogy of what first proposed by *Farquhar* (1989). *Farquhar* (1989) demonstrated that the equation describing whole-leaf photosynthesis would have the same form as for individual chloroplasts across a leaf, when the distribution of chloroplast photosynthetic capacity is in proportion to the profile of absorbed irradiance and the shape of the response to irradiance is identical in all layers. Questioning this assumption, *de Pury and Farquhar* (1997) demonstrated that the optimal distribution of canopy nitrogen, which is in linear proportion with photosynthetic capacity is an invalid basis for the simplifications in big-leaf models. Instantaneous profiles of absorbed

irradiance in canopies, indeed, do not follow Beer's law because of both sunfleck penetration and leaf angles (*de Pury and Farquhar*, 1997). Since the distribution of absorbed irradiance is always changing, there cannot be a fixed distribution of photosynthetic capacity. For instance, this distribution cannot be optimal simultaneously for maximizing daily and instantaneous photosynthesis. Leaf photosynthetic capacity, in fact, reallocated between leaves on time scale larger than instantaneous irradiance variation (*de Pury and Farquhar*, 1997). Consequently, big-leaf models cannot be considered truly scaled models (*Raupach*, 1995). Furthermore, *Wang and Leuning* (1998) argue that photosynthesis of shaded leaves has an essentially linear response to absorbed PAR, while photosynthesis of sunlit leaves is often light saturated and so independent of absorbed PAR. Hence at least two different classes of leaves, sunlit and shaded, are necessary to reduce the error in the final predicted canopy photosynthesis. The partitioning of available energy and photosynthesis are also non-linearly related to the leaf temperature difference. Sunlit leaves can be several degrees warmer than shaded leaves, thus ignoring the temperature difference between sunlit and shaded leaves will bias the estimates of photosynthesis and heat fluxes for the canopy (*Wang and Leuning*, 1998). These canopy features can be explicitly incorporated by dividing the canopy into sunlit and shaded fractions and modeling each fraction separately in a "two big-leaves" model. These model are more complex than a big-leaf model, but it has been demonstrated that two-leaf approach is comparable to those of a multi-layers model and significantly better than those of big-leaf models (*de Pury and Farquhar*, 1997; *Wang and Leuning*, 1998; *Dai et al.*, 2004).

Finally, the most accurate and computationally expensive approaches are those that divide the canopy in multiple layers, where all the quantities are estimated independently for each layer and integrated to obtain the fluxes at the canopy scale (*Leuning et al.*, 1995; *Baldocchi and Harley*, 1995; *Baldocchi and Meyers*, 1998; *Pyles et al.*, 2000; *Baldocchi et al.*, 2002).

As explained in Section 4.2.5, "Tethys" uses only a single prognostic value of temperature for all the surface components (bare soil, low and high layers of vegetation, etc). Therefore, a separate treating of the assimilation rates and stomatal conductances for sunlit and shaded leave does not seem convenient, for both computational and congruence reasons. Although, as discussed above, such subdivision is scientifically supported and recommended. A big-leaf model assumption is made in order to compute the energy, mass, and carbon fluxes within the canopy. Consequently, the non-linear coupling between the energy budget and the photosynthesis/stomatal conductance is partially neglected (see also Section: 4.4.5).

It should be remarked that *Friend* (2001) discussing the feasibility of the big-leaf model, states that is theoretically consistent to use the big-leaf assumption to calculate photosynthesis and canopy carbon fluxes, especially when nitrogen and leaf area distributions within the canopy are unknown. In fact, accurate prediction of canopy carbon fluxes would require the knowledge of such distributions and a photosynthesis/stomatal model completely coupled with the energy and water fluxes.

Scaling of nitrogen

Profiles of leaf properties have led to the hypothesis that leaves adapt or acclimate to their radiation environment such that a plant nitrogen resources may be distributed to maximize daily canopy photosynthesis (*de Pury and Farquhar*, 1997). It has been further hypothesized that the optimal distribution of nitrogen occurs when the nitrogen is distributed in proportion to the distribution of absorbed irradiance in the canopy, averaged over the previous several days to a week, the time over which leaves are able to adapt.

The canopy nitrogen profile is assumed to decay exponentially controlled by a factor K_N $[-]$, in analogy with the penetration of the direct beam radiation in the canopy that is assumed to decay exponentially and controlled by a light extinction parameter $K'_{opt} = \frac{G(\mu)}{\mu}\sqrt{1-\omega_{vis}^{veg}}$ (see Section 4.2.2). Since the maximum photosynthetic capacity has been shown to depend linearly on leaf nitrogen content (*Schulze et al.*, 1994; *White et al.*, 2000; *Reich et al.*, 1997; *Wright et al.*, 2004), the distribution of nitrogen in the canopy is used to scale photosynthesis from leaf to canopy level. A scaling factor, F_N, is provided:

$$F_N \;=\; \int_0^{LAI} e^{-K_N\,x} dx \;=\; \frac{1-e^{-K_N\,LAI}}{K_N}\,. \tag{4.126}$$

The above coefficients is used to obtain the estimate of photosynthesis quantities scaled from leaf to canopy. It follows that the canopy maximum Rubisco capacity at $25°C$ V_{max} $[\mu mol\, CO_2\; s^{-1}\; m^{-2}]$ is:

$$V_{max} \;=\; F_N\; V_{max}^L\;. \tag{4.127}$$

where V_{max}^L $[\mu mol\, CO_2\; s^{-1}\; m^{-2}]$ is the maximum Rubisco capacity at $25°C$ at leaf scale. Theoretically, another quantity, the maximum electron transport capacity at $25°C$, J_{max}^L $[\mu mol\, Eq\; s^{-1}\; m^{-2}]$, should be also scaled from leaf to canopy (*Wang and Leuning*, 1998; *Dai et al.*, 2004). Since, J_{max}^L depends on V_{max}^L (*Kattge and Knorr*, 2007), its scaling is implicit on V_{max}.

Biochemical model of photosynthesis and stomatal aperture

Plant metabolism is based on the photosynthetic reaction, in which photosynthetically active shortwave radiation energy is used to combine water and atmospheric CO_2 into sugars and other organic compounds. In order to achieve this task, plants must allow for the transfer of CO_2 from the atmosphere to the cellular sites of photosynthesis located inside the leaves. This flow requires an open pathway between the atmosphere and the water-saturated tissues inside the leaf, which leads to an inevitable loss of water vapor over the same route (*Sellers et al.*, 1997). The opening of this pathway is regulated by stomatal aperture. The complex mechanisms of stomatal movement depend on both plant physiology and environmental factors (*Daly et al.*, 2004; *Buckley*, 2005). A complete mechanistic model for their functioning has not been developed so far, although from the early eighties several

biochemical models have been proposed and the subject is still an area of active research (*Jones*, 1998; *Jarvis and Davies*, 1998; *Dewar*, 2002; *Gao et al.*, 2002; *Katul et al.*, 2003; *Tuzet et al.*, 2003; *Buckley et al.*, 2003; *Sperry et al.*, 2002; *Buckley*, 2005; *Zweifel et al.*, 2007; *Vico and Porporato*, 2008). For this reason simplified or empirical approaches are usually employed (*Daly et al.*, 2004). The driving factor is that plants control the opening of the stomata to regulate the CO_2 uptake for the photosynthesis process and in this transit transpiration occurs and thus plants lose water. The stomatal opening can be seen as a compromise between the necessity to maintain turgor and reduce dehydration as well as to control leaf temperature and at the same time to maximize carbon assimilation (*Sellers et al.*, 1997).

Three general approaches can be distinguished for stomatal aperture and photosynthesis modeling. First, the modeling of photosynthate production without treatment of leaf photosynthesis methods, for instance with prescribed value for light use efficiency, water use efficiency or use carbon assimilation (*Anderson et al.*, 2000; *LeRoux et al.*, 2001; *Arora*, 2002). Second, the use of empirical function correlating stomatal aperture to environmental factor, usually this approach is named as Jarvis-type (*Lhomme*, 2001), and third the use of explicit biochemical models (*Sellers et al.*, 1997; *Farquhar et al.*, 2001; *Daly et al.*, 2004).

In order to avoid the use of biochemical models, empirical equations have been often used to calculate stomatal conductance, g_s $[m\ s^{-1}]$. The latter use a product of functions of environmental conditions that exert a control on photosynthesis, such an approach is named Jarvis's type from the work of *Jarvis* (1976). The main assumption in Jarvis's type models is that the environmental control on stomatal aperture are independent each other, thus the total control is provided by the products of single functions:

$$g_s \;=\; g_{s,max} f(PAR_{abs}) f(T_V) f(\Delta e) f(\theta_R) f(CO_2) f(e_{rel}) f(N)\,, \tag{4.128}$$

where $g_{s,max}$ $[m\ s^{-1}]$ is the maximum stomatal conductance when all the other functions are equal to one. The variable PAR_{abs} is the absorbed photosynthetically active radiation, T_v is the leaf temperature, Δe is the vapor pressure deficit, θ_R is the soil moisture in the root zone, e_{rel} is a relative photosynthetic efficiency, CO_2 and N are general dependencies on CO_2 concentration and nutrients. Equation (4.128) captures the important responses of leaf stomata to the environment an it has been widely used in stomatal aperture modeling (*Jarvis*, 1976; *Noilhan and Planton*, 1989; *Schulze et al.*, 1994; *Sellers et al.*, 1997; *Lhomme et al.*, 1998; *Lhomme*, 2001; *LeRoux et al.*, 2001; *Daly et al.*, 2004). Specifically, g_s increases with PAR_{abs} monotonically from near zero at $PAR_{abs} = 0$ to an asymptote at high light levels, where the process becomes light saturated. The stomatal aperture is sensitive to humidity, almost all plants maintain open the stomata in humid air, when CO_2 can be taken up freely with a relatively small loss of leaf water vapor (*Sellers et al.*, 1997). As the external air dries, the stomata progressively close, and $f(\Delta e)$ decreases, presumably to protect the leaf from desiccation and to conserve water. The temperature dependent function, $f(T_V)$, reaches a maximum around the mean environmental growing

season temperature and tapers off to zero for warmer or cooler temperatures. This action is related to the enzyme kinetics of photosynthesis and conductance, which have been "tuned" through evolution to work efficiently at particular temperatures (*Sellers et al.*, 1997). The soil moisture dependent function, $f(\theta_R)$, takes into account that stomata tend to close when the root soil moisture θ_R decreases below a certain threshold and becomes limiting. The $f(CO_2)$ function expresses the dependance on CO_2 concentration, and $f(e_{rel})$ on leaf age. Stomata tend to close when a larger amount of carbon dioxide is available, moreover photosynthetic capacity and thus stomatal aperture seems to decrease with senescence (*Nouvellon et al.*, 2000; *Wilson et al.*, 2001; *Medvigy et al.*, 2009). Finally, $f(N)$ accounts for nitrogen limitations. It should remarked that commonly only the first four limitation factors are taken into account, as originally proposed by *Jarvis* (1976).

Notwithstanding their great popularity, Jarvis's type model have a great shortcoming, they do not provide a direct estimation of carbon assimilation process. Although, indirect evaluations of carbon assimilation based on Jarvis's type model have been proposed considering the linear relationship between net assimilation rate and stomatal conductance, g_s, (*Thornley*, 1991; *Nouvellon et al.*, 2000; *LeRoux et al.*, 2001; *Montaldo et al.*, 2005). Nonetheless, biochemical models show consistently better performances compared to the Jarvis-type schemes (*Niyogi and Raman*, 1997), for this reason in "Tethys" a biochemical model is used to describe the coupling between photosynthesis and stomatal resistance. Simplifications are introduced in order to reduce computational efforts and to account for the limitations imposed by the single prognostic temperature (Section 4.2.5).

Computational requirements of biochemical model of photosynthesis are typically elevated. There is, indeed, the necessity to solve iteratively for stomatal resistance, r_s, inside the non-linear numerical scheme used to determine leaf temperature or equivalently the surface temperature T_s (see Section 4.3.5). A complete coupling between energy, water, and carbon mass transfers requires large computational resources. Such a complex picture is partially simplified also in state of art land-surface models (*Bonan*, 1996; *Oleson et al.*, 2004). In the biochemical component of "Tethys", leaf temperature, T_v, is approximated with air temperature, T_a, and the value of aerodynamic resistance, r_a, that depends implicitly on surface temperature, is approximated with neutral aerodynamic resistance as explained later in this section.

Biochemical models of leaf photosynthesis describe assimilation by chloroplasts or leaves as rate-limited by enzyme kinetics. Specifically, the amount and cycle time of the carboxylating enzyme Rubisco, the electron transport and the efficiency of the leaf's light-intercepting apparatus (chlorophyll) are considered as limiting factors (*Farquhar et al.*, 1980; *vonCaemmerer and Farquhar*, 1981; *Collatz et al.*, 1991, 1992; *Farquhar and Wong*, 1984; *Farquhar et al.*, 2001). The biochemical model of canopy photosynthesis implemented within "Tethys" is based on *Farquhar et al.* (1980); *Collatz et al.* (1991, 1992) with some modification based on *Leuning* (1995); *Sellers et al.* (1996b); *Dai et al.* (2004); *Kattge and Knorr* (2007). The model describes the

net and gross photosynthetic rates, A_{nC}, A_C [$\mu mol\, CO_2\ s^{-1}\ m^{-2}$], as a function of three limiting rates (J_c, J_e and J_s). These rates describe the assimilation as limited by the efficiency of the photosynthetic enzyme system (Rubisco-limited), J_c, the amount of PAR captured by the leaf chlorophyll, J_e, that depends on turn on the the electron transport rate, J_{max}, and the capacity of the leaf to export or utilize the products of photosynthesis (triose phosphates), J_s, for C3 plants or PEP-carboxylase, J_s, for C4 plants.

The RuBP-carboxylase (Rubisco enzyme) limited carboxylation rate is formulated as:

$$J_c = V_m \left[\frac{c_i - \Gamma^*}{c_i + K_c(1 + O_i/K_o)} \right], \quad \text{for } C_3\,, \tag{4.129}$$

$$J_c = V_m\,, \quad \text{for } C_4\,. \tag{4.130}$$

The maximum rate of PAR captured by the leaf chlorophyll (i.e., the light limited rate) is:

$$J_e = J \left[\frac{c_i - \Gamma^*}{c_i + 2\Gamma^*} \right], \quad \text{for } C_3\,, \tag{4.131}$$

$$J_e = J\,, \quad \text{for } C_4\,, \tag{4.132}$$

where J is the smaller root of the quadratic equation:

$$\alpha_J J^2 - (PPFD + \frac{J_m}{4})\, J + PPFD\, \frac{J_m}{4}\,. \tag{4.133}$$

The export limited rate of carboxylation (for C_3 plants) and the PEP-carboxylase limited rate of carboxylation (for C_4 plants) are:

$$J_s = 0.5\, V_m\,, \quad \text{for } C_3\,, \tag{4.134}$$

$$J_s = 20000\, V_m \frac{c_i}{P_{atm}}\,, \quad \text{for } C_4\,. \tag{4.135}$$

In the above equations, c_i and O_i [Pa] are the partial pressures of CO_2 and O_2 in leaf interior, respectively. The quantity $PPFD = \epsilon\, \beta_Q\, PAR_{abs}$ [$\mu mol\, CO_2\ s^{-1}\ m^{-2}$] is the photosynthetic photon flux density, ϵ [$\mu molCO_2\ \mu mol^{-1}\, photons$] is the intrinsic quantum efficiency, and β_Q [$\mu mol\, photons\ J^{-1}$] is a quanta-to-energy converting factor between the measurement units, that depends on the wavelength, λ, and thus on the type of radiation. *Dye* (2004) shows that a value of $\beta_Q = 4.56$ can be employed for a wide range of cloud conditions with little or no error. The term PAR_{abs} [$W\ m^{-2}$] is the absorbed photosynthetically active radiation at canopy level calculated in Section 4.2.1 and α_J [$-$] is a shape parameter taken equal to $\alpha_J = 0.7$ as in *Bonan* (2002). The value of the intrinsic quantum efficiency, ϵ, depends on the photosynthesis pathway (C3, C4 or CAM plants). There are arguments about its variability among different plants (*Skillman*, 2008) but operational values of $\epsilon = 0.081$ [$\mu molCO_2\ \mu mol^{-1}\, photons$] for C3 and $\epsilon = 0.040$ [$\mu molCO_2\ \mu mol^{-1}\, photons$] are typically used (*Farquhar et al.*, 1980; *Collatz et al.*, 1991, 1992; *Cox*, 2001; *Arora*, 2002). Refer to *Öquist and Chow* (1992) and *Singsaas et al.* (2001) for a discussion

on ϵ.

The variables V_m [$\mu mol\, CO_2\ s^{-1}\ m^{-2}$] and J_m [$\mu mol\, Eq\ s^{-1}\ m^{-2}$] are the maximum Rubisco capacity and maximum electron transport capacity at canopy scale, respectively, after accounting for temperature dependence. The parameter Γ^* [Pa] is the CO_2 compensation point (*Sellers et al.*, 1996b; *Cox*, 2001; *Dai et al.*, 2004):

$$\Gamma^* = \frac{0.5\, O_i}{2600\ \left[0.57^{0.1(T_v-25)}\right]}\ , \tag{4.136}$$

where T_v [$^\circ C$] is the leaf temperature. The constant K_c and K_o [Pa] are the Michaelis-Menten constants for CO_2 and O_2, respectively, expressed as functions of leaf temperature, T_v [$^\circ C$], (*Leuning*, 1995; *Dai et al.*, 2004):

$$K_c = 30\ \left[2.1^{0.1(T_v-25)}\right]\ , \tag{4.137}$$

$$K_o = 30000\ \left[1.2^{0.1(T_v-25)}\right]\ . \tag{4.138}$$

The dependence of maximum catalytic capacity of Rubisco, V_m, on temperature, T_v, is accounted for with the equation provided by *Kattge and Knorr* (2007) who analyzed 36 different plants under various conditions (see also *Medlyn et al.* (2002)):

$$V_m = V_{max}\ \exp\Big[\frac{H_a(T_v - T_{ref})}{(T_{ref}\, R\, T_v)}\Big]\frac{1 + exp\left(\frac{T_{ref}\Delta S - H_d}{T_{ref}\, R}\right)}{1 + exp\left(\frac{T_v\Delta S - H_d}{T_v\, R}\right)}\ , \tag{4.139}$$

where $R = 8.314$ [$J\ mol^{-1}\ K^{-1}$] is the universal gas constant, V_{max} [$\mu mol\ CO_2\ m^{-2}\ s^{-1}$] is the value of maximum Rubisco capacity at $25^\circ C$, H_a [$kJ\ mol^{-1}$] is the activation energy, H_d [$kJ\ mol^{-1}$] is the deactivation energy. The deactivation energy, H_d, is generally assumed constant, $H_d = 200$ [$kJ\ mol^{-1}$] and describes the rate of decrease above the optimum temperature. The term ΔS [$kJ\ mol^{-1}\ K^{-1}$] is the so-called entropy factor, $T_{ref} = 273.15$ [K] is a reference temperature, and T_v [K] is in Kelvin.

Kattge and Knorr (2007) suggest for general application $H_a = 72$ [$kJ\ mol^{-1}$] and $\Delta S = 0.649$ [$kJ\ mol^{-1}\ K^{-1}$]. More generally, these quantities are species dependent with typical ranges of $H_a = 45 - 90$ [$kJ\ mol^{-1}$] and $\Delta S = 0.635 - 0.665$ [$kJ\ mol^{-1}\ K^{-1}$]. Their value influences the shape of the temperature dependent function as shown in Figure 4.25.

The parametrization of *Kattge and Knorr* (2007) improves the biochemical models of photosynthesis in comparison to use a Q_{10} function to account for temperature effects on photosynthesis (*Collatz et al.*, 1991). Besides, the parameter H_a and ΔS are physically meaningful, and not purely adjustment factors as the upper and lower temperature constraints proposed by (*Sellers et al.*, 1996a; *Cox*, 2001). Note also that the shape of the temperature dependent functions, shown in Figure 4.25, are similar to empirical equations of parameterizations of stomatal conductance temperature dependence (*Jarvis*, 1976; *Lhomme et al.*, 1998; *Nouvellon et al.*, 2000; *Matsumoto et al.*, 2005).

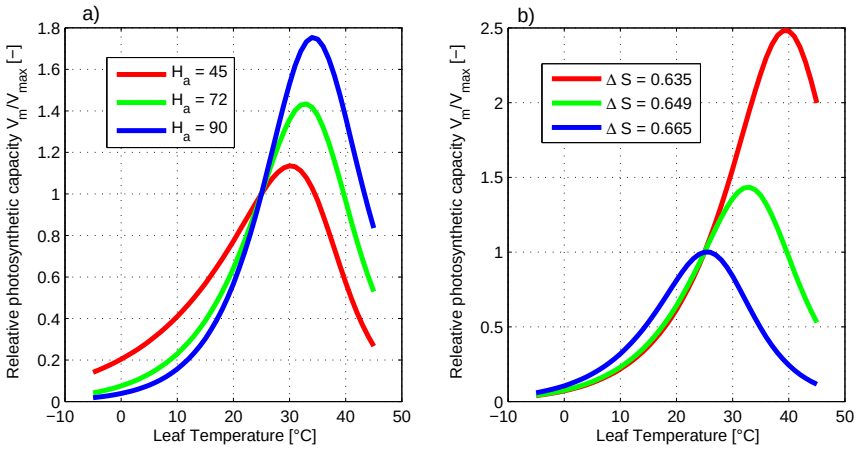

Figure 4.25: Values of relative maximum Rubisco capacity, V_m/V_{max}, function of leaf temperature, T_v [$°C$], for different values of activation energy, H_a [$kJ\ mol^{-1}$] with $\Delta S = 0.649$ (a), and entropy factor ΔS [$kJ\ mol^{-1}\ K^{-1}$] with $H_a = 72$ (b).

The maximum electron transport capacity, J_m [$\mu mol\ Eq\ s^{-1}\ m^{-2}$] is also computed as in *Kattge and Knorr* (2007):

$$J_m \;=\; J_{max}\,\exp\Big[\frac{H_a(T_v - T_{ref})}{(T_{ref}\,R\,T_v)}\Big]\,\frac{1 + exp\left(\frac{T_{ref}\Delta S - H_d}{T_{ref}\,R}\right)}{1 + exp\left(\frac{T_v\Delta S - H_d}{T_v\,R}\right)}\,, \tag{4.140}$$

where J_{max} [$\mu mol\ Eq\ s^{-1}\ m^{-2}$] is the maximum electron transport capacity at $25°C$ and the other symbols have been previously defined. *Kattge and Knorr* (2007) suggest for general application to use $H_a = 50$ [$kJ\ mol^{-1}$], $\Delta S = 0.646$ [$kJ\ mol^{-1}\ K^{-1}$], and $J_{max} = r_{jv}\,V_{max}$ [$\mu mol\ Eq\ s^{-1}\ m^{-2}$], with $r_{jv} = 1.97$ [$\mu mol\ Eq\ \mu mol\ CO_2^{-1}$].

The transition from one to another limiting rate (J_c, J_e, and J_s) is not abrupt. The coupling between the three processes leads to smooth curves. *Collatz et al.* (1991) describe this effect by combining the rate terms into two quadratic equations, which are then solved for their smaller roots:

$$\begin{aligned} \alpha_{ce} J_p^2 - J_p(J_c + J_e) + J_e J_c \;&=\; 0\,, \\ \alpha_{ps}(A^*)^2 - A^*(J_p + J_s) + J_p J_s \;&=\; 0\,, \end{aligned} \tag{4.141}$$

where J_p [μmol CO_2 m^{-2} s^{-1}] is the smoothed minimum of J_c and J_e, A^* [μmol $CO_2\,m^{-2}\,s^{-1}$] is the gross assimilation rate for unit canopy before accounting for moisture stress, α_{ce} and α_{ps} are the coupling coefficients. From *Sellers et al.* (1996a): $\alpha_{ce} = 0.98$, $\alpha_{ps} = 0.95$.

The net assimilation rate at canopy scale, A_{nC} [μmol CO_2 m^{-2} s^{-1}], is then given by:

$$A_{nC} \;=\; A_C - R_{dC}\,, \tag{4.142}$$

where $A_C = \beta_R\,A^*$ [μmol CO_2 m^{-2} s^{-1}] is the gross assimilation rate with β_R a soil moisture stress factor. The term R_{dC} [μmol CO_2 m^{-2} s^{-1}] is the leaf (dark)

respiration estimated following *Collatz et al.* (1991, 1992) as:

$$R_{dC} = 0.015\, V_{max}\, 2.0^{0.1(T_v-25)}\, f_2(T_v)\,, \quad \text{for } C_3\,, \tag{4.143}$$

$$R_{dC} = 0.025\, V_{max}\, 2.0^{0.1(T_v-25)}\, f_2(T_v)\,, \quad \text{for } C_4\,, \tag{4.144}$$

where $f_2(T_v)$ is a temperature inhibition function:

$$f_2(T_v) = \left[1 + e^{1.3\,(T_v-55)}\right]^{-1}\,. \tag{4.145}$$

Note that recent evidences suggest that the relation between leaf (dark) respiration, R_d, and temperature, T_v, is more complex, since the Q_{10} coefficient depends on temperature and acclimation effects may play an important role (*Tjoelker et al.*, 2001; *Wythers et al.*, 2005).

The factor β_R that limits canopy photosynthesis according to root zone soil moisture availability is introduced to reproduce the soil moisture control on transpiration as observed from experimental evidences (*Kurc and Small*, 2004; *Wullschleger and Hanson*, 2006). The equation used to compute the soil moisture stress factor, β_R $[-]$, is assumed to be very simple (*Bonan*, 1996; *Montaldo et al.*, 2005; *Ivanov et al.*, 2008a):

$$\beta_R = \max\left[0, \min\left(1, \frac{\theta_R - \theta_{wp}}{\theta_{ss} - \theta_{wp}}\right)\right]\,, \tag{4.146}$$

where θ_R $[-]$ is the soil moisture in the root zone (Section 4.7.3), and θ_{ss}, θ_{wp} $[-]$ are the soil moisture contents at the beginning of stomatal closure and at the complete stomatal closure, respectively. Other studies substitute the soil moisture water content, θ, with the correspondent water potential, Ψ (*Jarvis*, 1976; *Dai et al.*, 2004; *Daly et al.*, 2004). This produces different results, since the relationship $\Psi = f(\theta)$ is non-linear (Section: 4.7.4). Notwithstanding, the relationship described in equation (4.146) is only a proxy of the entire soil-root-xylem-leaf transfer process that controls stomatal aperture and photosynthesis and that it is still not completely understood (*Feddes et al.*, 2001; *Sperry et al.*, 2003; *Sack and Holbrook*, 2006). Attempts to consider carbon and water transfer in the soil-plant-atmosphere continuum in a more mechanistic fashion have been proposed (*Tuzet et al.*, 2003; *Buckley et al.*, 2003; *Katul et al.*, 2003; *Bohrer et al.*, 2005; *Verbeeck et al.*, 2007; *Vico and Porporato*, 2008). These studies point to reduce the empiricism and explicitly compute the leaf water potential, Φ_L $[kPa]$, or whole plant hydraulic control on stomata. Given the large number of parameters required from such approaches, the use of β_R is still preferred in this version of "Tethys". Note, that the factor β_R is applied to the assimilation rate, A^*, as proposed by *Daly et al.* (2004) and not to the maximum Rubisco capacity, V_m, as proposed by other authors (*Ivanov et al.*, 2008a).

The aperture of stomata has been experimentally shown to be related to net assimilation rate of CO_2, A_{nC}, environmental vapor pressure deficit, Δe $[Pa]$, and intercellular CO_2 concentration c_i $[Pa]$ (*Gao et al.*, 2002). Several empirical equations to calculate stomatal conductance have been proposed in literature (*Ball et al.*, 1987;

Tardieu and Davies, 1993; *Leuning*, 1990, 1995; *Tuzet et al.*, 2003). See also *Niyogi and Raman* (1997); *Dewar* (2002) for comparisons. All the empirical stomatal conductance relationships give a linear dependence between the net assimilation rate, A_{nC}, and stomatal conductance g_{s,CO_2}, while the other dependencies can change. In "Tethys" the equation proposed by *Leuning* (1990, 1995) is used:

$$g_{s,CO_2} = g_0 + a\frac{A_{nC}}{(c_i - \Gamma^*)} f(\Delta e)\, P_{atm}\,, \tag{4.147}$$

where g_{s,CO_2} $[\mu molCO_2\ m^{-2}\ leaf\ s^{-1}]$ is the stomatal conductance, $g_{s,CO_2} = 1/r_{s,co_2}$, a $[-]$ is an empirical parameter, Γ^* $[Pa]$ is the CO_2 compensation point, P_{atm} $[Pa]$ is the atmospheric pressure, and g_0 $[\mu mol\, CO_2\ m^{-2}\, leaf\ s^{-1}]$ is the cuticular conductance or minimum stomatal conductance when $A_{nC} \leq 0$. Measurements of g_0, i.e. when stomata are completely closed, are almost impossible to obtain in the field (*White et al.*, 2000). In biochemical models values of $g_{0,CO_2} = 0.01 - 0.04$ $[mol\, CO_2\ s^{-1}\ m^{-2}]$ are typically used (*Leuning*, 1995; *Sellers et al.*, 1996b) and are taken as a reference also in "Tethys".

The function that expresses sensitivity to vapor pressure deficit, $f(\Delta e)$, takes the form:

$$f(\Delta e) = \left(\frac{1}{1 + \Delta e/\Delta_0}\right), \tag{4.148}$$

where Δe $[Pa]$ is the vapor pressure deficit and Δ_0 $[Pa]$ is an empirical coefficient that represents the value of vapor pressure deficit at which $f(\Delta e) = 0.5$.

Equation (4.147) takes into account the correction of *Tuzet et al.* (2003) where the CO_2 concentration at the leaf surface, c_s $[Pa]$, is replaced by the leaf internal concentration, c_i $[Pa]$, that agrees better with observed stomatal response (*Assmann*, 1999; *Dewar*, 2002). Correct parameterizations of equation (4.147) provide close agreement between simulated and observed stomatal conductance and carbon assimilation rates (*Gao et al.*, 2002).

The photosynthesis rates and stomatal conductance depend on leaf interior partial pressure of CO_2, c_i $[Pa]$ that, a priori, is an unknown. A iterative procedure is thus required to estimate c_i. The determination of c_i can be formulated as a problem of finding the zero of a non-linear equation, once the resistance scheme between leaf interior and atmosphere is accounted for as shown in Figure 4.26. The correspondent equation in terms of carbon fluxes is:

$$A_{nC} = \frac{c_a - c_i}{P_{atm}\,(1.64\,\widehat{r_s} + 1.37\,\widehat{r_b} + r_a)} \tag{4.149}$$

where c_a $[Pa]$ is the atmospheric CO_2 concentration, the coefficients 1.37 and 1.65 are the ratios between the resistances of CO_2 and of water vapor for the leaf boundary layer resistance, $r_{b,CO_2}/r_{b,H_2O} = 1.37$, and stomatal resistance, $r_{s,CO_2}/r_{s,H_2O} = 1.64$, respectively (*vonCaemmerer and Farquhar*, 1981). The ratio between stomatal resistances corresponds exactly to the inverse of molecular diffusivity ratio between CO_2 and H_2O (see table 4.1). This follows from the diffusive nature of fluxes within

the leaf. The ratio between leaf boundary resistances is an intermediate value between laminar and turbulent inverse diffusivity ratios. Finally, since the transfer of carbon through aerodynamic surface layer is completely turbulent, $r_{a,CO_2} = r_{a,H_2O}$ (*Jones*, 1983). Note that when the subscript CO_2, or H_2O, is omitted the value refer always to water vapor. The quantity $\widehat{r_s}$ is already scaled to canopy level, the stomatal resistance for unit of leaf is $r_s = LAI\ \widehat{r_s}$ $[s\ m^{-1}]$. The same consideration holds true for leaf boundary resistance, i.e., $\widehat{r_b} = r_b/LAI$.

When the biochemical model is used to solve photosynthesis in one of the PFT belonging to a low-vegetation (L_v) layer surmounted by high vegetation (H_v), an undercanopy resistance, r'_a, must be added to equation (4.149). The introduction of this further resistance is shown in Figure 4.26. The solution of the non-linear equation that involves c_i to compute stomatal aperture and assimilation rate is realized with the *Matlab* command *fzero*. Further details about the numerical function are provided in Section 4.3.5.

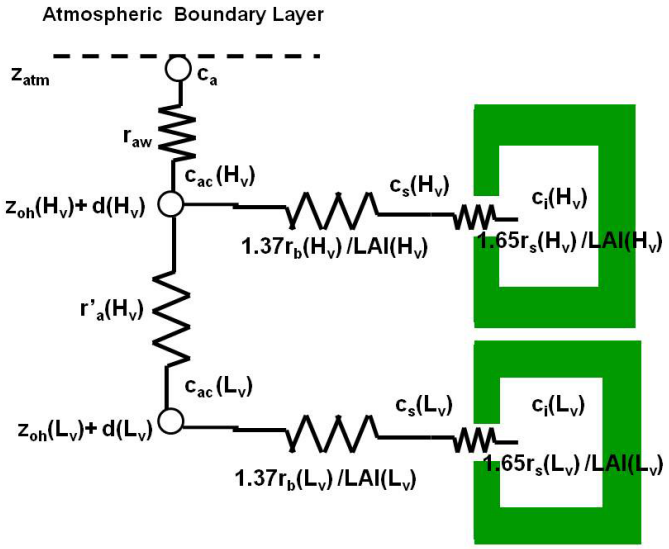

Figure 4.26: Diagram of the resistance scheme for CO_2 transfer from the leaf interior to the atmospheric surface layer for high and low vegetation layers. The variables c_a, c_{ac}, c_s, and c_i are the atmospheric, canopy space, leaf surface, and leaf interior CO_2 concentrations, respectively. The other variables are defined in the text.

The resistances of equation (4.149) are expressed in biochemical units of $[m^2\ s\ \mu mol^{-1}\ CO_2\ ]$. The conversion to common units $[s\ m^{-1}]$ is obtained using the following equation (*Sellers et al.*, 1996b):

$$r_x(s\ m^{-1}) \quad = \quad \frac{1}{0.0224}\frac{T_f\ P_{atm}}{(T+273.15)P_{atm,0}}10^6 r_x(m^2\ s\ \mu mol^{-1}\ CO_2)\,, \quad (4.150)$$

where P_{atm} $[Pa]$ is the atmospheric pressure, $P_{atm,0} = 101325$ $[Pa]$ is the reference atmospheric pressure, $T_f = 273.15$ $[K]$ is the freezing temperature, T $[^\circ C]$ is the leaf temperature for r_s or air temperature for r_b and r_a, and $r_x(\diamond)$ is a generic resistance with unit of measurements $(\diamond)$.

The leaf temperature, T_v, that represents the reference value for the temperature

of vegetation, is not explicitly calculated in "Tethys". For computational reasons only a single prognostic temperature is simulated. In this conditions, T_v is replaced with an approximate value. The radiative surface temperature, T_s, can be a proxy to replace T_v, unfortunately this value can differ significantly from T_v, especially when a basic computational element has a small vegetated fraction. In order to avoid unrealistic values of leaf temperature, T_v is approximated with the air temperature at the reference height, T_a. Such an approximation is justified by the fact that larger values of T_v enhance the sensible heat flux, that in turn gets warmer the surrounding air. Ultimately, the air temperature can be influenced by the vegetation temperature through feedback processes. Furthermore, replacing T_v with T_a, allows another simplification. The aerodynamic resistance, r_a, of equation (4.149) is calculated for neutral conditions (see Appendix C.2). The simplificative assumption described above permits to solve for photosynthesis and stomatal resistance outside the non-linear equation used to calculate the surface temperature, T_s. Such an approach diminishes the computational effort and is the reason why the approximation of T_v with T_a in the computation of stomatal resistance has been often used (*Noilhan and Planton*, 1989; *Nouvellon et al.*, 2000; *Daly et al.*, 2004; *Montaldo et al.*, 2005).

A fundamental parameter in the biochemical model is the maximum Rubisco capacity at $25°C$, V_{max} [μmol CO_2 m^{-2} s^{-1}]. Figure 4.27 provides an illustration of the sensitivity to this parameter. The maximum photosynthetic capacity, A_{max} [$\mu mol\, CO_2$ s^{-1} m^{-2}], i.e. the gross assimilation rate, A_C, for optimal conditions, and the minimum stomatal resistance, $r_{s,min}$ [s m^{-1}], are plotted against V_{max}. These quantities represent the rate of photosynthesis and the inverse of stomatal conductance when all the environmental conditions are non-limiting. The values obtained with the biochemical model described in this section are comparable to other modeling studies and direct measurements. The sensitivities of A_{max} and $r_{s,min}$ to two parameters, the atmospheric CO_2 concentration, c_a [ppm], and the empirical coefficient, a [$-$], that indicates the magnitude of the linear linkage between assimilation rate and stomatal conductance are shown in Figure 4.27.

The evaluation of photosynthetic capacity and stomatal response to c_a is important in understanding the sensitivity of the model. Although, the currently annual average value of $c_a = 387$ [ppm] ($= 387 \times 10^{-6}\, P_{atm}$ [Pa]) is similar all around the world, its value is continuously increasing and expected to further growth in the next decades due to greenhouse gas emissions. Understanding the consequences of an increase in c_a in the photosynthetic activity deserves a special attention (*Jarvis et al.*, 1999). As shown in Figure 4.27 such an increase sensibly enhances the productivity of the plants, without particularly influencing the stomatal aperture process. This implies that the plant water use efficiency, $WUE = A_C/T$, [$\mu mol\, CO_2$ s^{-1} m^{-2}]/[mm h^{-1}], i.e. the capacity of a plant to exploit water to photosynthesize will be higher in the future. A greater concentration of CO_2 allows to photosynthesize more carbon compounds with the same stomatal opening and thus potentially with the same transpiration rate. The sensitivity analysis to the coefficient a, instead, underlines as a exerts a direct control on plant water use effi-

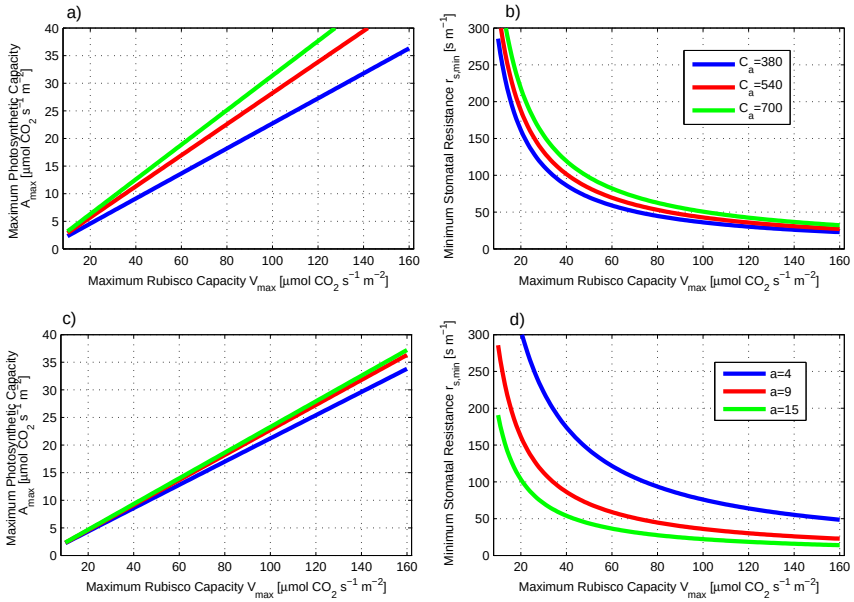

Figure 4.27: Values of maximum photosynthetic capacity, A_{max}, and minimum stomatal resistance, $r_{s,min}$, function of V_{max}. A sensitivity analysis to atmospheric CO_2 concentration, c_a $[ppm]$, and to the empirical coefficient, a $[-]$, is shown. The graphics are calculated with $LAI = 1$ $[-]$, $\epsilon = 0.081$ $[\mu molCO_2\ \mu mol^{-1}\ photons]$, $H_a = 72$ $[kJ\ mol^{-1}]$, $\Delta S = 0.649$ $[kJ\ mol^{-1}\ K^{-1}]$ for a C3 plant; $a = 9$ $[-]$ in the subplots (a) and (b); $c_a = 380$ $[ppm]$ in the subplots (c) and (d).

ciency, WUE. Lower values of a indicate a better capacity to use water to construct assimilation products. Similar photosynthetic capacities, A_{max}, are obtained with larger minimum stomatal resistances, $r_{s,min}$, thus with lower transpiration rates. This means that the value of a can be regarded as a specie dependent characteristic of water use efficiency.

The calculated values of A_{max} can be compared with values reported in literature. For instance *Reich et al.* (1997, 1998a) provide a wider overview of observed values, although it is always difficult that observed values of A_{max} would be not influenced by some limiting factor. Notwithstanding, observed A_{max} values are around 5-20 $[\mu mol\, CO_2\ s^{-1}\ m^{-2}]$, with higher values for deciduous plants than for evergreen. V_{max} and thus A_{max} are, in fact, positively correlated with the leaf nitrogen content and specific leaf area, typically lower in evergreen species and negatively correlated with leaf life span that is typically longer in evergreen species (see Chapter 5 for further details). Measurement of $r_{s,min}$ are also available for comparisons. *White et al.* (2000) stated that for natural vegetation types $r_{s,min}$ is remarkably similar across different species and proposed a constant value $r_{s,min} = 166$ $[s\ m^{-1}]$ following the study of *Kelliher et al.* (1995), who provided also a value for crops $r_{s,min} = 83$ $[s\ m^{-1}]$. *Montaldo et al.* (2005) used $r_{s,min} = 180$ $[s\ m^{-1}]$, *Viterbo and Beljaars* (1995) $r_{s,min} = 240$ $[s\ m^{-1}]$, *Schulze et al.* (1994) found values in the range $r_{s,min} = 80 - 250$ $[s\ m^{-1}]$ across different species. Sometimes also lower $r_{s,min}$ are used (*Lhomme et al.*, 1998; *Daly et al.*, 2004). As can be observed in Figure 4.27, the

proposed biochemical model reproduces the typical range of values both for $r_{s,min}$ and A_{max}, as available in the scientific literature.

The influence of c_a on photosynthesis and stomatal responses is further investigated in Figure 4.28 where the behavior of the net assimilation rate, A_{nC}, stomatal resistance, r_s, and leaf interior CO_2 concentration, c_i, are shown. Results confirm the strong influence of c_a on net assimilation rate up to a certain atmospheric CO_2 concentration, identifiable as three times the present atmospheric concentration. Stomatal resistance tends to increase linearly with c_a underlying the higher WUE obtainable in a CO_2 richer world, the ratio c_i/c_a is instead fairly constant across a wide range of CO_2 concentrations.

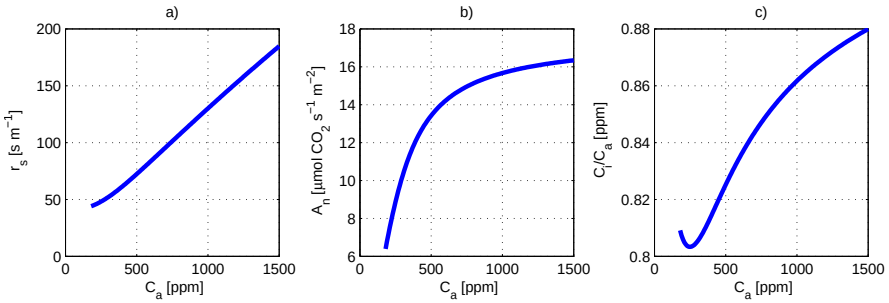

Figure 4.28: Sensitivity analysis of net assimilation rate, A_{nC}, stomatal resistance, r_s, and leaf interior CO_2 concentration, c_i, to atmospheric CO_2 concentration, c_a $[ppm]$. The relationships are calculated for a C3 plant in well watered conditions with $LAI = 1$ $[-]$, $T_v = 25$ $[°C]$, $\Delta e = 0$ $[Pa]$, $\epsilon = 0.081$ $[\mu molCO_2\ \mu mol^{-1}\, photons]$, $H_a = 72$ $[kJ\ mol^{-1}]$, $\Delta S = 0.649$ $[kJ\ mol^{-1}\ K^{-1}]$, $PAR_{abs} = 300$, $a = 9$ $[-]$, $g_0 = 0.02$ $[mol\, CO_2\ m^{-2}\, s^{-1}]$, $\Delta_0 = 1500$ $[Pa]$, $V_{max} = 60$ $[\mu mol\ CO_2\ m^{-2}\ s^{-1}]$, $r_a = 75$ $[s\ m^{-1}]$, and $r_b = 50$ $[s\ m^{-1}]$.

In order to better understand the sensitivity of the model to different environmental factors, a graphical illustration of the behavior of net assimilation rate, A_{nC}, stomatal resistance, r_s, internal leaf CO_2 concentration, c_i, and dark respiration, R_{dC}, as a function of the vapor pressure deficit, Δe $[Pa]$, and leaf temperature, T_v $[°C]$, is shown in Figure 4.29.

Figure 4.29 highlights the strong sensitivity of the biochemical model to leaf temperature with a pronounced decrease of assimilation rate, A_{nC}, and increase of stomatal resistance, r_s, when temperature departs from the optimum. The effect of vapor pressure deficit, for elevated Δe, is instead mitigated by larger gradients between internal leaf CO_2 concentration, c_i, and atmospheric concentration c_a. This provides a positive feedback that tends to reduce the control of vapor pressure deficit in reducing assimilation rate and increasing stomatal resistance. Foliage respiration, R_{dC}, is sensitive only to temperature, as can be easily observed in the equations (4.143-4.144). The sensitivity to absorbed photosynthetically active radiation, PAR_{abs}, and soil moisture in the root zone, θ_R, are shown in Figure 4.30. Assimilation rate, A_{nC}, and stomatal resistance, r_s, can be observed to respond abruptly to θ_R, after a certain threshold and more smoothly to PAR_{abs}.

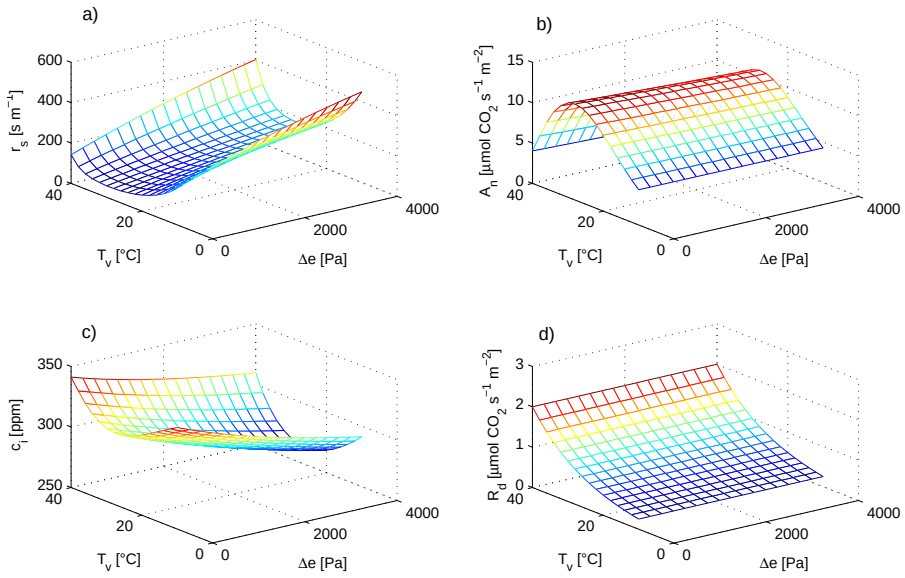

Figure 4.29: Sensitivity analysis of net assimilation rate, A_{nC}, stomatal resistance, r_s, internal leaf CO_2 concentration, c_i, and dark respiration, R_{dC}, to environmental factors such as Δe $[Pa]$ and T_v $[°C]$. The relationships are calculated for a C3 plant in well watered condition with $LAI = 1$ $[-]$, $\epsilon = 0.081$ $[\mu molCO_2\ \mu mol^{-1}\, photons]$, $H_a = 72$ $[kJ\ mol^{-1}]$, $\Delta S = 0.649$ $[kJ\ mol^{-1}\ K^{-1}]$, $c_a = 380$ $[ppm]$, $a = 9$ $[-]$, $g_0 = 0.02$ $[mol\, CO_2\ m^{-2}\, s^{-1}]$, $\Delta_0 = 1500$ $[Pa]$, $V_{max} = 60$ $[\mu mol\ CO_2\ m^{-2}\ s^{-1}]$, $PAR_{abs} = 300$ $[W\ m^{-2}]$, $r_a = 75$ $[s\ m^{-1}]$ and $r_b = 50$ $[s\ m^{-1}]$.

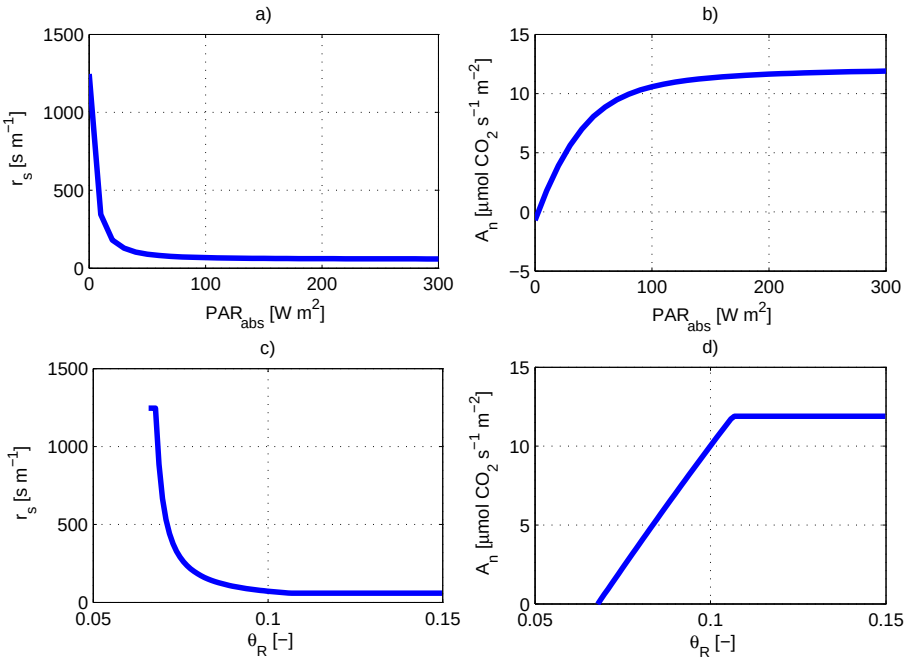

Figure 4.30: Sensitivity analysis of net assimilation rate, A_{nC}, and stomatal resistance, r_s, to environmental dependence such as PAR_{abs} $[W\ m^{-2}]$ and θ_R $[-]$. The relationship are calculated for a C3 plant with with $LAI = 1$ $[-]$, $T_v = 25$ $[^{\circ}C]$, $\Delta e = 0$ $[Pa]$, $\epsilon = 0.081$ $[\mu molCO_2\ \mu mol^{-1}\ photons]$, $H_a = 72$ $[kJ\ mol^{-1}]$, $\Delta S = 0.649$ $[kJ\ mol^{-1}\ K^{-1}]$, $c_a = 380$ $[ppm]$, $a = 9$ $[-]$, $g_0 = 0.02$ $[mol\,CO_2\ m^{-2}\,s^{-1}]$, $\Delta_0 = 1500$ $[Pa]$, $V_{max} = 60$ $[\mu mol$ $CO_2\ m^{-2}\ s^{-1}]$, $r_a = 75$ $[s\ m^{-1}]$, $r_b = 50$ $[s\ m^{-1}]$, $\Psi_{ss} = 400$ $[kPa]$, and $\Psi_{wp} = 4000$ $[kPa]$ in a generic sand loam soil.

4.5 Snow hydrology

When mountainous catchments or basins located at high latitudes are considered, a suitable model of the hydrological cycle must account for snow accumulation, melting, and for soil freezing. In order to extend the areas where "Tethys" can be applied, a snow hydrology module is included. The presence of snow modifies the energy and mass balances, and snowmelt may be responsible for most of the runoff in many mountain catchments (*Zanotti et al.*, 2004). Furthermore, the inclusion of a snow-hydrology component in an eco-hydrological model allows to investigate the interactions between snow dynamics and vegetation, because processes such as snow interception, net radiation modifications, albedo changes, and shadow effects are accounted for. The latter processes deserve a special attention in the study of the linkages between hydrology and vegetation, especially in a changing climate. The understanding and a quantitative evaluation of the controls that vegetation exerts on snow hydrology (and vice-versa) is still an open research field that requires new tools and studies (*Liston et al.*, 2002; *Strack et al.*, 2004; *Jost et al.*, 2007; *Veatch et al.*, 2009; *Molotch et al.*, 2009)

The formation of the snowpack and the snowpack melting are modeled with a physically-based approach (*Wigmosta et al.*, 1994; *Douville et al.*, 1995; *Essery et al.*, 1999; *Belair et al.*, 2003). The snow-hydrology module accounts for a single snowpack layer, neglecting the soil freezing and thawing cycles (see also Section: 4.3.3). The proposed approach preserves the physics governing the evolution of the snowpack, as compared to temperature index modeling (*Walter et al.*, 2005), but avoids the large computational resources required by complex multilayer snowpack models (*Marks et al.*, 1998, 1999; *Bartelt and Lehning*, 2002).

4.5.1 Precipitation partition

The partition of the incoming precipitation, P_r $[mm\ h^{-1}]$, into rain, $P_{r,liq}$ $[mm\ h^{-1}]$, and snow, $P_{r,sno}$ $[mm\ h^{-1}]$, (both in terms of water equivalence depth) is considered to be governed by air temperature, T_a $[^\circ C]$, at the reference height, z_{atm} $[m]$. This assumption is common in snowpack modeling (*Wigmosta et al.*, 1994; *Tarboton and Luce*, 1996), since it requires only the knowledge of the T_a. Generally, the partition between $P_{r,liq}$ and $P_{r,sno}$ depends on the actual profile of temperature in the lower troposphere, and on the weather system producing the precipitation event and can be significatively different also when T_a at the reference height, z_{atm}, is the same. The terms $P_{r,liq}$ and $P_{r,sno}$ are calculated as follows:

$$P_{r,sno} = P_r\,, \qquad \text{if } T_a \leq T_{min}, \tag{4.151}$$

$$P_{r,sno} = P_r \frac{T_{max} - T_a}{T_{max} - T_{min}}\,, \qquad \text{if } T_{min} < T_a < T_{max}, \tag{4.152}$$

$$P_{r,sno} = 0\,, \qquad \text{if } T_a \geq T_{max}, \tag{4.153}$$

$$P_{r,liq} = P_r - P_{r,sno}\,, \tag{4.154}$$

where T_{min} [$^{\circ}C$] is a threshold temperature below which all precipitation is in the form of snow, and T_{max} [$^{\circ}C$] is a threshold temperature above which all precipitation is rain. Between the threshold temperatures, precipitation is assumed to be a mix of rain and snow. The values of T_{min} and T_{max} can be parameterized for a specific location. However, *USACE* (1956) suggests typical values of -1.1 [$^{\circ}C$] and 3.3 [$^{\circ}C$] for T_{min} and T_{max}, respectively.

4.5.2 Snowpack energy and mass balance

Two different storages of snow are considered: the snowpack at the ground, which snow water equivalent is S_{WE} [mm] and the intercepted snow in the *high-vegetation* layer which snow water equivalent is identified by $In_{S_{WE}}$ [mm]. Since, as discussed, only a single prognostic surface temperature, T_s [$^{\circ}C$], is computed, also the energy balance of the two snow storages is unique. The eventual snowmelt flux resulting from the energy balance is then partitioned weighting the relative masses of the two packs.

The basic theory underlying all physically-based point snowmelt models lies in balancing the energy budget for the snowpack and converting the excess energy into snowpack temperature change, metamorphism, or melt (*Williams and Tarboton*, 1999). The seasonal snowpack dynamic can be separated into the cooling phase, the warming phase, the ripening phase, and the output phase (*Dingman*, 1994). During the cooling and warming phases, the net energy input raises or decreases the temperature of the snowpack, until a warming phase brings the whole pack to the melting point. In cooling and warming phases the temperature variation are controlled by heat transfer as:

$$dQ = \frac{c_i\,\rho_w(S^b_{WE} + In^b_{S_{WE}})dT_s}{1000dt}\,, \tag{4.155}$$

or equivalently:

$$dT_s = \frac{1000\,dQ\,dt}{c_i\,\rho_w(S^b_{WE} + In^b_{S_{WE}})}\,, \tag{4.156}$$

where dQ [$W\ m^{-2}$] is the net energy flux input to the snowpack, $c_i = 2093$ [$J\ kg^{-1}\ K^{-1}$] is the specific heat of ice, $\rho_w = 1000$ [$kg\ m^{-3}$] is the density of water, and S^b_{WE} [mm], $In^b_{S_{WE}}$ [mm] are the snow mass water equivalent of ground snowpack and intercepted snow, before accounting for melting. The term dt [s] is the time step, and $dT_s = T_s(t) - T_s(t-dt)$ [$^{\circ}C$] is the change in average temperature of the snowpack. Note that in equation (4.156) the temperature change dT_s can be positive or negative depending on the sign of dQ that in turn depends implicitly on T_s.

During the ripening phase and the output phases, the snowpack remains isothermal at the melting point temperature, $T_s = 0$ [$^{\circ}C$]. Additional energy input causes some

of the snow to change phase from ice to water according to the following equation:

$$dQ = \frac{\lambda_f \rho_w S_m}{1000}, \tag{4.157}$$

or equivalently:

$$S_m = \frac{1000 dQ}{\lambda_f \rho_w}, \tag{4.158}$$

where $\lambda_f = 333700$ $[J\ kg^{-1}]$ is the latent heat of melting of ice at 0 $[°C]$, and S_m $[mm]$ is the snow water equivalent converted to water. During the ripening phase, the liquid water is retained in the snowpack by surface-tension forces until the snow reaches its liquid holding capacity (Section 4.5.4). Once the snowpack voids are saturated the output phase begins and melt water flows out of the snowpack.

The snowmelt, S_m, is partitioned between snowmelt, S_{m1} $[mm]$, in the snowpack at the ground, i.e., from S^b_{WE}, and snowmelt, S_{m2} $[mm]$, in the intercepted snowpack, i.e., from $In^b_{S_{WE}}$, weighting the relative masses:

$$S_{m1} = \frac{S^b_{WE}}{S^b_{WE} + In^b_{S_{WE}}} S_m, \tag{4.159}$$

$$S_{m2} = \frac{In_{S^b_{WE}}}{S^b_{WE} + In^b_{S_{WE}}} S_m. \tag{4.160}$$

The net energy flux input to the snowpack, dQ $[W\ m^{-2}]$, is calculated considering all the different sources of incoming and outgoing heat with an energy balance equation (*Anderson*, 1968; *Bras*, 1990; *Wigmosta et al.*, 1994; *Dingman*, 1994; *Tarboton and Luce*, 1996; *Williams and Tarboton*, 1999; *Liston and Elder*, 2006):

$$dQ(T_s) = R_n(T_s) + Q_v(T_s) + Q_{fm}(T_s) - H(T_s) - \lambda E(T_s) - G(T_s), \tag{4.161}$$

where R_n $[W\ m^{-2}]$ is the net radiation energy absorbed by the total snow present, Q_v $[W\ m^{-2}]$ is the incoming heat with precipitation into the snow, G $[W\ m^{-2}]$ is the ground heat flux into the soil, H $[W\ m^{-2}]$ is the sensible heat flux from the snow, λE $[W\ m^{-2}]$ is the latent heat flux from the snow, and Q_{fm} $[W\ m^{-2}]$ is the heat released from melting (negative) or freezing (positive) of the liquid water content held by the snow (Section: 4.5.4). Note that all the above quantities depend implicity or explicitly on the surface temperature, T_s.

The mass balance of the snowpack, S_{WE} $[mm]$, is obtained as follows:

$$S^b_{WE}(t) = S_{WE}(t - dt) + P_{r,u,sno}(t) - E_{sno}(t) dt, \tag{4.162}$$

$$S_{WE}(t) = S^b_{WE}(t) - S_{m1}(t), \tag{4.163}$$

where $P_{r,u,sno}$ $[mm]$ is the snow precipitation that reach the ground, E_{sno} $[mm\ h^{-1}]$ is the evaporation-sublimation from the ground snowpack and dt $[h]$ is the time step. The term $P_{r,u,sno}$ is given by the total snow that precipitates, more the unloading of the intercepted snow, $U_{In_{S_{WE}}}$ $[mm]$, less the new intercepted snow, $In^N_{S_{WE}}$ $[mm]$,

(equation 4.164). Further details are given in Section 4.5.3. The flux E_{sno} results from equation (4.63) and accounts for the evaporation-sublimation of snow from the snowpack.

$$P_{r,u,sno} = P_{r,sno}\,dt\,[1 - C_{wat}] - In^{N}_{S_{WE}} + U_{In_{S_{WE}}}\,, \tag{4.164}$$

$$E_{sno} = \Big(1 - \sum_{i=1}^{n_c} C_{crown,i} - C_{wat}\Big) E_{sno,f} + \sum_{i=1}^{n_c} \big(C_{crown,i}\, E_{sno,v,i}\big)\,. \tag{4.165}$$

where the symbols of equation (4.165) are defined in Section 4.3.2.

As previously stated, all the quantities in equation (4.161) are function of the surface temperature, T_s, that a priori is an unknown. The unknown T_s depends also on the snow mass balance since it influences snowmelt and liquid water content of the snowpack. The solution of the energy balance is realized hypothesizing a initial value of T_s^i and then solving until the value of T_s obtained from equation (4.156) satisfies the equality $T_s = T_s^i$. Such a non-linear problem is solved with the *fzero* M-file command described in Section 4.3.5.

4.5.3 Snow interception

Interception by forest canopies can store up to 60% of cumulative snowfall by midwinter in cold boreal forests, which results in significative loss of snow over the winter in many coniferous forest (*Pomeroy et al.*, 1998a). Following interception, in fact, most snow remains in the canopy where it is exposed to a relatively warm and dry atmosphere (Figure 4.31). An underestimation of interception will result in a shorter exposure time for sublimation/evaporation and thus in a decrease in seasonal sublimation (*Pomeroy et al.*, 1998a).

Intercepted snow alters also the global surface albedo, since there is a significant decrease of the albedo once the intercepted snow is unloaded from the canopies. Note that given the difficulty on a separate treatment of canopy snow and surface snow most land surface schemes do not consider snow interception (*Pomeroy et al.*, 1998a). In "Tethys" only the *high-vegetation* layer (H_v) is assumed to have a storage of intercepted snow. A single value of intercepted snow, $In_{S_{WE}}$ $[mm]$, is considered and it represents the average of the intercepted snow between different PFT of the n_c *Crown Areas* that can be present within a basic computational element. The *low-vegetation* layers lack any specific storage of intercepted snow. When snow falls into the *low-vegetation* layers, it is considered to increment the ground snowpack layer and its contribution is added to the snow water equivalent, S_{WE} $[mm]$. It follows that the presence of snow at the ground, no matter its depth, is considered to hide completely the *low-vegetation* layer. Consequently, in such a situation the latent and sensible heat fluxes are estimated from the snow surface.

The snow interception model first proposed by *Hedstrom and Pomeroy* (1998) is applied in order to calculate the intercepted snow mass, $In_{S_{WE}}$. The considerations and adaptations of *Gelfan et al.* (2004) and *Liston and Elder* (2006) are also accounted for. The scheme consists of a physical based model of snow intercep-

Figure 4.31: An example of snow intercepted by vegetation. Picture taken in February in a mixed deciduous-evergreen wood in Tuscany.

tion, where $In_{S_{WE}}$ is related to snowfall characteristics, leaf area index, tree species, canopy density, air temperature, and wind speed (*Hedstrom and Pomeroy*, 1998; *Pomeroy et al.*, 1998b, 2002; *Gelfan et al.*, 2004). The model of the accumulation of intercepted snow permits the calculation from standard meteorological parameters of both, the existing load of intercepted snow, $In_{S_{WE}}(t)$, and the snow unloaded from the canopy, $U_{In_{S_{WE}}}$ $[mm]$. The model can be summarized as follows:

$$In'_{S_{WE}}(t) = In_{S_{WE}}(t-dt) + In^{N}_{S_{WE}}(t) - E_{In_{S_{WE}}}(t)dt\,, \tag{4.166}$$

$$In_{S_{WE}}(t) = In'_{S_{WE}}(t) - U_{In_{S_{WE}}}(t) - S_{m2}(t)\,, \tag{4.167}$$

where $In'_{S_{WE}}(t)$ $[mm]$ is the intercepted snow before unloading, $In^{N}_{S_{WE}}$ $[mm]$ is the new intercepted snow, $E_{In_{S_{WE}}}$ $[mm\ h^{-1}]$ is the sublimation/evaporation from intercepted snow, S_{m2} $[mm]$ is the snowmelt of the intercepted snow (Section 4.5.2), and dt $[h]$ is the time step. The sublimation/evaporation from intercepted snow, $E_{In_{S_{WE}}}$, results from equation (4.63):

$$E_{In_{S_{WE}}} = \Big(d_{w,sno}\sum_{i=1}^{n_c}\big(C_{crown,i}[LAI(H_{v,i}) + SAI(H_{v,i})]\big)\Big)E_{sno,f}\,, \tag{4.168}$$

where $E_{sno,f}$ is in $[mm\ h^{-1}]$, $d_{w,sno} = \min\left(1, In_{S_{WE}}/In^{M}_{S_{WE}}\right)$ $[-]$ is the fraction of vegetation in the *high-vegetation* layer covered by intercepted snow (*Lee and Mahrt*, 2004). The term, $d_{w,sno}$, is averaged on the n_c *Crown Areas*, and $In^{M}_{S_{WE}}$ $[mm]$ is the averaged (on the *Crown Areas*) snow interception capacity. Note, that in the presented formulation the sublimation/evaporation from intercepted snow is estimated similarly to evaporation from water surfaces, i.e. considering the snowpack surface

temperature and the effective latent heat of sublimation. Such a method is simplified when compared to more complete approaches that consider sublimation-losses for ice-spheres and canopy exposure coefficients (*Pomeroy et al.*, 1998b), nonetheless it also requires a minor number of parameters.

The new intercepted snow, $In^N_{S_{WE}}$ $[mm]$, depends on the difference between canopy snow interception capacity, $In^M_{S_{WE}}$ $[mm]$, and the initial snow load, $In_{S_{WE}}(t-1)$ $[mm]$. It is further related through an exponential function to snowfall and canopy coverage and density (*Hedstrom and Pomeroy*, 1998):

$$In^N_{S_{WE}} = c(t)\Big(In^M_{S_{WE}} - In_{S_{WE}}(t-1)\Big)\left(1 - e^{-\varsigma_p \frac{P_{r,sno}dt}{In^M_{S_{WE}}}}\right), \tag{4.169}$$

where ς_p $[-]$ is the canopy-leaf contact area per unit area of ground, which for no wind condition is proportional to canopy coverage and in high wind speeds is 1 (*Pomeroy et al.*, 1998b). For simplicity, $\varsigma_p = 1$ is assumed for any condition in "Tethys". The term $P_{r,sno}$ $[mm\ h^{-1}]$ is the snowfall on the canopy (considered equal to the open-area snowfall) (Section 4.5.1). The coefficient $c(t) = exp(-\overline{u}\ t_{sls})$ $[-]$ is a dimensionless snow unloading coefficient, where t_{sls} $[s]$ represents the time since last snowfall and $\overline{u}$ $[s^{-1}]$ the unloading rate. Note that equation (4.169) was originally developed to also account for the snow unload after a major precipitation, the reason why $c(t)$ was introduced. The unloading rate, $\overline{u}$, which is supposed to account for the unloaded snow after the snowfall is a term difficult to measure. Only averaged values of the global unload, $c(t)$, were provided (*Hedstrom and Pomeroy*, 1998; *Pomeroy et al.*, 1998b,a). For instance, *Hedstrom and Pomeroy* (1998) found a empirical value of $c = 0.678$, averaged for time between 0 and 7 days. Afterwards, *Pomeroy et al.* (1998a) suggested that a value of $c = 0.7$ is appropriate for hourly time-step. This value is used in the model to account for the immediate unload of the new intercepted snow at $t_{sls} = 0$ $[s]$. The unloaded snow from the canopy, $U_{In_{S_{WE}}}$ $[mm]$, at the successive time steps, $t_{sls} > 0$, is calculated using a linear reservoir model as first proposed by *Hedstrom and Pomeroy* (1998). The value of $U_{In_{S_{WE}}}$ for cold conditions is given by the difference between the intercepted snow, estimated with equation $dIn'_{S_{WE}}/dt = -\overline{u}In'_{S_{WE}}$ at two different time steps, $t - dt$ and t:

$$U_{In_{S_{WE}}}(t) = \left(1 - e^{-\overline{u}dt}\right) In'_{S_{WE}}(t)\,. \tag{4.170}$$

where $\overline{u}$ $[s^{-1}]$ can be now parameterized with a reference value $\overline{u} = 1.15\ 10^{-6}$ $[s^{-1}]$, obtained from the sensitivity analysis of *Hedstrom and Pomeroy* (1998). Note that in equation (4.170), valid in cold conditions, the wind speed is not considered in the unloading process (*Hedstrom and Pomeroy*, 1998). An example of unloading process under cold conditions is shown in Figure 4.32. All the mechanisms for unloading of intercepted snow increase dramatically for wet-snow conditions. Therefore, when the atmospheric dew point temperature, T_{dew} $[^\circ C]$, exceeds 0 $[^\circ C]$ and the wind speed, u_a $[m\ s^{-1}]$, is greater than 0.5 $[m\ s^{-1}]$ the intercepted snow in the canopy is

considered to be sufficiently ventilated to be isothermal at 0 [$°C$] and as suggested from *Gelfan et al.* (2004) is completely unloaded, i.e., $U_{In_{S_{WE}}}(t) = In'_{S_{WE}}(t)$. This mechanism is consistent with the unloading criteria underlined by *Storck et al.* (2002), is physically meaningful and computationally simple.

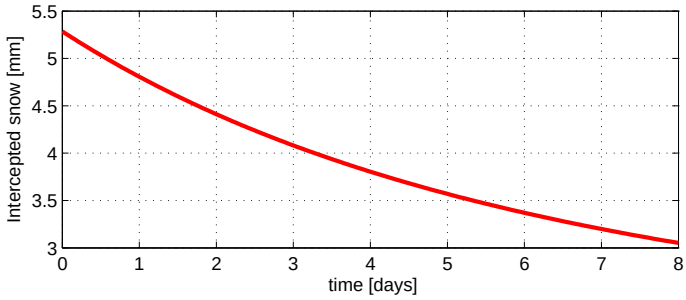

Figure 4.32: Temporal evolution of intercepted snow $In_{S_{WE}}$ after a snowfall of 10 [mm] in a evergreen forest with $LAI = 4.0$ and $T_a = -5°C$.

The canopy snow interception capacity, $In^M_{S_{WE}}$ [mm], is calculated as proposed by *Hedstrom and Pomeroy* (1998). The interception capacity of snow, $In^M_{S_{WE}}$, depends on LAI and on the maximum snow load per unit of stem and leaf area, $Sp_{sno,In}$ [$kg\,m^{-2}$] or equivalently [mm]:

$$In^M_{S_{WE}} = Sp_{sno,In} \sum_{i=1}^{n_c} \Big[C_{crown} [LAI(H_v) + SAI(H_v)] \Big] , \tag{4.171}$$

where $Sp_{sno,In}$ is composed of a mean specie value $\widehat{Sp}_{sno,In}$ corrected by a function that depends on snow density, ρ_{sno} [$kg\,m^{-3}$]. Since the snow density of the intercepted snow is not explicitly computed, it is always assumed to be the that of a potential new snow, ρ^{new}_{sno} (see Section 4.5.5 for a discussion):

$$Sp_{sno,In} = \widehat{Sp}_{sno,In} \left(0.27 + \frac{46}{\rho^{new}_{sno}} \right) . \tag{4.172}$$

Extensive measurements have suggested values of $\widehat{Sp}_{sno,In}$ between 5.9-6.6 [$mm\ m^2\ ground\ area\ m^{-2}\ leaf\ area$] (*Schmidt and Gluns*, 1991).

4.5.4 Snowpack water content

During the ripening phase, the liquid water is retained in the snowpack by surface-tension forces until the snow reaches its liquid holding capacity. In an accurate physically-based approach the outflow rate, W_r [mm], from the snowpack is determined through Darcy's law. In order to do that the saturated hydraulic conductivity and the relative saturation in excess of water retained by capillary forces must be known. These quantities, in turn depend on liquid water volume, capillary retention, and pore volume of the snowpack creating a quite complex system (*Tarboton and Luce*, 1996; *Essery et al.*, 1999; *Zanotti et al.*, 2004). In order to avoid excessive computational effort, a simple bucket model is used to account for the water content

in the snowpack, Sp_{wc} $[mm]$. The bucket approach provides outflow, W_r, when the maximum holding capacity, Sp^M_{wc} $[mm]$, is exceeded (*Wigmosta et al.*, 1994; *Belair et al.*, 2003). The maximum holding capacity of the snowpack, Sp^M_{wc}, is estimated as a function of the snow water equivalent, S_{WE} $[mm]$, and of a specific holding capacity coefficient, c^R $[-]$, that in turn depends on snow density, ρ_{sno} $[kg\,m^{-3}]$. The equations first proposed by *Belair et al.* (2003) are used:

$$Sp^M_{wc} = c^R\, S_{WE}\,, \tag{4.173}$$

$$c^R = c^R_{min}\Big(\rho_{sno} \geq \rho_e\Big) + \Big(c^R_{min} + (c^R_{max} - c^R_{min})\frac{\rho_e - \rho_{sno}}{\rho_e}\Big)\Big(\rho_{sno} < \rho_e\Big)\,, \tag{4.174}$$

where the snow density is defined in Section 4.5.5, the minimum specific holding capacity coefficient is $c^R_{min} = 0.03$ $[-]$, the corresponding maximum is $c^R_{max} = 0.1$ $[-]$, and the density threshold is $\rho_e = 200$ $[kg\,m^{-3}]$. The release of water from the snowpack, W_r, starts when the snowpack water content, Sp_{wc}, exceeds Sp^M_{wc}. At this point the output phase begins and the melted water, W_r, flows out of the snowpack. The released water is $W_r = (Sp_{wc} - Sp^M_{wc})$.

The time evolution of snowpack water content, Sp_{wc}, below its maximum threshold are given by the sum of the snowmelt and of the liquid precipitation directly falling in the snowpack:

$$Sp_{wc}(t) = Sp_{wc}(t-dt) + S_m + P_{r,liq}(t)dt\Big(1 - C_{wat} - \Big[\sum_{i=1}^{n_c} C_{crown}C_{fol,H_v}\Big]\big(1 - d_{w,sno}\big)\Big)\,, \tag{4.175}$$

where C_{fol,H_v} $[-]$ is the fractional vegetation cover for the *high-vegetation* layer defined in Section 4.6.1. The snowpack water content is considered to be in a liquid state when the surface temperature, T_s, is equal to 0 $[^\circ C]$ and to be in a frozen state otherwise. No mixed states are considered for the water held by the snowpack. Consequently, the heat released from the melting (negative) or the freezing (positive) of this water, Q_{fm} $[W\ m^{-2}]$, is estimated as:

$$Q_{fm}(t) = \frac{\lambda_f\,\rho_w\,Sp_{wc}(t-dt)}{1000\,dt}\,, \quad \text{if } T_s(t) < 0 \text{ and } T_s(t-dt) = 0\,, \tag{4.176}$$

$$Q_{fm}(t) = -\frac{\lambda_f\,\rho_w\,Sp_{wc}(t-dt)}{1000\,dt}\,, \quad \text{if } T_s(t) = 0 \text{ and } T_s(t-dt) < 0\,, \tag{4.177}$$

where $\rho_w = 1000$ $[kg\ m^{-3}]$ is the density of water, $\lambda_f = 333700$ $[J\ kg^{-1}]$ is the latent heat of melting-freezing and dt $[s]$ is the time step. Without phase change, $Q_{fm} = 0$.

4.5.5 Snow depth and density

The density of the snow is assumed to be constant with depth, as proposed by *Douville et al.* (1995). This assumption is consistent with considering only a single

layer of snowpack and avoids further computational efforts. The snow density, ρ_{sno} $[kg\ m^{-3}]$, evolves on time according to the conceptual formulation first presented by *Verseghy* (1991) in the *CLASS* model and successively applied in the *ISBA* model (*Douville et al.*, 1995; *Essery et al.*, 1999). The original procedure has been further enhanced by *Belair et al.* (2003). The snow density increases due to gravitational settling, following an exponential function of time and is updated when fresh snow falls in the snowpack. The mechanism of compaction due to the weight of new snow in the preexistent snowpack (*Anderson and Crawford*, 1964) is neglected. The snow density is calculated as:

$$\rho'_{sno} = \rho^{M}_{sno} - \left[\rho^{M}_{sno} - \rho_{sno}(t-dt)\right] e^{\left(-\tau_f \frac{dt}{\tau_1}\right)}, \text{ if } \rho_{sno}(t-dt) < \rho^{M}_{sno}, \quad (4.178)$$

$$\rho'_{sno} = \rho_{sno}(t-dt), \qquad \text{if } \rho_{sno}(t-dt) \geq \rho^{M}_{sno}, \quad (4.179)$$

where ρ'_{sno} $[kg\ m^{-3}]$ is an intermediate value of snow density, ρ^{M}_{sno} $[kg\ m^{-3}]$ is the maximum snow density, $\tau_f = 0.24$ $[-]$, and $\tau_1 = 86400$ $[s]$ are parameters proposed by *Verseghy* (1991) (see also Section 4.2.2), and dt $[s]$ is the time step. The maximum density of snow ρ^{M}_{sno} depends on snow depth and melting conditions (*Belair et al.*, 2003):

$$\rho^{M}_{sno} = \frac{1000}{\rho_w}\left[\rho^{M1}_{sno} - \frac{20.47}{S_{dep}}\left(1 - e^{-\frac{S_{dep}}{0.0673}}\right)\right], \quad \text{if } S_{m1} > 0, \quad (4.180)$$

$$\rho^{M}_{sno} = \frac{1000}{\rho_w}\left[\rho^{M2}_{sno} - \frac{20.47}{S_{dep}}\left(1 - e^{-\frac{S_{dep}}{0.0673}}\right)\right], \quad \text{if } S_{m1} = 0, \quad (4.181)$$

where $\rho_w = 1000$ $[kg\ m^{-3}]$ is the density of water, S_{dep} $[m]$ is the snow depth, S_{m1} $[mm]$ is the snow melt from the snowpack and ρ^{M1}_{sno}, ρ^{M2}_{sno} $[kg\ m^{-3}]$ are the maximum density allowed for snow in melting and freezing conditions, respectively. *Belair et al.* (2003) proposed typical values for these parameters, i.e., $\rho^{M1}_{sno} = 600$ and $\rho^{M2}_{sno} = 450$. The latter values are generally too large when compared to other references or measurements (*Dingman*, 1994; *Essery et al.*, 1999). Therefore, revised values of $\rho^{M1}_{sno} = 500$ and $\rho^{M2}_{sno} = 400$ are used in "Tethys".

The intermediate value of snow density, ρ'_{sno}, is used to update the snow density. When a new snowfall occurs, snow density is supposed to decrease due to fresh snow. The updated value of ρ_{sno} becomes:

$$\rho_{sno} = \frac{\rho^{new}_{sno} P_{r,sno}(t)dt + \rho'_{sno} S_{WE}(t-dt)}{P_{r,sno}(t)dt + S_{WE}(t-dt)}, \quad (4.182)$$

where $P_{r,sno}$ $[mm\ h^{-1}]$ is the snow precipitation, S_{WE} $[mm]$ is the snow water equivalent in the snowpack, dt in $[h]$, and the fresh snow density, ρ^{new}_{sno} $[kg\ m^{-3}]$, is calculated with the equation (*Bras*, 1990):

$$\rho^{new}_{sno} = 1000\left[0.05 + \left(\frac{1.8\,T_a + 32}{100}\right)^2\right], \quad (4.183)$$

where T_a is in $[^{\circ}C]$. Note that without a new snowfall, ρ_{sno} is simply equal to ρ'_{sno}.

The snow depth, S_{dep} $[m]$, is calculated from the obtained snow water equivalent

and snow density as:

$$S_{dep} = 0.001\, S_{WE}(t)\, \frac{\rho_w}{\rho_{sno}}\,. \tag{4.184}$$

Finally, the presence of snow at the ground modifies the roughness, z_{om} $[m]$, of the surface (Section: 4.4.1). The new roughness, z_{om}, in presence of snow becomes (*Strack et al.*, 2004):

$$z_{om} = z_{om,veg} \max\left[0, \left(1 - \frac{S_{dep}}{H_c}\right)\right] + z_{om,sno} \min\left[1, \frac{S_{dep}}{H_c}\right], \tag{4.185}$$

where $z_{om,veg}$ $[m]$ and $z_{om,sno}$ $[m]$ are the roughness of vegetation and snow in a open field (Section 4.4.1), H_c $[m]$ is the vegetation height, and S_{dep} in $[m]$. The relationship $z_{oh} = z_{ow} = 0.1 z_{om}$ continues to hold true.

4.6 Canopy interception and erosion

The interception of rainfall by vegetation canopies has been considered by hydrologists since long time ago (*Horton*, 1919). This process modifies the water balance at the surface, since water retained on the leaves rather than contribute to runoff and recharge through dripping, evaporates back into the atmosphere as a latent heat (*Mahfouf and Jacquemin*, 1989). Although interception has been often neglected in rainfall-runoff and hydrological model (*Ciarapica and Todini*, 2002; *Campo et al.*, 2006), on average can amount to 20-50% of the precipitation in temperate wet zone with frequent drizzles (*Link et al.*, 2004; *Savenije*, 2004; *Gerrits et al.*, 2007). Generally, interception is the sum of canopy interception, and forest floor interception, though traditionally the term interception refers only to the first contribution. Canopy interception considers water retained by vegetation leaves and stems, forest floor interception considers the water trapped by litter and dead biomass. Only the contribution of canopy interception is calculated in "Tethys". Nonetheless, since up two layers of vegetation can be considered also the interception of grass or very shallow vegetation species is accounted for. However, formally the proposed scheme neglects the forest floor interception related to litter, as well as the storage of water in ponds, puddles, and surface micro-depression. These might be important mechanisms that precede infiltration or runoff (*Kamphorst et al.*, 2000; *Gerrits et al.*, 2007), in updated versions of the model it can be useful to take into account also these processes. At the end of this Section, the methodology used to compute erosion due to rainfall impact is also presented. This is the first step for an evaluation of sediment production and soil depletion that can be very important in many hydrological applications.

4.6.1 Throughfall

Precipitation can be either intercepted by the canopy or falls to the ground as throughfall and stem flow. In order to distinguish between intercepted precipitation

and and free fall, a fractional vegetation cover should be introduced. The fractional vegetation cover, C_{fol} $[m^2\ vegetated\ area\ m^{-2}\ \ PFT\ area]$, represents the fraction $[0-1]$ of the area occupied by leaves and stems projected in the vertical direction. C_{fol} is a function of leaf area index, LAI $[m^2\ leaf\ area\ m^{-2}\ PFT\ area]$, and stem area index, SAI $[m^2\ stem\ area\ m^{-2}\ \ PFT\ area]$. *Mahfouf and Jacquemin* (1989) used the following empirical relationship to calculate C_{fol}:

$$C_{fol} \;=\; 1 - e^{-\kappa(LAI+SAI)}\,, \tag{4.186}$$

where κ $[-]$ is assumed to be equal to 0.8 (*Mahfouf and Jacquemin*, 1989). Other reference values have been proposed for κ, e.g. $\kappa = 0.5$ in the *BATS-CLM* model (*Dickinson et al.*, 1993; *Oleson et al.*, 2004). According to the study of *Ramírez and Senarath* (2000), $\kappa = 0.75$ is used in "Tethys".

Following the definition of C_{fol}, the fraction of rain which falls through gaps in the canopy is $P_r(1 - C_{fol})$ $[mm\ h^{-1}]$, and the intercepted fraction is $P_r\ C_{fol}$ $[mm\ h^{-1}]$. Consequently, the rainfall intercepted by the two vegetation layers is (see also the scheme of Figure 4.33):

$$P_{r,H_v} \;=\; C_{crown} P_{r,liq}(1 - d_{w,sno}) C_{fol,H_v}\,, \tag{4.187}$$

$$P_{r,L_v} \;=\; [1 - C_{sno}][(1 - C_{fol,H_v}) P_{r,H_v} + Dr_{H_v}] C_{fol,L_v}\,, \tag{4.188}$$

where P_{r,H_v} and P_{r,L_v} $[mm\ h^{-1}]$ are the precipitation reaching the vegetated surface in the *high* and *low-vegetation* layers, respectively. The latter terms will be generally indicated as $P_{r,fol}$ in the following. The quantity Dr_{H_v} $[mm\ \ h^{-1}]$ is the total drainage from the *high-vegetation* layer (Section 4.6.3).

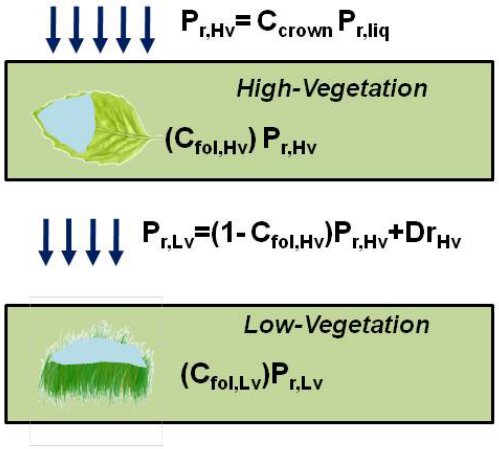

Figure 4.33: Scheme of the interception process in absence of snow where two vegetation layers, *high* and *low-vegetation* are considered. The variable P_{r,H_v} and P_{r,L_v} represent the precipitation reaching the high and low layers of vegetation. The other terms are defined in the text.

Note that since a number n_c of different *Crown Areas* can be simultaneously present within a basic computational element the calculation of the interception is made independently for each *Crown Area*.

4.6.2 Canopy storage capacity

The maximum allowed interception, called also canopy storage capacity, In^M $[mm]$, or equivalently $[kg\ m^{-2}]$ is calculated with the approach proposed by *Dickinson et al.* (1993):

$$In^M = S_{p,In}(LAI + SAI)\,, \tag{4.189}$$

where $S_{p,In}$ $[mm\ m^2\ PFT\ area\ m^{-2}\ leaf\ area]$ is the specific water retained by a vegetated area function of the PFT type. The assumption made in equation (4.189) is that the sum of leaf area index LAI, and stem area index SAI cannot retain more than In^M of liquid water. This relation is perhaps oversimplified because other factors such as wind speed can influence the interception (*Mahfouf and Jacquemin*, 1989). However, equation (4.189) agrees well with observed quantities (*Rutter et al.*, 1975) and has been widely applied in land surface and hydrological models (*Noilhan and Mafhouf*, 1996; *Oleson et al.*, 2004; *Ivanov et al.*, 2008a). References values of $S_{p,In}$ can be found in literature. For instance, *Rutter et al.* (1975) proposed a value of 0.2 $[mm]$. More generally, *Mahfouf and Jacquemin* (1989) suggested that values between 0.1-0.4 $[mm]$ apply for different vegetation types.

4.6.3 Model of interception

The canopy interception in each *Crown Area*, C_{crown}, and separately for the two vegetation layers (H_v and L_v) is estimated using the Rutter model (*Rutter et al.*, 1971, 1975) that has been widely used in hydrological applications (*Mahfouf and Jacquemin*, 1989; *Eltahir and Bras*, 1993; *Ivanov et al.*, 2008a). The equation describing interception storage dynamic is:

$$\frac{dIn}{dt} = P_{r,fol} - Dr - E_{In}\,. \tag{4.190}$$

Equation (4.190) is a non-linear ordinary differential equation that cannot be solved analytically. In order to avoid the efforts of the numerical integration, an approximate expression of (4.190) is used. First the updates due to precipitation and evaporation are considered and successively the drainage term is added:

$$In'(t) = In(t - dt) + P_{r,fol}(t)dt - E_{In}(t)dt\,, \tag{4.191}$$

$$In(t) = In'(t) - Dr(t)dt\,, \tag{4.192}$$

where dt $[h]$ is the time step, In and In' $[mm]$ are the intercepted water, and the first update of intercepted water, respectively. The flux E_{In} $[mm\ h^{-1}]$ is the evaporation rate from the wetted fraction of the canopy estimated using the equations (4.67)-(4.68). When E_{In} is negative is considered as dew on the foliage. The quantity $P_{r,fol}$ $[mm\ h^{-1}]$ is the rainfall rate falling into the vegetation. It is a function of the vegetation layer, i.e., $P_{r,fol} = P_{r,H_v}$ or $P_{r,fol} = P_{r,L_v}$ (Section 4.6.1). The flux Dr $[mm\ h^{-1}]$ is the canopy drainage, sum of the dripping from the canopy, Dr_d $[mm\ h^{-1}]$, and of the drainage from saturation excess, Dr_s $[mm\ h^{-1}]$. The dripping

from the canopy, Dr_d, is calculated as in the Rutter model:

$$Dr_d = K_c e^{g_c(In' - In^M)}, \tag{4.193}$$

where K_c $[mm\ h^{-1}]$ and g_c $[mm^{-1}]$ are the drainage rate coefficient and exponential decay parameter, and In^M $[mm]$ is the is the maximum interception capacity (Section 4.6.2). Since the drainage rate coefficient and the exponential decay parameter have a limited range of variability, prescribed values, i.e. $K_c = 0.06$ $[mm\ h^{-1}]$ and $g_c = 3.7$ $[mm^{-1}]$ are used (*Rutter et al.*, 1971; *Mahfouf and Jacquemin*, 1989). Note that the intercepted water, In $[mm]$, must be always inferior to the maximum interception capacity, In^M. Consequently, when this value is exceeded a storage excess drainage, Dr_s $[mm\ h^{-1}]$, is computed:

$$Dr_s = \frac{(In' - In^M)}{dt} (In > In^M), \tag{4.194}$$

with dt $[h]$ time step.

4.6.4 Rainfall erosion

The explicit computation of the erosion produced by the rainfall can be useful in specific model applications. For instance, the material displaced by splash erosion is one of the components that contributes to the sediment transport, the determination of the latter is often important at the watershed scale. Furthermore, plot scale erosion and soil depletion can be regarded as variables that deserve attention in several environmental studies. For these reasons a module of "Tethys" is dedicated to the evaluation of the erosion rate, E_r $[mm\ h^{-1}]$ or in mass units $[kg\ h^{-1}\ m^{-2}]$. At the basic element scale only erosion due to rainfall detachment is considered. Other possible erosion mechanisms, such as sheetflow, gully, and river erosion are meaningful only when an explicit topographic representation is considered and are not implemented yet in the model.

Rainfall detachment is related to the kinetic energy of rainfall. A distinct effect of leaf and stem drainage, and direct throughfall is considered to estimate soil detachment by raindrop impact. This permits to explicitly account for the effects of different vegetation characteristics such as height, H_c $[m]$, and fractional vegetation cover, C_{fol} $[-]$. It further met the purpose of properly include the vegetation role within the model. The free throughfall, $P_{r,TR}$ $[mm\ h^{-1}]$, and the drainage from leaves and stems, $P_{r,LD}$ $[mm\ h^{-1}]$, that reach the ground are:

$$\begin{aligned} P_{r,TR} &= [1 - C_{sno}] \sum_{i=1}^{n_c} \Big[P_{r,liq} C_{crown,i} (1 - C_{fol,H_v,i})(1 - C_{fol,L_v,i}) \Big] + \\ &\quad P_{r,liq} C_{bare} (1 - C_{sno}), \end{aligned} \tag{4.195}$$

$$P_{r,LD,H_v,i} = [1 - C_{sno}] \Big[Dr_{H_v,i} (1 - C_{fol,L_v,i}) \Big], \tag{4.196}$$

$$P_{r,LD,L_v,i} = [1 - C_{sno}] \Big[Dr_{L_v,i} \Big], \tag{4.197}$$

where $P_{r,LD}$ is subdivided between *low* and *high vegetation* layers. It is further assumed that the water released by the snowpack, given its natural slow dynamic does not induce erosion. The specific kinetic energy of rainfall reaching the ground as direct throughfall, $K_{E,TR}$ $[J\ m^{-2}\ mm^{-1}]$, is assumed to be the same as that of the natural rainfall. This term depends on rainfall intensity and raindrop size. Following *Brandt* (1990) which assumes a raindrop size distribution as described by *Marshall and Palmer* (1948), $K_{E,TR}$ can be evaluated as follows:

$$K_{E,TR} = 8.95 + 8.44 \log_{10}(P_{r,TR})\,. \tag{4.198}$$

The specific kinetic energy of the leaf and stem drainage, $K_{E,LD}$ $[J\ m^{-2}\ mm^{-1}]$, is estimated using the equation developed experimentally by *Brandt* (1990):

$$K_{E,LD} = 15.8\sqrt{H_c}\ - 5.87\,, \tag{4.199}$$

where H_c $[m]$ is the effective plant canopy height. Such a simple relationship is considered valid because, for a wide range of plants, the drop-size distribution of leaf drainage has been found invariant (*Brandt*, 1989). This statement is further reinforced by recent studies where it has been observed that plant architecture does not play an important role in soil detachment (*Foot and Morgan*, 2005). This means that the variations in the energy of leaf drainage are solely a function of the impact velocity of the raindrops which depends on the height of fall. The kinetic energy of leaf drainage is set to zero when the canopy height is less than $H_c < 0.14$ $[m]$ in order to avoid negative values, as suggested by *Morgan et al.* (1998). The total flux of kinetic energy, K_E $[J\ m^{-2}\ h^{-1}]$, of rainfall can be calculated multiplying the specific energies obtained from equations (4.198) and (4.199) by the respective intensities. These *"rainfall"* intensities are the direct throughfall and the leaf drainage from *low* and *high vegetation* layers:

$$\begin{aligned} K_E = {} & K_{E,TR}P_{r,TR} + \sum_{i=1}^{n_c} K_{E,LD,H_v,i}P_{r,LD,H_v,i} + \,, \\ & \sum_{i=1}^{n_c} K_{E,LD,L_v,i}P_{r,LD,L_v,i}\,. \end{aligned} \tag{4.200}$$

The same formulation of kinetic energy evaluation (equation 4.201) is used in the *LISEM* (*DeRoo et al.*, 1996) and *EUROSEM* (*Morgan et al.*, 1998) models. The total erosion rate, E_r $[kg\ h^{-1}\ m^{-2}]$, due to raindrop detachment in a basic computational element is:

$$E_r = K_E K_{ero}\Big[P_{r,TR} + \sum_{i=1}^{n_c} P_{r,LD,H_v,i} + \sum_{i=1}^{n_c} P_{r,LD,L_v,i}\Big]\,, \tag{4.201}$$

where K_{ero} $[kg\ h\ J^{-1}\ mm^{-1}]$ is an erodibility factor (Section 4.7.4) that needs to be multiplied again for the total rainfall intensity. The erosion rate, E_r, can be expressed in height of lost soil $[mm\ h^{-1}]$ dividing per the bulk density of soil, $\rho_d = \rho_{ss}(1-\theta_{sat})$ $[kg\ m^{-3}]$: $E_r = E_r\ 1000/\rho_d$; where θ_{sat} is the soil water content

at saturation, and $\rho_{ss} = 2650$ $[kg\ m^{-3}]$ is the solid soil density (Section 4.7.4). Note that the erodibility factor, K_{ero}, is scaled with the intensity of the rainfall. Since this intensity is already accounted for in the estimation of K_E would be probably better in successive version of the model consider a detachability coefficient, K_{det} $[g\ J^{-1}\ ]$, valid for every rainfall intensity as proposed in other studies (*Morgan*, 2001; *Gumiere et al.*, 2009). Corrections due to the presence of a possible thin sheet of water on the surface that reduces the erosive power of the drops are neglected (*Torri et al.*, 1987; *Wicks and Bathurst*, 1996; *Morgan et al.*, 1998). The uncertainties in the determination of a water depth correction factor are indeed too large (*Parsons et al.*, 2004). Furthermore, the storage of water in micro-depression or ponds is not considered. This makes the estimation of the water sheet on the surface problematic.

4.7 Subsurface water dynamics

Vadose zone dynamics exert a fundamental control on the hydrological cycle. The soil moisture profile, i.e. the value of soil moisture at different depths, $\theta(z_d)$, directly influences processes such as infiltration, storm runoff, lateral subsurface flow, and aquifer recharge. Furthermore, the energy balance is strongly controlled by the soil moisture distribution, the latter affects directly or indirectly (mainly determining the surface temperature, T_s) all the energy fluxes, e.g., net radiation, partition between latent heat and sensible heat, etc. Consequently, also evaporation and transpiration fluxes are mediated by the the value of soil moisture at different depths, $\theta(z_d)$. Therefore, the study of water movement in the vadose zone and its quantification is essential to solve correctly the energy balance and to quantify the partition between different hydrological components.

4.7.1 Infiltration and infiltration excess runoff

The influx of water, q_{ins} $[mm\ h^{-1}]$, at the soil surface is the sum of many components. Direct rainfall in non-vegetated areas, throughfall in the two vegetation layers, water released from the snowpack, drainage of intercepted water, and eventually dew. All these terms contribute to the flux q_{ins}. An ulterior flux, the runon, q_{runon} $[mm\ h^{-1}]$, can be added to the water influx at the ground. The runon, q_{runon}, for a given element is estimated as the sum of surface runoff produced in neighboring elements that flow towards the considered element. The runon component may become important in semi-arid environments where discontinuous and intermittent patterns of surface flow create conditions for the re-infiltration of a significant portion of runoff (*Howes and Abrahams*, 2003). When the analysis is led at element scale, the runon component cannot be calculated and is assumed equal to zero. The

equation of the water incoming at the soil surface becomes:

$$q_{ins} = [1 - C_{sno}] \sum_{i=1}^{n_c} \Big[\big(P_{r,liq} C_{crown,i} (1 - C_{fol,H_v,i}) + Dr_{H_v,i} \big) \big(1 - C_{fol,L_v,i} \big) + Dr_{L_v,i} \Big] + P_{r,liq} C_{bare} [1 - C_{sno}] + \frac{W_r}{dt} + \sum_{i=1}^{n_c} \left(Dr_{H_v,i} \right) [C_{sno}] + q_{runon} \,, \quad (4.202)$$

where all the symbols have been previously defined in this Chapter. Depending on the intensity of the incoming flux to the soil, soil properties, and on antecedent soil moisture condition, q_{ins} may either infiltrate or be lost from the soil as surface runoff (*Bonan*, 2002; *Daly and Porporato*, 2005; *Brutsaert*, 2005).

Numerous methods exist for the estimation of the water infiltration rate. Generally, these methods have been developed to study the infiltration dynamic throughout the entire vadose zone. In "Tethys" the infiltration term is only an upper boundary condition, at the soil surface. The proper computation of soil water dynamics is then realized with the numerical scheme described in the next Section 4.7.3 that allows to calculate the entire soil moisture profile $\theta(z_d)$.

Infiltration methods can be subdivided into three broad categories: empirical models, Green-Ampt models, and Richards equation models. For a review and comparison of different methods refer for instance to *Chow* (1988); *Clausnitzer et al.* (1998); *Mishra et al.* (2003). The infiltration flux, in "Tethys", is evaluated with the three parameter infiltration equation first proposed by *Parlange et al.* (1982) and successively applied in *KINEROS2* (*Smith et al.*, 1995). The *Parlange et al.* (1982) infiltration equation belongs to the Green-Ampt model category. The infiltration capacity, I_f^C $[mm\ h^{-1}]$, is a function of the depth of water infiltrated in the soil, F $[mm]$ and of three parameters:

$$I_f^C = K_{s\,v} \left[\frac{\exp[(\alpha F)/B] - 1 + \alpha}{\exp[(\alpha F)/B] - 1} \right] , \quad (4.203)$$

where $K_{s\,v}$ $[mm\ h^{-1}]$ is the vertical saturated hydraulic conductivity at the surface (Section 4.7.4), $B = G(\theta_{sat} - \theta_F)$ $[mm]$ combines the effects of net capillary drive, G $[mm]$, and storage capacity. The terms θ_{sat} and θ_F $[-]$ are the water content at saturation and the water content in the layer of soil interested by infiltration, respectively (Section 4.7.3). The parameter α $[-]$ represents the soil type. The value of α is near 0 for sand, in which case equation (4.203) approaches the Green-Ampt relation, and α is near 1 for a well-mixed loam, in which case equation (4.203) represents the Smith-Parlange infiltration equation (*Smith and Parlange*, 1978). In *KINEROS2*, *Smith et al.* (1995) use a value of α near 0.85 that best describes most of the soils, the same value is adopted in "Tethys". The net capillary drive, G $[mm]$, is defined as:

$$G = \int_{-\infty}^{0} \frac{K(\Psi)}{K_s} d\Psi \,. \quad (4.204)$$

A simplified expression is used to evaluate G, as first proposed in the *KINEROS2* model:

$$G = -\Psi_e \frac{2 + 3\lambda_\circ}{1 + 3\lambda_\circ}\,, \tag{4.205}$$

where $\lambda_\circ$ $[-]$ is the pore-size distribution index and Ψ_e $[mm]$ is the air entry bubbling pressure (Section: 4.7.4).

Empirical infiltration schemes or Green-Ampt type models often consider the soil column as a bucket. This means that a single value of soil moisture, θ, and infiltrated depth, F, are available. In the proposed approach the infiltration is only a boundary condition. Thus, the amount of rain already absorbed, F $[mm]$, is approximated by the water stored on the first portion of soil $F = d_{z,F}(\theta_F - \theta_{hy})$. The term θ_{hy} $[-]$ is the residual or hygroscopic water content and $d_{z,F}$ is the thickness of the layer interested by the infiltration process (Section 4.7.3). The depth $d_{z,F}$ is assumed to be 50 $[mm]$, although it can be regarded as a calibration parameter, larger values of $d_{z,F}$ induce a slower increase of I_f^C for drier soils. The values assumed by infiltration capacity, calculated with equation (4.203) for a sand loam soil, are shown in Figure 4.34 as a function of soil moisture. As can be observed, infiltration capacity exponentially increases when the soil get drier.

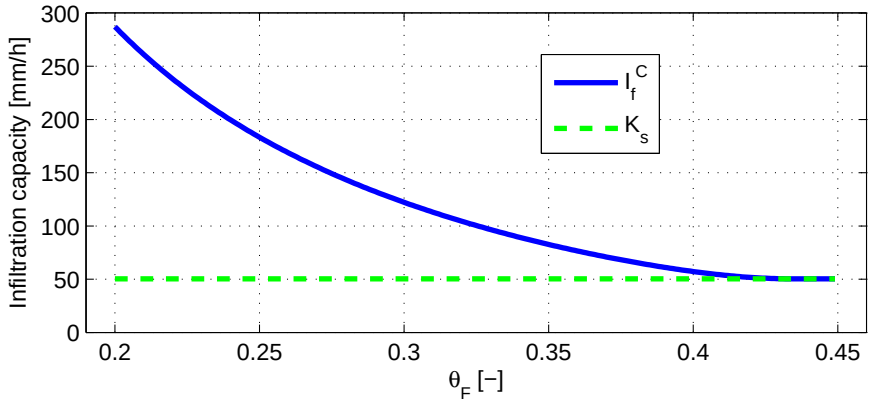

Figure 4.34: Infiltration capacity, I_f^C, varying with soil water content of the shallower part of soil, θ_F, values refer to a generic sand loam soil. The dashed line represent the vertical saturated hydraulic conductivity $K_{s\,v}$.

Surface sealing and soil crust mechanisms can be accounted for in the model and their conceptualization is described in Section 4.7.2. These phenomena tend to decrease infiltration rate, this in turn reduces the available water to the plants in the root zone, diminishes the natural recharge of aquifers, and increases runoff and soil erosion (*Assouline*, 2004). Therefore, considering soil sealing effects can be of paramount importance in eco-hydrological modeling, especially when arid and semiarid environments with large portions of bare exposed soil are investigated.

It has been further shown that vegetation density and distance from the vegetation are important variables in determining the infiltration capacity. The measured values of I_f^C can be quite different among vegetated and bare soil patches for similar

soils and environments (*Bhark and Small*, 2003; *Madsen et al.*, 2008; *Bedford and Small*, 2008). Nonetheless, this mechanism that leads to heterogeneous infiltration capacities because of a heterogeneous land cover composition is neglected in order to avoid further parameterizations.

Infiltration excess runoff, called also *Horton* runoff, R_H $[mm\ h^{-1}]$, is calculated as the difference between the actual infiltration rate, I_f $[mm\ h^{-1}]$, and the water influx to soil, q_{ins}. The actual infiltration rate is the minimum between infiltration capacity, I_f^C $[mm\ h^{-1}]$, and water influx to soil: $I_f = \min(q_{ins}, I_f^C)$. Consequently, R_H is obtained as:

$$R_H = q_{ins} - I_f\,. \tag{4.206}$$

4.7.2 Soil sealing and crust

The formation of a seal at the soil surface can result from different causes, such as rainfall, fire, biological activity, etc. The model accounts only for rainfall induced surface sealing as described in *Assouline* (2004). Structural seals are formed at the soil surface by the destruction of the soil aggregates exposed to the direct impact of the rain drops. Under the impact of raindrops the weaker soil aggregates breakdown, the soil undergoes a compaction and the pores are filled and clogged by wash-in of fine material. Consequently, soil develops surface seals that alter the surface hydraulic properties (*Assouline*, 2004). Successively, the seals on drying become crusts. A review of processes involved in seal formation, seal layer properties characterization, modeling approaches of dynamic seal layer and effects on soil water dynamics is provided by *Assouline* (2004). In arid and semi-arid environments with large portion of soil directly exposed to raindrop impacts soil sealing plays an important role decreasing the infiltration capacity (*Morin et al.*, 1989; *Robinson and Phillips*, 2001; *Assouline and Mualem*, 2001; *Assouline*, 2004; *Assouline and Mualem*, 2006). For this reason, surface seal effects are accounted for.

The conceptual model used to describe the surface seal layer is the one proposed by *Mualem and Assouline* (1989). The model of *Mualem and Assouline* (1989) is a theoretical one but it has been recently tested to be valid against accurate measurements (*Assouline*, 2004). They suggested that the seal is a nonuniform layer situated at the soil surface. It results from the rearrangement and compaction of the soil particles in the disturbed upper zone due to raindrop impact, and from fine soil particles percolating in-depth during infiltration. Consequently, the seal bulk density, ρ_{cr} $[kg\ m^{-3}]$, is the highest at the surface and decreases exponentially with depth, z_d $[mm]$, to that of the undisturbed soil $\rho_d = \rho_{ss}(1 - \theta_{sat})$ $[kg\ m^{-3}]$, where θ_{sat} is the soil water content at saturation, and $\rho_{ss} = 2650$ $[kg\ m^{-3}]$ is the solid soil density (Section 4.7.4).

$$\rho_{cr}(z_d) = \rho_d + \Delta\rho \exp(-\gamma_{cr} z_d)\,, \tag{4.207}$$

where $\Delta\rho$ $[kg\ m^{-3}]$ is the maximum change in bulk density at the soil surface ($z_d = 0$), and γ_{cr} $[mm^{-1}]$ is a characteristic parameter of the soil rainfall interaction. The seal thickness, d_{cr} $[mm]$, is identified with the depth at which the changes in hydraulic properties are insignificant, namely, where $\Delta\rho(z_d) \leq 0.001\Delta\rho$. It follows that $\gamma_{cr} = -\ln(0.001)/d_{cr}$.

The main purpose of including a seal modeling in "Tethys" is the possibility to simulate infiltration into a crust-topped profile or during seal formation. In order to simulate infiltration in a sealed soil, hydraulic properties of the seal must be recalculated. Following *Mualem and Assouline* (1989), the distributed hydraulic properties in the nonuniform seal layer depend on the undisturbed soil properties and on the modified seal bulk density, ρ_{cr}. The seal density in turn depends on the depth z_d according to equation (4.207). The undisturbed soil parameters are the saturation moisture content, θ_{sat} $[-]$, the residual or hygroscopic moisture content, θ_{hy} $[-]$, the pore-size distribution index, $\lambda_\circ$ $[-]$, the air entry bubbling pressure, Ψ_e $[mm]$, and the vertical saturated hydraulic conductivity, $K_{s\,v}$ $[mm\ h^{-1}]$ (Section 4.7.4). The correspondent parameters modified by the seal effect are indicated with the subscript *cr* and are calculated according to *Mualem and Assouline* (1989):

$$\theta_{sat,cr}(\rho_{cr}) = \theta_{sat} - \big[\rho_{cr}(z_d) - \rho_d\big]/\rho_{ss}\,, \tag{4.208}$$

$$\theta_{hy,cr}(\rho_{cr}) = \theta_{hy}\big[1 + (\rho_{cr}(z_d) - \rho_d)/\rho_d\big]\,, \tag{4.209}$$

$$\Psi_{e,cr}(\rho_{cr}) = \Psi_e\big[1 + (\rho_{cr}(z_d) - \rho_d)/\rho_d\big]^{3.72}\,, \tag{4.210}$$

$$\lambda_{\circ,cr}(\rho_{cr}) = \lambda_\circ - \mathcal{C}\big[\rho_{cr}(z_d) - \rho_d\big]\,, \tag{4.211}$$

$$K_{s\,v,cr}(\rho_{cr}) = K_{s\,v}\left[\frac{\theta_{sat,cr} - \theta_{hy,cr}}{\theta_{sat} - \theta_{hy}}\right]^{2.5}\left[\frac{\Psi_e}{\Psi_{e,cr}}\right]^2\left[\frac{\lambda_{\circ,cr}(1+\lambda_\circ)}{\lambda_\circ(1+\lambda_{\circ,cr})}\right]^2\,, \tag{4.212}$$

where $\mathcal{C}$ $[m^3\ kg^{-1}]$ is a fitting parameter. A value $\mathcal{C} = 2.5\,10^{-4}$ $[m^3\ kg^{-1}]$ is used, when no specific information for its calibration is available (*Assouline and Mualem*, 1997).

In order to calculate the hydraulic properties in the nonuniform seal, the seal must be characterized by the maximum change in bulk density at the soil surface, $\Delta\rho$ $[kg\ m^{-3}]$, and seal thickness, d_{cr} $[mm]$. These two variables are the result of soil and rainfall interaction. They evolve in time according to the seal development. *Mualem et al.* (1990) introduced a conceptual model for the dynamic of seal formation that is implemented in "Tethys". The model is based on equation (4.207) and accounts dynamically for the transfer of kinetic energy from the rainfall to the soil. The increase in the soil bulk density at the soil surface, $\Delta\rho$, and the seal thickness, d_{cr}, are considered to be function of the rainfall cumulative kinetic energy, E_K $[J\ mm^{-2}]$. The cumulative kinetic energy can be estimated from the total flux of direct throughfall and leaf drainage kinetic energy, K_E $[J\ m^{-2}\ h^{-1}]$, calculated in Section 4.6.4. The variable, E_K, is simply the time integration of K_E.

$$\Delta\rho(E_K) = \Delta\rho^*\big[1 - \exp(-\eta_{cr}E_K)\big]\,, \tag{4.213}$$

$$d_{cr}(E_K) = d^*_{cr}\big[1 - \exp(-\zeta_{cr}E_K)\big]\,, \tag{4.214}$$

where $\Delta\rho^*$ $[kg\ m^{-3}]$ and d_{cr}^* $[mm]$ are the maximal values of $\Delta\rho$, and d_{cr} reached after a long exposure to rainfall. The parameters η_{cr}, and ζ_{cr} depend on soil-rainfall characteristics. Theoretically, the values of $\Delta\rho^*$, d_{cr}^*, η_{cr}, and ζ_{cr} must be estimated from observations of seal formation (*Assouline*, 2004). Here, literature values of $\Delta\rho^* = 400$ $[kg\ m^{-3}]$, $d_{cr}^* = 10$ $[mm]$ $\eta_{cr} = 7000$ $[mm^2\ J^{-1}]$, and $\zeta_{cr} = 3500$ $[mm^2\ J^{-1}]$ are assumed as representative for every soil and rainfall type (*Mualem et al.*, 1990). It must be underlined that a more accurate model of seal formation has been proposed (*Assouline and Mualem*, 1997). This includes a characterization of raindrop size distribution, and the influence of soil mechanical properties in the evolution of the seal layer. Nevertheless, the simpler *Mualem et al.* (1990) model is preferred in "Tethys" given the general lack of experimental data to estimate the required parameters.

The time evolution of the saturated hydraulic conductivity, $K_{s\,v,cr}$, in the seal layer at different depths is shown in Figure 4.35. The behavior of Figure 4.35 is obtained with the *Mualem et al.* (1990) model after applying a constant rainfall of 30 $[mm\ h^{-1}]$ in a bare sandy-loam soil. It can be observed that for the applied rainfall intensity the sealing effects in reducing infiltration at the surface are really fast. Note that it is mainly the most superficial part of the soil to be interested by a change of soil hydraulic characteristics. Below $z_d = 5 - 6$ $[mm]$ the effect of the sealing can be fairly neglected.

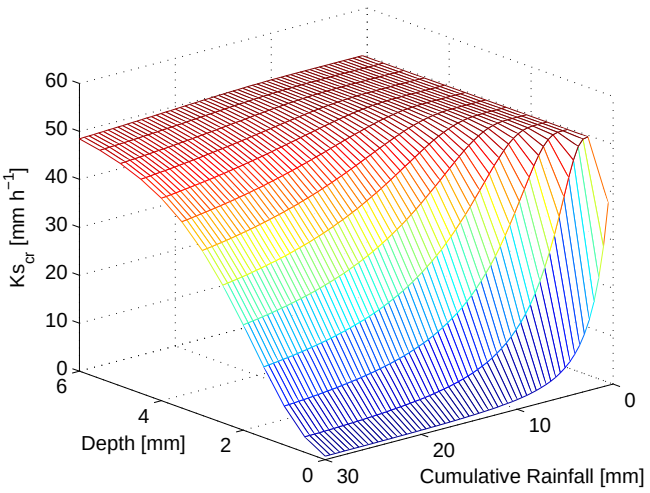

Figure 4.35: Values of saturated hydraulic conductivity, $K_{s\,v,cr}$ $[mm\ h^{-1}]$, of a sealed soil for a sandy-loam subject to a 30 $[mm\ h^{-1}]$ rainfall lasting one hour. The effects of cumulative rainfall at different depths are shown.

Models and subsequent applications of seal dynamic formation including the relative changes of soil-hydraulic properties have been developed and used at the event scale (*Mualem et al.*, 1990; *Mualem and Assouline*, 1989; *Assouline and Mualem*, 1997, 2001, 2006). Their extension over longer time intervals is required by the fact that "Tethys" is a long-lead hydrological model. This extension is realized re-

initializing the accumulation of cumulative kinetic energy, E_K [$J\ mm^{-2}$] for each event. A seal formation event is considered concluded, i.e., $E_K = 0$, when $K_E = 0$ for more than one hour. Otherwise, E_K evolves in time as the time integration of the fluxes of kinetic energy. This simplification neglects the possibility of persisting effects on seal layer, such as the formation of a soil crust when the surface soil dries, or the maintenance of an unmodified seal between two consequent but separated precipitation events. Little information, if any, exists on surface seal breaking and revert to the initial undisturbed conditions or conversely on its persistence on time. The study of such an effect could be important both for the infiltration and soil evaporation dynamics. Nonetheless, given the large uncertainties in the understanding of this phenomenon no attempt is made to model long-term seal/crust evolution.

As can be observed from Figure 4.35 the effect of soil sealing is confined to a thin superficial layer. For this reason, surface seal is considered to modify only the infiltration flux (Section 4.7.1) and have no importance on the subsurface soil-water dynamics (Section 4.7.3). After the formation of a seal layer the soil-hydraulic properties required in the calculation of the infiltration in Section 4.7.1 are changed. The new soil-hydraulic properties are obtained as the average of the properties at the seal surface, $z_d = 0$, (the ones indicated with the subscript cr) and the undisturbed properties. Geometric or arithmetic averages are used for the different soil-hydraulic properties. Averaging the properties between the surface and the undisturbed soil is a further simplification of the method, because it corresponds to assume an uniform equivalent seal layer case. Given, the large non-linearities present in soil-hydraulic properties using a uniform seal layer can be a coarse approximation. However, including a distributed seal would require a very fine spatial resolution of the soil column at the surface, unfeasible for long-term simulations. Furthermore, *Assouline and Mualem* (2001) show that assuming an uniform seal layer does not affect significantly the estimated infiltration curve when the dynamic phase of seal formation is simulated. Overestimation of infiltration rates is instead possible when a completely formed seal layer is considered.

As a final remark, it must be noted that the module of soil sealing implemented in "Tethys" depend on several parameters not easy to determine and on some restrictive assumption. Therefore, it must be intended more as a possibility to include the first order effect of the soil seal process than not as an effective realistic simulation of the latter. It would not be surprising to obtain infiltration or runoff fluxes different from the observed ones or if some of the parameters would need to be adjust to provide realistic results.

4.7.3 Governing equation

Within the soil, water moves according to gradients in soil water potential which are dominated by gravity at high soil water contents and by capillarity in drier conditions. Water can then be removed from the soil by evaporation and root uptake or be lost to deeper layers by drainage (*Daly and Porporato*, 2005). Infiltration from the water influx to the surface, together with evaporation, transpiration, and leakage

cause a continuous redistribution of water within the soils.

The most well-known methodology to describe this phenomenon is represented by the Richards equation (*Hillel*, 1998), which is based on homogeneous uniform soil characteristics, and describes the flow of liquid water in unsaturated soils under gravity and capillary forces in isothermal conditions (*Hillel*, 1998; *Daly and Porporato*, 2005). The basic equation, using one-dimensional approximation, written for vertical flows, was derived by *Richards* (1931) by combining the Darcy's law with the continuity equation, as:

$$\frac{\partial \theta}{\partial t} = \frac{\partial}{\partial z_d}\left[K(\theta)\frac{\partial \Psi(\theta)}{\partial z_d} + K(\theta)\right] = \frac{\partial}{\partial z_d}\left[D(\theta)\frac{\partial \theta}{\partial z_d}\right] + \frac{\partial K(\theta)}{\partial z_d}\,, \tag{4.215}$$

where θ $[-]$ is the soil moisture content, $K(\theta)$ $[mm\ h^{-1}]$ is the unsaturated hydraulic conductivity, $\Psi(\theta)$ $[mm]$ is the soil water potential, $D(\theta)$ $[mm^2\ h^{-1}]$ is the unsaturated water diffusivity, t $[h]$ is the time, and z_d $[mm]$ denotes the normal to the soil surface assumed to be positive upward.

The Richards equation is a highly nonlinear partial differential equation and its numerical solution is difficult also in one single dimension. Numerical methods to solve equation (4.215) are typically time consuming and they require a fine mesh of soil layers (*Celia et al.*, 1990; *Ross*, 2003; *Miller et al.*, 2006). Furthermore, Richards equation as described in equation (4.215) neglects infiltration, evaporation, transpiration, and lateral fluxes terms. The presence of inflow or outflow contributions makes the solution of (4.215) rather complex (*vanDam and Feddes*, 2000; *Varado et al.*, 2006; *Ivanov*, 2006) also when lateral and dispersion terms are neglected *Kumar* (2004). Given these inherent complexities, simplifications of Richards equation or alternative approaches have been proposed. For instance, the force-restore methods was applied also for soil moisture (*Noilhan and Planton*, 1989; *Montaldo and Albertson*, 2001). Many authors have used one or more buckets to represent the soil moisture dynamics with a volume-balance equation applied over the vadose zone (*Rodriquez-Iturbe et al.*, 1999; *Rodriguez-Iturbe*, 2000; *Albertson and Kiely*, 2001; *Guswa et al.*, 2002). An example of such an equation is given by:

$$d_{z,i}\frac{d\theta_i}{dt} = I_f(\theta_i) - T(\theta_i) - E(\theta_i) - L(\theta_i)\,, \tag{4.216}$$

where in this case $d_{z,i}$ $[mm]$ is the thickness of the soil in the bucket layer i, I_f $[mm\ h^{-1}]$ is the infiltration rate, T and E $[mm\ h^{-1}]$ the transpiration and evaporation rates, and L $[mm\ h^{-1}]$ the leakage.

The numerical scheme governing soil water dynamics within "Tethys" is a compromise between the correct representation of physical laws describing soil moisture fluxes in the vadose zone and the need to reduce the computational cost of a such realistic representation. Specifically, the governing equation of water fluxes into the soil is a simplification of the Richards equation, where capillary forces are neglected

and only gravity effects are considered:

$$d_z \frac{\partial \theta}{\partial t} = d_z \frac{\partial K(\theta)}{\partial z_d} - \Big[T_{H_v}(\theta) + T_{L_v}(\theta) + E_g(\theta) + E_{bare}(\theta)\Big] + Q_{l,in} - Q_{l,out}(\theta)\,, \tag{4.217}$$

where T_{H_v}, T_{L_v} $[mm\ h^{-1}]$ are the transpiration rates, E_g, E_{bare} $[mm\ h^{-1}]$ are the evaporation rates described in Section 4.3.2, and $Q_{l,in}$, $Q_{l,out}$ $[mm\ h^{-1}]$ are the incoming and outgoing subsurface lateral fluxes, as described later in Section 4.7.6. In order to evaluate the soil moisture contents, θ_i $[-]$, equation (4.217) is solved numerically using a system of ordinary differential equations, once the soil column is subdivided in $i = 1, ..., n_s$ layers.

Referring to Figure 4.36, each layer i can be characterized with a depth from the surface to the layer upper boundary, $Z_{s,i}$ $[mm]$, a layer thickness, $d_{z,i}$ $[mm]$, and a positive distance between the layer center and the precedent layer center, $D_{z,i}$ $[mm]$. The ordinary differential equations obtained from the discretization of equation (4.217) take the form:

$$d_{z,i} \frac{d\theta_i}{dt} = q_{i-1} - q_i - \left(\sum_{j=1}^{n_c} T_{H_v,j}\ r_{H_v,i,j}\right) - \left(\sum_{j=1}^{n_c} T_{L_v,j}\ r_{L_v,i,j}\right) - \left(\sum_{j=1}^{n_c} E_{g,j}\right)\ e_{f,i} - E_{bare}\ e_{f,i} + Q_{l,in,i} - Q_{l,out,i}\,, \tag{4.218}$$

where q_i $[mm\ h^{-1}]$ is the vertical outflow from a layer i. Water uptakes from the soil surface and root zone via the evaporation and transpiration processes can be subdivided in the following components: evaporation from the bare soil fraction, E_{bare} $[mm\ h^{-1}]$, described in equation (4.70); evaporation from the soil under the canopies, E_g $[mm\ h^{-1}]$ (equation 4.66), and transpiration from high and low vegetation layers, T_{H_v}, and T_{L_v} $[mm\ h^{-1}]$ (equation 4.64, and 4.65). The fractions of the root biomass contained in the soil layers, r_i $[-]$, and the evaporative fractions $e_{f,i}$ $[-]$ are described later in this section. The lateral outflows, $Q_{l,out,i}$ $[mm\ h^{-1}]$, are calculated according to the soil moisture content and to the basic element topographic slope. Their determination is described in Section 4.7.6. The incoming lateral subsurface fluxes, $Q_{l,in,i}$ $[mm\ h^{-1}]$, are the sum of subsurface water fluxes coming from the neighborhood elements.

According to the original Richards equation (4.215), the vertical outflow from layer i is function of the soil water potential and of the unsaturated conductivity that in turn depend on moisture θ_i and on the depth $Z_{s,i}$ as:

$$q_i = \overline{K_i}\left(1 + \frac{\Psi_i - \Psi_{i+1}}{Dz_{i+1}}\right)\,, \tag{4.219}$$

when the soil water potential, Ψ, is neglected, equation (4.219) becomes:

$$q_i = \overline{K_i}\,, \tag{4.220}$$

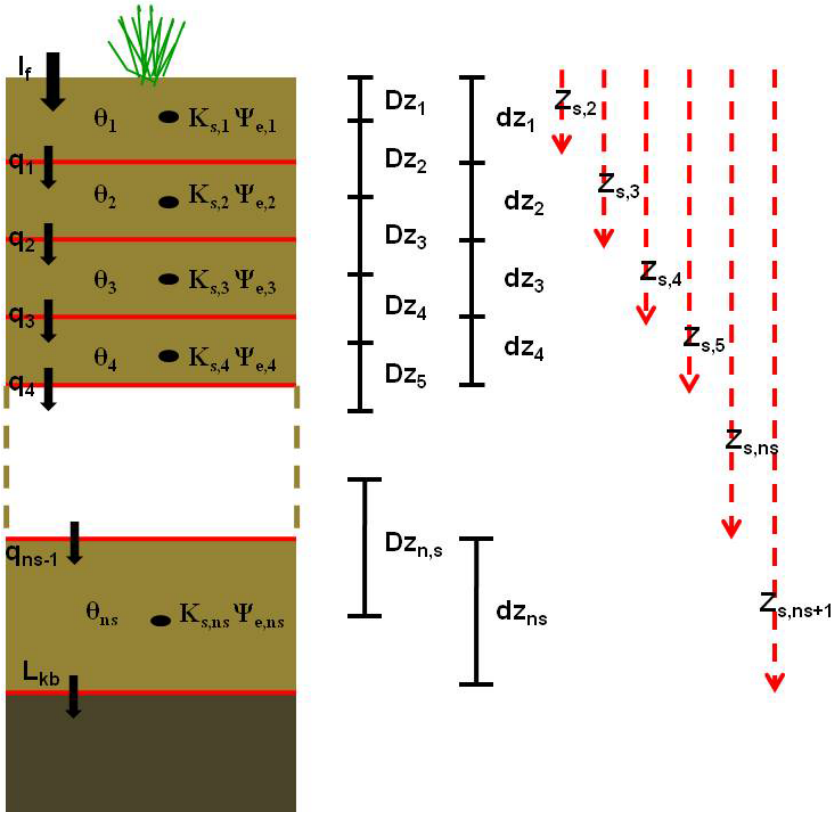

Figure 4.36: A graphical scheme illustrating the discrete soil column and the principal variables used in the computation of subsurface water dynamics. The subscript i identify the soil layer. The term $\Psi_{e,i}$ $[mm]$ is the water potential at the bubbling pressure at the center of the layer, $K_{s,i}$ $[mm\ h^{-1}]$ is the saturated conductivity at the center of layer (Section 4.7.4), L_{kb} $[mm\ h^{-1}]$ is the bottom leakage subsurface flow (Section 4.7.6). The soil water content is θ_i $[-]$, q_i $[mm\ h^{-1}]$ is the vertical outflow from layer i, $Z_{s,i}$ $[mm]$ is the depth from the surface to the layer upper boundary, $d_{z,i}$ $[mm]$ is the layer thickness, and $D_{z,i}$ $[mm]$ is a positive distance between the layer center and the precedent layer center. Note the first value of Z_s is always zero, corresponding to the surface. Rather than define the mesh resolution a priori, in each simulation the soil column can be properly subdivided. Typically between 8 and 20 layers are used with a coarser mesh resolution at greater depths for computational efficiency.

where $\overline{K_i}$ $[mm\ h^{-1}]$ is the unsaturated conductivity averaged from the layer i and $i+1$. Typically, arithmetic, geometric, or harmonic means are used to average the values of $K(\theta)$ between layers (*Zhu*, 2008). The averaging method is of a certain importance because $K(\theta)$ varies strongly with soil water content (see Section 4.7.4). Neglecting the water potential Ψ in equation (4.219) implies that neither geometric mean nor harmonic mean can be used to average $K(\theta)$. This limitation is related to the dryness of the lower layer, $i+1$, such dryness would inhibit the leakage from the upper layer i, leading to $\overline{K_i} \approx 0$ when one of the two layers is dry. This would create an unnatural process where the lower layer $i+1$ cannot receive water, because it is dry. Neither the arithmetic mean is suitable because high moisture contents in the lower layer, $i+1$, would induce a leakage from layer i, also when this layer is completely dry. For the reasons mentioned above, the average value $\overline{K_i}$ is calculated accounting only for the unsaturated conductivity in the upper layer i, i.e., $\overline{K_i} = K_i$. The value of the unsaturated conductivity, K_i, is calculated according to the depth of the layer and to the unsaturated conductivity curve (Section 4.7.4):

$$K_i \quad = \quad K_s(z_d)\Big(\frac{\theta_i}{\theta_{sat}}\Big)^{3+2/\lambda_\circ}, \tag{4.221}$$

where $K_s(z_d) = K_s\big(Z_{s,i} + 0.5 d_{z,i}\big)$ $[mm\ h^{-1}]$ is the saturated conductivity at the center of the layer i and for the other symbols refer to Section 4.7.4.

Note that the flow incoming to the first layer of soil is the infiltration term, I_f $[mm\ h^{-1}]$, that is assumed to be a boundary condition of the model (Section 4.7.1). Furthermore, the fluxes q_i,s are $n_s - 1$, since the vertical outflow from the last layer of soil is directed toward the bedrock and is identified as bottom leakage, L_{kb} (Section 4.7.6). The depth Z_{n_s+1} $[mm]$ is, indeed, the maximum soil depth simulated in the model and can be often assumed to encompass the regolith layer up to the bedrock boundary. The quantity L_{kb} represents the leakage between the vadose zone and the underneath bedrock, the latter can eventually contain a deep aquifer schematized as a lumped entity (see Section 4.7.6 for details). Consequently, in the last equation of the system described in (4.218), the term q_{n_s} is replaced with L_{kb} $[mm\ h^{-1}]$.

There may be cases where the last layer, n_s, or some intermediate layer becomes saturated, for instance when $L_{kb} = 0$ $[mm\ h^{-1}]$). In these conditions the water in excess is considered to saturate progressively the *"unsaturated"* zone starting from the interested layer toward the surface. This mechanism leads to the formation of a shallow water table depth, Z_{wt} $[mm]$, and of a saturated zone within the soil column that is explicitly considered in the model.

The adopted numerical methods operates on a mesh that is supposed to resolve the vertical variability of soil moisture. Since the numerical discretization permits multiple resolution, the soil profile is resolved at a high detail near the surface, which allows one to account for the high-frequency variability in the atmospheric forcing. The mesh has a coarser resolution at greater depths for computational efficiency. Typical mesh resolutions adopted in the model are composed by 10-20 layers with layer thickness varying from 50 to 400 $[mm]$.

Since the soil column is resolved at multiple number of points, the root biomass profile (equation 4.1) can be explicitly represented in the modeling of water dynamics in the vadose zone. The fractions of the root biomass at different depths are identified by r_i $[-]$, with $i = 1 \dots n_s$. The terms r_i can be calculated using the depth of the layer upper boundary, $Z_{s,i}$ $[mm]$, and the the rooting depth, Z_R $[mm]$. Note that to preserve the balance of mass $\sum_i^{n_s} r_i = 1$, although the rooting depth, Z_R $[mm]$, accounts only for the 95.02% of the root biomass (Section 4.1.2).

$$r'_i = e^{-\eta\,(Z_{s,i})} - e^{-\eta\,(Z_{s,i+1})}\,, \quad \text{if} \quad Z_R > Z_{s,i+1}\,, \tag{4.222}$$

$$r'_i = e^{-\eta\,(Z_{s,i})} - e^{-\eta\,Z_R}\,, \quad \text{if} \quad Z_{s,i} \leq Z_R \leq Z_{s,i+1}\,, \tag{4.223}$$

$$r'_i = 0\,, \quad \text{if} \quad Z_R < Z_{s,i}\,, \tag{4.224}$$

where the rooting depth, Z_R $[mm]$, and the decay rate of root biomass, η $[mm^{-1}]$, are function of the specific PFT and of the vegetation types $(H_v - L_v)$ as described in Section 4.1.2. Finally, the fractions of the root biomass, r_i, are obtained as $r_i = r'_i/(0.9502)$ $[-]$. Note that the the rooting depth, Z_R $[mm]$, for numerical reasons should be always shallower than Z_{s,n_s+1}. This is an acceptable assumption given the difficulties of roots to growth until considerable depths or in the bedrock. The fractions of root biomass, r_i, are the numerical representation of plant water uptake strategy. Using fractions proportional to the fine root biomass the strategy chosen is a static one since plants cannot adapt to non-optimal soil moisture distributions. It has been remarked that plants have the capability to compensate for water stress and to uptake water from wetter layers (*Guswa et al.*, 2002; *Teuling et al.*, 2006). Since a great uncertainty still remains regarding this behavior, a dynamic adaptability of root fractions is not accounted for in "Tethys". There is only an implicit adaptability strategy related to the possible lack of moisture in one or more layers. In this case the transpiration rate is reduced, given the impossibility to uptake water from dry layers. Consequently, the partition of transpiration does not perfectly follow the root fraction distribution.

In analogy to the fractions of root biomass, evaporative fractions, $e_{f,i}$ $[-]$, are defined. The latter rather than have a physical meaning, such as r_i, are a numerical artefact to extract water up to a certain depth, d_e $[mm]$. Neglecting, capillary forces in the soil moisture balance (equation 4.218) prevents an upward redistribution of soil moisture. For this reason, as described in Section 4.4.4, it is necessary to introduce a characteristic length of evaporation, d_e, i.e., a depth up to which is possible to uptake water. The evaporative fractions $e_{f,i}$ are nothing but the fractions occupied by each soil layer i up to the depth d_e.

The solution of the system of ordinary differential equations (4.218) is carried out with an explicit *Runge-Kutta(4,5)* formula, the Dormand-Prince pair (*Dormand and Prince*, 1980) using the *Matlab* M-file *ode45*. Since all the evaporation and transpiration fluxes implicitly depend on soil water content, a rigorous solution of soil water dynamic would require the computation of the energy fluxes within the differential numerical scheme of equation (4.218). In order to avoid this high time-demanding

solution the transpiration and evaporation fluxes in (4.218) are determined with the soil water content calculated at the precedent time step. Similarly, the lateral fluxes, $Q_{l,in,i}$, represent the outflows from neighborhood elements at the precedent time step.

Characteristic soil water contents necessary in the computation of the mass and energy fluxes between the atmospheric surface layer and the surface are calculated as the weighted soil moisture up to a certain depth. These are: the average soil moisture up to the characteristic length of evaporation, θ_e $[-]$, the soil moisture content averaged up to depth interested by the infiltration process, θ_F $[-]$, the soil moisture content averaged up to the dampening depth, θ_d, and the average soil moisture content available to roots, θ_R, that is PFT dependent. The soil moisture content available to roots zone is, in fact, obtained from the fraction of the root biomass r_i, as $\theta_R = \sum_{i=1}^{n_s} r_i \theta_i$.

4.7.4 Soil properties and pedotransfer functions

Soil texture is a key variable in the coupled dynamics of climate, soil, and vegetation (*Fernandez-Illescas et al.*, 2001; *Ivanov*, 2006). Suitable relationships to link soil texture properties to hydraulic characteristics are thus necessary and the estimation of soil water hydraulic characteristics from readily available physical parameters has been a long-term goal of soil physicists and engineers (*Saxton and Rawls*, 2006). Several equations have been developed to describe soil water hydraulic characteristics using a limited number of parameters related to soil texture composition (*Brooks and Corey*, 1964; *Campbell*, 1974; *Clapp and Hornberger*, 1978; *vanGenuchten*, 1980; *Saxton et al.*, 1986; *Mayr and Jarvis*, 1999; *Schaap and vanGenuchten*, 2006); see also *Hillel* (1998). Such equations are commonly applied in hydrologic analysis. *Saxton and Rawls* (2006) have recently proposed an update of the *Saxton et al.* (1986) soil water retention curve with new equations derived from a large *USDA* database of soils. They make use of commonly available variables such as soil texture and organic matter to describe the equation parameters. They further incorporate an improved conductivity equation including the effects of bulk density, gravel, and salinity, to provide a broadly applicable predictive system. The *Saxton and Rawls* (2006) curves and related parameterizations to describe soil hydraulic characteristics are used in "Tethys". Unsaturated hydraulic conductivity, K $[mm\ h^{-1}]$, and soil water potential, Ψ $[kPa]$, are related to the soil moisture content, θ $[-]$ or $[mm^3\ mm^{-3}]$.

Before discussing the retention and conductivity curves, definitions must be provide for three specific value of moisture content θ_{sat}, θ_{hy}, θ_{fc} $[-]$, and for the effective saturation s_e $[-]$. The saturation moisture content, θ_{sat}, is the maximum water content that a soil can store before saturation occurs, the residual or hygroscopic moisture content, θ_{hy}, is the amount of soil water that cannot be removed from soil neither by drainage nor by evaporation, finally the field capacity moisture content, θ_{fc}, is the water content at which the hydraulic conductivity becomes negligible

(*Laio et al.*, 2001). The effective saturation of a soil layer i, s_e $[-]$ is defined as:

$$s_e = \frac{\theta_i - \theta_{hy}}{\theta_{sat} - \theta_{hy}} . \tag{4.225}$$

Saxton and Rawls (2006) proposed the following empirical equations for the soil water retention curve $\Psi(\theta)$, (assuming isotropic media, drainage cycle, and neglecting hysteresis):

$$\Psi(\theta) = -33 + \left[\frac{(\theta - \theta_{33})(33 + \Psi_e)}{\theta_{sat} - \theta_{33}}\right], \quad \text{if } \Psi(\theta) > -33\ [kPa], \tag{4.226}$$

$$\Psi(\theta) = -A\,(\theta)^{-\frac{1}{\lambda_\circ}}, \quad \text{if } \Psi(\theta) \leq -33\ [kPa], \tag{4.227}$$

where Ψ_e $[kPa]$ is the air entry bubbling pressure, $A = \exp\big[\ln(33) + (\ln(33)/\lambda_\circ)\big]$ $[kPa]$, θ_{33} $[-]$ is the soil water content at -33 $[kPa]$, and $\lambda_\circ$ $[-]$ is the pore-size distribution index. The equation relating the unsaturated conductivity, $K_v(\theta)$ $[mm\ h^{-1}]$, and soil moisture content, θ $[-]$, is:

$$K_v(\theta) = K_{s\,v}\left(\frac{\theta}{\theta_{sat}}\right)^{\frac{2+3\lambda_\circ}{\lambda_\circ}} . \tag{4.228}$$

where $K_{s\,v}$ $[mm\ h^{-1}]$ is the saturated hydraulic conductivity in the normal to the soil surface. Note that equation 4.228) is similar to the ones proposed by *Campbell* (1974). An example of the soil water retention and unsaturated conductivity curves for a generic sand loam soil is presented in Figure 4.37. The curves obtained with the equation of *Saxton and Rawls* (2006) are compared with other parameterizations, such as *Brooks and Corey* (1964), *vanGenuchten* (1980), and *Campbell* (1974) (Figure 4.37). The parameters first calculated for the *Saxton and Rawls* (2006) equations have been converted to *Van Genuchten* equations using a parameter equivalence (*Morel-Seytoux et al.*, 1996), and have been considered valid, without modifications, for *Brooks and Corey* and *Campbell* equations.

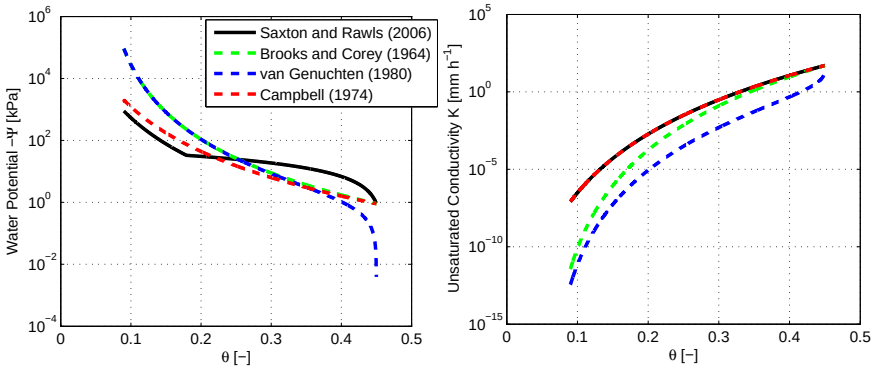

Figure 4.37: Soil water retention and unsaturated conductivity curves, i.e., unsaturated hydraulic conductivity K_v $[mm\ h^{-1}]$ (a) and soil water potential $-\Psi$ $[kPa]$ (b) function of soil water content, θ. The curves are calculated for a generic sand loam soil.

The value of the parameters θ_{hy} and θ_{fc} can be obtained from soil water char-

acteristic curves (equations 4.226-4.228) imposing a water potential equal to -10 $[MPa]$ for the residual-hygroscopic water content, i.e., $\theta_{hy} = \theta(\Psi = -10\ [MPa])$, and an unsaturated conductivity of 0.2 $[mm\ h^{-1}]$ for the field capacity, i.e., $\theta_{fc} = \theta(K_v = 0.2\ [mm\ h^{-1}])$ (*Laio et al.*, 2001). Generally, the characterization of these parameters is uncertain, especially for θ_{fc} which definitions is not mathematically rigorous. The threshold chosen above must be seen as a model assumption and can be eventually modified.

The unsaturated hydraulic conductivity, K_v, is assumed to exhibit an exponential decline with depth within the soil column (*Beven*, 1982; *Sivapalan et al.*, 1987; *Wigmosta et al.*, 1994):

$$K_v(z_d) \quad = \quad K_v(0)e^{-\tilde{f}(-z_d)}\,, \tag{4.229}$$

where z_d $[mm]$ is the considered depth (positive upward) and $\tilde{f}$ $[mm^{-1}]$ is a scaling parameter controlling the rate of decline $\tilde{f} = (\theta_{sat} - \theta_{hy})/m_f$ (*Vertessy and Elsenbeer*, 1999). The parameter m_f $[mm]$ expresses the magnitude of the decay and it is a property of the specific soil and location. The choice of an exponential decline of transmissivity is typical in literature since its first application in *TOPMODEL* (*Beven and Kirkby*, 1979; *Beven*, 1997). The exponential decay is a reasonable assumption for a wide range of soils (*Beven*, 1982), although it can be inappropriate for specific soils and alternative forms based on linear and parabolic functions have been derived (*Ambroise et al.*, 1996; *Wigmosta and Lettenmaier*, 1999). For this reason, in future versions of "Tethys" a wider flexibility on the parametrization of $K_v(z_d)$ decay behavior with depth is recommended. Note that scaling parameter, $\tilde{f}$, can be quite different from the one used in *TOPMODEL* applications. *TOPMODEL* applications, being at the catchment scale, often assume values of surface conductivity very large in comparison to the values obtainable from soil texture (*Niu et al.*, 2007), and this is reflected also on $\tilde{f}$. The effect of $K_v(z_d)$ decay with depth can be eliminated assuming very large values of m_f, that give a constant $K_v(z_d)$. Furthermore, evidences show that the saturation conductivity decay is mainly concentrated in the upper part of the soil column (*Scott et al.*, 2000). At greater depth $K_v(z_d)$ remains almost constant rather than continue to diminish. Therefore, the saturated hydraulic conductivities decline is stopped at a certain depth, Z_{Kv} $[mm]$. In order to avoid the introduction of a further parameter, Z_{Kv} is assumed to be the depth at which the saturated hydraulic conductivity reaches the 10% of its surface values, i.e., $Z_{Kv} = 2.30/\tilde{f}$. An illustration of the hydraulic conductivity decay with depth is shown in Figure 4.38.

Equations (4.226), (4.227), and (4.228) can be used once the parameters θ_{sat} $[-]$, $\lambda_\circ$ $[-]$, Ψ_e $[kPa]$, $K_{s\,v}(z_d = 0)$ $[mm\ h^{-1}]$, and θ_{33} $[-]$ are known. The above parameters are evaluated using the pedotransfer functions proposed by *Saxton and Rawls* (2006), neglecting the adjustments due to gravel, and salinity effects. The information required to estimate the soil hydraulic parameters is the textural composition of the soil. Specifically, the fractions of sand, F_{san} $[-]$, and clay F_{cla} $[-]$, and the percentage of organic material, P_{org} $[-]$, are required. The soil column is assumed

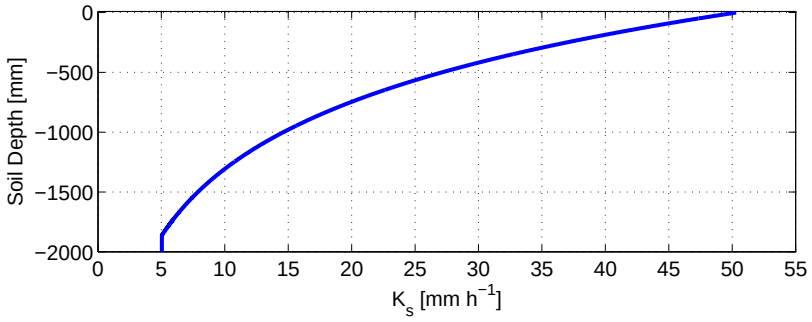

Figure 4.38: Illustration of the saturated hydraulic conductivity, $K_{s\,v}$, decay with soil depth, z_d, in a generic sand loam soil, values obtained with the parameter $m_f = 320$ $[mm]$.

to have a constant texture composition within its depth. The equations relating θ_{sat}, $\lambda_\circ$, Ψ_e, $K_{s\,v}(z_d = 0)$, and θ_{33} to the soil fractions F_{san}, F_{cla}, and P_{org} are described in page 1571 of *Saxton and Rawls* (2006).

Horizontal and vertical heterogeneities in hydraulic conductivity are accounted for with an anisotropy factor. The soil anisotropy, a_r $[-]$, is, indeed, defined as the ratio between the hydraulic conductivity in the directions parallel to the slope K_h and the hydraulic conductivity normal to the slope K_v:

$$a_r \quad = \quad \frac{K_h}{K_v} \,. \tag{4.230}$$

Typically $a_r > 1$. The value of K_h can be some order of magnitude larger then K_v, since it embeds also the effect of preferential flow paths (*Weiler and McDonnell*, 2007). Anytime the subscript h or v is omitted in the text, K refers to the hydraulic conductivity normal to the slope.

In Section 4.3.3 parameters depending on soil types have been introduced. These are the thermal conductivity of solid soil, λ_{soil} $[W\ m^{-1}\ K^{-1}]$, the volumetric heat capacity of soil, cv_{soil} $[J\ K^{-1}\ m^{-3}]$, and the thermal conductivity of dry soil, λ_{dry} $[W\ m^{-1}\ K^{-1}]$. The latter are necessary in the calculation of the soil heat fluxes and are estimated according to *de Vries* (1963); *Farouki* (1981) (see also *Oleson et al.* (2004) pages 93-95):

$$\lambda_{soil} \quad = \quad \left[8.8F_{san} + 2.92F_{cla}\right] / \left[F_{san} + F_{cla}\right] \ , \tag{4.231}$$

$$\lambda_{dry} \quad = \quad \left[0.135\rho_d + 64.7\right] / \left[2700 - 0.947\rho_d\right] \ , \tag{4.232}$$

$$cv_{soil} \quad = \quad 10^6 \left[2.128F_{san} + 2.385F_{cla}\right] / \left[F_{san} + F_{cla}\right] \ , \tag{4.233}$$

where F_{san}, F_{cla} $[-]$ are the soil fractions of sand and clay, and $\rho_d = \rho_{ss}(1 - \theta_{sat})$ $[kg\ m^{-3}]$ is the bulk density of soil, with $\rho_{ss} = 2650$ $[kg\ m^{-3}]$ soil solid density. Note that the information required to estimate soil thermal parameters is the same necessary for soil water hydraulic characteristics.

Finally, the soil erodibility factor, K_{ero} $[kg\ h\ J^{-1}\ mm^{-1}]$, utilized in Section 4.6.4 is borrowed from *Universal Soil Loss Equation*, *USLE*, equation (*Wischmeier*

and Smith, 1978; *Lenhart et al.*, 2005), and it is calculated with the pedotransfer functions of *Williams* (1995):

$$K_{ero} = 10^{-3} f_{sand}\, f_{cls}\, f_{orgC}\, f_{his}\,, \tag{4.234}$$

$$f_{san} = 0.2 + 0.3 \exp\left[-25.6 F_{san}(1 - F_{sil})\right], \tag{4.235}$$

$$f_{cls} = \left(\frac{F_{sil}}{F_{cla} + F_{sil}}\right)^{0.3}, \tag{4.236}$$

$$f_{orgC} = 1 - \frac{0.25 P_{orgC}}{P_{orgC} + \exp\left[3.72 - 2.95 P_{orgC}\right]}, \tag{4.237}$$

$$f_{his} = 1 - \frac{0.7(1 - F_{san})}{1 - F_{san} + \exp\left[-5.51 - 22.9(1 - F_{san})\right]}, \tag{4.238}$$

where the percentage of organic carbon content, P_{orgC} $[-]$ can be calculated as $P_{orgC} = P_{org}/1.72$ (*Williams*, 1995), and the fraction of silt is $F_{sil} = (1 - F_{san} - F_{cla} - P_{org}/100)$ $[-]$.

4.7.5 Saturation excess runoff

A generic soil layer i of soil column can become over-saturated, once reached the soil content θ_{sat} $[-]$ the inflow to the layer i is larger than the outflow. In this case there is a surplus of water that the layer i is unable to store. As anticipated in Section 4.7.3, the model assumption is that the exceeding water, W_{TR} $[mm\ h^{-1}]$, is transferred to the upper layer $i-1$. Consequently, the formation of a saturated zone in deeper soil layers starts to saturate progressively the unsaturated zone toward the surface. This mechanism can create a perched or shallow aquifer characterized by a certain water table depth, Z_{wt} $[mm]$, within the soil column. When the upward flux, W_{TR} $[mm\ h^{-1}]$, outflows from the first layer, 1, this component contributes to surface runoff and it is indicated as saturation excess runoff, R_D $[mm\ h^{-1}]$. Numerically the fluxes $W_{TR,i}$ are estimated at each time step after solving equation (4.218), and checking progressively from the bottom if the layer are over-saturated (Section 4.7.3).

4.7.6 Subsurface flow

Water transferred sideways from the column of soil, $Q_{l,out}$ $[mm\ h^{-1}]$, is indicated as lateral subsurface flow or hypodermic flow. These downslope flows within the unsaturated zone are often neglected in literature (*Beven and Kirkby*, 1979; *Sivapalan et al.*, 1987), although in soils close to saturation they can be very significant. The slope of the hydraulic head is assumed to be parallel to the soil surface, this assumption is commonly made in topographic subsurface routing method (*Beven and Kirkby*, 1979; *Sivapalan et al.*, 1987). However, its validity is strongly violated in shallow terrains (floodplain), especially when a portion or the entire soil column becomes saturated. For this reason in future version of the model it is recommended to include the possibility of a subsurface flow governed by the hydraulic head gradient (*Wigmosta and Lettenmaier*, 1999). According to the previous considerations,

the lateral subsurface flow from a layer i, $Q_{l,out,i}$ moves in the steepest direction toward the nearest elements:

$$Q_{l,out,i} = \frac{T_{r,i} \tan \beta_T}{a_T} , \tag{4.239}$$

where β_T $[rad]$ is the slope of the element, a_T $[mm]$ is the area of the basic element per unit contour length that drains through the location (*Beven and Kirkby*, 1979; *Sivapalan et al.*, 1987), and $T_{r,i}$ $[mm^2\ h^{-1}]$ is the total transmissivity of the layer i. The transmissivity, $T_{r,i}$, is obtained considering the unsaturated hydraulic conductivity $K(\theta_i, z_d)$ in direction parallel to the slope, K_h, at depth $Z_{s,i} + dz_i/2$ $[mm]$:

$$T_{r,i} = K_h(\theta_i,\ Z_{s,i} + dz_i/2)[dz_i] , \tag{4.240}$$

where dz_i is the depth of layer i, as described in Section 4.7.3. The total lateral subsurface flow from an element, $Q_{l,out}$, $[mm\ h^{-1}]$, is calculated integrating equation (4.239) in the $i = 1, ..., n_s$ layers. When a single basic computational element is considered the component $Q_{l,out}$ is lost as subsurface flow, for a flat element $Q_{l,out} = 0$.

According to Figure 4.36 the last layer of the soil column, n_s, is drained via a bottom leakage subsurface flow, L_{kb} $[mm\ h^{-1}]$. The latter represents the percolation from the soil column, regolith, toward the bedrock. The soil-bedrock interface leakage, although neglected for long-time, has been recently regarded has an important process of the subsurface dynamics (*Weiler and McDonnell*, 2004; *Tromp-van Meerveld and Weiler*, 2008). This flux is obtained as a geometric mean between the hydraulic conductivity of the last layer of soil, n_s, and the conductivity of the bedrock, K_{bot} $[mm\ h^{-1}]$, that might be eventually equal to zero for an impermeable bedrock. The condition $K_{bot} = 0$ avoids recharge to deeper aquifers, and the condition $K_{bot} = K_v(\theta_{n_s}, Z_{s,n_s+1})$ represents a free drainage.

$$L_{kb} = \exp\Big[0.5\big(ln[K_{bot}] + ln[K_v(\theta_{n_s}, Z_{s,n_s+1})]\big)\Big] . \tag{4.241}$$

The vertical subsurface flow L_{kb} is considered to provide a recharge to a very deep aquifer. The latter can be schematized as a lumped component at watershed or sub-watershed scale. The deep aquifer on turn returns a baseflow flux, Q_{sub} $[mm^3\ h^{-1}]$, according to a linear reservoir scheme characterized by a certain time parameter. The baseflow flux is successively distributed throughout the stream network. However, these components are meaningful only at the watershed scale. At the basic element scale L_{kb} is only indicated as recharge to deeper layers.

4.8 Surface water dynamics

The movement of surface water through a distributed model domain is strictly correlated to its topographic representation (Section 4.1.2). The runoff depth, R_{tot} $[mm]$, in a basic computational element is the sum of infiltration excess runoff, R_H $[mm\ h^{-1}]$, (Section 4.7.1) and saturation excess runoff, R_D $[mm\ h^{-1}]$ (Section 4.7.5) integrated on the time step. The flow depth, y $[mm]$, is then calculated spreading runoff depth over the entire cell grid for overland flow, $y = R_{tot}$. For cells that represent channels, a rectangular regular section of width, w_{ch} $[m]$, is assumed, i.e. $y = R_{tot}\, dx/w_{ch}$, where dx $[m]$ is the cell size. The runoff is successively routed using the kinematic wave approach, i.e. assuming the momentum equation $S_{fl} = \tan \beta_T$, where S_{fl} $[-]$ is the the energy gradient and β_T $[rad]$ is the slope of the element (*Chow*, 1988; *Bras*, 1990; *Brutsaert*, 2005). The water surface is thus assumed to be parallel to the cell bed. Further assuming local uniform flow and the Manning equation (4.242) as flow depth-discharge relationship is possible to calculate the flow velocity, U $[m\ s^{-1}]$, and consequently the time, t_R $[s]$, needed to move the water from a basic computational element to downstream elements (*Kollet and Maxwell*, 2006):

$$U = \frac{1}{n} R_{hy}^{2/3} {S_{fl}}^{1/2}, \tag{4.242}$$

where $R_{hy} \approx y$ $[mm]$ is the hydraulic radius approximated with the flow depth, and n $[s\ m^{-1/3}]$ is the Manning coefficient that depends on the superficial roughness. Consequently, the routing time is:

$$t_R = \frac{dx\, n}{y^{2/3} {\tan \beta_T}^{1/2}}, \tag{4.243}$$

where for simplicity the distance between the center of two cells is assumed to be equal to the cell size, dx, also for diagonal movements. The runoff depth, R_{tot} $[mm]$, present at a given time in the domain is routed according to the time t_R and to the flow directions calculated in Section 4.1.2. Obviously, it is possible that part of the runoff depth, R_{tot}, would remain within the domain at the end of the time step. In this case at the successive time step the portion of surface runoff still contained in the grid cells can be re-infiltrated as runon, q_{runon} $[mm\ h^{-1}]$. Runon is added to the water influx at the ground as described in Section 4.7.1. Finally, the rate at which runoff leaves the domain or pass trough a specific cell is identified as surface discharge $Q = \overrightarrow{R_{tot}}/dt$ $[mm\ h^{-1}]$, where $\overrightarrow{R_{tot}}$ $[mm]$ represent the routed part of R_{tot}. In order to respect the Courant condition a very fine time step must be used to route the water flow across the domain. The present version of "Tethys" adopts a 2 $[s]$ time step. It must be notice that this only improves the correctness of the flow routing, since runoff depth and eventual runon are still computed at hourly time scale from Section 4.7.

Chapter 5

"CHLORIS" A DYNAMIC VEGETATION MODEL

5.1 Introduction

Vegetation affects water, momentum, and energy exchanges by modifying the boundary conditions at the land surface. Consequently, it is of particular importance to explicitly consider the role of vegetation by taking into account its physiological properties, in particular, Leaf Area Index (LAI) and stomatal conductance. The developed model, named "Chloris" uses the photosynthesis rates computed in "Tethys" (Chapter: 4) to simulate the transient response of vegetation simulating productivity, respiration, allocation, and phenology processes. All the latter processes are strongly dependent on environmental conditions and they interact with hydrological components. "Chloris" is inspired to the group of models that simulate the distribution and structure of natural vegetation dynamically, using mostly mechanistic parameterizations of large-scale vegetation processes. These models are designed to facilitate the coupling, between hydrological/land surface models and the simulation of two-way bio-geophysical feedbacks between climate, hydrology and vegetation. Several among them can be quoted as principal references for "Chloris": *ORCHIDEE* (*Krinner et al.*, 2005), *LPJ* (*Sitch et al.*, 2003), *CLM-DGVM* (*Bonan et al.*, 2003; *Levis et al.*, 2004), *SEIB-DGVM* (*Sato et al.*, 2007), *Hybrid 3.0* (*Friend et al.*, 1997), *TRIFFID* (*Cox*, 2001), *IBIS*(*Foley et al.*, 1996), *BETHY* (*Knorr*, 2000), *TURC* (*Ruimy et al.*, 1996), *FBM* (*Lüdeke et al.*, 1994), *FOREST-BGC* (*Running and Coughlan*, 1988), *BIOME3* (*Haxeltine and Prentice*, 1996), *DOLY* (*Woodward et al.*, 1995), *ED2* (*Medvigy et al.*, 2009), *ANAFORE* (*Deckmym et al.*, 2008).

Atmospheric carbon dioxide is fixed into carbohydrates at each time-step, by means of photosynthesis at canopy scale. This uptake is constrained by biotic factors express as physiological and structural characteristics of the plants and through environmental factors that regulate the stomatal opening. The model of photosynthesis, described in Section 4.4.5, gives an estimation of the Gross Primary Production GPP, i.e. the rate at which the plants capture and store a given amount of chem-

ical energy as biomass, more tissue respiration. Some fraction of GPP is used by plants for growth and maintenance respiration of existing tissues. The remaining fixed biomass is referred to as Net Primary Production (NPP). When an excess in production is present ($NPP > 0$) the assimilated carbon is allocated to different vegetation compartments: foliage, living sapwood, fine roots, carbohydrate reserve, fruits, flowers, etc. Such a transfer typically follows dynamics and stress-dependent allocation patterns.

Along with these construction processes, tissue senescence and turnover are accounted for. Plants renew their living tissues and shed their green biomass, according to phenological pattern and life-spans. Foliage senescence is further enhanced by adverse hydro-meteorological conditions, which may impose additional controls on the fate of leaves and grass compartments.

The alternation of phenological states is considered in the model. Phenology represents the succession of periodic plant life cycle events and how these events are influenced by seasonal and inter-annual variations in climate. Phenological states strongly affect the regulatory mechanisms of the biochemical processes. Four different phenological states are represented: dormant, maximum growth, normal growth, and senescence states.

It must be noted that "Chloris" cannot be regarded as a fully vegetation dynamic model since it neglects all the long term dynamics of vegetation, i.e. the modifications that needs years or centuries to take place. For instance, seed production, dispersal and germination for the establishment of new species, species competition, plants mortality, and wildfire effects are not considered. Furthermore, the dynamic of vegetation structural attributes is simplified, plants height and stem area index evolution are not considered. Therefore, the term vegetation dynamics must be referred to the phenological dynamics and leaf area index evolution (*Arora*, 2002), rather than to a complete modeling of forest growth and plant competition (*Kirschbaum*, 199; *Sitch et al.*, 2003; *Levis et al.*, 2004; *Deckmym et al.*, 2008; *Medvigy et al.*, 2009).

The stationarity of vegetation fractions is indeed a strong limitation of "Tethys"-"Chloris". In the real world the extent of area occupied by a vegetation type is subject to changes due to species competition or mortality (*Tilman*, 1994; *Fernandez-Illescas and Rodriguez-Iturbe*, 2003, 2004; *Arora and Boer*, 2006). Neglecting species competition means that *Crown Areas* fractions (Section 4.1.2) are constant during the simulation period. This simplification avoids the introduction of uncertain and complex parameterizations required by an ecological model with interacting plant functional types. Modeling species competition is still an open problem, subject of scientific research in the ecological, and eco-hydrological communities (*Tilman*, 1994; *Fernandez-Illescas and Rodriguez-Iturbe*, 2003, 2004; *Arora and Boer*, 2006). A straightforward consequence of neglecting competition is that also the establishment of new individuals and the mortality of the plants is neglected. The proportion among vegetated and non-vegetated patches remains invariant. This assumption reduces the possibilities of investigation and research achievable with "Tethys"-

"Chloris". For instance, mortality events of vegetation have been observed worldwide (*Breshears et al.*, 2005; *McDowell et al.*, 2008; *vanMantgem et al.*, 2009). Such events can have long-term impacts on community dynamics and species interactions, and may feed back upon atmospheric CO_2 the climate (*Scholze et al.*, 2006). Although the consequences of tree mortality are readily apparent, the understanding of the causes of this process is still limited (*McDowell et al.*, 2008). This makes difficult to propose a parametrization of such a behavior in numerical models. Consequently, the current ability to predict when plant stress will result in widespread mortality is lacking, although it would be fundamental to assess potential climate-change impacts.

5.1.1 Model overview

"Chloris" simulates several characteristics of the physiological cycle of a plant, specifically it includes a description of the following components:

◇ **Vegetation processes**

- net primary production and plant respiration (Section 5.2.1);
- carbon allocation and translocation (Section 5.2.2);
- tissue turnover and stress-induced foliage loss (Section 5.2.3);
- carbon balance (Section 5.2.4);
- vegetation phenology (Section 5.3).

The photosynthesis-primary productivity process and the stomatal physiology are described in the Chapter 4, and they provide two canopy scale quantities: net assimilation rate, A_{nC} [$\mu mol\, CO_2\ s^{-1}\ m^{-2}$], and dark respiration, R_{dC} [$\mu mol\, CO_2\ s^{-1}\ m^{-2}$]. These rates are used as inputs for the vegetation model. "Chloris" operates at the daily time scale, vegetation affects the state of the land-surface mainly through changes of leaf area index. Photosynthesis and stomatal physiology are instead computed at the hourly time scale within the hydrological model (Section 4.4.5). An overview of the processes considered in the model and of the variables simulated is represented in Figure 5.1 with a flow chart, and in Figure 5.2 with a cartoon where a brief outline of the coupling among various plant life regulatory mechanisms is also illustrated.

5.1.2 Vegetation structure

The vegetated fraction, C_{veg}, of a basic computational element can contain different vegetation types. The model can account for an horizontal and vertical composition of the vegetation. The horizontal composition is made of units called *Crown Areas*, which fractions are C_{crown} [$-$]. The latter fractions identify specific vegetated patches with at most two different Plant Functional Types (PFT). The two

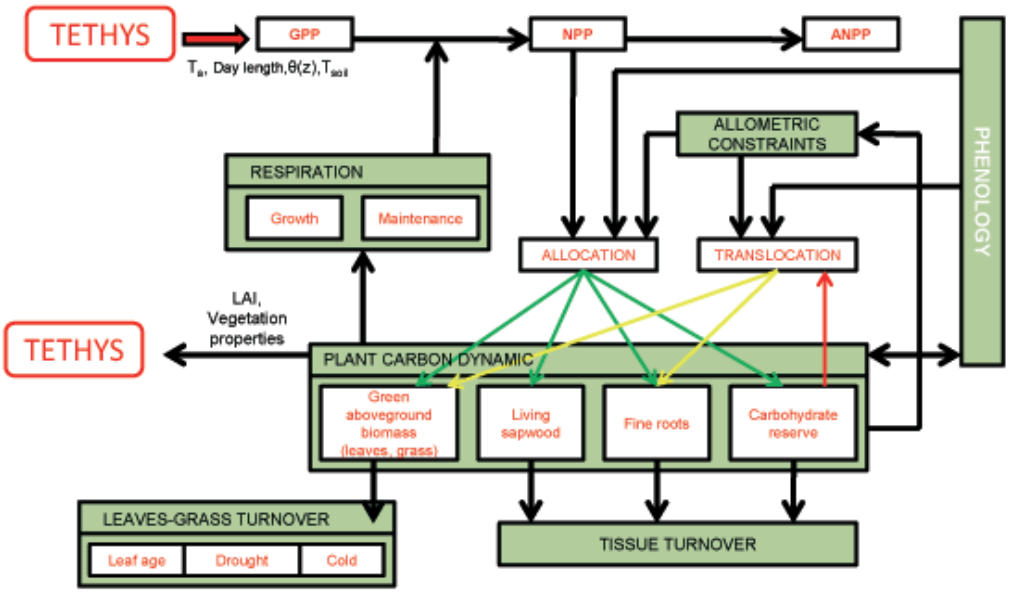

Figure 5.1: Components of "Chloris" showing the different biochemical and physiological processes. The model is forced with atmospheric and soil environmental conditions calculated in "Tethys". It returns the Leaf Area Index and vegetation properties. All the components and symbols are detailed in the text.

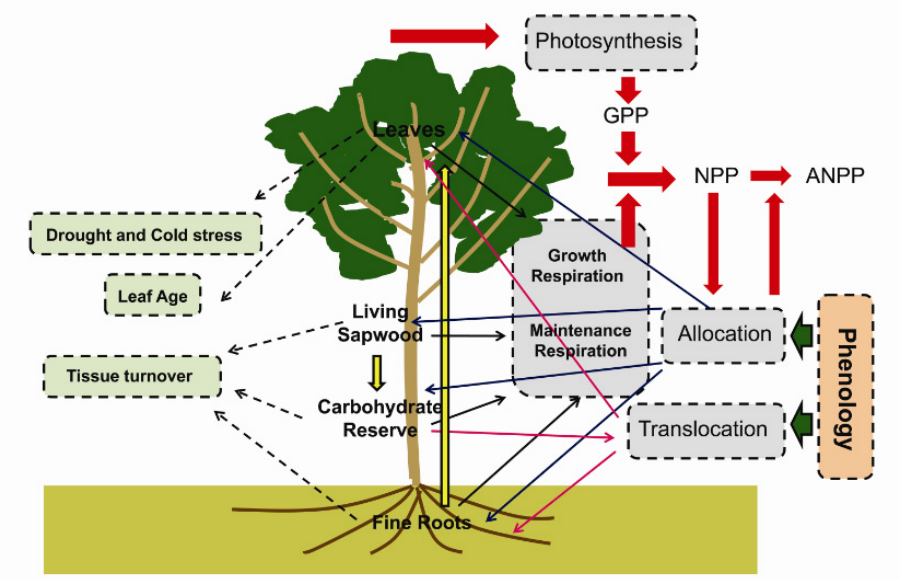

Figure 5.2: Conceptual diagram of carbon fluxes simulated by the model and of the involved processes. The four carbon pools are leaves, fine roots, living sapwood, and carbohydrate reserve. Boxes outlined with dashed lines illustrate processes that affect the carbon balance. The red arrows indicates the general patterns of productivity. The blue solid-line arrows show allocation fluxes, while the magenta ones show translocation. The black dashed-line arrows indicates turnover from carbon pools. The yellow arrows indicate allometric constraints and controls.

different *PFT*, one for the higher canopy layer, *High-vegetation*, (H_v), and one for the lower canopy layer, *Low-vegetation*, (L_v), catheterize the vertical composition of a given *Crown Area*. The described vegetation composition allows to summarize multiple species within the same *PFT* and to account for multiple *PFTs*, differentiating between upperstory and understory plants. Further details in the description of vegetation composition are provided in Section 4.1.2.

The simulation of vegetation dynamics is realized separately for each Plant Functional Type of the *High-vegetation* and *Low-vegetation* layers. As already pointed out in Section 4.1.2 the same *PFT* can belong to more than one *Crown Area*, because of a different vertical composition, for instance grass under deciduous and evergreen plants. In such a case, although the two *PFTs* in different *Crown Areas* share the same physiological parameters, they have separate carbon pool dynamics.

The actual version of the model does not explicitly include species competition as discussed in Section 5.1. Nonetheless, effects of competition can be appreciated in the productivity of the plants and in the soil moisture distribution. Competition for resources, such as water and light is indirectly accounted for in the hydrological model, as a consequence of vegetation characteristics, i.e. plant water uptake properties, rooting profiles, vertical composition, representation of foliage layers. This creates a dynamic and interacting framework also in absence of changes in the vegetated fraction and in its composition.

Carbon dynamics is represented by four carbon pools in each *PFT*. Carbon pools stored carbon as results of photosynthetic activity and consume it for maintenance, growth, tissue turnover, and reproduction. The represented carbon pools are the green aboveground biomass identified as leaves or grass, C_{leaf} [$g\,C\,m^{-2}\,PFT$], living sapwood, C_{sapw} [$g\,C\,m^{-2}\,PFT$], fine roots, C_{root} [$g\,C\,m^{-2}\,PFT$], and carbohydrate reserve, C_{hydr} [$g\,C\ \ m^{-2}\,PFT$]. The latter term identified the fraction of labile carbon in a plants, i.e., non-structural carbohydrates (glucose, fructose and sucrose, starch), lipids, and sugar alcohols (*Hoch et al.*, 2003; *Gough et al.*, 2009). The living sapwood components does not apply for grass species. Along with the carbon pools defined above there are other two carbon pools that are considered for allocation but which dynamics is not tracked explicitly. These carbon pools are the flower and fruit carbon pool, C_{flfr} [$g\,C\,m^{-2}\,PFT$], and the heartwood-dead sapwood carbon pool, C_{heaw} [$g\,C\,m^{-2}\,PFT$]. The first one takes into account the reproduction cost of a plant, C_{heaw} accounts for the death of the living sapwood and the conversion into structural wood such as in the trunk and in the coarse roots. Note that different schemes and number of carbon pools, simpler or more complex than in "Chloris", have been proposed (*Nouvellon et al.*, 2000; *Krinner et al.*, 2005; *Sato et al.*, 2007; *Ivanov et al.*, 2008a; *Medvigy et al.*, 2009). For instance, in the above subdivision litter carbon pools and standing dead leaves/grass are completely neglected. The latter typically plays a not negligible role in energy exchanges (*Nouvellon et al.*, 2000).

Vegetation structure evolves dynamically. In fact, the carbon amount in the different pools varies in function of the environmental conditions, stresses, seasonality

etc. This dynamic is directly reflected in vegetation attributes, as leaf and stem areas, canopy height, root profile, and leaf dimension. As anticipated in Section 4.1.2, although all the described attributes of vegetation are dynamic component (time-varying) only the LAI time-variations are considered in this version of the model. For each PFT the LAI $[m^2\, leaf\ area\, m^{-2}\, PFT\, area]$, is estimated as follows:

$$LAI \;=\; C_{leaf} S_{LAI}\,, \tag{5.1}$$

where S_{LAI} $[m^2\, LAI\ g\, C^{-1}]$ is the specific leaf area of biomass, PFT dependent. Vegetation models are quite sensitive to the values of S_{LAI}, since it represents the ability of plants to invest in new photosynthetic capacity. At a structural level species with low S_{LAI} have a thicker leaf blade or denser tissue, or both. Plants with low S_{LAI} needs more investment per unit leaf area. It has been found that S_{LAI} generally increases with photosynthetic capacity and leaf nitrogen content and generally decrease with leaf life span (*Schulze et al.*, 1994; *Reich et al.*, 1997; *Wright et al.*, 2004). The value of S_{LAI} is a trade-off between the photosynthetic capacity that increases with S_{LAI} and the disadvantage both energetically and competitively by maintaining long-lived foliage with high photosynthetic capacity. The latter option would impose a less than optimal allocation of resources. Furthermore, leaves with high nitrogen content are even nutritionally more attractive and thus subject to higher rates of herbivory (*Reich et al.*, 1997; *Wright et al.*, 2004). Variation in S_{LAI} are thus the result of a evolutionary adaptations to the range of environmental and external conditions that occur in different habitats. Reference values of S_{LAI} for several species can be found in *White et al.* (2000), typical values of S_{LAI} range between 0.005-0.050 $[m^2\, LAI\ g\, C^{-1}]$ (*Schulze et al.*, 1994; *Foley et al.*, 1996; *Kaduk and Heimann*, 1996; *Friend et al.*, 1997; *Reich et al.*, 1997, 1998a; *Kucharik et al.*, 2000; *Cox*, 2001; *Bonan et al.*, 2003; *Wright et al.*, 2004; *Sato et al.*, 2007; *Wramnebya et al.*, 2008).

In order to describe the dynamics of other vegetation attributes would be necessary to explicitly represent the heartwood carbon pool, subdividing it in aboveground and belowground components. Allometric relationships can be successively introduced to link the size of carbon pools to structural attributes of the plants (*Cox*, 2001; *Niklas and Enquist*, 2001; *Sitch et al.*, 2003; *Levis et al.*, 2004; *Deckmyn et al.*, 2006; *Sato et al.*, 2007; *Cheng and Niklas*, 2007; *Enquist et al.*, 2007). Such an approach is briefly outlined in Appendix D.1 but is not applied in this version of "Chloris". It is author opinion that although the ongoing research of biologist, plant physiologist, botanists attempting to find general or universal laws to relate leaf structure, plant growth, respiratory costs, allocation fractions to measurable leaf or plant characteristics is obtaining remarkable results (*Reich et al.*, 1997, 1998a,b; *Wright et al.*, 2004), further studies are necessary before applying such results in a numerical model of vegetation dynamics. This is the principal reason why the first version of "Chloris" avoids further parameterizations to characterize vegetation attributes different from LAI.

The nitrogen dynamics or more generally the nutrient dynamics is neglected and

nutrient pools are not tracked nor in the vegetation compartments neither in the soil. The water supply limitation is considered the most important actor in plant stress (*Rodriguez-Iturbe*, 2000; *Rodriguez-Iturbe et al.*, 2001; *Laio et al.*, 2001; *Porporato et al.*, 2001; *Eagleson*, 2002; *Rodriguez-Iturbe and Porporato*, 2004). This assumption is a rationale of eco-hydrologycal studies for arid and semi-arid environments. The validity of such an assumption in non water-limited ecosystems is generally questionable (*Rodriguez-Iturbe et al.*, 2001; *Mackay*, 2001; *Dickinson et al.*, 2002; *Eagleson*, 2002; *Rodriguez-Iturbe and Porporato*, 2004), although also the nutrient cycle is strongly mediated by water availability (*Porporato et al.*, 2003; *Tague and Band*, 2004; *Arain et al.*, 2006; *Wang et al.*, 2007b; *Manzoni and Porporato*, 2009). Nonetheless, in order to avoid the implementation of a full biogeochemistry component, nutrient supply is assumed to be directly dependent on water availability and thus nutrient dynamics is neglected in "Chloris". Results from the application of the model in environments where water is abundant should be carefully checked, since limiting factors different from water availability may occur.

In order to facilitate explanations later in this Chapter, each PFT is considered to belong to a broader category of vegetation types. Specifically "Chloris" distinguishes between four different broad vegetation categories identified with the symbol Ξ: evergreen plants ($\Xi = 0$), seasonal deciduous plants ($\Xi = 1$), grass species ($\Xi = 2$), and crops ($\Xi = 3$). This differentiation is necessary because different broad vegetation categories have substantially different phenological and carbon pool dynamics. These different dynamics imply particular parameterizations and changes to the modeling scheme.

5.2 Carbon pool dynamics

This section outlines the processes affecting the carbon balance in different vegetation compartments. These include evaluation of net primary production, plant respiration, carbon allocation, translocation and tissue turnover.

5.2.1 Net Primary Production and plant respiration

The net primary production, NPP [$g\,C\,m^{-2}\,PFT\,day^{-1}$], is defined as the gross plant photosynthesis, or gross primary production, GPP [$g\,C\,m^{-2}\,PFT\,day^{-1}$], minus autotrophic respiration, R_A [$g\,C\,m^{-2}\,PFT\,day^{-1}$] (*Ruimy et al.*, 1996; *Knorr*, 2000; *Arora*, 2002; *Sitch et al.*, 2003; *Levis et al.*, 2004; *Krinner et al.*, 2005; *Nobel*, 2009):

$$NPP = GPP - R_A\,, \tag{5.2}$$

$$GPP = \kappa(A_{nC} + R_{dC})\,, \tag{5.3}$$

where $\kappa = 1.0368$ [$g\,C\,s\,\mu mol\,CO_2^{-1}\,day^{-1}$] is used to convert the unit of net assimilation rate, A_{nC} [$\mu mol\,CO_2\,s^{-1}\,m^{-2}$], and dark respiration, R_{dC} [$\mu mol\,CO_2\,s^{-1}\,m^{-2}$], from the photosynthesis module (see Section 4.4.5). Vegetation autotrophic res-

piration R_A is estimated as the sum of maintenance respiration R_m and growth respiration R_g [$g\,C\,m^{-2}\,PFT\,day^{-1}$] rates:

$$R_A = R_m + R_g\,, \tag{5.4}$$

$$R_m = R_{mF} + R_{mS} + R_{mR} + R_{mH}\,, \tag{5.5}$$

$$R_g = \max\left[0, \omega_{grw}(GPP - R_m)\right]\,, \tag{5.6}$$

where ω_{grw} [$-$] is the growth respiration fraction, R_{mS}, R_{mR}, and R_{mH} [$g\,C\,m^{-2}\,PFT\,day^{-1}$] are the maintenance respiration rates for living sapwood, fine roots, and carbohydrate reserve respectively, and $R_{mF} = \kappa R_{dC}$ [$g\,C\,m^{-2}\,PFT\,day^{-1}$] is the rate of foliage maintenance respiration. The maintenance respiration R_m is, in fact, typically subdivided into living plant compartments (*Thornley*, 1970; *McCree*, 1970; *Ryan*, 1991; *LeRoux et al.*, 2001). In order to grow, plants require carbohydrates both for their plant-body construction and for biosynthesis (*Sato et al.*, 2007). Usually, the amount of growth respiration costs can be estimated by combining data on the biochemical composition of organs with knowledge on the biochemical costs of synthesis of all the major compounds, including cellulose, hemicellulose, lignin, protein, lipids, and organic acids (*Lambers et al.*, 1998). Since obtaining a physiological estimation of growth respiration cost is practically impossible, vegetation model schematize this cost as a fraction ω_{grw} of the gross primary production less maintenance respiration (*Ryan*, 1991; *Sitch et al.*, 2003; *Levis et al.*, 2004; *Ivanov et al.*, 2008a) or in same cases directly as a fraction of NPP (*Knorr*, 2000; *Arora*, 2002). The value assumed by the growth respiration fraction ω_{grw} [$-$] is usually between $0.15 - 0.30$ (*Ryan*, 1991; *LeRoux et al.*, 2001; *Sitch et al.*, 2003; *Krinner et al.*, 2005; *Ivanov et al.*, 2008a), but very often a value of $\omega_{grw} = 0.25$ is assumed (*Ryan*, 1991; *Cox*, 2001; *Bonan et al.*, 2003; *Sitch et al.*, 2003).

The maintenance respiration is defined as that required for maintenance and turnover of existing biomass (*LeRoux et al.*, 2001). The maintenance respiration rate, R_m, (i.e., the fraction of biomass that is lost during a given time interval) for living plant compartments is basically calculated as a function of temperature and biomass, once the prescribed nitrogen/carbon ratio of each tissue is known (*Ruimy et al.*, 1996; *Sitch et al.*, 2003; *Krinner et al.*, 2005). For a wide variety of plant organs, in fact, the maintenance respiration rate is linearly related to the nitrogen content of the living tissue (*Ryan*, 1991; *Ruimy et al.*, 1996; *Reich et al.*, 1998b, 2006). Furthermore, the maintenance respiration coefficient increases with temperature (air temperature for aboveground plant tissues; root-zone temperature for belowground tissues) (*Sitch et al.*, 2003; *Krinner et al.*, 2005). In "Chloris" the maintenance respiration rates are calculated as proposed in *Sitch et al.* (2003):

$$R_{mS} = r_m \frac{C_{sapw}}{N_s}\, g(T_a)\,, \tag{5.7}$$

$$R_{mR} = r_m \frac{C_{root}}{N_r}\, g(T_d)\,, \tag{5.8}$$

$$R_{mH} = r_m \frac{C_{hydr}}{N_s}\, g(T_a)\,, \tag{5.9}$$

where T_d [$^\circ C$] is the daily averaged temperature at dampening depth from Section 4.3.3, T_a [$^\circ C$] is the daily averaged air temperature at the reference height z_{atm} (Section 4.3). For a given PFT (H_v or L_v) within a *Crown area* of a basic computational element, the terms C_{sapw}, C_{root}, and C_{hydr} [$g\,C\ m^{-2}\ PFT$] represent the carbon pools of living sapwood, fine root, and carbohydrate reserves, respectively. Note that these quantities refer only to the area occupied by a given PFT and not to the entire element. The quantity r_m [$g\,C\ g\,N^{-1}\ day^{-1}$] is the respiration rate coefficients on a $10^\circ C$ base that is a specific PFT parameter. The value of r_m typically accounts for the observation that plants from warmer environments have lower respiration rates than plants from cooler environments (*Ryan*, 1991; *Reich et al.*, 1998b; *Sitch et al.*, 2003), r_m typically ranges between 0.033-0.066 [$g\,C\ g\,N^{-1}\ day^{-1}$] (*Sitch et al.*, 2003; *Bonan et al.*, 2003). The terms N_s and N_r [$g\,C\ g\,N^{-1}$] are the living sapwood and fine root carbon-nitrogen C:N mass ratios [$g\,C\ g\,N^{-1}$]. The temperature dependence $g(T)$ [$-$] is finally expressed with a modified Arrhenius equation, with T in [$^\circ C$]:

$$g(T) \quad = \quad e^{308.56\left(\frac{1}{56.02}-\frac{1}{T+46.02}\right)}. \tag{5.10}$$

The use of the modified Arrhenius equation instead of a fixed Q_{10} (*Nouvellon et al.*, 2000; *Arora*, 2002; *Deckmym et al.*, 2008) is preferred because of the evidence for a constant decline in the apparent Q_{10} of autotrophic respiration with temperature (*Sitch et al.*, 2003). Note that the hydrological model does not solve the complete thermal profile within the soil, therefore the temperature at dampening depth, T_d, is used as a proxy of the rooting depth temperature. Besides, the carbon-nitrogen mass ratio C:N for the carbohydrate reserve is assumed equal to the one of living sapwood and the reference temperature for carbohydrate respiration cost is assumed to be the air temperature, T_a. The latter approximation implicitly assumes that carbohydrate reserves are stored somewhere inside the sapwood and actually are not distinguishable from it concerning respiration behavior. This assumption is made for all vegetation categories except grass species ($\Xi = 2$), where carbohydrate reserve are assumed to be stored in the root compartment. In this case carbohydrate reserve respiration is calculated with the temperature at dampening depth. The value T_d substitutes T_a in equation (5.9). In a real plants carbohydrate reserve are likely to be distributed in both aboveground and belowground compartments and thus the previous assumption is partially violated. Nonetheless, the error in the calculation of respiration costs due to such an approximation is considered negligible compared to other uncertainties, i.e. the quantification of r_m.

Foliage respiration, R_{mF}, is estimated as the daily sum of the dark respiration, R_{dC}, that in turn is estimated at hourly scale along with photosynthesis and stomatal resistance (Section: 4.4.5). Dark respiration, R_{dC}, is calculated independently of the soil moisture state in the root zone (section 4.4.5) differently to what proposed by other authors (*Cox*, 2001). This is related to the necessity of plants to respire and to maintain operativity also in stressed conditions, for instance during a drought.

The carbon-nitrogen C:N mass ratios for living sapwood and fine root, N_s, N_r,

are estimated from a fixed ratio between these quantities and the foliage carbon-nitrogen C:N mass ratio, N_f $[g\,C\ g\,N^{-1}]$, as first proposed by *Friend et al.* (1997) and successively confirmed by *Sato et al.* (2007):

$$N_s = N_l/0.145\,, \tag{5.11}$$

$$N_r = N_l/0.860\,. \tag{5.12}$$

Typical values of C:N mass ratio for leaves and grasses, N_l, can be found in literature for different *PFTs* (*White et al.*, 2000; *Sitch et al.*, 2003; *Bonan et al.*, 2003) or can be retrieved from regressions on other leaf traits (*Wright et al.*, 2004). Usually the variability of N_l is confined to $N_l = 25 - 50$ $[g\,C\ g\,N^{-1}]$. Note that the one proposed above is only a simplification to reduce the tissue C:N mass ratios to a single value, N_l. Nonetheless, the model is quite flexible and also allows to use specific values for N_s and N_r once they are known.

As can be observed from equation (5.2), the net primary production is positive when carbon uptake from photosynthesis exceeds autotrophic respiration, a situation characteristic for favorable well-watered conditions. The value of NPP is negative during night time or when soil moisture deficit does not allow vegetation to effectively photosynthesize and maintenance costs are higher than gross carbon uptake.

5.2.2 Carbon allocation and translocation

The carbon assimilated through the photosynthetic process is allocated to the different carbon pools, i.e., green aboveground, fine roots, living sapwood, carbohydrate reserves, and fruits-flowers.

Carbohydrate allocation currently represents a central problem of carbon pool dynamics scheme in ecological, vegetation and plants models, since the physiological and biochemical mechanisms, as plant hormonal balance, that control allocation of photosynthate under resource stresses are only partially understood (*Friedlingstein et al.*, 1998). Hence, formulation of allocation remains a very thorny issue (*LeRoux et al.*, 2001; *Niklas and Enquist*, 2002; *Litton et al.*, 2007; *Fourcaud et al.*, 2008). In literature different approaches have been proposed to solve this problem, the simplest one is the use of constant fractions. Another way is to determine carbon allocation from allometric constraints or to allocate carbon in order to optimize growth, leaf area index, or to minimize environmental stresses (*Friedlingstein et al.*, 1998; *Arora and Boer*, 2005). Finally the most complex approaches provide functions of the interactions among sinks with different demands and/or import capacities (*Thornley*, 1991; *Lacointe*, 2000; *LeRoux et al.*, 2001).

Carbon allocation in "Chloris" is treated following *Friedlingstein et al.* (1998) and *Krinner et al.* (2005). They provide an allocation scheme which answers dynamically to resource modification. The use of dynamic stress-dependent schemes permits more flexible patterns of carbon redistribution and it is experimenting a certain popularity (*Arora and Boer*, 2005; *Ivanov et al.*, 2008a). The basic hypothesis in the model of *Friedlingstein et al.* (1998) is that a plant allocates carbon to its differ-

ent compartments essentially in response to external limitations: water, light, and nitrogen availability. Furthermore, carbon allocation is constrained by allometric relationships. For instance, the need that leaf biomass has to be supported by a sufficient quantity of transport tissue, or the need to maintain a minimum root:shoot ratio, i.e., the ratio of fine root carbon to foliage carbon (*Lüdeke et al.*, 1994; *Levis et al.*, 2004; *Arora and Boer*, 2005; *Ivanov et al.*, 2008a). Other allocation limits during the leaf onset season can be also considered. Some of these restrictions are considered in "Chloris" after the realization of a constraint free allocation.

The original allocation scheme of *Friedlingstein et al.* (1998) calculates the allocation fractions for three compartments (leaves, stems, roots), the modification carried out in *ORCHIDEE* (*Krinner et al.*, 2005) considers eight biomass compartments, toward six of which carbon can be allocated. In "Chloris" this scheme is further modified to allocate to the four carbon pools introduced previously. The limiting factors are: soil moisture availability, A_H [−], light availability, A_L [−], and nitrogen availability, A_N [−]. Since nitrogen dynamic is not computed in the model, the limits in carbon allocation due to the availability of nitrogen, A_N, are made dependent on the other environmental variables (*Krinner et al.*, 2005):

$$A_H = \max\left[0.1, \min\left(1, \frac{\theta_R - \theta_{wp}}{\theta_{ss} - \theta_{wp}}\right)\right], \tag{5.13}$$

$$A_L = \max\left[0.1, e^{-K_e\, LAI}\right], \tag{5.14}$$

$$A_N = A_{NH}\, A_{NT}, \tag{5.15}$$

where θ_R [−] is the daily averaged soil moisture in the root zone (Section 4.7.3), θ_{ss} and θ_{wp} [−] are the soil moisture content at the begin and at the complete stomatal closure calculated from Ψ_{ss} $[kPa]$ and Ψ_{wp} $[kPa]$ (Section 4.1.2) through the soil-water retention function (Section: 4.7.4). LAI $[m^2\, leaf\, area\, m^{-2}\, PFT\, area]$ is the leaf area index and $K_e = 0.5$ is a constant light extinction coefficient proxy for the optical depth K_{opt} (*Monsi and Saeki*, 2005) (Section 4.2.2). Nitrogen availability is parameterized as the product of a soil humidity parameter, A_{NH} [−], and a soil temperature parameter, A_{NT} [−]. The assumption is that the microbial decomposers are distributed in the soil following an exponential profile decreasing with depth and their activity increases with favorable moisture and temperature conditions. The pertinent soil moisture the decomposers feel, is calculated with the equation below:

$$A_{NH} = \min\left[1, \max\left(0.5, \frac{\theta_e - \theta_{wp}}{\theta_{sat} - \theta_{wp}}\right)\right], \tag{5.16}$$

where θ_e [−] is the daily averaged soil moisture up to the characteristic length of evaporation d_e. Therefore, it is assumed that microbial activity occurs in a shallow layer of the soil column. The temperature effect on nitrogen availability, A_{NT}, is neglected in "Chloris". However, the impact of assuming $A_{NT} = 1$ is considered to have a weak influence in the overall allocation process and furthermore the parametrization proposed by *Krinner et al.* (2005) for A_{NT} is rather unclear. The belowground availabilities A_N and A_H are combined to a single belowground

availability, $A_B = \min(A_N, A_H)$. The belowground and light availabilities are finally used to calculate preliminary allocation fractions for leaves-grasses, $\widetilde{f_l}$ [−], fine roots, $\widetilde{f_r}$ [−], and living sapwood, $\widetilde{f_s}$ [−]:

$$\widetilde{f_r} = \max\left[r_{min},\ r_0\frac{3A_L}{A_L + 2A_B}\right], \tag{5.17}$$

$$\widetilde{f_s} = s_0\frac{3A_B}{2A_L + A_B}, \tag{5.18}$$

$$\widetilde{f_l} = \max\left[a_{min}, \min\left(a_{max}, 1 - \widetilde{f_r} - \widetilde{f_s}\right)\right], \tag{5.19}$$

where $r_{min} = 0.15$, $a_{min} = 0.2$, $a_{max} = 0.5$, and $r_0 = s_0 = 0.3$ are coefficients provided by *Krinner et al.* (2005). The preliminary root allocation fraction is then recalculated as: $\widetilde{f_r} = 1 - \widetilde{f_l} - \widetilde{f_s}$, that gives $\widetilde{f_l} + \widetilde{f_r} + \widetilde{f_s} = 1$. For grasses species ($\Xi = 2$) there is no allocation to the living sapwood, in this case the computed $\widetilde{f_s}$ is partitioned among $\widetilde{f_l}$ and $\widetilde{f_r}$ with $\widetilde{f_s} = 0$. The scheme to calculate preliminary allocation fractions provides more carbon allocation to roots when soil moisture is limiting in order to increase the below ground biomass. More carbon is provided to sapwood when foliage significantly limits light penetration to lower levels of the canopy, this increases the canopy supporting structure.

During the maximum growth phenological state (see Section 5.3) all the preliminary fractions are modified to allocate everything to C_{leaf}, i.e., $\widetilde{f_l} = 1$ and $\widetilde{f_r} = 0$, $\widetilde{f_s} = 0$. This assumption permits to attain rapidly a relatively dense leaf cover to allow the plant to photosynthesize efficiently at the beginning of the new growing season (*Arora and Boer*, 2005; *Ivanov et al.*, 2008a). The translocation of carbon from the carbohydrate reserve, described below, contributes to the same purpose.

The final allocation fractions, f, are calculated using the preliminary fractions $\widetilde{f}$ as proposed by *Krinner et al.* (2005), with some additional modifications. Changes in allocation patterns are related to vegetation category (Ξ) and to phenological state (Section 5.3), i.e. which part of the phenological season the plant is undertaking. Allometric constraints are also considered. The final allocation fractions f are totally five: to green aboveground biomass, f_l, to living sapwood, f_s, to fine roots, f_r, to carbohydrate reserves, f_h, and to fruit and flowers, f_f. Since the fruit and flower carbon pool, C_{flfr}, is not explicitly simulated, the carbon allocated through f_f is simply lost and subtracted from the carbon balance. There is no allocation to the tree heartwood-dead sapwood pool as the latter is produced by the slow conversion of living sapwood.

The reproduction costs, i.e. the carbohydrate allocated to produce reproductive organs and propagules range between 5% and 20% (*Larcher*, 2001). *Sitch et al.* (2003) and *Krinner et al.* (2005) proposed to simple approximate this fraction as a 10% of the annual NPP. An allocation fraction to reproductive organs of $f_f = 0.1$ is adopted in "Chloris" during the maximum growth and normal growth seasons (Section 5.3), $f_f = 0$ otherwise. During senescence or dormant phenological states it is assumed that the plant does not produce fruit or flowers, i.e. does not invest in reproductivity. This assumption although coarse and invalid for specific species can

be considered fairly general and as valuable as other assumption made for f_f. The allocation toward the carbohydrate reserves, f_h, is tentatively parameterized as a function of the sum of the preliminary allocation fractions $\widetilde{f}_l$ and $\widetilde{f}_r$ (as the biomass will later be translocated toward the leaves and roots) (*Krinner et al.*, 2005):

$$f_h = (1-C)(1-f_f)\,, \tag{5.20}$$

with

$$C = \frac{1}{1+\varepsilon_{al}(\widetilde{f}_l+\widetilde{f}_r)}\,, \tag{5.21}$$

where ε_{al} $[0-1]$ is a tuning parameter for carbohydrate reserve allocation. *Krinner et al.* (2005) proposed a value of $\varepsilon_{al}=1$ for seasonal plants ($\Xi=1$) and $\varepsilon_{al}=0$ for evergreen plants ($\Xi=0$). Note that when $\varepsilon_{al}=0$, $C=1$. This implies that evergreen plants should not have carbohydrate reserve in the model, which is not true in reality as remarked by several studies (*Hansen and Beck*, 1990; *Chapin III et al.*, 1990; *Kobe*, 1997) and also stated by *Krinner et al.* (2005). Differently from *Krinner et al.* (2005) in "Chloris" the tuning parameter for allocation to carbohydrate reserves is considered to assume the value 1 for seasonal plants and a lower value for evergreen $\varepsilon_{al}=0.1-0.3$. Such a change allows to model the dynamics of carbohydrate reserves also for evergreen species, although the capability of these species to store reserve is assumed limited in comparison to seasonal plants (*Chapin III et al.*, 1990).

When a plant is out of the growing season, i.e. it is in the senescence or dormant phenological states (Section 5.3), there is no point in allocating carbon to leaves, roots, or living sapwood. The plant is considered to save as much carbon as possible and the total assimilate products are stored into the carbohydrate reserves, i.e., $f_h=1$, while all the other allocation fractions are set to zero (leaves, $f_l=0$, roots, $f_r=0$, living sapwood, $f_s=0$, fruits and flowers, $f_f=0$) (*Krinner et al.*, 2005). Note that during the senescence or dormant phenological states the carbon available for allocation is null or rather scarce due to unfavorable environmental conditions and leaf shedding. The latter rule does not apply to evergreen ($\Xi=0$) for which carbon is allocated to the different compartments throughout the year and the allocation toward carbohydrate reserves is always governed by equation (5.20). Evergreen, in fact, are considered to experiment a senescence-dormant phenological state different from other plant types (for details refer to Section 5.3). During the maximum growth phenological state (Section 5.3) the allocation to carbohydrate reserves is instead set equal to zero, $f_h=0$, imposing $C=1$. The final allocation fractions are calculated as:

$$f_l = \widetilde{f}_l(1-f_f)\,C\,, \tag{5.22}$$

$$f_r = \widetilde{f}_r(1-f_f)\,C\,, \tag{5.23}$$

$$f_s = \widetilde{f}_s(1-f_f)\,C\,, \tag{5.24}$$

with the equivalence $f_l + f_r + f_s + f_f + f_h = 1$.

In addition to the allocation processes described above, two allometric constraints are imposed to refine allocation dynamics. The first one concerns the maximum capacity to store carbohydrate reserves. *Krinner et al.* (2005) parameterized that no carbon should be allocated to the reserves when the reserve pool is larger than a prescribed value, function of the LAI. In "Chloris" the constraint about carbohydrate reserve, C_{hydr}, is parameterized following *Friend et al.* (1997). The maximum value for C_{hydr} is assumed to be 0.67 of the living sapwood carbon pool C_{sapw}. Note that this is congruent with estimates of the fraction of labile carbon in the sapwood that are typically around 2-10% in dry matter (*Hoch et al.*, 2003; *Körner*, 2003). Considering that on average about 10% of sapwood is alive and a conversion factor 0.5 $[gC/gDM]$ (*Kozlowski and Pallardy*, 1997; *Friend et al.*, 1997), this implies that the fraction of carbohydrate reserve to living sapwood is around $0.4 - 2$. These values are generally higher than 0.67, however 0.67 is probably a good approximation since a not negligible portion of reserves is sequestered rather than stored in the plant and thus not available for translocation (*Körner*, 2003). When the value of 0.67 is exceed, $f_h = 0$, and its calculated fraction is partitioned among the other pools during normal growth or it is transferred to sapwood during the senescence or dormant phenological states. This is valid for $\Xi = 0,\ 1$. For grasses species ($\Xi = 2$) the maximum carbohydrate reserve is assumed to be 0.67 of the fine root carbon pool, C_{root}, in this case there is no living sapwood and the carbohydrate are assumed to be mainly stored in the roots. As proposed for the other species when the limit threshold is exceed, $f_h = 0$, and the fraction allocated to reserves is partitioned among the other pools during normal growth and only to fine roots during senescence or dormant phenological states.

The second allometric constraint concerns the leaf-to-root or shoot-to-root ratio R_{ltr} $[-]$. Typically vegetation models introduce an allometric constraint on the shoot:root ratio, since there is a need from leaf biomass to be supported by a sufficient quantity of transport tissue (*Lüdeke et al.*, 1994; *Bonan et al.*, 2003; *Sitch et al.*, 2003; *Deckmym et al.*, 2008). Usually, a constant ratio is considered. This value can be regarded as an upper limit. In "Chloris" the allocation to C_{leaf} is constrained, anytime $C_{leaf} > R_{ltr}\ C_{root}$. In this case, $f_l = 0$ and its calculated value is partitioned among f_s and f_r proportionally to their biomasses. The range of variability proposed in literature for R_{ltr} is around $0.75 - 1.5$ depending on the PFT, with higher values for woody species ($\Xi = 0$ or 1) than grasses species ($\Xi = 2$) (*Sitch et al.*, 2003; *Bonan et al.*, 2003; *Sato et al.*, 2007). In order to maintain a certain quantity of leaves a minimum water-conducting tissue is necessary. This introduces a constraint on sapwood through a leaf to sapwood area ratio (*Bonan et al.*, 2003; *Sitch et al.*, 2003). The leaf to sapwood area ratio is often estimated using the pipe model theory (*Lacointe*, 2000; *LeRoux et al.*, 2001; *Deckmyn et al.*, 2006; *Deckmym et al.*, 2008). However, since no structural relationships are used to define the area of sapwood starting from its biomass, the possible constraint on the sapwood pool cannot be imposed in the model and is neglected.

The dynamics of storage and mobilization of carbohydrate reserves in plants have been investigated for a long time, nevertheless the knowledge of the process is merely qualitative (*LeRoux et al.*, 2001). There are evidences that carbohydrate reserves are formed through storage in late summer and fall, are partially depleted during winter through maintenance respiration and a massive mobilization occurs in spring to enhance the leaf cover and to permit to the plant to photosynthesize efficiently after leaf onset (*Chapin III et al.*, 1990; *Dickinson et al.*, 2002; *Pregitzer*, 2003; *Krinner et al.*, 2005). Other authors analyzing non-structural carbohydrates concentration find minor evidences of such a dynamic, and identify a mobilization of carbohydrate reserves only after strong environmental stresses (*Körner*, 2003). Yet, carbon-based models generally ignore, or treat very briefly, this aspect of the carbon balance (*Nouvellon et al.*, 2000; *LeRoux et al.*, 2001). An attempt to introduce the process of translocation from the carbohydrate reserve toward leaves and roots was made by *Krinner et al.* (2005) who parameterized seasonal trees and grasses to use carbohydrate reserves at the beginning of the growing season up to reach half of a prescribed value of the leaf area index LAI. In "Chloris" all the vegetation categories Ξ have a storage compartment. Therefore, translocation occurs also from evergreen and crops species. Since in literature an explicit quantification of the carbon translocation has been often neglected, convincing mechanistic parameterizations are lacking. A very simple scheme is adopted in "Chloris". Carbohydrate translocation is modeled to occur only during the maximum growth phenological state (Section 5.3) with a prescribed constant rate T_{rC} $[g\,C\,m^{-2}\,PFT\,day^{-1}]$, PFT dependent. The rate Tr_C is a parameter of the model and suitable values have been found in the order of 0.5-7 $[g\,C\,m^{-2}\,PFT\,day^{-1}]$, with higher values for plants which attain a faster growth after leaf onset (grasses, temperate deciduous). Assuming T_{rC} constant rather than dependent on reserve size has shown better results and it is probably due to the fact that translocation is sink and not source driven. The total carbohydrate translocation is then subdivided between translocation to green aboveground, Tr_l $[g\,C\,m^{-2}\,PFT\,day^{-1}]$, and fine roots, Tr_r $[g\,C\,m^{-2}\,PFT\,day^{-1}]$, inversely proportional to their biomasses as:

$$Tr_l = Tr_C \frac{C_{root}}{C_{leaf} + C_{root}}\,, \tag{5.25}$$

$$Tr_r = Tr_C \frac{C_{leaf}}{C_{leaf} + C_{root}}\,. \tag{5.26}$$

Obviously translocation of carbon from the reserve pool, C_{hydr}, is limited by the availability of reserves, i.e., $C_{hydr} \geq 0$. Note that the translocation from crops is substantially a model artifact, it mimics a source of carbon introduced with sowing and serves to simulate the very fast increase of green aboveground biomass after leaf onset, that would not be possible to achieve otherwise.

There are evidences that an inverse translocation of resources, especially nutrients, from leaves to reserve occurs at the end of the growing season (*Thomas and Stoddart*, 1980; *Chapin III et al.*, 1990; *Medvigy et al.*, 2009). This mechanism prevents the

lost of carbon and nutrients by leaves shedding, subtracting resources from the leaves before they offset. For the maintenance of nitrogen in plants the re-translocation process is fundamental, for carbon, evidences are much more contradictory, therefore no parametrization to describe such a mechanism is proposed in "Chloris".

5.2.3 Tissue turnover and leaf environmental stresses

A parametrization of leaves and fine roots transformation into litter, and sapwood conversion to heartwood is necessary to account for the turnover of organic matter (*Sitch et al.*, 2003; *Arora and Boer*, 2005; *Sato et al.*, 2007; *Ivanov et al.*, 2008a). The amount of tissue turnover of living sapwood biomass, i.e., the sapwood that die and it is later converted into heartwood biomass, S_{sapw} $[g\,C\,m^{-2}\,PFT\,day^{-1}]$, and the turnover of fine root biomass to litter, S_{root} $[g\,C\,m^{-2}\,PFT\,day^{-1}]$, are linear function of the biomasses and of parameters related to tissue longevity. The quantity of tissue turnover of green aboveground biomass, S_{leaf} $[g\,C\,m^{-2}\,PFT\,day^{-1}]$, is a linear function of C_{leaf} through three turnover rates. One turnover rate accounts for the phenology and it is related to leaf age, the other two are related to environmental stresses. The equations used to calculate the tissue turnovers are:

$$S_{leaf} = \left[d_{leaf,a} + d_{leaf,c} + d_{leaf,d}\right] C_{leaf}\,, \tag{5.27}$$

$$S_{sapw} = d_{sapw}\, C_{sapw}\,, \tag{5.28}$$

$$S_{root} = d_{root}\, C_{root}\,, \tag{5.29}$$

where d_{sapw} $[day^{-1}]$ is the living sapwood death rate, d_{root} $[day^{-1}]$ is the turnover rate for fine roots, $d_{leaf,a}$, $d_{leaf,c}$, and $d_{leaf,d}$ $[day^{-1}]$, represent the turnover rates of green aboveground biomass due to leaf age, cold stress, and drought stress respectively (*Levis et al.*, 2004; *Arora and Boer*, 2005; *Ivanov et al.*, 2008a). According to *Krinner et al.* (2005) living sapwood is converted into heartwood with a one year time constant, thus $d_{sapw} = 1/365$ $[day^{-1}]$. As a matter of fact this is not realistic for many species where the conversion rates are slower or no heartwood formation occurs at all (*Kozlowski and Pallardy*, 1997). In "Chloris", d_{sapw} refers to the rate at which living sapwood dies and only later it is converted into heartwood biomass. Given this assumption a one year time constant is used for d_{sapw}. The turnover rate of fine roots, d_{root}, is taken from *Gill and Jackson* (2000), where root turnover across climatic gradients and for plant functional groups have been tested using a database of 190 published studies. They found that root turnover decreased from tropical to high-latitude systems for all plant functional groups and typical values worldwide are $d_{root} = 1/240 - 1/1500$ $[day^{-1}]$, confirmed also by other studies (*Foley et al.*, 1996; *Kucharik et al.*, 2000; *Bonan et al.*, 2003; *Arora and Boer*, 2005; *Wramnebya et al.*, 2008).

A fraction of green aboveground biomass, i.e., leaves (or grass plus stalks) is lost at every time step as a function of the leaf age. This is based on the consideration that although meteorological conditions can remain favorable for leaf maintenance, plants, in particular evergreen trees, have to renew their leaves simply because old

leaves become inefficient (*Krinner et al.*, 2005). Typically, ecological and vegetation model do not calculate explicitly leaf age and a constant turnover rate, $d_{leaf,a}$ $[day^{-1}]$, is assumed (*Bonan et al.*, 2003; *Arora and Boer*, 2005; *Ivanov et al.*, 2008a). In "Chloris" the age of the leaves, Ag_L $[day]$, is explicitly simulated and $d_{leaf,a}$ is parameterized according to Ag_L with a modification of the approach first proposed by *Krinner et al.* (2005):

$$d_{leaf,a} = \frac{Ag_L}{A_{cr}^2}, \quad \text{if } \Xi = 0, \tag{5.30}$$

$$d_{leaf,a} = \min\left[0.99, \frac{1}{A_{cr}}\left(\frac{Ag_L}{A_{cr}}\right)^4\right], \quad \text{if } \Xi = 1, \tag{5.31}$$

$$d_{leaf,a} = \min\left[\frac{1}{A_{cr}}, \frac{Ag_L}{A_{cr}^2}\right], \quad \text{if } \Xi = 2, \tag{5.32}$$

where Ag_L $[day]$ is the leaf age, better described in Section 5.3, and A_{cr} $[day]$ is a critical age for leaf shed, PFT dependent. Typical values proposed in literature for A_{cr} range from 120 $[day]$ for grasses species to 910 $[day]$ or more for evergreen trees (*Foley et al.*, 1996; *Bonan et al.*, 2003; *Krinner et al.*, 2005; *Arora and Boer*, 2005; *Wramnebya et al.*, 2008), although wider ranges 50-1500 $[day]$ have been proposed (*Wright et al.*, 2004; *Sato et al.*, 2007). The turnover rate, $d_{leaf,a}$, is a function of the vegetation category (Ξ) as also shown in Figure 5.5. Deciduous plants ($\Xi = 1$) turnover rate follows the fourth power expression proposed by *Krinner et al.* (2005) (equation 5.31). For evergreen and grass categories equation (5.31) was found inadequate. It produces, indeed, a too fast green biomass shedding when the critical age threshold, A_{cr}, is exceeded, and conversely a rather slow turnover for relative young leaves. For these reasons a simpler linear relationship is proposed to estimate turnover for evergreen ($\Xi = 0$) (equation 5.30), and grass species ($\Xi = 2$) (equation 5.32). For grass species an upper limit to the turnover rate is imposed to account for a general resilience to ageing that grass shows when favorable conditions are met. The graphical behavior of the three turnover-age functions, in relative terms, is shown in Figure 5.5.

In crops ($\Xi = 3$) leaf age turnover, $d_{leaf,a}$, is neglected and all the green biomass is subtracted from the balance after the harvest (see Section 5.3 for details).

Environmental and meteorological conditions may impose additional controls on the green aboveground biomass shedding (*Kozlowski and Pallardy*, 2002; *Ivanov et al.*, 2008a). The turnover of C_{leaf} is also controlled by drought and cold stresses. Questions such as leaf foliage loss due to the severity of a drought or the effects of chilling in leaf shedding are still far to be properly answered and the physiological mechanisms are not completely understood. Conceptual parameterizations are used in the following, since mechanistic models are not available. The drought-induced foliage loss rate, $d_{leaf,d}$ $[day^{-1}]$, is parameterized as in *Arora and Boer* (2005); *Ivanov et al.* (2008a). The rate $d_{leaf,d}$ is a function of the, PFT-dependent, maximum

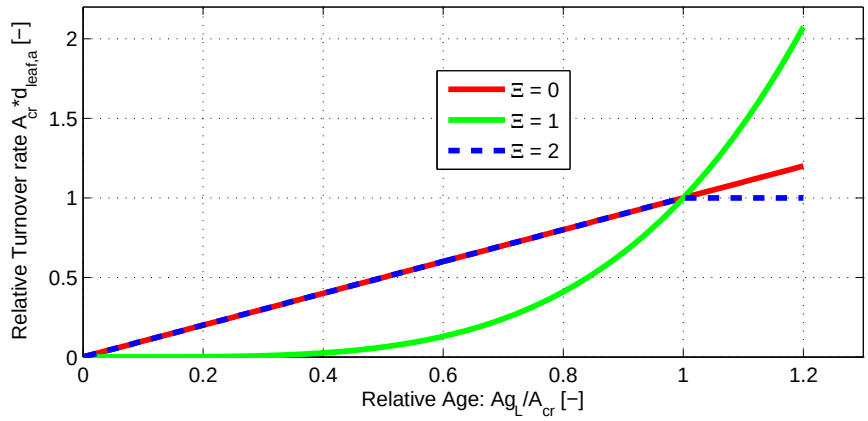

Figure 5.3: Behavior of relative senescence induced turnover, $d_{leaf,a} \cdot A_{cr}$ [−], function of the relative age, Ag_L/A_{cr} [−], for evergreen ($\Xi = 0$), deciduous ($\Xi = 1$), and grass species ($\Xi = 2$).

drought loss rate $d_{d\,max}$ $[day^{-1}]$ and of the root zone soil moisture factor β_R:

$$d_{leaf,d} \quad = \quad d_{d\,max}(1 - \beta_R)^{b_d}\,, \tag{5.33}$$

with:

$$\beta_R \quad = \quad \max\left[0, \min\left(1, \frac{\theta_R - \theta_{wp}}{\theta_{ss} - \theta_{wp}}\right)\right]\,, \tag{5.34}$$

where b_d [−] is the shape parameter reflecting the sensitivity of canopy to drought, θ_R [−] is the daily averaged soil moisture in the root zone (Section 4.7.3), θ_{ss} and θ_{wp} [−] are the soil moisture contents at the begin of stomatal closure and at the complete stomatal closure, respectively. A value of $b_d = 3$ was proposed by *Arora and Boer* (2005) and is used also in "Chloris". The parameter $d_{d\,max}$ $[day^{-1}]$ is difficult to determine, because it is a conceptual representation of a poorly understood mechanism. Values of $d_{d\,max} = 1/40 - 1/365$ $[day^{-1}]$ have been reported (*Arora and Boer*, 2005), however given the very large uncertainty in this process it would not be surprising if $d_{d\,max}$ would assume different values. As a general behavior, $d_{d\,max}$ is expected to be minor for drought tolerant species and for evergreen, where leaves are exposed for the entire year to environmental agents. Note that the drought stress is zero when the root zone contains a certain amount of soil moisture $\theta_R > \theta_{ss}$ and is maximum when $\theta_R \leq \theta_{wp}$.

The rate of foliage loss due to cold stress, $d_{leaf,c}$ $[day^{-1}]$, is assumed to be a linear function of air temperature below a certain threshold temperature (*Cox*, 2001):

$$d_{leaf,c} \quad = \quad d_{cold}(T_{cold} - T_a)(T_a \leq T_{cold})\,, \tag{5.35}$$

where d_{cold} $[day^{-1}\,{}^{\circ}C^{-1}]$ is a linear coefficient, PFT-dependent, for foliage loss due to cold temperatures and T_a $[^{\circ}C]$ is the air temperature. The temperature threshold, T_{cold} $[^{\circ}C]$, is a PFT-dependent parameter that demarcates the temperature below which cold-induced leaf loss begins. This parametrization assumes that leaf shedding

due to cold stress increase linearly with temperature once the threshold T_{cold} is exceeded (towards lower values). As stated for leaf shedding induced by drought, the underlaying physiological mechanisms governing these processes are not completely understood and no mechanistic model exists. Consequently, the assumption behind equation (5.35) is considered equivalent to other hypotheses used to model leaf loss induced by cold temperatures (*Cox*, 2001; *Arora and Boer*, 2005; *Ivanov et al.*, 2008a). The model is quite sensitive to the parameter d_{cold} $[day^{-1}\,{}^{\circ}C^{-1}]$ and to the threshold T_{cold}, especially for evergreen species ($\Xi = 0$) where leaves are exposed to environmental stresses also during the winter season. The threshold T_{cold} is, indeed, higher for cold intolerant plants, for vegetation located in warmer climates and for deciduous species compared to evergreen ones. The same consideration holds true for the parameter d_{cold} which has been found to be an order of magnitude larger in deciduous than for evergreen species, with typical values around $d_{cold} = 1/10 - 1/365$ $[day^{-1}\,{}^{\circ}C^{-1}]$.

5.2.4 Carbon balance

The carbon pool mass balance for green aboveground, C_{leaf} $[g\,C\;m^{-2}\,PFT]$, living sapwood, C_{sapw} $[g\,C\;m^{-2}\,PFT]$, fine roots, C_{root} $[g\,C\;m^{-2}\,PFT]$, and carbohydrate reserves, C_{hydr} $[g\,C\;m^{-2}\,PFT]$, is simulated using a system of ordinary differential equations (*Dickinson et al.*, 1998; *Cayrol et al.*, 2000; *Nouvellon et al.*, 2000; *Arora and Boer*, 2005; *Ivanov et al.*, 2008a). When net primary production is positive, the carbon change in the pools is obtained as follows:

$$\frac{dC_{leaf}}{dt} = f_l NPP - S_{leaf} + Tr_l\,, \tag{5.36}$$

$$\frac{dC_{sapw}}{dt} = f_s NPP - S_{sapw}\,, \tag{5.37}$$

$$\frac{dC_{root}}{dt} = f_r NPP - S_{root} + Tr_r\,, \tag{5.38}$$

$$\frac{dC_{hydr}}{dt} = f_h NPP - Tr_C\,, \tag{5.39}$$

where S_{leaf}, S_{sapw}, and S_{root} $[g\,C\;m^{-2}\,PFT\;day^{-1}]$ are the turnover rates, Tr_C $[g\,C\;m^{-2}\,PFT\;day^{-1}]$ is the translocation from carbohydrate reserves, subdivided into translocation to green aboveground, Tr_l $[g\,C\;m^{-2}\,PFT\;day^{-1}]$, and to fine roots, Tr_r $[g\,C\;m^{-2}\,PFT\;day^{-1}]$. The other carbon pools: flowers-fruits, C_{flfr}, and heartwood, C_{heaw}, are not explicitly resolved in the model. Their theoretical equations are described below:

$$\frac{dC_{flfr}}{dt} = f_f NPP - M_f\,, \tag{5.40}$$

$$\frac{dC_{heaw}}{dt} = S_{sapw} - W_m\,, \tag{5.41}$$

where M_f $[g\,C\;m^{-2}\,PFT\;day^{-1}]$ is a coefficient that accounts for maturation of fruits and loss of flowers, seasonally dependent, and W_m $[g\,C\;m^{-2}\,PFT\;day^{-1}]$ is

the dead wood turnover to litter, that depends on the age and health of the plant and in many external factors that can cause plant mortality, e.g., insect outbreaks, wildfires (*Hawkes*, 2000).

Another important metric of productivity is the Above-Ground Net Primary Production $ANPP$ [$g\,C\,m^{-2}\,PFT\,day^{-1}$]. The term $ANPP$ represents a characteristic of plant performance at a given location and provide a value that is possible to compare with in situ measurements, since estimation of $ANPP$ are generally easier than NPP or GPP measurements.

$$ANPP = \frac{dC_{leaf} + dC_{sapw} + dC_{hydr}}{dt} + S_{leaf} + S_{sapw}\,. \tag{5.42}$$

Note that in equation (5.42) is assumed that carbohydrate reserves and living sapwood are located completely in the aboveground fraction. This simplification is not generally true for many *PFTs*. This is accounted for in grass species considering that there is no living sapwood and eliminating the term relative to carbohydrate reserve in equation (5.42). For other vegetation typologies equation (5.42) is adopted regardless of where the actual carbohydrate reserves and living sapwood physical location is. This approximation probably leads to an overestimation of $ANPP$ when the portion of belowground living sapwood and reserves is considerably large. Conversely, the error is supposed to be limited when $ANPP$ is mainly due to green aboveground dynamics.

When NPP is negative, gross primary production, GPP, less eventually growth respiration rate, R_g, is partitioned among the pools. The respective maintenance respiration costs, R_m, are then subtracted from the carbon pools:

$$\frac{dC_{leaf}}{dt} = f_l(GPP - R_g) - \kappa R_{dC} - S_{leaf} + Tr_l\,, \tag{5.43}$$

$$\frac{dC_{sapw}}{dt} = f_s(GPP - R_g) - R_{mS} - S_{sapw}\,, \tag{5.44}$$

$$\frac{dC_{root}}{dt} = f_r(GPP - R_g) - R_{mR} - S_{root} + Tr_r\,, \tag{5.45}$$

$$\frac{dC_{hydr}}{dt} = f_h(GPP - R_g) - R_{mH} - Tr_C\,, \tag{5.46}$$

The system of ordinary differential equations (5.36)-(5.39) or (5.43)-(5.46) is solved with an explicit *Runge-Kutta(4,5)* formula, the Dormand-Prince pair (*Dormand and Prince*, 1980) using the *Matlab* M-file *ode45*.

A final note is dedicated to the possibility for the plants to experiment mortality within the model. Among the possible mechanisms proposed to explain tree mortality (*McDowell et al.*, 2008) solely carbon starvation is simulated. Carbon starvation can occur after an extended period of environmental stress, mainly drought, where negative NPP induces a deprivation of carbon in the various pools. When carbon content in the compartments, especially in the carbohydrate reserves, is extremely reduced, new favorable environmental conditions cannot be sufficient for the plant to recover and the consequence is plant mortality. The possibility that plants present an anisohydric behavior allowing leaf potential to significantly decrease in order to

maintain positive assimilation rates as soil water potential decreases is not accounted for. While using such a strategy prevents carbon starvation, it increases the possibility of hydraulic failure due to cavitation in the xylems, changing the possible cause of mortality (*Pockman and Sperry*, 2000; *McDowell et al.*, 2008). Not including such a mechanism represents a limitation of the model. Nevertheless carbon starvation has been regarded as the most probable mechanism for drought induce mortality (*Breshears et al.*, 2009), although doubts about the lack of direct evidences have been arisen (*Sala*, 2009).

5.3 Vegetation phenology

Leaf phenology describes the seasonal cycle of leaf functioning and it is essential for understanding the interactions between biosphere and hydrology. Accurate predictions of recurring vegetation cycles as a function of climate are, in fact, important in vegetation models. The timing of leaf onset, bud burst, leaf senescence, leaf abscission determines the length of the growing season, and this considerably affects NPP, the annual cycle of LAI, and consequently, the energy and water fluxes. It has been recognized that phenology is mainly influenced by meteorological conditions warmth and cold periods, soil moisture, length of photoperiod, benefits in terms of carbon gain, etc. (*Botta et al.*, 2000; *Arora and Boer*, 2005; *Ivanov et al.*, 2008a). Notwithstanding, leaf phenology remains one of the most difficult processes to parameterize in terrestrial ecosystem models because our understanding of the physical mechanisms that initiate leaf onset and senescence is incomplete (*Arora and Boer*, 2005). The identification of processes associated with senescence and flowering at the molecular level for selected plant species is still far to be accomplished (*Arora and Boer*, 2005). For instance, it is recognized that deciduous plants shed their leaves in fall primarily because the high costs involved in their maintenance would outweigh the benefits from photosynthesis during the winter period of low light availability and cold temperatures (*Thomas and Stoddart*, 1980). Nevertheless, it is still unclear why leaf shading should necessarily be preceded by the production of vivid autumn colors, and the function of the color change, an incredible familiar phenomenon has been a long standing enigma (*Lee and Gould*, 2002).

Phenology varies according to the characteristic of the *PFT*. For example evergreen, winter deciduous, drought deciduous, or raingreen vegetation types experiments a different relative importance of humidity or temperature factors. Typically, in literature the dates of leaf onset and offset are prescribed (*Ruimy et al.*, 1996) or parameterized with very simple methods (*Haxeltine and Prentice*, 1996; *Knorr*, 2000; *Sitch et al.*, 2003). The most common empirical parameterizations are based on chilly days or growing degree-days (GDD) (*Botta et al.*, 2000; *Arora and Boer*, 2005). The GDD approach made the assumption that before warmer temperatures begin to affect spring growth the positive sum of differences between the daily mean air (or soil) and some threshold temperature following a predetermined date must be exceeded (*Haxeltine and Prentice*, 1996; *Kucharik et al.*, 2000; *Sitch et al.*, 2003).

The chilling days criterion made the assumption that most trees must fulfil a chilling requirement (days with mean temperature below a certain threshold) (*Friend et al.*, 1997). Also combination of growing degree-days and chilling days have been proposed (*Kaduk and Heimann*, 1996; *Botta et al.*, 2000). The shortcoming of these methods is a certain lack of generality and that they may be implicit functions of current climate and therefore unsuitable for changing climate conditions. Climate warming is, in fact, expected to alter seasonal biological phenomena such as leaf onset and flowering (*Peuelas and Filella*, 2001; *Schwartz et al.*, 2006; *Cleland et al.*, 2007).

Mechanistic models of phenology state evolution have been proposed in literature based on a carbon gain approach. The essential assumption in carbon gain approach is that leaf onset starts when it is beneficial for a plant to produce leaves, in carbon terms, and leaf shedding starts when the production becomes unfavorable (*Arora and Boer*, 2005; *Ivanov et al.*, 2008a). The carbon gain approach requires the simulation of a virtual foliage to calculate photosynthesis patterns also in absence of a real foliage cover. In order to avoid such a complication a multi-criteria leaf phenological scheme is used based only on environmental conditions. Proxies for leaf onset such as thresholds of soil temperature, day length, soil moisture, number of consecutive days with net positive photosynthesis are used to determine phenological states (*Lüdeke et al.*, 1994; *Arora and Boer*, 2005; *Ivanov et al.*, 2008a).

Totally four phenological states are considered (*Arora and Boer*, 2005): dormant ($\Phi = 1$), maximum growth ($\Phi = 2$), normal growth ($\Phi = 3$), and senescence ($\Phi = 4$) as shown in Figure 5.4. The phenology states in turn determine plant behavior and allocation patterns as described earlier in this Chapter. Two vegetation categories deciduous plants ($\Xi = 1$) and grass species ($\Xi = 2$) experiment all the phenological states. Evergreen species ($\Xi = 0$) have a single senescence-dormant state. Crops ($\Xi = 3$) are considered to be harvested at a certain date coinciding with the end of normal growth state and to start a new phenological season after a certain amount of carbon is provided to the reserve pool with sowing. Since sowing and harvesting are human controlled actions, these should be accounted for differently in each specific case.

5.3.1 Dormant state to maximum growth

The passage from dormant to maximum growth state ($\Phi = 1 \rightarrow 2$), i.e., leaf onset for seasonal plants ($\Xi = 1, 2, 3$) or bud burst for evergreen takes place with the arrival of favorable weather in spring. *Baldocchi et al.* (2005) analyzing data from 12 sites worldwide, found that carbon uptake by temperate deciduous forest canopies corresponds with the time when the mean daily soil temperature equals the mean annual air temperature. On the basis of these results, in "Chloris" the most tightening criterion for the passage from dormant status to maximum growth is related to the comparison of the average soil temperature of the preceding 30 days, $T_{s,M}$ [$^{\circ}C$], with a certain prescribed threshold temperature $T_{s,LO}$ [$^{\circ}C$]. The passage $\Phi = 1 \rightarrow 2$ happens when $T_{s,M} > T_{s,LO}$. The threshold $T_{s,LO}$ can be tentatively

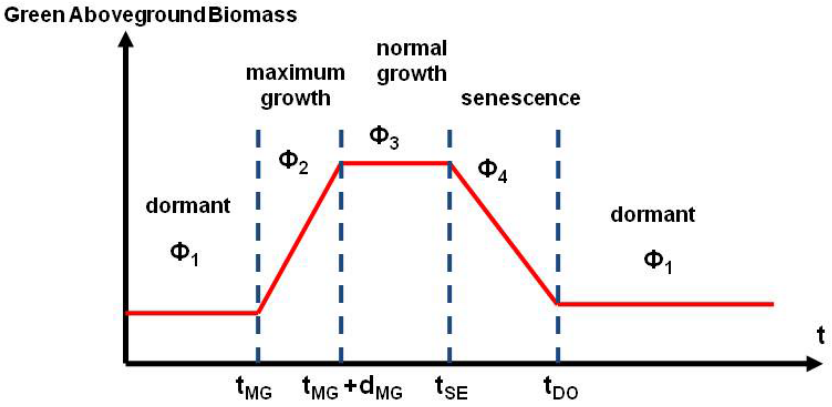

Figure 5.4: A conceptual scheme of phenology phases. The plant passes from the dormant state ($\Phi = 1$) to maximum growth ($\Phi = 2$) at the begin of the favorable season (t_{MG}). For deciduous species and grasses ($\Xi = 1,\ 2$) it corresponds to leaf onset. After a prescribed period d_{MG} $[day]$ the plant passes in a normal growth state ($\Phi = 3$), until the arrival of the unfavorable season, where a senescence state begins ($\Phi = 4$). In the senescence state (t_{SE}) leaf shed becomes dominant and carbon is allocated exclusively to carbohydrate reserves for $\Xi = 1,\ 2$. When all the leaves are shed (t_{DO}) the plants return into a dormant state ($\Phi = 1$) until the arrival of a new favorable season. In evergreen species ($\Xi = 0$) the senescence and dormant states are considered as a single state similar to normal growth in which carbon is still allocated to all the compartments but $f_f = 0$. In crops ($\Xi = 3$), the green biomass is lost after a prescribed harvesting date, thus senescence and dormant states do not exist.

prescribed as the mean annual temperature. However, since the calculation of $T_{s,M}$ is affected by uncertainties and moreover depends on the depth of the soil layer and on the length of the averaging period, $T_{s,LO}$ becomes essentially a calibration parameter. The second criterion for the beginning of maximum growth is related to the soil moisture conditions. A certain amount of moisture must be available to consider the environmental conditions favorable to start a new growing season. Specifically, in order to switch from the dormant to the maximum growth state the metric $\beta_{R,M}$ $[-]$ must be larger than a certain prescribed threshold $\beta_{R,M} > \beta_{LO}$, with:

$$\beta_{R,M} \quad = \quad \max\left[0, \min\left(1, \frac{\theta_{R,M} - \theta_{wp}}{\theta_{ss} - \theta_{wp}}\right)\right], \tag{5.47}$$

where $\theta_{R,M}$ $[-]$ is the average root zone soil moisture in the previous 7 days. Note that this criterion can be removed imposing $\beta_{LO} = 0$. The latter criterion is especially necessary in climates where the initiation of the growing season is due to the return of favorable wet conditions, e.g., arid-semiarid ecosystems or in tropical environments where temperature is never a limiting factor. A final criterion is imposed on the Julian day $J_{Day} < J_{Day,LO}$. Leaf onset cannot start after a certain prescribed date. This is mainly a model artefact, though a sort of genetic memory has been observed in plants (*Thomas and Stoddart*, 1980). This criterion prevents the beginning of a new growing season during late fall or winter when exceptional

fair conditions may occur.

5.3.2 Maximum growth to normal growth

The transition from the maximum to the normal growth state ($\Phi = 2 \rightarrow 3$) occurs when a certain biomass-dependent LAI has been attained. According to *Arora and Boer* (2005); *Ivanov et al.* (2008a) this LAI is approximately 40-50% of the maximum LAI a given stem and root biomass can support. *Krinner et al.* (2005) suggested to identify the maximum growth phase with a fixed number of days where all the carbon is allocated to aboveground green biomass and translocation from reserves occurs. They proposed a maximum growth period of 60 days for trees species and 30 days for grasses species. Following this idea, the passage ($\Phi = 2 \rightarrow 3$) is assumed to take place after a prescribed number of days, d_{MG} $[day]$, PFT dependent. Typical values are $d_{MG} = 20 - 40$ $[day]$.

5.3.3 Normal growth to senescence state

In the normal growth state, a PFT allocates products of photosynthesis to all the carbon compartments (leaves, fine roots, living sapwood, fruit-flowers, and carbohydrate reserves). The transition from normal growth to senescence state ($\Phi = 3 \rightarrow 4$) is triggered by incoming unfavorable weather conditions. This passage is even less understood than the one that leads to leaf onset and only few parameterizations have been proposed. A simple criterion based on the day length is implemented in "Chloris". When the length of the day goes down a certain threshold $D_{LH} < D_{LH,SE}$ $[h]$, the normal growth state is considered finished and senescence begins. This implies that there are no more expenses for reproduction, i.e., $f_f = 0$, and carbon is totally allocated to reserves. This consideration is valid for seasonal and grass species ($\Xi = 1,\ 2$). For crops ($\Xi = 3$) this transition coincides with the harvest and the senescence state does not exist. The evergreen ($\Xi = 0$) species experiment something different from a senescence or dormant state. This singular state coincides almost perfectly with normal growth, except for the fact that there is no allocation to reproductive tissues $f_f = 0$. According to the proposed method, for given geographical coordinates, the transition between normal growth and senescence state occurs the same day every year. It becomes a sort of genetically prescribed passage, unsensitive to environmental conditions. This is a strong assumption but it is the simplest one given the poor understanding of the process. Other conceptual approaches where the transition from normal growth to senescence depends on soil temperature, soil moisture, photosynthetic activity can be easily accounted for in "Chloris" but are not enabled in this first version.

5.3.4 Senescence to dormant state

In deciduous species ($\Xi = 1$) the end of the senescence is characterized by the reaching of a complete defoliation, i.e. when $LAI < LAI_{min}$ the plants is newly considered in a dormant state ($\Phi = 4 \rightarrow 1$). Grass species ($\Xi = 2$) theoretically

experiment both senescence and dormant states. However, given a certain resilience of many grass types to unfavorable condition and ageing, LAI can also remain above LAI_{min} during the winter season. In this case the passage to dormant state is forced externally. Moreover, grass can undergo more phenological cycles during the same year, due to moisture pulses triggering leaf onset in different seasons. For instance, grass growths during spring and fall in Mediterranean climates. The growth in the fall permits grass to recover from the vegetation dye-out induced by drought during summer (*Montaldo et al.*, 2008). Therefore, the condition $LAI < LAI_{min}$ implies a direct passage to dormant state, also when it occurs during the normal growth state $\Phi = 3 \rightarrow 1$. This allows the grass to be ready for a new leaf onset without experimenting the senescence stage.

5.3.5 Leaf age

Leaf age is parameterized similarly to *Krinner et al.* (2005). Leaf age is used to account for different effects on leaf shedding as described in Section 5.2.3. Leaves in the same tree can have different ages, as shown in Figure 5.5, and leaf age influence the turnover rate. Younger leaves if shed are, in fact, expected to be shed at a much slower rate then older ones. *Krinner et al.* (2005) introduced a multi-classes leaf age model where leaf mass is tracked for each different class. In "Chloris" a single leaf age value, Ag_L $[day]$, is computed in order to provide an average of the age of the green biomass standing each PFT:

$$Ag_L(t+dt) = \frac{\Big[LAI(t+dt) - N_{LAI}\Big]\Big[Ag_L(t)+dt\Big] + N_{LAI}\ dt}{LAI(t+dt)}, \qquad (5.48)$$

where N_{LAI} $[m^2\ leaf\ area\ m^{-2}\ PFT\, area]$ is the new leaf area onset between the time t $[day]$ and $t+dt$ $[day]$ with dt daily time step.

There are evidences that leaf age could affect the photosynthetic capacity reducing the latter. This occurs because as leaf age increase, the leaf nitrogen content diminishes, although the same reduction has been observed also when leaf nitrogen is essentially constant (*Nouvellon et al.*, 2000; *Wilson et al.*, 2001; *Krinner et al.*, 2005; *Warren*, 2006). Parameterizations of a relative photosynthetic efficiency, e_{rel} $[-]$, as a function of leaf age have been proposed (*Krinner et al.*, 2005; *Medvigy et al.*, 2009). Notwithstanding, given the numerous uncertainties of such a parametrization, "Chloris" always considers a full constant photosynthetic efficiency, $e_{rel} = 1$.

Figure 5.5: An example of leaves with different ages, picture taken in late October in a chestnut (Castanea sativa) deciduous wood in Tuscany.

Chapter 6

"TETHYS" AND "CHLORIS" (T&C) TESTING

6.1 Introduction

Joint applications of "Tethys" and "Chloris" (T&C, brief acronym) have been carried out for different climates and vegetation types worldwide. The objective is to assess the capability of the numerical tools to reproduce hydrologic and vegetation metrics, e.g., energy fluxes, soil moisture dynamics, snowpack evolution, vegetation production, Leaf Area Index seasonality, etc. Such a modeling exercise requires suits of observational data that are rarely captured by a single experimental field campaign. The interdisciplinary nature inherent in the models requires experimental sites where meteorological, hydrological, vegetation productivity, energy and carbon flux measurements are collected together. Furthermore, vegetation physiological and structural attributes, as well as soil texture profiles must be known. Such a completeness of data is unusual. Experimental scientists from different fields and a broad ensemble of instruments and facilities would be necessary. Scarcity of interdisciplinary data makes difficult or sometimes even impossible to test all the desired behavioral aspects of the models as already underlined by *Ivanov et al.* (2008a). A possibility to begin a corroboration of mechanistic ecohydrological models is offered by "FLUXNET", (www.fluxnet.ornl.govfluxnetindex.cfm). "FLUXNET" is a network that provides access to observations from micro-meteorological towers worldwide. The flux tower sites use eddy covariance methods to measure the exchanges of carbon dioxide, water vapor, and energy between terrestrial ecosystems and the atmosphere (*Baldocchi et al.*, 2001; *Friend et al.*, 2007). Another source of information is constituted by remote sensing data. The launch of the National Aeronautics and Space Administration's (NASA) Terra and Aqua platforms, has provided a new generation of satellite sensor data, helping to make progresses on large scale ecosystem and ocean observations. Among the sensors a great interest has been focused on the two Moderate Resolution Imaging Spectroradiometer (MODIS) (http:modis.gsfc.nasa.gov) that have provided substantially improved data for land cover mapping (*Justice et al.*, 1998; *Myneni et al.*, 2002). For these sensors

algorithms able to infer information about the structural properties of vegetation canopies, e.g., Leaf Area Index (LAI), and Fraction of Photosynthetically Active Radiation (fPAR) have been developed (*Knyazikhin et al.*, 1998; *Myneni et al.*, 2002). Vegetation properties retrieved from remote sensing can offer a further opportunity to test the capability of the model in reproducing LAI dynamics and vegetation phenology. Therefore, combining data from eddy covariance flux towers with measurements of soil moisture and vegetation attributes allows to evaluate the overall performance of the model and also to validate single components.

The consistency of the developed models is demonstrated in two different ways. First, a series of experiments in locations characterized by different climates and vegetation types and where detailed data are available is illustrated. It is shown that the model agrees well in reproducing the behavior of the observed variables and produces consistent results across a range of hydrological and plant behaviors. Second, it is demonstrated that the developed tools are able to capture the dynamics of vegetation-hydrology interaction according to the present scientific understanding of the processes. This is realized designing syntectic case studies. Several possible land covers and plant functional types are forced with the same climate. Differences in terms of energy flux partition, vegetation productivity, and hydrology components are highlighted.

Obviously, the objective of such a validation is not to assert that "Tethys"-"Chloris" are flawless models able to reproduce the ecohydrologic dynamic of multiple and complex ecosystem. The scope is rather to underline that the models behave consistently for the intended use and that their theoretical validity is acceptable for the present state of the art knowledge in hydrological and vegetation modeling. Although theoretical validity must always be regarded as provisional (*Rykiel*, 1996). It should be further remarked that not all the components of the model have been checked to produce consistent results. For instance, great uncertainties exist on the modeling of interaction among vegetation, radiation, and snowpack. Proper field experiments on this topic are not available so far, although efforts are underway (*López-Moreno and Latron*, 2008; *Musselman et al.*, 2008; *Veatch et al.*, 2009). Critical points emerge also in the impossibility to thoroughly verify the carbon allocation scheme, tissue turnovers rates, drought effects on stomatal closure. All this crucial aspects are not yet completely understood by ecologist and plant physiologist and are only partially testable (*LeRoux et al.*, 2001; *Sperry et al.*, 2002; *Katul et al.*, 2003; *Litton et al.*, 2007). Hence, the comparison and numerical experiments realized merely attempt to build confidence that the model performance is physically plausible. For the scope of the research, this is regarded as a sufficient criterium to consider reliable the obtained results.

6.2 Lucky Hills, Arizona, USA

The experimental site of Lucky Hills ($110.30\,W$, $31.44N$; elevation 1372 $[m\ a.s.l.]$) is a very small headwater catchment, 3.71 $[ha]$, located within the Walnut Gulch

Experimental Watershed, near Tombstone in the south-east of Arizona. The Walnut Gulch is a long term experimental watershed managed by the Southwest USDA-ARS (United States Department of Agriculture-Agriculture Research Service) where research in hydrology and soil erosion has been led since 1953 (*Renard et al.*, 2008). The climate at Lucky Hills can be classified as semiarid or steppe, hot, with a dry winter, though is quite close to be an arid or desert climate. Mean annual temperature at Lucky Hills from meteorological observation (1997-2008) is 17.2 $[°C]$ and mean annual precipitation is approximately 353 $[mm]$ (*Keefer et al.*, 2008). The Walnut Gulch watershed is located primarily in a high foothill alluvial fan portion of the San Pedro River watershed. In order to study carbon dioxide and water fluxes over the Walnut Gulch two flux towers have been established since 1997 (*Emmerich and Verdugo*, 2008). One of the towers is located in the divide of the Lucky Hills catchment and belongs to the FLUXNET network. The Lucky Hills flux tower footprint embraces a shrub plant community (Figure 6.1), mainly composed by evergreen shrubs as creosotebush (Larrea tridentata), tarbush (Flourensia cernua), and deciduous shrubs as whitethorn acacia (Acacia constricta) (*King et al.*, 2008; *Skirvin et al.*, 2008). Average vegetation height is estimated to be around 0.3-0.5 $[m]$ and vegetation cover fraction around 0.25-0.4 (*Weltz et al.*, 1994; *Su et al.*, 2001). In the numerical simulation crown area fractions, C_{crown}, equal to 0.175 for deciduous shrubs and 0.125 for evergreen shrubs have been assigned (see Section 4.1.2). Productiveness, behavior, physiological and structural characteristics of Whitethorn acacia and Creosote bush have been considered in order to decide the model parameters (*Chew and Chew*, 1965; *Cox et al.*, 1986; *Clarke et al.*, 1990; *Franco et al.*, 1994; *Housman et al.*, 2006; *Muldavin et al.*, 2008; *Hamerlynck and Huxman*, 2009).

The soil at this site is coarse-loamy with slopes around 3 to 8%. The surface horizon (0-6 $[cm]$) contains 650 $[g\ kg^{-1}]$ of sand, 290 $[g\ kg^{-1}]$ of silt, and 60 $[g\ kg^{-1}]$ of clay with 290 $[g\ kg^{-1}]$ of coarse fragments > 2 $[mm]$, 8 $[g\ kg^{-1}]$ of organic carbon,

Figure 6.1: Shrub plant community at the Lucky hills flux tower. Source: *www.tucson.ars.ag.govunitgiswg.html.*

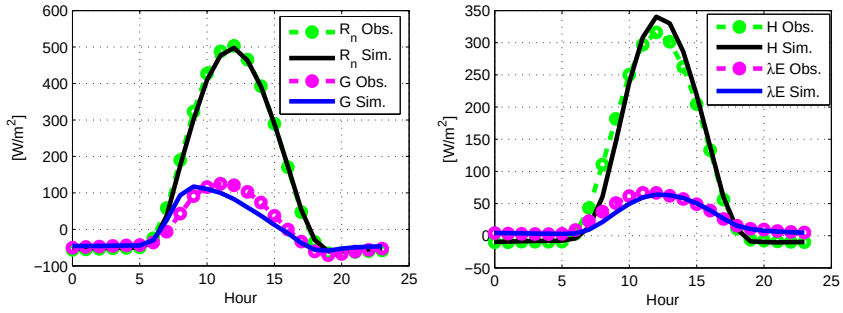

Figure 6.2: A comparison between observed and simulated average daily cycle of energy fluxes, where R_n is the net radiation, H the sensible heat, λE the latent heat, and G the ground heat.

and 21 $[g\ kg^{-1}]$ of inorganic carbon (*Emmerich and Verdugo*, 2008). The saturated conductivity has been observed to consistently diminish with soil depth (*Scott et al.*, 2000).

Results in terms of energy fluxes are highly satisfactory as testified from the capability of the models to reproduce the average daily cycle of net radiation, R_n, sensible heat, H, latent heat, λE, and ground heat, G, (Figure: 6.2). The determination coefficients, R^2, for the entire simulations are $R^2 = 0.96$ for R_n, $R^2 = 0.88$ for H, $R^2 = 0.56$ for λE, and $R^2 = 0.68$ for G. It should be remarked that such a performance is obtained for a period of simulation longer than 11 years. This is quite rare in comparison to analogous modeling exercise. The results maintain their reliability, when disaggregated at the monthly scale as shown in Figure 6.3, Figure 6.4, and Figure 6.5. An overestimation of sensible heat during the months of the growing season, and an underestimation of latent heat flux during August, balanced by an overestimation in July can be observed (Figure 6.4).

The performance of the model in reproducing soil moisture dynamics is illustrated in Figure 6.6 at three characteristic depths. An ensemble of four different observation dataset is shown in Figure 6.6. This ensemble is due to different sensors, trench positions, and collection periods of soil moisture measurements. The large spread of observations underlines once more the uncertainties in soil moisture measurements. The match between simulated and observed soil moisture at 5 $[cm]$ depth is satisfactorily (Figure 6.6). In deeper layer, 15-30 $[cm]$, the differences between the simulated and observed soil moisture becomes significant. Soil moisture is indeed generally overestimated. This can be the result of the numerous assumptions introduced to simplify the water dynamics in the unsaturated zone (see Chapter: 4). An uncorrect position of the sinks (evapotranspiration) in the soil column, or a poor parametrization of the hydraulic properties of soil, estimated from pedotransfer functions can be also the causes of such a mismatch.

The monthly partition between hydrological fluxes is shown in Figure 6.7. Evaporation and transpiration represent by far the largest components of the hydrological budget. Infiltration excess runoff can be observed during the summer months (mon-

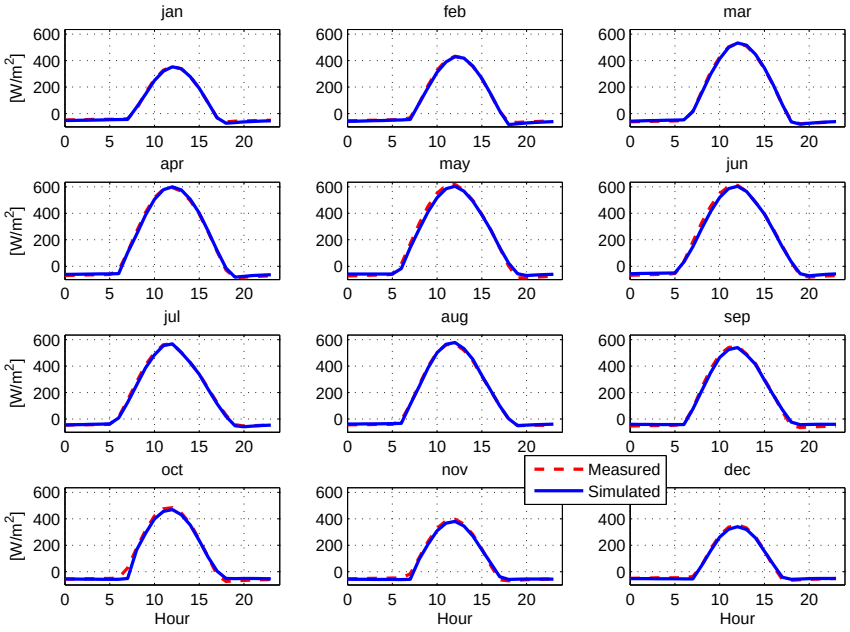

Figure 6.3: A comparison between observed and simulated monthly average daily cycle of net radiation, R_n.

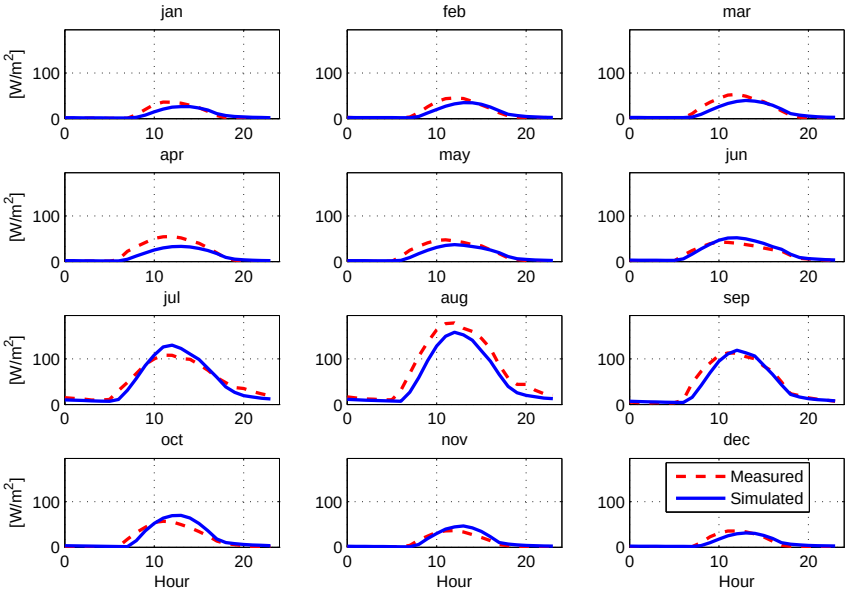

Figure 6.4: A comparison between observed and simulated monthly average daily cycle of latent heat, λE.

soon period) due to heavy precipitation and soil sealing. The average evapotranspiration flux during the simulation is 308 $[mm\ yr^{-1}]$ that represents about the 87%

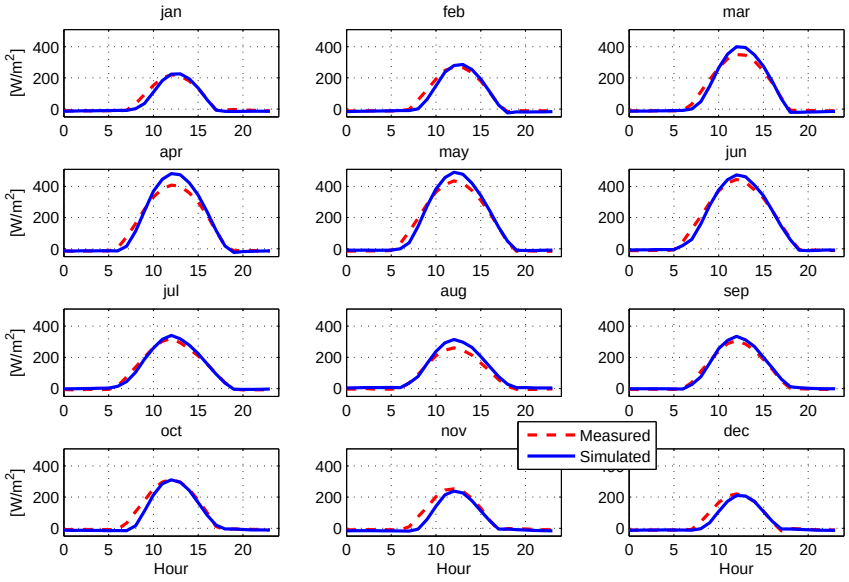

Figure 6.5: A comparison between observed and simulated monthly average daily cycle of sensible heat, H.

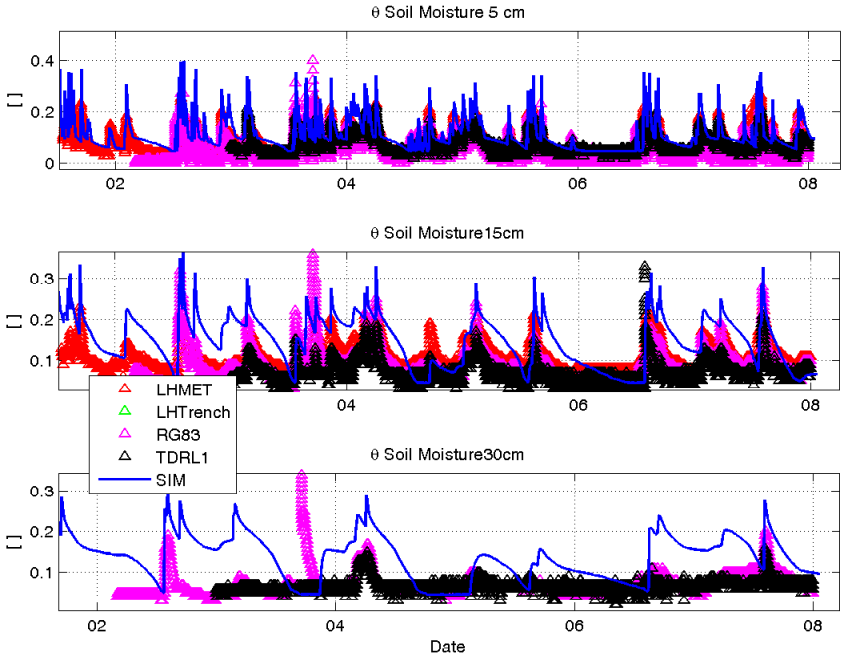

Figure 6.6: A comparison between observed and simulated soil water contents at different depths: 5 $[cm]$, top panel, 15 $[cm]$ central panel, 30 $[cm]$, bottom panel.

of annual precipitation. Recharge to deeper soil layers is estimated to be almost 22 $[mm\ yr^{-1}]$. Although, during the 11 years is mainly concentrated in two very wet

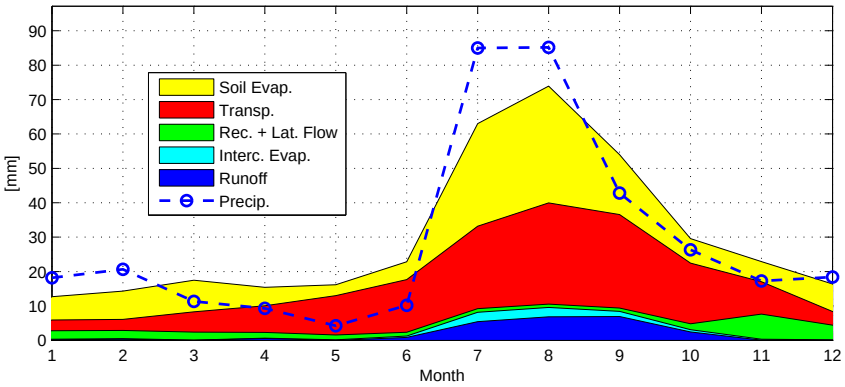

Figure 6.7: Monthly partition of the principal hydrological budget components expressed in $[mm\ yr^{-1}]$ averaged over the simulation period.

events. Plot scale runoff, generated from intense precipitation and soil sealing effects is estimated to be 23 $[mm\ yr^{-1}]$. This value is very close to the ones measured at very small watersheds in the Walnut Gulch (*Stone et al.*, 2008).

The calculated average annual Gross Primary Production (GPP) is 172 $[gC\ m^{-2}\, ground\ yr^{-1}]$, the Net Primary Production (NPP) is 92 $[gC\ m^{-2}\, ground\ yr^{-1}]$, and the Aboveground Net Primary Production (ANPP) is 65 $[gC\ m^{-2}\, ground\ yr^{-1}]$. As shown in Figure 6.8 these values are close to the ones estimated from remote sensing data (MODIS). The simulated inter-annual variability of vegetation productivity is generally limited. A sensible reduction in GPP and NPP can be appreciated in 2006 due to a prolonged drought period. In the satellite data, this effect seems postponed of one year although uncertainties on the reliability of remote sensing data exist. The leaf area index dynamic is captured as far as concern the magnitude and the inter-annual cycle, see Figure 6.9, where the calculated LAI is compared with satellite observations. The capability to capture the general phenology is demonstrated, although sensible difference in the length of the growing season and in the LAI peaks are appreciable. As already stated above, it should be noted that the corroboration of LAI simulations with remote sensing observations is always critical since mismatches in terms of footprint or disturbances can distort the reliability of the comparison.

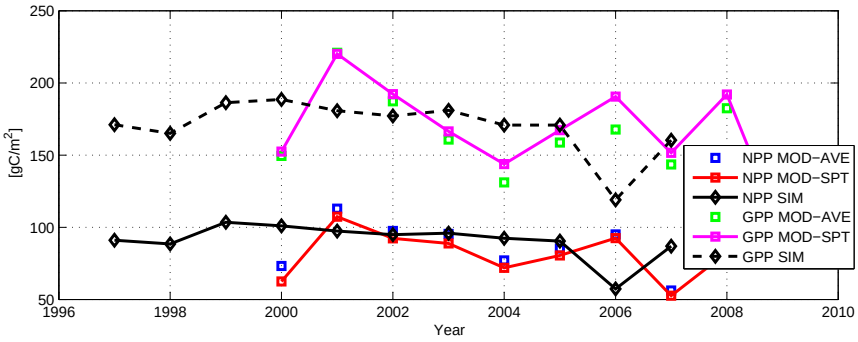

Figure 6.8: A comparison between simulated and remote sensing observations of GPP and NPP. MOD-SPT is the MODIS estimation of the vegetation productivity in the pixel containing the flux tower, MOD-AVE is the average in a surrounding area of 7x7 [km^2].

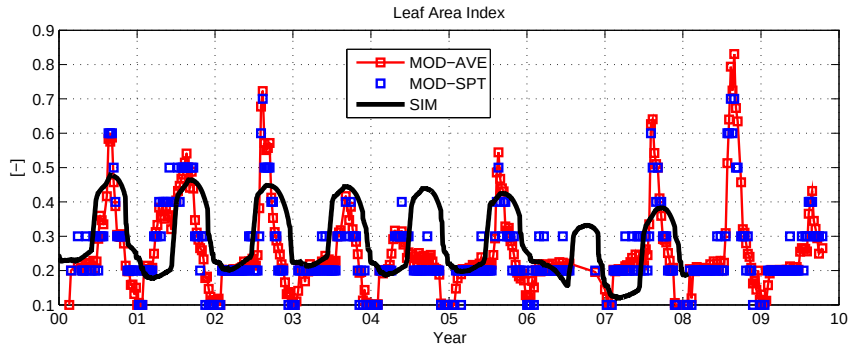

Figure 6.9: A comparison between simulated and remote sensing observation of Leaf Area Index. MOD-SPT is the MODIS estimation of LAI in the pixel containing the flux tower, MOD-AVE is the average in a surrounding area of 7x7 [km^2].

6.3 San Rossore, Italy

The flux tower of San Rossore (10.28E, 43.72N; elevation 4 [m $a.s.l.$]) is located within the Natural Park of San Rossore. The tower site is in proximity of the sea, 700 [m] east of the shoreline, and 10 [km] west of Pisa. It belongs to the FLUXNET network. The climate is Mediterranean sub-humid. In the recorded period (2001-2007) the average yearly temperature is 15.3 [$^{\circ}C$] and the average annual precipitation is about 823 [mm]. The area adjacent to the sea (Figure 6.10, left) is dominated by the presence of a Mediterranean evergreen needleleaf forest composed of both maritime pine (Pinus pinaster) and stone pine (Pinus pinea) (Figure 6.10). The measurement site is surrounded by an homogeneous maritime pine stand where canopy flux measurements are being collected by an eddy covariance tower. The average stand height is 18 [m], the average diameter at breast height of Pinus pinaster trees is 29 [cm], and the stand density is 565 [$number\,of\,individuals\,ha^{-1}$] (84% P. pinaster, 12% P. pinea and 4% Quercus ilex). The soil is composed prevalently by sand (*Tirone*, 2003; *Chiesi et al.*, 2007). From literature, the typical root depth of maritime pine trees is around 60-90 [cm] (*Bakker et al.*, 2006). Physiological and biochemical parameters characteristic of Pinus Pinaster have been reported in several studies and are used in the simulation set-up (*Medlyn et al.*, 2002; *Warren*, 2006).

The comparison between observed and simulated energy fluxes is very good both for net radiation, R_n, and latent heat, λE, as testified from Figure 6.11. The sensible heat flux is instead substantially overestimated (not shown). This can be explained only by uncertainties in the measurements, although temporary differences can be due to a considerable storage of heat in the forest layer. The observed energy balance is indeed far from be close, as can be often noticed for eddy covariance data. When the analysis is partitioned at the monthly scale, the quality of the results in terms of energy fluxes is still very good, as shown for the latent heat fluxes in Figure 6.12. There is an overestimation of the latent heat flux during the night probably due to an undervaluation of the stability conditions in the surface boundary layer. This can be a shortcoming related to the single value of prognostic temperature used in "Tethys" (see Chapter 4). Another explanation can be the poor quality of latent

Figure 6.10: Aerial view of the San Rossore flux tower, source: Google® maps (left); and illustrative details of maritime pine (Pinus pinaster) (right).

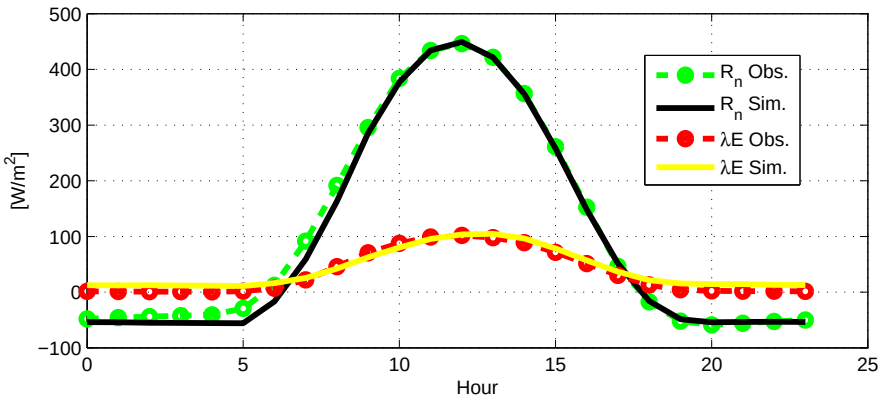

Figure 6.11: A comparison between observed and simulated average daily cycle of energy fluxes, where R_n is the net radiation, and λE the latent heat.

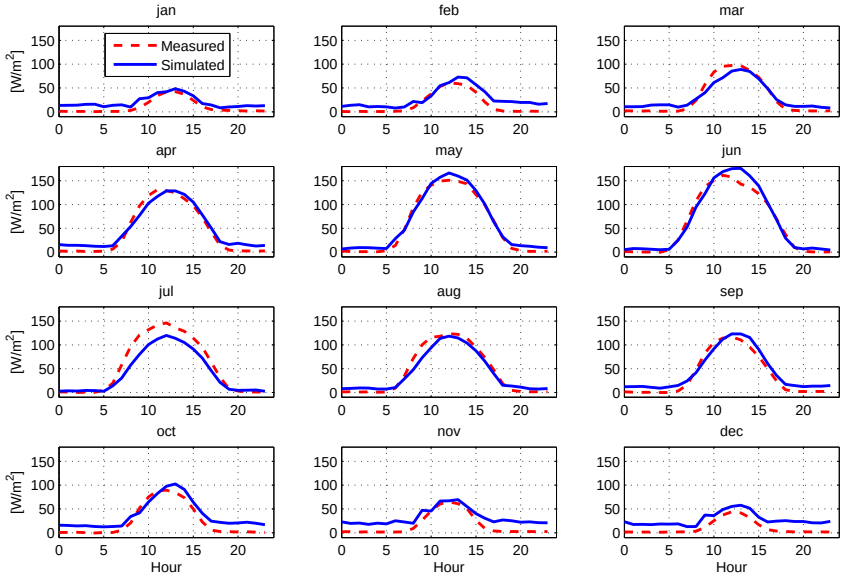

Figure 6.12: A comparison between observed and simulated monthly average daily cycle of latent heat, λE.

heat data during the nighttime, as measured with the eddy covariance technique. A slight underestimation of latent heat flux is also appreciable in the month of July. This can be the result of simulating a too strong effect of water stress on vegetation photosynthetic and transpiration activities or ignoring the effect of water table. The determination coefficients, R^2, for the entire simulation are $R^2 = 0.94$ for R_n, $R^2 = 0.60$ for H, and $R^2 = 0.39$ for λE.

The monthly partition between hydrological fluxes is shown in Figure 6.13. Transpiration and deep recharge represent the highest fractions of the hydrological budget. The average evapotranspiration flux during the simulation is 514 $[mm\ yr^{-1}]$ about the 62% of the annual precipitation. There is also a significant contribution

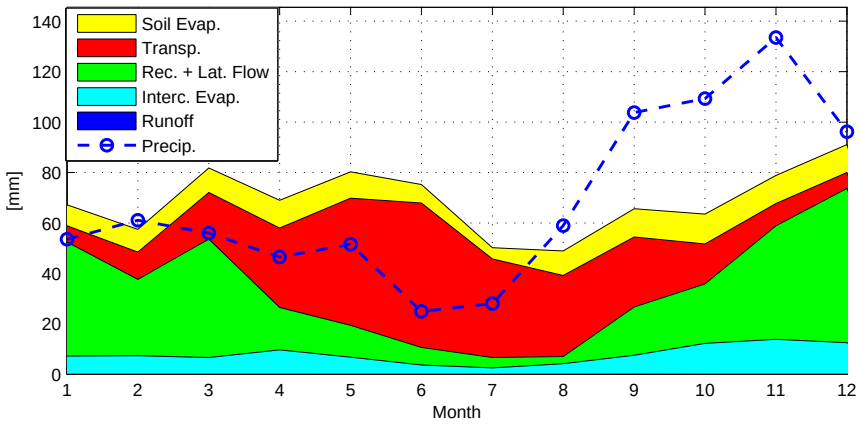

Figure 6.13: Monthly partition of the principal hydrological budget components expressed in $[mm\ yr^{-1}]$ averaged over the simulation period.

of evaporation from intercepted rainfall, that is estimated to be 95 $[mm\ yr^{-1}]$ more than 10% of the hydrological budget. This is a consequence of the presence of a dense vegetation cover of evergreen plants and of a mild winter that allows evaporation to occur also during the cold months.

The simulated average annual GPP is 1256 $[gC\ m^{-2}\, ground\ yr^{-1}]$, the NPP 594 $[gC\ m^{-2}\, ground\ yr^{-1}]$, and the ANPP 450 $[gC\ m^{-2}\, ground\ yr^{-1}]$. These values agree with remote sensing observation (Figure 6.14 bottom panel), although simulated GPP is generally larger than the MODIS observed and the opposite holds true for NPP. However, other estimations of GPP indicate that larger values are typical of that ecosystem (*Chiesi et al.*, 2007; *Chirici et al.*, 2007). In Figure 6.14 (top panel) is shown the comparison between the simulated LAI and the values obtained from MODIS. The comparison in terms of LAI seasonal cycle and magnitude is very good. There is a peak of water stress at the end of the summer 2003, where the Mediterranean and European regions were interested by persistent hot and dry conditions (*Granier et al.*, 2007). This water stress can be appreciated in the time series of the simulated, β_R, moisture stress factor (Section 4.4.5) as shown in Figure 6.14 (central panel).

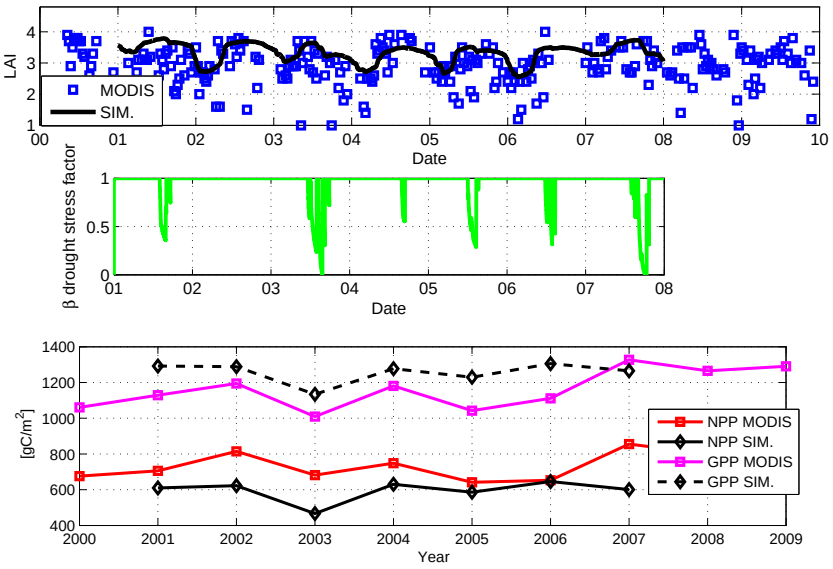

Figure 6.14: A comparison between simulated and remote sensing observations of Leaf Area Index (top panel), GPP and NPP (bottom panel) and the time evolution of simulated, β_R, moisture stress factor (central panel).

6.4 Reynolds Creek, Mountain East, Idaho, USA

The snow hydrology in "Tethys" has been tested using data recorded at the Reynolds Creek, Mountain East site (116.46W, 43.16N, elevation 2058 [m $a.s.l.$]), located in the Owyhee Mountains in Idaho, USA (*Seyfried et al.*, 2001a). The Reynolds Creek river basin is an experimental watershed of the USDA-ARS Northwest Research center (*Slaughter et al.*, 2001). This dataset is particularly appealing for testing snow models because contains high quality and long term measurements of snow water equivalent and snow depth and the correspondent meteorological and hydrological variables (*Hanson*, 2001; *Hanson et al.*, 2001; *Marks et al.*, 2001; *Seyfried et al.*, 2001b; *Marks and Winstral*, 2001; *Winstral and Marks*, 2002). At the Reynolds Creek snow water equivalent, S_{WE}, and snow depth, S_{dep}, have been measured in 8 sites every two weeks during the snow season for 35 years (1962-1996). In one location, S_{WE} has been recorded continuously by means of a snow pillow for almost 14 years (1983-1996) (*Marks et al.*, 2000, 2001). These snow pillow measurements are used to validate the snow hydrology component. The snow pillow device is located in proximity of a rain-gauge system constituted of a dual-gauge installations, unshielded and shielded, designed to more accurately measure snowfall (*Hanson*, 2001). Meteorological variables are observed in a station 400 [m] upstream at the elevation of 2097 [$ma.s.l.$] after scaling for the temperature lapse rate (*Hanson et al.*, 2001). The location where meteorological variables are collected is shown in Figure 6.15. Few meters from the meteorological station neutron probes were installed and 19 years (1977-1996) soil moisture measurements at different depths are available (*Seyfried et al.*, 2001b, 2000). The Reynolds Creek Mountain East is mainly dominated by sagebrush, as low sagebrush (Artemisia arbuscula), vaseyana sagebrush-Wyoming big sagebrush (Artemisia tridentata). Tall trees such as aspens and Douglas firs are also present. The fraction of vegetation cover is estimated to be around 0.6 (*Seyfried et al.*, 2001b). The snow course is situated in a clearing surrounded by sparse aspen (Populus tremuloides) grove bordering a sparse stand of Douglas fir (Psuedotsuga menziesii) to the south, about 90 meters north and about 250 meters to the east of a snow-drift accumulation area (*Seyfried et al.*, 2000; *Marks and Winstral*, 2001). The soil in Reynolds Creek, Mountain East area is a sandy-loam, loam, with elevated content of rocks and organic content (*Seyfried et al.*, 2001b). Mean annual temperature at Reynolds Creek, Mountain East site from meteorological observation (1983-1996) is 5.3 [$^{\circ}C$] and mean annual precipitation is approximately 966 [mm].

The capability of the model to reproduce the dynamics of snowpack and soil moisture are discussed in the following. Results are considered very satisfactory for both snow water equivalent and snow depth as shown in Figure 6.16 and 6.17. Although differences regarding the end of the melting season are present (not appreciable from the figures), these differences are generally limited to less than one week, 19 days in the worst case. The average error on S_{WE} during the snow season is 45 [mm] (15%) and the average error on S_{dep} is 24 [cm], (22%). The sublimation-evaporation

Figure 6.15: Climate, snow, and precipitation measurement site near fir forest in the southern, higher-elevation region of the Reynolds Creek Experimental Watershed, from *Slaughter et al.* (2001).

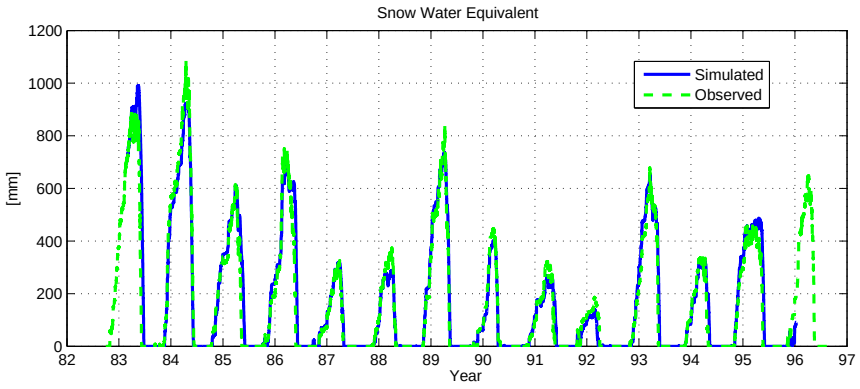

Figure 6.16: A comparison between simulated and observed snow water equivalent at the Reynolds Creek Mountain East snow pillow location.

from the snowpack is estimated to be 43 $[mm]$ per year. This value is less than the ones observed in other experimental sites (*Gelfan et al.*, 2004; *Strasser et al.*, 2008). However, it seems a realistic value given the absence of vegetation interception and the cold climate of the simulated area.

The comparison in terms of soil moisture dynamics is shown in Figure 6.18. The model captures quite well the timing and amplitude of the soil moisture pulses at shallow and intermediate depths 15-30 $[cm]$. The simulation in deeper layers shows a general overestimation of soil moisture. This can be related to topographic effects, not accounted for by the plot scale simulation and by the large uncertainty in the parametrization of the hydraulic properties of the soil.

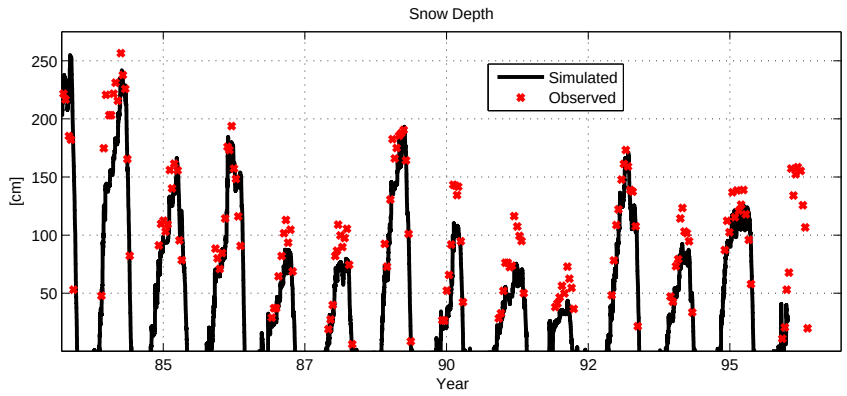

Figure 6.17: A comparison between simulated and observed snow depth at the Reynolds Creek Mountain East snow pillow location.

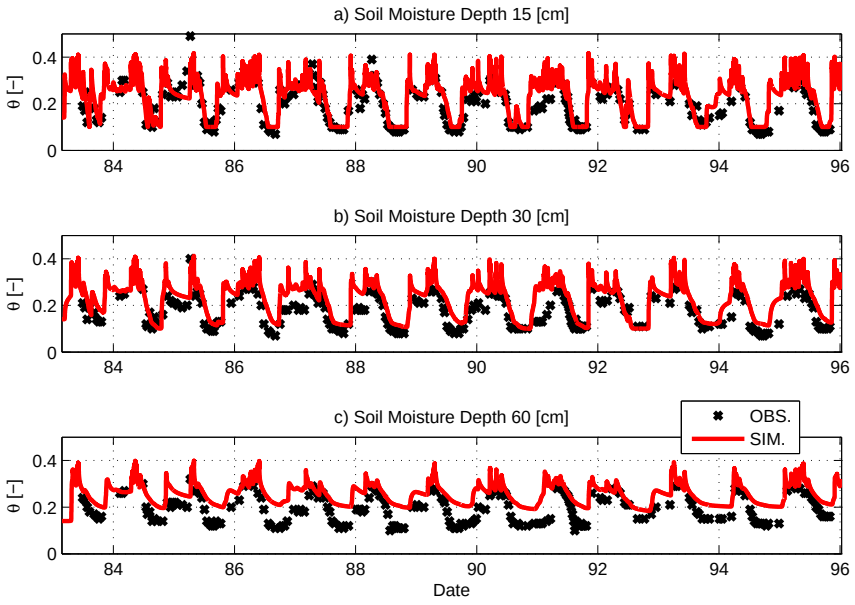

Figure 6.18: A comparison between simulated and observed soil moisture at the Reynolds Creek, Mountain East neutron probe location. a) Soil moisture at 15 [cm]. b) Soil moisture at 30 [cm]. c) Soil moisture at 60 [cm].

6.5 Bayreuth-Waldstein, Germany

The experimental site of Bayreuth-Waldstein ($11.52E$, $50.09N$; elevation 780 [m $a.s.l.$]) is located in an evergreen coniferous forest within the Lehstenbach catchment. Energy and carbon fluxes are observed with the eddy covariance technique. The flux tower belongs to the FLUXNET network. The climate is sub-oceanic, mountainous. In the recorded period (1996-1999), the average yearly temperature is 6.2 [$°C$] and average annual rainfall is about 996 [mm]. The area is dominated by the presence of Norway Spruce (Picea abies) and patches of wavy hairgrass (Deschampsia flexuosa) in the understorey (Figure 6.19) (*Alsheimer et al.*, 1998; *Köstner et al.*, 2002). The flux tower is located in an homogeneous Norway Spruce stand with average 40 years age. The average stand height is 19 [m] and the stand density is 1000 [$number\,of\,individuals\,ha^{-1}$] with a maximum leaf area index around 5.0. The soil is brown Earth (acidic cambisol) (*Alsheimer et al.*, 1998; *Köstner et al.*, 2002).

The results in terms of fluxes of net radiation, R_n, (Figure 6.20), and sensible heat, H, (not shown) are very good during the warm season. The assumption to exclude the vegetation not covered by snow from the energy budget is clearly appreciable during the winter period. As discussed in Section 4.2.4, in presence of snow, $C_{sno} = 1$, the net radiation absorbed by uncovered vegetation parts is neglected in the energy budget. It is assumed that this part of absorbed net radiation is exactly counterbalanced by the emitted sensible heat flux. Such an assumption implies an underestimation of the simulated net radiation and sensible heat, during the snowy season. This is especially true for vegetation types where the portion of uncovered canopy can be significant, e.g., evergreens. After the unloading of the intercepted snow, the snow is accumulated below the canopy and the plants with large LAI absorb a considerable part of net radiation, and emit sensible heat. However, as correctly hypothesized in Chapter 4 this outcome does not significantly affect the latent heat flux, λE. During wintertime, λE is indeed negligible (Figure 6.21).

Figure 6.19: Images of the forest stand and flux tower at the Bayreuth-Waldstein FLUXNET site. Source: *www.fluxnet.ornl.gov fluxnetCd-1web _start_here.html.*

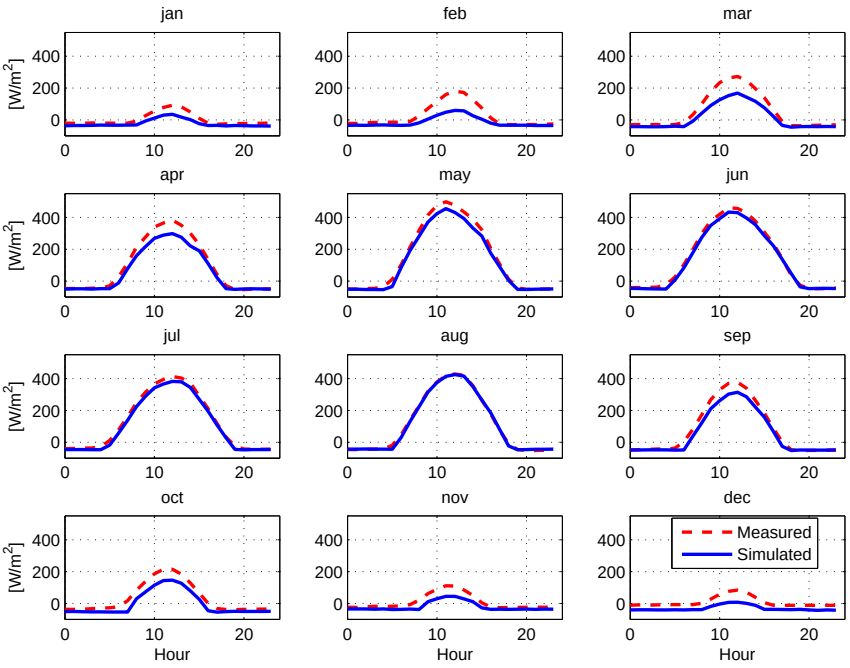

Figure 6.20: A comparison between observed and simulated monthly average daily cycle of net radiation, R_n.

Figure 6.21 also shows that the monthly average daily cycle of λE is captured by the model with only minor overestimation during the spring season. The determination coefficients, R^2, for the entire simulation are $R^2 = 0.90$ for R_n, $R^2 = 0.68$ for H, and $R^2 = 0.62$ for λE.

The monthly partition between hydrological fluxes is shown in Figure 6.22. Recharge to deeper layers represents the highest fraction of the hydrological budget ($\sim 66\%$). Recharge to aquifer is in phase with monthly precipitation. The latter outcome is explained by the limited capacity of soil to store incoming water. The soil is indeed near its field capacity throughout all the simulation period. The average evapotranspiration flux during the simulation is 322 $[mm\ yr^{-1}]$ about the 32% of the annual precipitation. This is close to the 330 $[mm\ yr^{-1}]$ obtained from observations. Note the differences in the relative importance of hydrological budget components, compared to a similar plant functional type, needleleaf evergreen forest, but in a different climate (Section: 6.3). The contribution of evaporation from intercepted rainfall is limited to the summer months, since during cold and wet periods potential evaporation is very small.

The simulated average annual GPP is 866 $[gC\ m^{-2}\ ground\ yr^{-1}]$, the NPP is 459 $[gC\ m^{-2}\ ground\ yr^{-1}]$ and the ANPP is 336 $[gC\ m^{-2}\ ground\ yr^{-1}]$. Note that these values are inferior to the needleleaf forest of San Rossore located in a warmer climate, although the LAI is higher in Bayreuth-Waldstein. GPP values are slightly larger ($\sim$ 10%) than reference values provided for Bayreuth-Waldstein by MODIS data

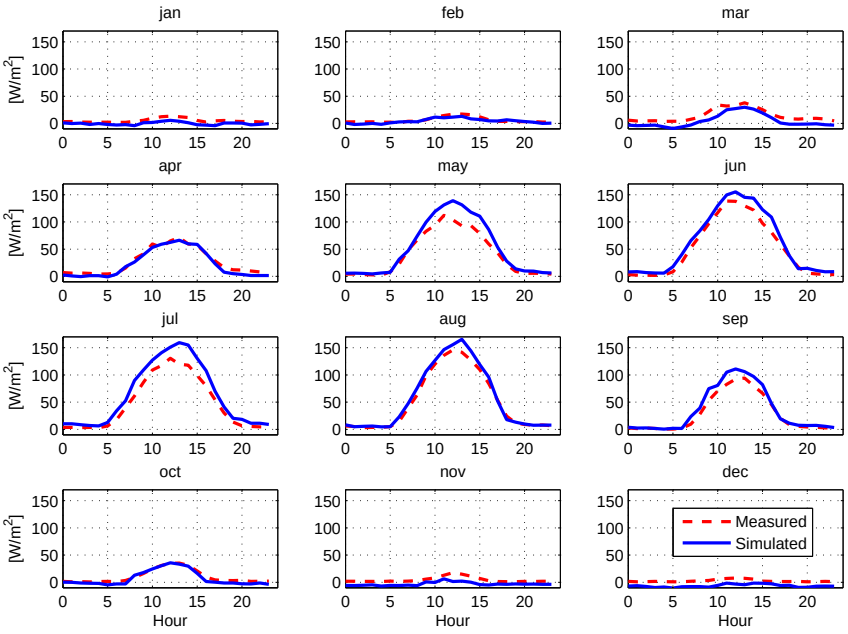

Figure 6.21: A comparison between observed and simulated monthly average daily cycle of latent heat, λE.

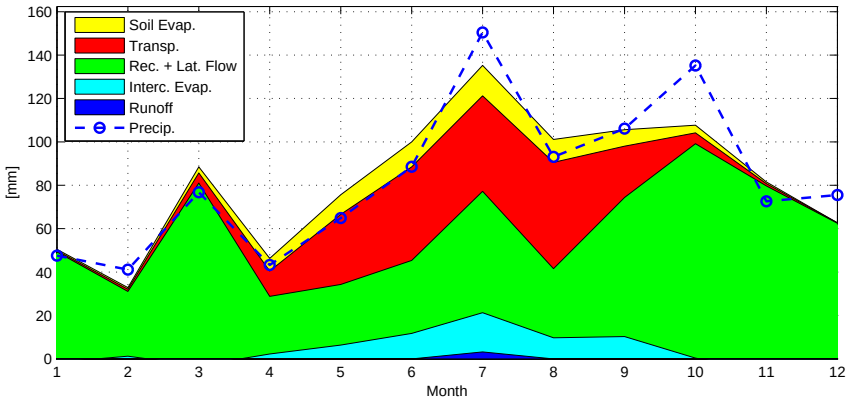

Figure 6.22: Monthly partition of the principal hydrological budget components expressed in $[mm\ yr^{-1}]$ averaged over the simulation period.

for the period 2000-2009. The opposite holds true for NPP, that is underestimated of almost the same percentage. The simulated Leaf Area Index ranges from 3.7 to 4.8 (Figure 6.23, top panel), that is close to the value of 5.0 estimated from field observations.

Contradictories are the results in terms of snow depth below the canopy (Figure 6.23 bottom panel). This variable in one hand seems to be simulated quite well during the winter 1997-98, corroborating the model performances. In the other hand, it appears strongly underestimated during the following winter. This underestimation

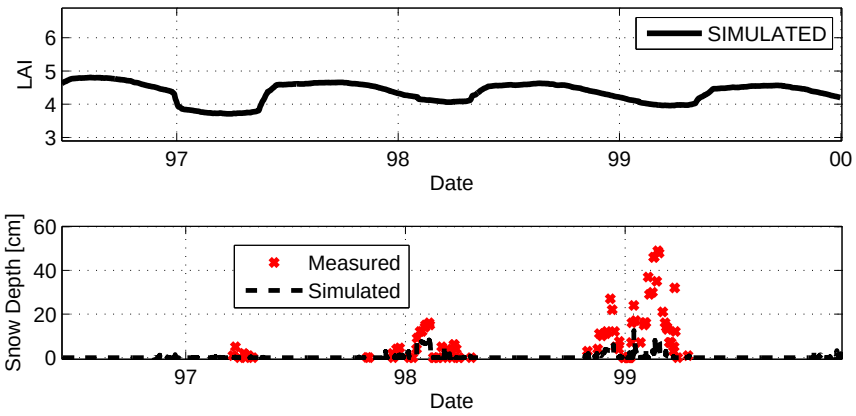

Figure 6.23: Simulated Leaf Area Index (top panel) and a comparison between observed and simulated snow depth below the canopy (bottom panel).

can be partially related to model flaws. However, inconsistencies or in the precipitation or in the snow depth measurements are very plausible. As a matter of fact, the total winter precipitation is inadequate to sustain such a snowpack, also when a bare soil area is considered. Better and more extensive field measurements are required to validate this component of the model.

6.6 Walker Branch, Tennessee, USA

The Walker Branch flux tower ($84.17\,W$, $35.57N$; elevation 365 [m $a.s.l.$]) is situated within an experimental watershed, the Walker Branch Watershed in Roane County, Tennessee. The site is located in the southern section of the temperate deciduous forest biome of eastern United States. Micro-meteorological and flux measurements were collected above a temperate deciduous forest continuously from 1995 through 1998 (Figure 6.24). The flux tower belongs to the FLUXNET network. The canopy height is approximately 26 [m] above the surface and maximum leaf area index is about 6.0 (*Wilson and Baldocchi*, 2000; *Wilson et al.*, 2001). The forest contains a mixed deciduous stand dominated in the overstory by oak (Quercus alba, Quercus prinus), maple (Acer Rubrum, Acer saccharum), and the remainder are primarily hickory (Carya spp.) and black Tupelo (Nyssa sylvatica) (*Wilson et al.*, 2001). The height in the understory is generally 2 [m] and it contributes to the overall LAI only marginally $LAI \simeq 0.3$ (*Misson et al.*, 2007). Dominant trees range from 60 to 120 years in age having regenerated from agricultural land. The upwind fetch of forest extends several kilometers in all directions. The soil is well drained and is classified as a typical Paleudult, which encompasses clayey and kaolinitic soils (*Wilson and Baldocchi*, 2000). Mean annual temperature from meteorological observation (1995-1998) is 14.6 [$°C$] and mean annual precipitation is approximately 1517 [mm]. This site has been widely used for research activity in ecology, plant physiology, and biogeochemestry, as testified by more than 80 publications (see for instance *Hanson et al.* (2004, 2005)). A more detailed description of the canopy architecture, species composition, climate and soil properties are provided in *Johnson and vanHook* (1989).

The comparison between observed and simulated energy fluxes is remarkably good as far as concern net radiation, R_n, (not shown) and latent heat, λE, (Figure 6.25). This is especially true during the summer months, although an earlier onset of evapotranspiration can be appreciated. The observed energy fluxes does not lead to the closure of the energy budget. This can be explained, in the short term, by a

Figure 6.24: Images of the Walker Branch deciduous forest during wintertime (left) and late summer (right).

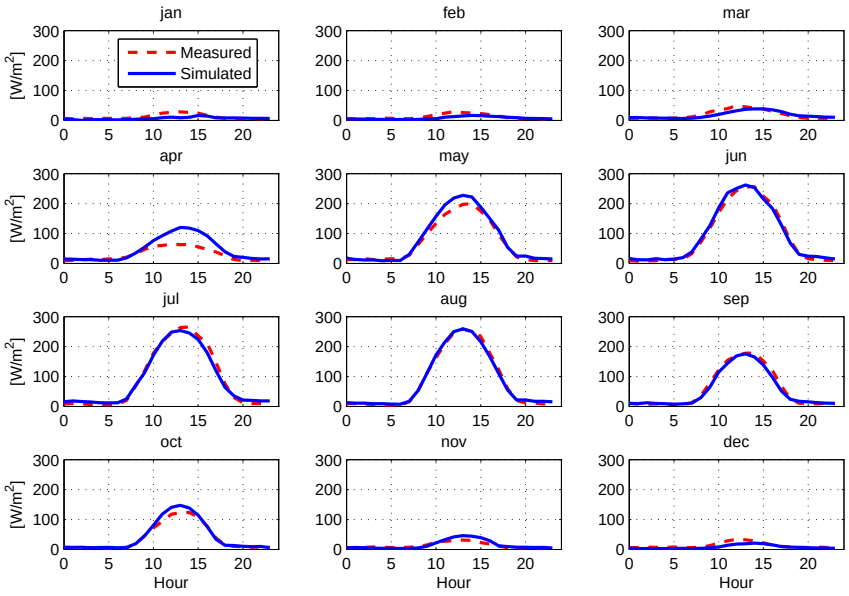

Figure 6.25: A comparison between observed and simulated monthly average daily cycle of latent heat, λE.

certain storage of heat within the canopy, and by uncertainties in the measurements in the long term. The sensible heat is strongly overestimated in comparison to observations (not shown). A similar behavior has been already observed for San Rossore (Section 6.3). In both sites the very dense vegetation cover may be the cause of this significant difference. However, it must be notice that the principal scope of the energy budget is to obtain reliable estimations of the latent heat, and this seems the case in the presented model. Determination coefficients, R^2, for the entire simulation are $R^2 = 0.97$ for R_n, $R^2 = 0.64$ for H, and $R^2 = 0.73$ for λE. Note the very good performance in the simulation of λE underlined by a rather elevated R^2.

The total evapotranspiration flux during the simulation period is 589 $[mm\ yr^{-1}]$, about the 39% of the annual precipitation. This is slightly higher than observed evapotranspiration estimated to be around 550-560 $[mm\ yr^{-1}]$. The evaporation of interception accounts only for 77 $[mm\ yr^{-1}]$, 5% of the total budget. The majority of the rain is lost as lateral subsurface flow or deep recharge.

Figure 6.26 shows the comparison between the simulated LAI and the values calculated from observations of light extinction factors. Errors in the order of 7-15 days in the dates of leaf onset and leaf shedding can be appreciated. This is mainly a shortcoming of the very simple criterium adopted for leaf onset, where the driving factor is soil temperature. Nonetheless, the comparison in term of LAI seasonal cycle and magnitude is good and it is considered to further corroborate the model.

The simulated average annual GPP is 960 $[gC\ m^{-2}\, ground\ yr^{-1}]$, the NPP is 411 $[gC\ m^{-2}\, ground\ yr^{-1}]$ and the ANPP 318 $[gC\ m^{-2}\, ground\ yr^{-1}]$. The pre-

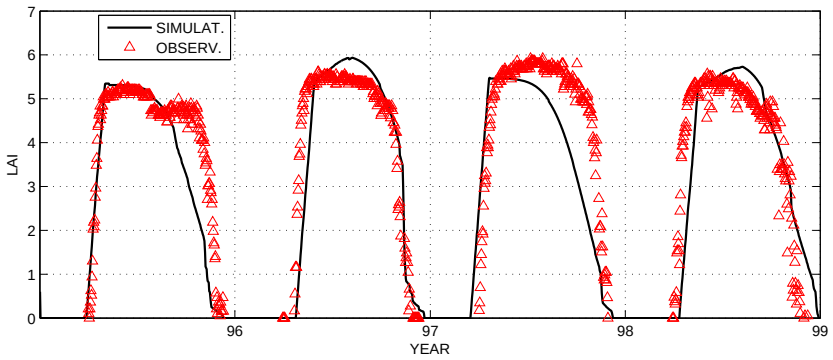

Figure 6.26: A comparison between observed and simulated Leaf Area Index.

dicted values of GPP and NPP are significantly smaller than the ones provided in literature study of this area, about 1400 $[gC\ m^{-2}\, ground\ yr^{-1}]$ for GPP and 700 $[gC\ m^{-2}\, ground\ yr^{-1}]$ for NPP. This points to question the model capabilities to simulate GPP and NPP in a such humid environment. The reasons can be related to the presence of processes that are not captured or underestimated by the model or to model structural flaws. Despite the overall performance in the simulation of LAI there can be parameters that assume values very different from the one set up in the model. Finally, it should be remarked that the Walker Branch is a wet environment, where soil moisture is almost never a limiting factor. In these conditions the hypothesis of a water controlled system is violated and other constraints, as nutrients, might play a major role (*Mackay*, 2001). The violation of such an hypothesis could be the explantation for some of the inconsistencies. However, globally the results of the model are considered acceptable, highlighting the quality of the proposed tool.

6.7 Sensitivity to land cover composition

In order to test the capability of the model to reproduce consistent realizations of hydrological and energy fluxes for different land uses and vegetation types, a series of syntectic case studies has been designed. The forcing climate has been assumed equal for all the cases and input variables are derived from the station *Firenze University* ($11.15E$, $43.47N$; elevation 91 [m $a.s.l.$]). The observations cover a period of eight years (2001-2008) for which a complete set of hydro-meteorological variables is available. However, in order to average the response of the different systems in a climatic time horizon "Tethys" and "Chloris" have been forced with 15 years of data. The 15-years long time series have been obtained using the weather generator described in Chapter 2, which parameters are estimated using the observations. Mean annual temperature in the simulated period is 14.6 [$^{\circ}C$] and mean annual precipitation is 745.6 [mm].

Eight syntectic cases corresponding to eight possible land covers are simulated. The choice attempts to consider the principal plant functional types of the Tuscany region. This should ensure a certain correspondence between the forcing climate and the simulated vegetation. Bare soil and water land covers are also simulated for comparison. In summary, the different cases are: bare soil (1), water surface (2), temperate deciduous forest (3), temperate evergreen forest (4), temperate grassland (5), generic crop (6), deciduous trees with grass underneath (7), and a mixed wood of deciduous and evergreen plants. The parameters used in the simulations for each plant functional type are described in Table 6.1. Vegetation physiological and structural parameters are derived from literature values and are based on author personal judgement. For a review of literature references refer to Chapter 4 and Chapter 5. The soil used in the simulations is a sandy-loam soil. A column 2 [m] deep with a saturated conductivity of 50 [$mm\ h^{-1}$] at the surface and a bottom free drainage condition is assumed in all the cases. A list of hydrological parameters is provided in Table 6.2.

The results of the simulations are subdivided in Table 6.3 among the analyzed syntectic case studies. In order to give a brief overview of the results only averaged quantities of the most significant variables are presented. The latter are total evapotranspiration, net radiation, latent and sensible heats, 1.2 [m] integrated soil water content, and three indexes of vegetation productivity, GPP, NPP, and ANPP. Evapotranspiration, ET, ranges between 224 [$mm\ yr^{-1}$] for the bare soil case study to 841 [$mm\ yr^{-1}$] for a open water surface. These quantities represent 30% and 112% of the annual precipitation respectively. The water surface ET can be regarded as the potential evapotranspiration for the examined climate and it is a reference value for the other cases. The vegetated cases have values of ET between 50% and 75% of annual precipitation, with the lower extreme represented by grassland and the higher by evergreen forest. Deciduous forest and mixed vegetation lay between these two values. These estimates of ET are very likely for vegetation in a temperate Mediterranean climate and are considered to corroborate the model. The differences

Table 6.1: List of the parameters used in the simulations for each PFT. The values are assigned according to literature values (see Chapter 5) and are based on author personal judgement.

Parameter	**Deciduous**	**Evergreen**	**Grass**	**Crop**
Ψ_{ss} $[kPa]$	-800	-650	-1000	-200
Ψ_{wp} $[kPa]$	-3000	-2500	-3500	-1500
Z_R $[mm]$	1200	900	300	300
SAI $[-]$	0.1	0.1	0.001	0.1
H_c $[m]$	15	20	0.3	0.5
d_{leaf} $[cm]$	3.5	0.25	0.8	3
K_N $[-]$	0.5	0.5	0.5	0.5
φ_p	C3	C3	C3	C3
V_{max}^L $[\mu mol\ \mathrm{CO_2}\ m^{-2}\ s^{-1}]$	40	35	65	90
ϵ $[\mu molCO_2\ \mu mol^{-1}\ phot]$	0.081	0.081	0.081	0.081
c_a $[ppm]$	380	380	380	380
O_i $[ppm]$	210000	210000	210000	210000
H_a $[kJ\ mol^{-1}]$	72	72	72	72
ΔS $[kJ\ mol^{-1}\ K^{-1}]$	0.649	0.649	0.649	0.649
Δ_0 $[Pa]$	1000	1000	1000	1000
a $[-]$	7	7	6	10
g_0 $[mol\,CO_2\ m^{-2}\ s^{-1}]$	0.01	0.01	0.01	0.01
S_{LAI} $[m^2\ LAI\ g\,C^{-1}]$	0.016	0.009	0.032	0.035
ω_{grw} $[-]$	0.25	0.25	0.25	0.25
r_m $[g\,C\ g\,N^{-1}\ day^{-1}]$	0.030	0.030	0.025	0.030
N_l $[-]$	30	42	20	30
ε_{al} $[-]$	1	0.2	1	1
R_{ltr} $[-]$	1	1	0.75	1
T_{rC} $[g\,C\ m^{-2}\ PFT\ day^{-1}]$	3.5	1.0	0.5	3.2
d_{root} $[day^{-1}]$	1/1095	1/1460	1/720	1/365
d_{sapw} $[day^{-1}]$	1/365	1/365	-	1/365
A_{cr} $[day]$	150	1460	250	120
$d_{d\,max}$ $[day^{-1}]$	1/365	1/600	1/360	1/160
d_{cold} $[day^{-1}\ {}^\circ C^{-1}]$	1/18.25	1/365	1/450	1/24
T_{cold} $[^\circ C]$	7	2	0	8
$T_{s,LO}$ $[^\circ C]$	12.9	12.7	11.3	11.7
β_{LO} $[-]$	0.95	0.95	0.95	0.95
$J_{Day,LO}$ $[-]$	180	180	260	180
d_{MG} $[day]$	35	30	25	35
$D_{LH,SE}$ $[h]$	12.3	10.05	10.05	9
LAI_{min} $[-]$	0.01	0.001	0.2	0.001
$S_{p,In}$ $[mm]$	0.2	0.2	0.2	0.2
$\widehat{Sp}_{sno,In}$ $[mm]$	5.9	5.9	5.9	5.9

are mainly related to the length of the period leaves can photosynthesize, the entire year for evergreen, and to the depth of the roots, significant shallower in grasses. In a temperate climate is possible to have transpiration and evaporation fluxes also during the winter season when favorable weather conditions are met. The average soil water content integrated in the first 1.2 $[m]$ of soil column directly reflects the differences in evapotranspiration. Its value ranges between 0.20 $[-]$ for evergreen, to 0.234 $[-]$ for grass, with an higher value for bare soil, i.e., 0.259 $[-]$. Note that these values are sensibly lower than the field capacity water content, estimated for the sandy-loam soil to be $\theta_{fc} = 0.29$ $[-]$. Although, not immediately appreciable the variability in the average soil water content among vegetation types is significant. The average difference in stored water in the 1.2 $[m]$ soil column between a grass meadow and an evergreen forest can indeed be about 40 $[mm]$. When the comparison is made between evergreen and bare soil, this difference raises to about 70 $[mm]$. Already, such a simple analysis highlights how different vegetation types can present, on average, quite different initial conditions in terms of stored water, this can be easily translated to runoff formation and response and can have important implications for flood risk mitigation.

Vegetation productivity, as expected, is higher in evergreen and lower in deciduous and grass species. In grass, GPP is about the 70% of the GPP of evergreen. The GPP indeed ranges between 817 to 578 $[gC\ m^{-2}\ yr^{-1}]$, and NPP ranges between 378 to 158 $[gC\ m^{-2}\ yr^{-1}]$ from an evergreen forest to a grassland. The total autotrophic respiration cost accounts for about 55% of GPP in evergreen, 51% in deciduous and 72% in grass species. The respiration cost for grass is generally larger than expected (*Litton et al.*, 2007), suggesting that the model capability to correctly reproduced this vegetation type must be improved. The GPP, NPP values simulated are generally significantly lower than what would be expected for the analyzed vegetation types in a Mediterranean temperate climate (*Bonan et al.*, 2003; *Krinner et al.*, 2005; *Chirici et al.*, 2007). This can be also appreciated in the simulated LAI generally comprise between 1 and 3 (Figure 6.27). In dense forest, LAI around 4-5 would be expected, consequently also the GPP and NPP values would be more similar to the ones estimated for the Tuscany area. This flaw of the model is worth of a thorough investigation in the future, since it can be the results of a model structural error or of a bug in the codes. For instance, it has been

Table 6.2: List of the parameters used to describe the hydrological properties in the simulations.

Hydrological parameter	
d_e $[mm]$	50
F_{san} $[-]$	0.65
F_{cla} $[-]$	0.1
P_{org} $[-]$	2.5
m_f $[mm]$	1000
K_{bot} $[mm\ h^{-1}]$	Free drainage

noted that the leaf dark respiration scheme might present some caveats, as discussed in Chapter 4. This might lead to underestimate maximum Rubisco capacity and consequently productivity, to compensate for higher respiration rates. The above ground net primary production, ANPP, ranges between 51-275 $[gC\ m^{-2}\ yr^{-1}]$. The considerations made for GPP and NPP can be extended to ANPP. A clarification for grass is useful, since grass has the ratio ANPP/NPP significant lower than other species. This is related to both the higher leaf respiration cost and to the fact that carbohydrate reserves are considered stored in the belowground compartment.

A comparison of the results in terms of LAI dynamic is shown in Figure 6.27. The LAI patterns obtained for various vegetation types are plausible in phenology timing and slightly underestimated in magnitude, given the climatic conditions imposed. Note the effect of a water stress period that influence LAI cover at the 3rd and 9th year. The effect is more appreciable in the grassland.

Net radiation, R_n, changes significantly between the analyzed synthetic cases. Net radiation reaches the maximum value of 92 $[W\ m^{-2}]$ for evergreen species the cooler surface and it decreases until 48 $[W\ m^{-2}]$ for bare soil the warmest surface. The variations are indeed explainable in terms of differences in albedo and outgoing longwave radiation. Albedo is generally lower in vegetated than in bare soil areas. This implies a larger absorption of shortwave radiation and thus a higher energy input into the systems. Outgoing longwave radiation is instead mainly determined by the surface temperature, T_s. Larger values of T_s imply large outgoing radiation fluxes and consequently a decrease in net radiation. Surface radiative temperatures are quite similar among the vegetation types and they are close to the mean annual air temperature. Larger T_s are appreciable in the bare soil case and also in the water surface. Note that for the water surface, this is mainly due to higher T_s values during the night and lower values in the daytime that on average produce a T_s similar to the one of the bare soil. The annual average Bowen ratio, B_R, i.e., $B_R = H/\lambda E$ $[-]$, for the vegetated case studies is on the order of $1.05 - 1.30$ lower for evergreen and larger for grasses. Bare soil and water surface represent the two extremes of Bowen Ratio with $B_R = 1.8$ and $B_R = 0.16$ respectively.

The results obtained for the eight synthetic case studies show the overall capability of the model to consistently reproduce hydrological components, energy fluxes, and vegetation productivity (slightly underestimated) for different land covers and vegetation types. Where consistently means that the results agree well with other studies, observed values for the examined area, and with the expected qualitative behavior.

Table 6.3: Synthetic experiment results, in terms of total evapotranspiration, ET, vegetation productivities, GPP, NPP, $ANPP$, soil moisture, θ, surface radiative temperature, T_s, net radiation, R_n, latent heat, λE, and sensible heat, H, for the different land covers. The wording D+G and D+E indicates deciduous trees with grass underneath, and a mixed wood of deciduous and evergreen plants, respectively.

	Bare s.	**Water**	**Dec.**	**Ev.**	**Grass**	**Crop**	**D+G**	**D+E**
P_r $[mm\ yr^{-1}]$	745.6	745.6	745.6	745.6	745.6	745.6	745.6	745.6
ET $[mm\ yr^{-1}]$	224.5	841.2	461.7	560.9	370.8	269.9	465.4	529.4
GPP $[gC\ m^{-2}\ yr^{-1}]$	-	-	581.8	817.8	578.7	186.2	676.2	712.7
NPP $[gC\ m^{-2}\ yr^{-1}]$	-	-	289.8	378.0	158.0	-	296.8	342.3
ANPP $[gC\ m^{-2}\ yr^{-1}]$	-	-	217.5	275.8	51.7	-	215.7	253.7
θ $[-]$ 0-1.2 $[m]$	0.259	-	0.210	0.200	0.234	0.245	0.208	0.204
T_s $[°C]$	18.2	17.9	14.6	14.3	15.1	15.0	14.6	14.3
R_n $[W\ m^{-2}]$	48.7	73.7	79.0	92.0	67.3	67.2	78.5	85.9
λE $[W\ m^{-2}]$	17.5	65.2	35.9	43.9	29.1	21.0	36.3	41.4
H $[W\ m^{-2}]$	31.5	10.6	42.6	47.0	38.1	46.1	42.0	43.8

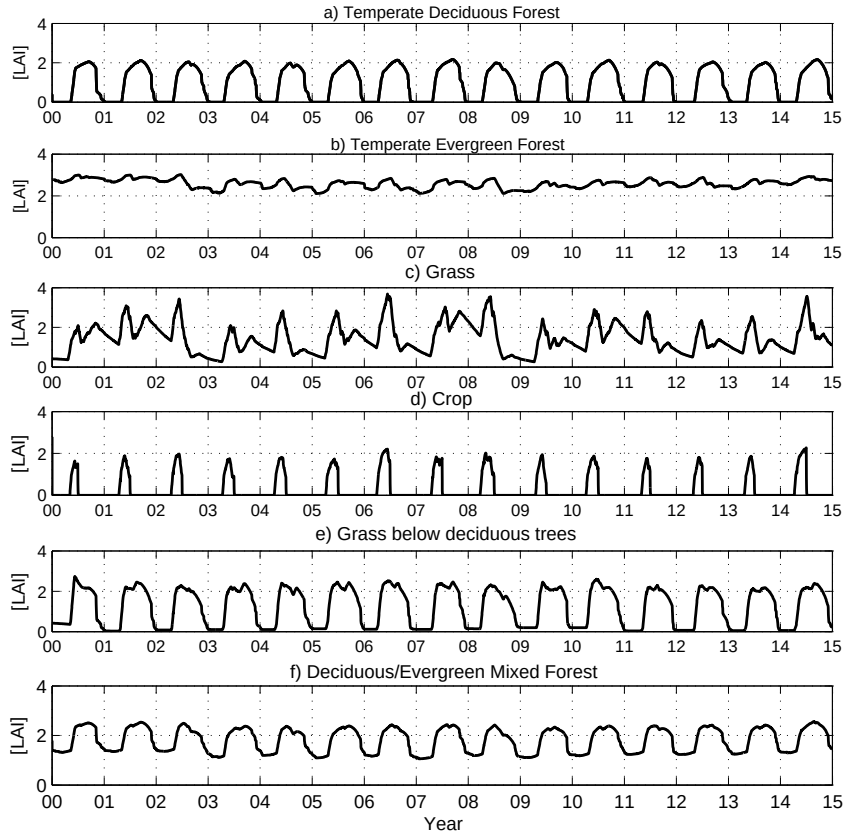

Figure 6.27: Simulated Leaf Area Index for the different vegetation types. a.) Temperate deciduous forest. b.) Temperate evergreen forest. c.) Grassland. d.) Crops. e.) Grass below deciduous trees. f.) Deciduous and evergreen mixed forest.

Chapter 7

USING CLIMATE CHANGE PREDICTIONS IN ECOHYDROLOGY, A CASE STUDY

7.1 Introduction

As discussed in Chapter 1 there is a growing interest to extend climate change predictions to smaller, catchment-size scales and identify their implications on hydrological and ecological processes. Small scale processes are, in fact, expected to mediate climate changes, producing local effects and feedbacks that can interact with the principal consequences of the change. This is particularly true, when a complex interaction, such as the inter-relationship between the hydrological cycle and vegetation dynamics, is considered. The tools and methodologies presented in the previous chapters are gathered to create a blueprint for studying climate change impacts, as inferred from climate models, on eco-hydrological dynamics at the catchment scale. A proof of concept of the proposed blueprint is discussed in this Chapter, analyzing a specific case study in a semiarid environment. Climate conditions, present and *future*, are imposed through input hydro-meteorological variables. These variables are simulated with the hourly weather generator (Chapter 2) as an outcome of a stochastic downscaling technique (Chapter 3). The generator is parameterized to reproduce the climate of southeastern Arizona for present (1961-2000) and future (2081-2100) conditions. The methodology provides the capability to generate ensemble realizations for the future that take into account the heterogeneous nature of climate predictions from different models. The generated time series of meteorological variables for the scenarios corresponding to the current and multiple expected futures serve as input to the coupled hydrological and vegetation dynamic model, "Tethys-Chloris" fully described in Chapter 4 and 5.

7.2 Case study characterization

The methodologies and numerical tools presented in this thesis are applied to a specific case study. Results and considerations are thus referred to a particular climate and ecosystem. The case study is represented by the semiarid climate of the south-east Arizona (USA) and by the plants characteristic of this area. The present climate is derived from 40 years (1960-2000) of observations at the meteorological station of Tucson airport ($110.91\,W$, $32.21N$; elevation 728 [m a.s.l.]). Tucson has a desert semi-arid climate with hot summers and temperate winters. Precipitation has a strong seasonality and falls for about 50% during the summer monsoon from July to September (*Sheppard et al.*, 2002). Mean annual temperature from meteorological observations in the considered period is 20.2 $[^{\circ}C]$ and mean annual precipitation is approximately 304 $[mm]$. The climate of Tucson airport is considered to effectively represent the portion of Sonoran desert of south-east Arizona as shown from the circle in Figure 7.1. The climate of Tucson airport is indeed used as a baseline for the generation of time series of present and future climates as described in Section 7.4.

The analyzed ecosystem is a community of desert shrubs. Desert shrubs have been chosen because sufficient data were available to test the performances of hydrological and vegetation models in reproducing their dynamics. The eco-hydrological model "Tethys-Chloris" has been validated at the experimental site of Lucky Hills ($110.30\,W$, $31.44N$; elevation 1372 $[m\ a.s.l.]$) located in the Walnut Gulch Experimental Watershed about 70 $[km]$ southeast of Tucson (Figure 7.1). The validation of the eco-hydrological model at the Lucky Hills location is described in other sections (7.3 and 6.2) and it is not further discussed here. The ecosystem analyzed is only partially vegetated ($\backsimeq 30\%$) (*Weltz et al.*, 1994; *Skirvin et al.*, 2008) and is composed of both deciduous and evergreen shrubs. As plant species representative of the two categories, Whitethorn acacia (Acacia constricta) (Figure 7.2) and Creosote bush (Larrea tridentata) (Figure 7.3) are considered in order to define plant structural and physiological properties (Section 6.2). Lucky Hills has a climate slightly different when compared to Tucson. In the period of observation (1997-2008) Lucky Hills mean annual temperature is 17.2 $[^{\circ}C]$ and mean annual precipitation is approximately 353 $[mm]$. The differences are mainly due to the higher elevation of Lucky Hills, 1372 $[m\ a.s.l.]$ vs 728 $[m\ a.s.l.]$, this entails a lower air temperature and stronger precipitation especially during the monsoon season. The Lucky Hills location is at the edge of the grassland and pine forests of south-east Arizona, as can be noted also in Figure 7.1. Nevertheless, transferring the properties of shrub plants validated at Lucky Hills to the Tucson area can be considered a fair assumption. Vegetation surrounding Tucson is also prevalently composed by sparse desert shrubs, as can be easily observed from Google® maps. Consequently, it can be expected that the physiological and structural properties of vegetation are preserved across this small distance and that the found results are not affected by the climate differences between the two locations.

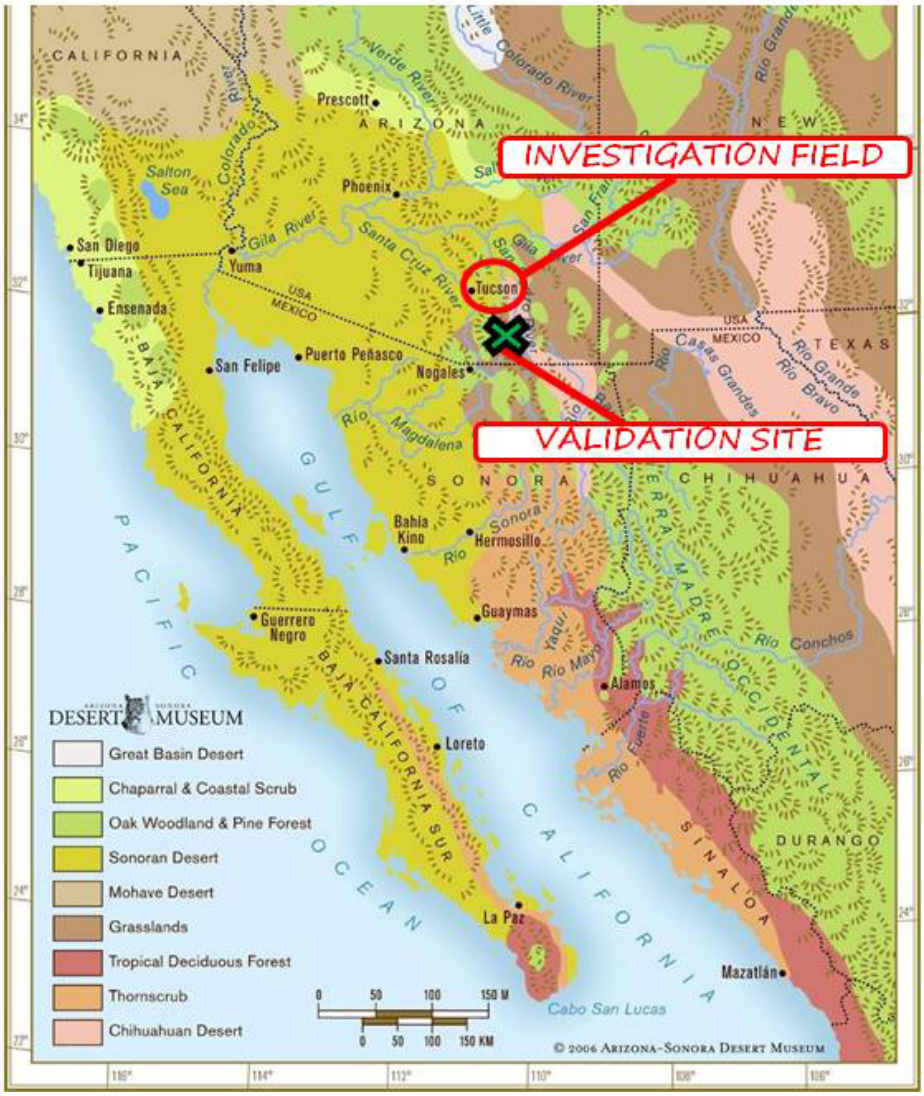

Figure 7.1: Deserts in the USA Southwest and Mexico Northwest. The circle indicates the area interested by the presented analysis, the cross indicates the location where the eco-hydrological model is validated. Source: *http://www. desertmuseum.org/desert/sonora.php*.

Southeast Arizona climate and desert shrubs can be regarded as a very specific case-study with scarce influences on human activities, water consumption, or flood risk. This is generally untrue, because semiarid ecosystems are expanding and currently represent 30% of global terrestrial surface area (*Scanlon et al.*, 2005). In semiarid environments the potential impacts of climate variability mainly affect subsurface components of the water cycle. For instance, the percolation below the root zone that can be assumed to represent the groundwater recharge. Recharge is essential for water resources planning in regions where water scarcity represents a big issue due to limited supplies and high demand (*Scanlon et al.*, 2005). Although, subsurface components are the most significant, semi-arid environments can be also affected by localized but severe flash floods (*Cohen and Laronne*, 2005). This entails

Figure 7.2: Plant of Whitethorn Acacia (Acacia Constricta).
Source: *http:// ag.arizona.edu/pima/gardening/ aridplants/Acacia_constricta.html.*

Figure 7.3: Plant of Creosote bush (Larrea Tridentata).
Source: *http://www. mojavenp.org/larrea_tridentata_ mojave_national_preserve.htm.*

a certain relevance of this study also for flood risk evaluation. In such a context vegetation dynamics cannot be neglected and are likely to play an important role. For example, *Scanlon et al.* (2005) in their study provide field evidence of the importance of vegetation dynamics in controlling the subsurface water cycle response to climate variability in semiarid and arid regions. Their results indicate that the presence of xeric vegetation is likely to maintain dry conditions and reducing episodic recharge. Similar results have been found in a modeling study by *Seyfried et al.* (2005) for areas dominated by xeric-shrub plant communities. The presence of vegetation patches in semi-arid landscapes has been also found to control at a certain extent run-on, infiltration, soil moisture storage, and consequently the related feedbacks on vegetation (*Valentin et al.*, 1999; *Ludwig et al.*, 2005; *Madsen et al.*, 2008;

Yu et al., 2008). Vegetation patches can also affect the inter-connectivity of overland flow, influencing the mechanism of discharge formation and the shape of the hydrograph (*Nora Mueller et al.*, 2007). Hence, it is not possible to disregard the two-way coupling between vegetation dynamics and the water cycle. The latter interaction is critical for predicting how climate variability will influence hydrology and water resources especially in water-limited landscapes.

A semi-arid environment also allows to preserve the hypothesis made in Chapter 5 about the water-limited ecosystem. The nutrient dynamics is, indeed, neglected in "Tethys-Chloris" and water limitations are considered the key factor in influencing plant behaviors. The desert-shrub community is expected to ensure the validity of such an assumption.

7.3 Ecohydrological modeling validation

The capability of the joint ecohydrological model "Tethys-Chloris" to produce consistent results in terms of many hydrological and ecological metrics has been demonstrated at the plot scale for several different environments (Chapter 6). Specifically, the performance obtained at the Lucky Hills experimental site in simulating a desert shrub ecosystem is considered very satisfactory. Energy fluxes, soil water content dynamics, and vegetation productivity are indeed simulated with an high degree of realism by the model (Section 6.2). The location and data description as well as the comparison between observed and simulated variables have been already presented in Section 6.2. In this Section, the validation is extended showing the spatial distributed results obtained for the Lucky Hills watershed. The Lucky Hills experimental watershed is a small watershed of 0.037 $[km^2]$. The elevation range is limited to about 10 $[m]$ as can be observed from the Digital Elevation Model (Figure 7.4a). The watershed has low to moderate slope < 0.1 $[-]$, except for the central part where steep hillslopes, around 0.4 $[-]$, can be observed (Figure 7.4b).

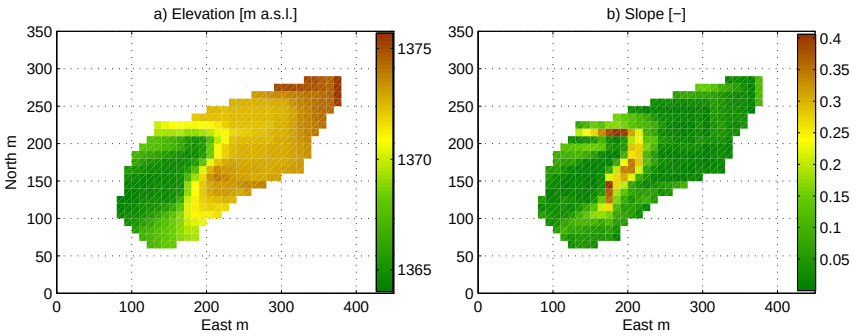

Figure 7.4: Representation of topographic attributes of the Lucky Hills experimental watershed. a.) Digital Elevation Model. b.) Slope fraction $[-]$ calculated with the maximum steepness method.

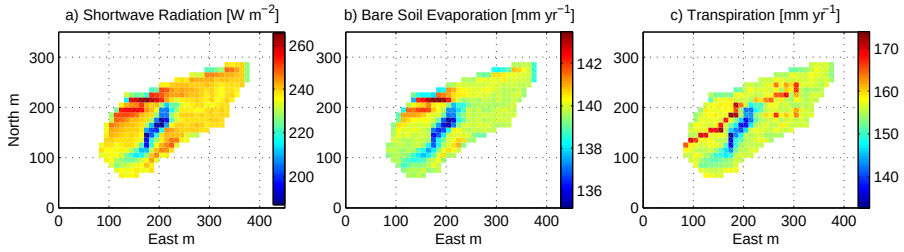

Figure 7.5: The results of spatially-distributed ecohydrological simulations averaged over the simulation period: a.) Incoming shortwave radiation. b.) Bare soil evaporation flux. c.) Transpiration flux.

Long term measurements of runoff and sediment transport have been collected at Lucky Hills for many years (1963-2008) (*Nearing et al.*, 2007; *Stone et al.*, 2008; *Nichols et al.*, 2008). The mean long term runoff is about 18.2 $[mm\,yr^{-1}]$ and the long term sediment transport is approximately 0.42 $[kg\,m^{-2}\,yr^{-1}]$ (*Nearing et al.*, 2007; *Stone et al.*, 2008). The watershed is dominated by shrubs; uniform soil and vegetation properties can be assumed. In the simulation all the hydrological and vegetation parameters are assumed equal to the plot scale application described in Chapter 6.

In a spatially-distributed application, hydro-meteorological inputs can vary among computational elements, due to the topographic or local meteorological conditions. In this case study, given the small watershed area, the incoming shortwave radiation is the only spatially variable input. Local and remote terrain effects on the incoming shortwave radiation are indeed accounted for in the simulation as discussed in Section A.9. Figure 7.5a shows that the inclusion of topography effect modifies the distribution of shortwave incoming radiation. As expected, steep slopes exposed to the south receive radiation that is about 40% larger than north exposed slope. This uneven distribution of radiation is directly reflected in the evaporation fluxes from bare soil (Figure 7.5b). To a relatively minor extent, this is also reflected in transpiration fluxes (Figure 7.5c). Transpiration is also controlled by lateral water redistribution. The latter process mainly occurs in deeper soil layers accessible only by plants, because of the relative fast vertical drainage of near surface soil characterized by an higher permeability.

Lateral redistribution of water in such a dry environment is dominated by the process of runoff-runon, rather than by the subsurface lateral flow. The subsurface lateral redistribution of soil water between neighbouring cells is only a small fraction of the annual budget (Figure 7.6a). It is generally less than 5.0 $[mm\ yr^{-1}]$ and peaks in correspondence of the steepest slope. Spatial differences in the mean annual infiltration rates are non-negligible and they are a consequence of localized runon (Figure 7.6b). Short, intense events during monsoon season can indeed produce infiltration excess runoff. The effect is achieved by using disaggregated rainfall at 5 $[min]$ time intervals with the model described in the Appendix A.1 and accounting for the formation of soil surface sealing (Chapter 4). Runoff produced after an intense

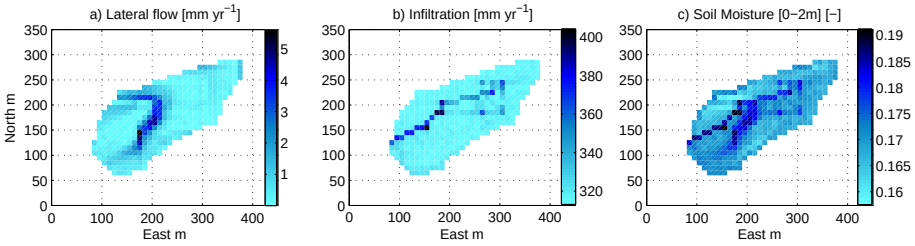

Figure 7.6: The results of spatially-distributed ecohydrological simulations averaged over the simulation period: a.) Lateral subsurface flow. b.) Infiltration flux. c.) Soil moisture content.

precipitation event is successively routed through the watershed toward the outlet. Although a large portion of runoff is lost from the watershed, there are favourable topographic niches with a near zero slope on convergent areas that allow water to be re-infiltrated as runon. Runon has the net effect of producing water redistribution within the watershed. This phenomenon takes place in several cells located in the hollow part of the catchment, where the total annual infiltration rates are larger than imposed spatially uniform precipitation (Figure 7.6b). Runon, lateral subsurface flows, and evapotranspiration fluxes contribute to create inequalities in the map of mean soil water content, as shown in Figure 7.6c. The wettest parts are in the channellized hollow, where runon occurs and the north slopes, where photosynthesis and consequently transpiration fluxes are smaller because of less light available.

The mean vegetation cover over the 11-year simulation period is the result of this adaption, with larger LAI in the wetter hollow and lower LAI in the steeper hillslopes (Figure 7.7a). Note that both the north and south facing slopes have smaller LAI values relative to the topographic hollow. This is due to the relatively drier conditions in the south-facing hillslopes and due to the light limitation in the north-facing slopes. Notwithstanding, given the smooth topography and the limited redistribution effects the relative variability in LAI is small ($\leq 10\%$). The ANPP has a similar spatial distribution of LAI, but a larger relative variability, with the maximum difference of 23% (Figure 7.7b). As can be observed from Figure 7.7c, the distribution of surface radiative temperature reflects the distribution of shortwave radiation, with only secondary effects due to the distribution of vegetation cover and soil moisture. The latter are indeed relatively uniform throughout the watershed.

The cumulative runoff simulated by the model in the last nine years of the simulation is compared to the observations in Figure 7.8. The mismatch between the simulated and observed values is evident, especially during the monsoon season of 1999 and 2000. During the period of 2000-2008, the annual simulated runoff is 12.5 $[mm\,yr^{-1}]$, while the observed runoff is 20.9 $[mm\,yr^{-1}]$. In absolute terms, such an error can be perceived as significant. However, given the lack of significant effort of model calibration, the uncertainty of the soil hydraulic properties and formation of surface sealing, and the uncertainty of rainfall disaggregation, the simulation results should be considered favourably. Furthermore, the simulated average runoff in the

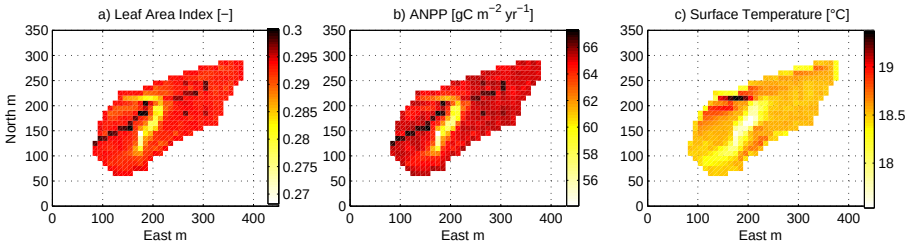

Figure 7.7: The results of spatially-distributed ecohydrological simulations averaged over the simulation period: a.) Leaf Area Index. b.) Above Ground Net Primary Productivity. c.) Surface radiative temperature.

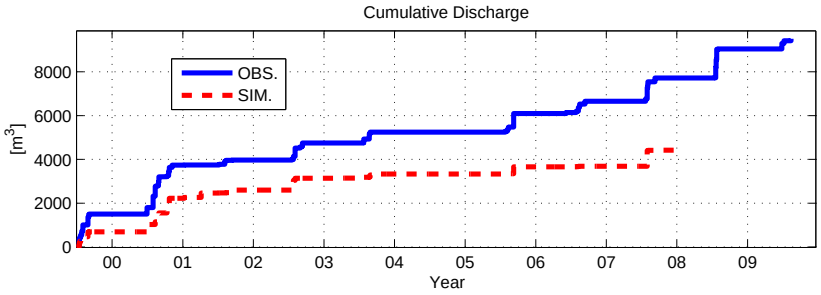

Figure 7.8: A comparison between the observed (solid line) and simulated (dashed line) cumulative runoff.

entire period is 18.4 $[mm\,yr^{-1}]$, a value very close to the long-term runoff measured at this site (*Stone et al.*, 2008). Producing runoff that is related to sporadic and intense events in a semi-arid system is indeed a challenging problem for many hydrological model. This is especially true when the objective is to effectively simulate all of the involved physical processes, i.e., getting appropriate answers for proper reasons.

As a final remark, it is important to note that the distributed application produces spatially-averaged fluxes and quantities, that are very similar to those obtained in the plot scale application. This is partially due to the small size of the watershed and the gentle topography. Furthermore, the limited influence of the subsurface flow is the principal reason of this result. It is very likely that extending simulations to larger watershed systems, e.g., those in the order of tens of square kilometers would provide similar results. Consequently, for the examined case study, plot scale simulated fluxes can be considered to be representative of a much larger area. Outlet runoff rate is instead dependent on the watershed area and no conclusion can be drawn for its behavior.

7.4 Generation of present and future climate with AWE-GEN

The stochastic downscaling methodology described in Chapter 3 combined with the weather generator AWE-GEN (Chapter 2) are used to generate long continuous time series of hydro-climatic variables for present and future climates. As stated previously the meteorological station of Tucson airport, where observations are available from 1961 to 2000, is considered to provide the reference climate for the south-east part of Arizona. The theoretical basis and procedural steps to downscaling climate models outputs and generate future climate predictions are discussed in detail in Chapter 3 and are not reported here. According to the proposed analysis distributions of factors of change for the station of Tucson airport are derived for several statistics of precipitation at different aggregation periods and for the mean monthly air temperature. Factors of change calculation is the result of the comparison between a control scenario, represented by eight GCM realizations in the present climate (1961-2000), and a predicted future climate, i.e., the realizations of eight GCMs for the period 2081-2100, emission scenario, A1B (see Chapter 3). The derived factors of change can be subsequently applied to the statistics of the observed climate to modify the latter and to obtain predictions of climate statistics for the future (Section 3.2.2). Once the required statistical properties are calculated for the future climate, a new set of "AWE-GEN" parameters can be estimated (Section 2.11). The re-parameterized weather generator is successively used to simulate hourly time series of hydro-climatic variables that are considered representative of the predicted future climate.

Predictions of the different members of the ensemble of climate models are weighted using the Bayesian approach described in Section 3.2.3. This stochastic downscaling produces Probability Density Function (PDF) of the factors of change rather than single factors of change. The preservation of this probabilistic information poses a challenge in the use of the weather generator in the reproduction of the future climate. The more straightforward application is to partially neglect the information contained in the factors of change PDFs and to use only the means or medians of the PDFs. Consequently, AWE-GEN can be applied to generate a certain number of years of predicted *mean/median* future climate, using a new parametrization derived from these means/medians of the PDFs. Note that such an approach produces a single set of weather generator parameters, thus a single, *most probable*, future climate.

The original idea was to generate more than a single *mean* future climate exploiting the information derived in the Bayesian approach to produce an ensemble of possible future climates. Transferring the uncertainty of the factors of change PDFs into time series generated by AWE-GEN can be regarded as the possibility to transfer the heterogeneous nature of climate predictions from different models into multiple hourly hydro-climatic time series and successively into eco-hydrological applications.

In order to preserve the information contained in the PDFs of factors of change

a Monte Carlo approach is required. A Monte Carlo application is computationally much more expensive than using a single value (mean, median) and demands assumptions about the dependence or independence of the factors of change. A numerical Monte Carlo must be used because it is not possible to find joint probability density functions that combine all the required factors of change. Furthermore, factors of change PDFs are derived empirically (Appendix B.1) and have no analytical expressions. Recently, joint distributions of factors of change for average seasonal temperature and average seasonal precipitation have been obtained numerically but are still too simplified to be suitable for the proposed stochastic downscaling (*Tebaldi and Sansó*, 2009). The application of a Monte Carlo entails the generation of random factors of change according to their distributions. The stochastic dowscaling technique implies the derivation of, totally, 170 PDFs of factors of change from the ensemble of climate models. These include 12 PDFs for the monthly air temperature, T_{mon}, one for each month, $12 \cdot 4$ PDFs for each precipitation statistics, i.e. mean $E_{Pr}(h)$, variance $VAR_{Pr}(h)$, frequency of non-precipitation, $\Phi_{Pr}(h)$, and skewness, $SKE_{Pr}(h)$, and 2 further PDFs for the coefficient of variation and the skewness of the annual precipitation process, $\overline{Pr_{yr}}$ (see Chapter 3). The number of PDFs describing each precipitation statistic is $12 \cdot 4$ because of the seasonality, 12 months, and because of the 4 different aggregation periods, i.e., $h = 24, 48, 72$ and, 96 hours. These are the aggregation periods at which precipitation statistics are required to successively extend them at shorter time-scale (see Section 3.2.5). One can note that $12 + 4 \cdot 12 \cdot 4 + 2 = 206$, however it must be considered that the product factors of change for mean precipitation, $E_{Pr}(h)$, are the same regardless of the aggregation period given the linearity of the mean operator. This reduces the total number of PDFs to 170, consequently the random selection of the factors of change is limited to these 170 PDFs.

The cross-correlation among factors of change poses a further challenge. The simplest way to solve the problem is to assume independence among the factors of change. For instance, although some degree of correlation must be expected between changes in precipitation and air temperature (*Tebaldi and Sansó*, 2009), the modifications of these two variables can be fairly assumed independent. Independence is harder to justify for changes of the same variable but in different months, e.g., air temperature delta-change in contiguous months cannot be assumed completely uncorrelated. The same consideration can be extended to changes of the same variable at different aggregation periods, e.g., variance of precipitation at 24 and 48 hours are undoubtedly strongly correlated. For this reason, one might simply assumes that all the factors of change are completely correlated, i.e., coefficient of correlation equal to one. This hypothesis, although acceptable for factors of change of the same variable at different months and aggregation periods seems inadequate for variable that depend on different physical processes, e.g., precipitation statistics and air temperature mean. For instance, imposing a complete correlation (e.g, the same random percentile in the Monte Carlo sampling) to a factor of change of mean monthly air temperature and 24 hours skewness of precipitation clearly lacks any

Table 7.1: Organization of dependent and independent factors of change in groups. Within each group factors of change are totally correlated, i.e., coefficient of correlation equal to one. Among different groups they are independent, i.e., correlation is equal to zero.

Group	**Variable**	**Number of factors of change**
1	T_{mon}	12
2	$VAR_{Pr}(h)$	$12 \cdot 4$
3	$\Phi_{Pr}(h)$	$12 \cdot 4$
4	$SKE_{Pr}(h)$	$12 \cdot 4$
5	$E_{Pr}(h)$	12
6	C_v of $\overline{Pr_{yr}}$	1
7	Skewness of $\overline{Pr_{yr}}$	1

scientific justification.

An universal acceptable solution to the issue arisen from the cross-correlation among factors of change is impossible to be found. Data do not exist and will never exist to support a decision, i.e., to explicitly calculate the cross-correlations among factors of change. Given the unavoidable uncertainty in the determination of these cross-correlations, an arbitrary and questionable assumption about the dependence or independence of the 170 factors of change is presented in the following. The 170 factors of change are reduced to 7 independent groups. Among groups the factors of change are assumed completely uncorrelated and within each group a total dependence among the factors of change is assumed.

The composition of the 7 groups is described in Table 7.1. Factors of change among different precipitation statistics and air temperature are considered to be independent. Factors of change for the different months and aggregation periods but for the same variable are instead assumed to be fully correlated, i.e., the changes in a statistic at different months and aggregation periods have cross-correlation equal to one.

Given the assumptions in the cross correlation among factors of change a Monte Carlo iteration consists in the generation of only 7 independent random probabilities, one for each group. Once generated a certain probability, p, this probability is used to estimate the correspondent factors of change for each PDF belonging to the group correspondent to p (see Table 7.1 for the group classification). For instance, in a Monte Carlo iteration, a random probability, p_1, is generated to estimate the additive factors of change of T_{mon} for each month. A random probability, p_2, is generated to estimate the product factors of change for $VAR_{Pr}(h)$ for each month and at the four aggregation periods, and analogous considerations can be extended to the other groups with p_3,...,p_7. Note that the same probability does not necessary imply the same factor of change, because the latter depends on the shape of the PDF. The factors of change PDFs are generally different within the same group and across groups. Details on how these PDFs are calculated are necessary given the empirical nature of these distributions. Totally, for each factor of change 1000 sample values are used to define a PDF and its integral, i.e., the Cumulative Distri-

bution Function (CDF). The 1000 samples are the result of the MCMC method as described in the Appendix B.1. To each sample empirical probabilities are assigned with the plotting position method (*Cunnane*, 1978). Once a random probability, p, distributed uniformly between zero and one has been generated in the Monte Carlo, a linear interpolation of the CDF is used to find the exact value of the factor of change corresponding to the probability p.

Totally, a number $\bar{N}$ of Monte Carlo iterations are simulated generating random probabilities, p. The outcome of each iteration is a set of factors of change obtained from the p and correlated as described above. Note again that the choice of the group subdivision and the assumptions about relative dependence or independence are subjective and made according only to the author best judgement. Each of the $\bar{N}$ set of factors of change is applied to the observed climate statistics in order to modify the latter and to obtain new statistics, representative of one of the possible future climates. The procedure is exactly equivalent to the use of a *mean* factor of change, only iterated $\bar{N}$ times. Once all the statistical properties are calculated for the future climates, $\bar{N}$ set of "AWE-GEN" parameters can be estimated (Section 2.11).

The new parameterizations of the weather generator are used to reproduce $\bar{N}$ times, 30 years long time series of hydro-climatic variables that are expression of the predicted future climate (2081-2100). Since the factors of change are randomly combined at each Monte Carlo iteration, the new parameterizations of AWE-GEN are all different. This implies that the $\bar{N}$ hourly, 30 years long, time series can differ for many characteristics such as mean precipitation, mean air temperature, inter-annual variability of precipitation, or internal structure of precipitation. As $\bar{N}$ increases the multiple combinations allow to explore a wider range of possible future scenarios. Therefore, the effects of the assumptions made about the cross-correlation of the factors of change tends to became less important. A number $\bar{N} = 100$ has been regarded as sufficient large and is used in the presented Monte Carlo analysis. It must be remarked that not all the combinations of factors of change obtained after the Monte Carlo directly lead to a set of AWE-GEN parameters. They exist particular combinations of factors of change of precipitation statistics that do not allow to estimate the weather generator parameters for rainfall (see Section 2.3.2). This issue has been encountered on about the 2% of Monte Carlo iterations. In this case the combination of factors of change is discarded and a new iteration is generated.

Along with the $\bar{N} = 100$, 30 years long, time series of future climates, (FUT), also one, 30 years long, control scenario, (CTS), time series representative of the present climate (1961-2000) has been simulated with the weather generator for comparison. Given, the relative large amount of information contained in the simulations (remind the hourly scale) only average statistics are illustrated in the following. The PDF of the 30 year means obtained for the future climates is compared with the mean of the control scenario and with the the mean of observational values.

Figures 7.9a and 7.9b show the comparison for the 30 year mean annual precip-

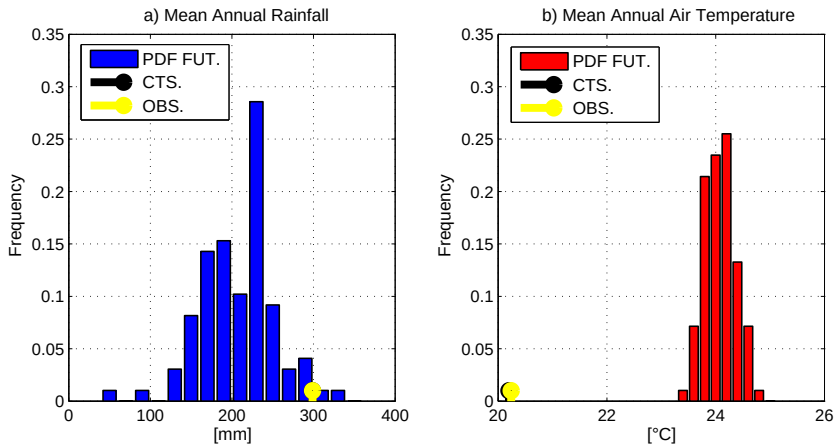

Figure 7.9: A comparison between the means of the observed (yellow dot) and simulated climatic variables for the control scenario (black dot) and the multiple future scenarios expressed as a PDF (blue (a) and red bars (b)). a.) Mean annual precipitation. b.) Mean air temperature.

itation and mean annual air temperature. It can be easily appreciated the large spread in the PDF of future mean annual precipitation, its range spans from less than 70 to 330 $[mm]$, with an average of about 223 $[mm]$. This very large uncertainty reflects the difficulties of climate models in correctly reproduced precipitation and the difference between model projections. Nonetheless, almost in all the simulations a sensible reduction of precipitation when compared to the control scenario and observation is appreciable. Note that for precipitation and air temperature the observed mean and the simulated control scenario mean are perfectly overlapped and not distinguishable from the graph (Figures 7.9a and 7.9b.). The PDF of future mean air temperature is more tighten, showing how the uncertainties in temperature projections are definitely smaller than in precipitation. All the simulated future mean temperatures are larger than the control scenario ones. The expected warming is comprised between 3.3 to 4.6 $[°C]$, underlining a good convergence among GCM predictions.

The PDFs obtained for mean vapor pressure and mean shortwave radiation are illustrated in Figure 7.10a and 7.10b. Changes in these variables are a consequence of statistical and causal relationships within the weather generator, because factors of change for e_a, R_{sw}, N, W_s, and P_{atm}, are not imposed in the stochastic downscaling as explained in Section 3.2.2. This simplification implies that only variations due to secondary effects, related to precipitation or air temperature changes, can be appreciated in e_a and R_{sw}. Their PDFs are, indeed, concentrated in a narrow set of values (Figure 7.10). Despite this limitation, it is possible to appreciate the feedbacks of precipitation and air temperature on these variables. For instance, vapor pressure is generally inferior to present conditions probably because of a drier climate, shortwave radiation is expected to increase because of the precipitation reduction and the consequent minor cloud cover.

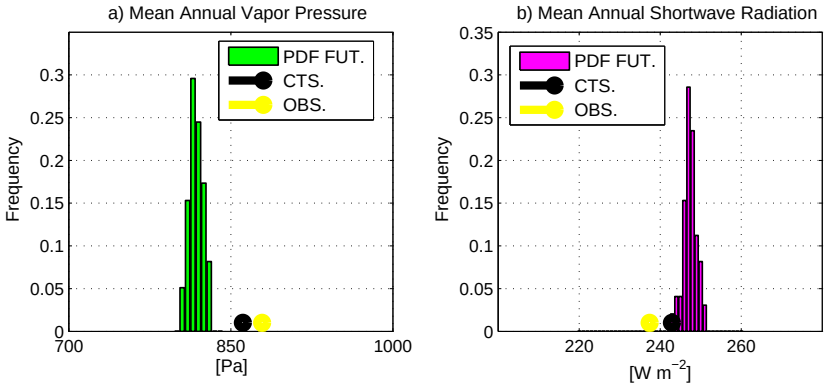

Figure 7.10: A comparison between the means of the observed (yellow dot) and simulated climatic variables for the control scenario (black dot) and the multiple future scenarios expressed as a PDF (green (a) and magenta (b)). a.) Mean vapor pressure. b.) Mean shortwave radiation.

Another important climatic variable, not directly simulated by the weather generator but imposed as external forcing is the atmospheric concentration of CO_2, c_a. A constant value of $c_a = 380$ $[ppm]$ is assumed for the control scenario, though this value is more representative of the end of the period. A constant value of $c_a = 700$ $[ppm]$ is instead assumed for all the future climates. Such a value is the one expected by 2100 for the emission scenario A1B (*Meehl et al.*, 2007b), i.e., the emission scenario used as baseline for GCM realizations in the stochastic downscaling.(Section 3.3).

A more detailed illustration of the characteristics of the future climate, including higher order statistics and finer temporal scale, is shown comparing the observations (40 years hourly time series) with the simulated CTS scenario (30 years hourly time series) and with the simulated *mean* future scenario (30 years hourly time series). The *mean* future scenario is realized using all the means of the factors of change PDF to re-parameterize AWE-GEN.

The annual cycle of the rainfall process is shown in Figure 7.11a. The simulated precipitation process perfectly preserves the mean but slightly underestimates the monthly variance of observations in almost every month (not shown). As pointed out previously and in Section 3.2.3, the simulated future scenario shows a general decrease of precipitation, which is quite appreciable for the July-September monsoon period. The mean of the total annual precipitation decreases from 300 $[mm]$, in the observation-control scenarios, to 223 $[mm]$, in the future scenario. The monthly variances of future precipitation realizations are comparable with those simulated in the control scenario Figure 7.11a.

The fractions of the total time that precipitation exceeds the depths of 1 and 10 $[mm]$ for different aggregation periods are shown in Figure 7.11b. In the simulation of future climate, these fractions are predicted to decrease along with a general reduction in the total precipitation amount. The distribution of dry spell duration (Figure 7.11c) is overestimated by 0.9 days in the control scenario simulation. Fur-

ther, the shape of the distribution somewhat deviates from the observed for the duration of one day as well as at intermediate durations. Although there is some inaccuracy in the simulation of dry spell duration, this does not influence the simulation performance of other variables dependent on precipitation, as testified by the results that follow. The projected future distribution of dry spell duration becomes flatter, leading to a remarkable increase in the mean from 12 days to more than 18 days. The distribution of wet spell duration (not shown) is usually better simulated and remains essentially unchanged in the future scenario.

A comparison between the observed and simulated cloud cover distributions is shown in Figure 7.11d. A very small decrease in the mean cloud cover is captured by the weather generator for the future scenario. This feedback is related to the predicted reduction in precipitation events during summer months.

The daily cycle and the probability density function of air temperature are very well reproduced, as shown in Figures 7.11e and 7.11f. As seen, the probability density function of air temperature for the future scenario is shifted towards higher temperature. This shift can be also observed in the daily cycle, while hourly standard deviations do not change (Figure 7.11f). The shift in the air temperature is a direct result of the application of factors of change only to the mean temperature, without including higher order statistics, as discussed in Section 3.2.2. Air temperature extremes for large return periods are reproduced less than optimally, a slight overestimation or underestimation is often present for minimum and maximum temperatures (not shown). These, however, is not expected to have appreciable effect on hydrology.

Extreme precipitation for different return periods and time aggregation intervals of 1 hour and 24 hours are shown in Figures 7.12a and 7.12b. There is a considerable overlap between the simulated and observed extreme precipitation, up to the return periods of 20-30 years (Figure 7.12a,b). The developed stochastic downscaling also allows one to make inferences about possible changes of high-frequency characteristics of climate, such as extreme precipitation. In fact, although the total precipitation is expected to reduce in future, the extremes seem to remain unchanged at the aggregation period of 1 hour and possibly increase for 24-hour periods (Figure 7.12a,b). Simulations for the future scenario point to a shift towards more extreme conditions in terms of dry spell durations. Wet spell durations appear to be relatively unchanged (Figure 7.12c,d).

The results obtained for other meteorological variables are illustrated in Figure 7.13. The daily cycles of shortwave radiation are shown in Figure 7.13a,b,c and are reproduced satisfactorily for the different components, i.e., global, direct, diffuse. The monthly average of global shortwave radiation (Figure 7.13d) is simulated properly, with occasional differences of 5-10 $[W\ m^{-2}]$. In the simulation of future climate, a slight increase in solar radiation can be noticed, due to the reduction in the mean of the cloud cover process.

In Figure 7.13e, the comparison between simulations and observations of the daily cycle of relative humidity highlights a good overlap, especially during day-time hours.

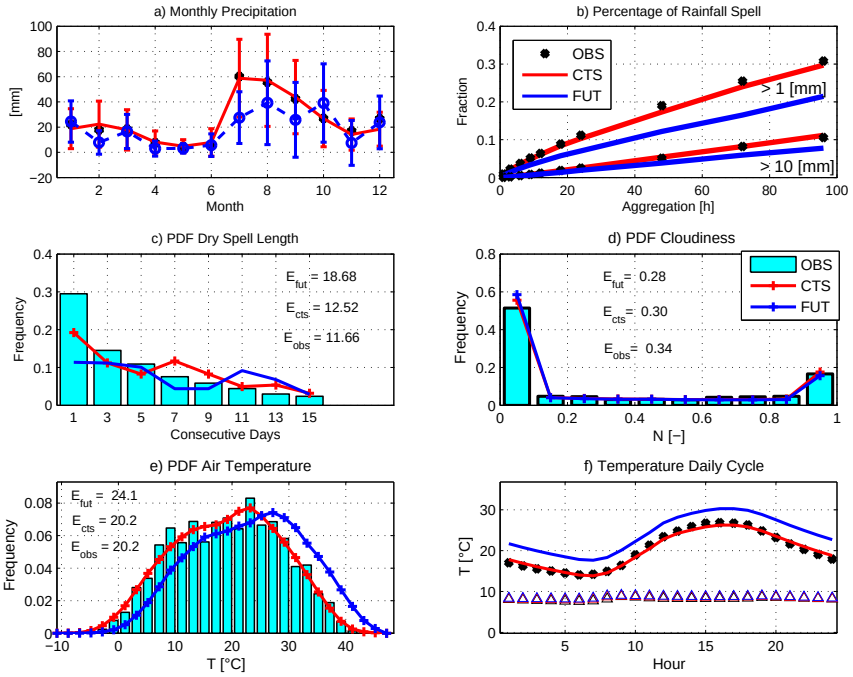

Figure 7.11: A comparison between the observed (black dots, subplots (a), (b), and (f), and cyan bars, subplots (c), (d), and (e)) and simulated meteorological variables for the CTS (red) and FUT (blue) scenarios. a.) The mean monthly precipitation, the vertical bars denote the standard deviations of monthly values. b.) The fraction of time with precipitation larger than a given threshold $[1 - 10mm]$ for different aggregation periods. c.) The frequency distribution of dry spell length. Dry spell duration is a number of consecutive days with precipitation depth lower than 1 $[mm]$. d.) The frequency distribution of cloud cover. e.) The frequency distribution of air temperature. f.) The mean daily cycle of air temperature. The triangle symbols denote the standard deviations of hourly values. E_{obs} is the observed mean, E_{cts} and E_{fut} are the simulated means for the control and future climate scenarios.

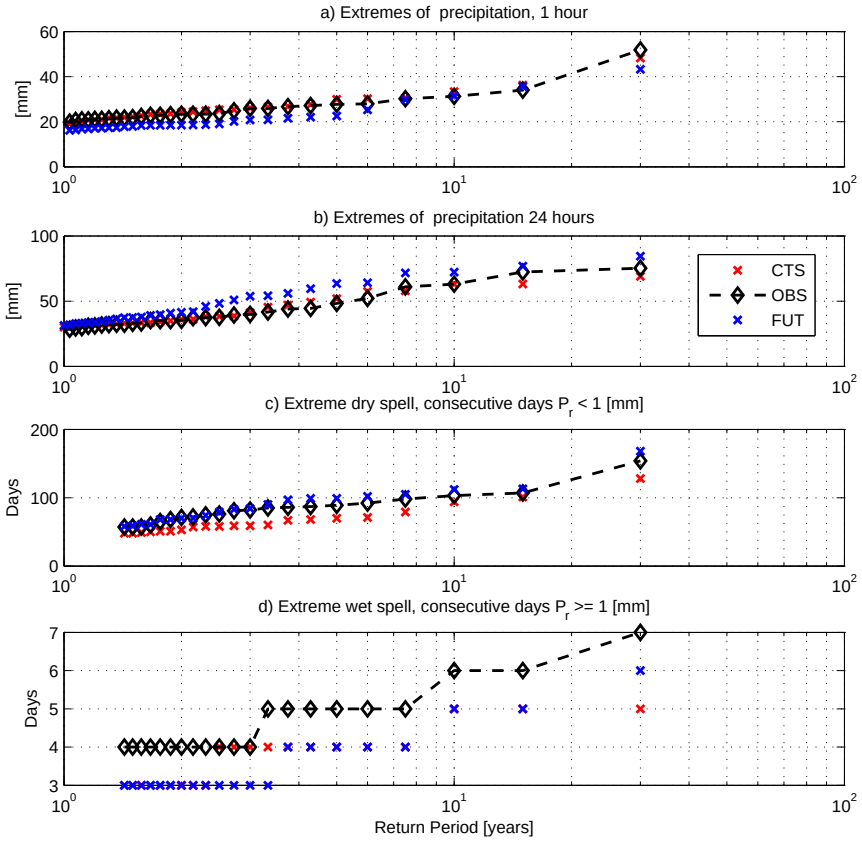

Figure 7.12: A comparison between the observed (dashed line with black diamonds) and simulated values of extreme precipitation for CTS (red crosses) and FUT (blue crosses) scenarios at (a) 1-hour and (b) 24-hour aggregation periods; (c) extremes of dry and (d) wet spell durations. Dry/Wet spell duration is the number of consecutive days with precipitation depth lower/larger than 1 [mm].

Overall the performance of AWE-GEN is very good also with regards to the simulation of the probability density function of vapor pressure (Figure 7.13f). Changes in the future scenario are detectable for both vapor pressure and relative humidity. The mean value of vapor pressure tends to decrease, since the future climate is drier and because the air temperature increase exerts a direct control on this variable. The daily cycle of relative humidity (Figure 7.13e) shifts toward lower values because vapor pressure decreases and air temperature increases.

The probability density function of wind speed is well captured (Figure 7.13g) as well as the first two statistical moments of the process (not shown). The wind speed daily cycle is also correctly reproduced (Figure 7.13h). Finally, the shape of the atmospheric pressure distribution is also correctly simulated as shown in Figure 7.13i. The differences between the control and future scenarios are practically not distinguishable (Figures 7.13g, 7.13h, and 7.13i).

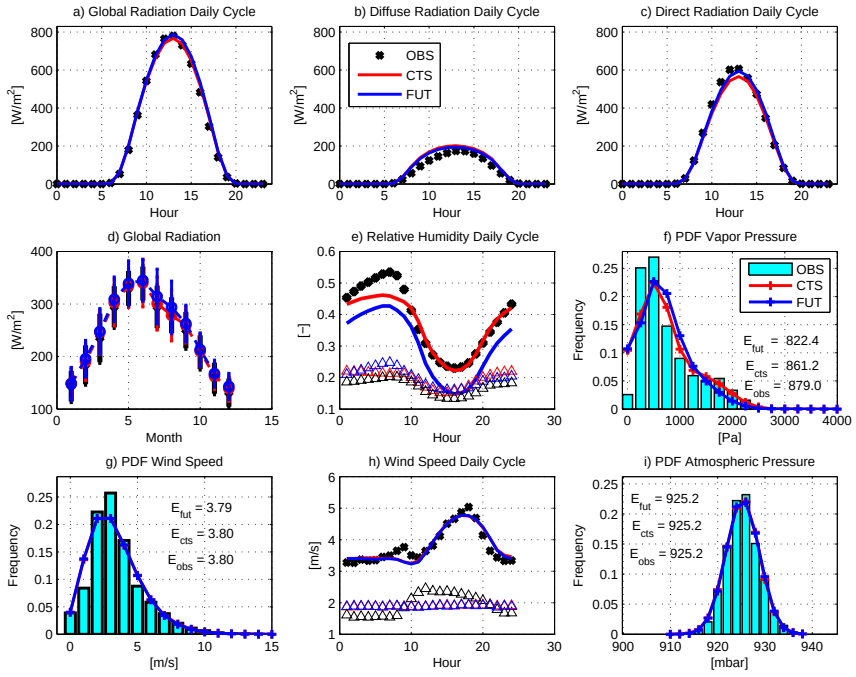

Figure 7.13: A comparison between the observed (black dots, subplots (a), (b), (c), (d), (e), and (h), and cyan bars, subplots (f), (g), and (i)) and simulated meteorological variables for CTS (red) and FUT (blue) scenarios. a.) The mean daily cycle of global radiation. b.) The mean daily cycle of direct beam radiation. c.) The daily cycle of diffuse radiation. d.) The mean monthly global shortwave radiation. The vertical bars denote the standard deviations of monthly values. e.) The daily cycle of relative humidity. The triangle symbols denote the standard deviations of hourly values. f.) The frequency distribution of vapor pressure. g.) The frequency distribution of wind speed. h.) The mean daily cycle of wind speed. The triangle symbols denote the standard deviations of hourly values. i.) The frequency distribution of atmospheric pressure. E_{obs} is the observed mean, E_{cts} and E_{fut} are the simulated means for the control and future climate scenarios.

7.5 Point scale results

The time series of hourly meteorological variables generated with AWE-GEN for the present and multiple future climates, as described in Section 7.4, serve as input to "Tethys-Chloris".

This section is organized in two parts. First the ecohydrological results obtained for the *mean* future climate are discussed in detail in the attempt to highlight the difference between present climate and *mean* future climate. Successively, the result for the $\bar{N} = 100$ Monte Carlo iterations are presented as 30 year averages in order to describe probabilistic changes in the hydrological balance components, energy fluxes, and indices of vegetation productivity. The ensemble of future climates allows one to transfer the uncertainty of climate predictions into uncertainty in the simulation of ecohydrological variables. Such a transfer of information is a novelty in climate change studies, as far as the author know, and can be regarded as a substantial contribution offered by this study. The results represented in the form of Probability Density Functions are the direct consequence of the ensemble of different *futures* forecasted by the presented methodology.

A discussion about the limitations and assumptions underlying the overall method is presented in the following before starting the result analysis. Such a discussion is considered important in order to regard the principal findings and the conclusion of this Chapter in the right perspective. In the coupled eco-hydrological model there are, in fact, important processes that have been completely neglected and other that are only simply conceptualized. These processes include the nutrient and soil carbon dynamics, vegetation mortality-plant competition, and carbohydrate translocation. All these aspects are likely to play an important role in controlling the interaction between hydrology and vegetation in a future different climate (*Dickinson et al.*, 2002; *Ostle et al.*, 2009). For instance, nutrient limitation can be regarded as the most important constraint to plant growth in a future where CO_2 concentration is expected to dramatically increase (*Ostle et al.*, 2009). Down-regulation of CO_2 uptake due to nitrogen limitations cannot be considered in the presented analysis as cannot be considered the effect that a warmer climate might have on soil carbon dynamics (heterotrophic respiration). The conceptualization adopted for carbohydrate translocation is also very simplified due to the lack of knowledge of this plant behavior (Chapter 5). This may represent a further issue, since carbohydrate translocation dynamics can be important for plant recover after periods of stress and can affect the long term capabilities of plants to produce and survive (*Körner*, 2003; *Ostle et al.*, 2009).

Another important model deficiency is the total lack of species competition and the simplified mechanism through which vegetation mortality can occur. As discussed in Chapter 5 it has been recently hypothesized that plant mortality can be related to two principal mechanisms, carbon starvation for isohydric plants and hydraulic failure for anisohydric plants (*McDowell et al.*, 2008). Anisohydric plants are generally relatively drought-tolerant and they usually maintain stomatal open

in drought conditions at very low water potential operating with narrower hydraulic safety margins. For this reason they can undergo to cavitation and hydraulic failure induced mortality. In the other hand, plants with isohydric regulation of water status avoid drought-induced hydraulic failure via stomatal closure. However, this can ultimately results in carbon starvation and plant death (*McDowell et al.*, 2008). In this study, vegetation die off can be only the result of carbon starvation since no mechanisms for hydraulic failure are included. This is mainly related to the way soil water potential controls stomatal closure. The empirical β_R function (Section 4.4.5) is a very simplified model of the water stress control on physiological activities (*Vico and Porporato*, 2008), and cavitation thresholds for minimum soil water potential are not defined, therefore hydraulic failure cannot occur.

The above limitations might be sufficient to strongly question the results of the presented analysis on hydrology-vegetation interaction under climate change. Although this eventuality cannot be completely dismissed, I strongly believe that in the presented case study, given the type of plant and the climate conditions the obtained results maintain a certain reliability despite the limiting assumptions. Furthermore, there is a certain confidence (Chapter 6) that the model can produce consistent outputs in terms of many ecohydrological variables in several different climates. For instance, the simplification on the mechanism of vegetation mortality can be a fairly acceptable hypothesis for the considered species. In fact, xeric species tend to have larger safety margin and generally lower water potential values for cavitation compared to other species (*Pockman and Sperry*, 2000). Moreover, carbon starvation has been hypothesized as the leading mechanism of vegetation die off in global change-type drought (*Adams et al.*, 2009; *Breshears et al.*, 2009).

Consequently, despite all the simplifications listed above the main conclusions of this study are considered to hold and be only partially dependent on model characteristics. Modeling artifacts have presumably only minor effects in the simulations, or better they are not expected to change the principal findings. Although, without the support of evidences I believe that similar results in terms of ecohydrological metrics can be obtained with a different physical-based mechanistic model. Therefore, in my opinion the obtained outcomes can be considered to a certain extent model independent. The unique hypotheses considered fundamental are the ones underlying the mechanistic modeling of photosynthesis and stomatal closure (Chapter 4). In case the relationship between stomatal opening and assimilation rate would be governed by other biochemical and physiological laws or be different in the future (*Wullschleger et al.*, 2002; *Hetherington and Woodward*, 2003) there is the serious possibility that the effect of CO_2 increase on plant will be different from what inferred from this study.

First the analysis of the comparison of the ecohydrological response for present and *mean* future climate is presented. Where *mean* future climate refers to the hydro-meteorologic variables simulated using the means of the factors of change as described in Section 7.4. This comparison is presented because being only between two 30 years simulation permits to highlight patterns and temporal evolutions that

would be rather difficult to show when the ensemble of 100 expected "future" climates is accounted for. The drawback is that showing only the *mean* future climate reduces consistently the space of investigation, for this reason later in the section all the members of the ensemble are analyzed in terms of temporally averaged properties.

The parameterizations of "Tethys-Chloris" for a partially vegetated desert shrubs system composed of Whitethorn acacia (Acacia constricta) and Creosote bush (Larrea tridentata) is fully described in Section 6.2 and 7.3. This ecosystem is forced with the climate of Tucson airport (Section 7.2). The original idea was to analyze separately the ecohydrological responses of the deciduous and evergreen shrubs to look at the possible behaviors. Nonetheless, it has been observed that only minor differences were appreciable in the response of the two plant functional types to climate change (not shown). Therefore, in the follows the analysis for an area covered by a mixed deciduous and evergreen shrub community (as in Section 6.2) is discussed. Being the climate of Tucson airport slightly different from Lucky Hills the partition of hydrological budget for the present climate (Figure 7.14) is not exactly the same described in Figure 6.7. Figure 7.14 shows the partition between hydrological budget components in absolute and relative terms. The bare soil evaporation and transpiration terms account for almost all of precipitated rainfall. Evaporation is predominantly over transpiration during period of low photosynthetic activity due to cold (winter months) and water stress (summer months). The opposite holds true during spring and early fall when vegetation experiments favorable conditions. Infiltration excess runoff during the Monsoon season is also appreciable but it is generally limited to less than 10% of monthly hydrological budget. In comparison to Lucky Hills, the lower amount of precipitation during the Monsoon makes evapotranspiration water limited in the summer and early fall months and reduce to negligible rates deep recharge.

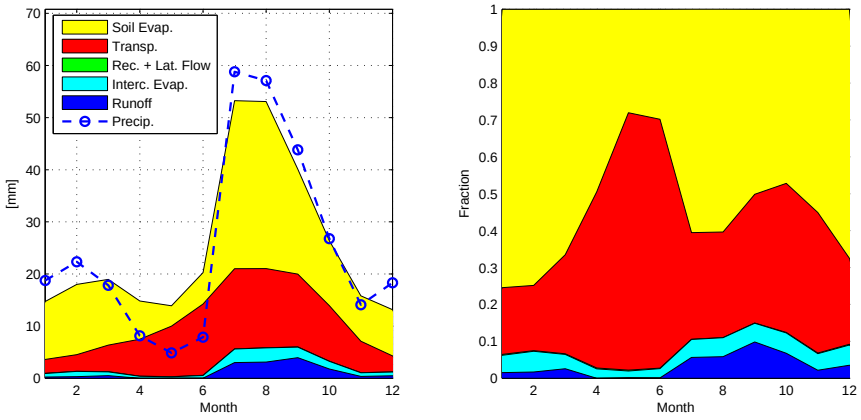

Figure 7.14: Monthly partition of the principal hydrological budget components averaged over the simulation period in $[mm\ yr^{-1}]$ (left panel) and in fractions (right panel). Results for the present climate.

The time series of Leaf Area Index is taken as representative of vegetation dynamics

and is shown in Figure 7.15. The seasonal dynamic due to deciduous shrub is clearly appreciable. During the 30 years of simulation there are several occasions in which drought stress causes a reduction on vegetation productivity which consequences are appreciable on the LAI. However, climate conditions generally allow plants to recover from the stress and to attain a pre-stress LAI in two-three years.

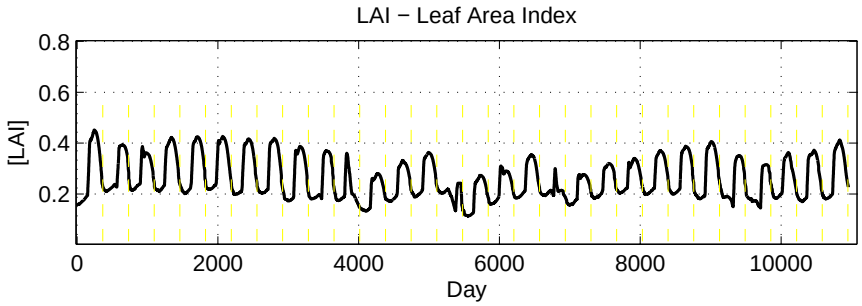

Figure 7.15: Time series of simulated Leaf Area Index. Results for the present climate. The vertical yellow dashed lines are one year equally spaced.

The monthly partition of the principal hydrological budget components for the *mean* future climate is shown in Figure 7.16. The major changes are driven by changes in total precipitation and its seasonality as already discussed in Section 7.4 and shown in Figure 7.11a. A significant reduction of precipitation is appreciable during the Monsoon season (July-September) that is partially counterbalanced by an increase in October, December and January. This results in a net reduction of precipitation of about 80 $[mm]$ per year. Evapotranspiration is consequently often limited by water availability and plants experiment prolonged water stress conditions. The partition between transpiration and evaporation in relative terms is mainly preserved in the future, while their absolute magnitudes are sensibly lower. The estimated runoff is expected to increase both in absolute and relative terms reaching about the 20% of monthly water balance from October to December. This augment is obtained despite the drier future conditions, underlining the important role of intensity and frequency of precipitation pulse in semi-arid ecosystem (*Huxman et al.*, 2004b).

The repeated water limited conditions entail a very irregular behavior of vegetation dynamics as illustrated by LAI time series in Figure 7.17. The LAI evolves according to several water stress episodes with different magnitude and duration. During the most prolonged drought periods LAI decays to very low values mainly caused by evergreen dynamics. Plants, indeed, need three four years before recovering from a major drought. There are also years in which no favorable conditions occur to initiate the growing season. This is appreciable by the absence of the spikes in the deciduous phenological dynamic. A certain resilience of vegetation and capacity to sustain production can be appreciated despite the prolonged and frequent water stresses.

The figures 7.16-7.17 already introduce the behavior of the analyzed ecosystem subjected to a changing climate. A detailed discussion of changes in vegetation,

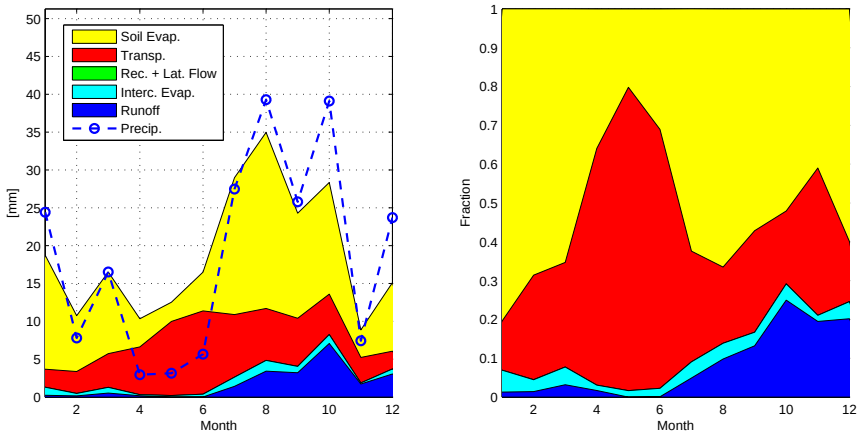

Figure 7.16: Monthly partition of the principal hydrological budget components averaged over the simulation period in $[mm\ yr^{-1}]$ (left panel), and in fractions (right panel). Results for the *mean* future climate.

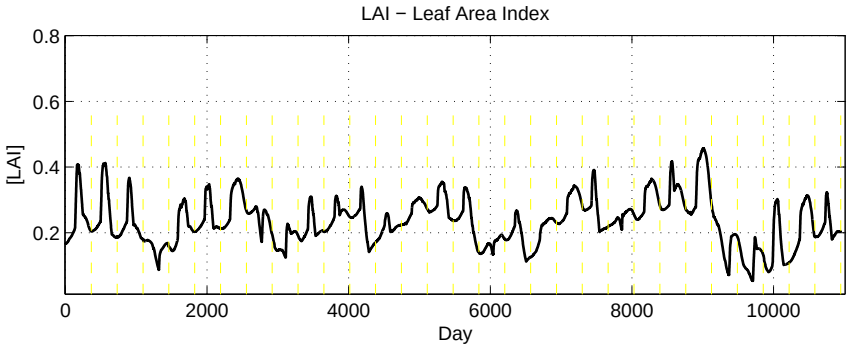

Figure 7.17: Time series of simulated Leaf Area Index. Results for the *mean* future climate. The vertical yellow dashed lines are one year equally spaced.

energy, and hydrological components is presented in the following in the scope of illustrating how the ensemble of future climates influence ecohydrological metrics. Therefore, hydrological and vegetation dynamics of the desert shrub ecosystem are tested using the $\bar{N} = 100$, 30 year long, hourly time series of expected "future" climate obtained in Section 7.4. Simulation details or the temporal evolution of each member of the ensemble are obviously impossible to show, given the large amount of variables and the total number of simulations. Nonetheless, the consistency of vegetation dynamics with regards to physical/ecological realistic states has been checked for each run of the ensemble. All the 100 Leaf Area Index time series have been visually inspected to produce plausible dynamics. This control also allows to identify cases where vegetation is subjected to strong water stress and eventually dies off, shedding the entire green biomass.

In the following results are presented in terms of multi-annual averaged values. Specifically, a 25 years average is considered. The first five years of each single Monte Carlo iteration are discarded in order to limit the effects of initialization. In ecohydrological studies initialization of vegetation biomass and of soil moisture in deep layers can be critical since their effects last for a long time. Considering the shrub vegetation type and the semi-arid climate a five year period is regarded as sufficient to avoid significant initialization effects in the results. Moreover, all the Monte Carlo iterations are initialized with the soil moisture and the vegetation biomass derived from the mean values of the 30 years of *mean* future climate. Where, the *mean* future climate initialization is in turn the result of a spin-up period of 30 years. The variables and the indexes shown in the following figures correspond to long-term averages (25 years) and their values must be regarded in a climate perspective. The results are generally organized to show comparisons between the control scenario and the ensemble of future scenarios. The control scenario corresponds to the present climate and is a unique 30 year average for each quantity. The ensemble of future climate produces instead 100, 25 year averages. The obtained distributions of hydrological and vegetation metrics correspond to the probability density functions of these metrics for the future. This is a direct consequence of the Monte Carlo methodology described in Section 7.4. The figures shown and discussed below are the final step that allows to appreciate the uncertainty of climate model predictions in terms of ecohydrological consequences.

The vegetation productivity metrics are shown in Figure 7.18. Averaged GPP, NPP, and ANPP are illustrated together with the average LAI. A first unexpected result emerges from the graphics, i.e., the vegetation productivity is very similar when present and future climates are compared. The mode of the PDF representing the possible futures is very close to the value of productivity in the control scenario, with slightly larger reductions appreciable for ANPP-NPP than for GPP. The vegetation cover expressed in terms of LAI appears also to be mainly preserved. These results are somehow different from expectations because of the consistent reduction in precipitation and the warmer climate forecasted in the downscaling (Figure 7.9). The predicted climate produces more frequent and intense conditions of stress for the

plants as appreciable also in a reduction of the β_R factor representing a significant increase in drought stress (Figure 7.19c). This extension and intensification of water stress does not produce strong consequences in vegetation because other factors tend to counterbalanced this stress. Specifically, the effect imposed by the increase of CO_2 atmospheric concentration results in an enhanced plant productivity and in a substantial maintenance of vegetation cover. According to the biochemical model of photosynthesis described in Section 4.4.5, elevated concentration of CO_2 allows to increase gross assimilation rate keeping stomatal relative close. This important physiological effect is discussed in detail later in this Section. The lengthening of the growing season is also one of the reason of the preservation of vegetation productivity. Leaves or buds are indeed expected to onset on average a 20 days earlier due to the warmer climate and winter precipitation (Figure 7.19a and Figure 7.19b). The lengthening of the growing season is more appreciable in evergreen than in deciduous plants because of a generally earlier bud burst for this kind of plant, as parameterized in the model. Future scenarios where water stress imposes a delay on leaf onset are also possible (Figure 7.19a). Note that the anticipation of the phenological leaf onset in a changing climate is consistent with other studies and observations (*Peuelas and Filella*, 2001; *Schwartz et al.*, 2006; *Morin et al.*, 2009). The differences between GPP (substantially invariant) and NPP (slight predicted decrease) are related to the respiration costs. A warmer climate requires major carbon expenses for plant to respire. Respiration functions are indeed temperature dependent (Chapter 5). Therefore, the ratio between NPP/GPP is very likely to be smaller in the future as predicted by this study, although acclimation effects could also intervene to modify this finding (*King et al.*, 2006; *Atkin et al.*, 210).

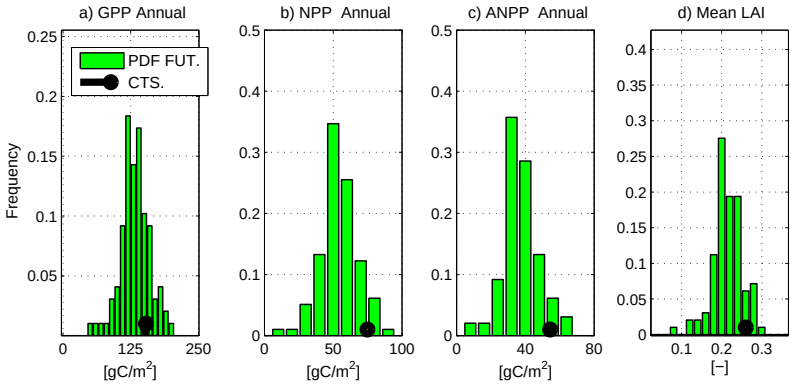

Figure 7.18: Vegetation productivity indexes for the control scenario (black dots) and an ensemble of future scenarios expressed as Probability Density Functions. a.) Gross Primary Production. b.) Net Primary Production c.) Aboveground Net Primary Production. d.) Leaf Area Index.

Figure 7.20 shows the comparison between control scenario and future climate as far as concern the fluxes of evapotranspiration (a), transpiration (b), and evaporation from bare soil (c). It can be appreciated in all the subplots how the control scenario lays in the right hand side of the PDF representing the future, i.e., despite uncertainties in the future climates, a reduction of the water fluxes from the surface

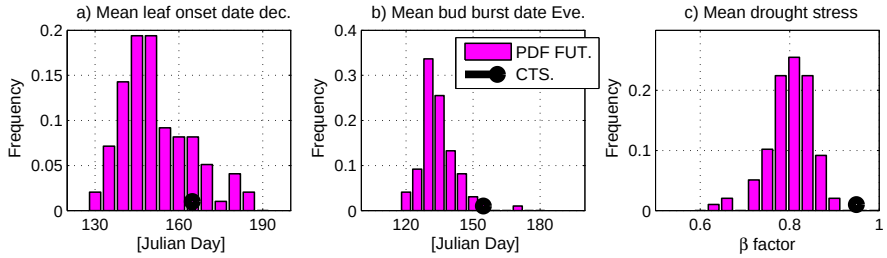

Figure 7.19: Drought stress and leaf onset dates for the control scenario (black dots) and an ensemble of future scenarios expressed as Probability Density Functions. a.) Leaf onset date for deciduous shrubs. b.) Bud burst date for evergreen shrubs. c.) Drought stress coefficient, β_R.

to the atmosphere is very likely for this area. This is a direct consequence of the decrease in the precipitation amount, shown in Figure 7.9. Evapotranspiration is almost totally controlled by rainfall inputs in such ecosystems and equal the amount of water stored in the soil. This is not surprising given the semi-arid climate conditions with elevated energy inputs and dry soils. This statement is further supported by the simulated Horton index, H_i, that is almost equal to one both in the control scenario and in the ensemble of future scenarios (not shown). Where Horton index refers to the ratio between total evapotranspiration and precipitation less storm runoff, $H_i = ET/(P_r - R_H - R_D)$ (*Troch et al.*, 2009). The partition of ET between transpiration and soil evaporation is expected to remain almost constant and it seems slightly affected by the different climate (not shown). This could be due to an overall preservation of vegetation cover as shown in Figure 7.18 and to adaptive capacities of the system.

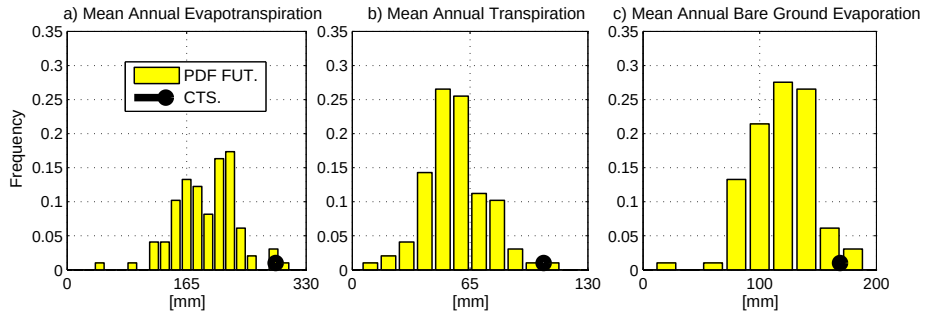

Figure 7.20: Evaporation and transpiration fluxes for the control scenario (black dots) and an ensemble of future scenarios expressed as Probability Density Functions. a.) Total evapotranspiration. b.) Transpiration from plants. c.) Bare soil evaporation.

The response of the ecohydrological system in terms on energy fluxes, latent heat (a), net radiation (b), and sensible heat (c), is shown in Figure 7.21. The same consideration presented for evapotranspiration continue to hold true for latent heat. In a drier climate latent heat is going to be significantly less. The control scenario is a point in the right tail of the PDF representing future. Net radiation flux is also predicted to significantly decrease (Figure 7.21b). The PDF representing future is shifted toward lower values of R_n and its position is distant from the present climate

also in the wetter scenarios, when latent heat is preserved. Since the incoming shortwave radiation remains unchanged or slightly increase in the future (Figure 7.10), explanations must be searched into albedo and longwave radiation effects. A substantial preservation of the LAI, points to investigate bare soil albedo rather than albedo of vegetated areas. In fact, the predicted drier soil surface (Figure 7.22) entails an increase of the albedo and a consequent reduction of the absorbed energy. However, albedo effects are unlikely to be the only explanation for such a significant reduction of R_n. Longwave radiation effects are also responsible with warmer surface and air that interact in a non linear fashion, leading to an overall decrease in the absorbed longwave radiation. The changes in sensible heat fluxes are the consequences of changes in net radiation and latent heat. The final result is that the mode of the PDF of "future" sensible heat flux generally indicates a small reduction of H, although in very dry scenarios larger H are also encountered (Figure 7.21c).

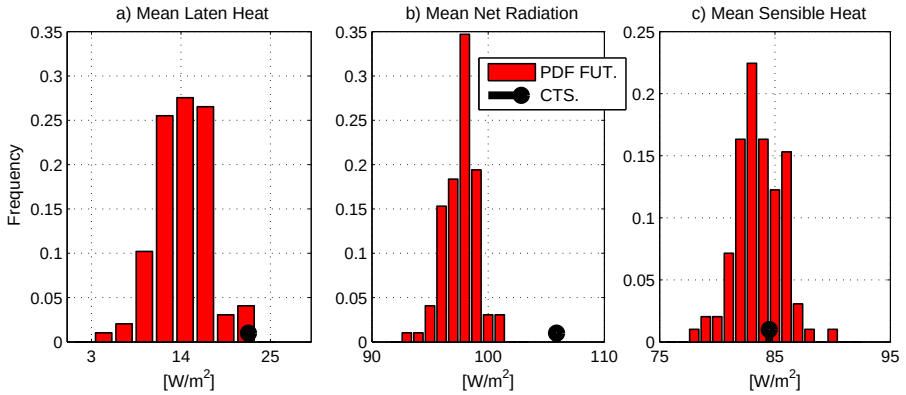

Figure 7.21: Energy fluxes for the control scenario (black dots) and an ensemble of future scenarios expressed as Probability Density Functions. a.) Latent heat flux. b.) Net radiation flux. c.) Sensible heat flux.

The reduction in precipitation combined with a substantial preservation of the vegetation cover in the future scenarios produces a depletion of soil moisture in the entire soil column, as can be observed in Figure 7.22. There is a remarkable uncertainty on "future" soil water contents, especially at intermediate depths underlined by spread distributions. Despite this uncertainty, all the predicted future climates lead to drier conditions highlighted by the sensible reduction in soil water content. In this context, the control scenario represents the wettest extreme of the distribution at all the depths. This outcome can have important consequences on deep recharge. An average reduction of soil water content can indeed affect considerably the recharge to aquifer and thus long-term water availability in semi-arid systems. In the analyzed point scale case the simulated recharge to deeper layers is almost zero also for the present climate (not shown), therefore it is not possible to provide quantitative evidences of the above consideration. However, more generally areas where recharge to aquifer is possible due to particular local situation, e.g., topographic convergence zones, will likely suffer this issue.

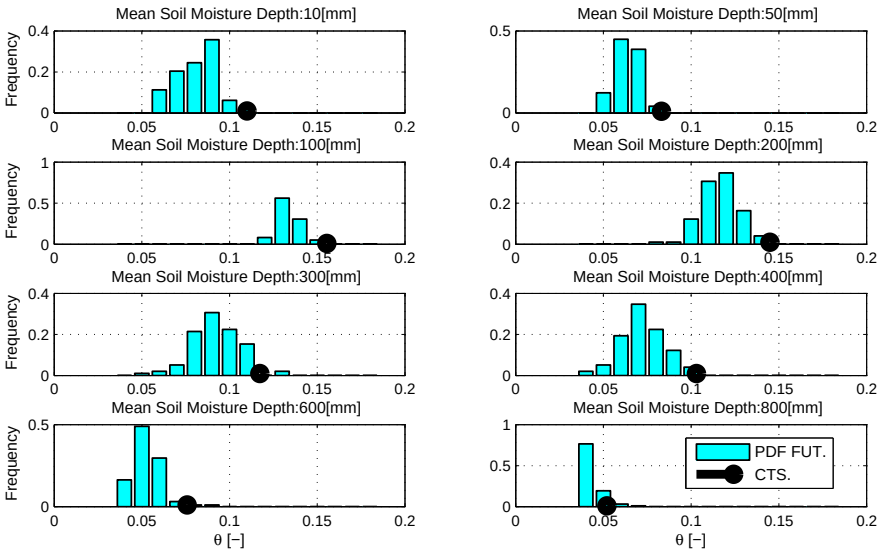

Figure 7.22: Soil water content at different depths of the soil column for the control scenario (black dots) and an ensemble of future scenarios expressed as Probability Density Functions.

Figure 7.23 shows the effect of the predicted climate change on the fraction of precipitation re-evaporated to the atmosphere and on the infiltration excess runoff, R_H. Remind that R_H is concentrated in few events and consists of the totality of runoff for such an environment. The consequences on R_H are totally unexpected. As can be seen in Figure 7.23a the mode of expected "future" runoff has a value of R_H similar to the control scenario with a positive skewed PDF, i.e., there are many possible scenarios for which the runoff is even larger than at the present. This happens despite the reduction in total precipitation. The spread of the results in Figure 7.23b is large with an expected increase of R_H with annual precipitation. However, the diamond representing present climate is in the lower boundary of the cloud representing the future, i.e., given the same amount of precipitation an higher runoff rate is expected. This is really important, because it is related to intra-annual characteristic of precipitation such as frequency and intensity of rainfall spells. In the specific case the role of extreme events can be of paramount importance. Extreme precipitation amounts were predicted to be similar between present and *mean* future climates (Figure 7.12). However, the larger runoff in the simulations can be the result of an increased number of events able to produce runoff although not statistically extremes or extreme precipitations can indeed be more frequent and intense in several future scenarios different from the *mean* one. The downscaling of fine time scales and high order moments of precipitation statistics is the reason why the proposed methodology is able to capture such an outcome. This agrees well with qualitative considerations about enhancement of extreme events because of climate change (*IPCC*, 2007a). The surplus value of the proposed methodology is the effective quantification, though with uncertainty, of changes in extremes at

the local scale.

The fraction of precipitation re-evaporated to the atmosphere is governed by the runoff since almost zero deep percolation occurs. This fraction decreases in each of the simulated future scenarios, although with drier conditions it would be expected to be higher (Figure 7.23c and 7.23d), the reason of this incongruence is the increase of runoff as a fraction of precipitation.

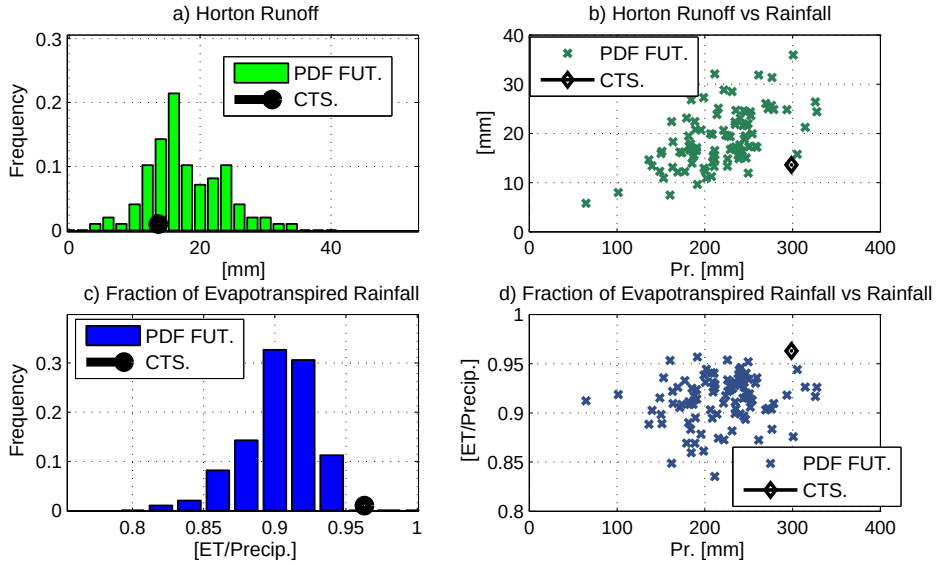

Figure 7.23: Fraction of precipitation re-evaporated to the atmosphere and infiltration excess runoff (Horton Runoff) for the control scenario (black dots (a,c); black diamonds (b,d)) and an ensemble of future scenarios (PDFs (a,c); crosses (b,d)).

The important beneficial effect of higher CO_2 concentrations demands a more insightful discussion on this simulated behavior. It has been shown that an elevated concentration of CO_2 allows to preserve higher gross assimilation rates with minor stomatal apertures. This should be reflected in an enhanced capability of plants to exploit water in the future. In this regard, Figure 7.24 investigates how vegetation productivity, i.e., GPP, NPP, ANPP, and water and rain use efficiency are expected to change. Where, Water Use Efficiency, WUE, is calculated as the ratio between the 25 year averages of NPP and transpiration. Rain Use Efficiency, RUE, is calculated as the ratio between 25 year averages of ANPP and precipitation (*Huxman et al.*, 2004a; *Troch et al.*, 2009). Note that here WUE represents a long term value and is calculated differently from the short term WUE as defined in Section 4.4.5. Despite the differences in the equations the concept underlying WUE is exactly the same. Vegetation productivity in the long-term is linearly correlated with precipitation as shown for GPP, NPP, and ANPP, in Figure 7.24a,b,c. Given the semi-arid climate this correlation was expected and similar linear correlations for climates with annual precipitation lower than 500 $[mm]$ have been observed also at the yearly scale (*Knapp and Smith*, 2001; *Fang et al.*, 2001; *Huxman et al.*, 2004a; *Yang et al.*, 2008). What is interesting to note is the fact that the diamond representing control scenario is at

the very edge of the cloud of points representing "future". This is more evident for GPP because the effect on GPP is not counterbalanced by an augment of respiration costs. The graph highlights the increased capacity of vegetation to produce carbon compounds given the same amount of precipitation inputs. Despite the uncertainties the possible future states are all different from the present underlining the non-negligible effects of climate change.

Figure 7.24c and 7.24d confirm the previous statements. The capacity of plants to exploit water, expressed as WUE, will be higher in the future. The behavior of RUE is more irregular, because although it generally increases for the same reasons of the WUE increase, its growth is limited by the larger portion of rainfall lost as runoff. The obtained values for $RUE \approx 0.2$ $[gCm^{-2}mm^{-1}]$ are close to what observed by other studies (*Huxman et al.*, 2004a; *Troch et al.*, 2009). Note that while RUE does not depend on long-term average precipitation, WUE has a tendency to increase in drier climates.

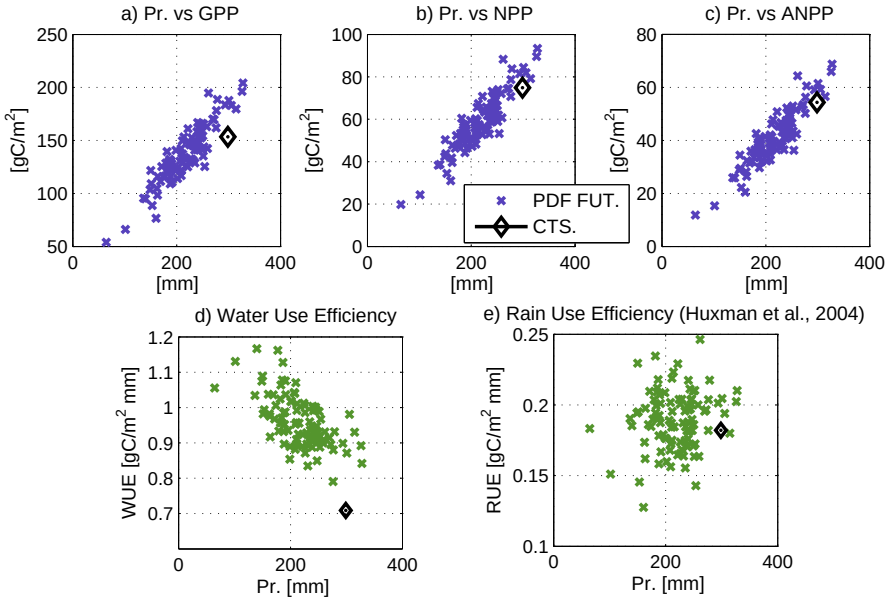

Figure 7.24: Vegetation productivity indexes vs precipitation and water and rain use efficiencies for the control scenario (black diamonds) and an ensemble of future scenarios (crosses). a.) Gross Primary Production vs precipitation. b.) Net Primary Production vs precipitation c.) Aboveground Net Primary Production vs precipitation. d.) Water Use Efficiency. e.) Rain Use Efficiency.

The conclusions about plant behavior in the future with a CO_2 richer atmosphere are hardly verifiable. The effects of elevated CO_2 on plants has been the subject of several hundreds of ecological and plant physiologist studies (*Körner*, 2006). However, a comprehensive understanding of this effect has not been reached so far. There are evidences of an enhancement of terrestrial vegetation growth in the middle and high latitudes of the Northern Hemisphere over the past two decades (*Zhou et al.*, 2001; *Nemani et al.*, 2003; *Piao et al.*, 2006). Although, the mechanisms underlying this phenomenon are still under debate, modeling studies suggest that CO_2

is the dominant controller for the greening trend during the recent period (*Piao et al.*, 2006). They show that the CO_2 effect is the most important compared to air temperature and precipitation. *Piao et al.* (2006) further highlight that precipitation use efficiency and atmospheric CO_2 fertilization effect on the greening trend of Northern Hemisphere increase as soil moisture becomes limiting. Another study shows that generally a reduction of stomatal conductance moderates or cancels the water losses caused by a warmer and drier climate. However, photosynthesis stimulation counteracts this stomatal effect, especially in the mid-to-high latitudes, because of enhanced LAI, resulting in a small net impact on increasing evapotranspiration (*Kergoat et al.*, 2002). These findings strongly support the results of this study, where the CO_2 fertilization partially offsets the effect of rainfall reduction. A reason why the detected shift in water use efficiency is such significant could be the very dry climate analyzed. Continue water stress conditions near the limit of plant surviving might contribute to exalt the CO_2 fertilization effect, that in different ecosystem could be nuanced. Note that in all the future scenarios the CO_2 concentration level is set to 700 $[ppm]$ for the entire 25 years of simulation. This is almost the double of present days carbon dioxide concentration and might also boost the simulated behavior. Observational evidence of larger WUE, RUE, with dry conditions and higher CO_2 have been also recently found by *Huxman et al.* (2004a); *Troch et al.* (2009); *Brooks et al.* (2009).

It must be noted how other studies are much more conservative in predicting such a strong fertilization effect due to CO_2 increase, arguing that the adaptation effects or the limitations imposed by nutrients might became fundamental in the future (*Wullschleger et al.*, 2002; *Körner*, 2003; *Hetherington and Woodward*, 2003; *Luo et al.*, 2004; *Körner*, 2006; *Thornton et al.*, 2007). *Shaw et al.* (2002) show that when favorable conditions such as precipitation, temperature, and nutrients are imposed, the increase in productivity with elevated CO_2 concentration is less than with present CO_2 concentration. This points to the fact that the net result of climate change rather than be the sum of multiple effects, such as CO_2 fertilization, warmer temperature etc., is the outcome of many complex interactions. This is remarked also by *Körner* (2006) that underlines how the straightforward photosynthetic response to CO_2 increase does not translate in an equal plant growth and productivity response. The CO_2 enrichment effects are mediated not only by other climatic variables but also by many ecophysiological factors such as carbon allocation, tissue turnovers, nutrient recycling, forest boundary conditions, etc., that can strongly influence the fate of the extra carbon. In this respect I believe that the developed ecohydrological model is able to include many feedbacks providing a comprehensive picture of the expected future, with two important exceptions, i.e., nutrient dynamics and plant adaptation strategies. It is likely that neglecting these two processes represents the major limitation of the conclusion. Nonetheless, the main findings are considered to hold true especially for the analyzed ecosystem.

The quite scattered cloud of points representing the 25 year averaged combinations of precipitation and vegetation productivity shown in Figure 7.24a,b,c leads to

another important remark. Note that the graphics contain a different information with respect to one year total because they are averaged over long periods of time. The fact that climates with the same long term amounts of precipitation produce different long term rates of vegetation productivity is an important aspect to investigate. This can be partially explained by differences in the other variables such as air temperature. However, the range of variability of temperature among the ensemble members is very narrow (Figure 7.9), and even less variability is simulated for the other meteorological variables. Consequently, the role of inter-annual and intra-annual differences in precipitation intensity and occurrence can be the leading factor in controlling productivity of this ecosystem. Each member of the ensemble of future climates has a specific internal structure, a different seasonality, and also a different inter-annual variability, of precipitation. The combination of these factors leads to observe a significant scatter in the values of vegetation productivity metrics, even when the 25 year average precipitation is almost the same. An important effect of duration, frequency, and intensity of precipitation pulses in shaping the productivity and carbon exchange in water limited ecosystem such as the Sonoran desert, has been already remarked by *Huxman et al.* (2004b). However, the considerations presented refer to an extended period of time and must be seen in a climate perspective. This is important and can have implications for long term ecosystem studies, not limited to climate change investigations. The role of precipitation structure, especially inter-annual variability has not always been considered as a critical factor. Understating which component of precipitation structure mainly affect the long-term variability in GPP, NPP, and ANPP, can be the objective of future studies.

7.6 Distributed results

The time series of meteorological inputs estimated at the Section 7.4 are used in the following to simulate the ecohydrologic dynamics in a distributed domain. Such analysis is presented in order to better understand possible implications of climate change on the spatial variability of hydrological and energy fluxes and in the patterns of vegetation. The distributed domain used for the analysis is the Lucky Hills experimental watershed for which a detailed description and an eco-hydrological analysis have been presented in Section 7.3. The distributed domain can be regarded as characteristic of the topography of South-East Arizona and is small enough to allow a discussion of specific topographic features. The simulation realized in the distributed domain includes a comparison between 30 years of the present climate and 30 years of the *mean* future climate. The latter is obtained through the means of the factors of change for each downscaled statistical property (Section 7.4). The large computational efforts required by distributed applications of "Tethys-Chloris" do not allow to use all the $\bar{N} = 100$ time series of the Monte Carlo as presented in the point scale application in Section 7.5. Consequently, a probabilistic description of metrics associated to future conditions is not feasible for the distributed domain.

A simple comparison of the control and mean future scenarios is presented in the following. The hydrological and vegetation parameters for the mixed deciduous and evergreen desert shrub community required in the model are assumed equivalent to the plot scale application and have been already described in Section 7.2. The initialization of soil moisture states and biomass carbon pools is realized with the long-term averages obtained from the point scale application (Section 7.5). This entails that at the beginning of the simulation vegetation and soil moisture are spatially homogeneous. Although, this is unrealistic, especially for vegetation, it has been observed that in two-three years vegetation adapts to local conditions and thus the effect of an homogeneous initial state is quickly dissipated. Therefore, the results of the simulations, lasting 30 years, are considered independent from the chosen initial state.

The simulated time series of variables averaged over the spatial domain have been compared with the same variable simulated at the plot scale. Such a comparison allows to analyze if there is a relevant impact of the distributed domain on the hydrological and vegetation response. The idea is to provide quantitative evidences for the the point-scale representativeness of larger domain. This is very important because in case spatially averaged and point scale fluxes would have similar dynamics and magnitudes, the point scale applications can be regarded as informative of an area much larger than the one effectively analyzed. This implies a different relevance of the results of the study that can be extended to wider spatial scales with a certain confidence. This concept was anticipated in Section 7.3 without providing any numerical support. The determination coefficients, R^2, obtained comparing point and distributed application in the control, CTS, and future, FUT, scenarios are shown in the first two columns of table 7.2. It can be easily observed that in the present climate the difference between spatially averaged and point scale simulations is fairly negligible for many energy and hydrological fluxes, as well as for vegetation productivity metrics. The R^2 are generally larger than 0.9, except for soil moisture and deep recharge, L_{kb}, quantities. The mild topography and the weak subsurface lateral fluxes contribute to maintain a fairly homogenous environment where above and below average fluxes tend to compensate each other, ultimately producing a spatial average similar to a flat topography.

The temporal averages of the spatial standard deviations for the control scenario are listed in the third column of table 7.2. The standard deviations show that a certain spatial variability is present in the system. However, this variability is distributed in a way to produce averages similar to a flat element. Considering a distributed domain is very important for soil moisture and recharge effects. The formation of special niches of favorableness produces conditions that depart significantly from the mean and that are not appreciable with a point scale simulation.

The spatial standard deviations for the future climate are different than in the control scenario and point to a stronger influence of the domain shape on the system response, especially with regards to metrics of vegetation productivity. The standard deviations listed in the fourth column of table 7.2 are larger in the future for almost

Table 7.2: Determination coefficients, R^2, between the simulations at the point scale and spatially averaged in the distributed domain for the principal ecohydrological variables (column 1-2). Temporal averages of spatial standard deviations for the principal ecohydrological variables (column 3-4). The control and future scenarios are indicated with CTS and FUT, respectively. *) The standard deviations for the metrics of vegetation productivity are calculated separately for deciduous and evergreen species. These values are successively averaged using the Crown Area fractions as weights. Given the non-linearity of standard deviation operator the obtained values are not correct in absolute terms but are still useful for comparison.

	R^2, **CTS**	R^2, **FUT**	**StD, CTS**	**StD, FUT**
R_{sw} $[W\ m^{-2}]$	0.998	0.998	13.5	14.0
R_n $[W\ m^{-2}]$	0.998	0.998	10.1	10.4
λE $[W\ m^{-2}]$	0.993	0.984	1.6	1.6
H $[W\ m^{-2}]$	0.989	0.988	13.8	15.1
T_H $[mm\ yr^{-1}]$	0.972	0.915	14.0	15.6
E_g $[mm\ yr^{-1}]$	0.996	0.991	8.4	7.6
θ $[-]$ $[0-1.6m]$	0.770	0.802	0.0069	0.0051
T_s $[^\circ C]$	0.998	0.997	0.40	0.43
I_f $[mm\ yr^{-1}]$	0.994	0.946	20.3	26.4
L_{kb} $[mm\ yr^{-1}]$	0.024	0.033	1.2	0.25
$Q_{l,out}$ $[mm\ yr^{-1}]$	-	-	0.15	0.07
A_{nC} $[\mu molCO_2\ m^{-2}\ s^{-1}]$	0.977	0.909	$0.025^\star$	$0.061^\star$
GPP $[gC\ m^{-2}\ yr^{-1}]$	0.948	0.754	$8.4^\star$	$24.2^\star$
NPP $[gC\ m^{-2}\ yr^{-1}]$	0.923	0.795	$5.1^\star$	$13.7^\star$
$ANPP$ $[gC\ m^{-2}\ yr^{-1}]$	0.914	0.755	$4.8^\star$	$11.0^\star$
LAI $[-]$	0.957	0.694	$0.0098^\star$	$0.0251^\star$

all the variables, depicting a significant enhanced spatial heterogeneity. This is also observable in the determination coefficients of vegetation metrics that are around 0.75 significantly less than in present conditions. The point scale results are indeed only partially representative of the averages of the distributed domain. There are local topographic effects that contributes to create inequalities between point-scale and distributed simulations.

A comparison between the time series of LAI simulated at the point scale and spatially averaged in the distributed domain is shown in Figure 7.25 for present climate and in Figure 7.26 for the *mean* future climate. For the present climate the two time series of LAI are almost identical as underlined by the very large R^2. Small differences are only appreciable during the transient initial period and during the most intense droughts (Figure 7.25).

The same comparison in the future climate highlights two patterns that after 12-13 years of simulation shown an evident dissimilar dynamic. In the drier and warmer predicted future a severe drought around the middle of the simulation is capable to induce mortality in deciduous vegetation in a large part of the domain where most unfavorable conditions occur. This smooths out the seasonal peaks of LAI that is related to deciduous species and allows evergreen to be the only vegetation specie in a part of the domain. This is visible in the last ten years of simulation and is

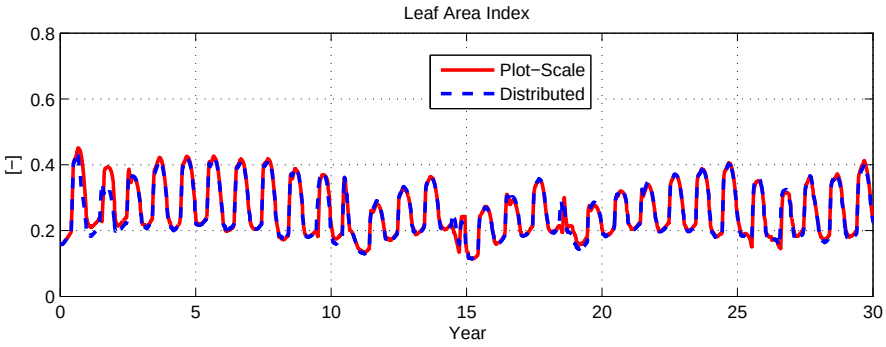

Figure 7.25: Time series of simulated Leaf Area Index. Results for the present climate. Point scale results (red line) and spatially averaged results over the distributed domain (blue dashed line).

the principal reason for the larger values of spatial standard deviations and minor correlations observed in the future. Such a kind of evolution has indeed a certain relevance and cannot be captured by a point scale simulation.

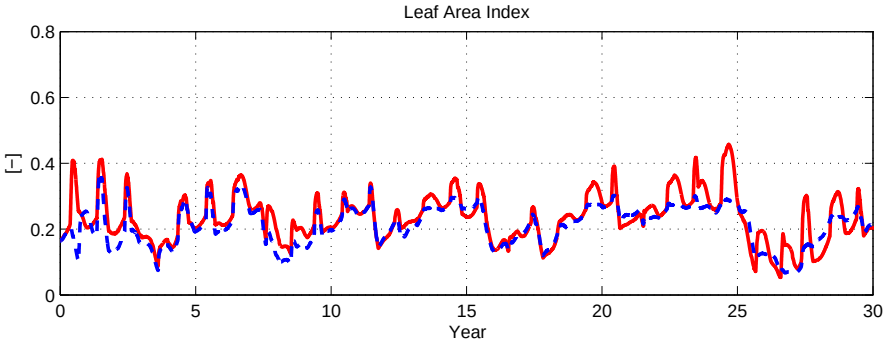

Figure 7.26: Time series of simulated Leaf Area Index. Results for the *mean* future climate. Point scale results (red line) and spatially averaged results over the distributed domain (blue dashed line).

The comparison between point-scale and distributed simulations is considered relevant because allows to understand the importance of the spatial variability and the feasibility to extend point scale results to larger domains. The limited subsurface water dynamics and the gentle topography provide support for this extension. Although, such an extension is possible for the present climate, the significant variability in vegetation behavior and the possibility that vegetation undergoes mortality in unfavorable topographic locations lead to question this approach for the future climate. This does not mean that the principal findings discussed in Section 7.5 should be questioned but only that must be regarded for what they are, simulations in a single cell.

Clarified the relevance of analyzing a distributed domain a comparison between the control and future scenarios is presented looking at the spatial differences of temporal averaged fluxes and states. Figure 7.27 shows the comparison in terms of mean soil moisture integrated in the soil column $[0 - 1.6m]$. It clearly emerges once more how the *mean* future is expected to be significantly drier than the present.

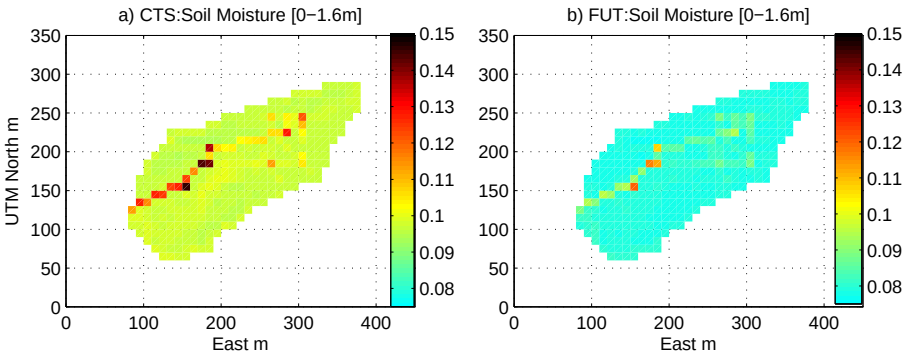

Figure 7.27: Spatial distribution of soil moisture, time averaged quantities for each basic computational element. A comparison between the control, CTS, (a) and future, FUT, scenarios (b).

Drier conditions are not only the results of a significant precipitation reduction ($\approx 25\%$) but also of an increase in runoff production and discharge at the outlet. In figure 7.28 the difference in cumulative runoff at the Lucky Hills outlet underlines how the future scenario might present a larger number of intense rainfall events despite the decrease of mean annual rainfall. This result was already anticipated in the point scale application (Section 7.5) but the simulated magnitude of discharge increase in the distributed domain is surprisingly large passing from 10.3 $[mm\ yr^{-1}]$ in the CTS scenario to 32.0 $[mm\ yr^{-1}]$ in the FUT scenario. This three-fold increase of runoff is mainly due to changes in the internal structure of precipitation with an increase of events able to producing runoff in the winter months. However, the soil sealing formation and evolution might contribute to create a positive feedback, in fact, heavier precipitation events lead to more pronounced soil seals that can consequently increase runoff.

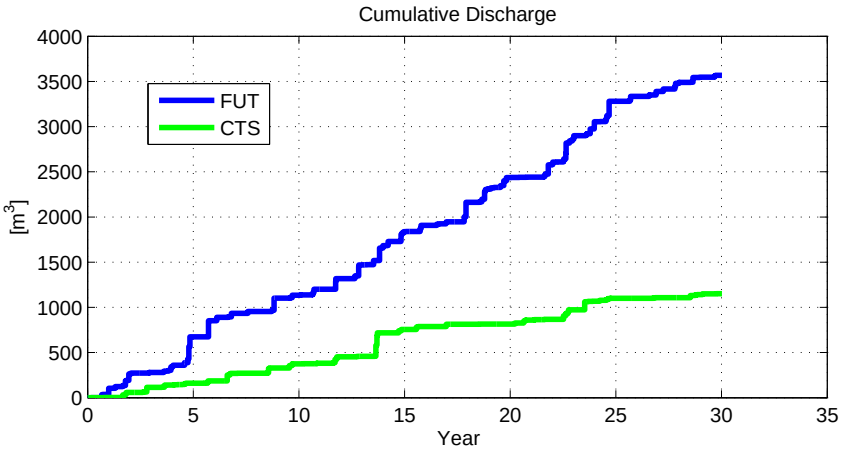

Figure 7.28: A comparison between the cumulative discharge simulated at the Lucky Hills outlet in the control (green line) and future (blue line) scenarios.

Spatially distributed infiltration rates for present and future scenarios are illustrated in Figure 7.29. In the topographic divergent portion of the watershed the infiltration rate is mainly governed by precipitation minus infiltration excess runoff. In this part the differences between the two cases are significant because are governed by the precipitation reduction. Appreciable differences between CTS and FUT scenarios are also detected in the hollow where infiltration is generally larger than precipitation because of runon. This happens regardless of the larger runoff in the FUT scenario. In quantitative terms runon accounts for 41% of runoff in CTS and for 34% of runoff in the FUT scenarios, pointing to a positive soil sealing feedback. The runoff-runon mechanism mediates the distribution of soil moisture. The hollow in the convergent part of the topography has a larger water content in both the scenarios (Figure 7.27). Lateral subsurface flows are indeed negligible, less than 0.8 $[mm\ yr^{-1}]$, (not shown). Consequently, the redistribution of soil moisture in such an arid environment is mainly due to topographic flat area or other obstructions (not considered in the model) that create favorable conditions for re-infiltration of surface overland flow.

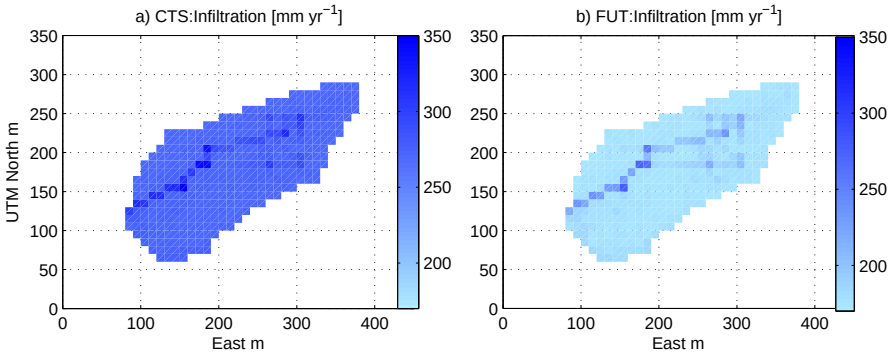

Figure 7.29: Spatial distribution of infiltration rates, time averaged quantities for each basic computational element. A comparison between the control, CTS, (a) and future, FUT, scenarios (b).

The presence of cells where soil water content is much larger than the surrounding zones allows for episodic recharge to deeper soil layers and ultimately to aquifers. In the model this flux is indicated as soil bottom leakage. This component in the point scale application was almost zero also in the CTS scenario (Section 7.5). Only speculative considerations about a possible reduction of deep recharge were indeed formulated in that Section. In the distributed domain the latter considerations are supported by evidences. The cells where conditions for recharge occur are significantly less in the future and also the intensity of the fluxes is expected to diminish (Figure 7.30). Such a scenario can have noticeable implications for semi-arid areas where aquifers might undergo a progressive depletion for the lack of zones where deep percolation is possible.

The analysis of spatially distributed energy fluxes does not provide particular insights in comparison to the point scale simulations. Point scale energy fluxes are indeed strongly correlated to their spatial means as can be observed from the R^2

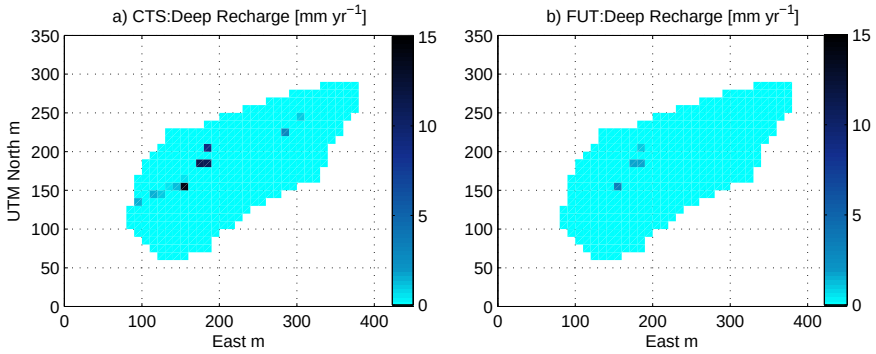

Figure 7.30: Spatial distribution of deep recharge fluxes, time averaged quantities for each basic computational element. A comparison between the control, CTS, (a) and future, FUT, scenarios (b).

in table 7.2. For this reason the spatial distributed maps of shortwave incoming radiation, net radiation, sensible heat, and latent heat, are not shown in the following. Only a note about bare ground evaporation is necessary. Given the high permeability of the shallow portion of the soil column in the domain the bare ground evaporation is not influenced by runon effects. Consequently, soil evaporation does not show consistent variation throughout the domain.

Very interesting to observe are the consequences that a drier and warmer climate with larger runoff rates has on vegetation dynamics. Figure 7.31 shows the comparison between the spatial distribution of Leaf Area Index in CTS and FUT scenarios. A significant increase of spatial heterogeneity in vegetation leaf cover can be appreciated. The future scenario presents LAI values larger than the present in the wettest convergent part of the watershed but it has considerably less vegetation in the remaining portions. The favorable moisture conditions in the topographic niches where re-infiltration occurs contribute to reduce vegetation water stress. In such a way plants can profit from the richer CO_2 atmospheric concentration to enhance their productivity, as thoroughly discussed in Section 7.5. Conversely, in the portion of the watershed where extremely dry conditions occur, plant are continuously experimenting water stress conditions and their productivity is dramatically reduced. As discussed previously the decrease in productivity is also related to mortality of deciduous vegetation species during the simulation in several computational elements. The range between maximum and minimum temporally averaged LAI simulated across the domain passes from 14% to 35%. The distribution of vegetation is more heterogenous in the predicted future and characteristic patterns of arid system such as a banded vegetation are more pronounced.

Vegetation productivity and LAI are slightly larger in the hollow portion of the watershed also in the present climate, nonetheless it is in the future that this pattern starts to significantly emerge (Figure 7.31 and 7.33). Semiarid landscapes with distinctly banded vegetation patterns are typical in nature and their dynamics have been the subject of several studies (*Valentin et al.*, 1999; *Ludwig et al.*, 2005; *Saco*

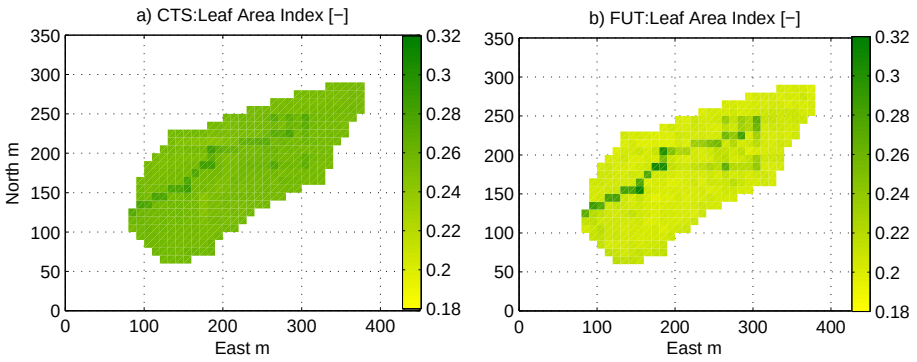

Figure 7.31: Spatial distribution of Leaf Area Index, time averaged quantities for each basic computational element. A comparison between the control, CTS, (a) and future, FUT, scenarios (b).

et al., 2007; *Kletter et al.*, 2009; *McDonald et al.*, 2009). The formation of vegetation patches organized in bands along the topographic gradient or in convergent areas is the result of pedological, hydrological, geomorphological, and eco-physiological processes and is an important feature of arid and semi-arid systems. This study shows how a drier climate might lead to accentuate the emergence of a banded vegetation starting from homogenous conditions. Major droughts are suggested as a triggering mechanism for vegetated band initiation. It is likely that once the development of a banded vegetation pattern is triggered, the process will be able to self sustain through the enhanced water and sediment interception and higher permeability in vegetated patches as discussed by *Ludwig et al.* (2005). Banded vegetation patterns are interesting landscape organization mechanisms of semi-arid and arid system and their study can be the topic of future researches. It is important to note that obtaining such an evolution with a physically-based model is far from be common in literature and effectively opens new opportunities of investigation.

The spatial distribution of LAI is directly reflected in the rates of transpiration as shown in Figure 7.32. Values of present climate transpiration are preserved only in the convergent topography area where runon ensures a sufficient soil moisture. The difference between the higher and lower long term averaged transpiration rate across the domain increases significantly passing from 36% in the present to 61% in the future scenario.

Vegetation productivity is affected and in turn affects the predicted spatial distribution of vegetation as shown in Figure 7.33 for ANPP, and in Figure 7.34 for GPP. The observed changes are indeed similar to the one observed for the LAI, with a slightly augmented productivity in favorable areas and a significant reduction elsewhere. The range of maximum to minimum simulated ANPP is 22% in CTS, and 50% in FUT scenarios.

These results underline how the relationships between LAI, transpiration, and

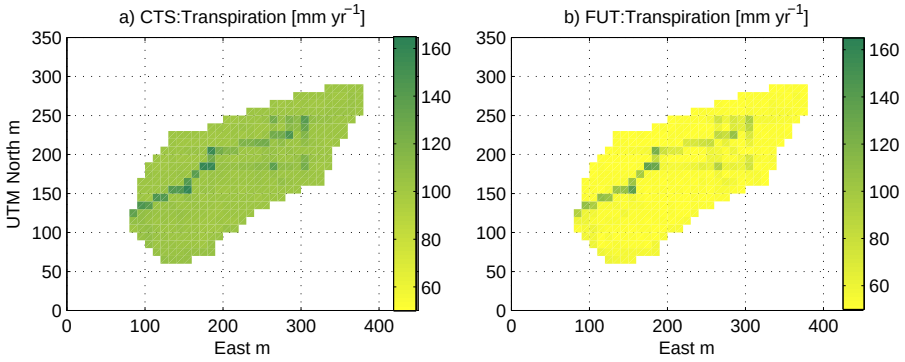

Figure 7.32: Spatial distribution of transpiration rates, time averaged quantities for each basic computational element. A comparison between the control, CTS, (a) and future, FUT, scenarios (b).

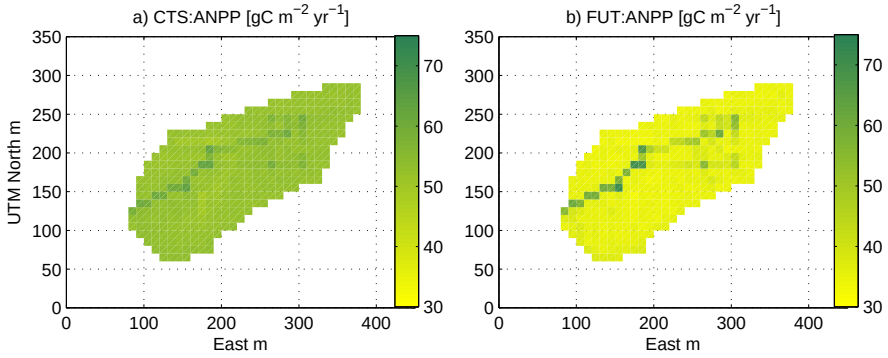

Figure 7.33: Spatial distribution of ANPP, time averaged quantities for each basic computational element. A comparison between the control, CTS, (a) and future, FUT, scenarios (b).

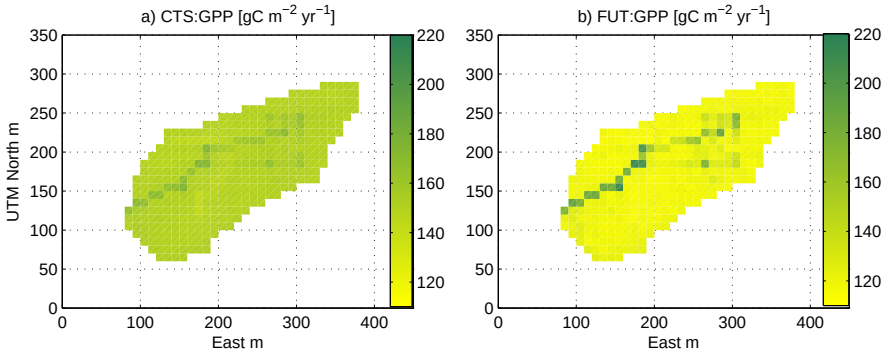

Figure 7.34: Spatial distribution of GPP, time averaged quantities for each basic computational element. A comparison between the control, CTS, (a) and future, FUT, scenarios (b).

vegetation productivity, are highly non-linear and how all the components are important in the control of the the overall eco-hydrological response of the system. Hydrological processes in water controlled ecosystems are indeed rather complex and interconnected with vegetation. In this respect, mechanistic-based ecohydrological models that include multiple processes can help in quantitative analysis and can be regarded as a very important tool for detailed investigations.

Chapter 8

CONCLUSIONS AND OUTLOOKS

How climate fluctuations influence hydrological and ecological dynamics has been a long-standing goal of scientific research (*Eagleson*, 1978). The interest on this topic is dramatically increased when anthropogenic climate change has began to become an evident reason of concern for our society. This "external" influence on the Earth climate has contributed to question the hypothesis of stationarity and to reconsider our way to make predictions, with the unavoidable consequences on long-term design. Non-stationarity is critical for disciplines such as hydrology and ecology were long-term projections are fundamental for both practical and theoretical problems. Contemporaneously to the recognized importance of climate non-stationarity an emerging discipline, named ecohydrology, that links physiological and plant dynamics to hydrological processes, has begun to develop. Ecohydrological studies in the last decade have significantly contributed to enlarge our understanding of the interaction between vegetation and hydrology highlighting several fundamental connections.

In this regard, this study has attempted to combine knowledge from multiple disciplines and to summarize it in a sounding methodology. Such a complex approach is required by the inherent difficulty to investigate climate change effects on vegetation-hydrology dynamics. This problem is further exacerbated by the evident gap that results from the necessity to investigate climate non-stationarity at local spatial scales and fine temporal resolutions typical of ecohydrologial studies, and the coarse (in space and time) scales of predictions available from climate models. The developed *blueprint* allows one starting from climate model outputs, to infer hourly time series of meteorological variables representing a predicted "future" and to propagate this information into the ecohydrological system. Each of these passages requires specific numerical tools that are described in detail in the thesis, e.g., the stochastic downscaling with the weather generator, the hydrological and the vegetation models. The presented blueprint can be regarded as an important landmark for local-scale climate change studies, because it delineates steps and the possible shortcomings and deficiencies of a downscaling methodology extended at the hourly

scale. More specifically, it offers a new powerful tool such as the weather generator and the possibility to include the uncertainty of climate model predictions, at least the part that derives by the use of multiple models, in the form of PDFs. This is also considered very important in climate change studies and allows one to give a probabilistic representation of future projections and to account for different "scenarios". Note that the proposed methodology is thought to extend the forecasted uncertainty to local ecohydrological predictions. Despite the numerous underlying assumptions, this represents a very up-to-date attempt in this field of research, especially at the level of detail provided by this study

The predictions made for meteorological forcing, hydrological, and ecological dynamics in a non-stationary climate have also noticeable implications, as far as the risk evaluation concerns. As discussed in the introduction the determination of the hazard according only to observations of the past is very incautious when climate change is expected to have a significant impact, and hazard quantification is fundamental for the entire risk management chain. This study offers an opportunity to re-evaluate the local climate forcing accounting for the climate changes predicted by GCMs. Uncertainty, and modeling assumptions are not negligible, but the challenging task of long-term projections leaves room to little or none alternatives.

The new developed tools, i.e., AWE-GEN, Tethys, and Chloris, have also a scientific relevance per se. For instance, it should be noticed that AWE-GEN capabilities to reproduce characteristics of a given climate represent a novelty development on its own. To author's knowledge, the presented weather generator is the only tool capable of generating such a wide set of hourly meteorological variables, capturing their statistical properties over a large range of temporal scales, such as extremes and low-frequency inter-annual variability. These characteristics make AWE-GEN suitable for applications in several fields of geosciences such as hydrology, ecology, geomorphology, and agriculture. AWE-GEN has indeed been tested in several locations with a quite different climate and has generally produced very consistent results in terms of many meteorological variables and temporal scales.

The modeling of hydrology and vegetation dynamics has been realized with Tethys and Chloris. Although the original idea was to keep separate to some extent the two models, and in this way they are presented throughout the thesis, the applications and the nature of the encountered problems suggest to consider the two models as a single numerical tool "Tethys"-"Chloris". The acronym *T&C* has been already introduced at the beginning of Chapter 6. *T&C* can be regarded as an "ecohydrological model" in the most up-to-date meaning of this expression. It is undoubtable that the structure of the model and many components that constitute *T&C* are not newly developed in this thesis. Nonetheless, the effort in accounting for the state of the art in hydrological and vegetation modeling, and the level of detail with which many components are presented is considered to have a scientific relevance. This is underlined from the large body of literature quoted in the thesis and from the inclusion of several new scientific contributions used to refine many components of *T&C*. In this context, there is also originality in the model organization and struc-

ture and in the type of processes that are considered, e.g., two layers of vegetation, snowpack-vegetation interaction, soil sealing, translocation of carbohydrates, leaf age, etc. These are non-conventionally included in ecohydrological studies. To author's knowledge, there are few mechanistic ecohydrological model worldwide that have capabilities similar to *T&C* in simulating the hydrology and vegetation interaction and it is probably the first one to include the treatment of snow in ecohydrology. Besides these positive aspects, *T&C* has many tightening assumptions that limit its performance. In this regard the model is still incomplete, and future ameliorations, and addition of components will be necessaries. The most critical assumptions that would need improvements are listed below.

- The spatial representation of basic computational elements with a regular square grid, though does not represent an issue in its own, it is not computationally parsimonious. In this scope non conventional methods to make the topographic partition of the watershed can be used or developed "ad hoc". As far as the use of a regular square grid concerns, advanced methods to calculate flow directions are available in literature and could be introduced (Section 4.1.2). Moreover, in the actual version of *T&C* the basic computational element area corresponds to the area projected from above. This is not an issue for flat topography but might become an important imprecision in very steep terrains.

- The use of a single prognostic temperature for the calculation of the energy budget is a great limitation of the model (Section 4.2.5). The use of a scheme that considers multiple temperatures to describe the different elements such as bare soil, snow, shaded and sunlit vegetation, is highly recommended. This amelioration will also permit to make a partition of the canopy with a more sounding two big leaves scheme (Section 4.4.5).

- The scheme used to describe the soil resistance to evaporation is empirical. It further depends on a parameter of difficult quantification that represents the characteristic soil depth subjected to the evaporation process (Section 4.4.4). A better or mechanistic parametrization of this phenomenon is thus desirable, although problems arises also from the lack of a complete scientific understanding.

- The parametrization adopted to link stomatal aperture to the availability of soil moisture in the soil is highly empirical. As discussed in Section 4.4.5 the use of β_R factor represents only a proxy of the entire soil-root-xylem-leaf transfer process that controls stomatal aperture and photosynthesis. This control is fundamental in ecohydrology because it expresses the major link between plant physiology and soil moisture. A mechanistic parametrization of this control is regarded as a very important amelioration of *T&C*.

- There are evidences that the dependencies of leaf (dark) respiration on maximum Rubisco capacity and temperature are more complex of the ones imple-

mented in *T&C*. This can have some relevance in the vegetation productivity and their revision according to new scientific results might be important.

- Evaporation and sublimation from snow are calculated in a traditional fashion, more detailed approaches, where sublimation-loss rates are properly accounted for, could be implemented within *T&C* (Section 4.5.3). Furthermore, redistribution of snow due to wind-topography interactions or avalanches is completely neglected. This can be a new component for a future *T&C* version.

- The geomorphic and erosion modules of *T&C* are restricted to splash erosion. The inclusion of sediment transport dynamics due to overland and channeled flows at the watershed scale can enlarge the possibility of analysis of such a model.

- In the subsurface water flow dynamics (Section 4.7) one of the most limiting assumption is to neglect capillarity effects in order to simplify the numerical scheme. This is a quite strong assumption and can be relaxed only solving the Richards equation. The price to pay is to considerably increase the computational burden. A similar consideration regards the implementation of a numerical scheme for groundwater flow. Although, the actual version of *T&C* accounts for saturated zones, the subsurface routing is still governed by topographic features and not by hydraulic heads. An hydraulic head subsurface routing would require a recalculation of flow directions at each time step, further increasing computational cost.

- Theoretically the possibility to consider spatially heterogeneous parameters such as soil texture properties, soil depth, and bedrock leakage is already included in the model. However, the general lack of information about these quantities would require a statistic approach rather than a deterministic one to describe their variability. Moreover, from the practical point of view introducing variability in soil depth presents a noticeable computational challenge, since it makes the description of connections among subsurface basic elements highly heterogenous.

- Another limit of *T&C* is the absence of a component that simulates nutrient and soil carbon dynamics. Including an explicit treatment of biogeochemistry would permit a better modeling of vegetation functions. This is the most desirable improvement for the model. In *T&C*, only four carbon pool are tracked right now. The consideration of other carbon and nutrient pools such as below- and above-ground heartwood, litter, standing dead biomass, soil carbon, soil nitrogen, etc. would produce noticeable benefits in the control of model performances and in the simulation of the whole carbon budget. This would also permit to simulate forest growth dynamic, and species competition once other mechanisms such as plant mortality, seed recruitment, and dispersal are considered. The explicit consideration of other carbon pools would also

help to delineate structural properties of the plants required in the water and energy budget, making hydrology and ecology even more tighten. A first attempt of such a schematization is provided in Appendix D.1.

- Some of the components governing the carbon balance and the phenology evolution could be refined, once a better knowledge of the underlying phenomena will be achieved from biologists, plant physiologists, and botanists. This is the case for processes such as carbon translocation, tissue turnover induced by environmental stresses, loss of photosynthetic capacity with age, phenology of leaf onset, senescence, etc. The latter are all parameterized very easily because a basic lack of information.

- The possibility for the model to include urban and rock covered surfaces is indicate in Section 4.1.2, and no further mentioned. The inclusion of these land covers could be an ulterior improvement.

Despite the limitations listed above there is confidence that AWE-GEN, Tethys, and Chloris can produce reliable results in many environments and for numerous metrics. The list above should be seen as a proof of the author awareness of model limitations rather than as a questioning of the model capabilities. It is also an incitement and a guideline for model improvements. As testified from the applications in Chapter 6 and 7, *T&C* is able to capture the ecohydrology dynamics of different ecosystems subjected to various climates with an elevated degree of realism and can be regarded as a very promising and useful tool. Undoubtedly, ulterior validations and tests will be necessary to prove or disprove components of *T&C*. This will be possible once better and larger datasets will be available (see Section 6.1). Finally, note that the possibility of investigation offered by the developed numerical tools extends far beyond the thesis scope and they can be used as the starting point for future scientific researches.

A considerable effort in the development of *T&C* has been also devoted to its numerical implementation. This hidden work is not discussed throughout the thesis but represents a not negligible part of the entire research. For instance, a parallel version of *T&C* for spatial distributed applications has been carried out. Along this line further efforts are required, because the computational demand of *T&C* is still very large. The latter issue places limits on the size of the analyzed watersheds.

As emphasized in the previous statements and generally in the thesis, the principal objective of this work was the realization of a *blueprint* for using climate change predictions on ecohydrology. However, the first application of such a blueprint has led to interesting results. The principal findings of the analysis of a desert shrub community in the semi-arid southeastern Arizona are summarized in the list below.

- For the analyzed case study, the largest uncertainty in climate model predictions is related to precipitation. Air temperature is simulated more consistently across models and the related uncertainty is significantly lower. There is a noticeable disagreement among GCMs precipitation projections that leads

to have a very spread distribution of this variable for the future scenario. This lack of skill in simulating precipitation is not surprising what is considered important is its quantification through PDFs. Despite the uncertainties, the projected future climate (2081-2100) for south Arizona is estimated to be significant warmer ($\approx +4\,[^{\circ}C]$) and drier ($\approx -25\%$ of total precipitation) than the control scenario (1961-2000). The reduction of mean precipitation does not lead to a reduction in extreme precipitation. Conversely, it is very likely that in the future a larger number of intense events able to trigger runoff would take place. The amount of runoff is indeed expected to be larger due to less frequent but more intense precipitations. Note that the predicted transition to a more arid climate in the southwestern regions of North America is very consistent with projections from other studies carried out at different scales (*Seager et al.*, 2007).

- The drier and warmer climate has a direct consequence in the vegetation stress that is expected to be stronger and more continuous in the predicted future. At the energy budget level, the increases of air temperature and surface temperature interact in a non-linear fashion, leading to enhance outgoing longwave radiation and to decrease the net radiation input to the system.

- Despite the supposedly unfavorable conditions vegetation productivity and vegetation cover is partially preserved in the future. This is a very important aspect to remark. As discussed in detail in Section 7.5 the enhancement of atmospheric CO_2 concentration in the future almost offsets the larger stress of the plant. CO_2 could have a fertilization effect on vegetation productivity. The capacity of plants to exploit water, WUE, is expected to increase sensibly, especially in a semi-arid system where soil moisture is often the limiting factor. Furthermore, it has been observed from the ensemble of future climates, that vegetation productivity can have long-term averages significantly different, for similar long-term precipitation amounts. This points to emphasize the role of precipitation structure in controlling vegetation dynamics. Inter-annual and intra-annual variations of precipitation can be indeed of paramount importance. Further research is required to investigate this simulated behavior.

- The results obtained for the control scenario simulation in the distributed domain have spatially averaged quantities similar to the point scale simulation. In the future scenario this similarity is weaker. In the latter major droughts lead deciduous vegetation in unfavorable topographic zones to die. This entails considerable differences with the point scale application. The distributed application highlights the significant larger amount of runoff in the future and how the recharge to deeper soil layers could diminish as a consequence of a drier soil. The larger atmospheric CO_2 concentration has a positive effect on vegetation productivity in zones where soil moisture is available due to re-infiltration following local runoff-runon effects. In the remaining areas soil moisture stress overcomes the positive effect of CO_2. The overall results of these two combined

mechanisms is the reinforcing of a banded vegetation pattern in the predicted future. Heterogeneity in hydrological fluxes is increased by the concentration of vegetation in convergent topography and by its rarefication in upslope areas.

Appendix A

APPENDIX CHAPTER TWO

A.1 Rainfall disaggregation

High resolution precipitation data are often required for practical design, e.g., urban drainage network design, or for accurate simulations of hydrological processes. Typically, high resolution rainfall data are rare. Therefore, stochastic simulation tools to disaggregate rainfall records or to generate new rainfall series with statistical properties similar to the observed ones are required. Rainfall simulation models, especially point process, as the Neyman-Scott Rectangular Pulse are widely discussed in Section 2.3.1. The focus here is concentrated in rainfall disaggregation techniques that use scale invariance theory (multifractality) to generate synthetic traces of high resolution rainfall from rainfall observed (or generated) at a coarser resolution. The utility of introducing a rainfall disaggregator is related to the possibility to force some components of the hydrological model described in Chapter 4 with rainfall at very fine temporal resolutions. For instance, the simulation of processes such as infiltration (Section 4.7.1), soil sealing (Section 4.7.2), or erosion (Section 4.6.4) would benefit from sub-hourly rainfall inputs. Furthermore, the rainfall disaggregator can be used in conjunction with the hourly weather generator, AWE-GEN, providing a tool able to simulate rainfall characteristics from inter-annual to sub-hourly timescales.

In the last three decades a substantial body of literature has dealt with the topic of rainfall disaggregation, mainly using multiplicative cascades to generate simple fractal and multifractal rainfall fields and time series (*Schertzer and Lovejoy*, 1987; *Gupta and Waymire*, 1993; *Over and Gupta*, 1994, 1996; *Olsson*, 1998; *Deidda*, 2000; *Menabde and Sivapalan*, 2000; *Veneziano and Iacobellis*, 2002; *Veneziano et al.*, 2002; *Onof et al.*, 2005; *Molnar and Burlando*, 2005; *Veneziano et al.*, 2006; *Gaume et al.*, 2007; *Rupp et al.*, 2009). Despite the major attention on multiplicative cascades, different techniques have been also introduced to disaggregate rainfall (*Koutsoyiannis and Onof*, 2001; *Koutsoyiannis et al.*, 2003; *Onof et al.*, 2005). See *Koutsoyiannis* (2003b) for a review. In the follow only rainfall disaggregation methods based on multiplicative random cascades are discussed.

A.1.1 Random cascade dissagregation model

Discrete multiplicative random cascade models distribute mass on successive regular subdivisions of an interval in a multiplicative manner (*Schertzer and Lovejoy*, 1987; *Gupta and Waymire*, 1993; *Over and Gupta*, 1994, 1996; *Molnar and Burlando*, 2005; *Gaume et al.*, 2007; *Rupp et al.*, 2009). The rainfall pulse, R_0 $[mm]$, occurring over a time interval T is divided among a number of smaller intervals of equal size. The number of subintervals, b, is known as the branching number. This method assumes that the amount of rain falling in the b subintervals of a given interval is determined by multiplying the interval rainfall R_0 by a dimensionless cascade weight, W $[-]$. After n levels of subdivision, totally b^n intervals of width T/b^n are created. The dimensionless scale, λ, can be defined as the ratio between the maximum scale intervals and the intervals on the cascade (*Gupta and Waymire*, 1993; *Over and Gupta*, 1994, 1996; *Molnar and Burlando*, 2005). Thus, at level n, $\lambda = b^{-n}$ and at the level 0, $\lambda = 1$.

The distribution of mass occurs via a multiplicative process through all levels, n, of the cascade, so that the mass in subinterval i at level n is:

$$R_{i,n} = R_0 \prod_{j=1}^{n} W_j(i)\,, \tag{A.1}$$

where $i = 1, 2, ..., b^n$, R_0 is the rainfall depth at $n = 0$, and W_j are the cascade weights (*Gaume et al.*, 2007; *Rupp et al.*, 2009). The basic structure of the discrete multiplicative random cascade model is illustrated in Figure A.1, with $b = 2$, branching number, and $n = 0, 1, 2$.

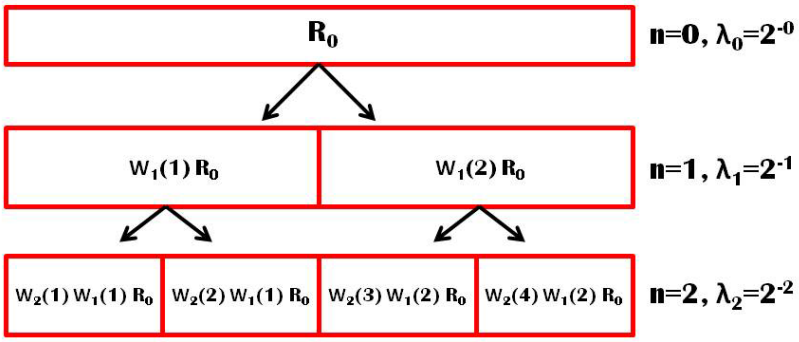

Figure A.1: Graphical representation of a two branches multiplicative random cascade process.

Multiplicative random cascades can be constructed so that the weights of each branch of a cascade sum to 1 only on the average (canonical cascade), or so that they sum to exactly one in each split (microcanonical cascade) (*Schertzer and Lovejoy*, 1987). In the microcanonical case, the weights are complementary. This implies that where there are two branches, $W_1 = W$ and $W_2 = 1 - W$, where W is a random variable $\in [0, 1]$. Both methods have been proposed in literature. Examples of

canonical models are given by *Gupta and Waymire* (1993); *Over and Gupta* (1994, 1996); *Onof and Townend* (2004); *Onof et al.* (2005); *Molnar and Burlando* (2005). Microcanonical cascade models are described in *Olsson* (1998); *Menabde and Sivapalan* (2000); *Molnar and Burlando* (2005); *Paulson and Baxter* (2007); *Gaume et al.* (2007).

Properties of the cascade generator, W, for the canonical case, can be generally estimated from the moment scaling behavior across scales (*Gupta and Waymire*, 1993; *Over and Gupta*, 1996; *Molnar and Burlando*, 2005; *Gaume et al.*, 2007; *Sivakumar and Sharma*, 2008). The statistical moment, $M(\lambda, q)$, as a function of scale, λ, and moment order, q, is defined as $M(\lambda) = \sum_i R(i,\lambda)^q$, where the summation is over i intervals of aggregated precipitation depth, $R(i,\lambda)$, at scale λ. For a scaling field $M(\lambda, q)$ behaves as:

$$M(\lambda, q) \sim \lambda^{-\tau(q)}\,, \tag{A.2}$$

where $\tau(q)$ may be regarded as a characteristic function of the scaling behavior, and is given by the slope of the log $M(\lambda, q)$ versus log λ plot. Such an analysis should be limited to the analysis of lower moments ($q \leq 4$) because the higher empirical moments can be poor estimators of the true moments (*Onof et al.*, 2005; *Gaume et al.*, 2007). If $\tau(q)$ versus q is a straight line, the time series exhibits mono-scaling. If $\tau(q)$ versus q is a convex function, then the time series exhibits multiscaling (*Molnar and Burlando*, 2008; *Sivakumar and Sharma*, 2008). Closed form solutions for $\tau(q)$ exist for some discrete multiplicative random cascades (*Gupta and Waymire*, 1993; *Molnar and Burlando*, 2005; *Gaume et al.*, 2007). An example of the scaling behavior of a rainfall time series is shown in Figure A.2, where the moment scaling relationship is calculated for different q (Figure A.2a) and the $\tau(q)$ function exhibits a multiscaling behavior, well approximated by the Mandelbrot-Kahane-Peyriere (MKP) function (Figure A.2b) (*Over and Gupta*, 1994; *Molnar and Burlando*, 2005).

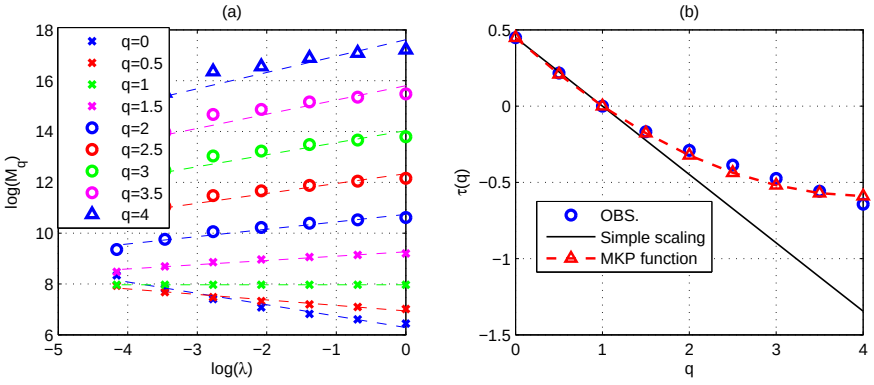

Figure A.2: Moment scaling relationships (a), and the $\tau(q)$ function compared with simple scaling and Mandelbrot-Kahane-Peyriere (MKP) function (b). Results are obtained with observed rainfall at Lucky Hills (AZ) for a ten years (1999-2009) period and aggregation time 1 minute.

Parameters of canonical cascade generator, such as the intermittent lognormal β-model (*Gupta and Waymire*, 1993; *Over and Gupta*, 1994, 1996; *Molnar and Burlando*, 2005), or the log-Poisson cascade model (*Onof and Townend*, 2004; *Onof et al.*, 2005; *Gaume et al.*, 2007; *Sivakumar and Sharma*, 2008) are estimated from the $\tau(q)$ function.

In microcanonical generator the cascade weights, W, are estimated from the empirical breakdown (or partition) distribution. The breakdown distribution is calculated as the ratio between the rainfall depth at two successive scales λ and $\lambda\, b$. In a single cascade subdivision is:

$$W(\lambda, i) = \frac{R(\lambda, i)}{R(\lambda\, b, j)}\,, \tag{A.3}$$

where the two intervals i are completely contained in j. By definition, W is bounded between 0 and 1, and the Probability Density Function (PDF), $f(W)$, may vary between scales (*Menabde and Sivapalan*, 2000). The relative frequencies, or probabilities, that the weights W equaled 0, 1, 0 or 1, or not 0 or 1, are successively calculated. The weights that are equal to 0, 1, 0 or 1, and not 0 or 1, are denoted by W_0, W_1, W_{01} and W_x, respectively. The corresponding probabilities of each of these subsets of W are denoted as P_0, P_1, P_{01}, and P_x. Parameters of a symmetrical microcanonical cascade generators are computed starting from the empirical values of P_{01}, or P_x, and from the distribution of W_x (*Molnar and Burlando*, 2005; *Paulson and Baxter*, 2007; *Rupp et al.*, 2009).

In this study, a random cascade microcanonical model is preferred because it conserves mass exactly at each branch. This is important for hydrological applications. It allows, for instance, to disaggregate 5-minutes rainfall from observed hourly values preserving the total mass at each hour. Furthermore, the performances of the used microcanonical model (Section A.1.2) have been compared against two different canonical cascade generators. The accuracy of the results of the microcanonical model is generally superior or comparable for several rainfall statistical properties (results not shown). This agrees well with conclusions from other studies (*Gaume et al.*, 2007).

A.1.2 Microcanonical model

The used discrete multiplicative random cascade is based on the studies of *Menabde and Sivapalan* (2000); *Molnar and Burlando* (2005). The cascade generator, W, is a random variable, which is constrained in a way that in every subdivision into b subintervals at level n, the model preserves mass exactly. The distribution of W in this case is identical to that of the breakdown (or partition) coefficients (*Menabde and Sivapalan*, 2000). Intermittency in the microcanonical model is preserved by accounting for the probability P_{01}. Assuming symmetry in the breakdown coefficients, the microcanonical model disaggregates every nonzero rainfall amount in the interval j at scale $n-1$ into $b=2$ intervals (i and $i+1$) at scale n. In this case, two situations can occur. First, the intermittency emerges in one interval only at

the scale n with probability P_{01}. Second, the intermittency does not emerge, and both intervals i and $i+1$ have W_x different from 0 and 1. A particularly suitable probability density function for W_x under the symmetric case is the Beta distribution with the parameter a governing the variance of W_x (*Menabde and Sivapalan*, 2000; *Molnar and Burlando*, 2005):

$$f(W_x) = \frac{1}{\beta(a)} W_x^{a-1}(1-W_x)^{a-1}\,, \tag{A.4}$$

where $\beta(a)$ is the Beta function. The distribution has a mean $E(W_x) = 0.5$ and variance $\sigma^2(W_x)$. For $a = 1$, this distribution is exactly uniform; for $a > 1$, it is bell-shaped symmetrically around $E(W_x)$. The parameter a can be obtained by numeric optimization fitting several moments (*Paulson and Baxter*, 2007) or fitting only the second moment:

$$a = \frac{1}{8\sigma^2(W_x)} - 0.5\,. \tag{A.5}$$

The intermittency parameter of the microcanonical model (i.e., the probability P_{01}) and the distribution parameter, a, of the cascade generator are estimated from the empirical breakdown coefficients. The probability P_{01} that one of the intervals in disaggregation is dry and the Beta parameter, a, are computed between scales $n-1$ and n. The P_{01} values estimated for scales between 16 $[h]$ ($n = 0$) and 15 $[min]$ ($n = 6$) are shown starting from 1 minute observed precipitation (Figure A.3a). The distribution parameter a of the cascade generator at the same time scales is shown in Figure A.3b.

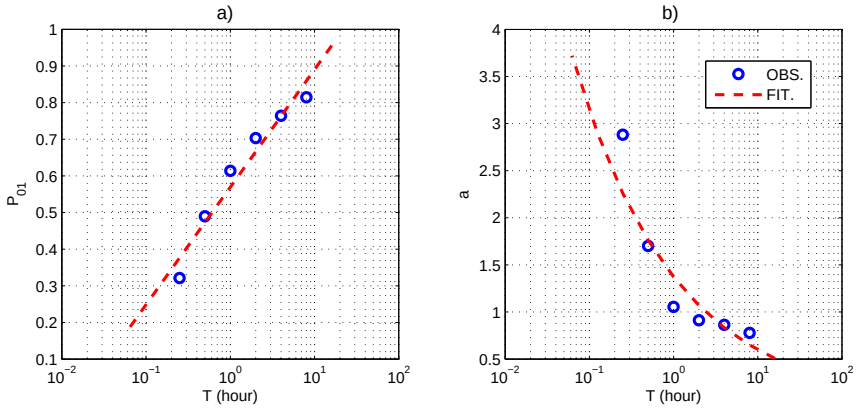

Figure A.3: Parameters of the microcanonical model. a.) Probability that the cascade weight, W, is 0 or 1, P_{01}, against the time scale, T. The solid circles indicate the time scales over which the model disaggregates rainfall, and the dashed line is a fitted logarithmic function. b.) Beta distribution parameter, a, for the weights, W_x, against the time scale, T. The open circles indicate the time scales over which the model disaggregates rainfall, and the dashed line is a fitted power law. The time scale, T, refer to the scale, n, in the breakdown $n-1 \rightarrow n$. Results are obtained with observed rainfall at Lucky Hills (AZ) for a ten years (1999-2009) period and aggregation time 1 minute.

The simplest random cascade is the one in which the weights, W, are assumed

independent and identically distributed both in time and across all cascade levels (*Rupp et al.*, 2009). Unfortunately, this is not the case in practice. The cascade weights are strongly dependent on time scale, rainfall intensity, seasonality, etc, (*Menabde and Sivapalan*, 2000; *Molnar and Burlando*, 2005, 2008; *Rupp et al.*, 2009). Here, only the scale dependance is accounted for fitting scale-dependent behavior with a logarithmic function for P_{01}, and with a power law for a:

$$P_{01}(T) = P_{01}^0 + \kappa \ln T\,, \tag{A.6}$$

$$a(T) = a_0 T^{\gamma}\,, \tag{A.7}$$

where the time scale T refers to the temporal resolution at which disaggregation is occurring at any level within the cascade, and P_{01}^0, κ, a_0, and γ, are constant parameters (*Menabde and Sivapalan*, 2000; *Paulson and Baxter*, 2007; *Rupp et al.*, 2009). Note that with increasing n, i.e., finer scales, it is possible to observe a substantial decrease in the variance of the cascade generator W_x (high a) and a smaller probability that intermittency will occur (Figure A.3).

A.1.3 Results

The rainfall disaggregation method described in the previous subsections is tested with three high resolutions time series of rainfall. Two located in Tuscany,(Italy), Livorno and Firenze Ximeniano stations where 24 years (1962-1986) of 5 min rainfall data are available, and one in Arizona (USA), Lucky Hills, where ten years (1999-2009) of 1 minute rainfall is available. Results are shown only for Lucky Hills. The accuracy for the other stations is generally superior. The rainfall disaggregation parameters P_{01}^0, κ, a_0, and, γ, are estimated using the breakdown distributions for scales between 16 $[h]$ and 15 $[min]$ (Figure A.3). Subsequently, starting from the observed rainfall aggregated at 1 $[h]$, a disaggregation to 3.75 $[min]$ is realized with the proposed method. The 3.75 $[min]$ simulated precipitation is then re-interpolated to obtain a 5 $[min]$ time series. The main scope of the rainfall disaggregator is indeed to generate 5 $[min]$ rainfall time series from hourly values. Hourly rainfalls can be the outcome of a weather generator simulation or observed values. It must be remarked that theoretically the rainfall disaggregation parameters can be estimated fitting only time scales larger than 1 hour, i.e. $T \geq 1$ $[h]$. Equation (A.6) and (A.7) can be successively used to extrapolated the value of $a(T)$ and $P_{01}(T)$ at shorter time scales. For instance, in the proposed example, a 3.75 $[min]$ disaggregation is realized using data aggregated at 15 $[min]$. The finer resolutions (1 minute) available are used only to test the results. Generally, using time scales $T \geq 1$ $[h]$ can worsen the performances of the rainfall disaggregation models but it does not require sub-hourly rainfall data to estimate the parameters.

Figure A.4a shows the comparison between observed and simulated 5 $[min]$ survival functions. The frequency of non precipitation (not shown) and the distribution of rainfall spells with an exceeding probability larger than 10^{-5} is reproduced well. Figure A.4b shows that also the simulation of the fractions of time with precipitation

larger than a given threshold is accurate. Note, that obviously above one hour the observed and simulated values are the same, because the disaggregation starts from hourly observed rainfall.

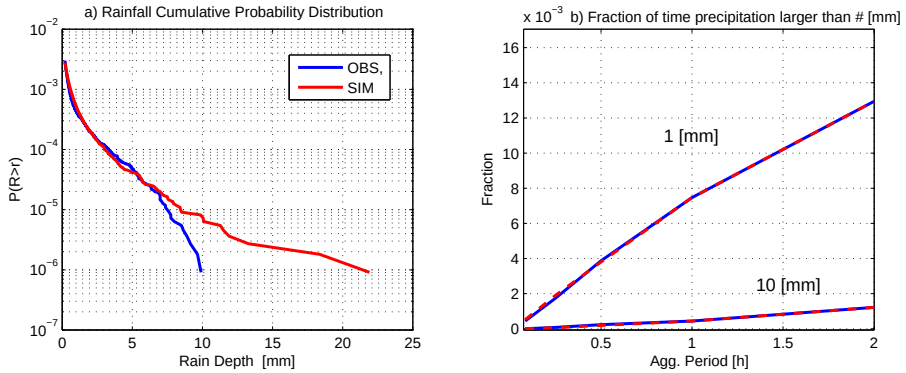

Figure A.4: A comparison between observed (blue) and simulated (red) cumulative distribution function of 5-min rainfall amounts from observations and a simulation with the microcanonical model (a). Fractions of time with precipitation larger than a given threshold 1, 10 $[mm]$ at different aggregation periods. Results obtained with observed rainfall at Lucky Hills (AZ) for a ten years (1999-2009) period and aggregation time 1 minute.

Rainfall extremes (Figure A.5a and A.5b) are generally overestimated. Although, this overestimation cannot be acceptable in engineering design, it becomes much less important when the scope is to use high resolution rainfall to force specific components of the hydrological model (Chapter 4). It must be noted that the simulations realized for the other stations, Livorno and Firenze Ximeniano compare much better with observations, including the simulation of extreme rainfalls. This is probably due to the longer time period available to estimate the parameters or to a different accuracy in recording rainfall.

It can be concluded that the performance obtained with the rainfall disaggregator are enough satisfactorily to use its results as forcing of specific components of the hydrological model. Such good performances are probably related to the small range of scales simulated, 1 $[h]$ to 5 $[min]$. Focusing in a narrow interval of aggregation periods, results in a simpler scaling behavior of rainfall and preserves the validity of the model parameters. This provides an advantage in comparison to typical applications of random cascade dissagregation models that encompass wider ranges of scale (*Molnar and Burlando*, 2005; *Rupp et al.*, 2009).

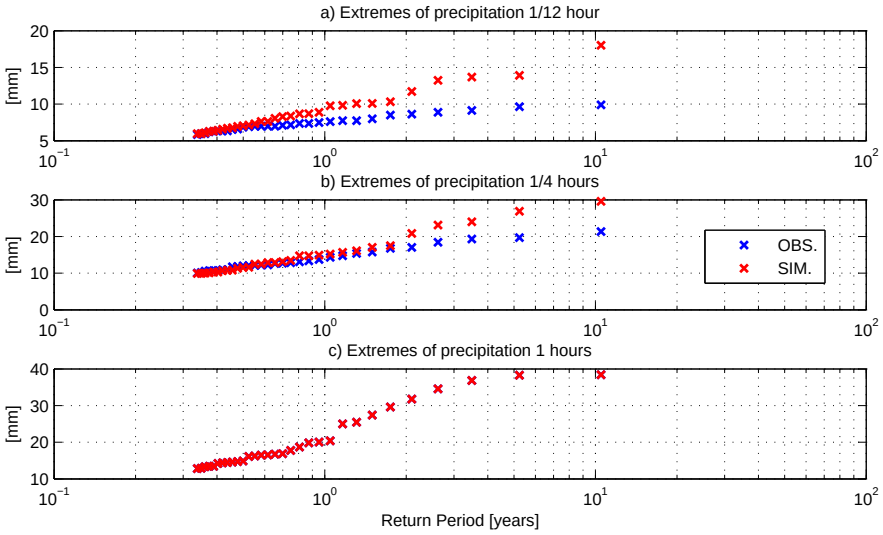

Figure A.5: A comparison between the observed (red crosses) and simulated values of extreme precipitation (blue crosses) at (a) 5 minutes, (b) 15 minutes, and (c) 1 hour aggregation periods. Note that for 1 hour the simulated and observed values are the same. Results obtained with observed rainfall at Lucky Hills (AZ) for a ten years (1999-2009) period and aggregation time 1 minute.

A.2 Statistical properties of the *NSRP* model

Referring to Section 2.3.1 the coefficient $A(h,l)$ and $B(h,l)$ necessary to calculate the second moment of the Neymann-Scott rectangular pulse model are defined in *Cowpertwait* (1998) as:

$$\begin{aligned} A(h,l) &= h\eta + e^{-\eta h} - 1\,, \qquad \text{if } l = 0\,, \\ A(h,l) &= 0.5\left(1 - e^{-\eta h}\right)^2 e^{-\eta h(l-1)}\,, \quad \text{if } l > 0\,, \end{aligned} \tag{A.8}$$

$$\begin{aligned} B(h,l) &= h\beta + e^{-\beta h} - 1\,, \qquad \text{if } l = 0\,, \\ B(h,l) &= 0.5\left(1 - e^{-\beta h}\right)^2 e^{-\beta h(l-1)}\,, \quad \text{if } l > 0\,, \end{aligned} \tag{A.9}$$

where h is the time aggregation and $l \geq 0$ is a integer lag of the autocorrelation. The third moment, $\xi_h = E\{[Y_h - E\{Y_h\}]^3\}$, is also defined in *Cowpertwait* (1998):

$$\begin{aligned} \xi_h &= E\{[Y_h - E\{Y_h\}]^3\} = 6\lambda\mu_c\, E\{X^3\}(\eta h - 2 + \eta h e^{-\eta h} + 2e^{-\eta h})/\eta^4 \\ &\quad +3\,\lambda E\{X\}E\{X^2\}E\{C(C-1)\}f(\eta,\beta,h)/[2\eta^4\beta(\beta^2-\eta^2)^2] \\ &\quad +\lambda E\{X\}^3 E\{(C^2-C)(C-2)\}g(\eta,\beta,h) \\ &\quad /[2\eta^4\beta(\eta^2-\beta^2)(\eta-\beta)(2\beta+\eta)(\beta+2\eta)]\,, \end{aligned} \tag{A.10}$$

where the function $f(\eta,\beta,h)$ and $g(\eta,\beta,h)$ are listed below:

$$\begin{aligned} f(\eta,\beta,h) &= -2\eta^3\beta^2 e^{-\eta h} - 2\eta^3\beta^2 e^{-\beta h} + \eta^2\beta^3 e^{-2\eta h} + 2\eta^4\beta e^{-\eta h} \\ &\quad +2\eta^4\beta e^{-\beta h} + 2\eta^3\beta^2 e^{-(\eta+\beta)h} - 2\eta^4\beta e^{-(\eta+\beta)h} - 8\eta^3\beta^3 h + 11\eta^2\beta^3 - 2\eta^4\beta \\ &\quad +2\eta^3\beta^2 + 4\eta\beta^5 h + 4\eta^5\beta h - 7\beta^5 - 4\eta^5 + 8\beta^5 e^{-\eta h} - \beta^5 e^{-2\eta h} \\ &\quad -2h\eta^3\beta^3 e^{-\eta h} - 12\eta^2\beta^3 e^{-\eta h} + 2h\eta\beta^5 e^{-\eta h} + 4\eta^5 e^{-\beta h}\quad , \end{aligned} \tag{A.11}$$

$$\begin{aligned} g(\eta,\beta,h) &= 12\eta^5\beta e^{-\beta h} + 9\eta^4\beta^2 + 12\eta\beta^5 e^{-\eta h} + 9\eta^2\beta^4 + 12\eta^3\beta^3 e^{-(\eta+\beta)h} \\ &\quad -\eta^2\beta^4 e^{-2\eta h} - 12\eta^3\beta^3 e^{-\beta h} - 9\eta^5\beta - 9\eta\beta^5 - 3\eta\beta^5 e^{-2\eta h} \\ &\quad -\eta^4\beta^2 e^{-2\beta h} - 12\eta^3\beta^3 e^{-\eta h} + 6\eta^5\beta^2 h - 10\eta^3\beta^4 h + 6\eta^2\beta^5 h \\ &\quad -10\eta^4\beta^3 h + 4\eta\beta^6 h - 8\beta^2\eta^4 e^{-\beta h} + 4\beta\eta^6 h + 12\beta^3\eta^3 \\ &\quad -8\beta^4\eta^2 e^{-\eta h} - 6\eta^6 - 6\beta^6 - 2\eta^6 e^{-2\beta h} - 2\beta^6 e^{-2\eta h} \\ &\quad +8\eta^6 e^{-\beta h} + 8\beta^6 e^{-\eta h} - 3\beta\eta^5 e^{-2\beta h}\,. \end{aligned} \tag{A.12}$$

The probability that an arbitrary interval of length h is dry, $\Phi(h) = P(Y_h = 0)$, was derived from *Cowpertwait* (1991); *Cowpertwait et al.* (1996). It is here modified to take into account the use of the Geometrical distribution instead of the Poisson distribution for the generation of the random number of cells:

$$\begin{aligned} \Phi(h) &= \exp\Big(-\lambda\, h + \lambda\, \beta^{-1}\mu_c^{-1}[1 - e^{(-\mu_c + \mu_c e^{-\beta h})}] \\ &\quad -\lambda \int_0^\infty \big[1 - p_h(t)\big]dt\Big)\,, \end{aligned} \tag{A.13}$$

where $p_h(t)$ is function of h, β, η and μ_c:

$$p_h(t) = \left[e^{-\beta(t+h)} + 1 - (\eta e^{-\beta t} - \beta e^{-\eta t})/(\eta - \beta)\right] \cdot \exp\left[-\mu_c \beta (e^{-\beta t} - e^{-\eta t})/(\eta - \beta) - \mu_c e^{-\beta\, t} + \mu_c e^{-\beta(t+h)}\right]. \quad \text{(A.14)}$$

A.3 Cloud cover parameter estimation

This description of cloud cover parameter estimation follows *Ivanov et al.* (2007). The parameters used by the cloud cover model are M_0, σ_m^2, $\rho_m(1)$, $\gamma = \varsigma$, J_1, a, and b.

The existence of a stationary interstorm fairweather cloud cover process is the central assumption of the model. The identification of sequences of the fairweather periods in series of meteorological data therefore becomes essential. The methodology proposed by *Curtis and Eagleson* (1982) employs an iterative approach that uses records of the total cloud cover during periods between successive precipitation events. The essence of the method is in estimating the mean value of cloud cover for some sub-region Δt within an interstorm period (Figure A.6).

Each interstorm period of length $T_{is} = \Delta t_0$ $[h]$ (Figure A.6) is considered to be constrained by the last hour of the first rainfall event and by the first hour of the following rainfall event. By successively eliminating one hour from both ends of any given interstorm period ($\Delta\tau_1 = 1$ *hour*, $\Delta\tau_2 = 2$ *hours*, ...), a number of sub-regions, not exceeding in total $(T_{is}/2 - 1)$, can be defined for each interstorm period. For any given sub-region, Δt_k, corresponding to k number of eliminated hours from each end (Figure A.6), a mean value of the cloud cover is estimated over all interstorm periods in the considered precipitation record whose duration exceeds $2k$ hours. Since $k \in [0, T_{is\,\max}/2 - 1]$, where $T_{is\,\max}$ is the maximum duration of an interstorm period in the considered record, a vector of the mean values of cloud cover of length $(T_{is\,\max}/2 - 1)$ is obtained.

Curtis and Eagleson (1982) argue that with the increasingly larger number of eliminated hours, the estimated mean value stabilizes, reaching some constant, or the fairweather mean value, M_0. The number of hours, T_r, eliminated from both ends of all interstorm periods (whose duration exceeds $2T_r$) after which there is no significant change in the mean cloudiness value, is considered to be the length of the *transition* period. Consequently, a necessary condition for an interstorm period to contain a fairweather cloud cover sequence is to be of duration $T_{is} > 2T_r$ $[h]$.

A note has to be made regarding a particular case of sub-regions within certain interstorm periods for which the described approach fails. Sometimes, passing atmospheric precipitation systems do not necessarily result in rainfall at a given location. However, the cloud cover process is obviously non-stationary during such periods and the estimated mean value can be significantly affected. The discussed approach cannot identify such periods, which would, perhaps, require auxiliary information about cloud vertical structure and spatial information about the precipitation process. Nonetheless, the procedure is efficient for most of interstorm periods and

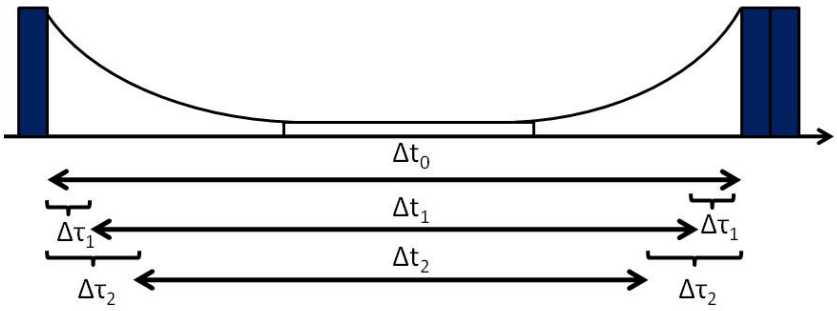

Figure A.6: An illustration of the procedure used to identify the *fairweather* cloud cover period.

results in reasonable estimates of the transition period as long as the above situation does not occur often. Caution has to be taken when interpreting the results of this method. Figure A.7 illustrate the outlined procedure.

For the selected values of T_r, both the empirical and observed transition function, $J(t)$, are plotted in Figure A.8. Some differences in comparison to the work of *Ivanov et al.* (2007) are discernible. The exponential form of $J(t)$ fits the observed cloud cover transition quite well in many months. The determination of the critical length, T_R, of the transition period in *Ivanov et al.* (2007) was left to the subjectivity of the user. T_R, indeed, is the length after which the fair weather region could be identified. In AWE-GEN, T_R is identified with an objective criterion. A threshold on the derivative of the smoothed mean cloud cover, $\widetilde{E\{N(t)\}}$, defines the begin of the fair weather region (Figure A.7).

Once T_r is established, the fairweather sequences contained in the interstorm periods of length $T_{is} > 2T_r$ are combined in a new time series containing only fairweather cloud cover values. For these series, created for each month or the entire period of analysis, the parameters M_0, σ_m^2, $\rho_m(1)$ and J_1 are determined by conventional methods. The parameter $\gamma = \varsigma$, is estimated according to the equation proposed by *Curtis and Eagleson* (1982) (see also Section 2.4):

$$\gamma = \frac{4.61}{T_r}\,. \tag{A.15}$$

The parameters a and b are estimated by analyzing random deviates, $\varepsilon(t)$, which are computed from the observed cloud cover series by inverting equation (2.11) and (2.14). The estimation of $\varepsilon(t)$ is conditioned by the cloud cover at time $(t-1)$. Therefore, 11 vectors of deviates are composed from the cloud cover records in the different months. Each vector corresponds to one of the values of $N(t-1)$: 0.0, 0.1, ..., 1.0. For each $N(t-1)$, the corresponding distribution of deviates is approximated by the *Beta* distribution with parameters a and b estimated from these deviates. The mean and standard deviation of the PDFs are essentially constant throughout the entire range of $N(t-1)$ values, the skewness of the deviates varies significantly, changing its sign from positive to negative. As can also be seen in

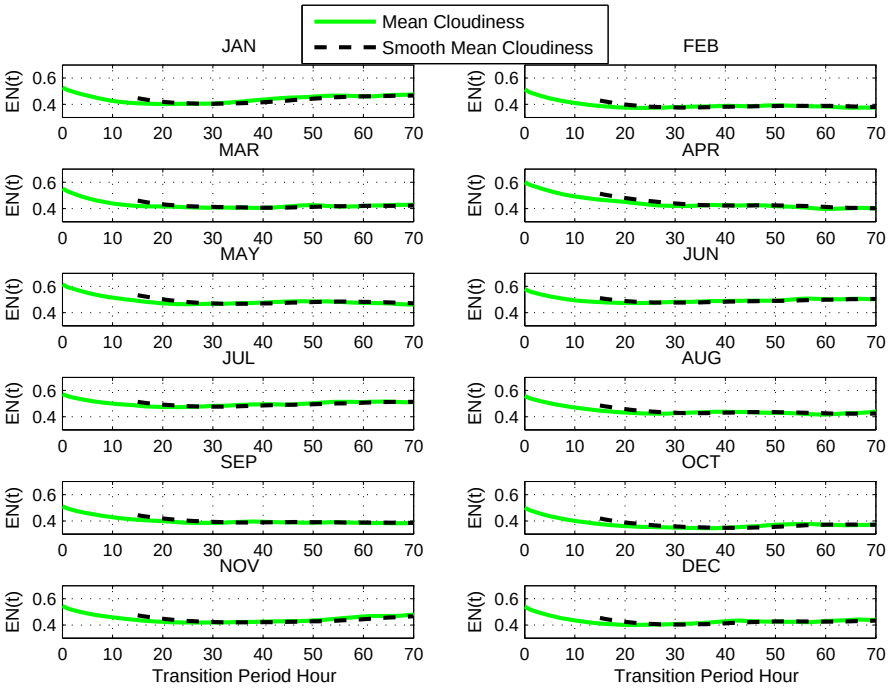

Figure A.7: Estimated mean cloud cover value $E\{N(t)\}$ (continuous line) and the smoothed function $\widetilde{E\{N(t)\}}$ (dashed line) as a function of the length of transition period.

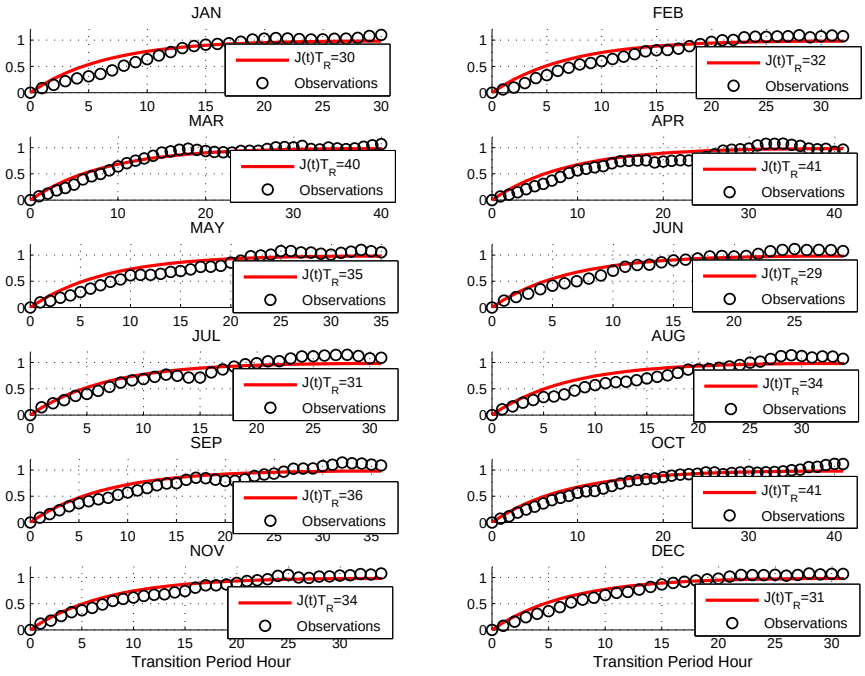

Figure A.8: Analytical (continuous line) and observed (circles) transition functions $J(t)$ corresponding to the estimated transition period lengths.

Figure A.9, the probability density functions of the *Beta* distribution, corresponding to the 11 $N(t-1)$ have significant different shapes. Moreover, since the variability is quite substantial for most months (for all stations), the values of a and b are estimated on a monthly basis.

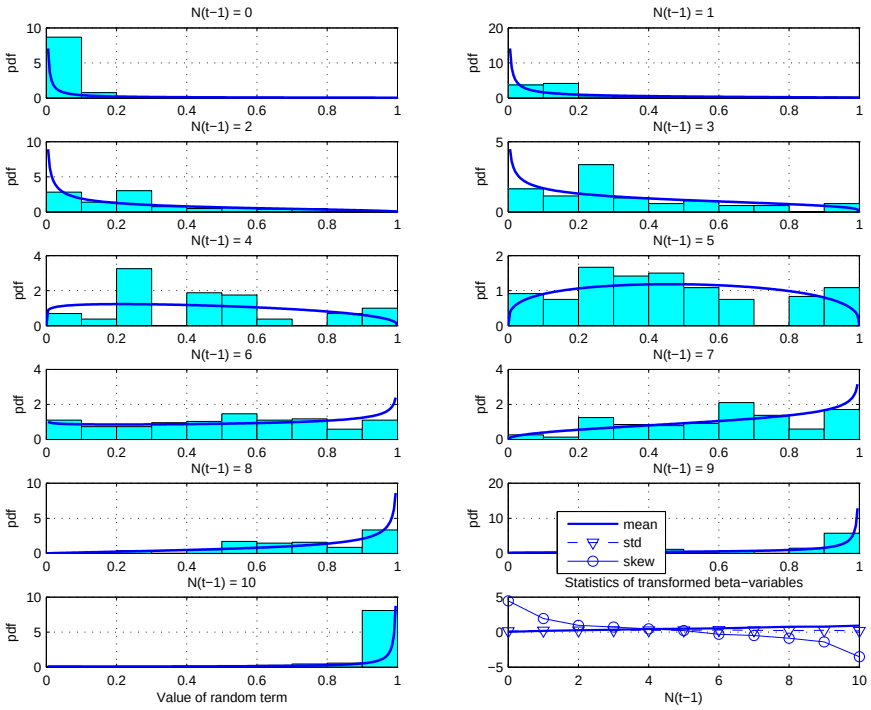

Figure A.9: An histogram of deviates $\varepsilon(t)$ in the cloud cover model and the corresponding probability density function (solid line) approximated with the *Beta* distribution. The cloud cover $N(t-1)$ for the month of *November* is given on a [0, 10] basis.

A.4 Definition of sun variables

Equations to define solar variables are taken from the auxiliary material of *Ivanov et al.* (2007), with some adjustment concerning the limits of integration of solar hour angle, altitude and azimuth.

Several variables are introduced that define the Sun's position with respect to a location on Earth. The declination of the Sun, δ $[rad]$, i.e., the angular distance between the celestial equator plane and the Sun, measured from the former (and positive when the Sun lies north of the equator) and along the hour circle (*Eagleson*, 2002) is defined as:

$$\delta = \frac{23.45\pi}{180} \cos\left[\frac{2\pi}{365}(172 - J_{Day})\right] . \tag{A.16}$$

The angular distance between the planes of the meridian and the Sun's hour circle (*Eagleson*, 2002) is known as the hour angle of the Sun, $\tau_S(t)$ $[rad]$:

$$\tau_S(t) = \frac{15\pi}{180}(t + 12 - \Delta t_{SL}) , \qquad \text{if} \qquad t < 12 + \Delta t_{SL} , \tag{A.17}$$

$$\tau_S(t) = \frac{15\pi}{180}(t - 12 - \Delta t_{SL}) , \qquad \text{if} \qquad t > 12 + \Delta t_{SL} , \tag{A.18}$$

where t $[h]$ is the standard time in the time zone of the observer counted from midnight and Δt_{SL} $[h]$ is the time difference between the standard and local meridian:

$$\Delta t_{SL} = \frac{\xi}{15} \left[\ 15|\Delta GMT| - |\Phi'|\ \right] , \tag{A.19}$$

where ΔGMT $[h]$ is the time difference between the local time zone and Greenwich Mean Time, Φ' $[angular\ degree]$ is the local longitude, and ξ is equal to -1 for west longitude and +1 for east longitude. The solar altitude, i.e., an angle of radiation with respect to an observer's horizon plane, h_S $[rad]$, is defined as

$$\sin h_S = \sin\Phi \sin\delta + \cos\Phi \cos\delta \cos\tau_S , \tag{A.20}$$

where Φ $[rad]$ is the local latitude. The mean value of solar altitude $h_{S,\,\Delta t}$ over a time interval Δt $[h]$ is often needed in practical applications. It is obtained integrating equation (A.20) in the interval $\Delta t = [t - t_{bef}]\,, [t + t_{aft}]$:

$$h_{S,\,\Delta t} = \int_{t-t_{bef}}^{t+t_{aft}} \arcsin[\sin h_S]\ dt , \tag{A.21}$$

where t_{bef} $[h]$ and t_{aft} $[h]$ are the backward and forward difference between the standard time in the time zone t $[h]$ and the limits of integration of the sun variables. Note the implicit dependence of h_S from the standard time within τ_S.

The Sun's azimuth ζ_S $[rad]$ is obtained from the "hour angle method" as the clockwise angle from north:

$$\zeta_S = \arctan\left(\frac{-\sin\tau_S}{\tan\delta\cos\Phi - \sin\Phi\cos\tau_S}\right) . \tag{A.22}$$

Note that also ζ_S should be integrated in the interval $\Delta t = [t - t_{bef}], [t + t_{aft}]$ to obtain the average value.

The sunrise time, $T_{H\,rise}$ [*local hour*], the sunset time, $T_{H\,set}$ [*local hour*], and the total day length D_{LH} [h] are also required in applications:

$$T_{H\,rise} = \frac{180}{15\pi}[2\pi - \arccos(-\tan\delta\tan\Phi)] - 12\,, \tag{A.23}$$

$$T_{H\,set} = \frac{180}{15\pi}\arccos(-\tan\delta\tan\Phi) + 12\,, \tag{A.24}$$

$$D_{LH} = \frac{360}{15\pi}\arccos(-\tan\delta\tan\Phi)\,. \tag{A.25}$$

A.5 Solution of the ODE for deterministic air temperature

Equation (2.17) in Section 2.5.1 is a first order differential equation, the solution to which can be found if the initial condition, i.e., the initial temperature, $\widetilde{T}(t^*)$, is given. *Curtis and Eagleson* (1982) provide the following equation:

$$\widetilde{T}(t) = \widetilde{T}(t^*)e^{-b_1(t-t^*)} + e^{-b_1 t}G(t,t^*)\,, \tag{A.26}$$

where:

$$\begin{aligned} G(t,t^*) &= b_0\int_{t^*}^{t} e^{b_1\tau}d\tau + b_2\int_{t^*}^{t} e^{b_1\tau}K(\tau)s(\tau)d\tau + \\ &\quad b_3\int_{t^*}^{t} e^{b_1\tau}K(\tau)r(\tau)d\tau + b_4 q(t-1)\int_{t^*}^{t} e^{b_1\tau}d\tau \\ &= I_1(t) + I_2(t) + I_3(t) + I_4(t)\,. \end{aligned} \tag{A.27}$$

By using the *full*, non-zero expressions for $s(t)$ and $r(t)$ (the system of equations 2.19) *Curtis and Eagleson* (1982) derived the following expressions for the terms of $G(t,t^*)$:

$$I_1(t) = b_0\int_{t^*}^{t} e^{b_1\tau}d\tau = \frac{b_0}{b_1}\left[e^{b_1 t} - e^{b_1 t^*}\right], \tag{A.28}$$

$$\begin{aligned} I_2(t) &= b_2\int_{t^*}^{t} e^{b_1\tau}K(\tau)s(\tau)d\tau \\ &= K(t)\,[\,K_2\,(e^{b_1 t} - e^{b_1(t-1)}) - K_3\,e^{b_1 t}\cos\frac{\pi t}{12} - K_4\,e^{b_1 t}\sin\frac{\pi t}{12} + \\ &\quad K_3\,e^{b_1(t-1)}\cos\frac{\pi(t-1)}{12} + K_4\,e^{b_1(t-1)}\sin\frac{\pi(t-1)}{12}\,] + I_2(t-1)\,, \end{aligned} \tag{A.29}$$

$$
\begin{aligned}
I_3(t) &= b_3 \int_{t^*}^{t} e^{b_1\tau} K(\tau) r(\tau) d\tau \\
&= K(t)\,[\, K_6\, e^{b_1 t} \sin\frac{\pi t}{12} - K_5\, e^{b_1 t} \cos\frac{\pi t}{12} - \\
&\quad K_6\, e^{b_1(t-1)} \sin\frac{\pi(t-1)}{12} + K_5\, e^{b_1(t-1)} \cos\frac{\pi(t-1)}{12}\,] + I_3(t-1) \qquad \text{(A.30)} \\
I_4(t) &= b_4 \int_{t^*}^{t} e^{b_1\tau} q(\tau) d\tau \;=\; \frac{b_4}{b_1} q(t-1)(1-e^{b_1}) e^{b_1 t} + I_4(t-1)\,,
\end{aligned}
\qquad \text{(A.31)}
$$

where

$$
\begin{aligned}
p &= \frac{\pi}{12}\,, \qquad K_1 = \frac{b_0}{b_1}\,, \qquad K_2 = \frac{b_2}{b_1}\sin\delta\sin\Phi\,, \\
K_3 &= \frac{b_1 b_2}{b_1^2 + p^2}\cos\delta\cos\Phi\,, \qquad K_4 = \frac{p b_2}{b_1^2 + p^2}\cos\delta\cos\Phi\,, \\
K_5 &= \frac{p^2 b_3}{b_1^2 + p^2}\cos\delta\cos\Phi\,, \qquad K_6 = \frac{p b_1 b_3}{b_1^2 + p^2}\cos\delta\cos\Phi\,.
\end{aligned}
\qquad \text{(A.32)}
$$

Equation (A.31) linearizes the integral $I_4(t)$ that contains $q(t)$, which is a non-linear function of the temperature, by using the value from the previous hour $q(t-1)$. Besides, the one-hour integration interval is considered short enough to allow variables $K(t)$ and $q(t-1)$ to be brought outside their respective integrals (equations A.29-A.31).

The full, non-zero expressions for $s(t)$ and $r(t)$ (the system of equations 2.19) were used to obtain the above general equations (A.29) - (A.30). Since $s(t)$ and $r(t)$ can be equal to zero during certain periods of the day, it can be seen that the integrals $I_2(t)$ and $I_3(t)$ may have different forms depending on time of the day. The ranges over which each form is valid are delimited by several critical times. *Curtis and Eagleson* (1982) identify five critical times: 1) t_0 is the value of t in local time corresponding to midnight in standard time; 2) t_R is the earliest standard hour that does not precede local sunrise $T_{H\,rise}$, ($t_R \geq T_{H\,rise}$); 3) t_{12} is the value of t at the earliest standard hour that does not precede local noon ($t_{12} \geq 12$); 4) t_S is the value of t at the earliest standard hour that does not precede local sunset, $T_{H\,set}$ ($t_S \geq T_{H\,set}$); 5) t_{23} is the value corresponding to 23.00 local standard time. The integrals $I_2(t)$ and $I_3(t)$ are evaluated according to the above time ranges using the system of equations (2.19), which leads to different forms for $G(t, t*)$.

A.6 Air temperature parameter estimation

The parameters of the air temperature component are: the regression coefficients b_i ($i = 0, 1, \ldots, 4$), $\overline{dT}_h$, $\sigma_{dT,h}$, and ρ_{dT}. The procedure of parameter estimation follows *Curtis and Eagleson* (1982). The same is described also in the auxiliary material of *Ivanov et al.* (2007).

According to *Curtis and Eagleson* (1982), equation (A.26) can be re-written to obtain:

$$\widetilde{T}(t) = e^{-b_1}\widetilde{T}(t-1) + e^{-b_1 t}G(t,t-1)\,. \tag{A.33}$$

The hourly temperature change, $Y(t) = T(t) - T(t-1)$, is obtained if temperature $T(t-1)$ is subtracted from both sides of equation (A.33). *Curtis and Eagleson* (1982) show that an equation for $Y(t)$ can be represented in the regression form:

$$Y(t) = a_0 + a_1 X_1(t) + \ldots + a_4 X_4(t)\,, \tag{A.34}$$

where the coefficients a_i-s ($i = 0,\, 1,\, \ldots,\, 4$) are:

$$\begin{aligned} a_1 &= e^{-b_1} - 1\,, \\ a_i &= -\frac{a_1}{b_1} b_i\,, \qquad i = 0, 2, \ldots, 4\,, \end{aligned} \tag{A.35}$$

and the predictors $X_i(t)$ are:

$$\begin{aligned} X_1(t) &= \widetilde{T}(t-1)\,, \\ X_2(t) &= \int_{t-1}^{t} K(\tau)s(\tau)d\tau\,, \\ X_3(t) &= \int_{t-1}^{t} K(\tau)r(\tau)d\tau\,, \\ X_4(t) &= q(t-1)\,. \end{aligned} \tag{A.36}$$

As above, the one-hour integration interval is considered to be short enough to allow variable $q(t-1)$ to be brought outside its integral. Similarly to the previous discussion, the terms $X_2(t)$ and $X_3(t)$ containing $s(t)$ and $r(t)$ have different form depending on time of the day. From a set of linear equations (A.34), the regression coefficients a_i-s ($i = 0,\, 1,\, \ldots,\, 4$) can be found with conventional methods. Once a_i-s ($i = 0,\, 1,\, \ldots,\, 4$) have been estimated, the regression parameters, b_i, can be easily obtained from (A.35). The b_i-s are estimated on a monthly basis.

Once the regression parameters have been estimated, equation (2.17) can be used to simulate the deterministic component of the hourly temperature model. Equation (2.17) is applied each day to compute temperatures for each hour starting from midnight ($t = 0$). The initial temperature, $\widetilde{T}(t^*)$, is taken as the deterministic temperature component estimated at 23 h of the previous day. According to (2.16), the difference between the observed and estimated deterministic temperature components defines the temperature random deviates. Consequently, series of deviates can be estimated for each period of interest, e.g., for each month, season, and also hour of the day. The parameters $\overline{dT}_h$, $\sigma_{dT,h}$, and ρ_{dT}, are obtained using conventional estimation techniques.

A.7 Clear sky radiation parameterizations

The transmittances in band $\Lambda 1$ and band $\Lambda 2$ required to estimate direct beam radiation at normal incidence, $R_{Bn,\Lambda}$, and the incedent diffuse irradiance, $R_{Dp,\Lambda}$, are calculated as in *Gueymard* (2008).

A.7.1 Direct beam irradiance

The ozone absorption transmittances, $T_{o,\Lambda}$, are:

$$\begin{aligned} T_{o,\Lambda 1} &= (1 + f_1\, m_O + f_2\, {m_O}^2)/(1 + f_3\, m_O)\,, \\ T_{o,\Lambda 2} &= 1.0\,, \end{aligned} \tag{A.37}$$

where m_O is the ozone absorption air mass and the other parameter are function of the ozone amount in atmospheric column, u_o $[cm]$:

$$\begin{aligned} f_1 &= u_o(10.979 - 8.5421 u_o)/(1 + 2.0115 u_o + 40.189 u_o^2)\,, \\ f_2 &= u_o(-0.027589 - 0.005138 u_o)/(1 - 2.4857 u_o + 13.942 u_o^2)\,, \\ f_3 &= u_o(10.995 - 5.5001 u_o)/(1 + 1.6784 u_o + 42.406 u_o^2)\,. \end{aligned} \tag{A.38}$$

The nitrogen dioxide absorption transmittances, $T_{n,\Lambda}$, are:

$$\begin{aligned} T_{n,\Lambda 1} &= \min\left[1, (1 + g_1\, m_W + g_2\, m_W^2)/(1 + g_3\, m_W)\right], \\ T_{n,\Lambda 2} &= 1.0\,, \end{aligned} \tag{A.39}$$

where m_W is water vapor air mass and the other parameters are function of the nitrogen dioxide amount in atmospheric column, u_n $[cm]$:

$$\begin{aligned} g_1 &= (0.17499 + 41.654 u_n - 2146.4 u_n^2)/(1 + 22295.0 u_n^2)\,, \\ g_2 &= u_n(-1.2134 + 59.324 u_n)/(1 + 8847.8 u_n^2)\,, \\ g_3 &= (0.17499 + 61.658 u_n + 9196.4 u_n^2)/(1 + 74109.0 u_n^2)\,. \end{aligned} \tag{A.40}$$

The Rayleigh scattering transmittances, $T_{R,\Lambda}$, are:

$$\begin{aligned} T_{R,\Lambda 1} &= 1 + 1.8169\, m'_R - 0.033454\, m'^2_R)/(1 + 2.063\, m'_R + 0.31978\, m'^2_R)\,, \\ T_{R,\Lambda 2} &= (1 - 0.010394\, m'_R)/(1 - 0.00011042\, m'^2_R)\,, \end{aligned} \tag{A.41}$$

where $m'_R = (P_{atm}/P_{atm,\,0}) m_R$ is calculated from the Rayleigh scattering and uniformly mixed gas air mass, m_R, after correcting atmospheric pressure for the difference in pressures between the reference point, P_{atm} $[mbar]$, and sea level, $P_{atm,\,0} = 1013.25$ $[mbar]$. The equation to scale atmospheric pressure with elevation is $P_{atm}/P_{atm,\,0} = \exp\left[-g Z_{ref}/(R_d\, T_m)\right]$, with $g = 9.81$ $[m\ s^{-2}]$ acceleration of gravity, $R_d = 287.05$ $[J\ kg^{-1}; K^{-1}]$, air gas constant, T_m average value of air temperature between sea level and Z_{ref}, where Z_{ref} $[m]$ is the elevation of the reference point. Assuming on average $T_m = 288.15$ $[K]$ we have $P_{atm}/P_{atm,0} = \exp\left[-g Z_{ref}/8434.5\right]$.

The uniformly mixed gas absorption transmittances, $T_{g,\Lambda}$, are:

$$\begin{aligned} T_{g,\Lambda 1} &= (1 + 0.95885\, m'_R - 0.012871\, m'^2_R)/(1 + 0.96321\, m'_R + 0.015455\, m'^2_R)\,, \\ T_{g,\Lambda 2} &= (1 + 0.27284\, m'_R - 0.00063699\, m'^2_R)/(1 + 0.30306\, m'_R)\,. \end{aligned} \tag{A.42}$$

The water vapor absorption transmittances, $T_{w,\Lambda}$, are:

$$\begin{aligned} T_{w,\Lambda 1} &= (1 + h_1\, m_W)/(1 + h_2\, m_W)\,, \\ T_{w,\Lambda 2} &= (1 + c_1\, m_W + c_2\, m_W^2)/(1 + c_3\, m_W + c_4\, m_W^2)\,, \end{aligned} \tag{A.43}$$

where m_W is again the water vapor air mass and the other parameters are function of precipitable water in atmospheric column, w $[cm]$:

$$\begin{aligned} c_1 &= w(19.566 - 1.6506w + 1.0672w^2)/(1 + 5.4248w + 1.6005w^2)\,, \\ c_2 &= w(0.50158 - 0.14732w + 0.047584w^2)/(1 + 1.1811w + 1.0699w^2)\,, \\ c_3 &= w(21.286 - 0.39232w + 1.2692w^2)/(1 + 4.8318w + 1.412w^2)\,, \\ c_4 &= w(0.70992 - 0.23155w + 0.096514w^2)/(1 + 0.44907w + 0.75425w^2)\,, \\ h_1 &= w(0.065445 + 0.00029901w)/(1 + 1.2728w)\,, \\ h_2 &= w(0.065687 + 0.0013218w)/(1 + 1.2008w)\,. \end{aligned} \tag{A.44}$$

Since the precipitable water in atmospheric column, w, is a variable not routinely measured, it is estimated from the dew point temperature, T_{dew} $[^\circ C]$, according to an empirical model of *Iqbal* (1983): $w = \exp(0.07\, T_{dew} - 0.075)$ $[cm]$.

Aerosol extinction transmittances, $T_{a,\Lambda}$, are modeled as in *Gueymard* (2008). The band-average spectral aerosol optical depth, $\tau_{a\Lambda}$, is expressed with the same formalism of the original Ångström law, linearized for discrete aerosol channel (see also Section 2.6.1), but considering an effective wavelength for the entire bands $\Lambda 1_e$ and $\Lambda 2_e$:

$$\begin{aligned} \tau_{a\Lambda 1} &= \beta_{\Lambda 1} \Lambda 1_e^{-\alpha_{\Lambda 1}}\,, \\ \tau_{a\Lambda 2} &= \beta_{\Lambda 2} \Lambda 2_e^{-\alpha_{\Lambda 2}}\,, \end{aligned} \tag{A.45}$$

where $\alpha_{\Lambda 1}$, $\alpha_{\Lambda 2}$, $\beta_{\Lambda 1}$, and $\beta_{\Lambda 2}$, are the Ångström turbidity parameters for the two bands $\Lambda 1$ and $\Lambda 2$:

$$\begin{aligned} \beta_{\Lambda 1} &= \beta_A 0.7^{\alpha_{\Lambda 1} - \alpha_{\Lambda 2}}\,, \\ \beta_{\Lambda 2} &= \beta_A\,. \end{aligned} \tag{A.46}$$

As in *Gueymard* (2008) no distinction is made between the two α_Λ, that are taken equal to the reference Ångström turbidity α_A: $\alpha_{\Lambda 1} = \alpha_{\Lambda 2} = \alpha_A$, consequently also $\beta_{\Lambda 1} = \beta_{\Lambda 2} = \beta_A$. The effective wavelength for the entire bands, $\Lambda 1_e$, and $\Lambda 2_e$, are essentially function of a parameter $u_A = \ln[1 + m_A\, \beta_\Lambda]$ (*Gueymard*, 1989), where m_A is the air mass for aerosol extinction. The aerosol extinction transmittances $T_{a,\Lambda}$

for each band are thus:

$$\begin{aligned} T_{a,\Lambda 1} &= e^{-m_A \tau_{a,\Lambda 1}}\,, \\ T_{a,\Lambda 2} &= e^{-m_A \tau_{a,\Lambda 2}}\,. \end{aligned} \tag{A.47}$$

The revised functions used here to obtain u_A are as in *Gueymard* (2008):

$$\begin{aligned} \Lambda 1_e &= (d_0 + d_1\, u_A + d_2\, u_A^2)/(1 + d_3\, u_A^2)\,, \\ \Lambda 2_e &= (e_0 + e_1\, u_A + e_2\, u_A^2)/(1 + e_3\, u_A)\,, \end{aligned} \tag{A.48}$$

where:

$$\begin{aligned} d_0 &= 0.57664 - 0.024743\alpha_{\Lambda 1}\,, \\ d_1 &= (0.093942 - 0.2269\alpha_{\Lambda 1} + 0.12848\alpha_{\Lambda 1}^2)/(1 + 0.6418\alpha_{\Lambda 1})\,, \\ d_2 &= (-0.093819 + 0.36668\alpha_{\Lambda 1} - 0.12775\alpha_{\Lambda 1}^2)/(1 - 0.11651\alpha_{\Lambda 1})\,, \\ d_3 &= \alpha_{\Lambda 1}(0.15232 - 0.087214\alpha_{\Lambda 1} + 0.012664\alpha_{\Lambda 1}^2)/(1 - 0.90454\alpha_{\Lambda 1} + 0.26167\alpha_{\Lambda 1}^2)\,, \\ e_0 &= (1.183 - 0.022989\alpha_{\Lambda 2} + 0.020829\alpha_{\Lambda 2}^2)/(1 + 0.11133\alpha_{\Lambda 2})\,, \\ e_1 &= (-0.50003 - 0.18329\alpha_{\Lambda 2} + 0.23835\alpha_{\Lambda 2}^2)/(1 + 1.6756\alpha_{\Lambda 2})\,, \\ e_2 &= (-0.50001 + 1.1414\alpha_{\Lambda 2} + 0.0083589\alpha_{\Lambda 2}^2)/(1 + 11.168\alpha_{\Lambda 2})\,, \\ e_3 &= (-0.70003 - 0.73587\alpha_{\Lambda 2} + 0.51509\alpha_{\Lambda 2}^2)/(1 + 4.7665\alpha_{\Lambda 2})\,. \end{aligned} \tag{A.49}$$

In the above equations individual optical masses, m_R, m_O, m_W, and m_A, are used for Rayleigh (molecular) scattering and uniformly mixed gases absorption, ozone absorption, water vapor absorption, and aerosol extinction, respectively (*Gueymard*, 2008). Individual optical masses rather than a single air mass are considered to better characterize the solar rays' pathlength through the atmosphere. The values of the optical masses are obtained from the sun's solar altitude, h'_S [*angular degree*], with the same functions of the *REST* model (*Gueymard*, 2003). Note that molecular optical mass, m_R, sometimes is called "relative air mass", or simply "air mass":

$$\begin{aligned} m_R &= \left[\sin(h'_S) + (0.48353\; Z^{0.09584})/(96.741 - Z^{1.1754})\right]^{-1}\,, \\ m_O &= \left[\sin(h'_S) + (1.0651\; Z^{0.6379})/((101.8 - Z)^{2.2694})\right]^{-1}\,, \\ m_W &= \left[\sin(h'_S) + (0.10648\; Z^{0.11423})/((93.781 - Z)^{1.9203})\right]^{-1}\,, \\ m_A &= \left[\sin(h'_S) + (0.16851\; Z^{0.18198})/((95.318 - Z)^{1.9542})\right]^{-1}\,, \end{aligned} \tag{A.50}$$

where $Z = 90 - h'_S$ [*angular degree*] is the sun's zenith angle.

A.7.2 Diffuse irradiance

Aerosol extinction is mostly caused by scattering, and by absorption for the remaining part. The aerosol scattering transmittances are:

$$\begin{aligned} T_{as,\Lambda 1} &= e^{-m_A \omega_{\Lambda 1} \tau_{a\Lambda 1}}\,, \\ T_{as,\Lambda 2} &= e^{-m_A \omega_{\Lambda 2} \tau_{a\Lambda 2}}\,. \end{aligned} \tag{A.51}$$

where $\omega_{\Lambda 1}$ and $\omega_{\Lambda 2}$ are the single scattering albedos. The forward scattering fractions for Rayleigh extinction are indicated with $B_{R,\Lambda}$. In the absence of multiple scattering, they would be exactly 0.5 because molecules scatter equally in the forward and backward directions. Multiple scattering is negligible in $\Lambda 2$ (so that $B_{R,\Lambda 2} = 0.5$), but not in $\Lambda 1$. Using a simple spectral model to describe this effect $B_{R,\Lambda 1}$ is obtained after spectral integration and parametrization as in *Gueymard* (2008):

$$B_{R,\Lambda 1} = 0.5\,(0.89013 - 0.0049558\,m_R + 0.000045721\,m_R^2)\,. \tag{A.52}$$

The aerosol forward scatterance factor, B_a, is the same as *Gueymard* (2008):

$$B_a = 1 - \exp\left[-0.6931 - 1.8326\sin(h_S)\right]. \tag{A.53}$$

The correction factors, F_Λ, to compensate for multiple scattering effects and shortcomings for the simple approach are (*Gueymard*, 2008):

$$\begin{aligned} F_{\Lambda 1} &= (g_0 + g_1\tau_{a\Lambda 1})/(1 + g_2\tau_{a\Lambda 1})\,, \\ F_{\Lambda 2} &= (h_0 + h_1\tau_{a\Lambda 2})/(1 + h_2\tau_{a\Lambda 2})\,, \\ g_0 &= (3.715 + 0.368\,m_A + 0.036294\,m_A^2)/(1 + 0.0009391\,m_A^2)\,, \\ g_1 &= (-0.164 - 0.72567\,m_A + 0.20701\,m_A^2)/(1 + 0.0019012\,m_A^2)\,, \\ g_2 &= (-0.052288 + 0.31902\,m_A + 0.17871\,m_A^2)/(1 + 0.0069592\,m_A^2)\,, \\ h_0 &= (3.4352 + 0.65267\,m_A + 0.00034328\,m_A^2)/(1 + 0.034388\,m_A^{1.5})\,, \\ h_1 &= (1.231 - 1.63853\,m_A + 0.20667\,m_A^2)/(1 + 0.1451\,m_A^{1.5})\,, \\ h_2 &= (0.8889 - 0.55063\,m_A + 0.50152\,m_A^2)/(1 + 0.14865\,m_A^{1.5})\,. \end{aligned} \tag{A.54}$$

The sky albedo, $\rho_{s,\Lambda}$, parameterizations are again from *Gueymard* (2008):

$$\begin{aligned} \rho_{s,\Lambda 1} &= \frac{0.13363 + 0.00077358\alpha_{\Lambda 1} + \beta_{\Lambda 1}(0.37567 + 0.22946\alpha_{\Lambda 1})/(1 - 0.10832\alpha_{\Lambda 1})}{1 + \beta_{\Lambda 1}(0.84057 + 0.68683\alpha_{\Lambda 1})/(1 - 0.08158\alpha_{\Lambda 1})}\,, \\ \rho_{s,\Lambda 2} &= \frac{0.010191 + 0.00085547\alpha_{\Lambda 2} + \beta_{\Lambda 2}(0.14618 + 0.062758\alpha_{\Lambda 2})/(1 - 0.19402\alpha_{\Lambda 2})}{1 + \beta_{\Lambda 2}(0.58101 + 0.17426\alpha_{\Lambda 2})/(1 - 0.17586\alpha_{\Lambda 2})}\,. \end{aligned} \tag{A.55}$$

The reduction factor for direct beam, M_B, and global, M_G, radiation between the first band radiation and PAR adopted in equation (2.33) and (2.34) are (*Gueymard*,

2008):

$$\begin{aligned} M_B &= (t_0 + t_1\beta_e + t_2\beta_e^2)/(1 + t_3\beta_e^2)\,, \\ M_G &= (v_0 + v_1\beta_e + v_2\beta_e^2)/(1 + v_3\beta_e^2)\,, \end{aligned} \tag{A.56}$$

where the effective turbidity coefficient, β_e, is obtained from the previously defined $\alpha_{\Lambda 1}$, $\beta_{\Lambda 1}$, and $\Lambda 1_e$ as: $\beta_e = \beta_{\Lambda 1}(\Lambda 1_e^{1.3-\alpha_{\Lambda 1}})$ and the other parameters are function of $m_{15} = \min(m_R, 15)$:

$$\begin{aligned} t_0 &= \frac{0.90227 + 0.29\, m_{15} + 0.22928\, m_{15}^2 - 0.0046842\, m_{15}^3}{1 + 0.35474\, m_{15} + 0.19721\, m_{15}^2}\,, \\ t_1 &= \frac{-0.10591 + 0.15416\, m_{15} - 0.048486\, m_{15}^2 + 0.0045932\, m_{15}^3}{1 - 0.29044\, m_{15} + 0.026267\, m_{15}^2}\,, \\ t_2 &= \frac{0.47291 - 0.44639\, m_{15} + 0.1414\, m_{15}^2 - 0.014978\, m_{15}^3}{1 - 0.37798\, m_{15} + 0.052154\, m15^2}\,, \\ t_3 &= \frac{0.077407 + 0.18897\, m_{15} - 0.072869\, m_{15}^2 + 0.0068684\, m_{15}^3}{1 - 0.25237\, m15 + 0.020566\, m_{15}^2}\,, \end{aligned}$$

$$\begin{aligned} v_0 &= \frac{0.82725 + 0.86015\, m_{15} + 0.00713\, m_{15}^2 + 0.00020289\, m_{15}^3}{1 + 0.90358\, m_{15} + 0.015481\, m_{15}^2}\,, \\ v_1 &= \frac{-0.089088 + 0.089226\, m_{15} - 0.021442\, m_{15}^2 + 0.0017054\, m_{15}^3}{1 - 0.28573\, m_{15} + 0.024153\, m_{15}^2}\,, \\ v_2 &= \frac{-0.05342 - 0.0034387\, m_{15} + 0.0050661\, m_{15}^2 - 0.00062569\, m_{15}^3}{1 - 0.32663\, m_{15} + 0.029382\, m_{15}^2}\,, \\ v_3 &= \frac{-0.17797 + 0.13134\, m_{15} - 0.030129\, m_{15}^2 + 0.0023343\, m_{15}^3}{1 - 0.28211\, m_{15} + 0.023712\, m_{15}^2}\,. \end{aligned} \tag{A.57}$$

Note that this parametrization to estimate PAR was originally developed only for clear sky condition. In the weather generator is applied indifferently for clear and cloudy sky conditions.

A.8 Overcast sky radiation parameterizations

According to *Stephens* (1978), the cloud optical thickness, τ_N, is one of the most important parameters needed to describe the radiative properties of clouds. Approximate range for τ_N is $5 < \tau_N < 500$. By considering a set of "standard" cloud types, *Stephens* (1978) derives that τ_N can be approximately parameterized in terms of the effective radius of cloud-droplet size distribution, r_e $[\mu m]$, and liquid water path, LWP $[g\, m^{-2}]$:

$$\tau_N \approx \frac{1.5\ LWP}{r_e}\,. \tag{A.58}$$

Liquid water path can be formally defined as the integral of the liquid water content from the cloud base to the cloud top. By considering two spectral intervals $[0.29 \div 0.75\,\mu m]$ and $[0.75 \div 4.0\,\mu m]$ for the set of "standard" cloud types, *Stephens*

(1978) also derives the following relationships:

$$\log_{10}(\tau_{N1}) = 0.2633 + 1.7095 \ln\big[\log_{10}(LWP)\big] , \quad (A.59)$$

$$\log_{10}(\tau_{N2}) = 0.3492 + 1.6518 \ln\big[\log_{10}(LWP)\big] , \quad (A.60)$$

where expression (A.59) refers to the first considered spectral band, where absorption by cloud droplets is extremely small, and expression (A.60) refers to the second band, where absorption is significant. It follows from equations (A.58), (A.59), and (A.60) that the knowledge of LWP allows one to obtain an approximate estimate of r_e. *Slingo* (1989) introduced a parametrization that provided an accurate estimate of cloud radiative properties based on r_e. This parametrization is used in the following.

Slingo (1989) considered four spectral bands, one in *UV/VIS*, $[0.25 \div 0.69\,\mu m]$, and three in *NIR* wavelength intervals: $[0.69 \div 1.19\,\mu m]$, $[1.19 \div 2.38\,\mu m]$, $[2.38 \div 4.0\,\mu m]$ with the following respective fractions, λ_i, $i = 1, \ldots, 4$, of solar irradiance at the top of the atmosphere: 0.460, 0.326, 0.181, 0.033. Note the slight differences with *Ivanov et al.* (2007). Following the parametrization of *Slingo* (1989), cloud transmittances and reflectances are estimated separately for each of these spectral intervals. The radiative fluxes computed for these four bands are then scaled to the two principal bands $\Lambda 1$ $[0.29 \div 0.7\,\mu m]$ and $\Lambda 2$ $[0.70 \div 4.0\,\mu m]$, considered in the model (Section 2.6.2).

A.8.1 Direct beam irradiance

For a given spectral interval, the single scattering properties of typical water clouds can be parameterized in terms of the liquid water path (provided r_e is known):

$$\tau_\lambda = LWP(a_\lambda + \frac{b_\lambda}{r_e}) , \quad (A.61)$$

$$\tilde{\omega_\lambda} = 1 - (c_\lambda + d_\lambda r_e) , \quad (A.62)$$

$$g_\lambda = e_\lambda + f_\lambda r_e , \quad (A.63)$$

where τ_λ is the cloud optical depth, $\tilde{\omega_\lambda}$ is the single scatter albedo, g_λ is the asymmetry parameter, and a_λ, b_λ, c_λ, d_λ, e_λ, f_λ are the coefficients of the parametrization (provided in Table A.1).

Thus the transmissivity for the direct beam radiation, $T_{B,\lambda}$, is:

$$T_{B,\lambda} = e^{\left[-(1-\tilde{\omega_\lambda}\Upsilon_\lambda)\frac{\tau_\lambda}{\sin h_S}\right]} . \quad (A.64)$$

where h_S $[rad]$ is the solar height and $\Upsilon_\lambda = g_\lambda^2$.

A.8.2 Diffuse irradiance

Using the same notation as in A.8.1 and omitting the subscripts λ that denote a particular spectral band it is possible to introduce:

$$\beta_0 = \frac{3}{7}(1-g)\,, \tag{A.65}$$

$$\beta(h_S) = 0.5 - \frac{3\sin h_S\, g}{4(1+g)}\,, \tag{A.66}$$

$$\Upsilon = g^2\,, \tag{A.67}$$

$$U_1 = \frac{7}{4}\,, \tag{A.68}$$

$$U_2 = \frac{7}{4}\left[1 - \frac{(1-\tilde{\omega})}{7\tilde{\omega}\beta_0}\right]\,, \tag{A.69}$$

$$\alpha_1 = U_1[1-\tilde{\omega}(1-\beta_0)]\,, \tag{A.70}$$

$$\alpha_2 = U_2\tilde{\omega}\beta_0\,, \tag{A.71}$$

$$\alpha_3 = (1-\Upsilon)\tilde{\omega}\beta(h_S)\,, \tag{A.72}$$

$$\alpha_4 = (1-\Upsilon)\tilde{\omega}(1-\beta(h_S))\,, \tag{A.73}$$

$$\epsilon = \sqrt{\alpha_1^2 - \alpha_2^2}\,, \tag{A.74}$$

$$M = \frac{\alpha_2}{\alpha_1+\epsilon}\,, \tag{A.75}$$

$$E = e^{-\epsilon\tau}\,, \tag{A.76}$$

$$\gamma_1 = \frac{(1-\tilde{\omega}\Upsilon)\alpha_3 - \sin h_S\,(\alpha_1\alpha_3+\alpha_2\alpha_4)}{(1-\tilde{\omega}\Upsilon)^2 - \epsilon^2\sin^2 h_S}\,, \tag{A.77}$$

$$\gamma_2 = \frac{-(1-\tilde{\omega}\Upsilon)\alpha_4 - \sin h_S\,(\alpha_1\alpha_4+\alpha_2\alpha_3)}{(1-\tilde{\omega}\Upsilon)^2 - \epsilon^2\sin^2 h_S}\,, \tag{A.78}$$

where the U_1 and U_2 are the reciprocals of the effective cosines for the diffuse upward and downward fluxes respectively, β_0 is the fraction of the scattered diffuse radiation, which is scattered into the backward hemisphere, and $\beta(h_S)$ is the same for the direct radiation.

The diffuse transmissivity for direct beam and incident diffuse radiation are $T_{DB,\lambda}$ and $T_{DD,\lambda}$ respectively. The diffuse reflectivity for direct beam and diffuse incident radiation are $A_{B,\lambda}$ and $A_{D,\lambda}$ respectively, as defined in *Slingo* (1989). The diffuse reflectivity for diffuse incident radiation is:

$$A_{D,\lambda} = \frac{M_\lambda(1-E_\lambda^2)}{1-E_\lambda^2 M_\lambda^2}\,. \tag{A.79}$$

The diffuse transmissivity for diffuse incident radiation is:

$$T_{DD,\lambda} = \frac{E_\lambda(1-M_\lambda^2)}{1-E_\lambda^2 M_\lambda^2}\,. \tag{A.80}$$

Table A.1: The values of coefficients in equations (A.61) - (A.63) (from *Slingo* (1989)).

Band	a_λ $[10^{-2}\, m^2\, g^{-1}]$	b_λ $[\mu m\, m^2\, g^{-1}]$	c_λ	d_λ $[\mu m^{-1}]$	e_λ	f_λ $[10^{-3}\, \mu m^{-1}]$
$[0.25 \div 0.69\ \mu m]$	2.817	1.305	-5.62×10^{-8}	1.63×10^{-7}	0.829	2.482
$[0.69 \div 1.19\ \mu m]$	2.682	1.346	-6.94×10^{-6}	2.35×10^{-5}	0.794	4.226
$[1.19 \div 2.38\ \mu m]$	2.264	1.454	4.64×10^{-4}	1.24×10^{-3}	0.754	6.560
$[2.38 \div 4.00\ \mu m]$	1.281	1.641	2.01×10^{-1}	7.56×10^{-3}	0.826	4.353

The diffuse transmissivity for direct beam incident radiation is:

$$T_{DB,\lambda} = -\gamma_{2,\lambda} T_{DD,\lambda} - \gamma_{1,\lambda} T_{B,\lambda} A_{D,\lambda} + \gamma_{2,\lambda} T_{B,\lambda}\,. \tag{A.81}$$

Finally, the diffuse reflectivity for direct beam radiation is:

$$A_{B,\lambda} = -\gamma_{2,\lambda} A_{D,\lambda} - \gamma_{1,\lambda} T_{B,\lambda} T_{DD,\lambda} + \gamma_{1,\lambda}\,. \tag{A.82}$$

A.9 Terrain effects

Solar radiation originating from the sun travels through the atmosphere, and is modified by topography and other surface features. Solar radiation at the ground surface can be intercepted as direct beam, $R^T_{B,\Lambda}$, diffuse, $R^T_{D,\Lambda}$, and reflected radiation, $R^T_{R,\Lambda}$. As anticipated in Section 2.6.2, incoming solar radiation is function of the local topography through site aspect and slope, and of the surrounding terrain through sky view factor, $S_{vf}(\vec{x})$, and shadow effect, $S_h(\vec{x}, t)$, where $\vec{x}$ is the position and t is the local time. A brief description of incoming solar radiation components and topographic effects is provided in Figure A.10. In this section all the symbols will refer to clear sky conditions, nevertheless results are valid also in cloudy conditions.

The importance of topographic variability in hydrological and biophysical processes is well known (*Bertoldi et al.*, 2006a; *Ivanov et al.*, 2008b). For such a reason the quantities useful to take into account topographic influences on solar radiation are delineated in the following.

The principal variable controlling incident radiation on a slope, in mountainous terrain, is the local solar illumination angle, $\varphi_{S,T}$ $[rad]$, that is defined as the angle between the sun beam and the normal to the slope surface (*Dozier and Frew*, 1990), given by :

$$\cos\varphi_{S,T} = \cos\beta_T \sin h_S + \sin\beta_T cosh_S \cos(\zeta_S - \zeta_T)\,, \tag{A.83}$$

where β_T $[rad]$ is the slope of the site, ζ_T $[rad]$ is the local aspect (clockwise direction from north), and h_S $[rad]$, ζ_S $[rad]$ are the solar altitude and azimuth angles respectively.

Another important parameter is the sky view factor, S_{vf} for which two definitions

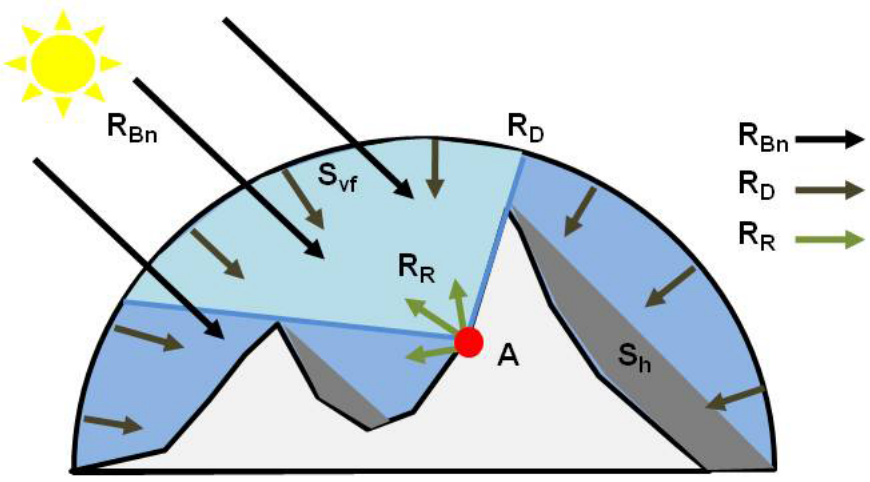

Figure A.10: Components of incoming solar radiation on a slope: direct beam radiation at normal incidence, R_{Bn}, diffuse radiation, R_D, and diffuse and direct radiations reflected off by nearby terrain, R_R. The reflected contribution from a generic A location is shown as example. Sky view factor, S_{vf}, from A and shadow effects, S_h, in the represented landscape are also shown. The figure is adapted from *Dubayah and Loechel* (1997).

have been proposed (*Chen et al.*, 2006). The first one assumes a surface with a unique slope receiving diffuse radiation isotropically, and posits that total diffuse radiation should be proportional to the fraction of sky dome viewed by the inclined surface. If β_T is the surface slope angle, then this sky view factor is given by the following equation: $S'_{vf} = (1+\cos\beta_T)/2$ [−] (*Bonan*, 2002). However, the sky dome viewed by the slope surface in mountainous terrain can be obstructed by neighboring surfaces. *Dozier and Frew* (1990) provide a method to take this effect into account, defining the sky-view factor, S_{vf}, as:

$$S_{vf} \approx \frac{1}{2\pi}\int_0^{2\pi}\Big[\cos\beta_T \sin^2 H_\zeta + \sin\beta_T \cos(\zeta-\zeta_T)(H_\zeta - \sin H_\zeta \cos H_\zeta)\Big]d\zeta\,, \tag{A.84}$$

where H_ζ is the horizon angle (Figure A.11), measured from the zenith downward to the local horizon, for direction ζ. Further details on the calculation of (A.84) are provided in *Dozier and Frew* (1990). Equation (A.84) includes the possibility to account for a variable horizon angle surrounding the point of interest, and not only for a constant horizon as assumed in the other derivation. Therefore, (A.84) is used to calculate S_{vf}.

Dozier and Frew (1990) derived also a terrain configuration factor, C_t [−], which approximates the total area between the point and the surrounding terrain for which the points are mutually visible:

$$C_t \approx \frac{1+\cos\beta_T}{2} - S_{vf}\,. \tag{A.85}$$

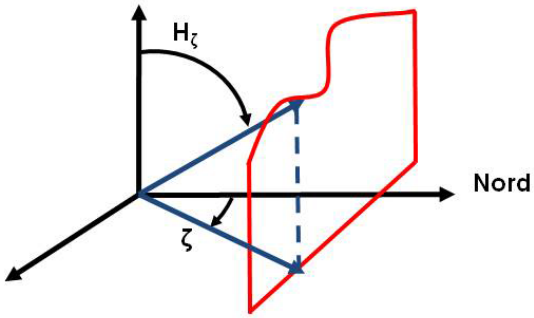

Figure A.11: Horizon angle, H_ζ, for a direction ζ, adapted from *Dozier and Frew* (1990).

As counterpart of sky view factor, the terrain configuration factor, C_t, estimates the fraction of the surrounding terrain visible to the point and varies from 0 (only sky visible) to 1 (only terrain visible). Further details on the calculation of (A.85) are provided from *Dozier and Frew* (1990). The shadow effect, S_h [0/1], is finally calculated as a binary coefficient which value is zero when the sloping surface is shadowed by neighboring terrain, while equal to one otherwise (*Dubayah and Loechel*, 1997; *Chen et al.*, 2006).

The direct beam, $R_{dir,\Lambda} = R^T_{B,\Lambda}$, flux on a general slope is thus given by:

$$R^T_{B,\Lambda} \;=\; S_h \;\cos\varphi_{S,T}\; R_{Bn,\Lambda}\,. \tag{A.86}$$

Wherever $\cos\varphi_{S,T}$ is negative, the point is "self-shadowed", i.e. the sun is below the local horizon caused by the slope itself. When instead $S_h = 0$ is cast shadowed, i.e. the shadow is caused by nearby terrain blocking the sun (*Dubayah and Loechel*, 1997). Note that when there is no shadow effect and the surface is flat $\beta_T = 0$, equation A.86 reduces to $R^T_{B,\Lambda} = \sin h_S \; R_{Bn,\Lambda}$. The latter is what the weather generator calculates by default.

The diffuse sky irradiance, $R^T_{D,\Lambda}$, on a surface oriented in space is composed of three components: the circumsolar, the circumzenith, and isotropic irradiation (*Olseth et al.*, 1995; *Olseth and Skartveit*, 1997), and for each of these components a specific topographic correction should be applied, see for example *Olseth and Skartveit* (1997) or a simplified version in the auxiliary material of *Ivanov et al.* (2007). Frequently, for simplicity the entire incident diffuse radiation $R_{D,\Lambda}$ is considered as isotropic (*Dozier and Frew*, 1990; *Dubayah and Loechel*, 1997; *Chen et al.*, 2006) and is given by:

$$R^T_{D,\Lambda} \;=\; S_{vf}\; R_{D,\Lambda}\,. \tag{A.87}$$

Another diffuse irradiance contribution comes from the reflected radiation, $R^T_{R,\Lambda}$, on surrounding topography. Incoming energy, in fact, may be reflected from nearby terrain toward the point of interest and can rarely be expected to be isotropic. However, in order to account for this effect, an approximate terrain configuration

factor, C_t, is usually employed (equation A.85) (*Dozier and Frew*, 1990; *Dubayah and Loechel*, 1997). This is due to the complexity in determining the geometric relationships between a particular location and all the surrounding terrain elements. Therefore, the reflected radiation, $R^T_{R,\Lambda}$, from surrounding terrain is estimated as:

$$C_t \; R^T_{R,\Lambda} = C_t \; \rho_g \big(R_{Bn,\Lambda} \cos(\varphi_{S,T}) + (1 - S_{vf}) R_{D,\Lambda} \big) \,, \tag{A.88}$$

where ρ_g is the average ground albedo refereing to a large area of 5-50 $[km]$ radius around the point (*Gueymard*, 2008). Note that when an unobscured flat surface is considered $C_t = 0$, because of $\beta_T = 0$ and $S_{vf} = 1$, i.e. all the sky dome is visible. Consequently the reflected radiation component is $R^T_{R,\Lambda} = 0$.

Summing the diffuse shortwave radiation on a slope that is the contribute of two components: $R_{dif,\Lambda} = R^T_{D,\Lambda} + C_t \; R^T_{R,\Lambda}$, and the global shortwave radiation, $R_{sw,\Lambda}$, we have:

$$R_{sw,\Lambda} = R_{dir,\Lambda} + R_{dif,\Lambda} = R^T_{B,\Lambda} + R^T_{D,\Lambda} + C_t \; R^T_{T,\Lambda} \,. \tag{A.89}$$

The parameter necessary to evaluate the previous equations, such as local site slope, $\beta_T(\vec{x})$ $[rad]$, local site aspect, $\zeta_T(\vec{x})$ $[rad]$, and horizon angle, $H_\zeta(\vec{x}, \zeta)$ $[rad]$, can be obtained from the analysis of Digital Elevation Models (DEM) (see Section: 4.1.2). Specifically, in order to calculate the horizon angle, $H_\zeta(\vec{x}, \zeta)$, the viewsheds for each cell $\vec{x}$ of an input DEM should be calculated. A viewshed is the angular distribution of sky visibility versus obstruction. This is similar to the view provided by upward-looking hemispherical (fisheye) photographs. A viewshed is calculated by searching in a specified set of directions around a location of interest. The resolution of the viewshed array must be sufficient to adequately represent all sky directions but small enough to enable rapid calculations, for the following examples a code with eight direction is implemented. Horizon angles for other directions are calculated using interpolation. The penumbral effects are neglected in the code, penumbral refers to decreased direct beam radiation at the edge of shadow due to partial obscuration of the solar disc, considering that the solar disc radius is 0.00466 $[rad]$.

An example of the values assumed by the above mentioned variables is provided in Figure A.12 and in Figure A.13 for the *Versilia* watershed in Tuscany (Italy). Sky-view factor, S_{vf}, terrain configuration factor, C_t, and shadow effect, S_h, for a particular date and hour are calculated from the DEM.

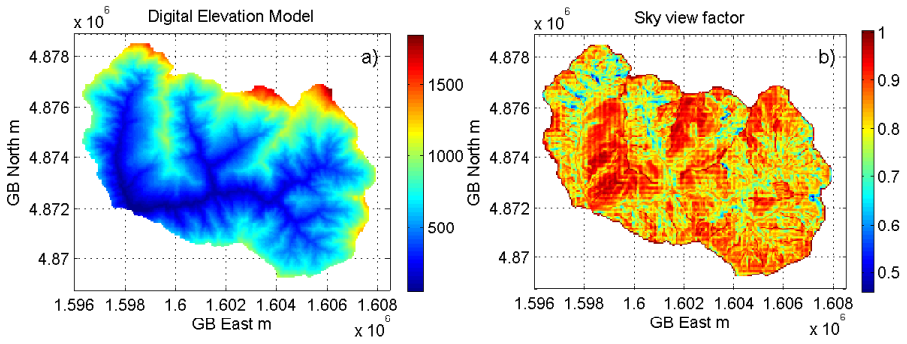

Figure A.12: Digital Elevation Model (a), and sky-view factor, S_{vf}, (b) for the the *Versilia* watershed in Tuscany (Italy).

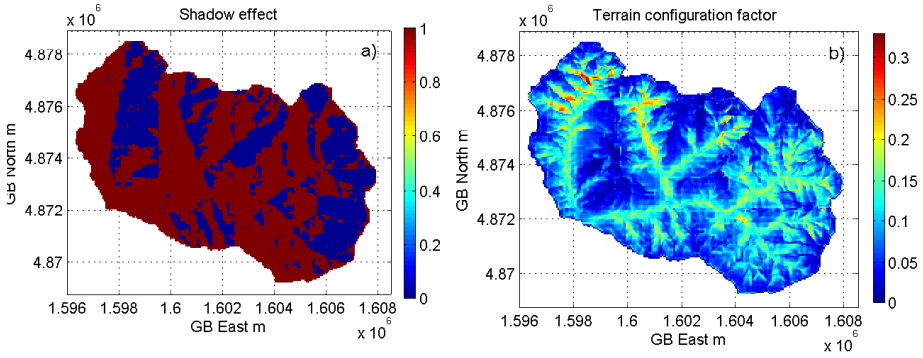

Figure A.13: Shadow effect, S_h, (a) and terrain configuration factor, C_t, (b) for the the *Versilia* watershed in Tuscany (Italy). The shadow effect is calculated with sun height in the barycenter of the watershed, the 26 April 1982 at 8 am, local time.

Appendix B

APPENDIX CHAPTER THREE

B.1 Posterior PDF calculation using MCMC simulations

The joint posterior distributions derived from the Bayesian multi-model ensembles described in Section 3.2.3 are not members of any known parametric family. However, the distributional forms (Gaussian, $\mathcal{N}$, Uniform, $\mathcal{U}$, and Gamma, $\mathcal{GA}$) chosen for the likelihoods and priors are conjugate, thus allowing for closed-form derivation of all full conditional distributions (the distributions of each parameter, as a function of the remaining parameters assuming fixed deterministic values). In the following are listed such distributions, for the robust model that includes a correlation between X_i and Y_i in the form of regression equation (*Tebaldi et al.*, 2005).

$$\lambda_i|... \sim \mathcal{GA}\Big(a+1, \big[b+0.5(X_i-\mu)^2+0.5\theta[Y_i-\nu-\beta(X_i-\mu)]^2\big]^{-1}\Big), \quad \text{(B.1)}$$

$$\mu|... \sim \mathcal{N}\Big(\overline{\mu}, \big[\sum\lambda_i+\theta\beta^2\sum\lambda_i+\lambda_0\big]^{-1}\Big), \quad \text{(B.2)}$$

$$\nu|... \sim \mathcal{N}\Big(\overline{\nu}, \big[\theta\sum\lambda_i\big]^{-1}\Big), \quad \text{(B.3)}$$

$$\beta|... \sim \mathcal{N}\Big(\overline{\beta}, \big[\theta\sum\lambda_i(X_i-\mu)^2\big]^{-1}\Big), \quad \text{(B.4)}$$

$$\theta|... \sim \mathcal{GA}\Big(c+0.5n_{mod}, \big[d+0.5\sum\lambda_i[Y_i-\nu-\beta(X_i-\mu)]^2\big]^{-1}\Big), \quad \text{(B.5)}$$

where the above shorthand notation $\overline{\mu}, \overline{\nu}$ and $\overline{\beta}$ are:

$$\overline{\mu} = \frac{\sum\lambda_iX_i-\theta\beta\sum\lambda_i(Y_i-\nu-\beta X_i)+\lambda_0X_0}{\sum\lambda_i+\theta\beta^2\sum\lambda_i+\lambda_0}, \quad \text{(B.6)}$$

$$\overline{\nu} = \frac{\sum\lambda_i[Y_i-\beta(X_i-\mu)]}{\sum\lambda_i}, \quad \text{(B.7)}$$

$$\overline{\beta} = \frac{\sum\lambda_i(Y_i-\nu)(X_i-\mu)}{\sum\lambda_i(X_i-\mu)^2}. \quad \text{(B.8)}$$

The Gibbs sampler can be easily coded so as to simulate iteratively from this sequence of full conditional distributions. After a series of random drawings during which the MCMC process forgets about the arbitrary set of initial values for the parameters (the burn-in period), the values sampled at each iteration represent a draw from the joint posterior distribution of interest, and any summary statistic can be computed to a degree of approximation. The latter is a direct function of the number of sampled values available and inverse function of the correlation between successive samples. In order to minimize this correlation, I saved only one iteration result every 50, after running the sampler for a total of 75 000 iterations, and discarding the first 25 000 as a burn-in period. These many iterations are probably not needed for this particular application but by performing them I eliminate any possibility of bias resulting from too few MCMC iterations. The convergence of the Markov chain to its stationary distribution (the joint posterior of interest) has been verified by *Tebaldi et al.* (2005) with standard diagnostic tools .

Appendix C

APPENDIX CHAPTER FOUR

C.1 Parameters of canopy radiative transfer model

The following parameters are obtained in *Sellers* (1985), note the in *Sellers* (1985) there is an error in h_4.

$$
\begin{aligned}
b &= 1-\omega_\Lambda+\omega_\Lambda\beta_\Lambda\,,\\
c &= \omega_\Lambda\beta_\Lambda\,,\\
d &= \omega_\Lambda\bar{\mu}K\beta_{0,\Lambda}\,,\\
f &= \omega_\Lambda\bar{\mu}K(1-\beta_{0,\Lambda})\,,\\
h &= \frac{\sqrt{b^2-c^2}}{\bar{\mu}}\,,\\
\sigma &= (\bar{\mu}K)^2+c^2-b^2\,,\\
u_1 &= b-\frac{c}{\alpha^{\mu}_{s\Lambda}}\ \text{(direct beam)}\quad\text{or}\quad u_1 = b-\frac{c}{\alpha_{s\Lambda}}\ \text{(diffuse)}\,,\\
u_2 &= b-c\alpha^{\mu}_{s\Lambda}\ \text{(direct beam)}\quad\text{or}\quad u_2 = b-c\alpha_{s\Lambda}\ \text{(diffuse)}\,,\\
u_3 &= f+c\alpha^{\mu}_{s\Lambda}\ \text{(direct beam)}\quad\text{or}\quad u_3 = f+c\alpha_{gs\Lambda}\ \text{(diffuse)}\,,\\
s_1 &= e^{-h(LAI+SAI)}\,,\\
s_2 &= e^{-K(LAI+SAI)}\,,
\end{aligned}
$$

$$
\begin{aligned}
p_1 &= b+\bar{\mu}h\,,\\
p_2 &= b-\bar{\mu}h\,,\\
p_3 &= b+\bar{\mu}K\,,\\
p_4 &= b-\bar{\mu}K\,,\\
d_1 &= \frac{p_1(u_1-\bar{\mu}h)}{s_1}-p_2(u_1+\bar{\mu}h)s_1\,,\\
d_2 &= \frac{(u_2+\bar{\mu}h)}{s_1}-(u_2-\bar{\mu}h)s_1\,,
\end{aligned}
$$

$$
\begin{aligned}
h_1 &= -dp_4 - cf\,, \\
h_2 &= \frac{1}{d_1}\left[\left(d - \frac{h_1}{\sigma}p_3\right)\frac{(u_1 - \bar{\mu}h)}{s_1} - p_2\left(d - c - \frac{h_1}{\sigma}(u_1 + \bar{\mu}K)\right)s_2\right], \\
h_3 &= -\frac{1}{d_1}\left[\left(d - \frac{h_1}{\sigma}p_3\right)(u_1 + \bar{\mu}h)s_1 - p_1\left(d - c - \frac{h_1}{\sigma}(u_1 + \bar{\mu}K)\right)s_2\right],
\end{aligned}
$$

$$
\begin{aligned}
h_4 &= -fp_3 - cd\,, \\
h_5 &= -\frac{1}{d_2}\left[\frac{h_4(u_2 + \bar{\mu}h)}{\sigma s_1} + \left(u_3 - \frac{h_4}{\sigma}(u_2 - \bar{\mu}K)\right)s_2\right], \\
h_6 &= \frac{1}{d_2}\left[\frac{h_4}{\sigma}(u_2 - \bar{\mu}h)s_1 + \left(u_3 - \frac{h_4}{\sigma}(u_2 - \bar{\mu}K)\right)s_2\right], \\
h_7 &= \frac{c(u_1 - \bar{\mu}h)}{d_1 s_1}\,, \\
h_8 &= -\frac{c(u_1 + \bar{\mu}h)s_1}{d_1}\,, \\
h_9 &= \frac{(u_2 + \bar{\mu}h)}{d_2 s_1}\,, \\
h_{10} &= -\frac{s_1(u_2 - \bar{\mu}h)}{d_2}\,.
\end{aligned}
$$

In order to compute the above parameters the following quantities have to be specified: the vegetation leaf and stem reflectances, $(\alpha_\Lambda^{leaf}, \alpha_\Lambda^{stem})$, transmittances, $(\tau_\Lambda^{leaf}, \tau_\Lambda^{stem})$, the leaf angles distribution parameter, χ_L, and the albedos for the direct beam, $\alpha_{s\Lambda}^{\mu}$, and diffuse, $\alpha_{s\Lambda}$, radiative fluxes of the surface underneath the vegetation.

C.2 Aerodynamic resistance to momentum

The derivation of the aerodynamic resistance to momentum, r_{am}, follows the same procedure of the aerodynamic resistance for heat transfer. The flux of momentum in the atmospheric surface layer, τ, can be calculated as:

$$
\tau = \rho_a K_m \frac{\partial u}{\partial z} = \rho_a C_d u^2\,, \tag{C.1}
$$

where C_d $[-]$ is the drag coefficient and the other symbols are described in Section 4.4.1, note that equation C.1 already assumed $u(z = 0) = 0$. Elaborating from equation (4.86) and (4.89) it can be obtained:

$$
K_m/\partial z = C_d u_a = 1/r_{am} \;\Rightarrow\; \tau = \rho_a \frac{u_a}{r_{am}}\,, \tag{C.2}
$$

$$
\begin{aligned}
r_{am} &= \rho_a \frac{u_a}{\tau} = \frac{u_a}{u^{*2}} = \frac{1}{k^2 u_a}\Big[\ln\Big(\frac{z_{atm} - d}{z_{om}}\Big), \\
&\quad -\psi_m\big(\frac{z_{atm} - d}{\Lambda}\big) + \psi_m\big(\frac{z_{om}}{\Lambda}\big)\Big]^2\,.
\end{aligned} \tag{C.3}
$$

For neutral condition, r_{am}, assumes the well known expression:

$$r_{am} = \frac{1}{k^2 u_a}\left[\ln\left(\frac{z_{atm} - d}{z_{om}}\right)\right]^2 . \tag{C.4}$$

C.3 Model parameters

Table C.1: List of parameters used in "Tethys".

Parameter	**Description**	**Typical Range**
	Hydrological parameter	
d_e	characteristic length of evaporation	50-150 $[mm]$
F_{san}	fraction of sand	0-1 $[-]$
F_{cla}	fraction of clay	0-1 $[-]$
P_{org}	percentage of organic material	0-10 $[-]$
$S_{p,In}$	specific rainfall interception	0.1-0.4 $[mm]$
m_f	parameter for decay of saturated conductivity	100-2000 $[mm]$
$Z_{s,i}$	soil layer mesh	- $[mm]$
K_{bot}	conductivity of the bedrock	- $[mm\ h^{-1}]$
a_r	soil anisotropy ratio	1-1000 $[-]$
β_T	slope of the element	- $[rad]$
a_T	area of the basic element per unit contour length	- $[mm]$
$\widehat{Sp}_{sno,In}$	specific snow interception	5.9-6.6 $[mm]$
	PFT- dependent parameter	
Ψ_{ss}	soil water potential at the begin of stomatal closure	(-0.03)-(-2) $[MPa]$
Ψ_{wp}	soil water potential at the complete stomatal closure	(-1.5)-(-10) $[MPa]$
Z_R	rooting depth	300-2000 $[mm]$
SAI	stem area index	0-0.05 $[-]$
H_c	canopy height	0.1-30 $[m]$
d_{leaf}	leaf dimension	0.1-10 $[cm]$
	Photosynthesis parameter	
K_N	canopy nitrogen decay	0.5 $[-]$
φ_p	photosynthesis pattern	C3, C4 or CAM
V_{max}^L	maximum Rubisco capacity at $25°C$	10-120 $[\mu mol\ CO_2\ m^{-2}\ s^{-1}]$
ϵ	intrinsic quantum efficiency	0.040-0.081 $[\mu molCO_2\ \mu mol^{-1}\, phot]$
c_a	atmospheric CO_2 concentration	- $[ppm]$
O_i	O_2 partial pressure	210000 $[ppm]$
H_a	activation energy	45-90 $[kJ\ mol^{-1}]$
ΔS	entropy factor	0.635-0.665 $[kJ\ mol^{-1}\ K^{-1}]$
Δ_0	vapor pressure deficit coefficient	700-2000 $[Pa]$
a	empirical parameter for $A_n - g_s$ relationship	2-15 $[-]$
g_0	cuticular conductance	0.01-0.04 $[mol\, CO_2\ m^{-2}\ s^{-1}]$

Appendix D

APPENDIX CHAPTER FIVE

D.1 Vegetation structural properties

Allometric relationships linking the size of carbon pools to structural attributes of the plants are necessary to describe the temporal evolution of these attributes in woody species. Specifically, stem area index, SAI $[m^2\, stem\ area\ m^{-2}\, PFT\, area]$, canopy height, H_c $[m]$, and *Crown Area* fraction, C_{crown} $[m^2\ PFT\, m^{-2}\ ground]$ can be dynamically determined. The carbon pools that form the woody part of the aboveground plant are the aboveground heartwood carbon pool, $C_{heaw,a}$ $[g\, C\ m^{-2}\, PFT]$, the aboveground sapwood, $C_{sapw,a}$ $[g\, C\ m^{-2}\, PFT]$ and the aboveground carbohydrate reserve $C_{hydr,a}$ $[g\, C\ m^{-2}\, PFT]$. Considering the woody part of the plant halfway from a cylinder and a cone:

$$V_{tree} = \frac{C_{crown}}{T_\rho}\left(\frac{C_{heaw,a}}{\rho_{heaw,a}} + \frac{C_{sapw,a}}{\rho_{sapw}} + \frac{C_{hydr,a}}{\rho_{sapw}}\right), \tag{D.1}$$

$$V_{tree} = \frac{\pi D^2 H_c}{6}, \tag{D.2}$$

where V_{tree} $[m^3\,,\ number\, of\, individuals^{-1}]$ is the volume of wood of a representative tree, $\rho_{heaw,a}$ and ρ_{sapw} $[g\, C\ m^{-3}]$ are the heartwood and sapwood carbon wood density respectively, D $[m]$ is the average wood trunk diameter, T_ρ $[number\, of\, individuals\ m^{-2}\ ground]$ is the PFT population density, C_{crown} is the *Crown Area* fraction, expressed by $C_{crown} = T_\rho A_{crown}$ $[m^2\ PFT\, m^{-2}\ ground]$, with $C_{crown} \leq 1$; and A_{crown} $[m^2\ PFT\,,\ \ number\, of\, individuals^{-1}]$ is the average crown extension of an individual belonging to the PFT. Equations (D.1) and (D.2) contain several implicit assumptions about the forms of the tree parts and the density of different tissues. Most important, it is assumed that the aboveground heartwood, carbohydrate reserve, and sapwood biomasses are known, that it is not true for "Chloris". Equations (D.1) and (D.2), that can be considered as a single independent equation, generally, have three unknowns: D, A_{crown}, and H_c. Therefore, two further allometric relationships are necessary to estimate the vegetation structural parameters. Equations relating A_{crown} and H_c to D have been made available in literature (*Sitch et al.*,

2003; *Sato et al.*, 2007):

$$A_{crown} = k_1 D^{k_3}\,, \tag{D.3}$$

$$H_c = k_2 D^{k_4}\,, \tag{D.4}$$

where k_1 $[m^{2-k_3}]$, k_2 $[m^{1-k_4}]$, k_3 $[-]$, and k_4 $[-]$ are allometric constants, PFT dependent. Typical values assumed by the allometric constants are: $k_1 = 100 - 200$, $k_2 = 28 - 40$, $k_3 = 1.6$, $k_4 = 0.5 - 0.83$, (*Sitch et al.*, 2003; *Sato et al.*, 2007). For the scaling parameter k_3 and k_4, theoretical values of $k_3 = 1.33$ and $k_4 = 0.66$ based on universal scaling in tree and vascular plant allometry have been also calculated (*Enquist*, 2002; *West et al.*, 2009). Substituting equation (D.3) and (D.4) in (D.1)-(D.2) allows to solve iteratively for D. Consequently, a dynamic structural representation of the canopy including time varying canopy fraction, C_{crown}, can be achieved. When $T_\rho A_{crown} > 1$ only (D.4) is substituted into (D.1).

The stem area index, SAI $[m^2\, SAI\ m^{-2}\, ground\ area]$, that is a structural attribute can be successively computed as:

$$SAI = \left((1 - f_v)(DH_c) + (f_v)\frac{\pi D^2}{4}\right) T_\rho\,, \tag{D.5}$$

where the coefficient f_v $[-]$ is the fraction of stem and branches that can be regarded as prevalently vertical. SAI in $[m^2\, SAI\ m^{-2}\, PFT]$ can be obtained dividing SAI from equation (D.5) by the *Crown Area* fraction C_{crown}.

The method outlined above is not applied in "Chloris" because the model does not track heartwood carbon pool and neither other aboveground carbon pools, that are the basis of such an approach. Moreover, in order to obtain a dynamic evolution of vegetation the population density, T_ρ $[number\, of\, individuals\ m^{-2}\ ground]$, should evolve on time according to species competition, mortality (self-thinning, wildfire, insect outbreaks) and new individuals establishment factors (seedling, colonizable area, etc...) (*Lüdeke et al.*, 1994; *Bonan et al.*, 2003; *Sitch et al.*, 2003). The above method is valid only for woody species. Grass species do not have heartwood and sapwood carbon pools and their carbohydrate reserves are considered stored belowground. In grass the vegetation height depends directly on LAI, $SAI = 0$ and the *Crown Area* fraction depends on the effective portion of basic computational element occupied by the plant. When the basic computational element is completely occupied by grass, $C_{crown} = 1$. Note that the same is not generally true for woody species.

D.2 Model parameters

Table D.1: List of parameters used in "Chloris".

Parameter / PFT	**Description**	**Typical Range**
	Structural and Respiration parameter	
Ξ	broader vegetation category	0 (evergr.); 1 (decid.); 2 (grass); 3 (crops)
S_{LAI}	specific leaf area of biomass	0-0.05 $[m^2\,LAI\;g\,C^{-1}]$
ω_{grw}	growth respiration fraction	0.15-0.30 [–]
r_m	respiration rate coefficients	0.025-0.066 $[g\,C\;g\,N^{-1}\;day^{-1}]$
N_l	C:N mass ratio for leaves and grasses	20-50 [–]
	Soil moisture parameters	
Ψ_{ss}	soil matrix potential at the begin of stomatal closure	(-0.03)-(-2.0) $[MPa]$
Ψ_{wp}	soil matrix potential at the complete stomatal closure	(-1.5)-(-10) $[MPa]$
d_e	characteristic length of evaporation	50-300 $[mm]$
	Allocation parameters	
ε_{al}	tuning parameter for carbohydrate reserve allocation	0-1 [–]
R_{ltr}	maximum shoot-to-root ratio	0.75-1.5 [–]
T_{rC}	translocation rate	0-8 $[g\,C\;m^{-2}\,PFT\;day^{-1}]$
	Stress-induced foliage loss parameters	
d_{root}	turnover rate of fine roots	1/240 - 1/1500 $[day^{-1}]$
d_{sapw}	turnover rate of living sapwood	1/365 $[day^{-1}]$
A_{cr}	critical leaf age	120-1500 $[day]$
$d_{d\,max}$	maximum drought loss rate	1/40 - 1/365 $[day^{-1}]$
d_{cold}	linear coefficient for cold foliage loss	1/10-1/365 $[day^{-1}\,{}^{\circ}C^{-1}]$
T_{cold}	temperature threshold below which cold-induced leaf loss	-10 $[^{\circ}C]$ - +10 $[^{\circ}C]$
	Phenology parameters	
$T_{s,LO}$	soil temperature threshold to start growth	- $[^{\circ}C]$
β_{LO}	moisture stress threshold to start growth	0-1 [–]
$J_{Day,LO}$	Julian day threshold	- [–]
d_{MG}	days of maximum growth state	20-40 $[day]$
$D_{LH,SE}$	day length to start senescence	- $[h]$
LAI_{min}	minimum LAI	0.001 - 0.05 [–]

Bibliography

Abbott, M. B., J. C. Bathurst, J. A. Cunge, P. E. O'Connell, and J. Rasmussen (1986a), An introduction to the european hydrologic system-systeme hydrologique europeen, SHE, 1: History and philosophy of a physically-based, distributed modeling system, *Journal of Hydrology*, *87*, 45–59.

Abbott, M. B., J. C. Bathurst, J. A. Cunge, P. E. O'Connell, and J. Rasmussen (1986b), An introduction to the european hydrologic system-systeme hydrologique europeen, SHE, 2: Structure of a physically-based, distributed modeling system, *Journal of Hydrology*, *87*, 61–77.

Abdella, K., and N. A. McFarlane (1996), Parameterization of the surface-layer exchange coefficients for atmospheric models, *Boundary-Layer Meteorology*, *80*, 223–248.

Adams, H. D., M. Guardiola-Claramonte, G. A. Barron-Gafford, J. C. Villegas, D. D. Breshears, C. B. Zou, P. A. Troch, and T. E. Huxman (2009), Temperature sensitivity of drought-induced tree mortality portends increased regional die-off under global change-type drought, *Proc. Natl Acad. Sci. USA*, *106*(17), 7063–7066, doi:10.1073/pnas.0901438106.

Albertson, J. D., and G. Kiely (2001), On the structure of soil moisture time series in the context of land surface models, *Journal of Hydrology*, *243*, 101–119.

Alexander, L. V., X. Zhang, T. C. Peterson, J. Caesar, B. Gleason, A. M. G. K. Tank, M. Haylock, D. Collins, B. Trewin, F. Rahimzadeh, A. Tagipour, K. R. Kumar, J. Revadekar, G. Griffiths, L. Vincent, D. B. Stephenson, J. Burn, E. Aguilar, M. Brunet, M. Taylor, M. New, P. Zhai, M. Rusticucci, and J. L. Vazquez-Aguirre (2006), Global observed changes in daily climate extremes of temperature and precipitation, *Journal of Geophysical Research*, *111*(D05109), doi:10.1029/2005JD006290.

Alo, C. A., and G. Wang (2008), Hydrological impact of the potential future vegetation response to climate changes projected by 8 GCMs, *Journal of Geophysical Research*, *113*(G03011), doi:10.1029/2007JG000598.

Alsheimer, M., B. Köstner, E. Falge, and J. D. Tenhunen (1998), Temporal and spatial variation in transpiration of Norway spruce stands within a forested catchment of the Fichtelgebirge, Germany, *Annales des Sciences Forestieres*, *55*, 103–123.

Ambroise, B., K. Beven, and J. Freer (1996), Towards a generalization of the TOPMODEL concepts: topographic indices of hydrological similarity, *Water Resources Research*, *32*(7), 2135–2145.

Anderson, E. A. (1968), Development and testing of snowpack energy balance equations, *Water Resources Research*, *4*(1), 19–37.

Anderson, E. A., and N. H. Crawford (1964), The synthesis of continuous snowmelt runoff hydrographs on a digital computer, *Tech. Rep. 36*, Stanford, California Stanford University Dep. of Civil Engineering.

Anderson, M. C., J. M. Norman, T. P. Meyers, and G. R. Diak (2000), An analytical model for estimating canopy transpiration and carbon assimilation fluxes based on canopy light-use efficiency, *Agricultural and Forest Meteorology*, *101*, 265–289.

Aoki, T., A. Hachikubo, and M. Hori (2003), Effects of snow physical parameters on shortwave broadband albedos, *Journal of Geophysical Research*, *108*(D19,4616), doi:10.1029/2003JD003506.

Arain, M. A., F. Yuan, and T. A. Black (2006), Soil-plant nitrogen cycling modulated carbon exchanges in a western temperate conifer forest in Canada, *Agricultural and Forest Meteorology*, *140*, 171–192.

Arora, V. K. (2002), Modelling vegetation as a dynamic component in soil-vegetation-atmosphere- transfer schemes and hydrological models, *Reviews of Geophysics*, *40*(2), doi:10.1029/2001RG000103.

Arora, V. K., and G. J. Boer (2003), A representation of variable root distribution in dynamic vegetation models, *Earth Interactions*, *7*(6), 1–19.

Arora, V. K., and G. J. Boer (2005), A parameterization of leaf phenology for the terrestrial ecosystem component of climate models, *Global Change Biology*, *11*(1), 39–59.

Arora, V. K., and G. J. Boer (2006), Simulating competition and coexistence between plant functional types in a dynamic vegetation model, *Earth Interactions*, *10*, 1–30.

Arya, S. P. (2001), *Introduction to Micrometeorology*, 2nd ed., Academic Press.

Assmann, S. M. (1999), The cellular basis of guard cell sensing to rising CO_2, *Plant, Cell and Environment*, *22*, 629–637.

Assouline, S. (2004), Rainfall-induced soil surface sealing: A critical review of observations, conceptual models, and solutions, *Vadose Zone Journal*, *3*, 570–591.

Assouline, S., and Y. Mualem (1997), Modeling the dynamics of seal formation and its effect on infiltration as related to soil and rainfall characteristics, *Water Resources Research*, *33*, 1527–1536.

Assouline, S., and Y. Mualem (2001), Soil seal formation and its effect on infiltration: Uniform versus nonuniform seal approximation, *Water Resources Research*, *37*, 297–305.

Assouline, S., and Y. Mualem (2006), Runoff from heterogeneous small bare catchments during soil surface sealing, *Water Resources Research*, *42*(W12405), doi:10.1029/2005WR004592.

Atkin, O., H. Millar, and M. Turnbull (210), Plant respiration in a changing world, *New Phytologist*, *187*, 268–272.

Baker, D. G., D. L. Ruschy, and D. B. Wall (1990), The albedo decay of prairie snows, *Journal of Applied Meteorology*, *29*, 179–187.

Bakker, M. R., L. Augusto, and D. L. Achat (2006), Fine root distribution of trees and understory in mature stands of maritime pine (Pinus pinaster) on dry and humid sites, *Plant Soil*, *286*, 37–51, doi:10.1007/s11104-006-9024-4.

Baldocchi, D., and T. Meyers (1998), On using eco-physiological, micrometeorological and biogeochemical theory to evaluate carbon dioxide, water vapor and trace gas fluxes over vegetation: a perspective, *Agricultural and Forest Meteorology*, *90*, 1–25.

Baldocchi, D., E. Falge, L. Gu, R. Olson, D. Hollinger, S. Running, P. Anthoni, C. Bernhofer, K. Davis, R. Evans, J. Fuentes, A. Goldstein, G. Katul, B. Law, X. Lee, Y. Malhi, T. Meyers, W. Munger, W. Oechel, U. K. T. Paw, K. Pilegaard, H. P. Schmid, R. Valentini, S. Verma, T. Vesala, K. Wilson, and S. Wofsy (2001), FLUXNET: A new tool to study the temporal and spatial variability of ecosystem-scale carbon dioxide, water vapor, and energy flux densities, *Bulletin of the American Meteorological Society*, *82*(11), 2415–2434.

Baldocchi, D., K. Wilson, and L. Gu (2002), How the environment, canopy structure and canopy physiological functioning influence carbon, water and energy fluxes of a temperate broad-leaved deciduous forestan assessment with the biophysical model CANOAK, *Tree Physiology*, *22*, 1065–1077.

Baldocchi, D. D., and P. C. Harley (1995), Scaling carbon dioxide and water vapour exchange from leaf to canopy in a deciduous forest. II: Model testing and application, *Plant, Cell and Environment*, *18*, 1157–1173.

Baldocchi, D. D., T. A. Black, P. S. Curtis, E. Falge, J. D. Fuentes, A. Granier, L. Gu, A. Knohl, K. Pilegaard, H. P. Schmid, R. Valentini, K. Wilson, S. Wofsy, L. Xu, and S. Yamamoto (2005), Predicting the onset of net carbon uptake by deciduous forests with soil temperature and climate data: a synthesis of FLUXNET data, *International Journal of Biometeorology*, *49*, 377–387, doi: 10.1007/s00484-005-0256-4.

Ball, J. T., I. E. Woodrow, and J. A. Berry (1987), A model predicting stomatal conductance and its contribution to the control of photosynthesis under different environmental conditions, in *Progress in photosynthesis research*, edited by Biggins, pp. 221–224, Martinus Nijhoff, Netherlands.

Band, L. E., P. Patterson, R. Nemani, and S. W. Running (1993), Forest ecosystem processes at the watershed scale: incorporating hillslope hydrology, *Agricultural and Forest Meteorology*, *63*, 93–126.

Barnett, T. P., D. W. Pierce, H. G. Hidalgo, C. Bonfils, B. D. Santer, T. Das, G. Bala, A. W. Wood, T. Nozawa, A. A. Mirin, D. R. Cayan, and M. D. Dettinger (2008), Human-induced changes in the hydrology of the Western United States, *Science*, *319*, 1080–1083, doi:0.1126/science.1152538.

Bartelt, P., and M. Lehning (2002), A physical SNOWPACK model for the Swiss avalanche warning. Part I: numerical model, *Cold Regions and Technology*, *35*, 123–145.

Bates, B. C., Z. W. Kundzewicz, S. Wu, and J. P. Palutikof (2008), Climate change and water, *Technical paper*, Intergovernmental Panel on Climate Change, IPCC Secretariat, Geneva.

Bavay, M., M. Lehning, T. Jonas, and H. Löwe (2009), Simulations of future snow cover and discharge in Alpine headwater catchments, *Hydrological Processess*, *23*, 95–108, doi: 10.1002/hyp.7195.

Becchi, I., E. Caporali, L. Castellani, and F. Castelli (1994), Multiregressive analysis for the estimation of the spatial zero rainfall probability, in *Workshop on Climate change and hydrogeological hazards in the Mediterranean area*, Perugia, 27-28 June.

Becker, S. (2001), Calculation of direct solar and diffuse radiation in Israel, *International Journal of Climatology*, *21*(12), 1561–1576.

Bedford, D. R., and E. E. Small (2008), Spatial patterns of ecohydrologic properties on a hillslope-alluvial fan transect, central New Mexico, *Catena*, *73*, 34–48, doi:10.1016/j.catena.2007.08.005.

Belair, S., R. Brown, J. Mailhot, B. Bilodeau, and L.-P. Crevier (2003), Operational implementation of the ISBA land surface scheme in the Canadian regional weather forecast model. Part II: Cold season results, *Journal of Hydrometeorology*, *4*, 371–386.

Beljaars, A. C. M., and A. A. M. Holtslag (1991), Flux parameterization over land surfaces for atmospheric models, *Journal of Applied Meteorology*, *30*, 327–341.

Bertoldi, G., R. Rigon, and T. M. Over (2006a), Impact of watershed geomorphic characteristics on the energy and water budgets, *Journal of Hydrometeorology*, *7*, 389–403.

Bertoldi, G., R. Rigon, D. Tamanini, and F. Zanotti (2006b), GEOtop version 0.875: Technical description and programs guide, *Tech. Rep. dica-06-001*, University of Trento E-Prints.

Beven, K. J. (1982), On subsurface stormflow: An analysis of response times, *Hydrological Sciences Journal*, *4*, 505–521.

Beven, K. J. (1997), TOPMODEL: A critique, *Hydrological Processes*, *11*, 1069–1085.

Beven, K. J. (2001), How far can we go in distributed hydrological modelling?, *Hydrology and Earth System Sciences*, *5*, 1–12.

Beven, K. J. (2002), Towards an alternative blueprint for a physically based digitally simulated hydrologic response modelling system, *Hydrological Processes*, *16*, 189–206, doi:10.1002/hyp.343.

Beven, K. J. (2006), Searching for the Holy Grail of scientific hydrology: $Q_t = H(\vec{S}, \vec{R}, \Delta t)A$ as closure, *Hydrology and Earth System Science*, *10*, 609–618.

Beven, K. J., and J. Freer (2001), A dynamic TOPMODEL, *Hydrological Processes*, *15*, 1993–2011, doi: 10.1002/hyp.252.

Beven, K. J., and M. J. Kirkby (1979), A physically based, variable contributing area model of basin hydrology, *Hydrological Sciences Bulletin*, *24*, 43–69.

Bhark, E. W., and E. E. Small (2003), Association between plant canopies and the spatial patterns of infiltration in shrubland and grassland of the Chihuahuan desert, New Mexico, *Ecosystems*, *6*, 185–196, doi:10.1007/s10021-002-0210-9.

Bittelli, M., F. Ventura, G. S. Campbell, R. L. Snyder, F. Gallegati, and P. Pisa, Rossi (2008), Coupling of heat, water vapor, and liquid water fluxes to compute evaporation in bare soils, *Journal of Hydrology*, *362*, 191–205, doi:10.1016/j.jhydrol.2008.08.014.

Boé, J., L. Terray, E. Martin, and F. Habets (2009), Projected changes in components of the hydrological cycle in French river basins during the 21st century, *Water Resources Research*, *45*(W08426), doi:10.1029/2008WR007437.

Bohrer, G., H. Mourad, T. A. Laursen, D. Drewry, R. Avissar, D. Poggi, R. Oren, and G. G. Katul (2005), Finite element tree crown hydrodynamics model (FETCH) using porous media flow within branching elements: A new representation of tree hydrodynamics, *Water Resources Research*, *41*(W11404), doi:10.1029/2005WR004181.

Bonan, G. (2002), *Ecological Climatology: Concept and Applications*, Cambridge Univ. Press, New York.

Bonan, G. B. (1995), Land-atmosphere interactions for climate system models-coupling biophysical, biogeochemical, and ecosystem dynamical processes, *Remote Sensing of Environment*, *51*(1), 57–73.

Bonan, G. B. (1996), A land surface model (LSM version 1.0) for ecological, hydrological, and atmospheric studies: Technical description and user's guide, *Tech. Rep. NCAR Tech. Note NCAR/TN-417*, Natl. Cent. for Atmos. Res., Boulder, Colorado.

Bonan, G. B. (2008), Forests and climate change: Forcings, feedbacks, and the climate benefits of forests, *Science*, *320*, 1444–1449, doi:10.1126/science.1155121.

Bonan, G. B., S. Levis, L. Kergoat, and K. W. Oleson (2002), Landscapes as patches of plant functional types: An integrating concept for climate and ecosystem models, *Global Biogeochemical Cycles*, *16*(2,1021), doi:10.1029/2000GB001360.

Bonan, G. B., S. Levis, S. Sitch, M. Vertenstein, and K. W. Oleson (2003), A dynamic global vegetation model for use with climate models: concepts and description of simulated vegetation dynamics, *Global Change Biology*, *9*, 1543–1566, doi: 10.1046/j.1529-8817.2003.00681.x.

Bond, B. (2003), Hydrology and ecology meet-and the meeting is good, *Hydrological Processes*, *17*, 2087–2089, doi:10.1002/hyp.5133.

Bony, S., R. Colman, V. M. Kattsov, R. P. Allan, C. S. Bretherton, J.-L. Dufresne, A. Hall, S. Hallegatte, M. M. Holland, W. Ingram, D. A. Randall, B. J. Soden, G. Tselioudis, and M. J. Webb (2006), How well do we understand and evaluate climate change feedback processes?, *Journal of Climate*, *19*, 3445–3481.

Boone, A., V. Masson, T. Meyers, and J. Noilhan (2000), The influence of the inclusion of soil freezing on simulations by a soil-vegetation-atmosphere transfer scheme, *Journal of Applied Meteorology*, *39*, 1544–1569.

Botta, A., N. Viovy, P. Ciais, and P. Friedlingstein (2000), A global prognostic scheme of leaf onset using satellite data, *Global Change Biology*, *6*, 709–726.

Bouraoui, F., G. Vachaud, L. Z. X. Li, H. L. Treut, and T. Chen (1999), Evaluation of the impact of climate changes on water storage and groundwater recharge at the watershed scale, *Climate Dynamics*, *15*, 153–161.

Bovard, B. D., P. S. Curtis, C. S. Vogel, H.-B. Su, and H. P. Schmid (2005), Environmental controls on sap flow in a northern hardwood forest, *Tree Physiology*, *25*, 31–38.

Brandt, A. R., and A. E. Farrell (2007), Scraping the bottom of the barrel: greenhouse gas emission consequences of a transition to low-quality and synthetic petroleum resources, *Climatic Change*, *84*, 241–263, doi: 10.1007/s10584-007-9275-y.

Brandt, C. J. (1989), The size distribution of throughfall drops under vegetation canopies, *Catena*, *16*, 507–524.

Brandt, C. J. (1990), Simulation of the size distribution and erosivity of raindrops and throughfall drops, *Earth Surface Processes and Landforms*, *15*, 687–698.

Bras, R. L. (1990), *Hydrology, An introduction to hydrologic science*, Addison-Wesley, Reading, MA.

Braud, I., A. C. Dantas-Antonino, M. Vauclin, J. L. Thony, and P. Ruelle (1995), A simple soil-plant-atmosphere transfer model (SiSPAT) development and field verification, *Journal of Hydrology*, *166*, 213–250.

Brekke, L. D., E. P. Maurer, J. D. Anderson, M. D. Dettinger, E. S. Townsley, A. Harrison, and T. Pruitt (2009), Assessing reservoir operations risk under climate change, *Water Resources Research*, *45*(W04411), doi:10.1029/2008WR006941.

Breshears, D. D., N. S. Cobb, P. M. Rich, K. P. Price, C. D. Allen, R. G. Balice, W. H. Romme, J. H. Kastens, M. L. Floyd, J. Belnap, J. J. Anderson, O. B. Myers, and C. W. Meyer (2005), Regional vegetation die-off in response to global-change type drought, *Proceedings of the National Academy of Sciences, USA*, *102*(42), 15,144–15,148.

Breshears, D. D., O. B. Myers, C. W. Meyer, F. J. Barnes, C. B. Zou, C. D. Allen, N. G. McDowell, and W. T. Pockman (2009), Tree die-off in response to global change-type drought: mortality insights from a decade of plant water potential measurements, *Frontiers in Ecology and the Environment*, *7*(4), 185–189, doi:10.1890/080016.

Bronstert, A. (2003), Floods and climate change: Interactions and impacts, *Risk Analysis*, *23*(3), 545–557.

Brooks, P. D., P. A. Troch, M. Durcik, E. L. Gallo, B. G. Moravec, M. E. Schlegel, and M. Carlson (2009), Predicting regional-scale ecosystem response to changes in precipitation: Not all rain is created equal, abstract presented at the American Geophysical Union Fall Meeting, San Francisco, CA, 14-18 December.

Brooks, R. H., and A. T. Corey (1964), Hydraulic properties of porous media, *Hydrology Paper 3*, Colorado State University, Ft. Collins, CO.

Brunetti, M., M. Colacino, M. Maugeri, and T. Nanni (2001a), Trends in the daily intensity of precipitation in Italy from 1951 to 1996, *International Journal of Climatology*, *21*, 299–316.

Brunetti, M., M. Maugeri, and T. Nanni (2001b), Changes in total precipitation, rainy days and extreme events in Northeastern Italy, *International Journal of Climatology*, *21*, 861–871, doi:10.1002/joc.660.

Brutsaert, W. (1982), *Evaporation into the atmosphere*, D. Reidel.

Brutsaert, W. (2005), *Hydrology. An Introduction*, Cambridge University Press, Cambridge, UK.

Buckley, T. N. (2005), The control of stomata by water balance, *New Phytologist*, *169*, 275–292, doi: 10.1111/j.1469-8137.2005.01543.x.

Buckley, T. N., K. A. Mott, and G. D. Farquhar (2003), A hydromechanical and biochemical model of stomatal conductance, *Plant, Cell and Environment*, *26*, 1767–1785.

Burlando, P., and R. Rosso (2002), Effects of transient climate change on basin hydrology. 1. Precipitation scenarios for the Arno river, central Italy, *Hydrological processes*, *16*, 1151–1175.

Burton, A., C. G. Kilsby, H. J. Fowler, P. S. P. Cowpertwait, and P. O'Connell (2008), RainSim: A spatial-temporal stochastic rainfall modelling system, *Environmental Modelling & Software*, *23*, 1356–1369, doi:10.1016/j.envsoft.2008.04.003.

Businger, J. A., J. C. Wyngaard, Y. Izumi, and E. F. Bradley (1971), Flux profile relationships in the atmospheric surface layer, *Journal of the Atmospheric Sciences*, *28*, 181–189.

Camillo, P. J., R. J. Gurney, and T. J. Schmugge (1983), A soil and atmospheric boundary layer model for evapotranspiration and soil moisture studies, *Water Resources Research*, *19*, 371–380.

Campbell, G. S. (1974), A simple method for determining unsaturated conductivity from moisture retention data, *Soil Science*, *117*, 311–314.

Campo, L., F. Caparrini, and F. Castelli (2006), Use of multi-platform, multi-temporal remote sensing data for calibration of a distributed hydrological model: an application in the Arno basin, Italy, *Hydrological Processes*, *20*, 2693–2712.

Cannon, A. J., and P. H. Whitfield (2002), Downscaling recent streamflow conditions in British Columbia, Canada using ensemble neural network models, *Journal of Hydrology*, *259*, 136–151.

Cayrol, P., L. Kergoat, S. Moulin, G. Dedieu, and A. Chehbouni (2000), Calibrating a coupled SVAT-vegetation growth model with remotely sensed reflectance and surface temperature-A case study for the HAPEX-Sahel grassland sites, *Journal of Applied Meteorology*, *39*(12), 2452–2472.

Celia, M. A., E. T. Bouloutas, and R. L. Zarba (1990), A general mass-conservative numerical solution for the unsaturated flow equation, *Water Resources Research*, *26*(7), 1483–1496.

Chaiwiwatworakul, P., and S. Chirarattananon (2004), An investigation of atmospheric turbidity of Thai sky, *Energy and Buildings*, *36*, 650–659.

Chapin III, F. S., E.-D. Schulze, and H. A. Mooney (1990), The ecology and economics of storage in plants, *Annual Review of Ecology and Systematics*, *21*, 423–447.

Chapin III, F. S., J. T. Randerson, A. D. McGuire, J. A. Foley, and C. B. Field (2008), Changing feedbacks in the climatebiosphere system, *Frontiers in Ecology and the Environment*, *6*(6), 313–320, doi:10.1890/080005.

Chen, Y., A. Hall, and K. N. Liou (2006), Application of three-dimensional solar radiative transfer to mountains, *Journal of Geophysical Research*, *111*(D21111), doi:10.1029/2006JD007163.

Cheng, D.-L., and K. J. Niklas (2007), Above- and below-ground biomass relationships across 1534 forested communities, *Annals of Botany*, *99*, 95–102, doi:10.1093/aob/mcl206.

Chew, R. M., and A. E. Chew (1965), The primary productivity of a desert-shrub (Larrea tridentata) community, *Ecological Monographs*, *35*(4), 355–375.

Chiesi, M., F. Maselli, M. Moriondo, L. Fibbi, M. Bindi, and S. Running (2007), Application of BIOME-BGC to simulate Mediterranean forest processes, *Ecological Modelling*, *206*, 179–190, doi:10.1016/j.ecolmodel.2007.03.032.

Chiew, F. H. S., J. Teng, J. Vaze, D. A. Post, J. M. Perraud, D. G. C. Kirono, and N. R. Viney (2009), Estimating climate change impact on runoff across southeast Australia: Method, results, and implications of the modeling method, *Water Resources Research*, *45*(W10414), doi:10.1029/2008WR007338.

Chirici, G., A. Barbati, and F. Maselli (2007), Modelling of italian forest net primary productivity by the integration of remotely sensed and GIS data, *Forest Ecology and Management*, *246*, 285–295, doi:10.1016/j.foreco.2007.04.033.

Choudhury, B. J., and J. L. Monteith (1988), A four-layer model for the heat budget of homogeneous land surfaces, *Quarterly Journal of the Royal Meteorological Society*, *114*, 378–398.

Chow, V. T. (1988), *Applied Hydrology*, McGraw-Hill Science Engineering.

Christensen, N. S., A. W. Wood, N. Voisin, D. P. Lettenmaier, and R. N. Palmer (2004), Effects of climate change on the hydrology and water resources of the Colorado river basin, *Climatic Change*, *62*, 337–363.

Ciarapica, L., and E. Todini (2002), TOPKAPI: a model for the representation of the rainfall-runoff process at different scales, *Hydrological Processes*, *16*, 207–229.

Cichota, R., E. A. Elias, and Q. de Jong van Lier (2004), Testing a finite-difference model for soil heat transfer by comparing numerical and analytical solutions, *Environmental Modelling & Software*, *19*, 495–506.

Clapp, R. B., and G. M. Hornberger (1978), Empirical equations for some soil hydraulic properties, *Water Resources Research*, *14*(4), 601–604.

Clark, J. S., S. R. Carpenter, M. Barber, S. Collins, A. Dobson, J. A. Foley, D. M. Lodge, M. Pascual, J. R. Pielke, W. Pizer, C. Pringle, W. V. Reid, K. A. Rose, O. Sala, W. H. Schlesinger, D. H. Wall, and D. Wear (2001), Ecological forecasts: An emerging imperative, *Science*, *293*, 657–660.

Clarke, H. D., D. S. Seigler, and J. E. Ebinger (1990), Acacia constricta (Fabaceae: Mimosoideae) and related species from the Southwestern U.S. and Mexico, *American Journal of Botany*, *77*(3), 305–315.

Clausnitzer, V., J. W. Hopmans, and J. L. Starr (1998), Parameter uncertainty analysis of common infiltration models, *Soil Science Society of America Journal*, *62*, 1477–1487.

Cleland, E. E., I. Chuine, A. Menzel, H. A. Mooney, and M. D. Schwartz (2007), Shifting plant phenology in response to global change, *Trends in Ecology and Evolution*, *22*(7), 357–365, doi:10.1016/j.tree.2007.04.003.

Cohen, H., and J. B. Laronne (2005), High rates of sediment transport by flash-floods in the Southern Judean desert, Israel, *Hydrological Processes*, *19*, 1687–1702, doi:10.1002/hyp.5630.

Collatz, G. J., J. T. Ball, C. Grivet, and J. A. Berry (1991), Physiological and environmental regulation of stomatal conductance, photosynthesis and transpiration-a model that includes a laminar boundary-layer, *Agricultural and Forest Meteorology*, *54*, 107–136.

Collatz, G. J., M. Ribas-Carbo, and J. A. Berry (1992), Coupled photosynthesis-stomatal conductance model for leaves of C4 plants, *Australian Journal of Plant Physiology*, *19*, 519–538.

Collins, D. B. G., R. L. Bras, and G. E. Tucker (2004), Modeling the effects of vegetation-erosion coupling on landscape evolution, *Journal of Geophysical Research*, *109*(F03004), doi:10.1029/2003JF000028.

Coppola, E., and F. Giorgi (2009), An assessment of temperature and precipitation change projections over Italy from recent global and regional climate model simulations, *International Journal of Climatology*, -, doi:10.1002/joc.1867.

Costa-Cabral, M., and S. J. Burges (1994), Digital elevation model networks (DEMON): A model of flow over hillslopes for computation of contributing and dispersal areas, *Water Resources Research*, *30*, 1681–1692.

Cowpertwait, P. S. P. (1991), Further developments of the Neyman-Scott clustered point process for modeling rainfall, *Water Resources Research*, *27*, 1431–1438.

Cowpertwait, P. S. P. (1994), A generalized point process model for rainfall, *Proceedings of the Royal Society of London, Series A*, *447*, 23–27.

Cowpertwait, P. S. P. (1995), A generalized spatial-temporal model of rainfall based on a clustered point process, *Proceedings of the Royal Society of London, Series A*, *450*, 163–175.

Cowpertwait, P. S. P. (1998), A Poisson-cluster model of rainfall: high order moments and extreme values, *Proceedings of the Royal Society of London, Series A*, *454*, 885–898.

Cowpertwait, P. S. P. (2004), Mixed rectangular pulses models of rainfall, *Hydrology and Earth System Sciences*, *8*, 993–1000.

Cowpertwait, P. S. P. (2006), A spatial-temporal point process model of rainfall for the Thames catchment, *Journal of Hydrology*, *330*, 586–595.

Cowpertwait, P. S. P., P. O'Connell, A. Metcalfe, and J. Mawdsley (1996), Stochastic point process modelling of rainfall: I. Single-site fitting and validation, *Journal of Hydrology*, *175*, 17–46.

Cowpertwait, P. S. P., C. Kilsby, and P. O'Connell (2002), A space-time Neyman-Scott model of rainfall: empirical analysis of extremes, *Water Resources Research*, *38*(8), 1–14.

Cowpertwait, P. S. P., V. Isham, and C. Onof (2007), Point process models of rainfall: developments for fine-scale structure, *Proceedings of the Royal Society of London, Series A*, *463*(2086), 2569–2587.

Cox, J. R., G. W. Fraiser, and K. G. Renard (1986), Biomass distribution at grassland and shrubland sites, *Rangelands*, *8*(2), 67–69.

Cox, P. M. (2001), Description of the TRIFFID Dynamic Global Vegetation Model, *Technical Note 24*, Hadley Centre.

Cox, P. M., R. A. Betts, C. B. Bunton, R. L. H. Essery, P. R. Rowntree, and J. Smith (1999), The impact of new land surface physics on the GCM simulation of climate and climate sensitivity, *Climate Dynamics*, *15*, 183–203.

Cox, R., B. L. Bauer, and T. Smith (1998), A mesoscale model intercomparison, *Bulletin of the American Meteorological Society*, *79*(2), 265–283.

Crawford, N., and R. Linsley (1966), Digital simulation on hydrology: Stanford watershed model IV, *Technical Report 39*, Stanford University, Palo Alto, CA.

Cunnane, C. (1978), Unbiased plotting positions–a review, *Journal of Hydrology*, *37*, 205–222.

Curtis, D. C., and P. S. Eagleson (1982), Constrained stochastic climate simulation, *Tech. Rep. 274*, Mass. Inst. of Technol. Dep. of Civ. and Environ. Eng. Ralph M. Parsons Lab., Cambridge Mass. USA.

Dai, Q., and S. Sun (2006), A generalized layered radiative transfer model in the vegetation canopy, *Advances in Atmospheric Sciences*, *23*(2), 243–257.

Dai, Q., and S. Sun (2007), A comparison of two canopy radiative models in land surface processes, *Advances in Atmospheric Sciences*, *24*(3), 421–434.

Dai, Y., R. E. Dickinson, and Y.-P. Wang (2004), A two-big-leaf model for canopy temperature, photosynthesis, and stomatal conductance, *Journal of Climate*, *17*, 2281–2299.

Daly, E., and A. Porporato (2005), A review of soil moisture dynamics: from rainfall infiltration to ecosystem response, *Environmental Engineering Science*, *22*(1), 9–24.

Daly, E., A. Porporato, and I. Rodriguez-Iturbe (2004), Coupled dynamics of photosynthesis, transpiration, and soil water balance. part I: Upscaling from hourly to daily level, *Journal of Hydrometeorology*, *5*, 546–558.

Darula, S., R. Kittler, and C. A. Gueymard (2005), Reference luminous solar constant and solar luminance for illuminance calculations, *Solar Energy*, *79*(5), 559–565.

de Pury, D. G. G., and G. D. Farquhar (1997), Simple scaling of photosynthesis from leaves to canopies without the errors of big-leaf models, *Plant, Cell and Environment*, *20*(5), 537–557.

de Vries, D. A. (1963), Thermal properties of soils, in *Physics of the Plant Environment*, edited by W. van Wijk, North-Holland, Amsterdam.

Deardorff, J. W. (1978), Efficient prediction of ground surface temperature and moisture with inclusion of a layer of vegetation, *Journal of Geophysical Research*, *83*, 1889–1903.

Deaves, D. M., and I. G. Lines (1997), On the fitting of low mean windspeed data to the Weibull distribution, *Journal of Wind Engineering and Industrial Aerodynamics*, *66*, 169–178.

Deckmym, G., H. Verbeeck, M. O. de Beeck, D. Vansteenkiste, K. Steppe, and R. Ceulemans (2008), ANAFORE: A stand-scale process-based forest model that includes wood tissue development and labile carbon storage in trees, *Ecological Modelling*, *215*, 345–368, doi:10.1016/j.ecolmodel.2008.04.007.

Deckmyn, G., S. P. Evans, and T. J. Randle (2006), Refined pipe theory for mechanistic modeling of wood development, *Tree Physiology*, *26*, 703–717.

Deidda, R. (2000), Rainfall downscaling in a space-time multifractal framework, *Water Resources Research*, *36*, 1779–1794, doi:10.1029/2000WR900038.

DeRoo, A. P. J., C. G. Wesseling, and C. J. Ritsema (1996), LISEM: a single-event physically based hydrological and soil erosion model for drainage basins: I: Theory, input and output, *Hydrological Processes*, *10*, 1107–1117.

Dewar, R. C. (2002), The Ball-Berry-Leuning and Tardieu-Davies stomatal models: synthesis and extension within a spatially aggregated picture of guard cell function, *Plant, Cell and Environment*, *25*, 1383–1398.

Dickinson, R. E. (1983), Land surface processes and climate-surface albedos and energy balance, *Advances in Geophysics*, *25*, 305–353.

Dickinson, R. E. (1988), The force-restore method for surface temperature and its generalization, *Journal of Climate*, *1*, 1086–1097.

Dickinson, R. E. (2008), Determination of the multi-scattered solar radiation from a leaf canopy for use in climate models, *Journal of Computational Physics*, *227*, 3667–3677.

Dickinson, R. E., A. Henderson-Sellers, and P. J. Kennedy (1993), Biosphere-atmosphere transfer scheme (BATS) version 1E as coupled to the NCAR Community Climate Model, *Tech. Rep. NCAR/TN-387+STR*, Natl. Cent. for Atmos. Res., Boulder, Colorado.

Dickinson, R. E., M. Shaikh, R. Bryant, and L. Graumlich (1998), Interactive canopies for a climate model, *Journal of Climate*, *11*, 2823–2836.

Dickinson, R. E., J. A. Berry, G. B. Bonan, G. J. Collatz, C. B. Field, I. Y. Fung, M. Goulden, W. A. Hoffmann, R. B. Jackson, R. Myneni, P. J. Sellers, and M. Shaikh (2002), Nitrogen controls on climate model evapotranspiration, *Journal of Climate*, *15*, 278–294.

Dingman, S. L. (1994), *Physical Hydrology*, Prentice-Hall, New Jersey.

Dorman, J. L., and P. J. Sellers (1989), A global climatology of albedo, roughness length and stomatal resistance for atmospheric general circulation models as represented by the simple biosphere model (SiB), *Journal of Applied Meteorology*, *28*, 833–855.

Dormand, J. R., and P. J. Prince (1980), A family of embedded Runge-Kutta formulae, *Journal of Computational and Applied Mathematics*, *6*, 19–26.

Douville, H., J.-F. Royer, and J.-F. Mahfouf (1995), A new snow parameterization for the Meteo-France climate model. Part I: Validation in stand-alone experiments, *Climate Dynamic*, *12*, 21–35.

Dozier, J., and J. Frew (1990), Rapid calculation of terrain parameters for radiation modeling from digital elevation data, *IEEE Transactions on Geoscience and Remote Sensing*, *28*, 963–969.

Dubayah, R., and S. Loechel (1997), Modeling topographic solar radiation using GOES data, *Journal of Applied Meteorology*, *36*, 141–154.

Dubrovský, M., J. Buchtele, and Z. Žalud (2004), High-frequency and low-frequency variability in stochastic daily weather generator and its effect on agricultural and hydrologic modelling, *Climatic Change*, *63*, 145–179.

Ducoudré, N. I., K. Laval, and A. Perrier (1993), SECHIBA, a new set of parameterizations of the hydrologic exchanges at the land atmosphere interface within the lmd atmospheric general circulation model, *Journal of Climate*, *6*, 248–272.

Dupont, S., and P. G. Mestayer (2006), Parameterization of the urban energy budget with the submesoscale soil model, *Journal of Applied Meteorology and Climatology*, *45*, 1744–1765.

Dye, D. G. (2004), Spectral composition and quanta-to-energy ratio of diffuse photosynthetically active radiation under diverse cloud conditions, *Journal of Geophysical Research*, *109*(D10203), doi:10.1029/2003JD004251.

Dyer, A. J. (1974), A review of flux-profile relationships, *Boundary-Layer Meteorology*, *7*, 368–372.

Eagleson, P. S. (1978), Climate, soil, and vegetation 1. Introduction to water balance dynamics, *Water Resources Research*, *14*(5), 705–712.

Eagleson, P. S. (2002), *Ecohydrology: Darwinian Expression of Vegetation Form and Function*, Cambridge University Press, Cambridge, U.K.

EEA (2007), Climate change and water adaptation issues, *Technical report 2/2007*, European Environment Agency.

Elshamy, M. E., H. S. Wheater, N. Gedney, and C. Huntingford (2006), Evaluation of the rainfall component of a weather generator for climate impact studies, *Journal of Hydrology*, *326*, 1–24, doi:10.1016/j.jhydrol.2005.09.017.

Eltahir, E. A. B., and R. L. Bras (1993), A description of rainfall interception over large-areas, *Journal of Climate*, *6*, 1002–1008.

Emmerich, W. E., and C. L. Verdugo (2008), Long-term carbon dioxide and water flux database, Walnut Gulch Experimental Watershed, Arizona, United States, *Water Resources Research*, *44*(W05S09), doi:10.1029/2006WR005693.

Enquist, B. J. (2002), Universal scaling in tree and vascular plant allometry: toward a general quantitative theory linking plant form and function from cells to ecosystems, *Tree Physiology*, *22*, 1045–1064.

Enquist, B. J., A. J. Kerkhoff, S. C. Stark, N. G. Swenson, M. C. McCarthy, and C. A. Price (2007), A general integrative model for scaling plant growth, carbon flux, and functional trait spectra, *Nature*, *449*(218-222), doi:10.1038/nature06061.

Entekhabi, D., I. Rodriguez-Iturbe, and P. S. Eagleson (1989), Probabilistic representation of the temporal rainfall process by a modified Neyman-Scott rectangular pulses model: Parameter estimation and validation, *Water Resources Research*, *25*(2), 295–302.

Essery, R., E. Martin, H. Douville, A. Fernandez, and E. Brun (1999), A comparison of four snow models using observations from an alpine site, *Climate Dynamic*, *15*, 583–593.

Ewen, J., G. Parkin, and P. E. O'Connell (2000), SHETRAN: Distributed river basin flow and transport modeling system, *Journal of Hydrological Engineering*, *5*(3), 250–258.

Fang, J. Y., S. L. Piao, Z. Y. Tang, C. H. Peng, and W. Ji (2001), Interannual variability in net primary production and precipitation, *Science*, *293*, 1723.

Farouki, O. T. (1981), The thermal properties of soils in cold regions, *Cold Regions Science and Technology*, *5*, 67–75.

Farquhar, G. D. (1989), Models of integrated photosynthesis of cells and leaves, *Philosophical Transactions of the Royal Society of London. Series B. Biological Sciences*, *323*, 357–367.

Farquhar, G. D., and S. C. Wong (1984), An empirical model of stomatal conductance, *Australian Journal of Plant Physiology*, *11*, 191–210.

Farquhar, G. D., S. V. Caemmerer, and J. A. Berry (1980), A biochemical model of photosynthetic CO_2 assimilation in leaves of C3 species, *Planta*, *149*, 78–90.

Farquhar, G. D., S. vonCaemmerer, and J. A. Berry (2001), Models of photosynthesis, *Plant Physiology*, *125*, 42–45.

Feddes, R. A., H. Hoff, M. Bruen, T. Dawson, P. de Rosnay, P. Dirmeyer, R. B. Jackson, P. Kabat, A. Kleidon, A. Lilly, and A. J. Pitmank (2001), Modeling root water uptake in hydrological and climate models, *Bulletin of the American Meteorological Society*, *82*(12), 2797–2809.

Fensham, R. . J. ., R. J. Fairfax, and D. P. Ward (2009), Drought-induced tree death in savanna, *Global Change Biology*, *15*, 380–387, doi:10.1111/j.1365-2486.2008.01718.x.

Fernandez-Illescas, C. P., and I. Rodriguez-Iturbe (2003), Hydrologically driven hierarchical competition colonization models: The impact of interannual rainfall fluctuations, *Ecological Monographs*, *73*(2), 207–222.

Fernandez-Illescas, C. P., and I. Rodriguez-Iturbe (2004), The impact of interannual rainfall variability on the spatial and temporal patterns of vegetation in a water-limited ecosystem, *Advances in Water Resources*, *27*, 83–95.

Fernandez-Illescas, C. P., A. Porporato, F. Laio, and I. Rodriguez-Iturbe (2001), The ecohydrological role of soil texture in a water-limited ecosystem, *Water Resources Research*, *37*(12), 2863–2872.

Fiering, M. B., and B. B. Jackson (1971), Synthetic hydrology, *Water resourc. monogr.*, Americ. Geophys. Union.

Foley, J., I. Prentice, N. Ramankutty, S. Levis, D. Pollard, S. Sitch, and A. Haxeltine (1996), An integrated biosphere model of land surface processes, terrestrial carbon balance, and vegetation dynamics, *Global Biogeochemical Cycles*, *10*, 603–628.

Foley, J. A., S. Levis, M. H. Costa, W. Cramer, and D. Pollard (2000), Incorporating dynamic vegetation cover within Global Climate Models, *Ecological Applications*, *10*(6), 1620–1632.

Foot, K., and R. P. C. Morgan (2005), The role of leaf inclination, leaf orientation and plant canopy architecture in soil particle detachment by raindrops, *Earth Surface Processes and Landforms*, *30*, 1509–1520, doi: 10.1002/esp.1207.

Forsythe, G. E., M. A. Malcolm, and C. B. Moler (1976), *Computer Methods for Mathematical Computations*, Prentice-Hall.

Foufoula-Georgiou, E., and D. Lettenmaier (1987), A Markov renewal model for rainfall occurrences, *Water Resources Research*, *23*(5), 875–884.

Fourcaud, T., X. Zhang, A. Stokes, H. Lambers, and C. Körner (2008), Plant growth modelling and applications: The increasing importance of plant architecture in growth models, *Annals of Botany*, *101*, 1053–1063, doi:10.1093/aob/mcn050.

Fowler, H. J., C. G. Kilsby, and P. E. O'Connel (2000), A stochastic rainfall model for the assessment of regional water resource systems under changed climatic conditions, *Hydrology and Earth System Science*, *4*(2), 263–282.

Fowler, H. J., C. G. Kilsby, P. E. O'Connel, and A. Burton (2005), A weather-type conditioned multi-site stochastic rainfall model for the generation of scenarios of climatic variability and change, *Journal of Hydrology*, *308*, 50–66.

Fowler, H. J., S. Blenkinsop, and C. Tebaldi (2007), Linking climate change modelling to impacts studies: recent advances in downscaling techniques for hydrological modelling, *International Journal of Climatology*, *27*, 1547–1578, dOI: 10.1002/joc.1556.

Franco, A. C., A. G. deSoyza, R. A. Virginia, J. F. Reynolds, and W. G. Whitford (1994), Effects of plant size and water relations on gas exchange and growth of the desert shrub Larrea tridentata, *Oecologia*, *97*, 171–178.

Frank, P. (2008), A climate of belief, *Skeptic*, *14*(1), 22–30.

Freeze, R. A., and R. L. Harlan (1969), Blueprint for a physically-based, digitally-simulated hydrologic response model, *Journal of Hydrology*, *9*, 237–258.

Freidenreich, S. M., and V. Ramaswamy (1999), A new multiple-band solar radiative parameterization for general circulation models, *Journal of Geophysical Research*, *104*(D24), 31,389–31,409.

Friedlingstein, P., G. Joel, C. B. Field, and I. Fung (1998), Toward an allocation scheme for global terrestrial carbon models, *Global Change Biology*, *5*, 755–770.

Friedlingstein, P., P. M. Cox, R. A. Betts, L. Bopp, W. VonBloh, V. Brovkin, P. Cadule, S. Doney, M. Eby, I. Fung, G. Bala, J. John, C. D. Jones, F. Joos, T. Kato, M. Kawamiya, W. Knorr, K. Lindsay, H. D. Matthews, T. Raddatz, P. Rayner, C. Reick, E. Roeckner, K.-G. Schnitzler, R. Schnur, K. Strassmann, A. J. Weaver, C. Yoshikawa, and N. Zeng (2006), Climate-carbon cycle feedback analysis: Results from the C4MIP model intercomparison, *Journal of Climate*, *19*(14), 3337–3353.

Friend, A. D. (2001), Modelling canopy CO_2 fluxes: are 'big-leaf' simplifications justified?, *Global Ecology & Biogeography*, *10*, 603–619.

Friend, A. D., A. K. Stevens, R. G. Knox, and M. G. R. Cannell (1997), A process-based, terrestrial biosphere model of ecosystem dynamics (Hybrid v3.0), *Ecological Modelling*, *95*, 249–287.

Friend, A. D., A. Arneth, N. Y. Kiang, M. Lomas, J. Ogée, C. Rödenbeck, S. W. Running, J.-D. Santaren, S. Sitch, N. Viovy, F. I. Woodward, and S. Zaehle (2007), FLUXNET and modelling the global carbon cycle, *Global Change Biology*, *13*, 610–633, doi: 10.1111/j.1365-2486.2006.01223.x.

Furrer, R., R. Knutti, S. R. Sain, D. W. Nychka, and G. A. Meehl (2007), Spatial patterns of probabilistic temperature change projections from a multivariate Bayesian analysis, *Geophysical Research Letter*, *34*(L06711), doi:10.1029/2006GL027754.

Gao, Q., P. Xhao, X. Zeng, X. Cai, and W. Shen (2002), A model of stomatal conductance to quantify the relationship between leaf transpiration, microclimate, and soil water stress, *Plant, Cell and Environment*, *25*, 1373–1381.

Gardner, A. S., and M. J. Sharp (2010), A review of snow and ice albedo and the development of a new physically based broadband albedo parameterization, *Journal of Geophysical Research*, *115*(F01009), doi:10.1029/2009JF001444.

Garratt, J. R. (1992), *The Atmospheric Boundary Layer*, Cambridge University Press.

Garrote, L., and R. L. Bras (1995), A distributed model for real-time flood casting using digital elevation models, *Journal of Hydrology*, *167*, 279–306.

Gaume, E., N. Mouhous, and H. Andrieu (2007), Rainfall stochastic disaggregation models: Calibration and validation of a multiplicative cascade model, *Advances in Water Resources*, *30*, 1301–1319, doi:10.1016/j.advwatres.2006.11.007.

Gelfan, A. N., J. W. Pomeroy, and L. S. Kuchment (2004), Modeling forest cover influences on snow accumulation, sublimation, and melt, *Journal of Hydrometeorology*, *5*, 785–803.

Gerrits, A. M. J., H. H. G. Savenije, L. Hoffmann, and L. Pfister (2007), New technique to measure forest floor interception - an application in a beech forest in Luxembourg, *Hydrology and Earth System Science*, *11*, 695–701.

Gill, R. A., and R. B. Jackson (2000), Global patterns of root turnover for terrestrial ecosystems, *New Phytologist*, *147*, 13–31.

Giorgi, F., and L. Mearns (2002), Calculation of average, uncertainty range and reliability of regional climate changes from AOGCM simulations via the 'reliability ensemble averaging' (REA) method, *Journal of Climate*, *15*, 1141–1158.

Giorgi, F., and L. Mearns (2003), Probability of regional climate change calculated using the reliability ensemble average (REA) method, *Geophysical Research Letter*, *30*, 1629–1632, doi:10.1029/2003GL017130.

Goudriaan, J. (1977), Crop micrometeorology: A simulation study, *Tech. rep.*, Wageningen Center for Agricultural Publishing and Documentation.

Gough, C. M., C. E. Flower, C. S. Vogel, D. Dragoni, and P. S. Curtis (2009), Whole-ecosystem labile carbon production in a north temperate deciduous forest, *Agricultural and Forest Meteorology*, *149*, 1531–1540, doi:10.1016/j.agrformet.2009.04.006.

Grachev, A. A., E. L. Andreas, C. W. Fairall, P. S. Guest, and P. O. G. Persson (2007), On the turbulent Prandtl number in the stable atmospheric boundary layer, *Boundary-Layer Meteorology*, *125*, 329–341, doi: 10.1007/s10546-007-9192-7.

Granier, A., M. Reichstein, N. Breda, I. A. Janssens, E. Falge, P. Ciais, T. Grunwald, M. Aubinet, P. Berbigier, C. Bernhofer, N. Buchmann, O. Facini, G. Grassi, B. Heinesch, H. Ilvesniemi, P. Keronen, A. Knohl, B. Kostner, F. Lagergren, A. Lindroth, B. Longdoz, D. Loustau, J. Mateus, L. Montagnani, C. Nys, E. Moors, D. Papale, M. Peiffer, K. Pilegaard, G. Pita, J. Pumpanen, S. Rambal, C. Rebmann, A. Rodrigues, G. Seufert, J. Tenhunen, T. Vesala, and Q. Wang (2007), Evidence for soil water control on carbon and water dynamics in European forests during the extremely dry year: 2003, *Agricultural and Forest Meteorology*, *143*, 123–145, doi:10.1016/j.agrformet.2006.12.004.

Greene, A., L. Goddard, and U. U. Lall (2006), Probabilistic multimodel regional temperature change projections, *Journal of Climate*, *19*, 4326–4343, doi:10.1175/JCLI3864.1.

Grimaldi, S., F. Nardi, B. F. Di, E. Istanbulluoglu, and R. L. Bras (2007), A physically-based method for removing pits in digital elevation models, *Advances in Water Resources*, *30*, 2151–2158, doi:10.1016/j.advwatres.2006.11.016.

Groisman, P. Y., R. W. Knight, T. R. Karl, D. R. Easterling, B. Sun, and J. H. Lawrimore (2004), Contemporary changes of the hydrological cycle over the contiguous United States: Trends derived from in situ observations, *Journal of Hydrometeorology*, *5*(1), 64–85.

Gueymard, C. A. (1989), A two-band model for the calculation of clear sky solar irradiance, illuminance, and photosynthetically active radiation at the earth's surface, *Solar Energy*, *43*, 253–265.

Gueymard, C. A. (2001), Parameterized transmittance model for direct beam and circumsolar spectral irradiance, *Solar Energy*, *71*, 325–346.

Gueymard, C. A. (2003), Direct solar transmittance and irradiance predictions with broadband models. Part 1: Detailed theoretical performance assessment, *Solar Energy*, *74*, 355–379, corrigendum: *Solar Energy* 76, 513 (2004).

Gueymard, C. A. (2008), REST2: High-performance solar radiation model for cloudless-sky irradiance illuminance and photosynthetically active radiation - validation with a bechmark dataset, *Solar Energy*, *82*, 272–285.

Gumiere, S. J., Y. Le Bissonnais, and D. Raclot (2009), Soil resistance to interrill erosion: Model parameterization and sensitivity, *Catena*, *77*, 274–284, doi:10.1016/j.catena.2009.02.007.

Gupta, V. K., and E. C. Waymire (1993), A statistical analysis of mesoscale rainfall as a random cascade, *Journal of Applied Meteorology*, *32*, 251–267.

Guswa, A. J., M. A. Celia, and I. Rodriguez-Iturbe (2002), Models of soil moisture dynamics in ecohydrology: A comparative study, *Water Resources Research*, *38*(9), doi:10.1029/2001WR000826.

Hamerlynck, E. P., and T. E. Huxman (2009), Ecophysiology of two Sonoran Desert evergreen shrubs during extreme drought, *Journal of Arid Environments*, *73*, 582–585, doi:10.1016/j.jaridenv.2008.11.012.

Hamlet, A. F., and D. P. Lettenmaier (2007), Effects of 20th century warming and climate variability on flood risk in the western U.S., *Water Resources Research*, *43*(W06427), doi:10.1029/2006WR005099.

Hamlet, A. F., P. W. Mote, M. P. Clark, and D. P. Lettenmaier (2007), Twentieth-century trends in runoff, evapotranspiration, and soil moisture in the Western United States, *Journal of Climate*, *20*, 1468–1486, doi:10.1175/JCLI4051.1.

Hanan, N. P. (2001), Enhanced two-layer radiative transfer scheme for a land surface model with a discontinuous upper canopy, *Agricultural and Forest Meteorology*, *109*, 265–281.

Hansen, J., and E. Beck (1990), The fate and path of assimilation products in stem of 8-year-old Scots pine (Pinus sylvestris L.) trees, *Trees*, *4*, 16–21.

Hansen, J. W., and T. Mavromatis (2001), Correcting low-frequency variability bias in stochastic weather generators, *Agricultural and Forest Meteorology*, *109*, 297–310.

Hanson, C. L. (2001), Long-term precipitation database, Reynolds Creek Experimental Watershed, Idaho, United States, *Water Resources Research*, *37*(11), 2831–2834.

Hanson, C. L., D. Marks, and S. S. VanVactor (2001), Long-term climate database, Reynolds Creek Experimental Watershed, Idaho, United States, *Water Resources Research*, *37*(11), 2839–2841.

Hanson, P. J., J. S. Amthor, S. D. Wullschleger, K. B. Wilson, R. F. Grant, A. Hartley, D. Hui, E. R. Hunt, D. W. Johnson, J. S. Kimball, A. W. King, Y. Luo, S. G. McNulty, G. Sun, P. E. Thornton, S. Wang, M. Williams, D. D. Baldocchi, and R. M. Cushman (2004), Oak forest carbon and water simulations: model intercomparisons and evaluations against independent data, *Ecological Monographs*, *74*(3), 443–489.

Hanson, P. J., S. D. Wullschleger, R. J. Norby, T. J. Tschaplinski, and C. A. Gunderson (2005), Importance of changing CO_2, temperature, precipitation, and ozone on carbon and water cycles of an upland-oak forest: incorporating experimental results into model simulations, *Global Change Biology*, *11*, 1402–1423, doi: 10.1111/j.1365-2486.2005.00991.x.

Hawkes, C. (2000), Woody plant mortality algorithms: description, problems and progress, *Ecological Modelling*, *126*, 225–248.

Haxeltine, A., and I. C. Prentice (1996), BIOME3: An equilibrium terrestrial biosphere model based on ecophysiological constraints, resource availability, and competition among plant functional types, *Global Biogeochemical Cycles*, *10*(4), 693–709.

Hayhoe, K., C. P. Wake, T. G. Huntington, L. Luo, M. D. Schwartz, J. Sheffield, E. Wood, B. Anderson, J. Bradbury, A. DeGaetano, T. J. Troy, and D. Wolfe (2007), Past and future changes in climate and hydrological indicators in the US Northeast, *Climate Dynamics*, pp. 381–407, doi: 10.1007/s00382-006-0187-8.

He, W., and T. Kobayashi (1998), A rational parameterization of evaporation from dry, bare soil, *Journal of the Meteorological Society of Japan*, *76*(6), 955–963.

Hedstrom, N. R., and J. W. Pomeroy (1998), Measurements and modelling of snow interception in the boreal forest, *Hydrological Processes*, *12*, 1611–1625.

Hetherington, A. M., and F. I. Woodward (2003), The role of stomata in sensing and driving environmental change, *Nature*, *424*, 901–908.

Hillel, D. (1998), *Environmental Soil Physics: Fundamentals, Applications, and Environmental Considerations*, Academic Press, London, UK.

Hoch, G., A. Richter, and C. Körner (2003), Non-structural carbon compounds in temperate forest trees, *Plant, Cell and Environment*, *26*, 1067–1081.

Holben, B. N., T. F. Eck, I. Slutsker, D. Tanr, J. P. Buis, A. Setzer, E. Vermote, J. A. Reagan, Y. J. Kaufamn, T. Nakajima, F. Lavenu, I. Jankowiak, and A. Smirnov (1998), AERONET-A federated instrument network and data archive for aerosol characterization, *Remote Sensing of Environment*, *66*, 1–16.

Hopp, L., C. Harman, S. L. E. Desilets, C. B. Graham, J. J. McDonnell, and P. A. Troch (2009), Hillslope hydrology under glass: confronting fundamental questions of soil-water-biota co-evolution at Biosphere 2, *Hydrology and Earth System Science*, *13*, 2105–2118.

Horton, R. E. (1919), Rainfall interception, *Monthly Weather Review*, *47*(9), 603–623.

Housman, D. C., E. Naumburg, T. E. Huxman, T. N. Charlet, R. S. Nowak, and S. D. Smith (2006), Increases in desert shrub productivity under elevated carbon dioxide vary with water availability, *Ecosystems*, *9*, 374–385, doi:10.1007/s10021-005-0124-4.

Howes, D. A., and A. D. Abrahams (2003), Modeling runoff and runon in a desert shrubland ecosystem, Jornada Basin, New Mexico, *Geomorphology*, *53*, 45–73, doi:10.1016/S0169-555X(02)00347-1.

Hu, Z., and S. Islam (1995), Prediction of ground surface temperature and soil moisture content by the force restore-method, *Water Resources Research*, *31*(10), 2531–2539.

Hunt, J. C. R. (2002), Floods in a changing climate: a review, *Philosophical Transactions of the Royal Society of London, Series A*, *360*, 1531–1543, doi:10.1098/rsta.2002.1016.

Huxman, T. E., M. D. Smith, P. A. Fay, A. K. Knapp, M. R. Shaw, M. E. Loik, S. D. Smith, D. T. Tissue, J. C. Zak, J. F. Weltzin, W. T. Pockman, O. E. Sala, B. M. Haddad, J. Harte, G. W. Koch, S. Schwinning, E. E. Small, and D. G. Williams

(2004a), Convergence across biomes to a common rain use efficiency, *Nature*, *429*, 651–654.

Huxman, T. E., K. A. Snyder, D. Tissue, A. J. Leffler, K. Ogle, W. T. Pockman, D. R. Sandquist, D. L. Potts, and S. Schwinning (2004b), Precipitation pulses and carbon fluxes in semiarid and arid ecosystems, *Oecologia*, *141*, 254–268, doi:10.1007/s00442-004-1682-4.

Idso, S. B. (1981), A set of equations for full spectrum and 8- to 14-μm and 10.5- to 12.5 μm thermal radiation from cloudless skies, *Water Resources Research*, *17*(2), 295–304.

Ineichen, P. (2006), Comparison of eight clear sky broadband models against 16 independent data banks, *Solar Energy*, *80*, 468–478.

IPCC (2000), *Special Report on Emissions Scenarios. A Special Report of Working Group III of the Intergovernmental Panel on Climate Change*, Cambridge University Press, Cambridge, United Kingdom and New York, NY, USA,.

IPCC (2001), *Climate Change 2001: The scientific basis. Contribution of Working Group I to the Third Assessment Report of the Intergovernmental Panel on Climate Change*, Cambridge University Press, Cambridge, United Kingdom.

IPCC (2007a), *Climate Change 2007: The Physical Science Basis. Contribution of Working Group I to the Fourth Assessment Report of the Intergovernmental Panel on Climate Change*, Cambridge University Press, Cambridge, United Kingdom and New York, NY, USA.

IPCC (2007b), *Climate Change 2007: Impacts, Adaptation and Vulnerability. Contribution of Working Group II to the Fourth Assessment Report of the Intergovernmental Panel on Climate Change*, Cambridge University Press, Cambridge, United Kingdom and New York, NY, USA.

Iqbal, M. (1983), *An Introduction to Solar Radiation*, Academic Press, Toronto.

Istanbulluoglu, E., D. G. Tarboton, and R. T. Pack (2004), Modeling of the interactions between forest vegetation, disturbances, and sediment yields, *Journal of Geophysical Research*, *109*(F01009), doi:10.1029/2003JF00004.

Ivanov, V. Y. (2006), Effects of dynamic vegetation and topography on hydrological processes in semi-arid areas, Ph.D. thesis, Department of Civil and Environmental Engineering, MIT.

Ivanov, V. Y., E. R. Vivoni, R. L. Bras, and D. Entekhabi (2004a), Catchment hydrologic response with a fully-distributed triangulated irregular network model, *Water Resources Research*, *40*(11), W11,102, doi:10.1029/2004WR003218.

Ivanov, V. Y., E. R. Vivoni, R. L. Bras, and D. Entekhabi (2004b), Preserving high-resolution surface and rainfall data in operational-scale basin hydrology: a fully-distributed physically-based approach, *Journal of Hydrology*, *298*, 80–111, doi:10.1016/j.jhydrol.2004.03.041.

Ivanov, V. Y., R. L. Bras, and D. C. Curtis (2007), A weather generator for hydrological, ecological, and agricultural applications, *Water Resources Research*, *43*, W10,406, doi: 10.1029/ 2006WR005,364.

Ivanov, V. Y., R. L. Bras, and E. R. Vivoni (2008a), Vegetation-hydrology dynamics in complex terrain of semiarid areas: 1. A mechanistic approach to modeling dynamic feedbacks, *Water Resources Research*, *44*(W03429), doi:10.1029/2006WR005588.

Ivanov, V. Y., R. L. Bras, and E. R. Vivoni (2008b), Vegetation-hydrology dynamics in complex terrain of semiarid areas: 2. Energy-water controls of vegetation spatiotemporal dynamics and topographic niches of favorability, *Water Resources Research*, *44*(W03430), doi:10.1029/2006WR005595.

Iziomon, M. G., H. Mayer, and A. Matzarakis (2003), Downward atmospheric longwave irradiance under clear and cloudy skies: Measurement and parameterization, *Journal of Atmospheric and Solar-Terrestrial Physics*, *65*, 1107–1116, doi:10.1016/j.jastp.2003.07.007.

Jackson, R. B., J. Canadell, J. R. Ehleringer, H. A. Mooney, O. E. Sala, and E. D. Schulze (1996), A global analysis of root distributions for terrestrial biomes, *Oecologia*, *108*(3), 389–411.

Jacquemin, B., and J. Noilhan (1990), Sensitivity study and validation of a land surface parameterization using the HAPEX-MOBILHY data set., *Boundary-Layer Meteorology*, *52*, 93–134.

Jarvis, A. J., and W. J. Davies (1998), The coupled response of stomatal conductance to photosynthesis and transpiration, *Journal of Experimental Botany*, *49*, 399–406.

Jarvis, A. J., T. A. Mansfield, and W. J. Davies (1999), Stomatal behaviour, photosynthesis and transpiration under rising CO_2, *Plant, Cell and Environment (1999) 22, 639648*, *22*, 639–648.

Jarvis, P. G. (1976), The interpretation of the variances in leaf water potential and stomatal conductance found in canopies in the field, *Philosophical Transactions of the Royal Society of London, Series B*, *273*, 593–610.

Johnson, D. W., and R. I. vanHook (1989), *Analysis of Biogeochemical Cycling Processes in Walker Branch Watershed.*, Springer-Verlag, New York.

Jones, H. G. (1983), *Plants and Microclimate*, Cambridge University Press, New York.

Jones, H. G. (1998), Stomatal control of photosynthesis and transpiration, *Journal of Experimental Botany*, *49*, 387–398.

Jost, G., M. Weiler, D. R. Gluns, and Y. Alila (2007), The influence of forest and topography on snow accumulation and melt at the watershed-scale, *Journal of Hydrology*, *347*, 101–115, doi:10.1016/j.jhydrol.2007.09.006.

Jun, M., R. Knutti, and D. W. Nychka (2008), Spatial analysis to quantify numerical model bias and dependence: how many climate models are there?, *Journal of the American Statistical Association*, *103*, 934–947, doi:10.1198/016214507000001265.

Justice, C. O., E. Vermote, J. R. G. Townshend, R. Defries, D. P. Roy, D. K. Hall, V. V. Salomonson, J. L. Privette, G. Riggs, A. Strahler, W. Lucht, R. B. Myneni, Y. Knyazikhin, S. W. Running, R. R. Nemani, Z. Wan, A. R. Huete, W. vanLeeuwen, R. E. Wolfe, L. Giglio, J.-P. Muller, P. Lewis, and M. J. Barnsley (1998), The Moderate Resolution Imaging Spectroradiometer (MODIS): land remote sensing for global change research, *IEEE, Transactions on Geoscience and Remonte Sensing*, *36*, 1228–1249.

Kaduk, J., and M. Heimann (1996), A prognostic phenology scheme for global terrestrial carbon cycle models, *Climate Research*, *5*, 1–19.

Kampf, S. K., and S. J. Burges (2007), A framework for classifying and comparing distributed hillslope and catchment hydrologic models, *Water Resources Research*, *43*(W05423), doi:10.1029/2006WR005370.

Kamphorst, E., V. G. Jetten, J. Guerif, J. Pitkanen, B. Iversen, J. Douglas, and A. Paz (2000), Predicting depressional storage from soil surface roughness, *Soil Science Society of America Journal*, *64*, 1749–1758.

Kasten, F., and G. Czeplak (1980), Solar and terrestrial radition dependent on the amount and type of cloud, *Solar Energy*, *24*, 177–189.

Kattge, J., and W. Knorr (2007), Temperature acclimation in a biochemical model of photosynthesis: a reanalysis of data from 36 species, *Plant, Cell and Environment*, *30*, 1176–1190, doi: 10.1111/j.1365-3040.2007.01690.x.

Katul, G. G., R. Leuning, and R. Oren (2003), Relationship between plant hydraulic and biochemical properties derived from a steady-state coupled water and carbon transport model, *Plant, Cell and Environment*, *26*, 339–350.

Katz, R. W. (1996), Use of conditional stochastic models to generate climate change scenarios, *Climatic Change*, *32*, 237–255.

Katz, R. W., and M. B. Parlange (1993), Effects of an index of atmospheric circulation on stochastic properties of precipitation, *Water Resources Research*, *29*, 2335–2344.

Katz, R. W., and M. B. Parlange (1998), Overdispersion phenomenon in stochastic modeling of precipitation, *Journal of Climate*, *11*, 591–601.

Keefer, T. O., M. S. Moran, and G. B. Paige (2008), Long-term meteorological and soil hydrology database, Walnut Gulch Experimental Watershed, Arizona, United States, *Water Resources Research*, *44*(W05S07), doi:10.1029/2006WR005702.

Kelliher, F. M., R. Leuning, M. R. Raupach, and E.-D. Schulze (1995), Maximum conductances for evaporation from global vegetation types, *Agricultural and Forest Meteorology*, *73*, 1–16.

Kelly, A. E., and M. L. Goulden (2008), Rapid shifts in plant distribution with recent climate change, *Proc. Natl Acad. Sci. USA*, *105*(33), 11,823–11,826, doi:10.1073/pnas.0802891105.

Kergoat, L., S. Lafont, H. Douville, B. Berthelot, G. Dedieu, S. Planton, and J.-F. Royer (2002), Impact of doubled CO_2 on globalscale leaf area index and evapotranspiration: Conflicting stomatal conductance and LAI responses, *Journal of Geophysical Research*, *107*(D24), doi:10.1029/2001JD001245.

Kharecha, P. A., and J. E. Hansen (2008), Implications of "peak oil" for atmospheric CO_2 and climate, *Global Biogeochemical Cycles*, *22*(GB3012), doi:10.1029/2007GB003142.

Kiely, G., J. D. Albertson, M. B. Parlange, and R. W. Katz (1998), Conditioning stochastic properties of daily precipitation on indices of atmospheric circulation, *Meteorological Applications*, *5*.

Kilsby, C. G., P. Jones, A. Burton, A. Ford, H. Fowler, C. Harpham, P. James, A. Smith, and R. Wilby (2007), A daily weather generator for use in climate change studies, *Environmental Modelling & Software*, *22*, 1705–1719.

Kimball, J. S., S. W. Running, and R. Nemani (1997), An improved method for estimating surface humidity from daily minimum temperature, *Agricultural Forest Meteorology*, *85*, 87–98.

King, A. W., C. A. Gunderson, W. M. Post, D. J. Weston, and S. D. Wullschleger (2006), Plant respiration in a warmer world, *Science*, *312*, 536–537, doi:10.1126/science.1114166.

King, D. M., S. M. Skirvin, C. H. Collins, M. S. Moran, S. H. Biedenbender, M. R. Kidwell, M. A. Weltz, and A. Diaz-Gutierrez (2008), Assessing vegetation change temporally and spatially in southeastern Arizona, *Water Resources Research*, *44*(W05S15), doi:10.1029/2006WR005850.

Kirschbaum, M. F. (199), CenW, a forest growth model with linked carbon, energy, nutrient and water cycles, *Ecological Modelling*, *118*, 17–59.

Kleidon, A., K. Fraedrich, and M. Heimann (2000), A green planet versus a desert world: estimating the maximum effect of vegetation on the land surface climate, *Climatic Change*, *44*, 471–493.

Kletter, A. Y., J. vonHardenberg, E. Meron, and A. Provenzale (2009), Patterned vegetation and rainfall intermittency, *Journal of Theoretical Biology*, *256*, 574–583, doi:10.1016/j.jtbi.2008.10.020.

Knapp, A. K., and M. D. Smith (2001), Variation among biomes in temporal dynamics of aboveground primary production, *Science*, *291*, 481–484.

Knorr, W. (2000), Annual and interannual CO_2 exchanges of the terrestrial biosphere: Process based simulations and uncertainties, *Global Ecology and Biogeography*, *9*, 225–252.

Knutti, R. (2008), Should we believe model predictions of future climate change?, *Philosophical Transactions of the Royal Society A*, *366*, 4647–4664, doi:10.1098/rsta.2008.0169.

Knyazikhin, Y., J. V. Martonchik, R. B. Myneni, D. J. Diner, and S. W. Running (1998), Synergistic algorithm for estimating vegetation canopy leaf area index and fraction of absorbed photosynthetically active radiation from MODIS and MISR data, *Journal of Geophysical Research*, *103*, 32,257–32,275.

Kobe, R. K. (1997), Carbohydrate allocation to storage as a basis of interspecific variation in sapling survivorship and growth, *Oikos*, *80*(2), 226–233.

Kollet, S. J., and R. M. Maxwell (2006), Integrated surface-groundwater flow modeling: A free-surface overland flow boundary condition in a parallel groundwater flow model, *Advances in Water Resources*, *29*, 945–958, doi:10.1016/j.advwatres.2005.08.006.

Kondo, J., and S. Ishida (1997), Sensible heat flux from the Earth's surface under natural convective conditions, *Journal of the Atmospheric Sciences*, *54*, 498–509.

Kondo, J., N. Saigusa, and T. Sato (1990), A parametrization of evaporation from bare soil surfaces, *Journal of Applied Meteorology*, *29*, 385–389.

Körner, C. (2003), Carbon limitation in trees, *Journal of Ecology*, *91*, 4–17.

Körner, C. (2006), Plant CO_2 responses: an issue of definition, time and resource supply, *New Phytologist*, *172*, 393–411, 10.1111/j.1469-8137.2006.01886.x.

Köstner, B., E. Falge, and J. D. Tenhunen (2002), Age-related effects on leaf areasapwood area relationships, canopy transpiration and carbon gain of Norway spruce stands (Picea abies) in the Fichtelgebirge, Germany, *Tree Physiology*, *22*(8), 567–574.

Kot, S. C., and Y. Song (1998), An improvement of the louis scheme for the surface layer in an atmopsheric modelling system, *Boundary-Layer Meteorology*, *88*, 239–254.

Koutsoyiannis, D. (2000), A generalized mathematical framework for stochastic simulation and forecast of hydrologic time series, *Water Resource Research*, *36*(6), 1519–1533.

Koutsoyiannis, D. (2003a), Climate change, the Hurst phenomenon, and hydrological statistics, *Hydrological Sciences Journal*, *48(1)*(6), 3–24.

Koutsoyiannis, D. (2003b), Rainfall disaggregation methods: Theory and applications, in *Workshop on Statistical and Mathematical Methods for Hydrological Analysis*, edited by R. Universit degli Studi di Roma, La Sapienza.

Koutsoyiannis, D., and C. Onof (2001), Rainfall disaggregation using adjusting procedures on a Poisson cluster model, *Journal of Hydrology*, *246*, 109–122.

Koutsoyiannis, D., D. Kozonis, and A. Manetas (1998), A mathematical framework for studying rainfall intensity-duration-frequency relationships, *Journal of Hydrology*, *206*, 118–135.

Koutsoyiannis, D., C. Onof, and H. S. Wheater (2003), Multivariate rainfall disaggregation at a fine timescale, *Water Resources Research*, *39*(7), doi:10.1029/2002WR001600.

Koutsoyiannis, D., A. Efstratiadis, N. Mamassis, and A. Christofides (2008), On the credibility of climate predictions, *Hydrological Sciences Journal*, *53*(4), 671–684.

Kozlowski, T. T., and S. G. Pallardy (1997), *Physiology of Woody Plants*, Academic Press.

Kozlowski, T. T., and S. G. Pallardy (2002), Acclimation and adaptive responses of woody plants to environmental stresses, *The Botanical Review*, *68*(2), 270–334.

Krinner, G., N. Viovy, N. de Noblet-Ducoudre, J. Ogee, J. Polcher, P. Friedlingstein, P. Ciais, S. Sitch, and I. C. Prentice (2005), A dynamic global vegetation model for studies of the coupled atmosphere-biosphere system, *Global Biogeochemical Cycles*, *19*(GB1015), doi:10.1029/2003GB002199.

Kucharik, C., J. Foley, C. Delire, V. Fisher, M. Coe, J. Lenters, C. Young-Molling, N. Ramankutty, J. Norman, and S. Gower (2000), Testing the performance of a dynamic global ecosystem model: Water balance, carbon balance, and vegetation structure, *Global Biogeochemical Cycles*, *14*, 795–825.

Kumar, L., A. K. Skidmore, and E. Knowles (1997), Modeling topographic variation in solar radiation in a GIS environment, *International Journal of Geographic Information Science*, *11*, 475–497.

Kumar, P. (2004), Layer averaged Richard's equation with lateral flow, *Advances in Water Resources*, *27*, 521–531, doi:10.1016/j.advwatres.2004.02.007.

Kurc, S. A., and E. E. Small (2004), Dynamics of evapotranspiration in semiarid grassland and shrubland ecosystems during the summer monsoon season, central New Mexico, *Water Resources Research*, *40*(W09305), doi:10.1029/2004WR003068.

Kyselý, J., and M. Dubrovský (2005), Simulation of extreme temperature events by a stochastic weather generator: effects of interdiurnal and interannual variability reproduction, *International Journal of Climatology*, *25*, 251–269.

Lacointe, A. (2000), Carbon allocation among tree organs: A review of basic processes and representation in functional-structural tree models, *Annals of Forest Science*, *57*, 521–533.

Laio, F., A. Porporato, L. Ridolfi, and I. Rodriguez-Iturbe. (2001), Plants in water-controlled ecosystems: active role in hydrological processes and response to water stress. II. Probabilistic soil moisture dynamics, *Advances in Water Resources*, *24*, 707–723.

Lambers, H., I. F. S. Chapin, and T. L. Pons (1998), *Plant Physiological Ecology*, Springer, New York.

Lambert, S. J., and G. J. Boer (2001), CMIP1 evaluation and intercomparison of coupled climate models, *Climate Dynamics*, *17*, 83–106, doi:10.1007/PL00013736.

Larcher, W. (2001), *Physiological Plant Ecology*, 4th ed., Springer, New York.

Launiainen, J. (1995), Derivation of the relationship between the Obukhov stability parameter and the bulk Richardson number for flux-profile studies, *Boundary-Layer Meteorology*, *76*, 165–179.

Leander, R., and T. A. Buishand (2007), Resampling of regional climate model output for the simulation of extreme river flows, *Journal of Hydrology*, *332*, 487–496, doi:10.1016/j.jhydrol.2006.08.006.

LeCam, L. (1961), A stochastic description of precipitation, in *Proceedings of Fourth Berkeley Symposium on Mathematical Statistics and Probability*, vol. 3, edited by J. Neyman, pp. 165–176, Univ. of Calif. Press Berkeley.

Lee, D. W., and K. S. Gould (2002), Why leaves turn red, *American Scientist*, *90*, 524–531.

Lee, Y.-H., and L. Mahrt (2004), An evaluation of snowmelt and sublimation over short vegetation in land surface modelling, *Hydrological Processes*, *18*, 3543–3557, doi: 10.1002/hyp.5799.

Lehmann, P., S. Assouline, and D. Or (2008), Characteristic lengths affecting evaporative drying of porous media, *Physical Review E*, *77*(056309), doi: 10.1103/PhysRevE.77.056309.

Lehner, B., P. Döll, J. Alcamo, T. Henrichs, and F. Kaspar (2006), Estimating the impact of global change on flood and drought risks in Europe: a continental integrated analysis, *Climatic Change*, *75*, 273–299, doi:10.1007/s10584-006-6338-4.

Lenhart, T., A. VanRompaey, A. Steegen, N. Fohrer, H.-G. Frede, and G. Govers (2005), Considering spatial distribution and deposition of sediment in lumped and semi-distributed models, *Hydrological Processes*, *19*, 785–794, doi: 10.1002/hyp.5616.

Leonard, M., M. F. Lambert, A. V. Metcalfe, and P. S. P. Cowpertwait (2008), A space-time Neyman-Scott rainfall model with defined storm extent, *Water Resources Research*, *44*(W09402), doi:10.1029/2007WR006110.

LeRoux, X., A. Lacointe, A. Escobar-Gutirrez, and S. LeDizs (2001), Carbon-based models of individual tree growth: A critical appraisal, *Annals of Forest Science*, *58*, 459–506.

Leuning, R. (1990), Modelling stomatal behaviour and photosynthesis of eucalyptus grandis, *Australian Journal of Plant Physiology*, *17*, 159–175.

Leuning, R. (1995), A critical appraisal of a combined stomatal- photosynthesis model for C3 plants, *Plant, Cell and Environment*, *18*, 357–364.

Leuning, R., F. M. Kelliher, D. G. G. Pury, and E.-D. Schulze (1995), Leaf nitrogen, photosynthesis, conductance and transpiration: Scaling from leaves to canopies, *Plant, Cell and Environment*, (18), 1183–1200.

Levis, S., G. B. Bonan, M. Vertenstein, and K. W. Oleson (2004), The Community Land Model's Dynamic Global Vegetation Model (CLMDGVM): Technical description and user's guide, *Tech. note*, NCAR/TN-459+IA, Natl. Cent. for Atmos. Res., Boulder, Colorado.

Lhomme, J. P. (2001), Stomatal control of transpiration: Examination of the Jarvis-type representation of canopy resistance in relation to humidity, *Water Resources Research*, *37*, 689–699.

Lhomme, J. P., E. Elguero, A. Chehbouni, and G. Boulet (1998), Stomatal control of transpiration: Examination of Monteith's formulation of canopy resistance, *Water Resources Research*, *34*, 2301–2308.

Li, Y., W. Ye, M. Wang, and X. Yan (2009), Climate change and drought: a risk assessment of crop-yield impacts, *Climate Research*, *39*, 31–46, doi: 10.3354/cr00797.

Liebethal, C., and T. Foken (2007), Evaluation of six parameterization approaches for the ground heat flux, *Theoretical and Applied Climatology*, *88*(43-56), doi: 10.1007/s00704-005-0234-0.

Lin, J. D. (1980), On the force-restore method for prediction of ground surface temperature, *Journal of Geophysical Research*, *85*, 3251–3254.

Link, T. E., M. Unsworth, and D. Marks (2004), The dynamics of rainfall interception by a seasonal temperate rainforest, *Agricultural and Forest Meteorology*, *124*, 171–191, doi:10.1016/j.agrformet.2004.01.010.

Liston, G. E., and K. Elder (2006), A distributed snow-evolution modeling system (SnowModel), *Journal of Hydrometeorology*, *7*, 1259–1276.

Liston, G. E., J. P. McFadden, M. Sturm, and R. A. P. Sr. (2002), Modelled changes in arctic tundra snow, energy and moisture fluxes due to increased shrubs, *Global Change Biology*, *8*, 17–32.

Litton, C. M., J. W. Raich, and M. G. Ryan (2007), Carbon allocation in forest ecosystems, *Global Change Biology*, *13*, 2089–2109, doi: 10.1111/j.1365-2486.2007.01420.x.

Liu, S., L. Lu, D. Mao, and L. Jia (2007), Evaluating parameterizations of aerodynamic resistance to heat transfer using field measurements, *Hydrology and Earth System Science*, *11*, 769–783.

Loague, K., C. S. Heppner, B. B. Mirus, B. A. Ebel, Q. Ran, A. E. Carr, S. H. BeVille, and J. E. VanderKwaak (2006), Physics-based hydrologic-response simulation: foundation for hydroecology and hydrogeomorphology, *Hydrological Processes*, *20*, 1231–1237, doi:10.1002/hyp.6179.

López-Moreno, J. I., and J. Latron (2008), Influence of canopy density on snow distribution in a temperate mountain range, *Hydrological Processes*, *22*, 117–126, doi:10.1002/hyp.6572.

LoSeen, D., A. Chehbouni, E. Njoku, S. Saatchi, E. Mougin, and B. Monteny (1997), An approach to couple vegetation functioning and soil-vegetation-atmopshere-transfer models for semiarid grasslands during the HAPEX-Sahel experiment, *Agricultural and Forest Meteorology*, *83*, 49–74.

Louis, J.-F. (1979), A parametric model of the vertical eddy fluxes in the atmosphere, *Boundary-Layer Meteorology*, *17*, 187–202.

Louis, J.-F., M. Tiedtke, and J. F. Geleyn (1982), A short history of the operational PBL parameterization of ECMWF, in *Workshop on Planetary Boundary Layer Parameterization*, pp. 59–79, Shinfield Park, Reading, Berkshire, UK, European Centre for Medium Range Weather Forecasts.

Lüdeke, M. K. B., F.-W. Badeck, R. D. Otto, C. Häger, S. Dönges, J. Kindermann, G. Würth, T. Lang, U. Jäkel, A. Klaudius, P. Ramge, S. Habermehl, and G. H. Kohlmaier (1994), The Frankfurt biosphere model: A global process-oriented model of seasonal and long-term CO_2 exchange between terrestrial ecosystems and the atmosphere. I. Model description and illustrative results for cold deciduous and boreal forests, *Climate Research*, *4*(2), 143–166.

Ludwig, J. A., B. P. Wilcox, D. D. Breshears, D. J. Tongway, and A. C. Imeson (2005), Vegetation patches and runoff-erosion as interacting ecohydrological processes in semiarid landscapes, *Ecology*, *86*(2), 288–297.

Luo, Y., B. Su, W. S. Currie, J. S. Dukes, A. Finzi, U. Hartwig, B. Hungate, R. E. McMurtrie, R. Oren, W. J. Parton, D. E. Pataki, M. R. Shaw, D. R. Zak, and C. B. Field (2004), Progressive nitrogen limitation of ecosystem responses to rising atmospheric carbon dioxide, *BioScience*, *54*(8), 731–739.

Mackay, D. S. (2001), Evaluation of hydrologic equlibrium in a mountainous watershed: incorporating forest canopy spatial adjustment to soil biogeochemical processes, *Advances in Water Resources*, *24*, 1211–1227.

Mackay, D. S., and L. E. Band (1997), Forest ecosystem processes at the watershed scale: Dynamic coupling of distributed hydrology and canopy growth, *Hydrological Processes*, *11*, 1197–1217.

Madsen, M. D., D. G. Chandler, and J. Belnap (2008), Spatial gradients in ecohydrologic properties within a pinyon-juniper ecosystem, *Ecohydrology*, *1*, 349–360, doi: 10.1002/eco.29.

Mahfouf, J.-F., and B. Jacquemin (1989), A study of rainfall interception using a land surface parameterization for mesoscale meteorological models, *Journal of Applied Meteorology*, *28*, 1282–1302.

Mahfouf, J.-F., and J. Noilhan (1991), Comparative study of various formulations from bare soil using in situ data, *Journal of Applied Meteorology*, *30*, 1354–1365.

Manning, L. J., J. W. Hall, H. J. Fowler, C. G. Kilsby, and C. Tebaldi (2009), Using probabilistic climate change information from a multimodel ensemble for water resources assessment, *Water Resources Research*, *45*(W11411), doi:10.1029/2007WR006674.

Manzoni, S., and A. Porporato (2009), Soil carbon and nitrogen mineralization: Theory and models across scales, *Soil Biology & Biochemistry*, *41*, 1355–1379, doi:10.1016/j.soilbio.2009.02.031.

Marani, M. (2003), On the correlation structure of continuous and discrete point rainfall, *Water Resources Research*, *39*(5), doi:10.1029/2002WR001456.

Marani, M. (2005), Non-power-law-scale properties of rainfall in space and time, *Water Resources Research*, *41*(W08413), doi:10.1029/2004WR003822.

Marani, M., and S. Zanetti (2007), Downscaling rainfall temporal variability, *Water Resources Research*, *43*(W09415), doi:10.1029/2006WR005505.

Marks, D., and A. Winstral (2001), Comparison of snow deposition, the snow cover energy balance, and snowmelt at two sites in a semiarid mountain basin, *Journal of Hydrometeorology*, *2*(3), 213–227.

Marks, D., J. Kimball, D. Tingey, and T. Link (1998), The sensitivity of snowmelt processes to climate conditions and forest cover during rain-on-snow: a study of the 1996 Pacifc Northwest flood, *Hydrological Processes*, *12*, 1569–1587.

Marks, D., J. Domingo, D. Susong, T. Link, and D. Garen (1999), A spatially distributed energy balance snowmelt model for application in mountain basins, *Hydrological Processes*, *13*, 1935–1959.

Marks, D., K. R. Cooley, D. C. Robertson, and A. Winstral (2000), Snow measurements and monitoring, Reynolds Creek Experimental Watershed, Idaho, USA, *Tech. Rep. 2000-5*, Northwest Watershed Res. Cent., Agric. Res. Serv., U.S. Dep. of Agric., Boise, Idaho.

Marks, D., K. R. Cooley, D. C. Robertson, and A. Winstral (2001), Long-term snow database,Reynolds Creek Experimental Watershed, Idaho, United States, *Water Resources Research*, *37*(11), 2835–2838.

Marshall, I. S., and W. M. Palmer (1948), Relation of raindrop size to intensity, *Journal of Meteorology*, *5*, 165–166.

Mascart, P., J. Noilhan, and H. Giordani (1995), A modified parameterization of flux-profile relationships in the surface layer using different roughness lengthvalues for heat and momentum, *Boundary-Layer Meteorology*, *72*, 331–334.

Massman, W. J. (1997), An analytical one-dimensional model of momentum transfer by vegetation of arbitrary structure, *Boundary-Layer Meteorology*, *83*, 407–421.

Matsumoto, K., T. Ohta, and T. Tanaka (2005), Dependence of stomatal conductance on leaf chlorophyll concentration and meteorological variables, *Agricultural and Forest Meteorology*, *132*, 44–57, doi:10.1016/j.agrformet.2005.07.001.

Mavromatis, T., and J. W. Hansen (2001), Interannual variability characteristics and simulated crop response of four stochastic weather generators, *Agricultural and Forest Meteorology*, *109*, 283–296.

Mayr, T., and N. J. Jarvis (1999), Pedotransfer functions to estimate soil water retention parameters for a modified Brooks-Corey type model, *Geoderma*, *91*, 1–9.

McCree, K. J. (1970), An equation for the rate of respiration of white clover plants grown under controlled conditions, in *Proceedings of the technical meeting IBP,*

Trebon (CSK), 1969, edited by C. for Agricultural Publishing and N. Documentation, Wageningen, pp. 221–229.

McDonald, A. K., R. J. Kinucan, and L. E. Loomis (2009), Ecohydrological interactions within banded vegetation in the northeastern Chihuahuan Desert, USA, *Ecohydrology*, *2*, 66–71, doi:10.1002/eco.40.

McDonnell, J. J. (2003), Where does water go when it rains? Moving beyond the variable source area concept of rainfall-runoff response, *Hydrological Processes*, *17*, 1869–1875, doi:10.1002/hyp.5132.

McDonnell, J. J., M. Sivapalan, K. Vach, S. Dunn, G. Grant, R. Haggerty, C. Hinz, R. Hooper, J. Kirchner, M. L. Roderick, J. Selker, and M. Weiler (2007), Moving beyond heterogeneity and process complexity: A new vision for watershed hydrology, *Water Resources Research*, *43*(W07301), doi:10.1029/2006WR005467.

McDowell, N., W. Pockman, C. Allen, D. D. Breshears, N. Cobb, T. Kolb, J. Sperry, A. West, D. Williams, and E. Yepez (2008), Mechanisms of plant survival and mortality during drought: Why do some plants survive while others succumb to drought?, *New Phytologist*, *178*, 719–739, doi:10D1111/j.1469-8137D2008D02436.x.

McKague, K., R. Rudra, and J. Ogilvie (2003), CLIMGEN - A convenient weather generator tool for Canadian climate stations, in *Meeting of the CSAE/SCGR Canadian Society for engineering in agricultural food and biological systems, Montreal Quebec, July, 6-9*, 03-118, web-site: http://www.sipeaa.it/tools/ClimGen/CSAE03-118.pdf.

McMahon, T. A., and A. J. Miller (1971), Application of the Thomas and Fiering model to skewed hydrological data, *Water Resources Research*, *7*(5), 1338–1340.

Medlyn, B. E., D. Loustau, and S. Delzon (2002), Temperature response of parameters of a biochemically based model of photosynthesis. I. Seasonal changes in mature maritime pine (Pinus pinaster Ait.), *Plant, Cell and Environment*, *25*, 1155–1165.

Medvigy, D., S. C. Wofsy, J. W. Munger, D. Y. Hollinger, and P. R. Moorcroft (2009), Mechanistic scaling of ecosystem function and dynamics in space and time: Ecosystem Demography model version 2, *Journal of Geophysical Research*, *114*(G01002), doi:10.1029/2008JG000812.

Meehl, G. A., C. Covey, T. Delworth, M. Latif, B. McAvaney, J. F. B. Mitchell, R. J. Stouffer, and K. E. Taylor (2007a), THE WCRP CMIP3 Multimodel dataset: A new era in climate change research, *Bulletin of the American Meteorological Society*, *88*, 1383–1394, doi:10.1175/BAMS-88-9-1383.

Meehl, G. A., T. F. Stocker, W. D. Collins, P. Friedlingstein, A. T. Gaye, J. M. Gregory, A. Kitoh, R. Knutti, J. M. Murphy, A. Noda, S. C. B. Raper, I. G.

Watterson, A. J. Weaver, and Z. C. Zhao (2007b), *Global Climate Projections. In: Climate Change 2007: The Physical Science Basis. Contribution of Working Group I to the Fourth Assessment Report of the Intergovernmental Panel on Climate Change*, chap. X, Cambridge University Press Cambridge, United Kingdom and New York, NY, USA.

Melloh, R. A., J. P. Hardy, R. N. Bailey, and T. J. Hall (2002), An efficient snow albedo model for the open and sub-canopy, *Hydrological Processes*, *16*, 3571–3584, doi: 10.1002/hyp.1229.

Menabde, M., and M. Sivapalan (2000), Modeling of rainfall time series and extremes using the bounded random cascades and Levy-stable distributions, *Water Resources Research*, *36*(11), 3293–3300.

Menduni, G., A. Pagani, M. C. Rulli, and R. Rosso (2002), A non-conventional watershed partitioning method for semi-distributed hydrological modelling: the package aladhyn, *Hydrological Processes*, *16*, 277–291, doi:10.1002/hyp.340.

Mengelkamp, H.-T., K. Warrach, and E. Raschke (1999), SEWAB - a parameterization of the surface energy and water balance for atmospheric and hydrologic models, *Advances in Water Resources*, *23*, 165–175.

Merritt, W. S., Y. Alila, M. Barton, B. Taylor, S. Cohen, and D. Neilsen (2006), Hydrologic response to scenarios of climate change in sub watersheds of the Okanagan basin, British Columbia, *Journal of Hydrology*, *326*, 79–108, doi:10.1016/j.jhydrol.2005.10.025.

Meyer, C. R., C. S. Renshler, and R. C. Vining (2007), Implementing quality control on a random number stream to improve a stochastic weather generator, *Hydrological Processes*, *doi: 10.1002/hyp.6668*.

Middelkoop, H., K. Daamen, D. Gellens, W. Grabs, J. C. K. Kwadijk, H. Lang, B. W. A. H. Parmet, B. Schädler, J. Schulla, and K. Wilke (2001), Impact of climate change on hydrological regimes and water resources management in the Rhine basin, *Climatic Change*, *49*, 105–128.

Miller, C. T., C. Abhishek, and M. W. Farthing (2006), A spatially and temporally adaptive solution of Richards' equation, *Advances in Water Resources*, *29*, 525–545, doi:10.1016/j.advwatres.2005.06.008.

Milly, P. C. D., R. T. Wetherald, K. A. Dunne, and T. L. Delworth (2002), Increasing risk of great floods in a changing climate, *Nature*, *415*(6871), 514–517.

Milly, P. C. D., J. Betancourt, M. Falkenmark, R. M. Hirsch, Z. W. Kundzewicz, D. P. Lettenmaier, and R. J. Stouffer (2008), Stationarity is dead: Whither water management?, *Science*, *319*, 573–574, doi:10.1126/science.1151915.

Mishra, S. K., J. V. Tyagi, and V. P. Singh (2003), Comparison of infiltration models, *Hydrological Processes*, *17*, 2629–2652, doi: 10.1002/hyp.1257.

Misson, L., D. D. Baldocchi, T. A. Black, P. D. Blanken, Y. Brunet, J. Curiel, Yuste, J. R. Dorsey, M. Falk, A. Granier, M. R. Irvine, N. Jarosz, E. Lamaud, S. Launiainen, B. E. Lawi, B. Longdoz, D. Loustau, M. McKay, K. T. Paw, U, T. Vesala, D. Vickers, K. B. Wilson, and A. H. Goldstein (2007), Partitioning forest carbon fluxes with overstory and understory eddy-covariance measurements: A synthesis based on FLUXNET data, *Agricultural and Forest Meteorology*, *144*, 14–31, doi:10.1016/j.agrformet.2007.01.006.

Mölders, N., H. Luijting, and K. Sassen (2008), Use of atmospheric radiation measurement program data from Barrow, Alaska, for evaluation and development of snow-albedo parameterizations, *Meteorology and Atmopheric Physics*, *99*, 199–219, doi: 10.1007/s00703-007-0271-6.

Molnar, P., and P. Burlando (2005), Preservation of rainfall properties in stochastic disaggregation by a simple random cascade model, *Atmospheric Research*, *77*, 137–151, doi:10.1016/j.atmosres.2004.10.024.

Molnar, P., and P. Burlando (2008), Variability in the scale properties of high-resolution precipitation data in the Alpine climate of Switzerland, *Water Resources Research*, *44*(W10404), doi:10.1029/2007WR006142.

Molotch, N. P., P. D. Brooks, S. P. Burns, M. Litvak, R. K. Monson, J. R. McConnell, and K. Musselman (2009), Ecohydrological controls on snowmelt partitioning in mixed-conifer sub-alpine forests, *Ecohydrology*, *2*, 129–142, doi:10.1002/eco.48.

Monin, A. S., and A. M. Obukhov (1954), Dimensionless characteristics of turbulence in the surface layer of the atmosphere, *Trudy Geofiz. Inst. Akad. Nauk. SSSR*, *24*, 163–187, (In Russian).

Monsi, M., and T. Saeki (2005), On the factor light in plant communities and its importance for matter production, *Annals of Botany*, *95*, 549–567, originally published in German in Japanese Journal of Botany 14, 22-52, 1953.

Montaldo, N., and J. D. Albertson (2001), On the use of the Force-Restore SVAT model formulation for stratified soils, *Journal of Hydrometeorology*, *2*, 571–578.

Montaldo, N., R. Rondena, J. D. Albertson, and M. Mancini (2005), Parsimonious modeling of vegetation dynamics for ecohydrologic studies of water-limited ecosystems, *Water Resources Research*, *41*(W10416), doi:10.1029/2005WR004094.

Montaldo, N., J. D. Albertson, and M. Mancini (2008), Vegetation dynamics and soil water balance in a water-limited Mediterranean ecosystem on Sardinia, Italy, *Hydrology and Earth System Sciences*, *12*, 1257–1271.

Montanari, A., R. Rosso, and M. S. Taqqu (1997), Fractionally differenced ARIMA models applied to hydrologic time series: Identification, estimation and simulation, *Water Resources Research*, *33*(5), 1035–1044.

Montgomery, D. R., and W. E. Dietrich (1988), Where do channels begin?, *Nature*, *336*, 232–234.

Montgomery, D. R., and W. E. Dietrich (1989), Source areas, drainage density, and channel initiation, *Water Resources Research*, *25*, 1907–1918.

Morel-Seytoux, H. J., P. D. Meyer, M. Nachabe, J. Touma, M. T. vanGenuchten, and R. J. Lenhard (1996), Parameter equivalence for the Brooks-Corey and van Genuchten soil characteristics: Preserving the effective capillary drive, *Water Resources Research*, *32*(5), 1251–1258.

Morgan, R. P. C. (2001), A simple approach to soil loss prediction: a revised Morgan-Morgan-Finney model, *Catena*, *44*, 305–322.

Morgan, R. P. C., J. N. Quinton, R. E. Smith, G. Govers, J. W. A. Poesen, K. Auerswald, G. Chisci, D. Torri, and M. E. Styczen (1998), The european soil erosion model (EUROSEM): a dynamic approach for predicting sediment transport from fields and small catchments, *Earth Surface Processes and Landforms*, *23*, 527–544.

Morin, J., R. Karen, Y. Benjamini, M. Ben-Hur, and I. Shainberg (1989), Water infiltration as affected by soil crust and moisture profile, *Soil Science*, *148*, 53–59.

Morin, X., M. J. Lechowicz, C. Augspurger, J. O'Keefe, D. Viner, and I. Chuine (2009), Leaf phenology in 22 North American tree species during the 21st century, *Global Change Biology*, *15*, 961–975, doi: 10.1111/j.1365-2486.2008.01735.x.

Mualem, Y., and S. Assouline (1989), Modeling soil seal as a non-uniform layer, *Water Resources Research*, *25*, 2101–2108.

Mualem, Y., S. Assouline, and H. Rohdenburg (1990), Rainfall-induced soil seal. C. A dynamic model with kinetic energy instead of cumulative rainfall as independent variable, *Catena*, *17*, 289–303.

Muldavin, E. H., D. I. Moore, S. L. Collins, K. R. Wetherill, and D. C. Lightfoot (2008), Aboveground net primary production dynamics in a northern Chihuahuan Desert ecosystem, *Oecologia*, *155*, 123–132, doi:10.1007/s00442-007-0880-2.

Müller-Wohlfeil, D. I., G. Bürger, and W. Lahmer (2000), Response of a river catchment to climate change: application of expanded downscaling to northern Germany, *Climatic Change*, *47*, 61–89.

Muneer, T., M. S. Gul, and J. Kubie (2000), Models for estimating solar radiation and illuminance from meteorological parameters, *Journal of Solar Energy Engineering*, *122*, 146–153.

Musselman, K. N., N. P. Molotch, and P. D. Brooks (2008), Effects of vegetation on snow accumulation and ablation in a mid-latitude sub-alpine forest, *Hydrological Processes*, *22*, 2767–2776, doi:10.1002/hyp.7050.

Myneni, R. B., S. Hoffman, Y. Knyazikhin, J. L. Privette, J. Glassy, Y. Tian, Y. Wang, X. Song, Y. Zhang, G. R. Smith, A. Lotsch, M. Friedl, J. T. Morisette, P. Votava, R. R. Nemani, and S. W. Running (2002), Global products of vegetation leaf area and fraction absorbed PAR from year one of MODIS data, *Remote Sensing of Environment*, *83*, 214–231.

Nardi, F., S. Grimaldi, M. Santini, A. Petroselli, and L. Ubertini (2008), Hydrogeomorphic properties of simulated drainage patterns using digital elevation models: the flat area issue, *Hydrological Sciences Journal*, *53*(6), 1176–1193.

Nearing, M. A., M. H. Nichols, J. J. Stone, K. G. Renard, and J. R. Simanton (2007), Sediment yields from unit-source semiarid watersheds at Walnut Gulch, *Water Resources Research*, *43*(W06426), doi:10.1029/2006WR005692.

Nelder, J., and R. Mead (1965), A Simplex method for function minimization, *The Computer Journal*, *7*, 308–313.

Nemani, R. R., C. D. Keeling, H. Hashimoto, W. M. Jolly, S. C. Piper, C. J. Tucker, R. B. Myneni, and S. W. Running (2003), Climate-driven increases in global terrestrial net primary production from 1982 to 1999, *Science*, *300*, 1560–1563.

Nepstad, D., P. Lefebvre, S.-U. Lopes, Da, J. Tomasella, P. Schlesinger, L. Solórzano, P. Moutinho, D. Ray, and J. Guerreira, Benito (2004), Amazon drought and its implications for forest flammability and tree growth: a basin-wide analysis, *Global Change Biology*, *10*, 704–717, doi:10.1111/j.1529-8817.2003.00772.x.

Nichols, M. H., J. J. Stone, and M. A. Nearing (2008), Sediment database, Walnut Gulch Experimental Watershed, Arizona, United States, *Water Resources Research*, *44*(W05S06), doi:10.1029/2006WR005682.

Nicks, A. D., L. J. Lane, and G. A. Gander (1995), Weather generator, *USDA-Water Erosion Prediction Project: hillslope profile and watershed model documentation*, USDA-ARS National Soil Erosion Research Laboratory, chapter 2, 1-22.

Niklas, K. J., and B. J. Enquist (2001), Invariant scaling relationships for interspecific plant biomass production rates and body size, *Proc. Natl Acad. Sci. USA*, *98*, 2922–2927.

Niklas, K. J., and B. J. Enquist (2002), On the vegetative biomass partitioning of seed plant leaves, stems, and roots, *The American Naturalist*, *159*(5), 482–497.

Niu, G.-Y., Z.-L. Yang, R. E. Dickinson, L. E. Gulden, and H. Su (2007), Development of a simple groundwater model for use in climate models and evaluation with Gravity Recovery and Climate Experiment data, *Journal of Geophysical Research*, *112*(D07103), doi:10.1029/2006JD007522.

Niyogi, D. S., and S. Raman (1997), Comparison of four different stomatal resistance schemes using FIFE observations, *Journal of Applied Meteorology*, *36*, 903–917.

Nobel, P. S. (2009), *Physicochemical and Environmental Plant Physiology*, Elsevier Academic Press.

Noilhan, J., and J.-F. Mafhouf (1996), The ISBA land surface parameterisation scheme, *Global and Planetary Change*, *13*, 145–159.

Noilhan, J., and S. Planton (1989), A simple parameterization of land surface processes for meteorological models, *Monthly Weather Review*, *117*, 536–549.

Nora Mueller, E., J. Wainwright, and A. J. Parsons (2007), Impact of connectivity on the modeling of overland flow within semiarid shrubland environments, *Water Resources Research*, *43*(W09412), doi:10.1029/2006WR005006.

Northrop, P. (1998), A clustered spatial-temporal model of rainfall, *Proceedings of the Royal Society of London, Series A*, *454*, 1875–1888.

Nouvellon, Y., S. Rambal, D. L. Seen, M. S. Moran, J. P. Lhomme, A. Begue, A. G. Chehbouni, and Y. Kerr (2000), Modelling of daily fluxes of water and carbon from shortgrass steppes, *Agricultural and Forest Meteorology*, *100*, 137–153.

Núnez, C. M., E. A. Varas, and F. J. Meza (2010), Modelling soil heat flux, *Theoretical Applied Climatology*, *100*, 251–260, doi:10.1007/s00704-009-0185-y.

O'Callaghan, J. F., and D. M. Mark (1984), The extraction of drainage networks from digital elevation data, *Computer Vision, Graphics and Image Processing*, *28*, 323–344.

Oleson, K. W., Y. Dai, G. Bonan, M. Bosilovich, R. Dickinson, P. Dirmeyer, F. Hoffman, P. Houser, S. Levis, G. Y. Niu, P. Thornton, M. Vertenstein, Z. L. Yang, and X. Zeng (2004), Technical description of the community land model (CLM), *Tech. Rep. NCAR/TN-461+STR*, Natl. Cent. for Atmos. Res., Boulder, Colorado.

Oleson, K. W., G. B. Bonan, J. Feddema, M. Vertenstein, and C. S. B. Grimmond (2008a), An urban parameterization for a Global Climate Model. Part I: Formulation and evaluation for two cities, *Journal of Applied Meteorology and Climatology*, *47*, 1038–1060, doi:10.1175/2007JAMC1597.1.

Oleson, K. W., G.-Y. Niu, Z.-L. Yang, D. M. Lawrence, P. E. Thornton, P. J. Lawrence, R. Stockli, R. E. Dickinson, G. B. Bonan, S. Levis, A. Dai, and T. Qian (2008b), Improvements to the Community Land Model and their impact on the hydrological cycle, *Journal of Geophysical Research*, *113*(G01021), doi:10.1029/2007JG000563.

Olseth, J. A., and A. Skartveit (1997), Spatial distribution of photosynthetically active radiation over complex topography, *Agricultural and Forest Meteorology*, *86*, 205–214.

Olseth, J. A., A. Skartveit, and H. Zou (1995), Spatially continuous mapping of solar resources in a complex high latitude topography, *Solar Energy*, *55*(6), 475–485.

Olsson, J. (1998), Evaluation of a scaling cascade model for temporal rainfall disaggregation, *Hydrology and Earth System Sciences*, *2*, 19–30.

Onof, C., and J. Townend (2004), Modeling 5-min rainfall extremes, in *Hydrology: science and practice for the 21st century*, edited by B. H. Society, pp. 377–388.

Onof, C., E. Chandler, A. Kakou, P. Northrop, H. S. Wheater, and V. Isham (2000), Rainfall modeling using Poisson-cluster processes: a review of developments, *Stochastic Environmental Research and Risk Assessment*, *14*, 384–411.

Onof, C., J. Townend, and R. Kee (2005), Comparison of two hourly to 5-min rainfall disaggregators, *Atmospheric Research*, *77*, 176–187, doi:10.1016/j.atmosres.2004.10.022.

Öquist, G., and W. S. Chow (1992), On the relationship between the quantum yield of Photosystem II electron transport, as determined by chlorophyll fluorescence and the quantum yield of CO_2-dependent O_2 evolution, *Photosynthesis Research*, *33*, 51–62.

Orlandini, S., and G. Moretti (2009), Determination of surface flow paths from gridded elevation data, *Water Resources Research*, *45*(W03417), doi:10.1029/2008WR007099.

Orlandini, S., G. Moretti, M. Franchini, B. Aldighieri, and B. Testa (2003), Path-based methods for the determination of nondispersive drainage directions in grid-based digital elevation models, *Water Resources Research*, *39*(6), doi:10.1029/2002WR001639.

Ostle, N. J., P. Smith, R. Fisher, F. I. Woodward, J. B. Fisher, J. U. Smith, D. Galbraith, P. Levy, P. Meir, N. P. McNamara, and R. D. Bardgett (2009), Integrating plant-soil interactions into global carbon cycle models, *Journal of Ecology*, *97*, 851–863, doi: 10.1111/j.1365-2745.2009.01547.x.

Over, T. M., and V. K. Gupta (1994), Statistical analysis of mesoscale rainfall: Dependence of a random cascade generator on large-scale forcing, *Journal of Applied Meteorology*, *33*, 1526–1542.

Over, T. M., and V. K. Gupta (1996), A space-time theory of mesoscale rainfall using random cascades, *Journal of Geophysical Research*, *101*(D21), 26,319–26,331.

Parlange, J.-Y., I. Lisle, R. D. Braddock, and R. E. Smith (1982), The three-parameter infiltration equation, *Soil Science*, *133*(6), 337–341.

Parlange, M. B., and R. W. Katz (2000), An extended version of the richardson model for simulating daily weather variables, *Journal of Applied Meteorology*, *39*, 610–622.

Parsons, A. J., J. Wainwright, D. M. Powell, J. Kaduk, and R. E. Brazier (2004), A conceptual model for determining soil erosion by water, *Earth Surface Processes and Landforms*, *29*, 1293–1302, doi: 10.1002/esp.1096.

Paulson, K. S., and P. D. Baxter (2007), Downscaling of rain gauge time series by multiplicative beta cascade, *Journal of Geophysical Research*, *112*(D09105), doi:10.1029/2006JD007333.

Pederson, C. A., and J.-G. Winther (2005), Intercomparison and validation of snow-albedo parameterization schemes in climate models, *Climate Dynamic*, *25*, 351–362, doi: 10.1007/s00382-005-0037-0.

Peters-Lidard, C. D., E. Blackburn, X. Liang, and E. F. Wood (1998), The effect of soil thermal conductivity parameterization on surface energy fluxes and temperatures, *Journal of the Atmospheric Sciences*, *55*, 1209–1224.

Peuelas, J., and I. Filella (2001), Phenology: Responses to a warming world, *Science*, *294*(5543), 793–795, doi: 10.1126/science.1066860.

Philip, J. R. (1957), Evaporation, and moisture and heat fields in the soil, *Journal of Meteorology*, *14*, 354–366.

Piao, S., P. Friedlingstein, P. Ciais, L. Zhou, and A. Chen (2006), Effect of climate and CO_2 changes on the greening of the Northern Hemisphere over the past two decades, *Geophysical Research Letters*, *33*(L23402), doi:10.1029/2006GL028205.

Pirazzini, R., M. Nardino, A. Orsini, F. Calzolari, T. Georgiadis, and V. Levizzani (2001), Parameterization of the downward longwave radiation from clear and cloudy skies at Ny Ålesund (Svalbard), in *IRS 2000: Current Problems in Atmospheric Radiation*, edited by W. Smith and Y. M. Timofeyev, pp. 559–562, A. Deepack Publishing, Hampton, Virginia.

Plate, E. J. (2002), Flood risk and flood management, *Journal of Hydrology*, *267*, 2–11.

Pockman, W. T., and J. S. Sperry (2000), Vulnerability to xylem cavitation and the distribution of sonoran vegetation, *American Journal of Botany*, *87*(9), 1287–1299.

Pomeroy, J. W., D. M. Gray, K. R. Shook, B. Toth, R. L. H. Essery, A. Pietroniro, and N. Hedstrom (1998a), An evaluation of snow accumulation and ablation processes for land surface modelling, *Hydrological Processes*, *13*, 2339–2367.

Pomeroy, J. W., N. Parviainen, N. Hedstrom, and D. M. Gray (1998b), Coupled modeling of forest snow interception and sublimation, *Hydrological Processes*, *12*, 2317–2337.

Pomeroy, J. W., D. M. Gray, N. Hedstrom, and J. R. Janowicz (2002), Prediction of seasonal snow accumulation in cold climate forests, *Hydrological Processes*, *16*, 3543–3558.

Porporato, A., F. Laio, L. Ridolfi, and I. Rodriguez-Iturbe (2001), Plants in water-controlled ecosystems: active role in hydrologic processes and response to water stress III. Vegetation water stress, *Advances in Water Resources*, *24*, 725–744.

Porporato, A., P. D'Odorico, F. Laio, and I. Rodriguez-Iturbe (2003), Hydrologic controls on soil carbon and nitrogen cycles. I. Modeling scheme, *Advances in Water Resources*, *26*, 45–58.

Porporato, A., G. Vico, and P. A. Fay (2006), Superstatistics of hydro-climatic fluctuations and interannual ecosystem productivity, *Geophysical Research Letters*, *33*(L15402), doi:10.1029/2006GL026412.

Prata, A. J. (1996), A new long-wave formula estimating downward clear-sky radiation at the surface, *Quarterly Journal of the Royal Meteorological Society*, *122*, 1127–1151.

Pregitzer, K. S. (2003), Woody plants, carbon allocation and fine roots, *New Phytologist*, *158*(3), 421–424.

Prudhomme, C., N. Reynard, and S. Crooks (2002), Downscaling of global climate models for flood frequency analysis: Where are we now?, *Hydrological Processes*, *16*, 1137–1150.

Pyles, R., B. Weare, and K. Pawu (2000), The UCD advanced canopy-atmosphere-soil algorithm: comparisons with observations from different climate and vegetation regimes, *Quarterly Journal of the Royal Meteorological Society*, *126*(569), 2951–2980.

Quinn, P., K. Beven, P. Chevallier, and O. Planchon (1991), The prediction of hillslope flow paths for distributed hydrological modeling using digital terrain models, *Hydrological Processes*, *5*, 59–80.

Raff, D. A., T. Pruitt, and L. D. Brekke (2009), A framework for assessing flood frequency based on climate projection information, *Hydrology and Earth System Science*, *13*, 2119–2136.

Räisänen, J. (2007), How reliable are climate models?, *Tellus A*, *59*, 2–29, doi:10.1111/j.1600-0870.2006.00211.x.

Ramírez, J. A., and S. U. S. Senarath (2000), A statistical-dynamical parameterization of interception and land surface-atmosphere interactions, *Journal of Climate*, *13*, 4050–4063.

Randall, D. A., R. A. Wood, S. Bony, R. Colman, T. Fichefet, J. Fyfe, V. Kattsov, A. Pitman, J. Shukla, J. Srinivasan, R. Stouffer, A. Sumi, and K. Taylor (2007), *Cilmate Models and Their Evaluation. In: Climate Change 2007: The Physical Science Basis. Contribution of Working Group I to the Fourth Assessment Report of the Intergovernmental Panel on Climate Change*, chap. VIII, Cambridge University Press Cambridge, United Kingdom and New York, NY, USA.

Raupach, M. R. (1989), A practical acute "Lagrangian" method for relating scalar concentrations to source distributions in vegetation canopies, *Quarterly Journal Royal Meteorological Society*, *115*, 609–632.

Raupach, M. R. (1994), Simplified expressions for vegetation roughness length and zero-plane displacement as a function of canopy height and area index, *Boundary-Layer Meteorology*, *71*, 211–216.

Raupach, M. R. (1995), Vegetation-atmosphere interaction and surface conductance at leaf, canopy and regional scales, *Agricultural and Forest Meteorology*, *73*, 151–179.

Rebetez, M., H. Mayer, O. Dupont, D. Schindler, K. Gartner, J. P. Kropp, and A. Menzel (2006), Heat and drought 2003 in Europe: a climate synthesis, *Annals of Forest Science*, *63*, 569–577, doi: 10.1051/forest:2006043.

Reggiani, P., and J. Schellekens (2003), Modelling of hydrological responses: the representative elementary watershed approach as an alternative blueprint for watershed modelling, *Hydrological Processes*, *17*, 3785–3789, doi:10.1002/hyp.5167.

Reich, P. B., M. B. Walters, and D. S. Ellsworth (1997), From tropics to tundra: global convergence in plant functioning, *Proc. Natl. Acad. Sci. USA*, *94*, 13,730–13,734.

Reich, P. B., D. S. Ellsworth, and M. B. Walters (1998a), Leaf strucuture (specific leaf area) modulates photosynthesis-nitrogen realtions: evidence and across species and functional groups, *Functional Ecology*, *12*, 948–958.

Reich, P. B., M. B. Walters, D. S. Ellsworth, J. M. Vose, J. C. Volin, C. Gresham, and W. D. Bowman (1998b), Relationships of leaf dark respiration to leaf nitrogen, specific leaf area and leaf life-span: a test across biomes and functional groups, *Oecologia*, *114*, 471–482.

Reich, P. B., M. G. Tjoelker, J.-L. Machado, and J. Oleksyn (2006), Universal scaling of respiratory metabolism, size and nitrogen in plants, *Nature*, *339*, doi:10.1038/nature04282.

Reichler, T., and J. Kim (2008), How well do coupled models simulate today's climate?, *Bulletin of American Meteorological Society*, *89*, 303–311, doi:10.1175/BAMS-89-3-303.

Renard, K. G., M. H. Nichols, D. A. Woolhiser, and H. B. Osborn (2008), A brief background on the USDA Agricultural Research Service Walnut Gulch experimental watershed, *Water Resources Research*, *44*(W05S02), doi:10.1029/2006WR005691.

Rial, J. A., A. R. Pielke Sr., M. Beniston, M. Claussen, J. Canadell, P. Cox, H. Held, N. DeNoblet-Decoudré, R. Prinn, J. F. Reynolds, and J. D. Salas (2004), Nonlinearities, feedbacks and critical thresholds within the earth's climate system, *Climatic Change*, *65*, 11–38.

Richards, L. A. (1931), Capillary conduction of liquids through porous mediums, *Physics*, *1*, 318–333.

Richardson, C. W. (1981), Stochastic simulation of daily precipitation, temperature, and solar radiation, *Water Resources Research*, *17*, 182–190.

Richardson, C. W., and D. A. Wright (1984), WGEN: a model for generating daily weather variables, *ARS 8*, USDA-ARS.

Rigon, R., G. Bertoldi, and T. M. Over (2006), GEOtop: A distributed hydrological model with coupled water and energy budgets, *Journal of Hydrometeorology*, *7*(3), 371–388.

Robinson, D. A., and C. P. Phillips (2001), Crust development in relation to vegetation and agricultural practice on erosion susceptible, dispersive clay soils from central and southern italy, *Soil & Tillage Research*, *60*, 1–9.

Rodriguez, F., H. Andrieu, and F. Morena (2008), A distributed hydrological model for urbanized areas - Model development and application to case studies, *Journal of Hydrology*, *351*, 268–287, doi:10.1016/j.jhydrol.2007.12.007.

Rodriguez-Iturbe, I. (2000), Ecohydrology: A hydrological prespective of climate-soil-vegetation dynamics, *Water Resources Research*, *36*(1), 3–9.

Rodriguez-Iturbe, I., and P. S. Eagleson (1987), Mathematical models of rainstorm events in space and time, *Water Resources Research*, *23*(1), 181–190.

Rodriguez-Iturbe, I., and A. Porporato (2004), *Ecohydrology of Water-Controlled Ecosystems*, Cambridge University Press.

Rodriguez-Iturbe, I., D. Cox, and V. Isham (1987), Some models for rainfall based on stochastic point processes, *Proceedings of the Royal Society of London, Series A*, *410*, 269–288.

Rodriguez-Iturbe, I., D. Cox, and V. Isham (1988), A point process model for rainfall: further developments, *Proceedings of the Royal Society of London, Series A*, *417*, 283–298.

Rodriguez-Iturbe, I., A. Porporato, F. Laio, and L. Ridolfi (2001), Plants in water-controlled ecosystems: active role in hydrologic processes and response to water stress I. Scope and general outline, *Advances in Water Resources*, *24*, 695–705.

Rodriquez-Iturbe, I., P. D'Odorico, A. Porporato, and L. Ridolfi (1999), On the spatial and temporal links between vegetation, climate, and soil moisture, *Water Resources Research*, *35*, 3709–3722.

Ross, J. (1975), Radiative transfer in plant communities, in *Vegetation and the Atmosphere*, pp. 13–55, Academic Press.

Ross, P. J. (2003), Modeling soil water and solute transport-fast, simplified numerical solutions, *Agronomy Journal*, *95*, 1352–1361.

Ruimy, A., G. Dedieu, and B. Saugier (1996), TURC: A diagnostic model of continental gross primary productivity and net primary productivity, *Global Biogeochemical Cycles*, *10*, 269–285.

Running, S. W., and J. C. Coughlan (1988), A general model of forest ecosystem processes for regional applications, I, Hydrologic balance, canopy gas exchange, and primary production processes, *Ecological Modelling*, *42*, 125–154.

Rupp, D. E., R. F. Keim, M. Ossiander, M. Brugnach, and J. S. Selker (2009), Time scale and intensity dependency in multiplicative cascades for temporal rainfall disaggregation, *Water Resources Research*, *45*(W07409), doi:10.1029/2008WR007321.

Russell, P. B., J. Redemann, B. Schmid, R. W. Bergstrom, J. M. Livingston, D. M. M. S. A. Ramirez, S. Hartley, P. V. Hobbs, P. K. Quinn, C. M. Carrico, M. J. Rood, E. strm, K. J. Noone, W. V. Hoyningen-Huene, and L. Remer (2002), Comparison of aerosol single scattering albedos derived by diverse techniques in two North Atlantic experiments, *Journal of Atmospheric Sciences*, *59*, 609–619.

Rutter, A. J., K. A. Kershaw, P. C. Robins, and A. J. Morton (1971), A predictive model of rainfall interception in forests. 1. Derivation of the model from observation in a plantation of Corsican pine, *Agricultural Meteorology*, *9*, 367–384.

Rutter, A. J., A. J. Morton, and P. C. Robins (1975), A predictive model of rainfall interception in forests. 2. Generalization of model and comparison with observations in some coniferous and hardwood stands, *The Journal of Applied Ecology*, *12*(1), 367–380.

Ryan, M. G. (1991), Effects of cllimate change on plant respiration, *Ecological Applications*, *1*(2), 157–167.

Rykiel, E. R. (1996), Testing ecological models: The meaning of validation, *Ecological Modelling*, *90*(3), 229–244, doi:10.1016/0304-3800(95)00152-2.

Sack, L., and N. M. Holbrook (2006), Leaf hydraulics, *The Annual Review of Plant Biology*, *57*, 361–381, doi:10.1146/annurev.arplant.56.032604.144141.

Saco, P. M., G. R. Willgoose, and G. R. Hancock (2007), Eco-geomorphology of banded vegetation patterns in arid and semi-arid regions, *Hydrology and Earth System Science*, *11*, 1717–1730.

Saito, H., J. Šimunek, and B. P. Mohanty (2006), Numerical analysis of coupled water, vapor, and heat transport in the vadose zone, *Vadose Zone Journal*, *5*, 784–800, doi:10.2136/vzj2006.0007.

Sakaguchi, K., and X. Zeng (2009), Effects of soil wetness, plant litter, and under-canopy atmospheric stability on ground evaporation in the Community Land Model(CLM3.5), *Journal of Geophysical Research*, *114*(D01107), doi:10.1029/2008JD010834.

Sala, A. (2009), Lack of direct evidence for the carbon-starvation hypothesis to explain drought-induced mortality in trees, *Proceedings of the National Academy of Sciences, USA*, *106*(26), E68.

Salathé, E. P., Jr, P. W. Mote, and M. W. Wiley (2007), Review of scenario selection and downscaling methods for the assessment of climate change impacts on hydrology in the United States pacific northwest, *International Journal of Climatology*.

Sato, H., A. Itoh, and T. Kohyama (2007), SEIB-DGVM: A new Dynamic Global Vegetation Model using a spatially explicit individual-based approach, *Ecological Modelling*, *200*, 279–307.

Savenije, H. H. G. (2004), The importance of interception and why we should delete the term evapotranspiration from our vocabulary, *Hydrological Processes*, *18*, 1507–1511.

Saxton, K. E., and W. J. Rawls (2006), Soil water characteristic estimates by texture and organic matter for hydrologic solutions, *Soil Science Society of America Journal*, *70*, 1569–1578, doi:10.2136/sssaj2005.0117.

Saxton, K. E., W. J. Rawls, J. S. Romberger, and R. I. Papendick (1986), Estimating generalized soil water characteristics from texture, *Transactions of ASAE*, *50*, 1031–1035.

Scanlon, B. R., D. G. Levitt, R. C. Reedy, K. E. Keese, and M. J. Sully (2005), Ecological controls on water-cycle response to climate variability in deserts, *Proceedings of the National Academy of Sciences, USA*, *102*(17), 6033–6038.

Schaap, M. G., and M. T. vanGenuchten (2006), A modified Mualemvan Genuchten formulation for improved description of the hydraulic conductivity near saturation, *Vadose Zone Journal*, *5*, 27–34, doi:10.2136/vzj2005.0005.

Schenk, H. J., and R. B. Jackson (2002), The global biogeography of roots, *Ecological Monography*, *72*(3), 311–328.

Schertzer, D., and S. Lovejoy (1987), Physical modeling and analysis of rain and clouds by anisotropic scaling multiplicative processes, *Journal of Geophysical Research*, *92*, 9693–9714, doi:10.1029/JD092iD08p09693.

Schmidli, J., C. Frei, and P. L. Vidale (2006), Downscaling from GCM precipitation: a benchmark for dynamical and statistical downscaling methods, *International Journal of Climatology*, *26*, 679–689.

Schmidt, R. A., and D. R. Gluns (1991), Snowfall interception on branches of 3 conifer species, *Canadian Journal of Forest Research-Revue Canadienne De Recherche Forestiere*, *21*, 1262–1269.

Scholze, M., W. Knorr, N. W. Arnell, and I. C. Prentice (2006), A climate-change risk analysis for worlds ecosystems, *Proceedings of the National Academy of Sciences, USA*, *103*(35), 13,116–13,120.

Schuepp, P. H. (1993), Leaf boundary layers, *New Phytologist*, *125*, 477–507.

Schulze, E., F. M. Kelliher, C. Korner, J. Lloyd, and R. Leuning (1994), Relationships among maximum stomatal conductance, ecosystem surface conductance, carbon assimilation rate, and plant nitrogen nutrition: A global ecology scaling exercise, *Annual Reviews in Ecology and Systematics*, *25*, 629–662, doi:10.1146/annurev.es.25.110194.00321.

Schwanghart, W., and N. J. Kuhn (2010), Topotoolbox: A set of Matlab functions for topographic analysis, *Environmental Modelling & Software*, *25*, 770–781, doi:10.1016/j.envsoft.2009.12.002.

Schwartz, M. D., R. Ahas, and A. Aasa (2006), Onset of spring starting earlier across the Northern Hemisphere, *Global Change Biology*, *12*, 343–351, doi: 10.1111/j.1365-2486.2005.01097.x.

Scott, R. L., W. J. Shuttleworth, T. O. Keefer, and A. W. Warrick (2000), Modeling multiyear observations of soil moisture recharge in the semiarid american southwest, *Water Resources Research*, *36*(8), 2233.

Seager, R., M. Ting, I. Held, Y. Kushnir, J. Lu, G. Vecchi, H.-P. Huang, N. Harnik, A. Leetmaa, N.-C. Lau, C. Li, J. Velez, and N. Naik (2007), Model projections of an imminent transition to a more arid climate in Southwestern North America, *Science*, *316*, 1181–1184, doi:10.1126/science.1139601.

Seibert, J., and B. L. McGlynn (2007), A new triangular multiple flow direction algorithm for computing upslope areas from gridded digital elevation models, *Water Resources Research*, *43*(W04501), doi:10.1029/2006WR005128.

Sellers, P. J. (1985), Canopy reflectance, photosynthesis and transpiration, *International Journal of Remote Sensing*, *6*, 1335–1372.

Sellers, P. J., Y. Mintz, Y. C. Sud, and A. Dalcher (1986), A simple biosphere model (SiB) for use within general circulation models, *Journal of the Atmospheric Sciences*, *43*(6), 505–531.

Sellers, P. J., J. A. Berry, G. J. Collatz, C. B. Field, and F. G. Hall (1992a), Canopy reflectance, photosynthesis, and transpiration. III. A reanalysis using improved leaf models and a new canopy integration scheme, *Remote Sensing of Environment*, *42*(3), 187–216.

Sellers, P. J., M. D. Heiser, and F. G. Hall (1992b), Relations between surface conductance and spectral vegetation indices at intermediate (100 m^2 to 15 km^2) length scales, *Journal of Geophysical Research*, *97*(D17), 19,033–19,059.

Sellers, P. J., S. O. Los, C. J. Tucker, C. O. Justice, D. A. Dazlich, G. J. Collatz, and D. A. Randall (1996a), A revised land surface parameterization (SiB2) for atmospheric GCMs. 2. the generation of global fields of terrestrial biophysical parameters from satellite data, *Journal of Climate*, *9*(4), 706–737.

Sellers, P. J., D. A. Randall, G. J. Collatz, J. A. Berry, C. B. Field, D. A. Dazlich, C. Zhang, G. D. Collelo, and L. Bounoua (1996b), A revised land surface parameterization (SiB2) for atmospheric GCMs. 1. Model formulation, *Journal of Climate*, *9*(4), 674–705.

Sellers, P. J., R. E. Dickinson, D. A. Randall, A. K. Betts, F. G. Hall, J. A. Berry, G. J. Collatz, A. S. Denning, H. A. Mooney, C. A. Nobre, N. Sato, C. B. Field, and A. Henderson-Sellers (1997), Modeling the exchanges of energy, water and carbon between continents and the atmosphere, *Science*, *275*, 502–509.

Semenov, M. A. (2008), Simulation of extreme weather events by a stochastic weather generator, *Climate Research*, *35*, 203–212.

Semenov, M. A., and E. M. Barrow (1997), Use of a stochastic weather generator in the development of climate change scenarios, *Climatic Change*, *35*, 397–414.

Semenov, M. A., and E. M. Barrow (2002), *LARS-WG, A Stochastic Weather Generator for Use in Climate Impact Studies, Version 3.0*, user Manual. http://www.rothamsted.ac.uk/mas-models/download/LARS-WG-Manual.pdf.

Semenov, M. A., and J. R. Porter (1995), Climatic variability and the modelling of crop yields, *Agricultural and Forest Meteorology*, *73*, 265–283.

Semenov, M. A., R. J. Brooks, E. M. Barrow, and C. W. Richardson (1998), Comparison of the WGEN and LARS-WG stochastic weather generators for diverse climates, *Climate Research*, *10*, 95–107.

Seyfried, M., R. Harris, D. Marks, and B. Jacob (2001a), Geographic database, Reynolds Creek Experimental Watershed, Idaho, United States, *Water Resources Research*, *37*(11), 2825–2829.

Seyfried, M. S., R. C. Harris, D. Marks, and B. Jacob (2000), A geographic database for watershed research: Reynolds Creek Experimental Watershed, Idaho, USA, *Tech. Rep. 2000-3*, Northwest Watershed Res. Cent., Agric. Res. Serv., U.S. Dep. of Agric., Boise, Idaho.

Seyfried, M. S., M. D. Murdock, C. L. Hanson, G. N. Flerchinger, and S. V. Vactor (2001b), Long-term soil water content database, Reynolds Creek Experimental Watershed, Idaho, United States, *Water Resources Research*, *37*(11), 2847–2851.

Seyfried, M. S., S. Schwinning, M. A. Walvoord, W. T. Pockman, B. D. Newman, R. B. Jackson, and F. M. Phillips (2005), Ecohydrological control of deep drainage in arid and semiarid regions, *Ecology*, *86*(2), 277–287.

Sharpley, A. N., and J. R. Williams (1990), EPIC-Erosion/Productivity impact calculator: 1. Model documentation, *Technical Bulletin 1768*, US Department of Agriculture, 235 p.

Shaw, M. R., E. S. Zavaleta, N. R. Chiariello, E. E. Cleland, H. A. Mooney, and C. B. Field (2002), Grassland responses to global environmental changes suppressed by elevated CO_2, *Science*, *298*, 1987–1990, doi:10.1126/science.1075312.

Sheppard, P. R., A. C. Comrie, G. D. Packin, K. Angersbach, and M. K. Hughes (2002), The climate of the US Southwest, *Climate Research*, *21*, 219–238.

Shokri, N., P. Lehmann, and D. Or (2009), Critical evaluation of enhancement factors for vapor transport through unsaturated porous media, *Water Resources Research*, *45, number = W10433, note = doi:10.1029/2009WR007769,*.

Shuttleworth, W. J., and R. J. Gurney (1990), The theoretical relationship between foliage temperature and canopy resistance in sparse crops, *Quarterly Journal of the Royal Meteorological Society*, *116*, 497–519.

Sinclair, T. R., C. E. Murphy, and K. R. Knoerr (1976), Development and evaluation of simplified models for simulating canopy photosynthesis and transpiration, *Journal of Applied Ecology*, *13*, 813–829.

Singsaas, E. L., D. R. Ort, and E. H. Delucia (2001), Variation in measured values of photosynthetic quantum yield in ecophysiological studies, *Oecologia*, *128*, 15–23.

Sitch, S., B. Smith, I. C. Prentice, A. Arneth, A. Bondeau, W. Cramer, J. O. Kaplan, S. Levis, W. Lucht, M. T. Sykes, K. Thonicke, and S. Venevski (2003), Evaluation of ecosystem dynamics, plant geography and terrestrial carbon cycling in the LPJ dynamic global vegetation model, *Global Change Biology*, *9*, 161–185.

Sivakumar, B., and A. Sharma (2008), A cascade approach to continuous rainfall data generation at point locations, *Stochastic Environmental Research and Risk Assessment*, *22*, 451–459, doi:10.1007/s00477-007-0145-y.

Sivapalan, M. (2003), Process complexity at hillslope scale, process simplicity at the watershed scale: is there a connection?, *Hydrological Processes*, *17*, 1037–1041, doi:10.1002/hyp.5109.

Sivapalan, M., and J. M. Samuel (2009), Transcending limitations of stationarity and the return period: process-based approach to flood estimation and risk assessment, *Hydrological Processes*, *23*, 1671–1675, doi:10.1002/hyp.7292.

Sivapalan, M., K. J. Beven, and E. F. Wood (1987), On hydrologic similarity 2. A scaled model of storm runoff production, *Water Resources Research*, *23*(12), 2266–2278.

Skillman, J. B. (2008), Quantum yield variation across the three pathways of photosynthesis: not yet out of the dark, *Journal of Experimental Botany*, *59*(7), 1647–1661.

Skirvin, S., M. Kidwell, S. Biedenbender, J. P. Henley, D. King, C. H. Collins, S. Moran, and M. Weltz (2008), Vegetation data, Walnut Gulch Experimental Watershed, Arizona, United States, *Water Resources Research*, *44*(W05S08), doi:10.1029/2006WR005724.

Slaughter, C. W., D. Marks, G. N. Flerchinger, S. S. VanVactor, and M. Burgess (2001), Thirty-five years of research data collection at the Reynolds Creek Experimental Watershed, Idaho, United States, *Water Resources Research*, *37*(11), 2819–2823.

Slingo, A. (1989), A GCM parameterization for the shortwave radiative properties of water clouds, *Journal of Atmospheric Sciences*, *46*(10), 1419–1427.

Smith, J. B., S. H. Schneider, M. Oppenheimer, G. W. Yohe, W. Hare, M. D. Mastrandrea, A. Patwardhan, I. Burton, J. Corfee-Morlot, C. H. D. Magadza, H.-M. Füssel, A. B. Pittock, A. Rahman, A. Suarez, and J.-P. vanYperselen (2009a), Assessing dangerous climate change through an update of the Intergovernmental Panel on Climate Change (IPCC) "reasons for concern", *Proc. Natl Acad. Sci. USA*, *106*(11), 4133–4137, doi:10.1073/pnas.0812355106.

Smith, R., C. Tebaldi, D. Nychka, and L. Mearns (2009b), Bayesian modeling of uncertainty in ensembles of climate models, *Journal of the American Statistical Association*, *104*(485), 97–116, doi:10.1198/jasa.2009.0007.

Smith, R. E., and J.-Y. Parlange (1978), A parameter-efficient hydrologic infiltration model, *Water Resources Research*, *14*(3), 533–538.

Smith, R. E., D. C. Goodrich, D. A. Woolhiser, and C. L. Unkrich (1995), KINEROS - a kinematic runoff and erosion model, in *Computer Models of Watershed Hydrology*, edited by V. Singh, pp. 697–732, Water Resources Publications, Highlands Ranch, Colorado.

Sperry, J. S., U. G. Hacke, R. Oren, and J. P. Comstock (2002), Water deficits and hydraulic limits to water supply, *Plant, Cell and Environment*, *25*, 251–264.

Sperry, J. S., V. Stiller, and U. G. Hacke (2003), Xylem hydraulics and the soil-plant-atmosphere continuum: Opportunities and unresolved issues, *Agronomy Journal*, *95*, 1362–1370.

Spitters, C. J. T., H. A. J. M. Toussaint, and J. Goudriann (1986), Separating the diffuse and direct component of global radiation and its implications for modeling canopy photosynthesis. Part I. Components of incoming radiation, *Agricultural and Forest Meteorology*, *38*, 217–229.

Srikanthan, R., and T. A. McMahon (1982), Simulation of annual and monthly rainfalls a preliminary study at five Australian stations, *Journal of Applied Meteorology*, *21*, 1472–1479.

Srikanthan, R., and T. A. McMahon (2001), Stochastic generation of annual, monthly and daily climate data: a review, *Hydrology and Earth System Science*, *5*, 653–670.

Stephens, G. L. (1978), Radiation profiles in extended water clouds: 2. Parameterization schemes, *Journal of Atmospheric Sciences*, *35*(11), 2123–2132.

Stokes, V. J., M. D. Morecroft, and J. I. L. Morison (2006), Boundary layer conductance for contrasting leaf shapes in a deciduous broadleaved forest canopy, *Agricultural and Forest Meteorology*, *139*, 40–54, doi:10.1016/j.agrformet.2006.05.011.

Stone, J. J., M. H. Nichols, D. C. Goodrich, and J. Buono (2008), Long-term runoff database, Walnut Gulch Experimental Watershed, Arizona, United States, *Water Resources Research*, *44*(W05S05), doi:10.1029/2006WR005733.

Storck, P., D. P. Lettenmaier, and S. M. Bolton (2002), Measurement of snow interception and canopy effects on snow accumulation and melt in a mountainous maritime climate, Oregon, United States, *Water Resources Research*, *38*(11), doi:10.1029/2002WR001281.

Strack, J. E., G. E. Liston, and R. P. Sr. (2004), Modeling snow depth for improved simulation of snow-vegetation-atmosphere interactions, *Journal of Hydrometeorology*, *5*, 723–734.

Strasser, U., M. Bernhardt, M. Weber, G. E. Liston, and W. Mauser (2008), Is snow sublimation important in the alpine water balance?, *The Cryosphere*, *2*, 53–66.

Su, Z. (2002), The surface energy balance system (SEBS) for estimation of turbulent heat fluxes, *Hydrology and Earth System Sciences*, *6*(1), 85–99.

Su, Z., T. Schmugge, W. P. Kustas, and W. J. Massman (2001), An evaluation of two models for estimation of the roughness height for heat transfer between the land surface and the atmosphere, *Journal of Applied Meteorology*, *40*, 1933–1951.

Sugita, M., and W. Brutsaert (1993), Cloud effect in the estimation of instantaneous downward longwave radiation, *Water Resources Research*, *29*(3), 599–605.

Tague, C. L. (2009), Assessing climate change impacts on alpine stream-flow and vegetation water use: mining the linkages with subsurface hydrologic processes, *Hydrological Processes*, *23*, 1815–1819, doi:10.1002/hyp.7288.

Tague, C. L., and L. E. Band (2004), RHESSys: Regional Hydro-Ecologic Simulation System-An object- oriented approach to spatially distributed modeling of carbon, water, and nutrient cycling, *Earth Interactions*, *8*(19), 1–42.

Takle, E. S., and J. M. Brown (1978), Note on the use of Weibull statistics to characterize wind-speed data, *Journal of Applied Meteorology*, *17*, 556–559.

Tang, G., and P. J. Bartlein (2008), Simulating the climatic effects on vegetation: approaches, issues and challenges, *Progress in Physical Geography*, *32*(5), 543–556, doi:10.1177/0309133308100443.

Tarboton, D. G. (1997), A new method for the determination of flow directions and upslope areas in grid digital elevation models, *Water Resources Research*, *33*, 309–319.

Tarboton, D. G., and C. H. Luce (1996), Utah Energy Balance snow accumulation and melt model (UEB): Computer model technical description and user's guide, *Tech. rep.*, Utah Water Research Laboratory and USDA Forest Service Intermountain Research Station.

Tarboton, R. L. B., D. G., and I. Rodriguez-Iturbe (1991), On the extraction of channel networks from digital elevation data, *Hydrological Processes*, *5*(1), 81–100.

Tardieu, F., and W. J. Davies (1993), Integration of hydraulic and chemical signalling in the control of stomatal conductance and water status of droughted plants, *Plant, Cell and Environment*, *16*, 341–349.

Tebaldi, C., and R. Knutti (2007), The use of the multi-model ensemble in probabilistic climate projections, *Philosophical Transactions of the Royal Society A*, *365*(1857), 2053–2075, doi:10.1098/rsta.2007.2076.

Tebaldi, C., and B. Sansó (2009), Joint projections of temperature and precipitation change from multiple climate models: a hierarchical Bayesian approach, *Journal of the Royal Statistical Society A*, *172*, 83–106.

Tebaldi, C., L. Mearns, D. Nychka, and R. Smith (2004), Regional probabilities of precipitation change: a Bayesian analysis of multimodel simulations, *Geophysical Research Letter*, *31*(L24213), doi:10.1029/2004GL021276.

Tebaldi, C., R. L. Smith, D. Nychka, and L. O. Mearns (2005), Quantifying uncertainty in projections of regional climate change: A Bayesian approach to the analysis of multi-model ensembles, *Journal of Climate*, *18*, 1524–1540.

Tebaldi, C., K. Hayhoe, J. M. Arblaster, and G. A. Meehl (2006), Going to the extremes, an intercomparison of model-simulated historical and future changes in extreme events, *Climatic Change*, *79*, 185–211, dOI: 10.1007/s10584-006-9051-4.

Teuling, A. J., R. Uijlenhoet, F. Hupet, and P. A. Troch (2006), Impact of plant water uptake strategy on soil moisture and evapotranspiration dynamics during drydown, *Geophysical Research Letters*, *33*(L03401), doi:10.1029/2005GL025019.

Thomas, H., and J. L. Stoddart (1980), Leaf senescence, *Annual Review of Plant Physiology*, *31*, 83–111, doi:10.1146/annurev.pp.31.060180.000503.

Thornley, J. H. M. (1970), Respiration, growth and maintenance in plants, *Nature*, *227*, 304–305.

Thornley, J. H. M. (1991), A transport-resistance model of forest growth and partitioning, *Annals of Botany*, *68*, 211–226.

Thornton, P. E., J.-F. Lamarque, N. A. Rosenbloom, and N. M. Mahowald (2007), Influence of carbon-nitrogen cycle coupling on land model response to CO_2 fertilization and climate variability, *Global Biogeochemical Cycles*, *21*(GB4018), doi:10.1029/2006GB002868.

Tian, Y., R. E. Dickinson, and L. Zhou (2007), Four-stream isosector approximation for canopy radiative transfer, *Journal of Geophysical Research*, *112*(D04107), doi:10.1029/2006JD007545.

Tilman, D. (1994), Competition and biodiversity in spatially structured habitats, *Ecology*, *75*(1), 2–16.

Tirone, G. (2003), Stima del bilanco del carbonio di due ecosistemi forestali Mediterranei. Confronto tra una lecceta e una pineta, Ph.D. thesis, Department of Forest Science and Resources, University of Tuscia, Viterbo, Italy.

Tjoelker, M. G., J. Oleksyn, and P. B. Reich (2001), Modeling respiration of vegetation: evidence for a general temperature-dependent Q_{10}, *Global Change Biology*, *7*, 223–230.

Todini, E. (2007), Hydrological catchement modelling: past, present and future, *Hydrology and Earth System Sciences*, *11*(1), 468–482.

Todorovic, P., and D. A. Woolhiser (1975), A stochastic model of n-day precipitation, *Journal of Applied Meteorology*, *14*, 17–24.

Todorovic, P., and V. Yevjevich (1969), Stochastic process of precipitation, *Tech. rep.*, Colo. State Univ. Fort Collins, Fort Collins, Colorado.

Torri, D., M. Sfalanga, and M. DelSette (1987), Splash detachment: runoff depth and soil cohesion, *Catena*, *14*, 149–155.

Treut, H. L., R. Somerville, U. Cubasch, Y. Ding, C. Mauritzen, A. Mokssit, T. Peterson, and M. Prather (2007), *Historical Overview of Climate Change. In: Climate Change 2007: The Physical Science Basis. Contribution of Working Group I to the Fourth Assessment Report of the Intergovernmental Panel on Climate Change*, chap. I, Cambridge University Press Cambridge, United Kingdom and New York, NY, USA.

Troch, P. A., G. A. Carrillo, I. Heidbüchel, S. Rajagopal, M. Switanek, T. H. M. Volkmann, and M. Yaeger (2008), Dealing with landscape heterogeneity in watershed hydrology: A review of recent progress toward new hydrological theory, *Geography Compass*, *2*, doi:10.1111/j.1749-8198.2008.00186.x.

Troch, P. A., G. F. Martinez, V. R. N. Pauwels, M. Durcik, M. Sivapalan, C. Harman, P. D. Brooks, H. Gupta, and T. Huxman (2009), Climate and vegetation water use efficiency at catchment scales, *Hydrological Processes*, *23*, 2409–2414, doi:10.1002/hyp.7358.

Tromp-van Meerveld, I., and M. Weiler (2008), Hillslope dynamics modeled with increasing complexity, *Journal of Hydrology*, *361*, 24–40, doi:10.1016/j.jhydrol.2008.07.019.

Tucker, G. E., S. T. Lancaster, N. M. Gasparini, R. L. Bras, and S. M. Rybarczyk (2001), An object-oriented framework for distributed hydrologic and geomorphologic modeling using triangulated irregular networks, *Computers & Geosciences*, *27*(8), 959–973.

Tuzet, A., A. Perrier, and R. Leuning (2003), A coupled model of stomatal conductance, photosynthesis and transpiration, *Plant, Cell and Environment*, *26*, 1097–1116.

TVA (1972), Heat and mass transfer between a water surface and the atmosphere., *Tech. Rep. 14*, Tennessee Valley Authority Water Resources Research Engineering Laboratory, Norris, TN.

USACE (1956), Snow hydrology, summary report of the snow investigations, *Tech. rep.*, U.S. Army Corps of Engineers, North Pacific Division, Portland, Oregon.

Valentin, C., J. M. d'Herbès, and J. Poesen (1999), Soil and water components of banded vegetation patterns, *Catena*, *37*, 1–24.

van den Hurk, B. J. J. M., and A. A. M. Holtslag (1997), On the bulk parameterization of surface fluxes for various conditions and parameter ranges, *Boundary-Layer Meteorology*, *82*, 119–134.

vanDam, J. C., and R. A. Feddes (2000), Numerical simulation of infiltration, evaporation and shallow groundwater levels with the Richards equation, *Journal of Hydrology*, *233*, 72–85.

vanDijk, A. (2004), Ecohydrology: it's all in the game?, *Hydrological Processes*, *18*, 3683–3686, doi:10.1002/hyp.5762.

vanGenuchten, M. T. (1980), A closed-form equation for predicting the hydraulic conductivity of unsaturated soils, *Soil Science Society of America Journal*, *44*, 892–898.

vanMantgem, P. J., N. L. Stephenson, J. C. Byrne, L. D. Daniels, J. F. Franklin, P. Z. Ful, M. E. Harmon, A. J. Larson, J. M. Smith, A. H. Taylor, and T. T. Veblen (2009), Widespread increase of tree mortality rates in the Western United States, *Science*, *323*, 521–524.

vanRheenen, N. T., A. W. Wood, R. N. Palmer, and D. P. Lettenmaier (2004), Potential implications of PCM climate change scenarios for Sacramento - San Joaquin river basin hydrology and water resources, *Climatic Change*, *62*, 257–281.

Varado, N., I. Braud, and P. J. Ross (2006), Development and assessment of an efficient numerical solution of the richards' equation including root extraction by plants, *Journal of Hydrology*, *323*, 258–275.

Varis, O., T. Kajander, and R. Lemmela (2004), Climate and water: from climate models to water resources management and vice versa, *Climatic Change*, *66*, 321–344.

Veatch, W., P. D. Brooks, J. R. Gustafson, and N. P. Molotch (2009), Quantifying the effects of forest canopy cover on net snow accumulation at a continental, mid-latitude site, *Ecohydrology*, *2*(2), 115–128, doi:10.1002/eco.45.

Veneziano, D., and P. Furcolo (2002), Multifractality of rainfall and intensity-duration-frequency curves, *Water Resources Research*, *38*(12), doi:10.1029/2001WR000,372.

Veneziano, D., and V. Iacobellis (2002), Multiscaling pulse representation of temporal rainfall, *Water Resources Research*, *38*(8), doi: 10.1029/2001WR000,522.

Veneziano, D., P. Furcolo, and V. Iacobellis (2002), Multifractality of iterated pulse processes with pulse amplitudes generated by a random cascade, *Fractals*, *10*(2), 209–222.

Veneziano, D., A. Langousis, and P. Furcolo (2006), Multifractality and rainfall extremes: A review, *Water Resources Research*, *42*, W06D15, doi:10.1029/2005WR004,716.

Verbeeck, H., K. Steppe, N. Nadezhdina, M. O. DeBeeck, , G. Deckmyn, L. Meiresonne, R. Lemeur, J. Èermák, R. Ceulemans, and I. A. Janssens (2007), Stored water use and transpiration in scots pine: a modeling analysis with ANAFORE, *Tree Physiology*, *27*, 1671–1685.

Verseghy, D. L. (1991), CLASS-A Canadian land surface scheme for GCMs. I. Soil model, *International Journal of Climatology*, *11*, 111–133.

Vertessy, R. A., and H. Elsenbeer (1999), Distributed modeling of storm flow generation in an amazonian rain forest catchment: Effects of model parameterization, *Water Resources Research*, *35*(7), 2173–2187.

Vesala, T. (1998), On the concept of leaf boundary layer resistance for forced convection, *Journal of Theoretical Biology*, *194*, 91–100.

Vico, G., and A. Porporato (2008), Modelling C3 and C4 photosynthesis under water-stressed conditions, *Plant Soil*, *313*, 187–203, doi:10.1007/s11104-008-9691-4.

Viterbo, P., and A. C. M. Beljaars (1995), An improved land surface parameterization scheme in the ECMWF model and its validation, *Journal of Climate*, *8*, 2716–2748.

Vivoni, E. R., V. Y. Ivanov, R. L. Bras, and D. Entekhabi (2004), Generation of triangulated irregular networks based on hydrological similarity, *Journal of Hydrologic Engineering*, *9*(4), 288–302.

Vivoni, E. R., V. Y. Ivanov, R. L. Bras, and D. Entekhabi (2005), On the effects of triangulated terrain resolution on distributed hydrologic model response, *Hydrological Processes*, *19*(11), 2101–2122.

Vivoni, E. R., D. Entekhabi, R. L. Bras, and V. Y. Ivanov (2007), Controls on runoff generation and scale-dependence in a distributed hydrologic model, *Hydrology and Earth System Sciences*, *11*, 1683–1701.

Vivoni, E. R., C. A. Aragón, L. Malczynski, and V. C. Tidwell (2009), Semiarid watershed response in central New Mexico and its sensitivity to climate variability and change, *Hydrology and Earth System Science*, *13*, 715–733.

von Storch, H., E. Zorita, and U. Cubasch (1993), Downscaling of global climate change estimates to regional scales: an application to Iberian rainfall in wintertime, *Journal of Climate*, *6*, 1161-1171.

vonCaemmerer, S., and G. D. Farquhar (1981), Some relationships between the biochemistry of photosynthesis and the gas exchange of leaves, *Planta*, *153*, 376–387.

Wagener, T. (2007), Can we model the hydrological impacts of environmental change?, *Hydrological Processes*, *21*, 3233–3236, doi:10.1002/hyp.6873.

Wallis, T. W. R., and J. F. Griffiths (1997), Simulated meteorological input for agricultural models, *Agricultural and Forest Meteorology*, *88*, 241–258.

Walter, M. T., E. S. Brooksb, D. K. McCoolc, L. G. Kingd, M. Molnaub, and J. Bollb (2005), Process-based snowmelt modeling: does it require more input data than temperature-index modeling?, *Journal of Hydrology*, *300*, 65–75.

Walther, G.-R., E. Post, P. Convey, A. Menzel, C. Parmesank, T. J. C. Beebee, J.-M. Fromentin, O. Hoegh-Guldberg, and F. Bairlein (2002), Ecological responses to recent climate change, *Nature*, *416*, 389–395.

Wang, J., and R. L. Bras (1999), Ground heat flux estimated from surface soil temperature, *Journal of Hydrology*, *216*, 214–226.

Wang, W.-M., Z.-L. Li, and H.-B. Su (2007a), Comparison of leaf angle distribution functions: Effects on extinction coefficient and fraction of sunlit foliage, *Agricultural and Forest Meteorology*, *143*, 106–122.

Wang, Y. P. (2003), A comparison of three different canopy radiation models commonly used in plant modeling, *Functional Plant Biology*, *30*, 143–152.

Wang, Y.-P., and R. Leuning (1998), A two-leaf model for canopy conductance, photosynthesis and portioning of available energy I: Model description and comparison with a multi-layered model, *Agricultural and Forest Meteorology*, *91*, 89–111.

Wang, Y.-P., B. Z. Houlton, and C. B. Field (2007b), A model of biogeochemical cycles of carbon, nitrogen, and phosphorus including symbiotic nitrogen fixation and phosphatase production, *Global Biogeochemical Cycles*, *21*(GB1018), doi:10.1029/2006GB002797.

Warren, C. R. (2006), Why does photosynthesis decrease with needle age in pinus pinaster?, *Trees*, *20*, 157–164, doi: 10.1007/s00468-005-0021-7.

Waymire, E. C., and V. K. Gupta (1981a), The mathematical structure of rainfall representation, 1. A review of the stochastic rainfall models, *Water Resources Research*, *17*(5), 1261–1272.

Waymire, E. C., and V. K. Gupta (1981b), The mathematical structure of rainfall representation, 2. A review of the point process theory, *Water Resources Research*, *17*(5), 1273–1285.

Waymire, E. C., and V. K. Gupta (1981c), The mathematical structure of rainfall representation, 3. Some applications of the point process theory to rainfall processes, *Water Resources Research*, *17*(5), 1287–1294.

Weiler, M., and J. J. McDonnell (2004), Virtual experiments: a new approach for improving process conceptualization in hillslope hydrology, *Journal of Hydrology*, *285*, 3–18, doi:10.1016/S0022-1694(03)00271-3.

Weiler, M., and J. J. McDonnell (2007), Conceptualizing lateral preferential flow and flow networks and simulating the effects on gauged and ungauged hillslopes, *Water Resources Research*, *43*(W03403), doi:10.1029/2006WR004867.

Weltz, M. A., J. C. Ritchie, and H. D. Fox (1994), Comparison of laser and field measurements of vegetation height and canopy cover, *Water Resources Research*, *30*(5), 1311–1319.

West, G. B., B. J. Enquist, and J. H. Brown (2009), A general quantitative theory of forest structure and dynamics, *Proc. Natl Acad. Sci. USA*, *106*(17), 7040–7045, doi:10.1073/pnas.0812294106.

Wetzel, P. J., and J. T. Chang (1987), Concerning the relationship between evaporation and soil moisture, *Journal of Climate and Applied Meteorology*, *26*, 18–27.

Wheater, H., R. Chandler, C. Onof, V. Isham, E. Bellone, C. Yang, D. Lekkas, G. Lourmas, and M.-L. Segond (2005), Spatial-temporal rainfall modelling for flood risk estimation, *Stochastic Environmental Research and Risk Assessment*, *19*, 403–416.

White, M. A., P. E. Thornton, S. W. Running, and R. R. Nemani (2000), Parameterization and sensitivity analysis of the BIOME-BGC terrestrial ecosystem model: Net primary production controls, *Earth Interactions*, *4*(3), 1–85.

Wicks, J. M., and J. C. Bathurst (1996), SHESED: a physically based, distributed erosion and sediment yield component for the SHE hydrological modeling system, *Journal of Hydrology*, *175*, 213–238.

Wieringa, J. (1993), Representative roughness parameters for homogeneous terrain, *Boundary-Layer Meteorology*, *63*, 323–363.

Wigmosta, M. S., and D. P. Lettenmaier (1999), A comparison of simplified methods for routing topographically driven subsurface flow, *Water Resources Research*, *35*(1), 255–264.

Wigmosta, M. S., L. W. Vail, and D. P. Lettenmaier (1994), A distributed hydrology-vegetation model for complex terrain, *Water Resources Research*, *30*(6), 1665–1679.

Wilby, R. L., C. W. Dawson, and E. M. Barrow (2002), SDSM - a decision support tool for the assessment of regional climate change impacts, *Environmental & Modelling Software*, *17*(2), 145–157.

Wilks, D. (1989), Conditioning stochastic daily precipitation models on total monthly precipitation, *Water Resources Research*, *23*, 1429–1430.

Wilks, D. S. (1992), Adapting stochastic weather generation algorithms for climate changes studies, *Climatic Change*, *22*, 67–84.

Wilks, D. S. (1999), Interannual variability and extreme-value characteristics of several stochastic daily precipitation models, *Agricultural and Forest Meteorology*, *93*, 153–169.

Wilks, D. S., and R. L. Wilby (1999), The weather generation game: a review of stochastic weather models, *Progress in Physical Geography*, *23*, 329–357.

Williams, J. R. (1995), The EPIC model, in *Computer models of watershed hydrology*, edited by V. Singh, chap. 25, pp. 909–1100, Water Resources Publications, Highlands Ranch, Colorado.

Williams, K. S., and D. G. Tarboton (1999), The ABC's of snowmelt: a topographically factorized energy component snowmelt model, *Hydrological Processes*, *13*, 1905–1920.

Wilson, E. B., and M. M. Hilferty (1931), Distribution of Chi-square, *Proc. Natl. Acad. Sci. U.S.A.*, *17*, 684–688.

Wilson, K. B., and D. D. Baldocchi (2000), Seasonal and interannual variability of energy fluxes over a broadleaved temperate deciduous forest in North America, *Agricultural and Forest Meteorology*, *100*, 1–18.

Wilson, K. B., D. D. Baldocchi, and P. J. Hanson (2001), Leaf age affects the seasonal pattern of photosynthetic capacity and net ecosystem exchange of carbon in a deciduous forest, *Plant, Cell and Environment*, *24*, 571–583.

Winstral, A., and D. Marks (2002), Simulating wind fields and snow redistribution using terrain-based parameters to model snow accumulation and melt over a semi-arid mountain catchment, *Hydrological Processes*, *16*, 3585–3603, doi:10.1002/hyp.1238.

Wischmeier, W. H., and D. D. Smith (1978), Predicting rainfall-erosion losses: A guide to conservation planning, *Handbook 537*, US Department of Agriculture, Agriculture, US Government Printing Office, Washington DC.

Wiscombe, W. J., and S. G. Warren (1980), A model for the spectral albedo of snow. I. Pure snow, *Journal of Atmospheric Science*, *37*, 2712–2733.

Wood, A. W., L. R. Leung, V. Sridhar, and D. P. Lettenmaier (2004), Hydrologic implications of dynamical and statistical approaches to downscaling climate model outputs, *Climatic Change*, *62*, 189–216.

Woodward, F. I., T. M. Smith, and W. R. Emanuel (1995), A global land primary productivity and phytogeography model, *Global Biogeochemical Cycles*, *9*(4), 471–490.

Wramnebya, A., B. Smith, S. Zaehle, and M. T. Sykes (2008), Parameter uncertainties in the modelling of vegetation dynamics-effects on tree community structure and ecosystem functioning in european forest biomes, *Ecological Modelling*, *216*, 277–290.

Wright, I. J., P. B. Reich, M. Westoby, D. D. Ackerly, Z. Baruch, F. Bongers, J. Cavender-Bares, T. Chapin, J. H. C. Cornelissen, M. Diemer, J. Flexas, E. Garnier, P. K. Groom, J. Gulias, K. Hikosaka, B. B. Lamont, T. Lee, W. Lee, C. Lusk, J. J. Midgley, M. Navas, U. Niinemets, J. Oleksyn, N. Osada, H. Poorter, P. Poot, L. Prior, V. I. Pyankov, C. Roumet, S. C. Thomas, M. G. Tjoelker, E. J. Veneklaas, and R. Villar (2004), The worldwide leaf economics spectrum, *Nature*, *428*, 821–827.

Wu, A., T. A. Black, D. L. Verseghy, M. D. Novak, and W. G. Bailey (2000), Testing the α and β methods of estimating evaporation from bare and vegetated surfaces in CLASS, *Atmosphere-Ocean*, *38*, 15–35.

Wullschleger, S. D., and P. J. Hanson (2006), Sensitivity of canopy transpiration to altered precipitation in an upland oak forest: evidence from a long-term field manipulation study, *Global Change Biology*, *12*, 97–109, doi: 10.1111/j.1365-2486.2005.01082.x.

Wullschleger, S. D., T. J. Tschaplinski, and R. J. Norby (2002), Plant water relations at elevated CO_2- implications for water-limited environments, *Plant, Cell and Environment*, *25*, 319–331.

Wythers, K. R., P. B. Reich, M. G. Tjoelker, and P. B. Bolstad (2005), Foliar respiration acclimation to temperature and temperature variable Q_{10} alter ecosystem carbon balance, *Global Change Biology*, *11*, 435–449, doi: 10.1111/j.1365-2486.2005.00922.x.

Xu, C.-Y., E. Widn, and S. Halldin (2005), Modelling hydrological consequences of climate change-progress and challenges, *Advances in Atmospheric Sciences*, *22*(5), 789–797.

Yang, Y., J. Fang, W. Ma, and W. Wan (2008), Relationship between variability in aboveground net primary production and precipitation in global grasslands, *Geophysical Research Letters*, *35*(L23710), doi:10.1029/2008GL035408.

Yu, M., Q. Gao, H. E. Epstein, and X. S. Zhang (2008), An ecohydrological analysis for optimal use of redistributed water among vegetation patches, *Ecological Applications*, *18*(7), 1679–1688.

Zanotti, F., S. Endrizzi, G. Bertoldi, and R. Rigon (2004), The GEOTOP snow module, *Hydrological Processes*, *18*, 3667–3679, doi: 10.1002/hyp.5794.

Zeng, X., and R. E. Dickinson (1998), Effect of surface sublayer on surface skin temperature and fluxes, *Journal of Climate*, *11*, 537–550.

Zeng, X., and A. Wang (2007), Consistent parameterization of roughness length and displacement height for sparse and dense canopies in land models, *Journal of Hydrometeorology*, *8*, 730–737, doi: 10.1175/JHM607.1.

Zeng, X., R. Dickinson, M. Barlage, Y. Dai, G. Wang, and K. Oleson (2005), Treatment of undercanopy turbulence in land models, *Journal of Climate*, *18*, 5086–5094.

Zhao, W., and R. J. Qualls (2005), A multiple-layer canopy scattering model to simulate shortwave radiation distribution within a homogeneous plant canopy, *Water Resources Research*, *41*(W08409), doi:10.1029/2005WR004016.

Zhao, W., R. J. Qualls, and P. R. Berliner (2008), A two-concentric-loop iterative method in estimation of displacement height and roughness length for momentum and sensible heat, *International Journal of Biometeorology*, *52*, 849–858, doi:10.1007/s00484-008-0181-4.

Zhou, L. M., C. J. Tucker, R. K. Kaufmann, D. Slayback, N. V. Shabanov, and R. B. Myneni (2001), Variations in northern vegetation activity inferred from satellite data of vegetation index during 1981 to 1999, *Journal of Geophysical Research*, *106*, 20,069–20,083.

Zhu, J. (2008), Equivalent parallel and perpendicular unsaturated hydraulic conductivities: Arithmetic mean or harmonic mean?, *Soil Science Society of America Journal*, *72*, 1226–1233, doi:10.2136/sssaj2007.0337.

Zweifel, R., K. Steppe, and F. J. Sterck (2007), Stomatal regulation by microclimate and tree water relations: interpreting ecophysiological field data with a hydraulic plant model, *Journal of Experimental Botany*, *58*(8), 2113–2131, doi:10.1093/jxb/erm050.

LIST OF JOURNALS THAT IMPACTED THE THESIS

JOURNAL	Number of citations
Water Resources Research	91
Hydrological Processes	42
TECHNICAL REPORT	31
Journal of Hydrology	28
Agricultural and Forest Meteorology	27
Journal of Geophysical Research	23
Journal of Climate	20
BOOK	19
Plant, Cell & Environment	18
Journal of Applied Meteorology	17
Global Change Biology	16
Hydrology and Earth System Science	16
Climatic Change	15
Boundary Layer Meteorology	13
Science	13
Advances in Water Resources Research	12
Journal of Hydrometeorology	11
Proceeding National Academic of Science	11
Global Biogeochemical Cycle	10
Ecological Modelling	9
IN BOOK	9
International Journal of Climatology	9
Nature	9
Journal of Atmospheric Science	8
Proceedings of Royal Society, London, A	8
Solar Energy	8
Catena	7
Climate Dynmics	7
Geophysical Research Letters	7
New Phytologist	7
Climate Research	6
CONFERENCE	6
Oecologia	6
Tree Physiology	6
Bulltin of American Meteorological Society	5
Environmental Modeling & Software	5
Quarterly Journal of the Royal Meteorological Society	5
Soil Science American Journal	5
OTHERS	163